The Hashemite Kingdom of Jordan
Scientific Research Support Fund
The Hashemite University

JJEES

Jordan Journal of Earth and Environmental Sciences

Indexed by Scopus
ELSEVIER

Volume (17) Number (2)

Cover photo © Prof Mahmoud Abu-Allaban

JJEES is an International Peer-Reviewed Research Journal

ISSN 1995-6681 jjees.hu.edu.jo June 2026

Jordan Journal of Earth and Environmental Sciences (JJEES)

JJEES is an International Peer-Reviewed Research Journal, Issued by Deanship of Scientific Research, The Hashemite University, in corporation with, the Jordanian Scientific Research Support Fund, the Ministry of Higher Education and Scientific Research.

Editorial Board:

Associate Editorial Board: (Arranged Alphabetically)

International Advisory Board: (Arranged Alphabetically)

Editorial Board Support Team:

Submission address:

Manuscripts should be submitted electronically to the following e-mail:

jjees@hu.edu.jo

For more information and previous issues:

www.jjees.hu.edu.jo

Hashemite Kingdom of Jordan

Scientific Research Support Fund

Hashemite University

Jordan Journal of Earth and Environmental Sciences

JJEES

An International Peer-Reviewed Scientific Journal

Financed by the Scientific Research Support Fund

Volume 17 Number (2)

http:// jjees.hu.edu.jo/

ISSN 1995-6681

Cross-section of an ammonite fossil in Late Cretaceous limestone used as building stone in Jordan.
Photograph by Mahmoud Abu-Allaban (1 May 2026)

JJEES
Jordan Journal of Earth and Environmental Sciences

JJEES

JJEES (2026) 17 (2): 130-138
ISSN 1995-6681

Jordan Journal of Earth and Environmental Sciences

Application of the Erosion Potential Method to the Wadi Mubarak Basin in Aqaba Governorate, Jordan

Ahmed A. Thneibat

Department Of Geography, College of Social Sciences, Mutah University, Al-Karak, Jordan

Received on 20 March 2024; Accepted on 23 August 2025

Abstract

This study evaluates soil erosion and sediment yield in Wadi Mubarak Basin, located along the Aqaba Back Road in southern Jordan. The basin significantly impacts floodwater volumes and sedimentation levels. During intense, short-duration rainstorms, erosion leads to fatalities and infrastructure damage through box culvert and bridge blockages, leading to road deterioration and traffic disruption. The study employed the Erosion Potential Method (EPM), also known as the Gavrilovic Method. Key EPM parameters include the soil erosion coefficient, annual precipitation, and temperature coefficient. The soil erosion coefficient is based on the average slope coefficient, the erosion type and extent coefficient, soil protection coefficient, and the soil erodibility coefficient. Erosion intensity within the basin ranges from moderate to severe. Annual soil erosion is excessive in large Wadi beds within main channels (>42,000 m^3/km^2/year), accounting for about 0.5% of the total catchment surface area. The findings help to understand the spatial distribution of erosion across the basin and serve as a foundation for further research and environmental management programs.

Keywords: *Gavrilović, Erosion Potential Method; Soil Erosion; Wadi Mubarak; Sedimentation; Soil Protection Index.*

1. Introduction

Natural geomorphic processes, such as soil erosion, lead to the loss of topsoildue to the effects of runoff and precipitation. This separation and loss of soil particles occur through rainsplash or indirectly through sheet, rill, or gully erosion. Gully erosion has serious issues as its formations are deep, elongated, and narrow (Ali et al., 2016). Volumes of eroded material can be very destructive when large, as they may travel long distances. In most cases, erosion rates are higher on steep, long slopes (Tavares et al., 2021). In Jordan, soil erosion is caused by different natural and human factors. There are environmental effects of social, economic, and ecological implications (Al-Sababhah & Al maqablah, 2023).

The Wadi Mubarak basin is a hightly sensitive watershed that determines sediment volumes and flood discharge. Moreover, Wadi Mubarak has a transport zone that redirects heavy traffic and cargo to the east of Aqaba city. Thus, it improves the city's environment and protects coastal resort areas.

Nevertheless, the Wadi Mubarak basin presents significant challenges to infrastructure and human security due to intense, short-duration precipitation. These storms tend to exceed the drainage capability. This leads to obstruction of box culverts and bridges, thereby damaging roads and shoulders and leading to a major inconvenience in traffic movement and accessibility. This has been evidenced by the historical occurrence of floods.

On 21 March 1991, there was a major flood which had an estimated 6-7 year period of return following the completion of the road construction but before the official opening of the road, resulting in widespread destruction of the new infrastructure. In December 1993, another flood caused further damage (Farha, 1999). The recurrent floods are a testament to the need for robust infrastructure solutions to reduce the current number of threats posed by the Wadi Mubarak basin.

The presence of sparse vegetation cover is also a factor contributing to extensive soil erosion and sediment transport downstream (Thneibat, 2010)and the efficiency of engineering structures regarding these hazards. This work has been achieved through the analysis of remote sensing data, field work, laboratory work and field measurement, by utilizing standard techniques such as, (GPS. Critical factors in the infrastructure planning should be surface erosion and sediment yield (Dragičević et al., 2017)various methods for erosion intensity and sediment production assessment have been developed. The necessity for better model performance has led to the more frequent application of the method sensitivity and uncertainty assessments in order to decrease errors that arise from the model concept and its main assumptions. The analysis presented in this paper refers to the application of the Gavrilović method (Erosion Potential Method. The selection of models and parameter specifications of soil erosion requires accurate estimation. Over the last several decades, scholars have developed different empirical and physically based techniques of measuring erosion intensity and sediment production (Marouane et al., 2021). They depend on the input data required to perform their application (Deilami et al., 2012).

The most widely used empirical model for estimating soil erosion is the Universal Soil Loss Equation (USLE)

* Corresponding author e-mail: ahmedth@mutah.edu.jo

(Wischmeier and Smith, 1978). Since its creation, other models have been developed, such as RUSLE (Renard et al., 1991)has been the workhorse of erosion prediction and conservation planning technology in the U.S. and even worldwide. In 1985, at a meeting of U.S. Department of Agriculture (USDA, MUSLE (Williams, 1975), PSIAC (Pacific Southwest Inter-Agency Committee, 1968), WEPP (Water Erosion Prediction Project), SWAT (Soil and Water Assessment Tool), and EPM (Gavrilovic, 1988; da Silva et al., 2014). These models were developed and are still used today. The hilly topography, sparse vegetation cover, and prolonged droughts and erosive precipitation events increase land degradation in the study area (Ali et al., 2016).

At the research site, a few sediment gauging stations limit the ability to predict and evaluate watershed erodibility, thereby complicating the prioritisation of soil conservation in erosion and sediment yield assessment. Alternative models that are quantitative include the EPM. EPM, which has been used extensively in the Balkan countries, is effective in estimating the erosion rates, especially in the arid and semi-arid areas (Tavares et al., 2021). Although it is used in various settings, it was designed for dry and semi-arid areas of the southwestern United States and Iran (Yousefi et al., 2014).

The EPM was developed to calculate erosion coefficients, the measure of the erosion rates, and the mean annual sediment yield. Slovenia and Croatia have used the Gavrilović method to forecast soil erosion and the number of sediments at the basin level (Amini et al., 2010). The EPM is a suitable method of estimating erosion and sedimentation. The leading EPM parameters are the coefficient of soil erosion (z), the amount of precipitation per year (H) and the temperature coefficient (T). The soil erosion coefficient involves the mean slope coefficient (Ja), the soil protection coefficient (Xa), the erosion type and extent, and the soil erodibility coefficient (Loucks et al., 2005; Elbadaoui et al., 2023; Efthimiou et al., 2016; Jamal, 2020).

Gavrilović's method is straightforward and adaptable enough that the researcher can obtain significant results without relying on extensive historical data or complex modeling. It also provides a foundation for understanding erosion patterns and developing management strategies. In this context, the method uses annual parameters such as yearly precipitation and temperature data from King Hussein Airport in Aqaba, slope gradient and length measured from topographic maps, soil properties from geological maps, and land use data from the Aqaba Special Economic Zone maps. Notably, additional coefficients were calculated using empirical methods and tables developed by Gavrilović.

Soil erosion and sedimentation are not primary inputs to the planning process considered by regional development planners, and the focus is usually on flood hazard assessment. Planners rarely consider the dynamic nature of Earth's surface processes, including geomorphological processes, such as soil erosion, flooding, and increased sedimentation in hydraulic infrastructure (Farhan, 1999).

The goal was to reduce the errors in assessing soil erosion and sedimentation and to develop effective control strategies (Uddin et al., 2016). These advancements in GIS and remote sensing facilitate more precise calculation of EPM factors (soil erodibility, soil protection, slope, temperature, and precipitation) through spatial analysis techniques.

2. Materials and Methods

2.1. Study Area

The study area, located in Aqaba Governorate (Figure 1), lies between latitudes 29°24'46.77"N and 29°30'48.40"N and longitudes 34°58'35"E and 35°7'0"E. The basin covers 65 km2 with elevations ranging from 0 to 1250 m above sea level.

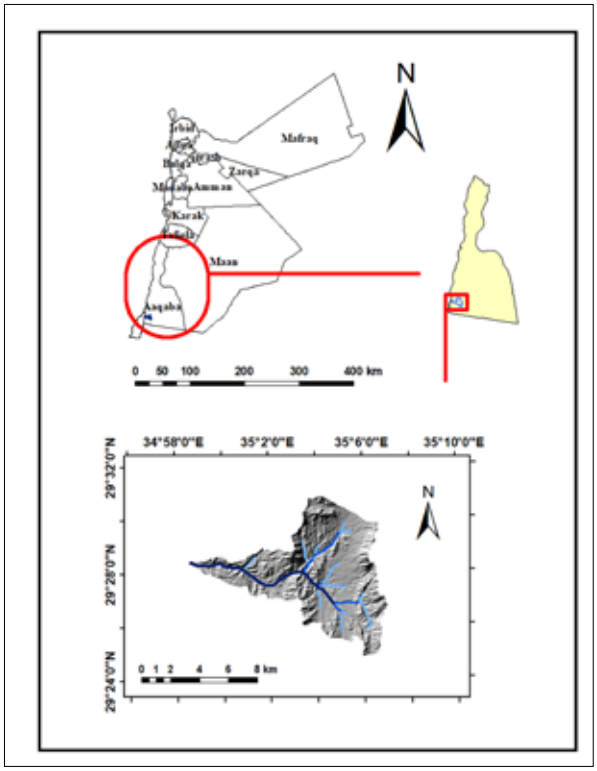

Figure 1. Location map of the study area in Aqaba, Jordan

2.2. Climatic data

Climate change in Jordan has led to shorter precipitation seasons with reduced precipitation frequency. Although most meteorological stations record decreasing precipitation trends, some locations experience extreme precipitation events (Salahat and Al-qinna, 2015; Oroud, 2011). Minor climate variations may lead to substantially different geomorphological responses (Saqqa & Atallah, 2013).

The study area has a hyper-arid climate with low mean annual precipitation and moderately high temperatures. According to the King Hussein International Airport station (1980-2018), the annual average temperature at the location is 24.8°C, and the annual precipitation is 23.4 mm.

2.3. The EPM

The Gavrilović Method, also known as the EPM method, is commonly used in watershed and land degradation studies in mountainous, dry, and semi-arid regions. It is calculated using Equation (1). The method is straightforward and requires minimal data, making it suitable for countries with limited data availability and offering an advantage over more

complex approaches (Efthimiou et al., 2016). This technique was chosen for the study because it is simple and convenient. It was used to evaluate soil erosion and sediment yield, as well as to examine its spatial distribution in the Wadi Mubarak Basin along the Aqaba Back Road in southern Jordan. To the best of the researcher's knowledge, this method has not yet been applied in Jordan. The work followed the steps outlined in the flowchart (Figure 2), based on the method developed by Gavrilović.

$$W = T * H * \pi * \sqrt{Z^3} \quad (1)$$

W = Average annual soil erosion (m3/km2/ year)

T = Temperature coefficient

The temperature coefficient (T) is calculated by Eq.2.

$$T = \sqrt{(\frac{t^0}{10} + 0.1)} \quad (2)$$

Where t^0 =the mean annual temperature (°C)

H = Average annual precipitation(mm)

Z = soil erosion coefficient (dimensionless) can be calculated from Eq.3.

$$Z = Y * Xa * (\varphi + \sqrt{Ja}) \quad (3)$$

Where:

Y = Soil erodibility coefficient (dimensionless).

Xa = Soil protection coefficient (dimensionless).

φ = coefficient of type and extent of erosion (dimensionless).

Ja = Average Slope coefficient (%)

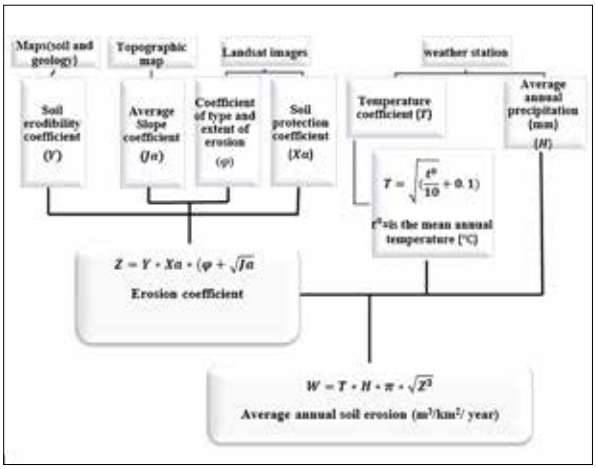

Figure 2. Flowchart which explaine the various processes involved in the computation of sediment production.

2.3.1 Temperature and precipitation parameters

Gavrilović incorporated temperature in the EPM because thermal variations contribute to material weathering and rock formation breakdown (Marouane et al., 2021)In Morocco, thewatersheds have very significant soil wastes, related to various physicaland anthropicfactors. The Oued Inaouene watershed is concerned because of its location in the eastern part of the Saïss basin, between the Middle Atlas and the Pre-Rif, where water erosion is more accentuated. This basin covers a total area of 3597.13 Km2 and it is marked by a semi-arid climate with relatively abundant (989.68 mm. Precipitation significantly influences water erosion, with intensity, duration, and frequency all playing a role. High-intensity precipitation events, though shorter, are more erosive than low-intensity ones due to increased flow energy (Elbadaoui et al., 2023).

2.3.2 Soil Protection Coefficient (Xa)

The soil protection coefficient, representing an area's erosion protection effectiveness, is determined by the land use and vegetation cover coefficients. These coefficients, reflecting land type and erosion control measures (especially in agriculture), are considered a single factor in assessing soil protection (Elbadaoui et al., 2023). : The soil protection coefficient in the study area was derived from the land-use map (Figure 3).

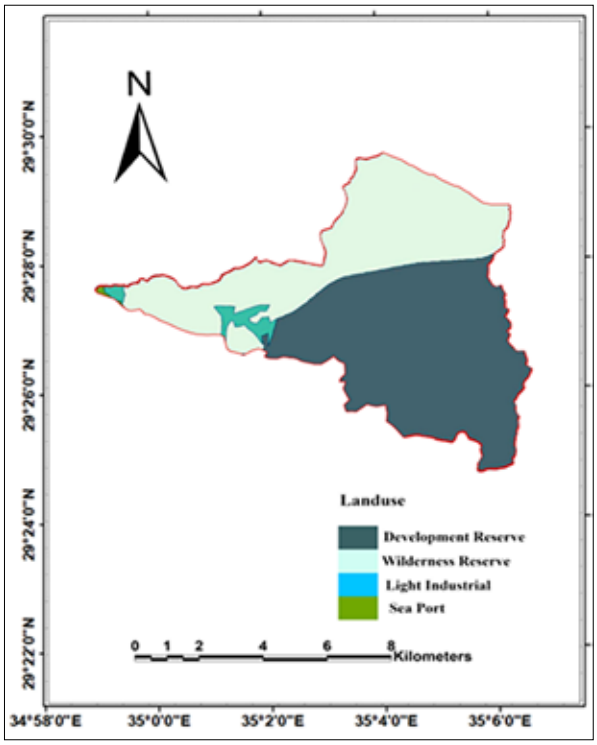

Figure 3. Landuse map of the study area as reported by Aqaba Special Economic Zone Authority.

2.3.3 Soil erodibility coefficient (Y)

Soil erodibility coefficient (Y) reflects a soil's susceptibility to erosion based on watershed geology (Marouane et al., 2021)In Morocco, thewatersheds have very significant soil wastes, related to various physicaland anthropicfactors. The Oued Inaouene watershed is concerned because of its location in the eastern part of the Saïss basin, between the Middle Atlas and the Pre-Rif, where water erosion is more accentuated. This basin covers a total area of 3597.13 Km2 and it is marked by a semi-arid climate with relatively abundant (989.68 mm. The formula was used to obtain the soil erodibility coefficient (Y) in the study area using the geological map scale of 1:50000 (Figure 4).

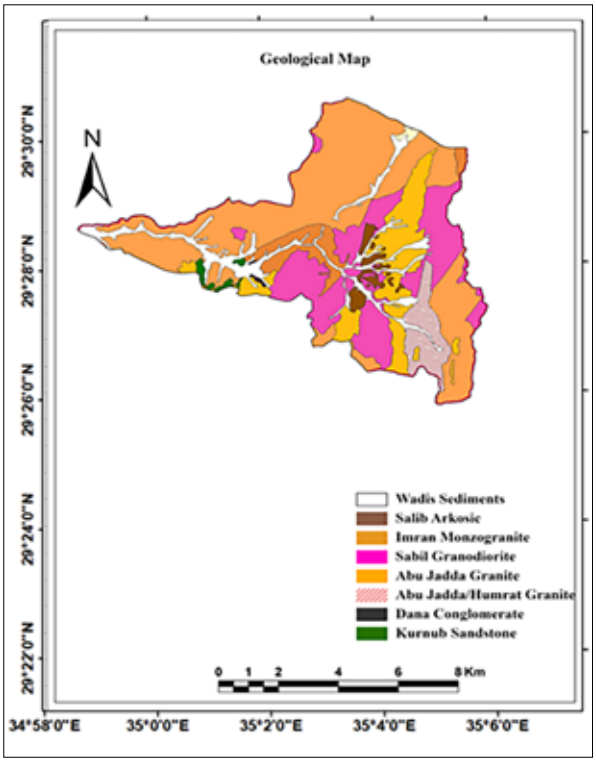

Figure 4. Geologecal map of the study areaas reported by the Jordanian Natural Resources Authority.

2.3.4 Coefficient of Type and Extent of Erosion (φ)

The Coefficient of Type and Extent of Erosions (φ) was determined through field observation. The coefficients of erosion processes were classified into five categories with an interval between 0.1 and 1.0 (Efthimiou et al., 2016). The study area values were obtained using Landsat and field values (Figure 5).

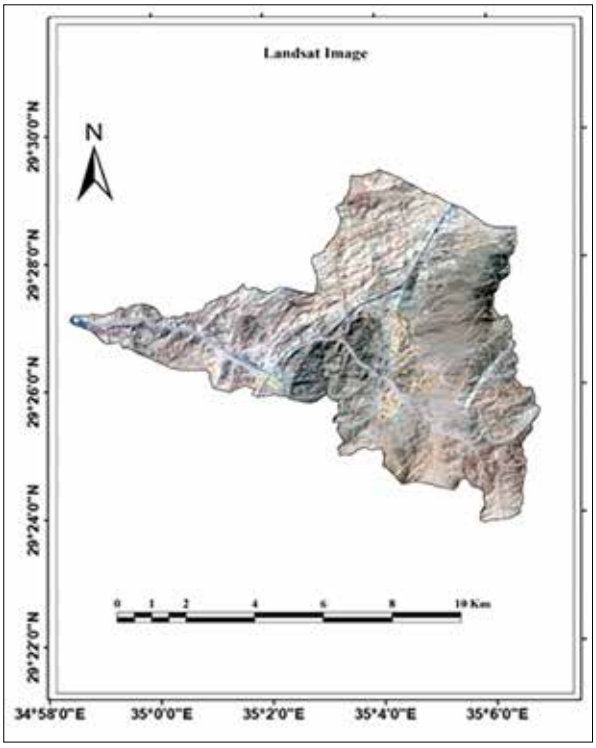

Figure 5. Landsat image of the study area, attained from the United States Geological Survey.

2.3.5 Average Slope Coefficient (,%)

Slopes are one of the most important factors in the EPM Method. The erosion rate generally increases when surface water runoff occurs on steeper terrain with longer slope lengths (Tavares et al., 2021). Understanding the slope-erosion relationship is crucial for predicting erosion patterns and their landscape impacts (Elbadaoui et al., 2023). The slope map in the study area was derived from a topographic map at a scale of 1:25,000 (Figure 6).

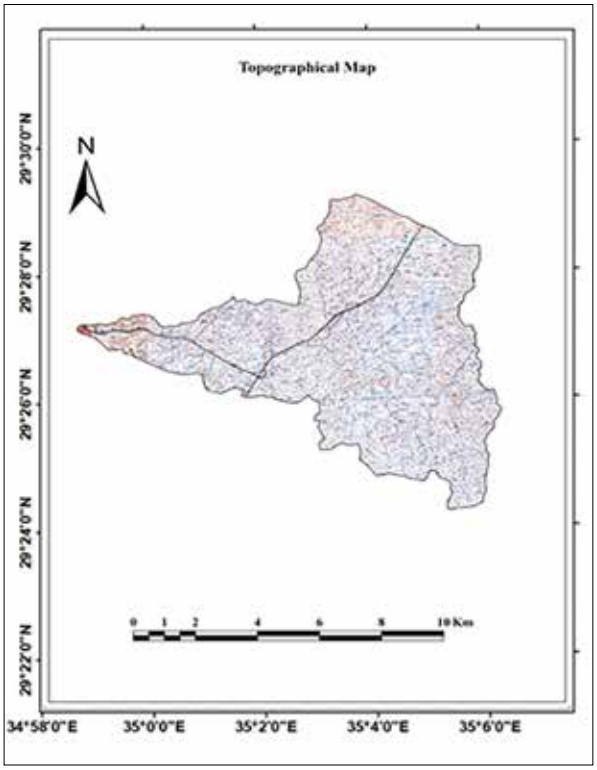

Figure 6. Topographical map of the study area attained from Royal Jordanian Geographic Center.

The coefficients X, Y, and ϕ values are presented in Table 1 and Figures 7, 8, 9, and 10; they are computed using tables proposed by Gavrilovic (1988) and reviewed by several researchers (e.g., Zemljic M, 1971; Globevnik et al., 2003; Fanetti and Vezzoli, 2007;Milanesi et al., 2015).

Erosion intensities are categorised as excessive, strong, medium, weak, very weak, or accumulating (Dragičević et al., 2017various methods for erosion intensity and sediment production assessment have been developed. The necessity for better model performance has led to the more frequent application of the method sensitivity and uncertainty assessments in order to decrease errors that arise from the model concept and its main assumptions. The analysis presented in this paper refers to the application of the Gavrilović method (Erosion Potential Method; da Silva et al., 2014 ; Globevnik et al., 2003; Gavrilovic et al., 2004; Amiri, 2010; Tošicá et al., 2012; Yousefi et al., 2014; Milanesi et al., 2015; Vacca and Dominici, 2015; Ali et al., 2016; Tadić and Šljuka, 2018; Jamal, 2020; Marko et al., 2022)geological, soil texture and land use types. The basin was subdivided into 5 sub-basins. Data required for this study were collected in part through published reports, whilst the remaining was derived by feld surveys. Necessary maps in EPM models were

prepared in Autocad-2006 medium and were transported to IILWIS, after some revision. After constructing topologies for all polygons, we entered weightings for all layers within the Arc-View software. Combinations of all layers were managed thereafter. Coeffcient of each factor was determined, and erosion intensity coeffcient (Z.

Table 1. Descriptive factors used in the EPM method (Gavrilovic, 1972; Lazarevic, 1985).

Soil Protection Coefficient	Xa
Mixed and dense forest	0.05-0.20
Thin forest with grove	0.05-0.20
Coniferous forest with little grove, scarce bushes, bushy prairie	0.20-0.40
Damaged forest and bushes, pasture	0.40-0.60
Damaged pasture and cultivated land	0.60-0.80
Areas without vegetal cover	0.80-1.00
Soil Erodibility Coefficient	Y
Hard rock, erosion resistance	0.1-0.3
Rock with moderate erosion resistance	0.3-0.5
Weak rock, schistose, stabilised	0.5-0.6
Sediments, moraines, clay, and other rocks with little resistance	0.6-0.8
Fine sediments and soils without erosion resistance	0.8-1.0
Coefficient Of Type and Extent Of Erosion	Φ
Little erosion on the watershed	0.1-0.2
Erosion in waterways on 20–50% of the catchment area	0.3-0.5
Erosion in rivers, gullies, and alluvial deposits, karstic erosion	0.6-0.7
of the catchment area is affected by surface 80%–50 erosion and landslides	0.8-0.9
The whole watershed is affected by erosion	1.0

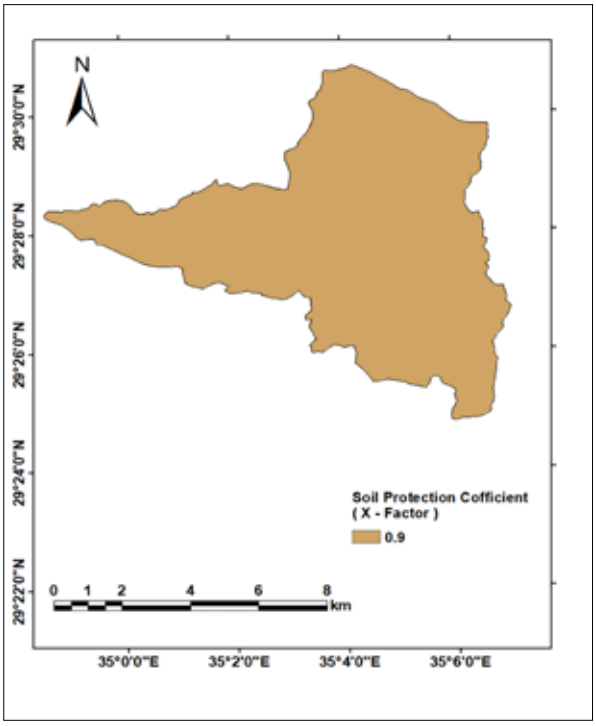

Figure 7. Soil protection coefficient (X)

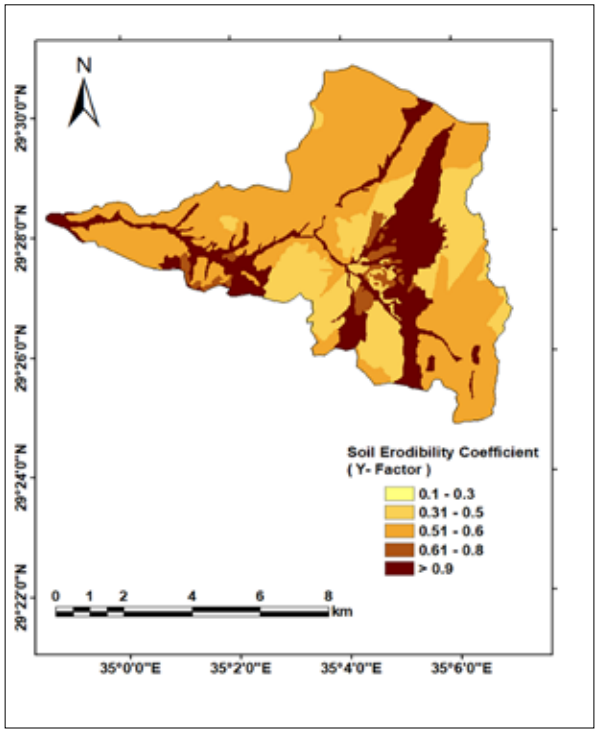

Figure 8. Soil erodibility coefficient (Y)

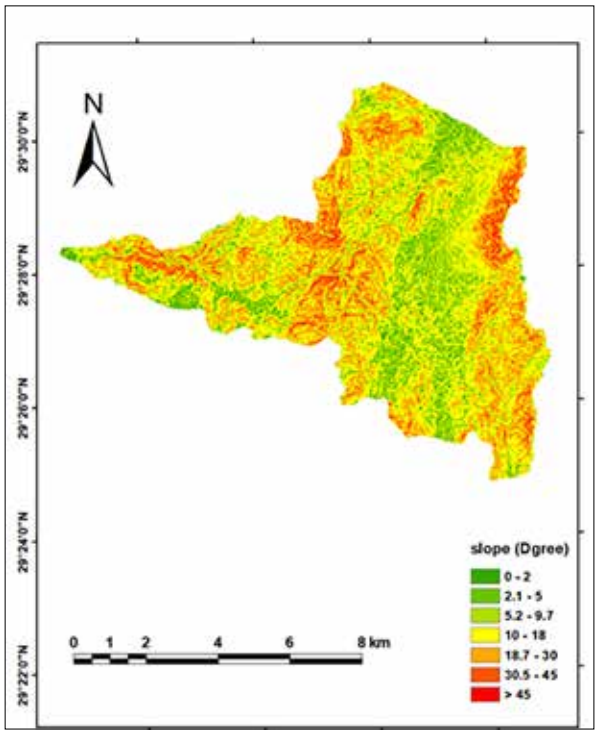

Figure 9. Average Slope coefficient (Ja)

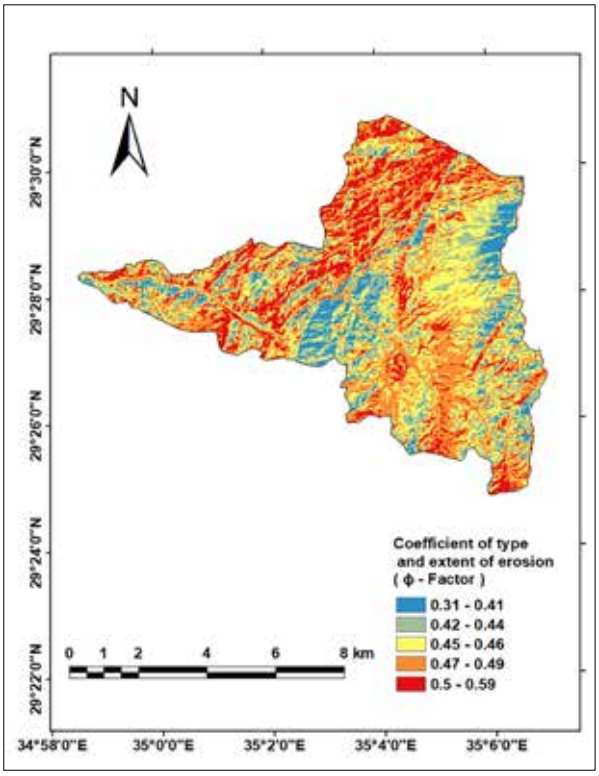

Figure 10. Coefficient of type and extent of erosion ().

3. Results and Discussion

Table 2 classifies erosion intensity using the non-dimensional coefficient Z, while Figure 11 shows its spatial distribution. Most of the basin area (83%, 54 km2) exhibits very low erosion intensity (Z < 0.2), followed by low (13%), moderate (2.4%), and high (1.1%) erosion intensities. Very high erosion intensity covers the smallest area (0.5%).

Table 2. The soil erosion intensity coefficient

Category	Erosion Intensity	Z value	Area (km2)	Area (%)
I	Very low	<0.2	54	83
II	Low	0.21 – 0.40	8.4	13
III	moderate	0.41 – 0.70	1.6	2.4
IV	High	0.71 – 1	0.7	1.1
V	Very high	> 1	0.3	0.5

Analysis of results in Table 4 and Figure 12 shows that most of the basins experience severe to extreme erosion when compared with Zachar's classification of sheet erosion based on soil removal intensity. Zachar identified six categories of water erosion based on the soil volume lost. Table 3 displays the erosion categories determined by Zachar based on erosion volume (Zachar, 1983). Erosion rates vary spatially within the basin depending on controlling factors.

Annual soil erosion reaches extreme levels in the main channels of large wadi beds (>42,000 m³/km²/year). The study area lacks vegetation cover, which makes the soils prone to erosion. Vegetation reduces the erosive force by dissipating the energy of erosive agents and increases water infiltration, which in turn reduces runoff. Main channels sloping wadi beds have sediments that have low soil resistance and steep side slopes. The granite underlying the Wadi Mubarak is bare, and sandstone has been completely stripped away in over 90% of the catchment.

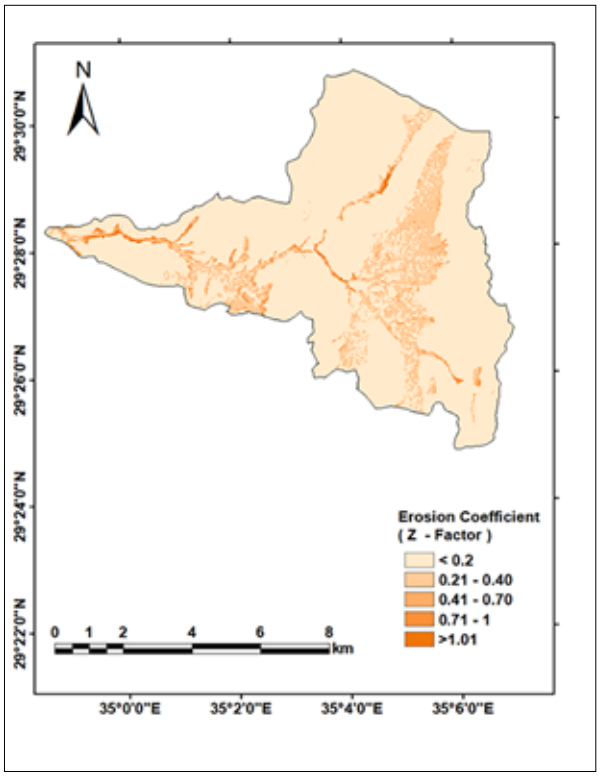

Figure 11. Spatial distribution of erosion intensity by using the Erosion Coefficient (Z).

These are higher rates than those in Table Zachar. The ranges of 20000-41000, 8100-19000, and 2900-8000 cover (1.1%), (7.7%), and (38%), respectively. However, the largest area has a rate below 2,800 m³/km²/year (52%). The annual average erosion rate is estimated at 22,092 m³/km²/year. According to Zachar's classifications, this value indicates a high level of erosion. Using this method, the highest and lowest erosion rates were 243 m³/km²/year and 163 m³/km²/year, respectively.

Table 3. Classification of sheet erosion and deflation by the intensity of soil removal. (Zachar, 1983)

Verbal assessment	Intensity of soil removal (m3 km2 year-1)	Grade
No erosion. Insignificant erosion	50 >	1
Slight erosion	50 - 500	2
Moderate erosion	500 – 1500	3
Severe erosion	1500 – 5000	4
Very severe erosion	5000 – 20000	5
Catastrophic erosion	20000 <	6

Table 4. Annual soil erosion in the basin of Wadi Mubarak

Class	W (m3/km2/year)	Area (km2)	Area
1	<2800	34	0.52
2	2900 - 8000	25	0.38
3	8100 – 19000	5	0.077
4	20000 – 41000	0.7	0.011
5	> 42000	0.3	0.005

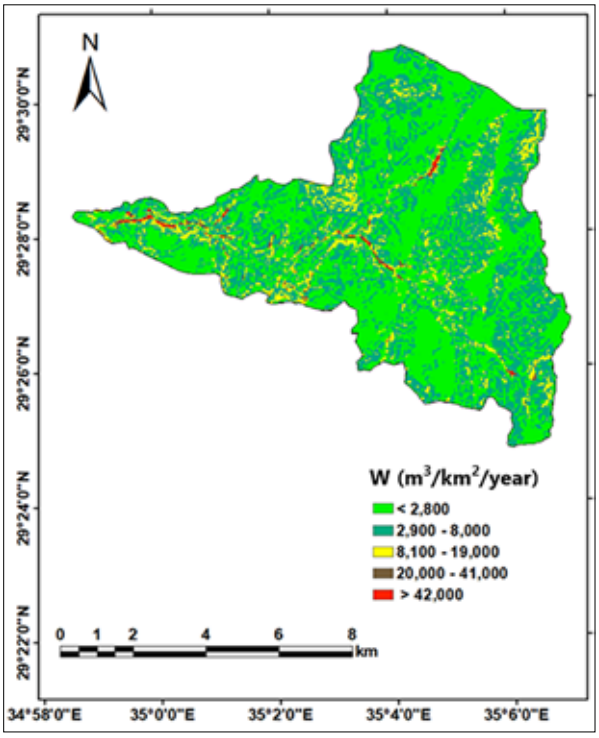

Figure 12. Annual erosion map of Wadi Mubarak

4. Conclusion

The primary aim of the study was to estimate soil erosion and to investigate its spatial distribution in the Wadi Mubarak Basin through the EPM Method. The research concluded that the EPM, when implemented with remote sensing and GIS methods, can be used to examine soil erosion in places like the Wadi Mubarak Basin. The rate of erosion at the Wadi Mubarak basin was estimated using key factors, such as soil erodibility, soil protection, slope, temperature and precipitation. The highest soil erosion is (>42000 m3/km2/year), and the lowest soil erosion is (2800 m3/km2/year). The damaged hydraulic structures indicate a lack of knowledge of the geomorphic conditions at the design stage, as well as the use of inappropriate specifications during construction, especially at the road crossings (see Figure 13).

Erosion assessment methods are needed in the catchment as essential tools for decision-making and for the construction of relevant check dams to control surface runoff in the upper alluvial piedmont. These devices reduce the erosive energy of floodwater. Appropriate hydrological systems that have the capacity to allow flood discharge, such as riprap, gabions, as well as appropriate drainage, will mitigate the volume and velocity of runoff. Landslides and rockfall can be prevented by fences and terraces, which reduce water runoff and control sediment transport.

The use of AI should be implemented in the future to enhance mitigation. To simulate future climate (e.g., RCP4.5 and RCP8.5) projections, EPM can be used to project future erosion at the current temperature and precipitation to show a higher sediment yield at higher temperature conditions. Environmental Impact Assessments (EIAs) of infrastructure projects, like dams, roads, and mining activities can also integrate EPM. The approach supports the sustainability evaluation of the proposed development zone (Marko et al., 2023).

Figure 13. Undercut erosion at the base of the road

References

Ali, S.S., Foad A. Al-Umary, Sarkawt G. Salar, Nadhir Al-Ansari, & Sven Knutsson. (2016). GIS Based Soil Erosion Estimation Using EPM Method, Garmiyan Area, Kurdistan Region, Iraq. Journal of Civil Engineering and Architecture 10: 291–308. https://doi.org/10.17265/1934-7359/2016.03.004

Al-Sababhah, N. M. A., & Al maqablah, M. M. (2023). Integrated Evaluation of Soil Erosion-prone Areas Based on the GIS Technique and the Analytic Hierarchy Process on Hillside Slopes, Northwest of Jordan. Jordan Journal of Earth and Environmental Sciences 14: 158–174.

Amini, S., Rafiei, B., Khodabakhsh, S., & Heydari, M. (2010). Estimation of erosion and sediment yield of Ekbatan Dam drainage basin with EPM, using GIS. Iranian Journal of Earth Sciences 2: 173–180. http://www.sid.ir/en/VEWSSID/J_pdf/1019920100209.pdf

Amiri, F. (2010). Estimate of erosion and sedimentation in semi-arid basin using empirical models of erosion potential within a geographic information system. Air, Soil and Water Research 3: 37–44. https://doi.org/10.4137/aswr.s3427

da Silva, R. M., Santos, C. A. G., & Silva, A. M. (2014). Predicting soil erosion and sediment yield in the Tapacurá catchment, Brazil (Vol. 8, Issue 1, pp. 75–82). https://doi.org/10.4090/juee.2014.v8n1.075082

Deilami, B. R., Liyaghat, M., Sheikhi, A., Al-saffar, M. R. A., & Barati, V. (2012). Estimation of Erosion and Sedimentation in Karoon Basin using EPM with in Geographic Information System. 2: 923–927.

Dragičević, N., Karleuša, B., & Ožanić, N. (2017). Erosion potential method (Gavrilović Method) sensitivity analysis [Soil and Water Research]. In Soil and Water Research 12. https://doi.org/10.17221/27/2016-SWR

Efthimiou, N., Lykoudi, E., Panagoulia, D., & Karavitis, C. (2016). Assessment of soil susceptibility to erosion using the epm and rusle models: The case of venetikos river catchment. Global Nest Journal 18: 164–179. https://doi.org/10.30955/gnj.001847

Elbadaoui, K., Mansour, S., Ikirri, M., Abdelrahman, K., Abu-Alam, T., & Abioui, M. (2023). Integrating Erosion Potential Model (EPM) and PAP/RAC Guidelines for Water Erosion Mapping and Detection of Vulnerable Areas in the Toudgha River Watershed of the Central High Atlas, Morocco. Land 12:. https://doi.org/10.3390/land12040837

Fanetti, D., & Vezzoli, L. (2007). Sediment input and evolution of lacustrine deltas: The Breggia and Greggio rivers case study (Lake Como, Italy). Quaternary International 173–174: 113–124. https://doi.org/10.1016/j.quaint.2007.02.008

Farhan, Y. (1999). Geomorphic Impacts of Highway Construction, Their Causes and Remedies: A Case Study from Aqaba, Southern Jordan. The Arab World Geographer 2: 1–25.

Gavrilovic, Z. (1988). Use of an Empirical Method Erosion Potential Method for Calculating Sediment Production and Transportation in Unstudied or Torrential Streams. International Conference on River Regime 411–422.

Gavrilovic, Z., Stefanovic, M., Milojevic, M., & Cotric, J. (2004). Erosion Potential Method. An Important Support For Integrated Water Resource Management. Institute Development of Water Resources 14.

Globevnik, L., Holjević, D., Petkovšek, G., & Rubinić, J. (2003). Applicability of the Gavrillović method in erosion calculation using spatial data manipulation techniques. IAHS-AISH Publication 279: 224–233.

Jamal, A. K. (2020). Estimation & Cartography the Water Erosion by Integration of the Gavrilovic " Epm " Model using a Gis in the Mediterranean Watershed : Oued Tleta (Western Rif , Morocco) 155: 265–278.

Loucks, D. P., van Beek, E., Stedinger, J. R., Dijkman, J. P. M., & Villars, M. T. (2005). Water Resources Systems Planning and Management and Applications: An Introduction to Methods, Models and Applications. 1nd Ed., Paris: UNESCO

Marko, O., Gjipalaj, J., & Shkodrani, N. (2022). Application of the Erosion Potential Method in Vithkuqi Watersheds (Southeastern Albania). Journal of Ecological Engineering 23: 17–24. https://doi.org/10.12911/22998993/146131

Marko, O., Gjoka, K., Shkodrani, N., & Gjipalaj, J. (2023). Climate Change Effect on Soil Erosion in Vjosa River Basin. Journal of Ecological Engineering 24: 92–100. https://doi.org/10.12911/22998993/156831

Marouane, L., Lahcen, B., & Valérie, M. (2021). Assessment and mapping of water erosion by the integration of the Gavrilovic "EPM" model in the Inaouene watershed, Morocco. E3S Web of Conferences 314:. https://doi.org/10.1051/e3sconf/202131403009

Milanesi, L., Pilotti, M., Clerici, A., & Gavrilovic, Z. (2015). Application of an improved version of the erosion potential method in alpine areas. Italian Journal of Engineering Geology and Environment 15: 17–30. https://doi.org/10.4408/IJEGE.2015-01.O-02

Oroud, I. M. (2011). Evaporation estimates from the Dead Sea and their implications on its water balance. Theoretical and Applied Climatology 106: 523–530. https://doi.org/10.1007/s00704-011-0452-6

Renard, K. G., Foster, G. R., Weesies, G. A., & and J.P. Porter. (1991). RUSLE: Revised soil loss equation. Journal of Soil and Water Conservation Society 46: 30–33. https://doi.org/10.1201/9780203739358

Salahat, M. A., & Al-qinna, M. I. (2015). Rainfall Fluctuation for Exploring Desertification and Climate Change : New Aridity Classification. Jordan Journal of Earth and Environmental Sciences Volume 7: 27–35.

Saqqa, W. A., & Atallah, M. Y. (2013). Tectonic Geomorphology of Alluvial Fans east of the Wadi Araba Fault (Dead Sea Transform), Jordan. Jordan Journal of Earth and Environmental Sciences 5: 79–86.

Tadić, E., & Šljuka, A. (2018). Erosion intensity assessment using erosion potential method and geographic information systems: A case study of Beočin municipality, Serbia. In Zbornik radova Departmana za geografiju, turizam i hotelijerstvo 47: 32–43. https://doi.org/10.5937/zbdght1801032t

Tavares, A. S., Uagoda, R. E. S., Spalevic, V., & Mincato, R. L. (2021). Analysis of the erosion potential and sediment yield using the intero model in an experimental watershed dominated by karst in brazil. Agriculture and Forestry 67: 153–162. https://doi.org/10.17707/AgricultForest.67.2.11

Thneibat, A.A. (2010). Geomorphological Evaluation of the Aqaba Back Road Area, Southern Jordan. Ph.D. Thesis, Jordan University. (Unpublished, in Arabic)

Tošicá, R., Dragićević, S., & Lovrić, N. (2012). Assessment of soil erosion and sediment yield changes using erosion potential model - case study: Republic of srpska (bih). Carpathian Journal of Earth and Environmental Sciences 7: 147–154.

Uddin, K., Murthy, M. S. R., Wahid, S. M., & Matin, M. A. (2016). Estimation of Soil Erosion Dynamics in the Koshi Basin Using GIS and Remote Sensing to Assess Priority Areas for Conservation. PLoS ONE 11: 1–19. https://doi.org/10.1371/journal.pone.0150494

Vacca, C., & Dominici, R. (2015). Preliminary considerations on the application of the Gavrilović method in GIS environment for the calculation of sediment produced by the catchment area of the Stilaro Fiumara (Calabria south-east). In Rendiconti Online Societa Geologica Italiana 33: 104–107. https://doi.org/10.3301/ROL.2015.25

Williams, J. E. (1975). Sediment-Yield Prediction With Universal Equation Using Runoff Energy Factor. 244–252.

Yousefi, S., Kivarz, N., Ramezani, B., Rasoolzadeh, N., Naderi, N., & Mirzaee, S. (2014). An estimation of sediment by using Erosion Potential Method and geographic information systems in Chamgardalan Watershed: A case study of Ilam province, Iran. Geodynamics Research International Bulletin 2: 34–41 . www.geo-dynamica.com

Zachar, D. (1983). Soil Erosion: Developments in Soil Science 10. Elsevier Scientific Publishing Company, Amsterdam and New York.

Zemljic M. (1971). Calcul du debit solide - Evaluation de la vegetation comme un des facteurs antierosifs. International Symposium Interpraevent,Villach, Austria.

JJEES

JJEES (2026) 17 (2): 139-154
ISSN 1995-6681

Jordan Journal of Earth and Environmental Sciences

Exploring Vulnerability of Coastal Livelihoods to Climate Change in Dacope Upazila, Khulna, Bangladesh: A Multidimensional Assessment Using Indices and Analytical Approaches

Md. Kamrul Hasan[1*], Md. Mizanur Rahman[2] and Abu Nayem Md. Kayes[1]

[1] Department of Urban and Regional Planning, Pabna University of Science & Technology, Pabna, Bangladesh
[2] Department of Geography and Environment, Jahangirnagar University, Savar, Dhaka, Bangladesh

Received on 5 June 2025; Accepted on 7 October 2025

Abstract

Life, livelihood, nature, and the onset of extreme climate change continue to pose challenges for the coastal residents of Dacope Upazila in Khulna district, Bangladesh, almost daily. As Dacope is one of the key areas affected by climate change, it is highly vulnerable to these changes. Recognizing the hardships faced by the community and the need for targeted support, this study evaluates the impacts of climate change on various livelihood assets using the Livelihood Vulnerability Index (LVI), LVI-IPCC, and Livelihood Effect Index (LEI) methods. Data were collected through a semi-structured household questionnaire survey covering nine unions within Dacope Upazila, with a sample of 400 households. Secondary data was obtained from the NASA Power website. Results show that Sutarkhali Union is the most vulnerable, with an LVI score of 0.584. Both the LVI-IPCC and LEI approaches ranked Sutarkhali as the most vulnerable. This study provides insight into living conditions and the factors that make the livelihoods of Dacope Upazila's residents vulnerable to climate change. Consequently, it offers valuable information for policymakers and development practitioners to design effective interventions for building resilience in coastal communities.

Keywords: *Climate Change; Vulnerability; Livelihood; LVI; LVI-IPCC; LEI*

1. Introduction

Climate change is a major global environmental challenge of the 21st century. Man-made greenhouse gas emissions, primarily from fossil fuel combustion and land-use changes, have led to higher global temperatures, rising sea levels, and extreme weather phenomena (IPCC, 2021). The Intergovernmental Panel on Climate Change (IPCC) warns that unmitigated changes could lead to devastating impacts for ecosystems, human health, and economies worldwide. Coastal regions around the world are experiencing significant challenges due to climate change, which has exacerbated environmental vulnerabilities and intensified socio-economic risks for dependent populations (IPCC, 2014). The southwest coastal region of Bangladesh is particularly vulnerable to climate-induced hazards, including cyclones, saline intrusion, and rising sea levels, all of which threaten the livelihoods of local communities (Islam & Hasan, 2016). The region's unique geographical position exposes it to both regular monsoon flooding and increasingly frequent natural disasters, making it a hotspot for climate vulnerability and livelihood insecurity (Hossain, 2024; Rahman & Rahman, 2022; Alam et al., 2017).

In Dacope Upazila, located in Khulna District, these challenges are especially severe. This area heavily relies on agriculture, fisheries, and forest resources for livelihood, all of which are highly sensitive to environmental changes (Ahmed et al., 2019). Recent studies have highlighted that communities in Dacope face multidimensional risks, including reduced agricultural productivity, fishery losses, and declining access to potable water due to salinity intrusion, all of which contribute to an increasingly precarious livelihood situation (Kabir et al., 2024). Vulnerability in this area is further intensified by socio-economic factors, such as limited access to markets, low adaptive capacity, and inadequate infrastructural resilience, which together exacerbate the impacts of environmental hazards on local livelihoods (Ali, 2019).

Although significant research by Haque et al. (2014), Alam et al. (2017), and Hossain et al. (2024) has addressed climate vulnerability in coastal Bangladesh, there is a lack of comprehensive analysis specifically focusing on livelihood vulnerability in Dacope Upazila. A targeted assessment is essential to understand the local aspects of vulnerability and identify specific factors that undermine livelihood sustainability. While studies have looked at coastal vulnerability using general indicators (e.g., agriculture, fisheries, or infrastructure damage) (Huq et al., 2015; Alam & Rabbani, 2015), the use of indices like the LVI and LEI to capture the multi-dimensional nature of livelihood vulnerability remains rare in Bangladesh's coastal zones. The LVI, which considers factors such as income, food security, resource access, and institutional support (Hann et al., 2009), has been applied in countries like Indonesia (Riantini et al., 2024) and India (Islam et al., 2024), but its use in Dacope Upazila—where diverse livelihoods are affected by both slow and rapid climate events—is limited. Additionally,

* Corresponding author e-mail: kamrul.urp@pust.ac.bd

while the LEI, which evaluates the direct and indirect effects of climate change on livelihoods (Scoones, 2009), has been used in some parts of Bangladesh (Ali, 2018), its specific application in the South-West coastal region and comparison with the LVI are largely unexplored.

Additionally, although there have been studies examining individual livelihood vulnerabilities to climate change in the coastal belt of Bangladesh, such as those by Rahman et al. (2020) and Sarker et al. (2019), most of these studies focus on sectoral impacts-agriculture or fisheries without offering an integrated view of how climate impacts interact across sectors. The combination of LVI and LEI could provide a more comprehensive understanding of how vulnerability manifests across various dimensions of livelihoods, including economic dependency on climate-sensitive sectors, social capital, adaptive capacity, and institutional responsiveness.

This study aims to evaluate the sensitivity of a portion of Bangladesh's coastal areas to the effects of climate change on the way people live there. The Livelihood Vulnerability Index (LVI), developed by Hahn et al. (2009), is applied in this research. This index derives its primary data from housing units and utilizes certain variables. As a result, it can measure not only the extent to which households are vulnerable to natural disasters and climatic variability, but also their capacity for adaptation and sensitivity to climate change. Additionally, the computation of this index is more straightforward than that of other indices because it utilizes primary data from residences (Akram et al., 2025). The study also examines livelihood vulnerability using the LVI-IPCC approach and attempts to identify the effects of climate change on various community capitals using the Livelihood Effect Index (LEI). Through this approach, the study aims to provide policymakers and development practitioners with valuable insights to design effective interventions that build resilience in coastal communities. The study is important in various dimensions, including focused action strategies, priority-driven policy development, and the fulfillment of the goals set by the IPCC. It supports the scientific community by delivering consistent insights on climate change, while also striving to alleviate the challenges faced by the most at-risk populations.

2. Materials and Methods

2.1 Study Area Profile

These areas are essentially vulnerable to climate change impacts and natural disasters that seriously affect the livelihood of the people living there (Swarnokar et al., 2025b). Vulnerability is increased by a lack of resources and infrastructure, and by economic dependence on climate-sensitive sectors (Islam et al., 2014). Dacope (Figure 1), an upazila amidst nine upazilas of Khulna district, is essentially a coastal area; hence, it is vulnerable to climate change. This situation underlines the challenges faced by the local population. More precisely, Dacope is situated between 22°24' and 22°40' north latitudes and between 89°24' and 89°35' east longitudes. It is bounded by Batiaghata Upazila to the north, Batiaghata and Rampal Upazilas to the east, the Sundarbans to the south, and Paikgachha Upazila to the west. It has an area of 991.98 sq. km., which is divided into 9 unions; the total number of households in this Upazila is 42186 (BBS, 2022).

The selection of Dacope Upazila as a case study area will be guided by its unique geographical location and proximity to a UNESCO World Heritage Site, which adds to its cultural and environmental significance. This area is considered highly vulnerable to the impacts of global warming (Swarnokar et al., 2025b); hence, it will be an important case for studying climate-related challenges. Second, the socioeconomic conditions in the Dacope Upazila provide such privileged ground for research; it is obvious that many of those factors will be strong variables when accounting for the resilience, adaptation capability, and development needs of that region.

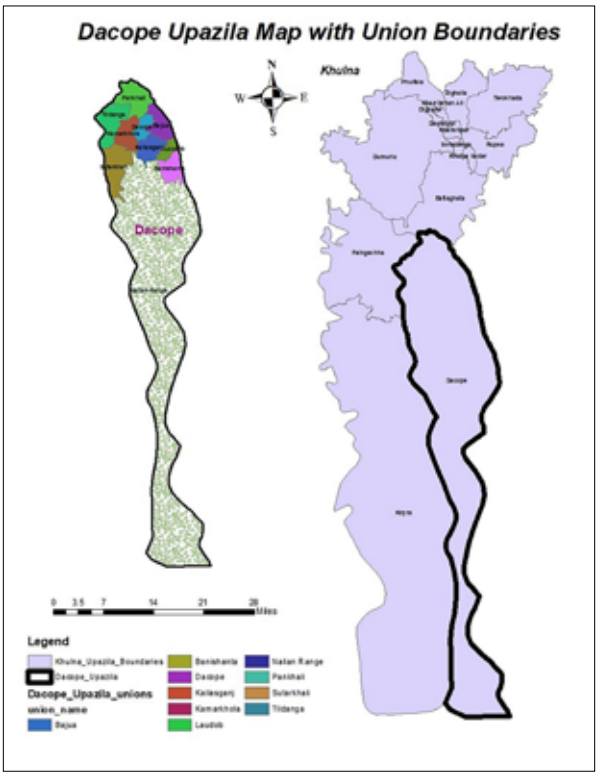

Figure 1. Map of Dacope Upazila.
Source: Hasan et al., 2025

2.2 Data Source, Sample Size, and Method of the Study

2.2.1 Data Sources

In the research study, primary data were collected through an intensive, semi-structured questionnaire survey at the household level, and approximately 400 data points were obtained from 9 unions of the Dacope Upazila, along with data sourced from the NASA Power website (maximum temperature, minimum temperature, and precipitation). The primary data were collected randomly to obtain a representative sample.

2.2.2 Sample Size for the Household Survey

According to BBS (2022), the number of households in the Dacope Upazila is 42186. Since the population size is known, the Yamane formula is suitable for determining sample size. Researchers widely utilise the Yamane formula (Kayes et al., 2025; Sultana & Hasan, 2024; Kayes et al., 2025h). The mathematical expression of the formula:

$$n = \frac{N}{1 - Ne^2} \quad (1)$$

(Yamane,1967)

In this equation, n denotes the required sample size, N is the total number of households in the study area, and e is the margin of error. For this study, taking a margin of error of 5% with a 95% confidence level, the sample was:

$$n = \frac{42186}{1 + 42186 \times (0.05)^2} = 397$$

So, the sample size was 397 for the household survey.

2.2.3 Method of vulnerability analysis

In 2009, Hahn et al. developed a framework that better represented community-level vulnerability by incorporating multiple components. This was immediately adopted by researchers the world over and remains one of the most popular among these researchers in related climate change research because of its structured approach, for example, Chowdhury et al. (2024), Phuong et al. (2022), and so many. The LVI became an instant hit, especially with many more aspiring researchers in this field, due to its composite structure. This enabled nuanced analysis across communities and regions in light of their vulnerabilities (Sullivan & Meigh, 2005). Therefore, this method is adopted in this study. Based on the conceptualization and literature review, 46 sub-components across 10 major components are included in this study. Where some major and sub-components are adopted from different research, and some are developed for this study. The ten major components are Socio-demographic profile (SDP), Livelihood strategies (LS), Social network (SN), Food security (FS), Water scarcity (WS), Income security (IS), Land (L), Physical facilities (PF), Health security (HS), and Natural disaster and climate variability (ND & CV). The data for sub-components are in different units and either have a positive or negative relationship with vulnerability. For that reason, we need to standardize the values of sub-components. There are two equations for the standardization, equation 2 is for positive sub-components and equation 3 for the negative sub-components:

$$Index\ X_{si} = \frac{X_{si} - MIN\ X_{sc}}{MAX\ X_{sc} - MIN\ X_{sc}} \quad (2)$$ *(Hahn et al.,2009)*

$$Index\ X_i = \frac{MAX\ X_{sc} - X_{si}}{MAX\ X_{sc} - MIN\ X_{sc}} \quad (3)$$ *(Adu et al.,2018;Hahn et al.,2009)*

In these two equations, Index Xsi is the standardized value of the sub-indicators, which ranges from 0 to 1; Xsi is the actual value of the sub-indicators; MAXsc is the maximum possible value for the sub-indicators; and MINsc is the minimum possible value for the sub-indicators. For example, for subcomponents taken as percentages, the maximum and minimum possible are 100 and 0, respectively.

Each of these major components consisted of several sub-components and was averaged using Equation 4. The consolidated value thus determined allowed comparison in vulnerability between the major components.

$$M_{cv} = \frac{\sum_{i=1}^{n} Index\ Xsi}{n} \quad (4)$$ *(Adu et al.,2018)*

In the equation 4, Mcv stands for the index value of major component (SDP, LS, SN, FS, WS, IS, L, PF, HS and ND & CV), "$\sum_{i=1}^{n} Index\ Xsi$" is the summation of the sub-indicators standardized value obtained by the equation 2 or 3. "n" stands for the number of sub-components under the respective major components after calculating the index value for each major component the overall LVI has been calculated by the equation 5.

$$LVI_d = \frac{W_{SDP}SDP_d + W_{LS}LS_d + W_{SN}SN_d + W_{FS}FS_d + W_{WS}WS_d + W_{IS}IS_d + W_LL_d + W_{PF}PF_d + W_{HS}HS_d + W_{ND\&CV}ND\&CV_d}{W_{SDP} + W_{LS} + W_{SN} + W_{FS} + W_{WS} + W_{IS} + W_L + W_{PF} + W_{HS} + W_{ND\&CV}} \quad (5)$$

(Hahn et al.,2009)

In this equation, LVI_d refers to the vulnerability index for study area d (Dacope), while "W ($_{SDP, LS, SN, FS, WS, IS, L, PF, HS, ND\&CV}$)" refers to the number of sub-components for relevant major components. SDP_d, LS_d, SN_d, FS_d, WS_d, IS_d, L_d, PF_d, HS_d, ND & CV_d represent the index value for each major component obtained from equation 4. For instance, the value of W_{SDP} is 6. The value from equation five is explained by the sequence of lower to higher value, from least vulnerable to most vulnerable.

2.2.4 LVI–IPCC: Based on IPCC Framework

The Intergovernmental Panel on Climate Change defines vulnerability as the susceptibility of a system to and inability of a system to cope with adverse effects of climate change, which includes the characteristics of the exposure in concerned areas and their sensitivity concerning the degree of impacts and adaptive capacity or the ability to adjust or manage impacts (IPCC, 2014). The highest magnitude of vulnerability arises from high exposure and sensitivity and from low adaptive capacity (IPCC, 2014).

Adaptive capacity contains the SDP, LS, and SN. Sensitivity contains FS, WS, IS, L, PF, and HS. And at last, exposure contains only one major component: natural disasters and climate variability. Equation (6) is the formula for calculating adaptive capacity, sensitivity, and exposure according to the IPCC framework, which is utilized in this study.

$$CF_d = \frac{\sum_{i=1}^{n} W_{cvi}\ M_{id}}{\sum_{i=1}^{n} W_{cvi}} \quad (6)$$ *(Hahn et al.,2009)*

In this equation, CF_d is the adaptive capacity, sensitivity, and exposure, W_{cvi} is the number of variables for each major component, Mid is the index value obtained by equation 4. $\sum_{i=1}^{n} W_{cvi}$ is the total sub-components under adaptive capacity, sensitivity, and exposure. After that the overall LVI – IPCC is calculated by equation 7:

$$LVI - IPCC = (Expo. - AC) * Sen. \quad (7)$$

Here, "Expo." is the exposure index, "AC" stands for the adaptive capacity index, and "Sen." means the sensitivity index. On the other hand, there exists a record by (Sultana & Hasan, 2024) that IPCC-VI uses the scale ranging from -1 to +1 where -1 stands as the least susceptible position, in other words when the adaptive capacity is more than the exposure, 0 for the moderately vulnerable and 1 stands for the severely vulnerable when the exposure would be much higher than the adaptive capacity.

2.2.5 Livelihood Effect Index (LEI)

The Livelihood Effect Index (LEI) is a composite indicator designed to assess the impacts of external factors. It captures various dimensions of livelihood security, including income, access to resources, employment, and quality of life (Scoones, 1998; Ellis, 2000). Likewise, LVI – IPCC, LEI are categorized in Human capital, Natural capital, Social capital, Financial capital and Physical capital.

The normalized values by equations 2 and 3, the capital values are obtained by equation 6 mentioned before. The LEI calculated by Equation 8:

$$LEI = \frac{\sum_{i=1}^{n} \text{capital value}}{\sum_{i=1}^{n} W_{sc}} \quad (8)$$

In this equation, LEI is the livelihood effect index and $\sum_{i=1}^{n} W_{sc}$ is the number of total sub-indicators. Figure 2 represents the methodological flowchart that followed during this research. The research started with the conceptualization of the topic climate change and vulnerability. Then, with proper literature review and standard survey tools, this study collects the required data from secondary sources and at the household level. The findings are validated with proper discussion.

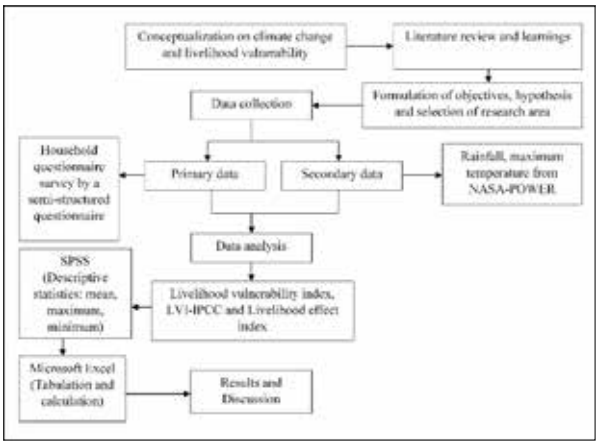

Figure 2. Methodological flowchart of the research

3. Results

3.1 Comparison of major Components of LVI among unions

According to the previous studies of Hahn et al. (2009; Nguyen & Leisz, 2021; Tewari et al., 2014; Hoang et al., 2020; Rahman, 2014; Piya et al., 2012; Thorpe et al., 2007; Toufique et al., 2013; Shah et al., 2013; Koirala et al., 2015). A total of 46 sub-components are selected under ten major components for calculating LVI.

3.1.1 Socio-demographic Profile (SDP):

Vulnerability is judged from aspects of the major and sub-components, as depicted in Table 1, across the nine unions. The highest values are an indication of more vulnerabilities, whereas lower values indicate less vulnerability. As indicated in Table 1, Sutarkhali is the most vulnerable area concerning the socio-demographic profile, with an LVI high value of 0.56. In contrast, Tildanga has the lowest vulnerability, with an LVI of 0.30. The second position for each is held by Bajua and Banishanta, with an LVI of 0.45, followed by Laudobe with an LVI of 0.44.

Sutarkhali has the highest values for four of the six sub-components: dependency ratio (0.43), presence of disabled members in the household (0.14), primary education level of the household head (0.59), and households with at least one female member lacking functional education (0.76). On the other hand, Tildanga has the lowest values in three sub-components: dependency ratio (0.14), households with girl children (0.26), and single-headed households (0.62).

Dacope, the Upazila town, and the surrounding areas exhibit average to low vulnerability, as indicated by moderate to low LVI values. These areas benefit from better employment opportunities, education, and communication infrastructure, resulting in lower levels of vulnerability.

3.1.2 Livelihood Strategies (LS):

Coming to the LS, Sutarkhali comes out to be the most vulnerable area, having an LVI value of 0.73. The unions of Dacope and Bajua have values quite near to the previous one, that is, 0.71 and 0.70, respectively. On the other hand, Tildanga shows the lowest vulnerability in livelihood strategies, with an LVI of 0.58.

The Livelihood Strategies component consists of four sub-components; three of them indicate a negative relationship with vulnerability. Therefore, in the case of higher values of these sub-indicators, it will reflect lower vulnerability. Thus, the lesser the value, the more vulnerable. Nevertheless, a higher general value of LVI signals greater vulnerability. In one such case, a household has a member working outside the area, providing a regular source of income and reducing its vulnerability.

The union with the lowest LVI is Laudobe, at 0.40, indicating it is the most vulnerable in livelihood diversification. The burden of loans is positively related to vulnerability; this means that a higher loan burden increases households' vulnerability . In this respect, Sutarkhali has the highest value, 0.81, making it the most vulnerable in terms of loan burdens, as nearly every household is indebted there (Table 1).

Agricultural livelihood diversification and non-agricultural livelihood diversification also reduce vulnerability. The lowest value, 0.71, belongs to Laudobe, which is the most vulnerable area, while Banishanta, Pankhali, and Dacope have the highest values at 0.81, which indicate that vulnerability is relatively low. It is because agricultural activities are less dominant in these areas, contributing to higher indices in non-agricultural livelihoods.

3.1.3 Social Network (SN):

The SN component is one of the primary determinants for vulnerability, comprising four sub-components, all of which are negatively associated with the vulnerability phenomenon. In this respect, Laudobe Union emerges as the most vulnerable, with an LVI value of 0.63, the highest for the areas, which indicates that, in terms of social networks, the vulnerability is marked. By contrast, Dacope Union has the lowest value, 0.50, indicating the least vulnerable area in this regard. Beyond that, LVI values for Koilashganj, Tildanga, Pankhali, and Sutarkhali are 0.62, 0.57, 0.56, and 0.55, respectively, indicating medium-to-high vulnerability.

Support from the neighbors, NGOs, and the government reduces vulnerability; hence, the relation is negative with this sub-component. As for the ratio of help provided to help received, Sutarkhali Union shows the lowest value of 0.63, indicating the highest vulnerability, while Pankhali Union shows a higher value, indicating a lower vulnerability.

It further reduces vulnerability, as membership in microcredit organizations offers small loans to help a household cope with adverse impacts of natural disasters. Reports show that Sutarkhali and Bajua unions have the highest membership value of 0.86, which indicates low vulnerability. On the other hand, Laudobe Union has reported the least value of 0.55, which reflects higher vulnerability with regard to access to micro-credit support.

Table 1. Major components, variables (sub-components), and average index values of nine Unions and their LVI values.

Sub- Components	Bajua	Banishanta	Laudobe	Pankhali	Dacope	Koilashganj	Kamarkhola	Sutarkhali	Tildanga	Major Component	Bajua	Banishanta	Laudobe	Pankhali	Dacope	Koilashganj	Kamarkhola	Sutarkhali	Tildanga
Avg. Number of Dependent members	0.29	0.29	0.14	0.29	0.14	0.14	0.29	0.43	0.14	Socio-Demographic Profile (SDP)	0.45	0.45	0.44	0.41	0.36	0.37	0.38	0.56	0.30
% of households have disabled persons	0.05	0.02	0.05	0.05	0.03	0.05	0.07	0.14	0.05										
% of households with no Primary Education of the household head	0.48	0.52	0.14	0.37	0.30	0.36	0.28	0.59	0.26										
% HH has a girl child aged 10-15 years	0.33	0.29	0.62	0.40	0.39	0.38	0.48	0.48	0.26										
% of single-headed elderly family	0.99	0.99	1.00	0.79	0.98	0.72	0.65	0.98	0.62										
% of HH having at least one female member with no functional education	0.55	0.59	0.67	0.56	0.32	0.55	0.52	0.76	0.48										
% of HH having at least 1 family member working outside the community	0.90	0.90	0.40	0.81	0.82	0.57	0.63	0.67	0.64	Livelihood Strategies (LS)	0.70	0.68	0.62	0.65	0.71	0.62	0.60	0.73	0.58
% of HH with burden of loan in the last 5 years	0.74	0.72	0.67	0.68	0.59	0.72	0.59	0.81	0.62										
Average agricultural and non-agricultural livelihood diversification	0.78	0.81	0.71	0.81	0.81	0.78	0.78	0.80	0.73										
% of HH changed sowing and cropping schedule	0.38	0.28	0.71	0.32	0.63	0.4	0.41	0.64	0.31										
Help received: Help provided	0.79	0.72	0.77	0.89	0.80	0.82	0.82	0.63	0.84	Social Network (SN)	0.53	0.52	0.63	0.56	0.50	0.62	0.51	0.55	0.57
% of households that did not apply to their local government for assistance in the past 12 months	0.24	0.17	0.36	0.19	0.27	0.19	0.17	0.29	0.4										
% of HH having no membership in Local Committee/ Samiti	0.07	0.36	0.62	0.33	0.07	0.55	0.28	0.24	0.38										
% of HH having no membership in the micro-credit organization	0.86	0.81	0.55	0.70	0.66	0.78	0.61	0.86	0.57										
% of HH having no access to at least a single social network platform	0.71	0.55	0.83	0.70	0.7	0.74	0.67	0.74	0.67										
Avg. no. of months households struggle to find food	0.42	0.42	0.17	0.42	0.67	0.25	0.42	0.50	0.17	Food Security (FS)	0.68	0.69	0.61	0.76	0.84	0.55	0.63	0.71	0.53
Household with primary irrigation source	0.23	0.14	0.72	0.5	0.95	0.07	0.3	0.37	0.31										
% of the HH with no ability to save harvested crops to eat during a different time of year	0.87	0.96	0.59	0.92	0.65	0.54	0.69	0.79	0.53										
% of HH having no ability to save seeds to grow the next year	1	0.96	0.72	0.96	0.95	0.89	0.83	0.95	0.72										
% of HH having no access to free seeds and fertilizer	0.87	0.96	0.86	1	1	1	0.9	0.95	0.91										
% of HH having no easy access of safe drinking water	1.00	1.00	0.57	0.98	0.96	1.00	1.00	0.98	0.53	Water Scarcity (WS)	0.42	0.39	0.38	0.53	0.44	0.52	0.49	0.39	0.35
Avg. distance to source of natural water	0.05	0.10	0.05	0.10	0.05	0.10	0.20	0.10	0.10										
% of HH experienced scarcity of water	0.60	0.36	0.83	0.88	0.66	0.86	0.65	0.43	0.71										
Avg. money spent by the households to get water	0.04	0.09	0.08	0.16	0.09	0.10	0.13	0.06	0.05										

Continuing from Table 1. Major components, variables (sub-components), and average index values of nine Unions and their LVI values.

Sub- Components	Bajua	Banishanta	Laudobe	Pankhali	Dacope	Koilashganj	Kamarkhola	Sutarkhali	Tildanga	Major Component	Bajua	Banishanta	Laudobe	Pankhali	Dacope	Koilashganj	Kamarkhola	Sutarkhali	Tildanga
% of HH members have loss of income	0.95	1	0.62	0.86	0.98	0.71	0.74	1	0.71	Income Security (IS)	0.46	0.61	0.36	0.51	0.53	0.43	0.53	0.62	0.36
% of HH having income lower than 12000 taka per month	0.41	0.62	0.45	0.35	0.55	0.41	0.72	0.57	0.33										
% of HH loss Income loss for Robbery	0.02	0.21	0	0.33	0.07	0.17	0.13	0.29	0.05										
% of landless HH	0.38	0.33	0.38	0.28	0.36	0.36	0.3	0.5	0.26	Land (L)	0.48	0.53	0.47	0.50	0.51	0.53	0.54	0.57	0.55
% HHs reporting land degradation by climate -related extremes during past 20 years	0.91	1	0.6	0.84	0.93	0.93	0.94	1	0.88										
% of HHs with small land (0.1–0.5 ha)	0.14	0.26	0.43	0.37	0.25	0.29	0.37	0.21	0.52										
% of HH having no Solar energy as a source of electricity	0.19	0.21	0.45	0.33	0.25	0.33	0.37	0.29	0.31	Physical Facilities (PF)	0.24	0.23	0.24	0.19	0.16	0.25	0.20	0.36	0.19
Avg. time to reach nearest primary school	0.32	0.28	0.08	0.03	0.02	0.21	0.04	0.61	0.06										
Avg. time to reach nearest vehicle station	0.19	0.19	0.19	0.19	0.19	0.19	0.19	0.19	0.19										
% of HH having at least one member getting illness due to disaster	0.79	0.98	0.17	0.37	0.05	0.31	0.57	1.00	0.29	Health Services (HS)	0.40	0.48	0.15	0.31	0.26	0.28	0.41	0.55	0.29
Avg. Number of chronically ill persons	0.60	0.98	0.33	0.42	0.36	0.50	0.54	1.00	0.57										
Avg. time needed to reach nearest health facility	0.31	0.31	0.12	0.20	0.52	0.32	0.45	0.22	0.27										
Avg. cost of reaching health facility	0.14	0.12	0.03	0.08	0.16	0.09	0.10	0.10	0.06										
% HH did not immunize their children	0.02	0.00	0.05	0.02	0.09	0.00	0.02	0.02	0.05										
% HH did not receive training on health facilities	0.55	0.50	0.17	0.79	0.39	0.45	0.80	0.95	0.50										
Avg. no. of natural disasters during the last 10 years	0.38	0.48	0.41	0.66	0.66	0.55	0.66	0.86	0.41	Natural Disaster and Climate Variability (ND & CV)	0.61	0.62	0.36	0.58	0.38	0.45	0.54	0.68	0.44
% HH that did not receive a warning about the pending natural disasters	0.00	0.00	0.00	0.00	0.00	0.00	0.00	0.00	0.00										
% of HH reported damaged or Loss of fish in crops, golphata, honey etc.	1.00	1.00	0.53	0.86	0.21	0.76	0.74	1.00	0.53										
% HH reported livestock damaged	1.00	1.00	0.38	0.84	0.82	0.76	0.78	1.00	0.74										
% of HH reported damaged or Loss of fish in ponds/gher	1.00	1.00	0.31	0.84	0.07	0.19	0.72	1	0.55										
Mean standard deviation (MSD) of average maximum temperature by month	0.49	0.49	0.49	0.49	0.49	0.49	0.49	0.49	0.49										
Mean standard deviation (MSD) of average precipitation by month	0.38	0.38	0.38	0.38	0.38	0.38	0.38	0.38	0.38										
LVI	0.509	0.529	0.422	0.507	0.463	0.456	0.487	0.584	0.417										

Source: Authors' calculation, 2026

3.1.4 Food Security (FS):

The fifth key component is food security, which consists of five sub-components that all show a positive relation to vulnerability; the higher the values, the greater the vulnerability. Based on the overall LVI, Dacope was identified as the most vulnerable, with an LVI score of 0.84, followed by Pankhali (0.76) and Sutarkhali (0.71) (Table 1). Tildanga thus has the lowest vulnerability to food security with an LVI value of 0.53.

Field observations show that most unions, excepting a few, are plagued by food security, and Dacope is the worst in terms of acute food scarcity, striving for food roughly 6 to 8 months of the year. The LVI for food scarcity is highest in Dacope, at 0.67, making it the most vulnerable to food scarcity. Sutarkhali, though the second most vulnerable area, has a value of 0.50, where households again have better access to natural resources than the average. Correspondingly, the bottom position is held by Laudobe and Tildanga, each with a value of 0.17, which means food struggle prevails in these areas for a few months of the year.

Savings from crops and access to free fertilizers will reduce food insecurity, lower costs, and improve food safety, thereby reducing household vulnerability. More than 80%, according to Table 1, in all unions either do not receive free fertilizers or cannot save crops for next year, and hence are more vulnerable.

3.1.5 Water Scarcity (WS):

In the coastal area, the crisis of water is enormous. Among them, Pankhali has been found to be the most vulnerable, with an index value of 0.53 (Table 1). Koilashganj is the second-most vulnerable area, with an index of 0.52 (Table 1). On the contrary, Laudobe has been recorded as the least vulnerable area since its water scarcity index is 0.38 (Table 1).

In these seven areas, 90–100% of households lack easy access to safe drinking water. Rainwater collected in plastic tanks and pond water treated with chemicals were the main sources. Though there are sources of water, they are way from the households, between 1 and 5 kilometers, and hence not reachable. Because of this, several households buy water either from the supply line or in bottled form. Above all, the residents of Pankhali bear the highest cost in securing water for consumption. This indicates that these areas are suffering from severe water scarcity, and this calls for a sustainable solution to enable them to access safe water.

3.1.6 Income Security (IS):

Due to climate change, the main sources of income have been hugely destroyed. Besides losses due to climate, robbery, especially in the Dacope area and the Sundarban region of Khulna District, is another concern that adds to economic insecurity. It therefore increases vulnerability because income instability is directly linked to greater vulnerability. Of the three sub-contributors of vulnerability, Sutarkhali bears the highest vulnerability regarding income security with an index value of 0.62, while Banisanta Union follows closely with an index value of 0.61 (Table 1). On the other hand, Laudobe and Tildanga, being in the heart of the upazila, were found to be the least vulnerable with an index value of 0.36 (Table 1). Sutarkhali and Banisanta are the most vulnerable sites, located very near the Sundarban forest and the Bay of Bengal. Because of their geography, they are particularly prone to various types of disasters.

In the studied areas, all households in the most vulnerable location report the rate of income loss due to natural disasters, while more than 90% of households face this problem in other areas. High dependence on natural resources for livelihoods has been coupled with increased natural disasters, which in turn have had a direct and significant impact on household income, further raising vulnerability. On average, more than half of households in the study area had incomes below 12,000 BDT, placing them below the extreme poverty line.

This is further compounded by robbery, which has also contributed to income loss and increased vulnerability in these communities. Of late, the incidence of robbery has decreased and is currently faced by less than 50% of households. In part, this decrease is attributed to livelihood adjustments, whereby many households have moved out of high-risk activities, such as fishing in the Sundarban region, and have concentrated on mainland fishing only. This has brought down their vulnerability to robbery, though the economic challenges remain.

3.1.7 Land (L):

In this case, the vulnerability for the major component of land has been measured using three selected sub-components. The results clearly indicate that Sutarkhali is the most vulnerable area, with an index value of 0.57, and Laudobe is the least vulnerable, with an index value of 0.47 (Table 1).

On average, Sutarkhali Union is characterized by a landlessness rate of 50%. Landlessness puts high-level stress on mental health, increases feelings of insecurity, and lowers coping ability with regard to disaster impacts; thus, it increases overall vulnerability. Over the last 20 years, land degradation has been observed across all study areas, contributing to increased migration. This type of migration, driven by land loss, further adds to the vulnerability of affected households.

In this case, as found in the field survey, a large number of respondents reported that land degradation has been worsening over time, which clearly indicates that land loss remains an ongoing challenge and impacts livelihoods and resilience in these communities.

3.1.8 Physical Facilities (PF):

Share of houses with solar energy, time to reach nearest vehicle station, and time to reach nearest primary school are physical facility subcomponents. These sub-components show that Sutarkhali is the most vulnerable of the nine unions, with an index value of 0.36, and Dacope Union is the least vulnerable, with 0.16 (Table 1). Two of the three energy subcomponents are positively associated with vulnerability, whereas energy access is negatively associated.

Pyra Power Plant near Dacope Upazila provides grid electricity to residents. Solar panels are too expensive for

many homeowners to install. The most vulnerable households for solar panel installation are Bajua, Banishanta, and Sutarkhali (Table 1). Laudobe has the lowest vulnerability at 0.43 (Table 1). The average travel time to the nearest vehicle station is 2 hours and 17 minutes to the nearest primary school. These two subcomponents increased vulnerability.

3.1.9 Health Services (HS)

Six sub-components of the second-to-last main health services component include household health status, distance to health facilities, and healthcare prices. Given these considerations, Sutarkhali Union is the most vulnerable with an index value of 0.55, whereas Laudobe Union is the least vulnerable, with an index value of 0.15 (Table 1).

100% of Sutarkhali families reported at least one person unwell due to disaster or chronic illness. Just 17% of Laudobe residents report this. At least one family member is unwell in 98% of Sutarkhali homes, increasing vulnerability. Because it takes 30–40 minutes to reach the nearest hospital, this lack of access is worse. Poor households are further hampered by healthcare transport fees of 50–100 BDT per person.

Fortunately, nearly 50% of households have immunized their children to decrease health risks. Most homes have not received a single day of health care instruction. In very vulnerable Sutarkhali, 95% of households had no primary health care training. However, certain areas received training, indicating resource and health access and utilization disparity between unions in the research area.

3.1.10 Natural Disaster and Climate Variability (ND & CV):

The final main component, Natural Disaster and Climate Variability, has seven subcomponents. As climatic or atmospheric influences, these sub-components directly affect vulnerability.

Table 1 shows that Sutarkhali Union has the highest natural-disaster and climatic-variability risk index, at 0.68 out of 1. Bajua and Banishanta rank next, with index values of 0.61 and 0.62, respectively. At 0.36, Laudobe has a low vulnerability index. These sites are more susceptible due to climate and natural factors.

Table 1 shows that the Sutarkhali Union averages 26 natural disasters per year. Most unions have over 20 natural disasters per year. According to Table 2, Sutarkhali has a standardised index value of 0.86, while Bajua has 0.38, based on local perceptions. The good news is that, in most cases, the government or NGOs warned people.

It harms fish, animals, crops, golpata, honey, and other resources. Table 1 shows Bajua, Banishanta, and Sutarkhali, which have damage values close to 1, signifying severe disasters.

Mean maximum temperature and mean precipitation had uniform standard deviations of 0.49 and 0.38 in all unions.

3.2 Outcomes of correlation

The correlation matrix of the major components of LVI across the unions of Dacope Upazila is shown in Figure 3.

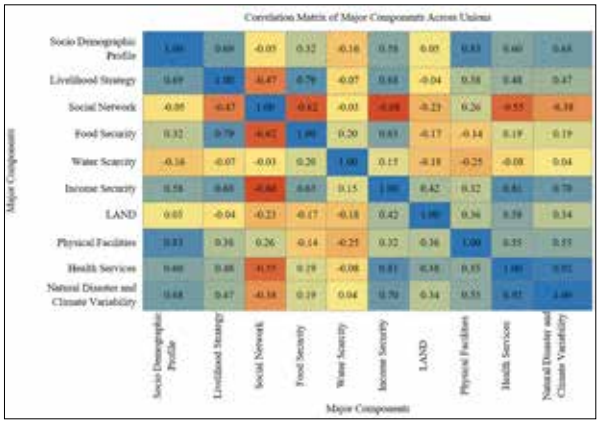

Figure 3. Correlation matrix of major components across unions.
Source: Authors' calculation, 2024

3.2.1 Strong Positive Correlations:

Physical Facilities (PF) and Socio Demographic Profile (SDP) show a strong positive correlation, suggesting that regions with better physical facilities tend to also have higher socio-demographic resilience (Figure 3).

Health Services (HS) and Natural Disaster and Climate Variability (ND & CV) are highly correlated (0.92), indicating that health services are closely linked to vulnerabilities from natural disasters and climate change. Food Security (FS) and Livelihood Strategies (LS) (0.79) also show a strong correlation, suggesting that food security is closely related to livelihood strategies.

3.2.2 Moderate Correlations:

Income Security (IS) and Health Services (HS) (0.81) have a moderate positive correlation, indicating a link between income stability and access to health services (Figure 3). Socio-demographic profile (SDP) and Livelihood Strategies (LS) (0.69) show a moderate correlation, meaning that better livelihood strategies can help improve socio-demographic factors.

3.2.3 Negative Correlations:

Social Networks (SN) and Livelihood Strategies (LS) (-0.47) have a negative correlation, suggesting that stronger social networks might not always align with certain livelihood strategies (Figure 3). Social Networks (SN) and Health Services (HS) (-0.55) also show a negative correlation, suggesting that stronger social networks may not always be associated with better health services.

3.3 Overall LVI in Dacope Upzila:

Among the nine analyzed unions, Sutarkhali is seen as the most vulnerable area to climate change from the total LVI represented in Table 2 with the highest index value of 0.584, followed by Banishanta with an index value of 0.529 and Bajua with a value of 0.509. The subsequent sequence of vulnerabilities includes Pankhali with an LVI of 0.507, followed by Kamarkhola with 0.487, Dacope with 0.463, and Koilashganj with 0.456. In contrast, Tildanga is the least vulnerable, with the smallest index value of 0.417, while Laudobe is the second least vulnerable, with an index value of 0.422. A livelihood vulnerability map is prepared showing the overall LVI score of all the unions of Dacope Upazila and is represented in Figure 4.

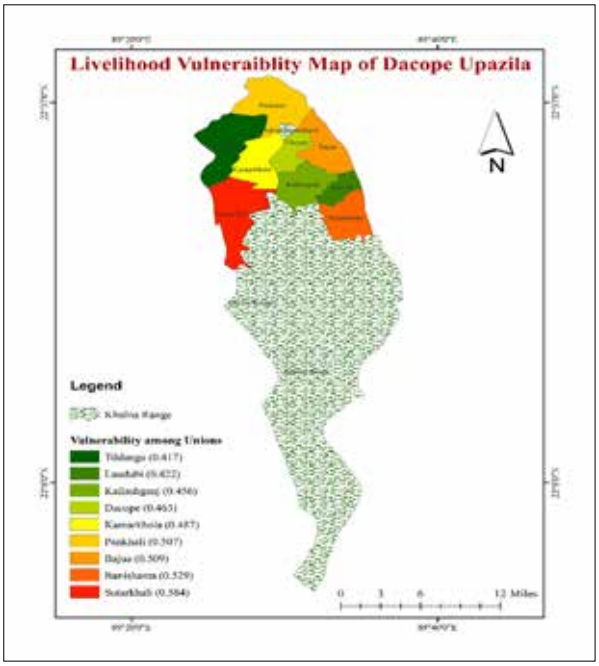

Figure 4. Union-wise livelihood vulnerability map of Dacope upazila

Table 2 shows the ranking of nine representative unions of Dacope Upazila according to their relative ranking of major components of LVI and overall Livelihood vulnerability to climate change. The ranking is based on values derived from the Livelihood Vulnerability Index (LVI), which shows the magnitude of vulnerability a community has to the consequences of climate change. The following is an assessment of the degree of vulnerability of the unions. A score ranging from one to nine has been used, with one representing the least vulnerable and nine the most vulnerable. The Table depicts Sutarkhali as the most vulnerable union in Dacope Upazila across seven major components: socio-demographic profile, livelihood strategies, income security, land resources, physical facilities, health services, and vulnerability to natural disasters and climatic variability. In contrast, Laudobe is the most vulnerable in the case of social networks, Dacope in food security, and Pankhali due to water scarcity.

3.4 LVI-IPCC

Under the LVI-IPCC framework, major components are categorized into three groups: adaptive capacity, sensitivity, and exposure. The socio-demographic profile, livelihood strategies, and social networks—the capacity of a community to adapt to changing conditions—make up the factors which, in turn, comprise adaptive capacity. The second category, sensitivity, consists of food security, water scarcity, income security, land availability, physical infrastructure, and health services. These aspects bring out a community's susceptibility to the impacts of climate change. The third one, exposure, has its key component in only one: natural disasters and climate variability, which estimates a community's degree of exposure to climate-related hazards. By applying the LVI-IPCC formula, these three groups are combined to produce the LVI-IPCC score, ranking areas from most vulnerable to least vulnerable. Results are shown in Table 3:

Table 2. Ranking of vulnerable area for each major component.

Unions	Major Components & Overall LVI										
	Socio-Demographic Profile	Livelihood Strategies	Social Network	Food Security	Water Scarcity	Income Security	Land	Physical Facilities	Health Services	Natural Disaster & Climatic Variability	Overall LVI
Bajua	8	7	4	5	5	4	2	6	6	7	7
Banishanta	7	6	3	6	4	8	5	5	8	8	8
Laudobe	6	3	9	3	2	2	1	7	1	1	2
Pankhali	5	5	6	8	9	5	3	3	5	6	6
Dacope	2	8	1	9	6	6	4	1	2	2	4
Koilashganj	3	4	8	2	8	3	6	8	3	4	3
Kamarkhola	4	2	2	4	7	7	7	4	7	5	5
Sutarkhali	9	9	5	7	3	9	9	9	9	9	9
Tildanga	1	1	7	1	1	1	8	2	4	3	1

Source: Authors' calculation, 2026

Compared with the LVI results in Table 1, the findings in Table 3 indicate that the ranks of the study areas by vulnerability have shifted. Despite an LVI rating of 0.046, Sutarkali remains the most vulnerable area in the region. With an index value of 0.044, Banishanta comes in as the second most vulnerable region after the region already mentioned. The LVI-IPCC value for Bajua is 0.029, which places it in third place. The fourth point is that Pankhali and Kamarkhola, both of which have the identical index value of 0.026, are the most vulnerable sections. With an exceptionally low LVI-IPCC rating of -0.069, Laudobe is the region with the least vulnerability.

Adaptive capacity, sensitivity, and exposure are the three primary categories described in the vulnerability triangle diagram shown in Figure 5. This diagram illustrates the diversity of scores observed across all study areas.

Table 3. LVI value calculated by IPCC definition (-1 least vulnerable) to (+1 most vulnerable).

Major components	Study area									IPCC contributing factors	Study area								
	Bajua	Banishanta	Laudobe	Pankhali	Dacope	Koilashganj	Kamarkhola	Sutarkhali	Tildanga		Bajua	Banishanta	Laudobe	Pankhali	Dacope	Koilashganj	Kamarkhola	Sutarkhali	Tildanga
SDP	0.45	0.45	0.44	0.41	0.36	0.37	0.38	0.56	0.30	Adaptive capacity	0.54	0.53	0.55	0.53	0.50	0.52	0.48	0.60	0.47
LS	0.70	0.68	0.62	0.65	0.71	0.62	0.60	0.73	0.58										
SN	0.53	0.52	0.63	0.56	0.50	0.62	0.51	0.55	0.57										
FS	0.68	0.69	0.61	0.76	0.84	0.55	0.63	0.71	0.53	Sensitivity	0.46	0.50	0.36	0.47	0.46	0.42	0.48	0.54	0.38
WS	0.42	0.39	0.38	0.53	0.44	0.52	0.49	0.39	0.35										
IS	0.46	0.61	0.36	0.51	0.53	0.43	0.53	0.62	0.36										
LAND	0.48	0.53	0.47	0.50	0.51	0.53	0.54	0.57	0.55										
PF	0.24	0.23	0.24	0.19	0.16	0.25	0.20	0.36	0.19										
HS	0.40	0.48	0.15	0.31	0.26	0.28	0.41	0.55	0.29										
NS & CV	0.61	0.62	0.36	0.58	0.38	0.45	0.54	0.69	0.44	Exposure	0.61	0.62	0.36	0.58	0.38	0.45	0.54	0.69	0.44
LVI-IPCC score											0.029	0.044	-0.069	0.026	-0.059	-0.029	0.026	0.046	-0.008

Source: Authors' calculation, 2026

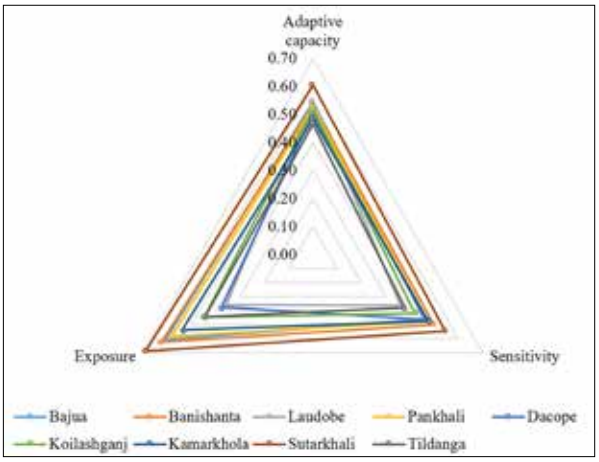

Figure 5. The vulnerability triangle of the components of the Livelihood Vulnerability Index - IPCC (LVI-IPCC) for Dacope Upazila

The comparative degree of vulnerability in the study areas presents sharp dissimilarities from the definition, presented by the IPCC, by its contributing factors, adaptive capacity, sensitivity, and exposure. After scoring, adaptive capacity is highest for Sutarkhali (0.60) and lowest for Tildanga (0.47), indicating stronger socio-demographic resilience, livelihood strategies, and social networks in Sutarkhali. Laudobe also has a relatively higher adaptive capacity, which is 0.55, hence indicating a better potential to cope with changing conditions than areas, like Kamarkhola, standing at 0.48. Sensitivity analysis has given Sutarkhali a value of 0.54; hence, it is the most sensitive area. This implies that the area is most at risk for health, food security, and access to water. It is closely followed by Banishanta at 0.50 and Kamarkhola at 0.48, whereas Laudobe has the lowest sensitivity, with a score of 0.36, making it the least susceptible to these various factors. Sutarkhali is again the most exposed to natural hazards and climate variability, with an exposure score of 0.69, placing it at higher risk due to potential climate impacts. On the other hand, Laudobe is the least exposed in relation to climate-related hazards, with a score of 0.36. Banishanta and Bajua are among the most exposed villages, having scores of 0.62 and 0.61, respectively. Whereas relatively lower exposure can be observed in the villages of Tildanga and Dacope, with scores of 0.44 and 0.38, respectively.

3.5 Differences in mean LVI and LVI-IPCC among unions

Table 4 shows the result from a one-way ANOVA test to compare the difference in mean value among the ten major components of the livelihood vulnerability index.

Table 4. Comparison of mean value of major components of LVI in Dacope.

Variable	Significance (levene statistics)	Sum of square	df	Mean square	F	Significance (P value)
Socio Demographic Profile	0.80	0.279	8	0.035	0.41	0.911
Livelihood Strategies	0.98	0.092	8	0.012	0.34	0.944
Social Network	0.984	0.078	8	0.01	0.13	0.997
Food Security	0.961	0.401	8	0.05	0.55	0.812
Water Scarcity	0.96	0.135	8	0.017	0.09	0.999
Income Security	0.998	0.221	8	0.028	0.21	0.986
Land	0.997	0.027	8	0.003	0.03	1
Physical Facilities	0.865	0.086	8	0.011	0.55	0.807
Health Services	0.256	0.542	8	0.068	0.76	0.638
Natural Disaster & Climate Variability	0.457	0.799	8	1	1.05	0.412

Source: Authors' calculation, 2026

Because the p-value is greater than 0.05, there are no discernible differences in the socio-demographic profiles of the nine unions. As a result, all unions are equally susceptible to socioeconomic factors. For the other major components, the P-values are as follows: livelihood strategies have a value of 0.944, social networks have a value of 0.997, food security has a value of 0.812, water scarcity has a value of 0.999, income security has a value of 0.986, land has a value of 1.000, physical facilities have a value of 0.807, health services have a value of 0.638, and natural disaster and climate variability has a value of 0.412. All of these values are greater than 0.05. The conclusion that can be drawn from this is that there is no statistically significant difference among the unions in these components, suggesting that the unions are equally vulnerable across all dimensions.

It is important to note that Table 5 presents the results of a t-test conducted on a single sample to compare the mean values of adaptive capacity, sensitivity, and exposure. The following is the hypothesis that is tested:

Null hypothesis (H_0): There is no significant difference in the mean value of adaptive capacity, sensitivity, and exposure.

Alternative hypothesis (H_A): There is a significant difference in the mean value of adaptive capacity, sensitivity, and exposure.

The p-values of all components are 0, less than 0.05. This therefore means rejecting the null hypothesis and proves that adaptive capacity, sensitivity, and exposure vary significantly among the nine unions.

Table 5. Comparison of the mean value of adaptive capacity, sensitivity and exposure

One-Sample Te One-Sample Test st						
Test Value = 0						
Value	t	df	Sig. (2-tailed)	Mean Difference	95% Confidence Interval of the Difference	
					Lower	Upper
Adaptive capacity	38.813	8	0.000	0.525	0.493	0.556
Sensitivity	23.472	8	0.000	0.453	0.409	0.498
Exposure	13.429	8	0.000	0.519	0.4298	0.6080

Source: Authors' calculation, 2024

3.6 Livelihood Effect Index (LEI):

The results from the calculation table of LEI shows that the overall LEI score ranges from 0.552, which makes Sutarkhali the most vulnerable area, up to 0.370, which makes Tildanga the least vulnerable one. Other areas, except Laudobe, are moderately vulnerable with close scores: Bajua 0.456, Banishanta 0.491, Pankhali 0.454, Dacope and Koilashganj 0.420, and Kamarkhola 0.445.

Table 6 shows the detailed Livelihood Effect Index values for the study area, indicating human capital as the highest contributing factor with three major components. It shows that Sutarkhali is the most vulnerable of the nine, with a capital value of 0.646, while Laudobe is the least, with a capital value of 0.415. About 55% of the households do not have easy access to health facilities. This area lacks large hospitals, and local markets typically house smaller health facilities far from residential areas, making them accessible to only 48% of households. The time and cost to reach the health facilities are also high compared to the areas with the least vulnerability. This percentage is found in areas located in the center of Dacope Upazila, which are closer to growth centers. In terms of livelihood strategies, the majority of these areas rely heavily on nature-based livelihoods, which are highly vulnerable to environmental conditions.

The second influencing factor comprises three major components: land, water, and natural disasters and climatic variability. Based on natural capital values, Sutarkhali again demonstrates higher vulnerability with a score of 0.579. Conversely, Laudobe remains the least vulnerable area, with the lowest score of 0.389. The scores for the other areas are quite close, as the geographical and economic conditions across Dacope are largely similar. In terms of land ownership, more than or nearly 50% of households do not own land. Additionally, 69% of households in Sutarkhali

Union are at risk from natural disasters and environmental changes.

The fourth capital in LEI is social capital, which is derived from two major components: socio-demographic profile and social networks. According to the table 6, Sutarkhali has the highest vulnerability in terms of social capital with an index score of 0.555, whereas Tildanga has the lowest vulnerability with an index score of 0.423. While Sutarkhali is the most vulnerable area in terms of socio-demographic factors, with a vulnerability score of 56%, Laudobe tops the list for social networks, with a vulnerability score of 63%.

Table 6. Livelihood effect of five capitals in Dacope.

Capital	Major Components	Bajua	Banishanta	Laudobe	Pankhali	Dacope	Koilashganj	Kamarkhola	Sutarkhali	Tildanga
Human	Health	0.40	0.48	0.15	0.31	0.26	0.28	0.41	0.55	0.29
	Livelihood Strategies	0.70	0.68	0.62	0.65	0.71	0.62	0.60	0.73	0.58
	Food	0.68	0.69	0.61	0.76	0.84	0.55	0.63	0.71	0.53
Human Capital Score		**0.564**	**0.598**	**0.415**	**0.544**	**0.564**	**0.449**	**0.529**	**0.646**	**0.438**
Natural	Land	0.48	0.53	0.47	0.50	0.51	0.53	0.54	0.57	0.55
	Water	0.42	0.39	0.38	0.53	0.44	0.52	0.49	0.39	0.35
	Natural Disasters and Climate Variability	0.61	0.62	0.36	0.58	0.38	0.45	0.54	0.69	0.44
Natural Capital Score		**0.528**	**0.535**	**0.389**	**0.549**	**0.425**	**0.487**	**0.526**	**0.579**	**0.438**
Social	Socio-Demographic Profile	0.45	0.45	0.44	0.41	0.36	0.37	0.38	0.56	0.30
	Social Networks	0.53	0.52	0.63	0.56	0.50	0.62	0.51	0.55	0.57
Social Capital Score		**0.486**	**0.482**	**0.526**	**0.478**	**0.424**	**0.484**	**0.439**	**0.555**	**0.423**
Financial	Income	0.46	0.61	0.36	0.51	0.53	0.43	0.53	0.62	0.36
Financial Capital Score		**0.46**	**0.61**	**0.36**	**0.51**	**0.53**	**0.43**	**0.53**	**0.62**	**0.36**
Physical	Physical Facilities	0.24	0.23	0.24	0.19	0.16	0.25	0.20	0.36	0.19
Physical Capital Score		**0.24**	**0.23**	**0.24**	**0.19**	**0.16**	**0.25**	**0.20**	**0.36**	**0.19**
Livelihood Effect Index (LEI)		**0.456**	**0.491**	**0.386**	**0.454**	**0.420**	**0.420**	**0.445**	**0.552**	**0.370**

Source: Authors' calculation, 2024

In conclusion, the two variables that contribute to vulnerability are financial capital and physical capital. With a score of 0.62 for physical capital and 0.36 for financial capital, Sutarkhali is the most vulnerable area and ranks as the most vulnerable neighbourhood overall. The level of income fluctuation in Sutarkhali is rather high; revenue losses are common due to thefts and natural calamities. When it comes to financial capital, Laudobe and Tildanga have a score of 0.36, indicating they are somewhat vulnerable. Dacope remains the area with the lowest vulnerability, with a physical capital score of 0.16. Figure 6 presents a comparison of the Livelihood Effect Index scores of various unions in Dacope Upazila. The following spider diagram summarizes all capital scores.

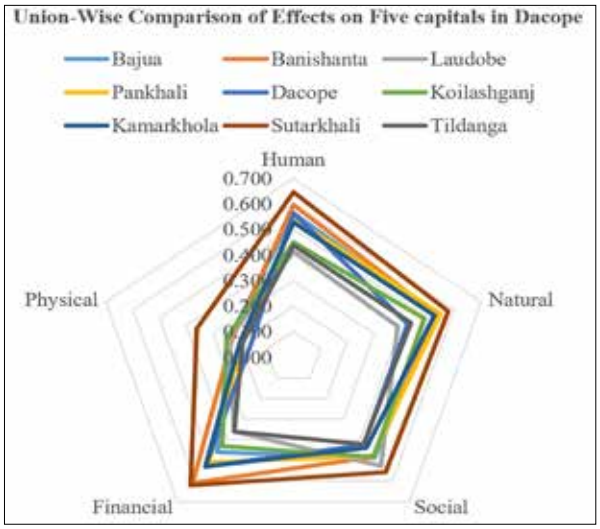

Figure 6. Comparison of the livelihood effect index in nine unions of Dacope

4. Discussion

The findings showed that areas remote from major rivers and forests are more vulnerable than other areas. These findings align with those of Sultana & Hasan (2023), Kayes et al. (2025), and Akram et al. (2025). Their identified vulnerable areas are also close to the sea, river, and forest. The findings of our study indicate that significant indicators, including food security, education, water scarcity, income insecurity, access to health services, exposure to natural disasters, and climate variability, are critical factors contributing to heightened vulnerability. According to Jui (2021), educational institutions in the coastal regions of Bangladesh encounter numerous obstacles stemming from recurrent natural disasters, the effects of climate change, and socio-economic vulnerabilities. This report also supports our findings.

The findings of this study strongly highlight that livelihood vulnerability is a multidimensional concept. Therefore, the local government and local NGOs alone cannot improve the community's livelihoods in Dacope Upazila. Effective collaboration among multiple government agencies and international NGOs, along with local governments and NGOs, can ensure the community's resilience, adaptive capacity, and sustainable mitigation strategies. Considering this importance, an action plan is provided in Figure 7, which includes the policy for specific wings of the government and NGOs. Where policy sections are symbolized as Slot1-4, which is discussed below in Figure 7.

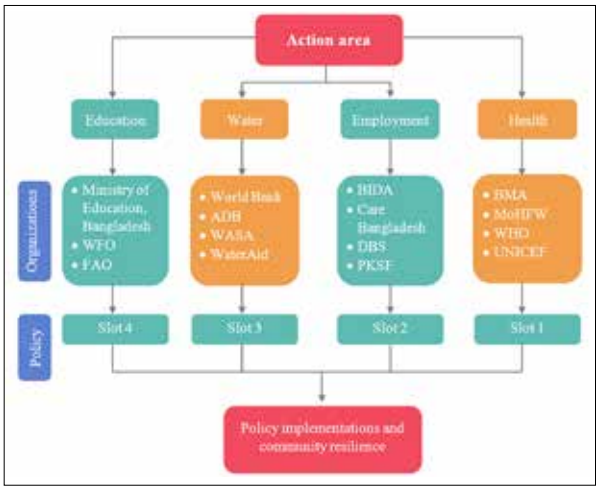

Figure 7. Action plan for climate resilience.

Slot-1: The World Health Organization (WHO), UNICEF, the Ministry of Health and Family Welfare (MoHFW), and the Bangladesh Medical Association (BMA) will work together to make sure the suggested policies are carried out. It is suggested that medical students be required to complete an internship in a seaside area after completing their final year of study. While the other organizations will provide financial, management, and coordination support, the BMA will be in charge of regulating this process.

Slot-2: The Bangladesh Investment Development Authority (BIDA), Care Bangladesh, Daridra Bimochon Shangstha (DBS), and Palli Karma-Sahayak Foundation (PKSF) are set to work together to enhance employment opportunities and diversify livelihoods in coastal regions. BIDA will spearhead the establishment of industries in these regions, while DBS will streamline access to loans. Care Bangladesh is committed to upholding transparency and accountability in the functions of both BIDA and DBS. Furthermore, PKSF will offer training and assistance for the overseas export of manpower.

Slot-3: The World Bank, Asian Development Bank (ADB), WASA, and WaterAid are joining forces to guarantee the availability of clean and sufficient water for the community. The project will receive funding from ADB and the World Bank, with WASA taking the lead in water purification efforts and ensuring access to clean water in vulnerable areas. WaterAid will assist WASA in implementing the project, maintaining transparency and accountability at every stage of the process.

Slot-4: The Ministry of Education in Bangladesh, along with the World Food Organization and the Food and Agriculture Organization, will work together to guarantee that everyone has access to fundamental education. The Ministry of Education plans to integrate disaster preparedness and response education into the school curriculum. The WFO and FAO will facilitate the implementation of current policies to ensure food provision for children in educational institutions. Furthermore, there will be ongoing workshops focused on disaster preparedness and essential actions at the community level throughout the year.

5. Conclusion

To assess how vulnerable different populations are to the consequences of climate change, this study used the LVI, LVI-IPCC, and LEI techniques. Every tactic provides an in-depth analysis of the factors that make people's ability to survive in a particular area so unstable. The goal in developing the LVI and LVI-IPCC calculation algorithms was to make them accessible to a wide audience in a variety of settings. More information can be found by using vulnerability spider and triangle diagrams to compare two or more research zones. Notable shortcomings of our methodology include the following: the subjective nature of sub-component selection; the inherently bidirectional nature of the sub-components' relationship to vulnerability; the masking of extreme values through the use of index calculation methods; and the possibility of selection bias as a result of the exclusion of vacant homes from the sample. What follows is a more in-depth discussion of each of these difficulties. To better understand how exposure, adaptability, and sensitivity evolve with the implementation of adaptation mechanisms, this study could be repeated in the same region at different intervals. To get a more accurate assessment of social ties in future research, it may be necessary to enhance the Social Networks and Natural Capacity subcomponents. It is also possible to assess the vulnerability of neighbourhoods using the LVI method. One useful instrument for city planners is the Livelihood Vulnerability Index (LVI). By doing so, they may determine which industries are most at risk from the impacts of climate change on local residents' livelihoods and work to mitigate those impacts. Furthermore, this study will provide a valuable resource for understanding the health,

socioeconomic, and demographic factors that influence climate sensitivity on a local or regional scale. Everyone from parliamentarians to development organizations and public health experts can use this tool to their advantage.

Knowledge Contribution:

This study presents the Livelihood Effect Index, a metric that has not been examined in prior investigations. Furthermore, the study presents a detailed action plan, specifying policies, institutions, and responsibilities to aid policymakers and government officials in decision-making, which can be used in other coastal areas of Bangladesh as well. This study addresses a significant gap left by previous investigations by providing a well-defined action plan for effective implementation.

Limitations of the study:

Historical rainfall and temperature data from the Bangladesh Meteorological Department are sparse, and most are unavailable or not readily accessible.

Further areas of research:

Future studies may focus on implementing the action plan, particularly on estimating the costs associated with each project, as significant capital is required for effective implementation. Furthermore, working alongside international organizations requires careful consideration and demands a high level of transparency. Future investigations could examine how the government will collaborate with international partners on these initiatives and identify which policies might affect national interests.

Declaration of Conflicting Interests:

The authors declared no potential conflicts of interest with respect to the research, authorship, and/or publication of this article.

Authorship contribution statement:

- Md. Kamrul Hasan: Conceptualization, investigation, data curation, methodology, software, and writing-original draft.
- Md. Mizanur Rahman: Resources, supervision, writing, review, and editing, and validation.
- Abu Nayem Md. Kayes: Formal analysis, writing-original draft, data presentation, software, and methodology.

Declaration of Conflicting Interests:

The authors declared no potential conflicts of interest with respect to the research, authorship, and/or publication of this article.

Ethics Statement:

Ethics approval was obtained from the Ethics Committee of the Department of Urban and Regional Planning, Pabna University of Science and Technology (Bangladesh). In addition, the participants provided their informed consent to participate in this study.

Acknowledgements:

We would like to express our heartfelt gratitude to all the individuals who generously shared their valuable insights, experiences, and data that were integral to the success of this research. We are also profoundly grateful to the University Grants Commission (UGC) for its financial assistance in funding this research.

References

Adu, D.T.; Kuwornu, J.K.M.; Anim-Somuah, H. & Sasaki, N. (2018). Application of livelihood vulnerability index in assessing smallholder maize farming households' vulnerability to climate change in Brong-Ahafo region of Ghana. Kasetsart J. Soc. Sci., 39, 22–32.

Ahmed, A., Abedin, M. A., & Rahman, M. M. (2019). Impacts of salinity intrusion on livelihoods in the southwest coastal region of Bangladesh. Environmental Management, 54(4), 1234-1245.

Akram, A., Tahir, A., Alam, A., & Waheed, A. (2025b). Livelihood vulnerability index: Assessment of climatic changes in flood affected areas of Mianwali district, Punjab, Pakitan. PLoS ONE, 20(3), e0315398. https://doi.org/10.1371/journal.pone.0315398

Alam, E., & Rabbani, G. (2015). Climate Change and Vulnerability in the Coastal Areas of Bangladesh. International Journal of Climate Change Strategies and Management, 7(2), 261-275.

Alam, M. Z., Carpenter-Boggs, L., Mitra, S., Haque, M. M., Halsey, J., Rokonuzzaman, M., Saha, B., & Moniruzzaman, M. (2017). Effect of salinity intrusion on food crops, livestock, and fish species at Kalapara Coastal Belt in Bangladesh. Journal of Food Quality, 2017, 1–23. https://doi.org/10.1155/2017/2045157

Ali, A. (2018). Assessing the Impacts of Climate Change on Livelihoods in Coastal Bangladesh Using the Livelihood Effect Index. Environmental Science & Policy, 88, 62-72.

Ali, A. (2019). Adaptation to climate change in Bangladesh: Future prospects and challenges. Asian Journal of Environment and Disaster Management, 11(2), 85-92.

Bangladesh Bureau of Statistics. (2011). Housing and population census 2011. Ministry of Planning, Government of the People's Republic of Bangladesh.

Chowdhury, K. J., Ali, M. R., Chowdhury, M. A., & Islam, S. L. U. (2024). Climate change induced risks Assessment of a coastal area: A "Socioeconomic and Livelihood Vulnerability Index" based study in Coastal Bangladesh. Natural Hazards Research. https://doi.org/10.1016/j.nhres.2024.06.005

Dasgupta, S., Hossain, M. M., Huq, M., & Wheeler, D. (2015). Climate change vulnerability in Bangladesh's southwest coastal region. World Bank Policy Research Working Paper, (2148), 21-29.

Ellis, F. (2000). Rural livelihoods and diversity in developing countries. Oxford University Press.

Hahn, B. M., Riederer, A. M., & Foster, S. O., 2009. The Livelihood Vulnerability Index: Apragmatic approach to assessing risks from climate variability and change—A case study in Mozambique. Global Environmental Change, 74-78

Haque, A. N., Dodman, D., & Hossain, M. M. (2014). Individual, communal and institutional responses to climate change by low-income households in Khulna, Bangladesh. Environment and Urbanization, 26(1), 112–129. https://doi.org/10.1177/0956247813518681

Hasan, K., Rahman, M., & Kayes, A. N. (2025d). Comprehensive assessment of local climate change adaptation with provision of sustainable adaptation plan in South-West Coastal region of Bangladesh: A study on Dacope Upazila, Khulna. Progress in Disaster Science, 100425. https://doi.org/10.1016/j.pdisas.2025.100425

Huong, N.T.L., Yao, S. & Fahad.S. (2019). Assessing household livelihood vulnerability to climate change: The case of Northwest Vietnam. Human and Ecological Risk Assessment: An International Journal, 25:5, 1157-1175, doi: 10.1080/10807039.2018.1460801.

Huq, S., & Hossain, M. (2015). Climate Change and Bangladesh: An Overview. Climate Change and Adaptation, 1(1), 1-15.

IPCC. (2014). Climate Change 2014: Impacts, Adaptation, and Vulnerability. Contribution of Working Group II to the Fifth Assessment Report of the Intergovernmental Panel on Climate Change.

IPCC. (2021). Sixth Assessment Report. Intergovernmental Panel on Climate Change.

Islam, M. R., & Hasan, M. R. (2016). Climate-induced displacement and migration in Bangladesh. Dhaka: Bangladesh Institute of Development Studies.

Jui, U. (2021, June 28). How Climate Change is Undermining Education in Coastal Areas of Bangladesh. The Business Standard. Retrieved September 25, 2025, from https://earthjournalism.net/stories/how-climate-change-is-undermining-education-in- coastal-areas-of-bangladesh

Kabir, M. A., Hossain, M. K., Hossain, M. A., Molla, M. O. F., Khatun, M. S., & Jamal, M. a. H. M. (2024). Impact of water and soil salinity on coastal agriculture in Bangladesh: Insights and mitigation Strategies. American Journal of Multidisciplinary Research and Innovation, 3(4), 36–48. https://doi.org/10.54536/ajmri.v3i4.2927

Kabir, M. A., Hossain, M. K., Hossain, M. A., Molla, M. O. F., Khatun, M. S., & Jamal, M. a. H. M. (2024). Impact of water and soil salinity on coastal agriculture in Bangladesh: Insights and mitigation Strategies. American Journal of Multidisciplinary Research and Innovation, 3(4), 36–48. https://doi.org/10.54536/ajmri.v3i4.2927

Kabir, R., Khan, H. T., Ball, E., & Caldwell, K. (2016). Climate change impacts on the livelihoods of rural Bangladeshis: A spatial and gender analysis. Environmental Hazards, 15(2), 173-183.

Kayes, A. N. M., Pramanik, M. A., & Mim, R. S. (2025). Assessing industrial linkage and strategic locations for sustainable economic development: A case study in North Corridor of Bangladesh. Journal of Urban Management. https://doi.org/10.1016/j.jum.2025.08.003

Kayes, M. a. N., Tabassum, T., & Khan, M. a. M. R. (2025h). Assessment of Climate- Induced vulnerabilities and poverty alleviation Potential of dry fish Industry: An Ecological and Socio-Economic study in Cox's Bazar District, Bangladesh. International Journal of Disaster Risk Management, 7(1), 461–483. https://doi.org/10.18485/ijdrm.2025.7.1.26

Koirala, S. (2015). Livelihood Vulnerability Assessment to the Impacts of Socio- Environmental Stressors in Raksirang VDC of Makwanpur District Nepal. Master 's Thesis, The Department of International Environment and Development Studies, Noragric, Norwegian University of Life Sciences, Trondheim, Norway. 2015.

Nguyen, Y.T.B., Leisz, S.J. (2021). Determinants of livelihood vulnerability to climate change: two minority ethnic communities in the northwest mountainous region of Vietnam. Environ. Sci. Policy 123, 11–20. doi:10.1016/j.envsci.2021.04.007, March.

Phuong, T. T., Tan, N. Q., Dinh, N. C., Van Chuong, H., Ha, H. D., & Hung, H. T. (2022). Livelihood vulnerability to climate change: Indexes and insights from two ethnic minority communities in Central Vietnam. Environmental Challenges, 10, 100666. https://doi.org/10.1016/j.envc.2022.100666

Piya, L., Maharjan, L.K., Niraj, J. (2012). Vulnerability of rural households to climate change and extremes: Analysis of Chepang households in the Mid-Hills of Nepal. In Proceedings of the International Association of Agricultural Economists (IAAE) Triennial Conference, Foz do Iguaçu, Brazil, 18–24.

Population and Housing Census 2022. (2024). In Bachelor of Business Studies. Retrieved May 8,2025,from http://nsds.bbs.gov.bd/storage/files/1/Publications/PHCensus/Khulna/District%20Rep ort%20khulna.pdf

Rahman, M. O., & Rahman, A. K. M. A. (2022). Adaptation Strategy with Climate Induced Salinity Disaster in the Coastal Area of Bangladesh. American Journal of Climate Change, 11(04), 284–306. https://doi.org/10.4236/ajcc.2022.114014

Rahman, M., Sultana, P., & Islam, S. (2020). Impacts of Climate Change on Coastal Livelihoods: Evidence from Bangladesh. Environmental Sociology, 8(2), 93-104.

Rahman, M.M. (2014). Community Perceptions and Adaptation to Climate Change in Coastal Bangladesh. Ph.D. Thesis, Curtin University, Bentley, Australia.

Riantini, M., Mardiharini, M., Saptana, N., Sudjarmoko, B., Kasymir, E., Nur'aini, L. G., Anindita, S. H., Syukur, M., Zulham, A., Wardono, B., Ardana, I. K., Indrawanto, C., & Wahyudi, A. (2024). Livelihood vulnerability household fishermen household due to climate change in Lampung Province, Indonesia. PLoS ONE, 19(12), e0315051. https://doi.org/10.1371/journal.pone.0315051

Sarker, M. A., Parveen, S., & Rahman, M. (2019). Coastal Agriculture under Climate Stress: A Study on Salinity and Waterlogging in Bangladesh. Agricultural Systems, 176, 102703.

Scoones, I. (1998). Sustainable rural livelihoods: A framework for analysis. IDS Working Paper No. 72. Institute of Development Studies.

Scoones, I. (2009). Livelihoods Perspectives and Rural Development. The Journal of Development Studies, 34(1), 79-99.

Shah K.U., Dulal H.B., Johnson et al. (2013). Understanding livelihood vulnerability to climate change: Applying the livelihood vulnerability index in Trinidad and Tobago. Geoforum 47:125–137. doi. org/10.1016/j.geoforum.2013.04.004.

Sullivan, C. A., and Meigh, J. R. (2005). Targeting attention on local vulnerabilities using an integrated index approach: The example of the Climate Vulnerability Index. Water Science and Technology, 51(5), 69-78.

Sultana, N., & Hasan, M.K. (2024). Identifying Climate Scenarios and an Index-Based Assessment of Household Vulnerability to Climate Change in the South-West Coastal Region of Bangladesh. Jordan Journal of Earth and Environmental Sciences, 15(2), 136-145.

Swarnokar, S. C., Mou, S. I., Sharmi, S. D., Iftikhar, A., & Jesmin, S. (2025b). Climate-induced risks, adaptation, and mitigation responses: a comparative study on climate-stressed coastal communities. Frontiers in Climate, 7. https://doi.org/10.3389/fclim.2025.1553579

Tewari, H.R. & Bhowmick, P.K. (2014). Livelihood vulnerability index analysis: An approach to study vulnerability in the context of Bihar. Jamba J. Disaster Risk Stud., 6, 1–13.

Thorpe, W., Erenstein, O., Singh, J. & Varma, A. (2007). Crop–Livestock Interactions and Livelihoods in the Gangetic Plainsof Bihar, India; International Livestock Research Institute: Nairobi, Kenya.

Toufique, A.K.; Yunus, M. (2013). Vulnerability of Livelihoods

in the Coastal Districts of Bangladesh; Development Studies, Bangladesh Institute of Development Studies (BIDS): Dhaka, Bangladesh. Volume 36, pp. 95–120.

Yamane, Y. (1967). Mathematical Formulae for Sample Size Determination.

JJEES

JJEES (2026) 17 (2): 155-166
ISSN 1995-6681

Jordan Journal of Earth and Environmental Sciences

Assessing Organic Carbon Stocks and Soil Quality in Response to Agroforestry Intervention

Anthony Tobore [1*], Noah Oyebamiji[2], Abdussalaam Sadiq[3], Ugonna C. Nkwunonwo[4], Ganiyu Oyerinde[5], Akinola Adesuji Komolafe[6]

[1] Department of Soil Science and Land Management, Federal University of Agriculture, Abeokuta, Abeokuta, Ogun State, Nigeria
[2] Department of Forestry Resource Management, Federal University of Agriculture, Abeokuta, Abeokuta, Ogun State, Nigeria.
[3] Department of Environmental Management and Toxicology, Federal University of Agriculture, Abeokuta, Abeokuta, Ogun State, Nigeria.
[4] Department of Geo-informatics and Surveying, Faculty of Environmental Studies, University of Nigeria, Enugu Campus, Nigeria.
[5] Department of Soil Science, Faculty of Agriculture, University of Abuja, Nigeria.
[6] Department of Remote Sensing and Geoscience Information System, Federal University of Technology, Akure, Nigeria

Received on 17 May 2025; Accepted on 15 October 2025

Abstract

Addressing the impacts of climate change on food security and poverty alleviation requires urgent action by institutions, such as the Federal University of Agriculture, Abeokuta (FUNAAB), Nigeria. Through its agroforestry initiatives, FUNAAB can play a vital role in promoting carbon sequestration and enhancing food production, thereby contributing to the achievement of Sustainable Development Goal 2 (Zero Hunger) by 2030. This study assessed Soil organic carbon (SOC) stock and soil quality within FUNAAB's agroforestry plots using geospatial techniques. Soil samples were collected at 0–20 cm depth across various topographic positions and analyzed for their physico-chemical properties. A dendrogram cluster and correlation matrix were employed to evaluate the spatial distribution of soil. The result of the soil quality index demonstrated that the studied soil was good (0.8), fair (0.6 – 0.4), and poor (< 0.4), approximately covering 249.4 (good), 51.9 (fair), and 5.6 (poor) hectares of the area. Consequently, SOC stocks of the area ranged from 124.41 to 59.22, 59.23 to 29.38, and 29.38 to 7.35 Mg C ha−1. The findings from this study concluded that soil nutrient management, like farmyard manure, should be adopted and tailored towards site-specific application to improve soil health and increase carbon stocks of the studied area. Further research on total SOC stocks beyond top-soils and various soil quality indices is necessary and expedient for specific and global empirical evidence to mitigate climate change pressures and ensure sustainable food production.

Keywords: *Soil degradation; Climate change; Cluster analysis; Above-ground biomass: FUNAAB Agroforestry*

1. Introduction

Agroforestry (AGF) is a land-use system that integrates trees with pastures and livestock (silvopastoral), aquatic farming (aquasilviculture), or combinations of trees, crops, and livestock (agrosilvopastoral) to deliver both environmental and socio-economic benefits (Shin et al., 2020; Sinclair, 1999). AGF plays a critical role in safeguarding terrestrial ecosystems, enhancing soil health, and promoting carbon sequestration (Stockmann et al., 2015; Pandit et al., 2013). However, its degradation presents significant threats to environmental sustainability and ecological resilience (Watson et al., 2000; Lal & Stewart, 2019). The extent and direction of climate change impacts on AGF systems remain uncertain, particularly in tropical developing countries (FAO, 2022). Ecosystem degradation, rapid population growth, and unplanned infrastructural development (Thapa, 2020) continue to intensify environmental deterioration at local, regional, and global scales (Chervier et al., 2024). These disruptions not only lead to ecological imbalances (Lal et al., 2012; MEA, 2005) but also significantly alter soil biogeochemical cycles (Zhang et al., 2019; Maharjan et al., 2024). This challenge is especially pronounced in Nigeria (Orobator, 2025), where unsustainable practices, such as extensive bush burning, high carbon dioxide (CO_2) emissions, and widespread land mismanagement are undermining both environmental and human well-being. These pressures contribute to the broader global crisis affecting an estimated 3.2 billion people, as linked to climate change vulnerabilities (Nayak et al., 2019; Lal, 2004).

Notably, AGF degradation is reported to affect 40% of Earth's areas (FAO/UNCCD 2022). The impacts of climate change on AGF systems have been evident for decades, contributing to the depletion of critical natural resources such as soil, air, and water (Obeidat & Awawdeh, 2021; Schuldt et al., 2020; Neumann et al., 2017; Lindner et al., 2014). As climate change intensifies, the need to preserve and expand green space becomes increasingly urgent to reduce atmospheric carbon levels and enhance AGF systems and their landscapes (Schelhas & Hitchner 2020). The connection between AGF and organic carbon sequestration is well-established, highlighting its significant role in climate change mitigation (Roose et al., 2015). There is a pressing need to address the multiple threats facing AGF systems ranging from natural factors such as topography, vegetation cover, and soil types to anthropogenic pressures including overgrazing, deforestation, and unsustainable agricultural practices (Guha et al., 2022; Lal, 2005; Tchotsoua, 1994; United Nations, 2014). Previous studies, conducted in tropical AGF regions,

* Corresponding author e-mail: anthonytobore@gmail.com

have reported considerable improvements in soil physical, chemical, and biological properties (Ofomola et al., 2024; Cardinal et al., 2017; Khaine & Woo, 2018; Ovung et al., 2021). Nevertheless, soil quality, within AGF systems, continues to decline across temporal and spatial scales (Lal, 2004; Fahad et al., 2022; Udawatta & Jose, 2012; Asabere et al., 2018). While AGF soils serve as vital reservoirs for organic carbon, the concurrent decline in food productivity particularly in sub-Saharan Africa presents a major challenge (Henry et al., 2009; Sharma et al., 2024; Tobore et al., 2024). Therefore, a comprehensive evaluation of AGF soil conditions is essential to support ecosystem resilience and promote sustainable food production (Ofomola et al., 2024; Tobore et al. 2021).

Advancements and innovations in modern technology have positioned Geographical Information Systems (GIS) as indispensable tools for analyzing spatial and temporal distributions of soil physical, chemical, and biological properties across natural and human-altered landscapes (Hengl et al., 2018; Zhang et al., 2016). Globally, GIS has empowered researchers to visualize complex historical landscapes and identify escalating ecological threats that could undermine ecosystem biodiversity and stability (Breiman, 2001). As a widely adopted approach for evaluating spatial point data, GIS enhances the precision of environmental assessments by reducing analytical uncertainty and improving sustainability metrics (Hengl et al., 2018; Breiman, 2001). In this context, the use of GIS to evaluate critical agroforestry (AGF) resources, particularly Soil Organic Carbon (SOC) stocks, has become a rational and non-trivial methodological advancement, offering a data-driven pathway for monitoring soil health and supporting climate-resilient land management practices (UNCCD, 2015).

Balancing the need between AGF and SOC stocks is a delicate global challenge (UNCCD, 2015). SOC represents the second-largest carbon reservoir on Earth, playing a critical role in enhancing agricultural productivity and supporting a healthy environment. However, understanding the contribution of AGF soils to carbon storage has become increasingly vital, especially in sub-Saharan Africa, where natural and unchecked human activities continue to degrade AGF systems (Lal, 2005; UNCCD, 2015; Jumaah et al., 2019). Addressing the impact of climate change on food security and poverty alleviation calls for immediate attention of the Federal University of Agriculture, Abeokuta (FUNAAB), Nigeria, through its Agroforestry landscape to facilitate carbon sequestration for a healthy environment and promote optimum food production to meet the Sustainable Development Goal (SDG 2) by 2030. Ultimately, spatially explicit information on safe and healthy food productivity is crucial for assessing soil quality and SOC stocks in the AGF to promote a healthy environment, and sustainability extends beyond the specific findings in the FUNAAB landscape. The study's objectives were to assess (i) soil quality of the area and (ii) evaluate the dynamics of SOC stocks. These insights are expected to support evidence-based local land management policies and contribute broadly to the global knowledge base on AGF and climate-resilient agriculture.

2. Methodology

2.1 Description of study area

The study area, encompassing a total area of 307 hectares (ha), is geographically situated within the Federal University of Agriculture, Abeokuta Agroforestry landscape, bounded by latitudes 7° 19' to 7° 26' and longitudes of 3° 42' to 3° 46'. The terrain features a mix of undulating and flat topography, interspersed with river valleys and seasonal depressions (Ufoegbune et al., 2010). Soil in the area are predominantly Ferric Luvisols, Ferric Cambisols, and Ferric Lixisols (Figure 1), while lowland areas are dominated by Gleyic Luvisols and Lithosols, which are subject to seasonal waterlogging and are generally less gravelly (Soil Science Division Staff, 2017; FAO, 2015; Tobore et al., 2025). The underlying geology is composed of basement complex rocks, with the region experiencing a humid tropical climate characterized by distinct wet and dry seasons (Smyth and Montgomery, 1962). Annual standardized precipitation index (SPI) revealed moderate and very-wet years of the area (Tobore et al., 2021) predominantly occupied by Tectona grandis, and Gmelina arborea (Figure 2).

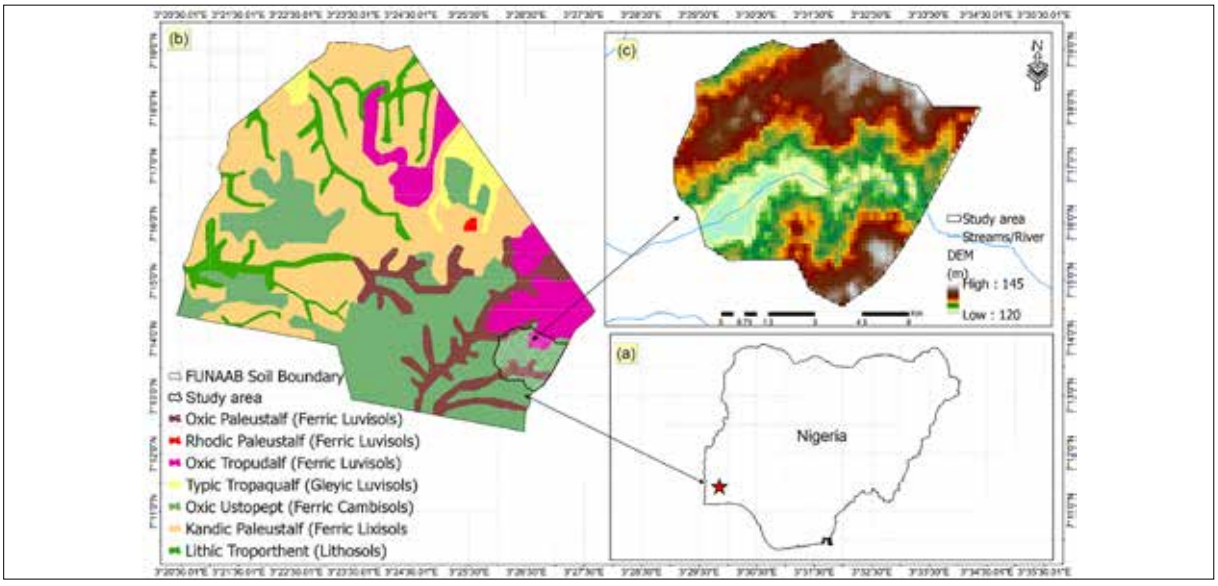

Figure 1. (**a**) Nigeria boundary enclosing FUNAAB as spot (**b**) map of FUNAAB showing soil types modified (Tobore et al,. 2025) and (**c**) study area digital elevation model extracted along the existing rivers and roads network

Figure 2. An example of Agroforestry components of the area

2.2 Soil sampling and design

A modified sampling design by Agroforestry (2023) was adopted to assess soils of the area (Vagen et al. 2013). Soil samples were collected using a grid pattern nested hierarchical approach (FAO, 2007). Sampling design was enabled to cover the studied area terrain and distribution of soil. A total of 48 soil samples were sampled through "create random point". The "create random point" through ArcGIS 10.5 toolbox was employed for statistical representativeness of the studied area for assessing soil properties including total nitrogen, soil pH, particle size distributions, available phosphorus, potassium and organic carbon (Table 1).

Surface soil were sampled from 0 to 20 cm depths along predominant toposequence to capture organic carbon sequestration potential an essential factor for understanding crop productivity and soil health (Sun et al., 2010; Gao et al., 2008). Additionally, three pedological pits (2 m × 1.5 m × 2 m) were excavated on representative slopes, with samples taken from bottom to top to prevent contamination, as recommended by FAO (2009). Elevation mapping was performed using a 30-meter resolution Shuttle Radar Topography Mission (SRTM) Digital Elevation Model (DEM), which helped classify the landscape into three distinct topographic zones (see Fig. 1). In-field assessments included soil structure, color, root concentration, and consistency following standard FAO procedures (2009). Soil bulk density was determined using a core ring sampler (7 cm diameter × 7 cm length) from undisturbed soil at 0–20 cm depth. Latitude and longitude geographic coordinates for representative soil samples were captured by Global positioning system device at <5 m. Subsequently, well labeled zip-locks polythene was used to collect samples for air-drying at controlled room temperature.

Table 1. Methods of soil properties analysis

Soil condition	Method
Total nitrogen	Kjeldahl method (Bremner & Mulvaney, 1982)
Soil texture	Hydrometer method (Gee & Bauder, 1986)
Soil pH	Potentiometry/ Glass calomel pH meter (McLean, 1982)
Organic carbon	Walkley and Black method (Nelson & Sommers, 1983)
Available phosphorus	Colourimetric after extraction with Bray 1 solution (Bray & Kurtz, 1945).
Potassium	Flame Photometer method (Thomas, 1983)
Bulk density	Core sampling method (Blake & Hartege, 1986)
Soil organic matter	Van Bemmelen factor of 1.724
ECEC	Summation of exchangeable cations and acidity
Base saturation	Summation of exchangeable bases divide by ECEC multiply by 100

ECEC: Effective cation exchanged capacity

2.3 Derived soil degradation parameters

In the study, soil vulnerability was assessed using Soil structural stability (SSSI), and Soil susceptibility (CSOM) degradation index (Serme et al., 2015). These two indices denote risk confronting SOC depletion and soil sensitivity to erosion (Isikwue et al., 2012).

SSSI

SSSI is a successful stable index used to assess aggregate resistance of soils after the degree of disruptive forces (Pieri, 1992). In this study, SSSI is expressed as proportion between soil organic carbon and fine soil particles of soil medium (Eq. 1). Consequently, the ranges between < 5% and 7% > values reflect low risk of structurally degraded soils and 7% represent high risk of soil structural degradation while >9% depict SOC with sufficient soils structural stability (Pieri, 1992).

$$SSSI = \frac{1.724\,SOC\ (\%)}{\text{Clay}\ (\%) + Silt\ (\%)} \times 100 \quad (1)$$

where SSSI is the soil structural stability index, SOC represent soil organic carbon.

CSOM

CSOM is a crucial indicator used to evaluate soil sensitivity to erosion (Brady et al., 2008; Pieri, 1992). In this study, CSOM was utilized to assess soil resistance to degradation based on Equation 2. CSOM values below 5% indicate soils that are highly susceptible to erosion, characterized by loose soil structure prone to rapid degradation. Values ranging between 5% and 7% reflect moderate susceptibility, suggesting partially stable structure but still vulnerable under stress conditions. Conversely,

CSOM values of 9% or greater indicate stable soil structures with enhanced resistance to erosion, indicating improved soil health and resilience to environmental pressures.

$$CSOM = \frac{SOM}{[\text{Clay (\%)} + Silt\ (\%)]\ content} \quad (2)$$

where (% Clay + % Silt) content value was obtained from soil texture classification, and SOM was converted (1.724) from the SOC data.

2.4 SOC stocks and soil quality development for the study area

In this study, SOC stocks of the area were calculated by (t ha-1) multiplying SOC (%) concentrations by respective bulk density (g/cm3) multiplied by soil depths (0 to 20 cm). Above-ground (AG) biomass in the studied area was estimated using an algorithm (Eq. 3) described by Chave et al. (2005). Additionally, AG biomass of saplings (Eq. 4) was assessed through the formula described by Haase and Haase (1995). On one hand, the study employed the soil quality index (SQI) to assess the soil quality of the area (Eq. 5) through a formula described by Bajracharya et al. (2006).

$$AGTB = 0.0509 * p\ D^2\ H \quad (3)$$

where AGTB = above-ground tree/pole biomass (kg), = Wood specific gravity (g cm− 3) as expressed by Jackson (1994) for each species, D = tree diameter at breast height (cm), H= tree height (m).

$$Y = aD^b \quad (4)$$

where Y denotes the total dry biomass (kg), D is the diameter at 15 cm above the ground (cm), and 'a ' and 'b' are the constant values represented as 4.264 and 1.0232, respectively.

$$SQI = [(a \times RSTC) + (b \times RpH) + (c \times ROC) + (d \times RNPK)] \quad (5)$$

where RSTC = assigned ranking values for soil textural class, RpH = assigned ranking values for soil pH, ROC = assigned ranking values for SOC, RNPK = assigned ranking values for nitrogen (N), potassium (K) and phosphorus (P). a = 0.2, b =0.1, c = 0.4 and d = 0.3.

3. Spatial distributions of soil properties and quality using GIS-based approach

GIS is a user-friendly technology employed to assess spatial variations of soil properties across extensive geographic areas (Zhang et al., 2019). In this study, the coordinates of the analyzed soil concentrations were interpolated using the Inverse Distance Weighted (IDW) technique in ArcGIS 10.5 (Li and Heap, 2008). IDW offers an unbiased, linear spatial prediction method for estimating point data (Radočaj et al., 2021). Following interpolation, soil property rasters were processed using raster math in the ArcGIS toolbox to derive Soil Quality Index (SQI), Soil Organic Carbon (SOC) stocks, Soil Structural Stability Index (SSSI), and Soil susceptibility (CSOM) across the study area. To further characterize soil variability, Hierarchical Cluster Analysis (HCA) was used to group soil properties based on the similarity of sampled points (Ibrahim, 2015). A correlation matrix was also generated to evaluate the strength and direction of relationships among the soil variables. All statistical analyses and data visualization were carried out using ArcGIS 10.5 and the R programming language (R Core Team, 2018)

4. Results and discussion

4.1 Spatial variation and morphological characteristics of soil properties in the AGF

Cumulative variance (CV) was computed to show variability of analyzed soil properties. Summary statistics of soil properties described high and low CV differences (Wilding 1985). CV indicates accurate normalization of the soil properties around means (Brejda et al., 2000). High variability (0.35) was observed for SOC, TN, P, K, ECEC, Mg, Ca, SOM, and clay concentrations. Conversely, soil pH, sand, and silt contents recorded the least (CV 0.15) variability (Table 2). We may trace variability in soils to inappropriate soil management practices and the intrusion of soil parent material due to the shocks and pressures of climate change (Tsu Wei et al., 2009).

Different soil types exhibits diverse behaviour due to nature and gradual changes in morphological characteristics (Ogunkunle, 2005). Characteristics of the studied soils varied with respect to depths, color, texture, structure and consistency etc. Soil depths showed a strong relationship with topography and thus ranged from 0 to 100 cm (upland), 0 to 110 cm (midland), and 0 to 90 cm (lowland), respectively. Variability of soil depths could be due to abrupt changes in topographic directions and different biological conditions over varying periods of time (Soil survey staff, 1993). Soil color varied from brown (7.5 YR 4/3), to dark brown (7.5 YR 3/3), and gradually changed to reddish color particularly at the sub-surface layers of the pedological pits. The reddish coloration observed in subsurface horizons may indicate oxidation of iron oxides due to the abundance of clay (Buol et al., 2003). Structure examination of the studied soils ranged from weak angular to sub-angular blocky. The soil consistency was not much varied, but clay tends to increase down the pits and thus is classified between slightly sticky and very plastic. The events of changes in the observed consistence especially at sub-surface horizons signify hardness or dryness of the soils especially in the dry state (Raji, 1995). Interestingly, soil boundaries of the profile showed easy demarcation because of clear color variations etc. The clarity in the soil boundaries could be pointing towards flora activities and melanisation of organic matter.

4.2 Physical and chemical soil conditions in the AGF

The soils within the study area exhibited varying textures along the toposequence, with sandy textures predominant in upland areas, sandy loam in midlands, and sandy clay in lowland regions. The particle size distributions of the studied soils were in the order sand > silt > clay. Results showed that clay soil had low values ranging from 2.60 to 25.60%, with a mean of 5.38%. Such textural values showed inadequacy of water retention since clay consolidates soil aggregates and can provides better resistance to water erosion (Tahirou et al., 2022; Tobore et al., 2025). In contrast, a higher value was obtained for sand ranging from 60.40 to 93.40 % with a mean value of 80.77. Also, silt had mean value of 13.85 and a ranged value of 2.40 to 20.00. Therefore, soil texture for the study is classed as sandy clay loam according to USDA (United States Department of Agriculture) criteria.

Eluviation – illuviation processes could be responsible for higher sand concentration obtained (Akinbola et al., 2009). Vulnerability of topography may directly act as a driver washing away surface finer materials and could be responsible for sand accumulation (Adu, 1995). Bulk density values ranged between 1.0 and 1.9 g/cm³. Soils with densities below 1.2 g/cm³ may support high humus content, whereas values approaching 1.9 g/cm³ suggest compaction, which restricts root penetration and water uptake and may affect nutrient cycling (Nam et al., 2021; Odey, 2018).

Table 2. Summary of physical and chemical properties of soils in the AGF. Abbreviation: CV, Coefficient of variation; SD, Standard deviation; SOC, Soil organic carbon; TN, Total nitrogen; SOM, Soil organic matter; ECEC, Effective cation exchanged capacity; Mg, Magnesium; P, Phosphorus; Ca, Calcium; BS, Base saturation.

Soil condition	Mean	Minimum	Maximum	SD	CV (%)
pH H20	6.35	4.68	7.35	0.69	0.10
SOC (%)	1.65	0.51	3.97	0.92	0.54
TN (%)	0.13	0.04	0.22	0.05	0.41
SOM (%)	2.84	0.88	6.84	1.59	0.56
Ca cmol kg -1	3.81	1.71	8.27	1.62	0.42
Mg cmol kg -1	1.60	0.66	3.20	0.94	0.59
P mg kg -1	6.66	2.32	28.00	5.69	0.86
K cmol kg -1	0.23	0.10	0.46	0.12	0.45
Sand (%)	80.77	60.40	93.40	6.70	0.08
Silt (%)	13.85	2.40	20.00	4.15	0.30
Clay (%)	5.38	2.60	25.60	4.75	0.88
Bulk density	1.31	0.67	1.72	0.23	17.53
ECEC cmol kg -1	8.50	3.26	17.66	4.46	0.52
BS (%)	80.95	20.72	99.68	28.13	0.35

Soil pH remains a master variable used to identify many chemical reactions across soil types (Brady & Weil, 2014). In the study, soil pH values ranged between strongly acidic (4.68), neutral (6.6 to 7.3), and alkaline (>7.3), with a mean value of 6.35. Total nitrogen concentration ranged from 0.04 to 0.22%, which means a "medium" to "high" supply for most plants. Variability obtained for soil pH could depict the presence of leaching like basic cations as well as the varying nature of the pedogenic processes (Abdenna et al., 2018). In addition, higher acidic pH could indirectly decrease total nitrogen (TN) as well as phosphorus (P) availability with the high risk of heavy metals contamination (Porta et al. 1994; Azeez et al., 2021). Nevertheless, plants thrive best in different soil pH ranges. Hence, the study pH requires different soil management techniques to achieve optimal agricultural productivity (MSU, 2011).

SOC concentration ranged from 0.51% to 3.91%, with a mean of 1.65%. Additionally, soil organic matter had a mean of 2.84% and ranged from 0.88% to 6.84%. The SOC variations may indirectly reveal the anthropized nature of tropical soils (Obidike-Ugwu et al., 2023; Safadoust et al., 2016). Nevertheless, calcium (Ca), magnesium (Mg), and potassium (K) had mean values of 3.81, 1.60, and 0.23 cmol kg -1 respectively. Effective cation exchanged capacity (ECEC) gave a mean value of 8.50 cmol kg 1 with ranged values between 3.26 and 17.66 cmol kg -1. For the base saturation, a mean value of 80.95 % was obtained, while phosphorus ranged from 2.32 to 28 mg kg -1 with a mean value of 6.6 mg kg -1. The correlation coefficient matrix was utilized to monitor the relevance of soil quality. Therefore, in the study, blue color intensity signifies positive correlation and red indicates a negative correlation among and within the matrix (Figure 3).

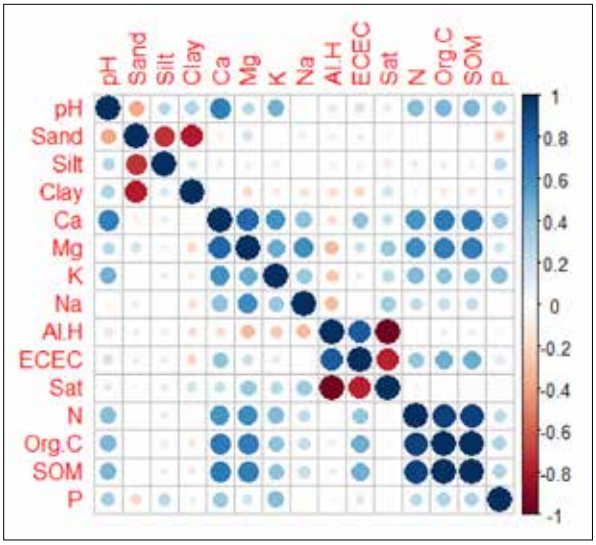

Figure 3. Correlation matrix of soil conditions in the AGF

4.3 Cluster analysis of soil condition in the AGF

Dendrogram (HCA) analysis was used to show the relationship between selected soil properties and a specific grouping of similar clusters (Figure 4). In this study, TN, SOC, P, K, pH, silt, clay and sand concentrations were selected with four major distinct clusters and sub-clusters. The selected soil properties showed that cluster 1 of the sub-cluster consists of SOC and TN, cluster 2 is characterized by silt and clay sub-clusters, while cluster 3 highlights soil pH and K sub-clusters. Cluster 4 signifies sub-clusters of sand and P.

4.4 Soil degradation vulnerability in the AGF

Vulnerability analysis of the present studied soils to degradation was calculated through GIS-based techniques. In

the study, SSSI and CSOM susceptibility to soil degradation ranged from 0.53 to 8.69%. Mean and standard deviation of SSSI and CSOM were 0.53 and 4.13. Consequently, SSSI ranged between 5 and 7% (low risk of structurally degraded soils), covering 158.2 ha -1, while sufficient SOC structural stability (9%) covered 148.8 ha -1 of the studied area. So far, CSOM indicated moderate vulnerability (5 and 7%) for the present study. We could trace SSSI and CSOM vulnerabilities to the fragile nature of the pedogenic processes (Sombroek & Zonneveld, 1971; Tesfahunegn & Gebru, 2020).

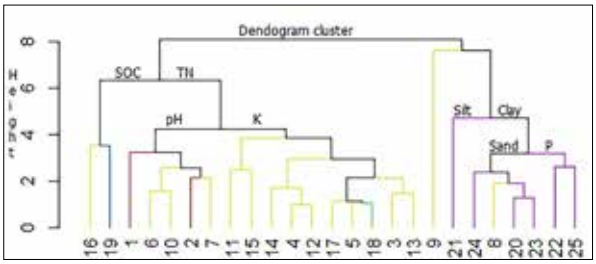

Figure 4. Spatial distribution of selected soil samples within each clusters

4.5 Above ground biomass and SOC stocks in the AGF

Tree basal area for the study was 71.24 m2 ha− 1 and vegetation density (tree and sapling) was 1450 ha− 1. Accordingly, value for above ground tree biomass (AGTB) was 87.96 ha− 1 and sapling biomass was 52.36 ha− 1. SOC stocks of the area varied along toposequence with increased in SOC stocks (Figure 5). So far, SOC stocks for up-land spanned from 124.41 Mg C ha−1 to 59.22 Mg C ha−1. In contrast, mid-land SOC stocks ranged from 59.23 Mg C ha−1 to 29.38 Mg C ha−1, while the low-land areas had SOC stocks of 29.38 Mg C ha−1 to 7.35 Mg C ha−1 (Figure 6). According to Sewerniak et al. (2017), topography indirectly affects variation of microclimates, underlying ecological processes and spatial distribution of soil properties.

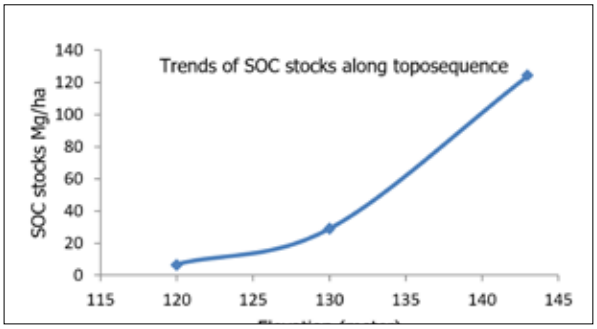

Figure 5. Trend of SOC stocks along topographic elevation

4.6 Soil quality analysis in the AGF

The spatial distribution map for the study soil quality is illustrated in Figure 7. Mean and standard deviation values of the soil quality index were 2.13 and 1.11. The result showed that SQI for the present studied soils ranged in the order of good (0.8) > fair (0.6 – 0.4) > poor (< 0.4), respectively. The good (0.8) soil quality was found mostly at central and southern parts of the area covering approximately 249.42 ha. In contrast, fair (0.6 – 0.4) and poor (< 0.4) soil qualities were located mostly at the northern part of the area, occupying 51.91 and 5.60 ha, respectively.

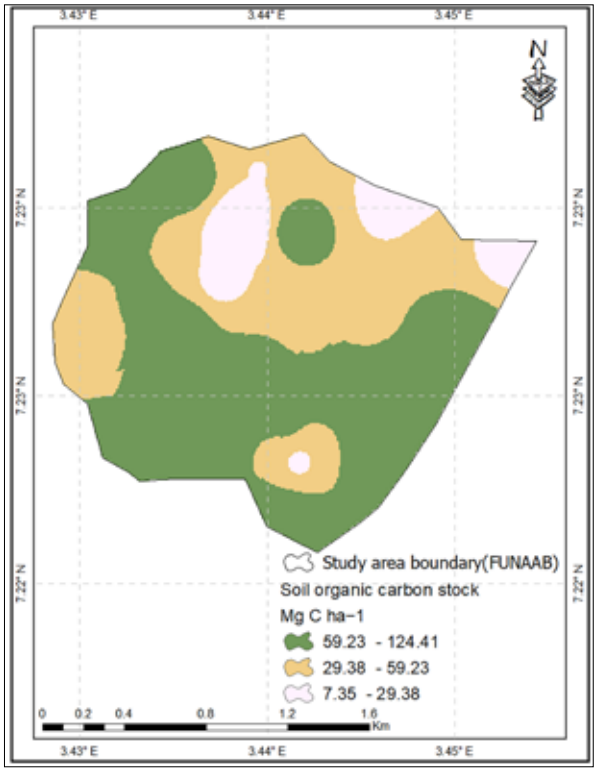

Figure 6. Spatial distributions of soil organic carbon stock in the AGF

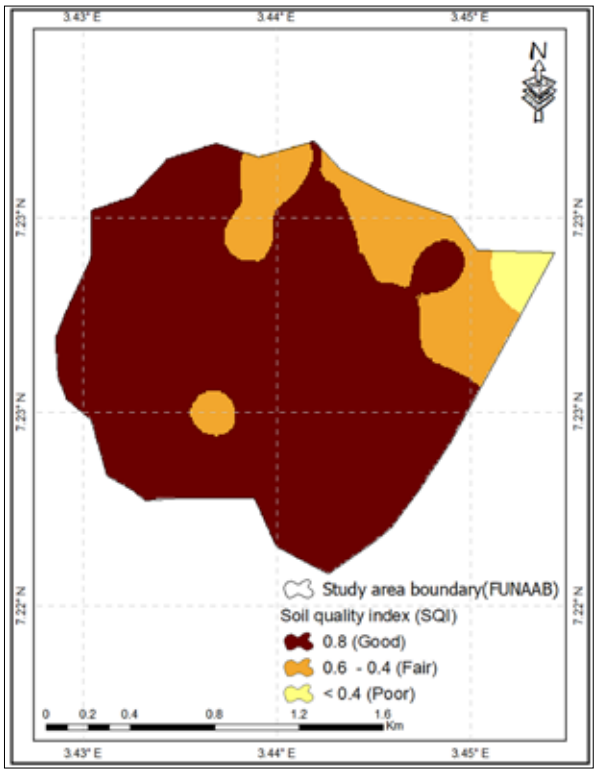

Figure 7. Spatial distribution of soil quality in the AGF

5. Discussion

The particle size distribution of the study area followed the trend of sand > silt > clay, with soils predominantly classified as sandy clay loam, derived from basement complex materials (Smyth & Montgomery, 1962). Such soils, common in Southwestern Nigeria, are often deep and heterogeneous, offering both opportunities and challenges for sustainable land management (Tobore, 2023; Ojanuga, 1979). The high sand content likely results from the underlying parent material and geomorphological processes (Greve et al., 2012), with elevation further influencing pedogenic differentiation (Seibert et al., 2007; Waswa et al., 2013). These findings underscore the role of terrain, geology, and climate-induced variability in shaping soil characteristics (Kosaki & Juo, 1989; Baltensweiler et al., 2020).

SSSI and CSOM mean values showed that the studied soils are classified as sufficient, moderate and low vulnerabilities. This indicates that some portions of the studied soil are susceptible to soil structural degradation. Additionally, absence of a stable soil structure class in the study showed less resistance of studied soils to erosion by water (Igwe and Obalum, 2013; Tobore et al., 2025). Nevertheless, these results are consistent with the findings of Folly (1995). The areas with low and moderate risk vulnerability could be traced to unchecked human actions on the fragile nature of the studied soils (Tobore 2023; Tesfahunegn and Gebru 2020). The dendrogram from Hierarchical Cluster Analysis (HCA) provided insights into the relationships among soil properties, suggesting distinct management needs for different clusters based on soil behavior and morphological variation (McNeill & Hewitt, 2015).

Soil pH is an essential indicator in assessing the fertility of a specific soil (Brady & Weil, 2014). About 75% of the area demonstrated a moderately acidic pH value of 5.69. The Acidic nature could be traced to the close vicinity of the study to major streams or rivers flowing in its valley from different direction (i.e., south, west, and north)s. Nkwunonwo et al. (2020) described the studied region to be naturally endowed with rivers and streams such as Ogun Rivers flowing along several tributaries. These tributaries have commonly been found to accommodate high levels of heavy metals (Olatunde et al., 2020). Nevertheless, Obiora et al. (2016) described Nigeria's soils and immediate environment to be intimidated with household and industrial wastes depositions and thereby leading to soil contamination by heavy metals. This was equally the view and conclusion of Olatunde et al. (2020). Our findings contrast with prior studies that reported that agroforestry soils should be less acidic due to the presence or abundance of vegetation cover (Muchane et al., 2020). On one hand, the present results corroborated the findings of Schwab et al., (2015) describing sub-Saharan Africa agroforestry soils to be higher in soil pH due to emissions of carbon dioxide, uncontrolled bush burning and continuous exploitation of fuel wood for livelihood (Khadijat et al., 2021). More importantly, findings from the study further suggested that nitrogen fertilizers, like ammonium based fertilizers can be used to decrease areas with high soil pH. This explains the availability of phosphorus sorption under low pH (Moody et al., 2008).

Total nitrogen (TN), phosphorus (P), and potassium (K) concentrations of the studied area ranged from medium to high. For instance, the obtained high TN contrasts with the fact that agroforestry lands possess less TN when compared to non-agroforestry lands because of prolonged urea application with a notion to attain high crop yield especially in emerging nations (Muchane et al. 2020; Kuyah et al., 2019). Also, the mineralization of leaf litters fall to bare-soil surface may significantly contributes to increase in the TN concentration of the studied area (Mulat et al., 2021). According to Sharma et al. (2022), increased in microbial activity increase TN because of quick decomposition of organic matter constituents thereby releasing ammonium and nitrate as forms of nitrogen (Maharajan et al., 2017). So far, recent studies in sub-Saharan Africa like Ethiopia and India re-affirmed that agroforestry soils have shown promising and continuous ways of enhancing P availability (Wolle et al., 2021; Dori et al., 2022). Besides, our result aligns perfectly with the previous findings of Chaudhry et al. (2007) and Lamichhane, (2013). Additionally, the application of inorganic phosphorus fertilizers may also be introduced to replenish and maintain P content in the present studied soils especially areas with medium phosphorus concentration (Sharma et al., 2022; Dagar et al., 2020). At the same time, the high K concentration in our study was consistent with prior agroforestry studies (Nath et al., 2015; Singh et al., 2018; Namgial et al., 2020).

High concentration of organic carbon was detected in the northern and southern regions, approximately covering 70 %. Moderate and low organic carbon concentrations covered 20 and 10 % of the area. The area with low organic carbon (OC) was classed below critical threshold limits. This further explains the vulnerability of the studied soils to structural degradation. Nevertheless, the OC concentration in the present study exceeded values reported by Schwab et al. (2015) and Magar et al. (2020) for tropical agroforestry. Interestingly, our study is consistent with the general instincts that proper adequate agroforestry practices can elevate soil organic carbon concentrations due to the abundance of woody trees. Additionally, woody trees deposit more leaf litter, thereby contributing to the decomposition of organic matter accumulation (Kassa et al., 2022). At the same time, the organic matter concentration of our studied soils ranged between high and low contents. Soil organic matter serves as a major contributor to the cation exchange capacity in the soil medium. The low and moderate OC concentration of the area could be traced to greenhouse gases, abrupt changes in slope positions, and lastly gradual to sudden increase of land surface temperature due to sea level rise intrusion (Tobore & Samuel 2022; Rezaei & Gilkes, 2005). Therefore, soils with low soil organic matter reduce water holding capacity and can cause soil nutrients to be unavailable (Tittonell et al., 2010).

SOC stocks of the area ranged between 7.35 and 124.41 Mg C ha−1 respectively. The variability in the SOC stocks might be traced to the differences in density of vegetative cover, tree populations and topography nature of the studied

soils (Feliciano et al., 2018). Although De Stefano and Jacobson (2018) asserted that healthy vegetative cover can grow taller trees and thus make them tap more sunlight, water, and nutrients easily to support above-ground biomass. Nevertheless, SOC stocks, obtained for our study, were higher than the reported studies of Besar et al. (2020). Although Kay et al. (2019) mentioned that adoption of different agroforestry system of practices plays a pivotal role in increasing SOC stocks stability and availability. A similar result was also obtained under agroforestry in Northern Ethiopia (Gebrerneskel et al., 2021). Hence, our study underscores the agroforestry potential systems of practicing healthy vegetation cover density, particularly to mitigate a changing climate and thus increase SOC stocks.

Spatial trends of soil quality for the present study showed more accurate areas classified as good (0.8), fair (0.6 – 0.4), and poor (<0.4). The portion covered by fair (0.6 – 0.4), and poor (<0.4) soil quality could be traced to unchecked human actions, leading to a low percentage of SOC and low soil structural stability. Zhang et al. (2016) described soil pH, bulk density, and SOC, among others, as the most influential predictors for accurate assessment of soil quality. This further confirmed the crucial importance of using these parameters in the present study. Moreover, the results obtained for our study also align with previous studies of agroforestry reported by Ramirez et al. (2022) and Guillot et al. (2021). More importantly, since soils are an essential medium for crop growth as well as a critical resource base where food supplies come from (Brevik 2013), developing soil nutrient recommendations for soils of agroforestry calls for immediate intervention of researchers to salvage the soil quality of the agroforestry. Interestingly, these actions will eventually help in reducing management cost and input wastage. Therefore, more emphasis should be placed on managing the potential of agroforestry resources and their significant contributions to carbon stocks for increasing food productivity and enhancing a sustainable environment.

6. Conclusion

The agroforestry system remains a multifunctional land-use strategy with significant benefits for both human well-being and environmental sustainability. Understanding the variability of soil properties and the extent of anthropogenic influence on agroforestry soils is essential for mitigating the impacts of climate change and enhancing food production. This study assessed soil quality and organic carbon (SOC) stocks at the Federal University of Agriculture, Abeokuta, Ogun State, Nigeria. A total of 48 soil samples were collected from 0–20 cm depth along a representative toposequence. The soils, derived from basement complex parent materials, were classified as sandy clay loam, exhibiting notable variations in physical and chemical properties. These variations significantly influenced SOC stocks and the overall soil quality across the study area. Spatial analysis revealed that SOC stocks ranged from 124.41 to 7.35 Mg C ha^{-1}, and the soil quality index (SQI) ranged from good (≥0.8), to fair (0.6–0.4), and poor (<0.4). Our findings demonstrate that agroforestry soil possesses considerable potential to enhance SOC stocks and improve soil quality—both of which are critical for climate change mitigation and sustainable food systems. The study underscores the importance of integrating sustainable soil fertility management practices, such as farmyard manure application or integrated soil fertility management techniques, to boost soil health and increase carbon sequestration capacity.

However, this study focused exclusively on surface soils (0–20 cm), thereby limiting our ability to assess SOC stocks in deeper horizons. Future research should incorporate deeper soil layers, quantify below-ground biomass, and examine the influence of climatic variables on SOC dynamics. Such efforts will provide robust empirical evidence at national, regional, and global scales—further strengthening the role of agroforestry in addressing climate change challenges, ecological resilience, and sustainable agricultural development.

Acknowledgment

The authors are sincerely grateful to the management of the Federal University of Agriculture, Abeokuta, for allowing us to carry out the study. The works of previous authors in this important research context and the invaluable contributions, insights, and resourcefulness of the editor and reviewers of this manuscript are vital to the completion of this research.

Declaration of Competing Interest

The author(s) declared no known competing moral or financial interests in relation to the work article.

Funding

The author(s) received no financial support for the research, authorship, and/or publication of this article

References

Abdenna D, Yli-Halla M, Muktar M, Lemma W.(2018). Soil classification of humid Western Ethiopia: a transect study along a toposequence in Didessa watershed. CATENA 2018; 163:184–195.

Agroforestry (2023). The Land Degradation Surveillance Framework Field Manual.

Adu S. (1995) Soils of the Nasia River Basin Northern Region1995.

Akinbola GE, Anozie HI, Obi JC.(2009) Classification and characterization of some pedons on basement complex in the forest environment of south-western Nigeria. Nigeria Journal of Soil Science 2009; Vol 19 no 1 pp 109 -117.

Azeez J, Aghorunse A, Ganiyu B, Anamezeonye M, Adegbite T, AbdulAzeez S (2021). Soil phosphorus availability indices and saturation ratio as an index of environmental risk assessment. Jordan Journal of Earth and Environmental Sciences 12 (3) 269 – 274. ISSN 1995 – 6681.

Bajracharya RM, Sharma S, Dahal BM. Sitaula BK, Rokaya K, Jeng A.(2006) Assessment of soil quality using physiochemical and biological indicators in a mid-hill watershed of Nepal. In: Proceedings of the International Seminar on Environmental and Social Impacts of Agricultural Intensification in Himalayan Watersheds, ; pp. 105–114.

Baltensweiler A, Heuvelink GBM, Hanewinkel M, Walthert L.,(2020). Microtopography shapes soil pH in flysch regions across Switzerland. Geoderma: 380, 114663. https://doi.org/10.1016/j.geoderma.2020.114663 Besar, N., Suardi, H., Phua, M., James, D., Mokhtar, M., Ahmed, M.,(2020).Carbon

Stock and Sequestration Potential of an Agroforestry System in Sabah, Malaysia. Forests. 2020: 11 (2), 210. https://doi.org/10.3390/f11020210

Blake GR, Hartege KH.(1986). Methods of soil analysis part 1. In: page, A.L. (Ed.), Physical and mineralogical methods agronomy monographs, 2nd.1. ASA SSSA, Madison, pp. 425–442

Brady NC, Weil RR (2008) The Nature and Properties of Soils. Prentice Hall, Upper Saddle River, NJ;

Bray RH, Kurtz LT,(1945) Determination of total, organic, and available forms of phosphorus in soils. Soil Sci. 1945: 59, 39–46. https://doi.org/10.1097/00010694- 194501000-00006

Bremner JM, Mulvaney CS, (1982). Nitrogen-Total. In: Page, A.L., Miller, R.H., Keeney, D.R. (Eds.), Methods of Soil analysis. Part 2. Chemical and Microbiological Properties. American Society of Agronomy, Soil Science Society of America, Madison, Wisconsin, pp. 595–624. Eds. https://www.scirp.org/reference/References Papers?ReferenceID=181829.

Breiman, L. (2000)..Some infinity theory for predictor ensembles. Technical Repor 579, Statistics Dept. UCB

Brevik EC.,(2013).The potential impact of climate change on soil properties and processes and corresponding influence on food security. Agriculture ; 3:398–417

Campos RC, Demattê JAM.,(2004). Soil color: approach to a conventional assessment method in comparison to an automatization process for soil classification. Rev. Bras. Ciênc. Solo 2004; 28, 853–863. https://doi.org/10.1590/S0100-06832004000500008

Cardinael R, Chevallier T, Cambou A, Beral C, Barthes BG, Dupraz C, Chenu C. (2017).Increased soil organic carbon stocks under agroforestry: a survey of six different sites in France. Agric. Ecosyst. Environ. 2017; 236, 243–255

Chaudhry, A.K., Khan, G.S., Ahmad, I.,. Effect of poplar tree intercropping at various densities on the post-harvest soil nutrient contents. Pakistan Journal of Agricultural Sciences 200744 (3), 468–472

Dagar, J.C., Gupta, S.R., Teketay, D. (Eds.),. Agroforestry For Degraded Landscapes. Springer, 1 and 2, 20201-475-1-554. https://link.springer.com/book/10.1007/978-981- 15-4136-0

De Stefano, A., Jacobson, M.G.,(2018). Soil carbon sequestration in agroforestry systems: a meta-analysis. Agrofor. System 92, 285–299. https://doi.org/10.1007/s10457-017- 0147-9

Demattê JAM, Morgan CLS, Chabrillat S, Rizzo R, Franceschini MHD, Terra F, Vasques GM, Wetterlind J, (2015).Spectral sensing from ground to space in soil science: State of the art, applications, potential, and perspectives. In: Thenkabail, P.S. (Ed.), Land Resources Monitoring, Modeling, and Mapping with Remote Sensing, Remote Sensing Handbook. CRC Press, pp. 661–732. https://doi.org/10.1201/ b19322-35

Fahad S, Chavan SB, Chichaghare AR, Uthappa AR, Kumar M, Kakade V, Poczai P. (2022).Agroforestry systems for soil health improvement and maintenance. Sustainability. 14 (22), 14877.

Feliciano, D., Ledo, A., Hillier, J., Nayak, D.R.,(2017) Which agroforestry options give the greatest soil and above ground carbon benefits in different world regions? Agriculture Ecosystems and Environment 2018: 254, 117–129. https://doi.org/10.1016/j. agee.2017.11.032

FAO. Status of the World's Soil Resources (SWSR) (2015).– Main Report. Food and Agriculture Organization of the United Nations and Intergovernmental Technical Panel on Soils

Food and Agriculture Organization (2007), Extent and causes of salt-affected soils in participating countries, AGL: Global network on integrated soil management for sustainable use of salt-affected soils. http://www.fao.org/ag/agl/agll/spush/topic2.html. (Accessed 15 September 2018).

Folly A.(1995) Estimation of erodibility in the savanna ecosystem, northern Ghana. Communication in Soil Science and. Plant Analysis. 1995: 26, 799–812. https://doi.org/10.1080/00103629509369336

Food and Agriculture Organization FAO,. (2022).World Food and Agriculture – Statistical Yearbook.. https://doi.org/10.4060/cc2211en.

Gao WQ, Lei XD, Fu LY.(2020). Impacts of climate change on the potential forest productivity based on a climate-driven biophysical model in northeastern China. J. For. Res. 31, 2273–2286. https://doi.org/10.1007/s11676-019-00999-6

Gbadebo AM, Oyedepo JA, Taiwo AM.,(2010). Variability of nitrate in groundwater in some parts of Southwestern Nigeria. Pac. J. Sci. Technol.; 11 (2), 572–584.

Gee GW, Bauder J, Klute A. (1986)Methods of soil analysis, part 1, physical and mineralogical methods. Soil science Society of America Book Series. American Society of Agronomy, Inc. and Soil Science Society of America, Inc. Madison, Wisconsin, 1986: pp. 404–410.

Guha S, Govil H, Taloor AK, Gill N, Dey A.. (2022)..Land surface temperature and spectral indices: A seasonal study of Raipur City. Geodesy and Geodynamics, 13(1), 72–82. https://doi.org/10.1016/j.geog.2021. 05.002.

Guillot, E., Bertrand, I., Rumpel, C., Gomez, C., Arnal, D., Abadie, J., Hinsinger, P.,. Spatial heterogeneity of soil quality within a Mediterranean alley cropping agroforestry system: comparison with a monocropping system. Eur. J. Soil Biol. 202; 105, 103330 https://doi.org/10.1016/j.ejsobi.2021.103330.

Haase R, Haase P.(1995) .Above-ground biomass estimates for invasive trees and shrubs in the Pantanal of Mato Grosso, Brazil. For. Ecol. Manage. 1995; 73 (1–3), 29–35. https:// doi.org/10.1016/0378-1127(94)03509-U.

Hengl T, Nussbaum M, Wright MN, Heuvelink GBM, Graler B.(2018). Random forest as a generic framework for predictive modeling of spatial and spatio-temporal variables. PeerJ 6, e5518. https://doi.org/10.7717/peerj.5518.

Henry M, Valentini R, Bernoux M.,(2009) Soil carbon stocks in eco-regions of Africa. J Biogeosci Discuss ; 6:797–823.

Ibrahim A.,(2015).Evaluation of surface water quality using multivariate techniques in terengganu river basin. International Journal of Development Research (IJDR). Int. J. Dev. Res., 2015; 5(2), 3421–3427.

Ibrahim RL, Al-Mulali U, Ajide KB, Mohammed A, Al-Faryan MAS.(2023). The implications of food security on sustainability: do trade facilitation, population growth, and institutional quality make or mar the target for SSA? Sustainability.15 (3), 2089. https://doi.org/10.3390/su15032089.

Jackson JK.(1994) Forest Manual of Afforestation in Nepal, 2. Research and Survey Centre, Ministry of Forest and Soil Conservation,pp. 631–639. https://frtc.gov. np/downloadfile/Manualofafforestration_nep_1597038827.pdf. pp.

Kassa, G., Bekele, T., Demissew, S., Abebe, T.,(2022). Leaves litterfall and nutrient inputs from four multipurpose tree/shrub species of homegarden agroforestry systems. Environ. Syst. Res. (Heidelb) 2022: 11 (1), 29.

Kay, S., Rega, C., Moreno, G., den Herder, M., Palma, J.H., Borek, R., Herzog, F.,(2019). Agroforestry creates carbon sinks whilst enhancing the environment in agricultural landscapes in Europe. Land. use policy; 83, 581–593. https://doi.org/10.1016/j.landusepol.2019.02.025

Khaine I, Woo SY .(2018). Exploration of the aboveground carbon sequestration and the growth estimation models of four species in agroforestry system of semi-arid region, Myanmar. Agrofor. Syst. ; 92, 183–194. https://doi.org/10.1007/s10457-016-00.

Khadijat A O, Tobore A O, Oyerinde G, Senjobi BA. (2021) Forest cover change in onigambari reserve, ibadan, Nigeria: application of vegetation index and Markov chain techniques. The Egyptian Journal of Remote Sensing and Space Sciences 24 (3), 983–990. https://doi.org/10.1016/j.ejrs.2021.08.004, 2.

Kosaki T, Juo ASR., (1989). Multivariate approach to grouping soils in small fields. I. Extraction of factors causing soil variation by principal component analysis. Soil Sci. Plant Nutrition. : 35, 469–477. https://doi.org/10.1080/00380768.1989.10434780

Kuyah S, Whitney CW, Jonsson M, Sileshi GW. Oborn, ¨ I., Muthuri, C.W., Luedeling,E.,(2019). Agroforestry delivers a win-win solution for ecosystem services in sub-Saharan Africa. A meta-analysis. Agron. Sustain. Dev. 2019: 39, 1. https://doi.org/ 10.1007/s13593-019-0589-8.

Lal R. Forest soils and carbon sequestration. For. Ecol. Manag. (2005); 220 (1–3), 242–258. https://doi.org/10.1016/j.foreco.2005.08.015

Lal R, Safriel U, Boer B.(2012).Zero net land degradation. A new sustainable goal for Rio + 20. A report prepared for the secretariat of the United Nations convention to combat desertification.

Lal R, and Stewart BA(.2019).soil Degradation and Restoration in Africa. CRC Press.https://doi.org/10.1201/b22321.

Lamichhane, K.,. Effectiveness of sloping agricultural land technology on soil fertility status of mid-hills in Nepal. J. For. Res. (Harbin) 201324 (4), 767–775. https:// doi.org/10.1007/s11676-013-0415-0.

Li J, Heap AD..(2008).A Review of Spatial Interpolation Methods for Environmental Scientists. Geoscience Australia, Record 2008; 23, 137 pp.

Lindner M, Fitzgerald JB, Zimmermann NE, Reyer C, Delzon S, van der Maaten E, Schelhaas MJ, Lasch P, Eggers J, van der Maaten-Theunissen M, Suckow F, Psomas A, Poulter B, Hanewinkel M. (2014). Climate change and European forests: what do we know, what are the uncertainties, and what are the implications for forest management? J. Environ. Manage. 146, 69–83. https://doi. org/10.1016/j.jenvman.2014.07.030

Magar, L.K., Kafle, G., Aryal, P.,(2020).Assessment of soil organic carbon in tropical agroforests in the Churiya Range of Makwanpur, Nepal. International Journal of Forestry Research 2020, 1–5. https://doi.org/10.1155/2020/8816433.

Maharajan, M., Sanaullah, M., Razavi, B.S., Kuzyakov, Y.,(2017). Effect of land use and management pratices on microbial biomass and enzyme activities in subtropical topand sub-soils. Appl. Soil. Ecology,113, 22–28.

McLean EO. (1986).pH and lime requirements. in: Page ALE, editor. Methods of soil analysis. Madison, WI, USA: American Society of Agronomists Inc. natural color image. In Poster session 3, GIS development proceedings, ACRS 1986.

Mississipi State University Extension Service (MSU) (2011). Vegetable gardening in Mississipi - Test soil to find its pH value. http;//msucares.com/lawn/gardevegetable/soil Ph 2011.

Muchane MN, Sileshi GW, Gripenberg S, Jonsson M, Pumarino L, Barrios E.,(2020) Agroforestry boosts soil health in the humid and sub-humid tropics: a meta-analysis. Agriculture, Ecosystems and Environment 295, 106899. https://doi.org/10.1016/j.agee.2020.106899.

Nath, A.J., Lal, R., Das, A.K.,(2015) Ethnopedology and soil properties in bamboo (Bambusa sp) based agroforestry system in North East India. Catena (Amst) 135, 92–99. https://doi.org/10.1016/j.catena.2015.07.001.

Namgial, J., Prabhakar, M., Gautam, K.L., Panda, S., Sharma, A.,(2020) Nutrient status of soil under different land use systems in Leh region of Himalayan cold desert. J Pharmacogn Phytochem ; 9 (4), 1192–1197

Nelson DW, Sommers LE, Sparks DL, Page AL, Helmke PA, Loeppert RH, Soltanpour PN, Tabatabai MA, Johnston CT, Sumner ME (1996) .Total carbon, organic carbon and organic matter. Methods Soil Anal ; 9:961–1010

Neumann M, Mues V, Moreno A, Hasenauer H, Seidl R (2017). Climate variability drives recent tree mortality in Europe. Glob. Chang. Biol. 23, 4788–4797. https:// doi.org/10.1111/gcb.1372

Obidike-Ugwu EO, Ogunwole JO, Eze PN.,(2023). Derivation and validation of a pedotransfer function for estimating the bulk density of tropical forest soils. Model. Earth Syst. Environ. 9 (1), 801–809. https://doi.org/10.1007/s40808-022-01531-2

Obiora SC, Chukwu A, Davies TC. (2016).Heavy metals and health risk assessment of arable soils and food crops around Pb–Zn mining localities in Enyigba, southeastern Nigeria. Journal of African Earth Sciences,: 116, 182–189. https://doi.org/10.1016/j.jafrearsci.2015.12.025.

Obeidat M & Awawdeh M (2021). Assessment of groundwater quality in the area surrounding Al-Zaatari Camp, Jordan, Using Cluster analysis and water quality index (WQI). Jordan Journal of Earth and Environmental Sciences 12 (3) 187 – 197. ISSN 1995 – 6681.

Odey S.(2018).Overview of Engineering Problems of Soil Compaction and Their Effects on Growth and Yields of Crops. 2018; doi: 10.13140/ RG.2.2.11522.22722

Ofomola, M.O, Abriku E.O, Utieyin B.S, Otheremu P, K, Anomohanran O. (2024). Combined Geophysical and Soil test Analysis Methods for soil precision mapping in the Delta State University, Centre for Entrepreneurial Studies (CES) farm, Abraka, Nigeria. Jordan Journal of Earth and Environmental Sciences 15 (4) 257 – 264. ISSN 1995 – 6681.

Ogunkunle AO. (2005).Soil survey and Sustainable land management. Invited paper at the 29th annual conference of SSSN held at University of Nigeria, Abeokuta.

Ojanuga AG.,(1997). Clay mineralogy of soils in the Nigerian tropical savanna regions. Soil Science Society of America Journal.: 43: 1237 – 1242.

Olatunde KA, Sosanya PA, Bada BS, Ojekunle ZO, Abdussalaam SA.,(2020). Distribution and ecological risk assessment of heavy metals in soils around a major cement factory, ibese, Nigeria. Scientific African, 2020: 9, 1–9.

Orobator P. O (2025). Effect of bushfire on soil physicochemical properties in Rubber (Hevea brasiliensis) plantation of Tropical Nigeria. Jordan Journal of Earth and Environmental Sciences 16 (2) 186 – 194. ISSN 1995 – 6681.

Oyerinde GT, Lawin AE, Tobore AO.,(2022) .Multiscale assessment of hydroclimatic modeling uncertainties under a changing climate. Journal of Water & Climate Change. : https://doi.org/10.2166/wcc.2022.266.

Pandit BH, Neupane RP, Sitaula BK, Bajracharya RM. (2013). Contribution of small-scale agroforestry systems to carbon pools and fluxes: a case study from middle hills of Nepal. Small-Scale Forestry.12 (3), 475–487. https://doi.org/10.1007/s11842-012-9224-

Pieri CJMG,(1992). Fertility of soils, Springer, Berlin Heidelberg. 1https://doi.org/10. 1007/978-3-642-84320-4.

Raji BA.(1995). Pedogenesis of Ancient Dune Soils in the Sokoto Sedimentary Basin, North Western Nigeria (unpublished) PhD. Thesis Ahmadu Bello University Zaria. 1995; 192p

R Core Team.(2018) A Language and Environment for Statistical Computing. R Foundation for Statistical Computing, Vienna, Austria. 2018; URL: https://www.R-project. Organization

Ramirez, M.A.J.P., Visco, R.G., Predo, C.D., Galang, M.A,. (2022). Assessment of soil condition using soil quality index of different land use types in Liliw, Laguna, Philippines. Philipp J Sci : (3), 151. https://doi.org/10.56899/151.03.29

Safadoust A, Doaei N, Mahboubi A.A, Mosaddeghi MR, Gharabaghi B, Voroney P, Ahrens B.(2016) Long-term cultivation and landscape position effects on aggregate size and organic carbon fractionation on surface soil properties in the semi-arid region of Iran. Arid Land Research and Management, 30(4), 345–361. https://doi. org/10.1080/15324982.2015.1016244

Schwab N, Schickhoff U, Fischer E.,(2015). Transition to agroforestry significantly improves soil quality: a case study in the central mid-hills of Nepal. Agriculture, Ecosystems and Environment, 57–69. https://doi.org/10.1016/j. agee.2015.03.004.

Sewerniak P, Stelter P, Bednarek R.(2017). Effect of site preparation method on dynamics of soil water conditions on inland dunes of the Toruń Basin. Sylwan,161(1): 52– 61. https://doi.org/10.26202/SYLWAN.2016086

Sharma, S., Phartiyal, M., Madhav, S., & Singh, P..(2021) Global wetlands: Categorization, distribution and global scenario. Wetlands Conservation: Current Challenges and Future Strategies, 2 1–16. https://doi.org/10.1002/ 9781119692621.ch1

Shin S, Soe KT, Lee H, Kim TH, Lee S, Park MS. (2020). A systematic map of agroforestry research focusing on ecosystem services in the Asia-Pacific region. Forests.;11 (4), 368. https://doi.org/10.3390/f11040368

Sinclair FL. A general classification of agroforestry practice. Agrofor. Syst. (1999) 46, 161–18

Singh, I., Rawat, P., Kumar, A., Bhatt, P., (2018). Soil physio-bio-chemical properties under different agroforestry systems in Terai region of the Garhwal Hiamalayas. J Pharmacogn Phytochem 7 (5), 2813–282

Namgial, J., Prabhakar, M., Gautam, K.L., Panda, S., Sharma, A.,(2020) Nutrient status of soil under different land use systems in Leh region of Himalayan cold desert. J Pharmacogn Phytochem ; 9 (4), 1192–1197

Kay, S., Rega, C., Moreno, G., den Herder, M., Palma, J.H., Borek, R., Herzog, F.,. Agroforestry creates carbon sinks whilst e

Smyth AJ, and Mongomery RF.(1962) Soils and land use in Central Western Nigeria. Government Press, Ibadan. Western Nigeria.:264pp

Soil Survey Staff. (1993).Keys to Soil Taxonomy, Soil Conservation Service. United States Department of Agriculture, Washington.

Soil Survey Staff. Digital Soil Mapping. In: Ditzler, C., Scheffe, K., Monger, H.C. (Eds.),(2017)Soil Survey Manual. Government Printing Office, Washington, DC: pp. 295–354

Spaargaren OC, Deckers J.(1998). The world reference base for soil resources. In: Soils of Tropical Forest Ecosystems. Springer, Berlin Heidelberg:pp. 21–28. https://doi. org/10.1007/978-3-662-03649-5_2

Sun Y, Zhou Q, Xie X, Liu R.(2010).Spatial, sources and risk assessment of heavy metal contamination of urban soils intypical regions of Shenyang, China. Journal of Hazardous Materials 174(1–3): 455–462. DOI: 10.1016/j. jhazmat.2009.09.074

Tahirou S, Zerbo P, Ouattara S, Ado MN.(2022), Caract´erisation des param`etres physico-chimiques du sol de la zone rizicole de Saga (Niamey) dans la vall´ee du fleuve Niger. Int. J. Biol. Chem. Sci. 2022; 16 (2), 842–854. https://doi.org/10.4314/ijbcs.v16i2.26.

Tchotsoua M.(1994) .Informal dynamics of urban space and accelerated erosion in a west tropical setting: the case of the City of Yaounde, Cameroon. Cahiers d'Outre-Mer.; 47 (185), 123–136. https://doi.org/10.3406/caoum.1994.3508.

Tesfahunegn GB, Gebru TA. (2020). Variation in soil properties under different cropping and other land-use systems in Dura catchment, Northern Ethiopia. PLoS One 15, e0222476. .https://doi.org/10.1371/journal.pone.0222476.

Thomas RL.(1983) Journal of Analytical Methods in Chemistry: ; 5, No 4

Tittonell, P., Muriuki, A., Shepherd, K.D., Mugendi, D., Kaizzi, K.C., Okeyo, J., Verchot, L., Coe, R., Vanlauwe, B.,(2009).The diversity of rural livelihoods and their influence on soil fertility in agricultural systems of East Africa a typology of smallholder farms. Agric. Syst. 2010: 103, 83–97. https://doi.org/10.1016/j.agsy.10.001

Tobore AO, Bamidele S.,(2022).Wetland change prediction of Ogun-River Basin, Nigeria: application of cellular automata Markov and remote sensing techniques. Watershed Ecology and the Environment : 4, 158–168

Tobore AO, Nkwunonwo UC, Senjobi, BA.(2024). Combined remote sensing and multi-criteria analysis of wetland soil potential for rice production: case study of Ogun river basin, Nigeria. African Geographical Review. 2024: https://doi.org/10.1080/19376812.2022.210473

Tobore AO, Senjobi BA, Ogundiyi, TO, Bamidele S P.(2021) Geospatial assessment of wetland soils for rice production in ajibode using geospatial techniques. Open Geosciences, 2021: 13(1), 310–320. https://doi.org/10.1515/geo-2020-0227

Tobore AO (2023). Spatio-temporal Assessment of Land use and Land cover Changes and their impacts on Land Suitability for Maize Production in Federal University of Agriculture Abeokuta, Ogun state, Nigeria. Ife Journal of Agriculture, Volume 35, Number 2, Page 45 - 77.

Tobore AO., Bolarinwa Senjobi. & Ganiyu, Oyerinde. (2021): Spatio Temporal Analysis and Simulation of Land Use and Land Cover Change in Odeda Peri- urban of Ogun State, Nigeria. Jordan Journal of Earth and Environmental Sciences (JJEES). Volume 12 (4) Page 326 – 336. ISSN 1996-6681.

Tobore AO., Adedeji O.H, Jones, S & Samuel B (2025): Assessing Land Use/ Cover Changes to soil erosion vulnerability using Machine learning and RUSLE model. Transaction in Earth, Environment, and Sustainability. Volume 2 Page 1 – 21. https://doi.org/10.1177/2754124X251331943

Tsu Wei, T., Marthandan, G., Yee-Loong Chong, A., Ooi, K., & Arumugam, S. (2009).What drives Malaysian mcommerce adoption? An empirical analysis. Industrial Management & Data Systems,; 109(3), 370–388. https://doi.org/10.1108/02635570910939399

Udawatta RP, Jose S.(2012.). Agroforestry strategies to sequester carbon in temperate North America. Agrofor. Syst.: 86 (2), 225–242. https://doi.org/10.1007/s10457- 012-9561-1

Ufoegbune GC, Oyedepo JA, Awomeso A, Eruola O.(21.0) Spatial Analysis of Municipal Water Supply in Abeokuta Metropolis, South Western Nigeria". REAL CORP 2010 Proceedings. Tagungsband: Vienna, Austria. http://www.corp.at. M. Schrenk, V. Vasily, P. Popovich, and P. Zeile (eds.)

UNCCD (2015). Report of the Conference of the Parties on its Twelfth Session

United Nations. Transforming our World (2014): The 2030 Agenda for Sustainable Development. Department of Economic; Social Affairs, Sustainable Development; UN, New York, NY, United Nations.

Waswa BS, Vlek PLG, Tamene LD, Okoth P, Mbakaya D, Zingore S. (2013).Evaluating indicators of land degradation in smallholder farming systems of western Kenya. Geoderma 195-196, 192–200. https://doi.org/10.1016/j. geoderma.2012.11.007.

Zeng R, Zhang GL, Li DC, Rossiter DG, Zhao YG.(2016) How well can VNIR spectroscopy distinguish soil classes? Biosyst. Eng. 2016: 152, 117–125. https://doi.org/10. 1016/j.biosystemseng.2016.04.019

Zhang C, Ren H, Dai X, Qin Q, Li J, Zhang T, Sun Y., (2019); Spectral characteristics of copper-stressed vegetation leaves

and further understanding of the copper stress vegetation index. International Journal of Remote Sensing,; 40(12), 4473–4488.

Zhang J, Li S, Sun X, Tong J, Fu Z, Li J. (2019). Sustainability of urban soil management: analysis of soil physicochemical properties and bacterial community structure under different green space types. Sustainability 11 (5), 1395. https://doi.org/10.3390/su11051395

JJEES

JJEES (2026) 17 (2): 167-177
ISSN 1995-6681

Jordan Journal of Earth and Environmental Sciences

Petrographic Characterization and Provenance of Sandstone from the Mukdadiya Formation, Eastern Iraq

Nael A. Al-Najjari*

Department of Geology, College of Science, University of Basrah, Basrah, Iraq

Received on 22 July 2025 ; Accepted on 2 November 2025

Abstract

Two surface sections of Mukdadiya Formation, Al-Band and Bajliah eastern Missan, were selected to conduct the petrography of sandstone units. Ten sandstone samples were analyzed using a polarized microscope on the thin sections prepared from all samples to determine their light mineral content for petrographic study. Petrographic analysis revealed that the Mukdadiya sandstone is primarily composed of rock fragments, along with quartz grains (both monocrystalline and polycrystalline), feldspars including K-feldspar (orthoclase and microcline), plagioclase, and is cemented with carbonates. Mukdadiya sandstone is classified as lithic Quartzarenite. The proposed provenance for Mukdadiya sandstone is mainly sedimentary and plutonic igneous rock, with a less dominant metamorphic source. These sandstones are considered to be mineralogically immature, and according to the stability of sandstone in both sections, are chemically and mechanically unstable. The QLF classifications, the tectonic provenance of the Mukdadiya sandstone is described as recycled orogeny, while the QmFLt classification is placed in the lithic recycled field. According to the paleoclimatic conditions affecting, all sandstone samples of Mukdadiya sandstone are fall in the semi-arid region. Mukdadiya Formation›s high percentage of carbonate rock fragments such as limestone and dolomite suggests that the parent rock is primally carbonate, indicating that the material was transported rapidly moved quickly within the area which occur only in areas with high relief and arid climate that the fragments could have originated in the overthrust belt, the Sanandaj-Sirgjan belt, or the northeastern Iraq in high Thrust belt, where the metamorphic fragments were most likely formed.

Keywords: *Mukdadiya, Sandstone, Igneous, Petrography, Weathering, Clastic, Mineralogy, Iraq*

1. Introduction

The study area is situated in the Al-Teeb District of the northeastern Missan Governorate, near the eastern international border between Iraq and Iran. The research area is situated within the Low Folded zone›s Hamrin Subzone-Foothill Zone of the Unstable Shelf (Al-Mutury and Al-Asadi, 2008). Iraq has significant exposure to the Upper Miocene-Pliocene Injana and Mukdadiya Formation. The Mukdadiya Formation consists of up to 2000 m of gravely sandstone, sandstone, and red mudstone. The sandstones are sometimes cross-bedded and contain channel lags and clay balls (Basi and Jassim, 1974). According to Jasim and Goff (2006), the Mukdadiya Formation was formed in a rapidly receding foredeep basin through river deposition. Sandstones constitute an important part of the Tertiary stratigraphic sequence in eastern and northeastern Iraq. Sandstone›s importance lies in its ability to be used primarily for construction. It is also used in varying proportions in the cement, ceramic, and glass industries, and is used in polishing, sharpening, and water purification processes. The Mukdadiyah Formation is one of the most important and widespread gravel formations in Iraq, containing sandstone and gravel. It is thick and contains quartz, feldspar, and other minerals such as barite and celestite, which are primary mineral sources of barium and strontium. They are also used to weigh drilling fluids in high- and medium-pressure oil wells.

Because of their widespread distribution, Mukdadiya Formations have been examined in a large number of publications, reports, papers, and scholarly dissertations (Bellen et al. 1959; Buday 1980; Al-Banna 1982). Most of which provide descriptions of the formations› lithofacies, sedimentology, and depositional environments, as well as geological overviews of the formations. Lower Bakhtiari Formation replaced with the Mukdadiya Formation and the Upper Bakhtiari Formation with the Bai Hassan Formation. Up to 2000 meters of fining upward cycles of gravely sandstone, sandstone, and red mudstone make up the Mukdadiya Formation. The sandstones are frequently heavily cross-bedded and are associated with clay balls and channel lags deposited in a rapidly subsiding foredeep basin (Jassim and Goff, 2006). The thickness of the formation in type section is 1411 meters, and it was measured close to Al-Mukdadiya City in the Diyala Governorate (Al-Rawi et al., 1992). Many previous investigations focused on the Mukdadiya Formation in different parts of Iraq, including Dohuk (Zawita and Amadya), Mosul, Tikrit, Dyala, and Wasit (Badra and Zurbatiya). These studies covered subjects such as : according to Al- Jassim (1969), the Mukdadiya formation was formed in central Iraqi flood plains and alluvial rivers; While Sadik (1977) examined the gravel content of the Mukdadiya and Dibdibba Formations, he discovered that the former had more quartz and chert gravels, whereas the latter had igneous rock fragments. Enad

* Corresponding author e-mail: nael.kareem@uobasrah.edu.iq

(2007) investigated the stratigraphy and sedimentology of the Mukdadiya Formation in the Badra area and proposed a fluvial environment there. Al-Shammary(2009) studied Mukdadiya Formation in south-east of Badra and shows that the conglomerate, sandstone, and mudstone facies repetitions in number of cycles with trough cross bedding and pebble size in all the studied section indication of typical variation of braided rivers activities through the deposition time. Al-Uqagdi (2011) compared the Mukdadiya and Injana Formations from the perspective of sedimentary sequences, stratigraphic environments and tectonic conditions in the northern Iraqi areas of Zakho and Ain Sefni. Al-Samaani (2011), in his study of mineralogy and geochemistry of the Mukdadiya Formation in northeast Missan, suggested that Mukdadiya Formation sediments sources primarily from the northeastern region of Iraq. Basi (2012) in his study of petrographic of the sandstones of Mukdadiya Formation indicates that they are immature, mostly poorly sorted and classified as litharenite. The predominant type of sedimentary fragments is carbonate. The source rocks, based on petrographical and heavy minerals studies, are interpreted to be composed essentially of sedimentary followed by igneous and metamorphic rocks , when studied in the Mukdadiya Formation in the central part of Iraq. Al-Salmani and Tamar-Agha (2018) in their study of Petrography and Provenance of the Sandstone of Injana and Mukdadiya Formations (Upper Miocene/Pliocene) at Duhok Governorate, Northern Iraq, indicate that the heavy minerals are derived from mafic igneous and metamorphic rocks mainly as well as acidic igneous and reworked sediments. The tectonic provenances of both Injana and Mukdadiya Formations can be described as transitional and lithic recycled of recycled orogen. Al-Dabbagh (2018) reported that the sandstone of the Mukdadiya Formation in the Zurbatiya area (east Iraq) is classified as litharinite, sedarinite, and calclithite, and the tectonic provenance is a lithic recycled. Al-Kalidi (2014) studied the petrographic and geochemical analysis, suggesting the semi-arid to semi-humid environments of immature to sub-mature sediments of the Mukdadiya Formation in the Zawita and Amaadya areas, which indicate a near-source area in northeast Iraq. Mahdi and Sultan (2021) in their study of gravel of Mukdadiya in Al-Teeb area confirmed that the origin of the derived gravels is from the Qulqula Formation, because of their content of radiolaria and the other characterizing fossils. Sandstones› petrological characteristics are an important instrument for classifying them and can be used with other factors to address a variety of sedimentological problems (Boggs, 2009). The features of the source, the sedimentary processes occurring in the basin, and the types of channels connecting the source and the basin all affect the composition of sandstones (Demange, 2012). This study in two selected sections, eastern of Missan governorate namely Al-Band (A) and Al-Bajalia (B) with in latitude (32° 25› 51» N & longitude 47° 13› 03» E to latitude 32° 15› 36» N & longitude 47° 27› 18» E) respectively (Figure 1). The aim of study focuses on the petrographic description of sandstone to identify the Provence , paleclimate, and tectonic setting for these two selected sections :Al-Band and Al-Bajalia (Figure 1).

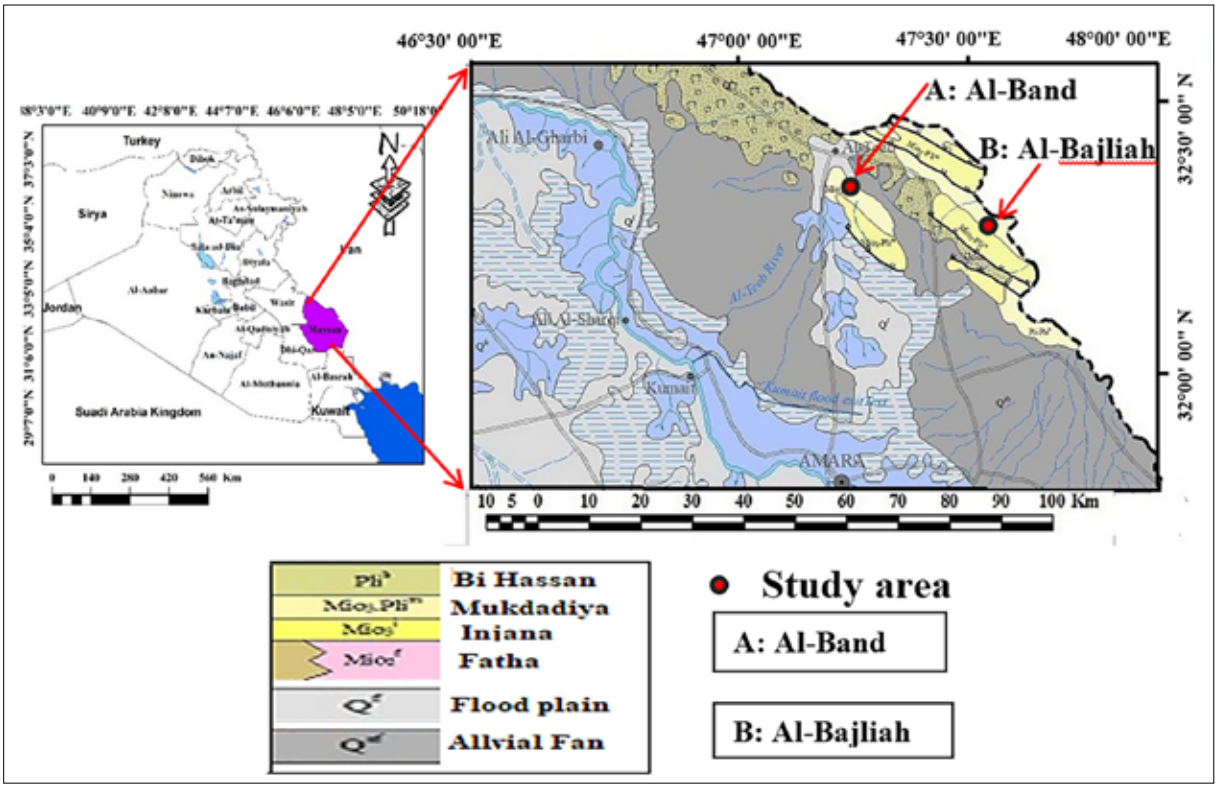

Figure 1. Geological map show the studied Area ***A:*** Al-Band and ***B:*** Al-Bajliah , modified after (Sissakian and Fouad,2012).

1.2. Geological and Tectonic Setting

According to Buday (1980), the Missan area is a part of the Makhul-Hemrine subzone (Low Folded Zone), which is sited outside the Arabian Plate form. According to Jassim and Goff (2006), Fouad (2008 and 2012), and Abdulnaby et al. (2021), the Mukdadiya Formation typically has a fluvial environment that quickly subsides in the foredeep basin. In late Miocene-Pliocene period, major thrusting occurred during collision of new Tethyan terranes and the Sanandaj-Sirjan zone with Arabian Plate resulting in the uplift of High Folded, Northern Thrust zones, and the NE part of Balambo-Tanjero zone (Figure 2). The Mukdadiya Formation in the Al-Teeb region (Figures 3 and 4) is made up of numerous sedimentary cycles, most of which consist of conglomerates, sandstone, and claystone arranged from bottom to top. Sand and gravel come in a variety of sizes, reflecting river environments and fining upward cycles. Range of sedimentary formations, such as load casts, trough cross-bedding, graded bedding, planer cross-bedding, and channeling that is periodically filled with gypsum. While Mukdadiya›s lower contact with Injana Formation is pebbly sandstone, the upper contact with Bai Hassan›s Formation is conformable and occasionally covered in Quaternary sediments. Most Quaternary sediments from the southern Iraqi Mesopotamian plain cover large areas of the unstable shelf (Al-Khafaji and Mhadi, 2019).

Figure 2. Correlation chart of the Neogene Period in Iraq (modified from Jassim & Buday, 2006; Jassim et al., 2006).

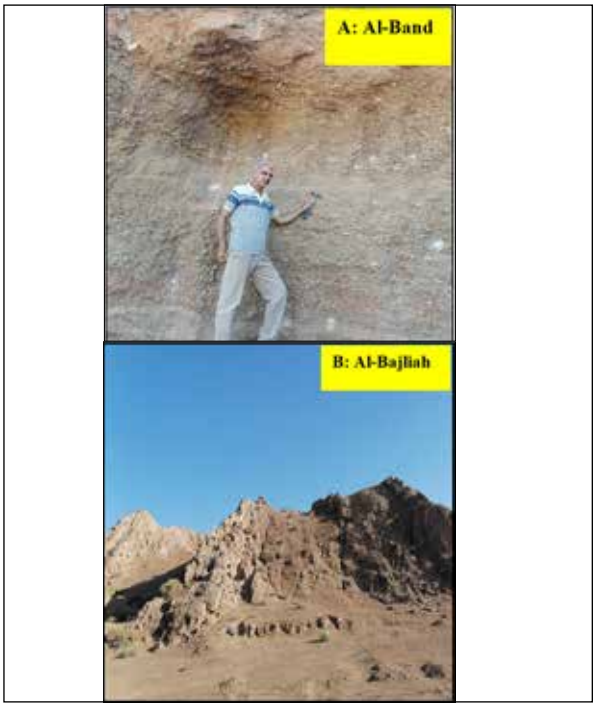

Figure 2. Correlation chart of the Neogene Period in Iraq (modified from Jassim & Buday, 2006; Jassim et al., 2006).

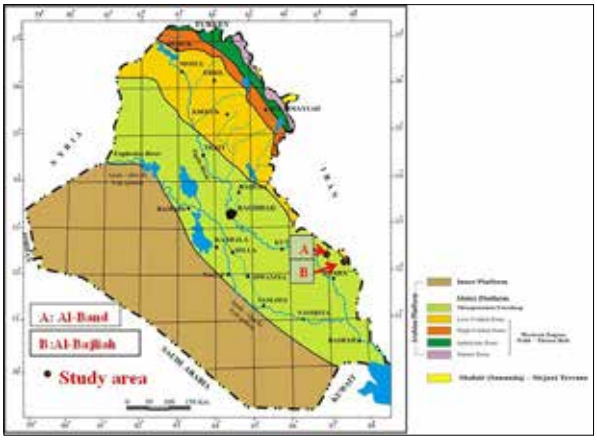

Figure 4. Location and tectonic map of the studied sections (after Fouad,2008; 2012 a and 2012 b)

2. Materials and Methods

The field work included the lithological description and measuring the thickness of sandstone units. Spot samples method were used for collections sandstone from the layers in the sections based on the variation in lithology, thickness, texture and color of the beds. Ten samples collected from both sections including five (5) samples of Al-Band section and five (5) samples of Al-Bajliah section (Figure 5) were chosen for preparing thin sections in the labratories of the Geology Department, College of Science, Baghdad University . The friable grains were consolidated on glass slide by saturated them with Araldite and Hardener materials (Moorland,1968). The components of thin section were counted according to the method of Gazzi-Dickinson (Dickinson, 1970), which is the most common method of counting point, using Polarized microscope (Type Optika) were used in order to identify the mineralogical components.

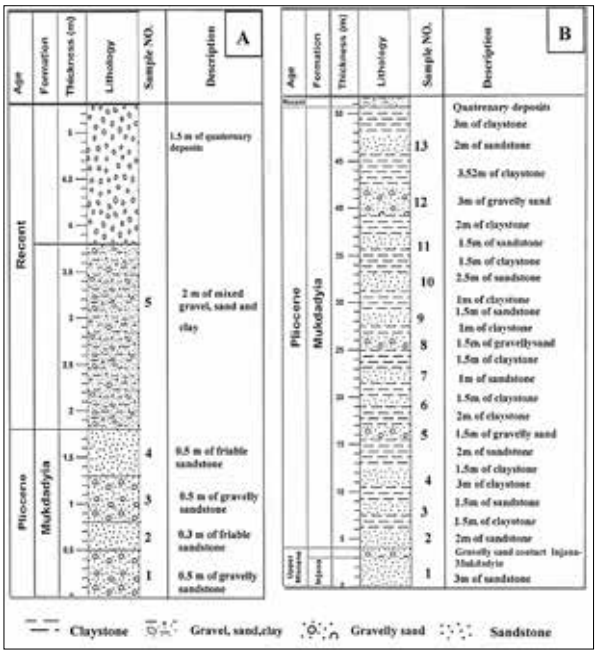

Figure 5. Stratigraphic column of Mukdadyia Formation in Al-Band (B), and Al-Bajliah (G).

3. Results and Discussion

3.1. Petrography of sandstone

Petrography is the most common geological method for understanding sediment formation, how sediments change during erosion, transport, deposition, and subsequent diagenesis. Morever , petrography is a fundamental method in sediment provenance studies (Dickinson et al. 1983; Garzanti, 2016, 2019; Augustsson, 2021). The only technique in sandstone provenance analysis that can give both mineralogical and textural data of the sandstone and its morphological components (small-scale original of the parent rock), enabling direct visualization and reconstruction of the source area (Garzanti, 2016). Sandstone fragmentation patterns can be connected to the plate tectonic setting of the sedimentary basins in which they were deposited (Dickinson & Suczek 1979; Dickinson et al. 1983; Dickinson 1985; Weltje & von Eynatten 2004; Weltje 2006); properties can be deduced to reflect source terranes and tectonic stratigraphic levels achieved through erosion in space and time. By examining the relative proportions of the three main constituents of sandstones: quartz (Q), feldspar (F), lithic or rock fragments (L), and carbonate cement, one can determine the modal composition of these rocks. Carbonate cement and matrix bind these components together (Boggs, 2009). Table 1 displays the averages and percentages of these components.

Table 1. Mineralogical components (%) of sandstone of Mukdadiya Formation Sandstone at Band (A) and Al-Bajalia

Components		Quartz			Feldspar				Rock fragments							Heavy Minerals	Opaque Minerals	Others
		Monocrystalline Quartz	Polycrystalline Quartz	Total Quartz	Orthoclase Feldspar	Microcline Feldspar	Plagioclase Feldspar	Total Feldspar	Carbonate Rock Fragments	Chert Rock Fragments	Igneous Rock Fragments	Metamorphic Rock Fragments	Mudstone Rock Fragments	Evaporites Rock Fragments	Total rock fragments			
Samples Number	A1	13.3	4.4	17.7	4.5	3.3	2.4	5.7	38.2	8.9	3.7	4.7	3.5	4.7	63.7	3.5	4.6	0.3
	A2	13.5	3.2	16.7	3.3	4.4	3.7	8.1	41.3	9.8	4.1	3.5	4.3	2.1	65.1	4.2	3.2	0.9
	A3	10.2	6.8	17	4.4	3.5	2.7	6.2	38.2	8.3	3.4	4.5	5.1	4.2	63.7	4.46	3.5	0.6
	A4	13.4	4.5	17.9	3.2	2.8	3.9	6.7	38.3	7.7	4.3	3.2	6.8	2.6	62.9	3.5	4.9	0.9
	A5	8.8	3.3	12.1	4.5	3.3	2.8	6.1	52.4	5.9	3.2	4.4	3.4	3.7	73	1.3	2.7	0.2
	mim	8.8	3.2	12	3.2	2.8	2.4	5.2	38.2	5.9	3.2	3.2	3.4	2.1	56	1.3	2.7	0.2
	max	13.5	6.8	20.3	4.5	4.4	3.9	8.3	52.4	9.8	4.3	4.7	6.8	4.7	82.7	4.46	4.9	0.9
	Av.	11.84	4.44	16.28	3.98	3.46	3.1	6.56	41.68	8.12	3.74	4.06	4.62	3.46	65.68	3.392	3.78	0.58
	B2	12.6	5.4	18	3.8	3.5	2.3	5.8	40.6	9.7	3.4	3.5	3.7	2.3	63.2	3.1	4.2	0.9
	B5	15.2	3.3	18.5	2.6	2.4	3.9	6.3	42.6	8.4	3.2	3.9	4.3	1.8	64.2	3.6	4.5	0.3
	B8	10.7	5.2	15.9	3.9	4.1	3.4	7.5	41.5	7.7	4.4	3.4	3.2	3.5	63.7	4.4	3.6	0.9
	B10	14.2	4.4	18.6	4.5	3.3	2.6	5.9	39.7	9.4	3.2	4.5	3.1	2.9	62.8	4.7	3.1	0.3
	B12	14.5	3.3	17.8	3.4	2.6	3.2	5.8	41.8	7.6	3.8	3.6	3.9	2.4	63.1	3.6	4.7	0.6
	min	10.7	3.3	14	2.6	2.4	2.3	4.7	39.7	7.6	3.2	3.4	3.1	1.8	58.8	3.1	3.1	0.3
	max	15.2	5.4	20.6	4.5	4.1	3.9	8	42.6	9.7	4.4	4.5	4.3	3.5	69	4.7	4.7	0.9
	Av.	13.44	4.32	17.76	3.64	3.18	3.08	6.26	41.24	8.56	3.6	3.78	3.64	2.58	63.4	3.88	4.02	0.6

Quartz is the main component of the Mukdadiya Formation sandstone is averaging 16.28% in the Band (A) section and 17.76% in the Al-Bajalia (B) section (Table 1). There are two types: polycrystalline quartz and monocrystalline quartz. The average monocrystalline type in the Band (A) section is 11.84%, and the average monocrystalline type in the Al-Bajalia (B) section is 13.4%. The crystals are angular to sub-angular with dominant straight and wavy extinction. The type of source rock is one of the major factors that affect the undulation of quartz (Conolly, 1965).

Wavy extinction resulted from the stress that was subjected to the quartz grain, which suggests that they are derived from plutonic igneous rock or metamorphic igneous rock (Asiedu et al., 2000; Folk, 1974). The occurrence of inclusions in monocrystalline quartz grains may reflect their derivation from plutonic igneous rock. (Figure 6-A).

These grains show polycrystalline type of quartz with an average in the Band (A) section is 4.44%, and the average polycrystalline type in the Al-Bajalia (B) section is 4.32%. It also has a sub-angular to sub-rounded shape, with a wavy extinction. Most of the quartz grains have a semi-angular shape, indicating that the transport distance is short to medium. Therefore, the probable source of polycrystalline quartz is metamorphic rocks, such as schist, gneiss, metaquartzite, and plutonic igneous rocks (Blatt, 1967; Folk, 1974). The amount of polycrystalline quartz presented in sandstones is a function of grain size and increases with increasing grain size (Conolly, 1965) (Figure 6-B).

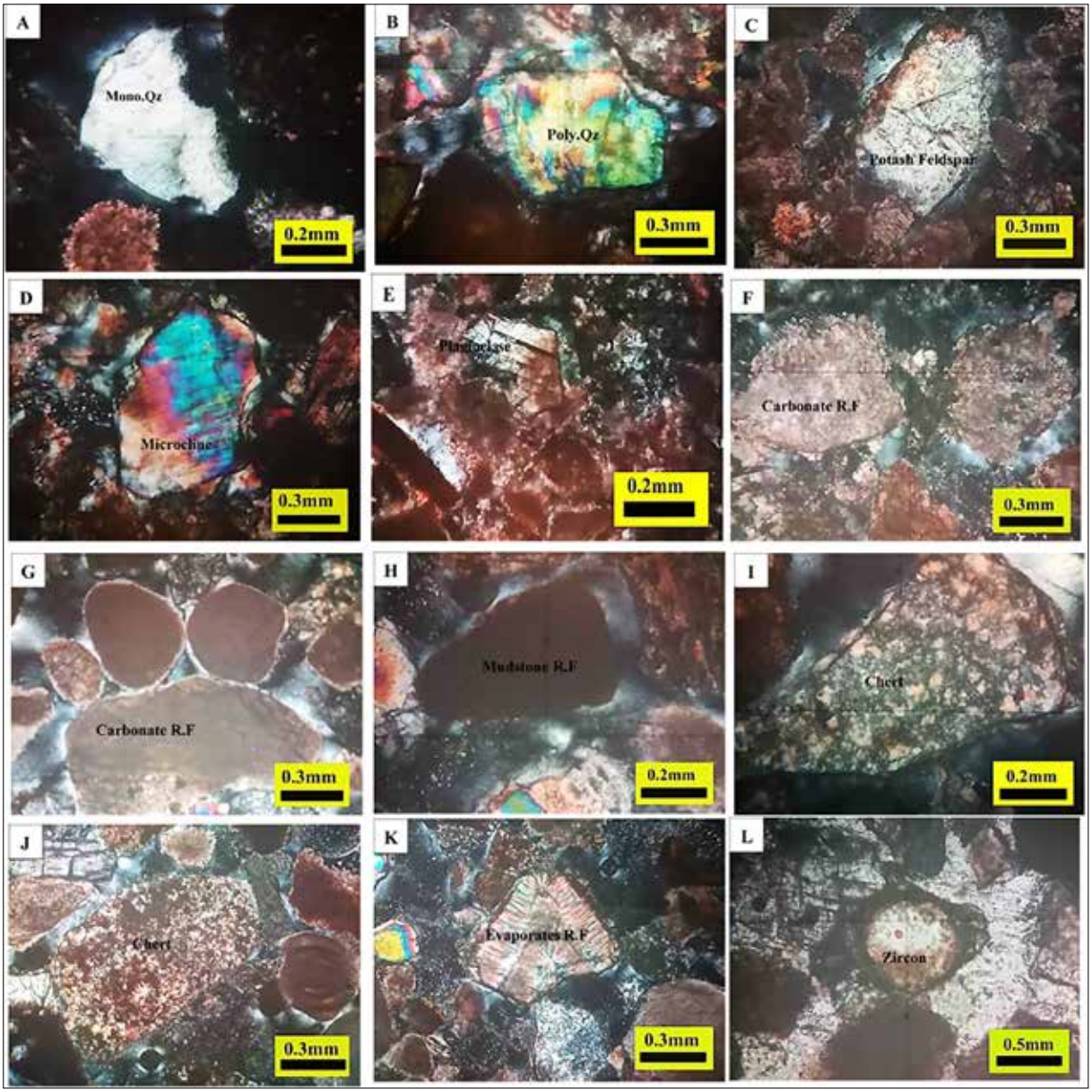

Figure 6. A: Angular, monocrystalline quartz, sample number (A1), XPL. **B:** Sub Angular, Polycrystalline quartz, sample number (B2), XPL. **C:** Angular, potash Feldspar, sample number (A 3), XPL. **D:** Sub angular, Micocline, sample number (B5), XPL. **E:** Angular, Plagioclase, sample number (A2), XPL. **F:** Sub-rounded carbonate Rock fragment, sample number (B10), XPL. **G:** Sub-rounded carbonate Rock fragment, sample number (A1), XPL. **H:** Sub rounded Mudstone Rock fragment, sample number (B12), XPL. **I:** Angular chert fragment, sample number (A5), XPL. **J:** Angular chert fragment, sample number (B12), XPL. **K:** Angular Evaporite fragment , sample number (B8), XPL. **L:** Sub-rounded Zircon, sample number (A4), XPL.

Feldspars are common in sedimentary, igneous, and metamorphic rocks. They are less stable under the influence of surface conditions, especially in sedimentary environments. Mechanically, the stability of feldspar mineral is less than that of quartz in the process of erosion; on the other hand, Chemical weathering of feldspar may produce clay. Therefore, feldspar minerals refer to short distances of transportation (Pettijohn, 1975). Feldspars in Mukdadiya Formation sandstone have an averaging 6.5% in the Band (A) section and 6.26% in the Al-Bajalia (B) section (Table 1).

The occurrence of alkali feldspar (Potassium feldspars), including orthoclase and microcline, suggests semi-arid paleoclimate conditions or a high relief source area subjected to rapid erosion (Pettijohn et al., 1987). Orthoclase in the Band (A) section ranges from 3.2–4.5%, with an average of 3.98%. while in Al-Bajalia (B), sections ranged between 2.6-4.5%, with an average of 3.64%. Orthoclase grains are subangular to subrounded with dusty color due to decomposition into clay minerals.(Figure 6-C).

Microcline in the Band (A) section ranges between 2.8– 4.4%with an average 3.46 %. while in Al-Bajalia (B), sections ranged between 2.4-4.1%, with an average of 3.18%. Microcline grains show a cross-hatching twinning, and are observed as subangular, with degrees of alteration. A slight difference in percentages was observed in the sample of Band (A), and Al-Bajalia (B) (Figure 6-D). Plagioclase in the studied samples was observed as very angular to subangular. The fresh feldspars may indicate fragmentation from igneous rocks, accompanied by short-distance transport (Pettijohn, 1975) (Figure 6-D). Plagioclase in the Band (A)

section ranges between 2.4– 3.9% with an average 3.1 %. While in Al-Bajalia (B) sections, ranging between 2.3-3.9%, with an average of 3.08%. Feldspar information alone is insufficient to identify source rocks; however, orthoclase and plagioclase may be derived from plutonic igneous rock or metamorphic rocks (Boggs, 2002). Microcline and perthite are more commonly found in the plutonic igneous rocks and metamorphic rocks, and are found to be rare in the formation of volcanic rocks. It can be said that the origin of the feldspar in the sandstones of the Mukdadiya Formation are from plutonic and metamorphic rocks (Figure 6-E).

The rock fragments include pieces of old source rocks that have been broken down and are indivisible into individual mineral grains. They are important in the study of the origin rocks because they are easy to distinguish and are a good indicator of the type of source rocks compared to individual minerals, such as quartz and feldspar (Boggs, 1995). Rock fragments are considered a material that indicates the clastic source. Location of the source rocks affects the percentage of rock fragments within the sandstone. This percentage increases when the source rock area was near the sedimentary basin or has high topography (Stephen, 2000). Rock fragments are common in the Mukdadiya Sandstone composition. The percentage ranges from 56% to 82.7.8% in the Band (A) section, with an average of 65.6%. It ranges from 58.8% to 69% in the Al-Bajalia (B) section, with an average of 63.4%.

A- Carbonate rock fragments

Carbonate rock fragments are common in clastic sedimentary rocks and clastic sediment in Iraq due to the widespread outcrops of these rocks in many areas of Iraq, these rock fragments represent special conditions of rapid mechanical erosion rather than chemical dissolution (Pettijohn et al., 1987). The Arabian shelf beneath Mesozoic carbonates is a likely source of carbonate fragments, which could have originated from adjacent areas. Carbonate source-rock fragments show a pattern of rapid mechanical erosion rather than chemical decomposition (Pettijohn et al., 1987). The presence of such fragments in the sediments indicates that the material was rapidly transported locally (Al-Juboury, 1994). Dickinson (1985) pointed out that high folds and thrusts in collision zones between colliding plates are formed, a process sometimes called recycling orogeny. Fold-thrust belts may expose igneous rocks, and the source rocks of the collision highs are sedimentary and metamorphic rocks that existed at the continental margin before the collision.

Carbonate rock fragments in the Band (A) section, ranges between 38.2– 52.4% with an average 41.6%, while in Al-Bajalia (B) section, it ranges from 39.7% to 42.9% with an average of 41.24% (Figures 6-F and -G).

B- Chert

The types of chert rock fragments, sub-rounded and rounded that were identified in the studied samples, including chalcedonic macrocrystalline and microcrystalline chert rock fragments in the Band (A) section,ranging between 5.9.– 5.8% with an average 8.1 %, while in Al-Bajalia (B) section, it ranges between 7.6-9. 7% with an average of 8.5% (Figures 6-I and -J).

C- Mudstone rock fragments

Mudstone rock fragments in the Band (A) section range between 3.4–6.8% with an average 4.6 %. While in Al-Bajalia (B) sections, ranging between 3.1- 4.3% with an average of 3.64% (Figures 6- H).

D- Igneous Rock Fragments:

Igneous rock fragments in the Band (A) section range between 3.2– 4.3%, with an average 3.74 %. While in Al-Bajalia (B) sections ranging between 3.2- 4. 4% with an average 3.6%

E- Metamorphic Rock Fragments

Metamorphic rock fragments in the Band (A) section range between 3.2– 4.7% with an average 4.07 %. while in Al-Bajalia (B) section, they range between 3.4- 4. 5% with an average of 3.78%.

F- Evaporates rock fragment

Evaporate rock fragments in the Band (A) section range between 2.1– 4.7% with an average of 3.46 %, while in Al-Bajalia (B) section, it ranges between 1.8- 3. 5% with an average of 2.58%. (Figures 6-K).

Opaque minerals

Opaque minerals in the Band (A) section range between 2.7– 4.9% with an average 3.78 %. while in Al-Bajalia (B) sections ranging between 3.1- 4. 7% with an average 4.028% (Figure 6-L)

3.2 Discussion:

Rock fragments are often unstable in the sedimentary setting, and their existence in sandstone provides good evidence of the original rock. (Boggs, 1995). It is clear that sedimentary rock fragments, particularly carbonate rock fragments, are the most abundant in the samples studied. This implies that they transformed from older layers with high carbonate content, which were exposed to the surface by tectonic activity such as folding and faulting (Dickinson, 1985); (Al-Juboury, 1994); and Zattin and Zuffa (2004). The presence of chert is attributed to the sediments of the chert that were subjected to the folding process or to the Chert nodules concretions located in the layers of carbonate rocks that were exposed (Dickinson, 1985; Blatt, 1987). AL-Juboury (1994) pointed out that the rocks of some Mesozoic formations in the thrust zone, possibly the Qulqula series, may be a source of chert. The chert fragments may be originated from carbonate deposits, containing chert nodules and chert in the northeastern overthrust belt sequence, in particular in the Qulqula Group (Al-Juboury, 1994). This shows that the Mukdadiya formation›s rocks, originated primarily from sedimentary rocks, with metamorphic and igneous rocks, contribute as secondary sources. The variety in mineral components reflects the diversity of their source rocks (Hendrix, 2000).

3.3 Classification of Sandstones

Based on the percentage of the main sandstone components, such as quartz, feldspar, and lithic pieces, the Mukdadiya Formation›s sandstone types (Table 1) were classified using Garzanti›s (2016). All of the Mukdadiya sandstone samples were classified as immature Quartzolithic sandstone as a result of this classification (Figure 7). Because sandstone is immature, this suggests that the sediments were

deposited quickly and moved a short distance from their source (Garzanti, 2019). According to Boggs (1995), the lithic component of sandstone is compositionally immature sandstone formed by the production and deposition of several moderately unstable minerals. The predominance of carbonates and feldspars in the sections under study suggests that low-intensity physical and chemical weathering predominated in arid to semiarid climates, while tectonic uplift of thrust rocks and collisions between continents dominated the deposition of carbonates and solid rocks. Carbonate-rich sandstone indicated that the carbonate source was the primary source, with short-distance transportation and deposition occurring during the early stages of tectonic uplift. According to Arribas et al. (2000), dry and semi-dry climates preserve carbonate rocks, whereas wet climates reduce their abundance (Mack, 1981).

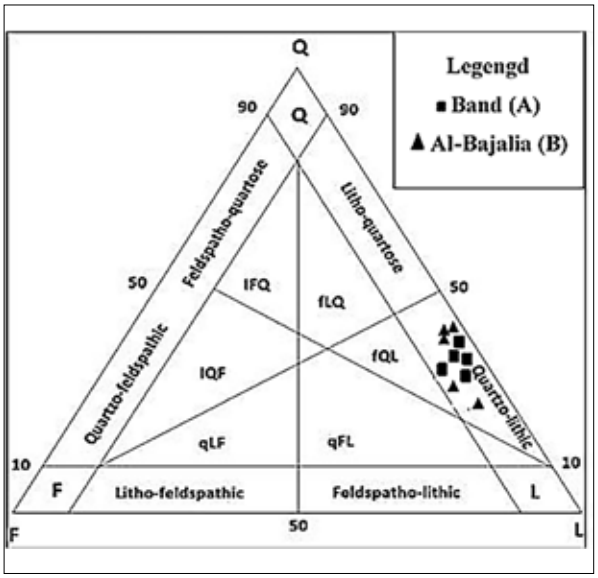

Figure 7. Classification of Mukdadiya Formation sandstone at Band (A) and Al-Bajalia (B) (Garzanti, 2016).

3.4 Stability of sandstone

Bjorlykke (1983) used a ternary diagram to classify sediment stability as chemical or mechanical (quartz-feldspar-rock fragments). He stated that a sandstone with a high percentage of quartz is chemically and mechanically stable, whereas a sandstone with a high percentage of feldspar is mechanically stable but chemically unstable, and a sandstone with a high percentage of rock fragments is chemically and mechanically unstable. According to this classification, Mukdadiya Formation sandstone in both sections is chemically and mechanically unstable due to the large percentage of rock fragments (Table 1and Figure 8).

3.5 Provenance of sandstone

The main aim of sediment provenance study is to remake and understand the geology of the source area, as well as to link the clasts› final burial to the host rock›s original erosion (Weltje & von Eynatten 2004). Most of the provenance investigations use petrographic analysis of quartz, feldspar, and rock fragments (Boggs, 2009). Due to its chemical stability, resistance to splitting, and relative hardness, quartz is a crucial mineral in the development of sandstones (Ibbeken & Schleyer 1991). Individual quartz crystals that exhibit wavy extinction, ranging from straight to oblique, are the primary means by which plutonic igneous rocks are identified in this study (Dickinson, 1985). Metamorphic rocks are indicated by wavy extinction > 5°, which is the greatest grade of wavy quartz (Folk, 1974). The wavy extinction of single quartz crystals and the disintegration of some of their grains under pressure could indicate that they originated in plutonic igneous and metamorphic rocks (Saftić et al. 2003). Polycrystalline quartz frequently displays straight or slightly curved intercrystalline borders, which suggests a plutonic origin (Tucker, 1985). Feldspar is seen as more relevant than quartz in detecting origin due to its less stable states (Boggs, 2009). Orthoclase and plagioclase can form from both plutonic and metamorphic igneous rocks, though microcline Microclene and plagioclase are more common in plutonic igneous rocks but uncommon in volcanic rocks (Garzanti, 2019). The presence of more feldspar could indicate that igneous rock fragmentation was accompanied by shorter transport routes (Pettijohn, 1975). According to Al-Juboury (1994), the flint fragments might have come from carbonate deposits that contained flint nodules and flint in the Qulqula group and the northeastern overthrust belt sequence . Carbonate particles that may have come from nearby regions are most likely to have come from the Arabian shelf beneath Mesozoic carbonates. Fragments of carbonate source rock exhibit a distinctive pattern of quick mechanical erosion as opposed to chemical breakdown (Pettijohn et al., 1987). The Mukdadiya Formation›s high percentage of carbonate fragments suggests that the parent rock is naturally carbonate-rich. The presence of these shards in the strata suggests that the material was moved quickly within the area (Al-Juboury, 1994). Volcanic fragments require quick erosion and incomplete weathering, which occur only in areas with high relief and arid climate (Pettijohn et al., 1973). Dickinson (1985) proposed that the fragments could have originated in the overthrust belt, the Sanandaj-Sirjan belt, or the northeastern overthrust belt, where the metamorphic fragments were most likely formed.

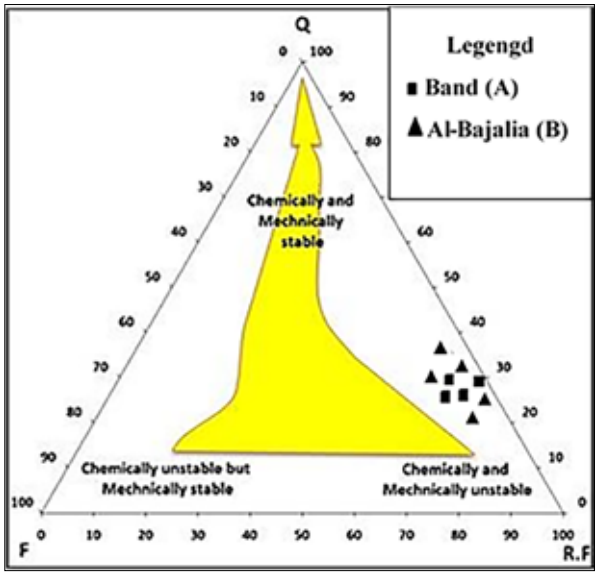

Figure 8. ternary diagram to classify sediment stability of Mukdadiya Formation sandstone at Band (A) and Al-Bajalia (B) Bjorlykke (1983) .

3.6 Tectonic setting

The source of the sandstone was identified in this work, using petrographical modal studies and QFL and QmFLt tectonec classification diagrams. The origin of Mukdadiya sandstone was explained using the ternary diagram of Ingersoll and Suczek (1979). The investigated samples plot in an undissected arc in this diagram (Figure 9). Additionally, the Dickinson and Suczek (1979) ternary diagram shows that the studied samples plot in lithic recycled (Figure 10). Uplifted terranes of folded and faulted strata, which are primarily composed of sedimentary and metamorphic rock, are the source of orogenic province deposits. However, igneous rock may be partially exposed (Dickinson and Suczek, 1979). The studied samples are lithic, recycled from transitional and undissected arcs, and show that the sand contains more rock fragments and less feldspar and quartz. In addition, the sand has a high concentration, due to the abundance of lithic fragments that are nearly solely volcanic clasts. The proportion of polycrystalline quartz and rock fragments and the low proportion of monocrystalline quartz and feldspar suggest that the sands may have derived from oceanic islands. High folds and thrusts develop in collision zones between colliding plates, a phenomenon often referred to as recycling orogeny, as noted by Dickinson (1985). Sedimentary and metamorphic rocks that were present at the continental margin before the collision are the source rocks of the collision highs, and fold-thrust belts may reveal igneous rocks (Dickinson1985). Tectonically uplifted, complex subduction zones behind volcanic arcs are the sources of transitional and lithospheric-recycled sediments. Sedimentary, metamorphic, and igneous rock exposed by thrust sheets and uplifting dominate these areas (Dickinson, 1970).

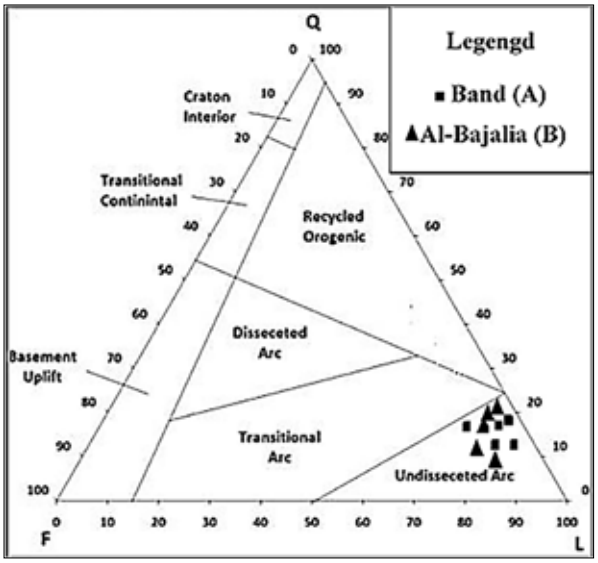

Figure 9. Tectonic provenance classification after Ingersoll and Suczek (1979) , and showing studied samples in Band (A) and Al-Bajalia (B) (after Garzanti, 2016).

3.7 Paleoclimate

Climate has a significant impact on skeletal mineralogy, even if tectonics is the primary determinant (Suttner and Dutta, 1986). According to Young (1975), the percentage of preservation in sands is a sensitive indicator of the type of paleoclimate. To identify the paleoclimatic circumstances that influenced the sandstones under study, the following is employed as a sensitive discriminator of sandstones with different climatic records. The ratios of Qt/F+R and Qp/F+R are low, indicating a low compositional maturity index and suggesting that the sandstone composition is immature. According to Suttner and Dutta›s (1986) bivariate double logarithmic plot of Qt/F+R and Qp/F+R, all of the Injana Formation›s sandstone samples are located in the semi-arid regions of the Tuz-Khurmatu and Basara sections (Figure 11 and Table 2). Tucker (1991) states that semi-humid conditions may contribute to the dominance of quartz and decrease the amount of feldspar and rock fragments, whereas dry conditions may support the dominance and stability of these unstable minerals.

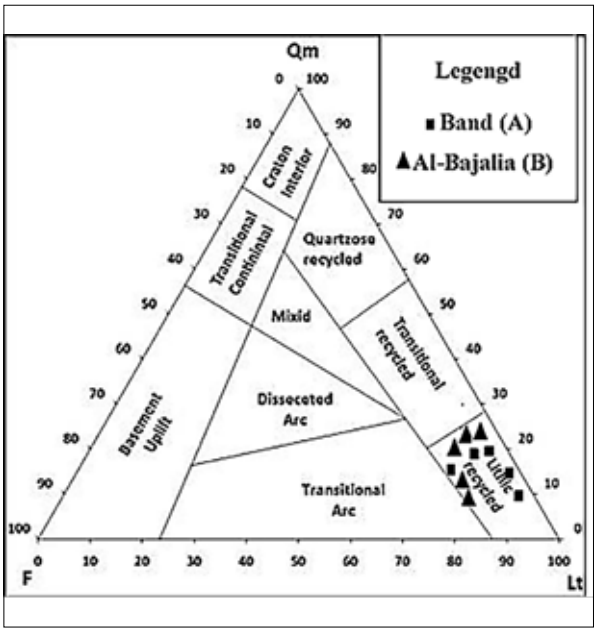

Figure 10. Tectonic provenance classification Dickinson and Suczek (1979), and showing studied samples in Band (A) and Al-Bajalia (B) . (Garzanti, 2016).

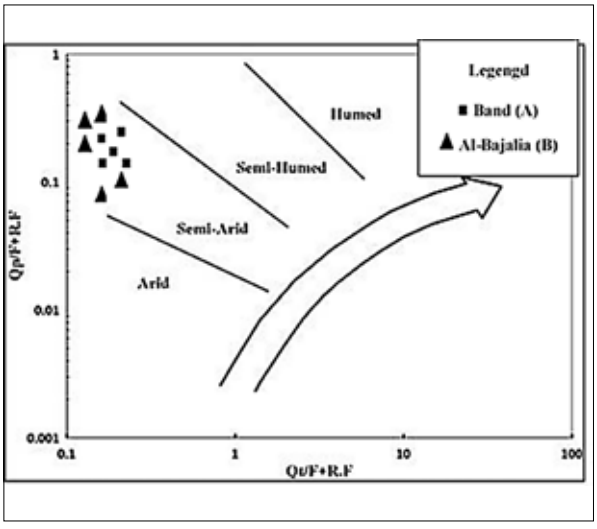

Figure 11. Bivariate log-log plot of Qt/F+R and Qp/F+R showing studied sample in Band (A) and Al-Bajalia (B) after (Suttner and Dutta, 1986).

Table 2. Main components (%) of sandstone of Mukdadiya Formation Sandstone at Band (A) and Al-Bajalia

	Total Quartz	Total Feldspar	Total rock fragments	F+RF	Q/F+RF
A1	17.7	5.7	63.7	69.4	0.25
A2	16.7	8.1	65.1	73.2	0.22
A3	17	6.2	63.7	69.9	0.24
A4	17.9	6.7	62.9	69.6	0.25
A5	12.1	6.1	73	79.1	0.15
min	12.1	5.7	62.9	68.6	0.17
max	6.8	3.9	4.7	8.6	0.79
Av.	16.28	6.56	65.68	72.24	0.22
B2	18	5.8	63.2	69	0.26
B5	18.5	6.3	64.2	70.5	0.26
B8	15.9	7.5	63.7	71.2	0.22
B10	18.6	5.9	62.8	68.7	0.27
B12	17.8	5.8	63.1	68.9	0.25
min	15.9	5.8	62.8	68.6	0.23
max	18.6	7.5	64.2	71.7	0.25
Av.	17.76	6.26	63.4	69.66	0.25

4. Discussion

The study area is situated in the Al-Teeb district in southern Iraq near the Iraqi-Iranian border. This study deals with the Mukdadiya Frmation in this area which Gravel, and sand sediments deposited by braided rivers make up these alluvial fans. The Mukdadiya Formation, located above the Fatha Formation and covered with Bai Hassan formations, which are found in the mountainous terrain along the border (Jassim and Goff, 2006). Field studies showed that the sediments consist mainly of gravel and sand, with the presence of clay. The changes in the grain size of sediments indicate that the differences in size are due to changes in the energy flow and sediment sorted in a relatively high energy environment. The large grain sizes indicate a high velocity for the current, which is strong enough to transport particles of this size (Friedman, 1967).

This study focuses on the petrographic description of sandstone to identify the Provence, paleoclimate ,and tectonic setting for Mukadya Formation in two selected sections: Al-Band and Al-Bajalia in Al-Teeb area by examining the proportions of the three main constituents of sandstones: quartz (Q), feldspar (F), lithic or rock fragments (L).

Most of the provenance investigations use petrographic analysis of quartz, feldspar, and rock fragments (Boggs, 2009).Sample of sandstone of Mukdadiya Formation shows quartz crystals with wavy extinction from straight to oblique, which means some of their grains› disintegration under pressure could indicate that they originated in plutonic igneous and metamorphic rocks (Saftić et al. 2003).Morover, Polycrystalline quartz frequently displays straight or slightly curved intercrystallite boundaries, which suggest a plutonic origin (Tucker, 1985). The presence of Feldspar could indicate that igneous rock fragmentation was accompanied by shorter transport routes (Pettijohn, 1975). Orthoclase and plagioclase can form from both plutonic and metamorphic igneous rocks, though microcline Microclene and plagioclase are more common in plutonic igneous rocks but uncommon in volcanic rocks (Garzanti, 2019). The presence of quartz and feldspar in the Muqdadiya Formation as clastic competes requires the presence of a nearby source containing igneous and metamorphic rocks that are exposed to weathering in order for the Muqdadiya Formation sediments to emerge from them, this source is located in northeastern Iraq in the high fold Zone . Moreover, the sandstone of Mukdadiya Formation›s high percentage of carbonate rock fragment and chert suggests that the source rock is consist of carbonate and chert that were subject to mechanical weathering and transport where Muqadiya Formation were deposited. This proposed source is the Qalqalah Formation, which consists of chert and limestone in northeastern Iraq and suggests that the material was moved quickly within the area (Al-Juboury, 1994). Mahdi and Sultan (2021) in their study of gravel of Mukdadiya in Al-Teeb area confirmed that the origin of the derived gravels is from the Qulqula Formation, because of their content of radiolaria and the other characterizing fossils.

Tectonically, The samples of current study are Lithic recycled and undissected arc which indicated the sand is high rock fragments and less quart and feldspar, moreover, the sand high in The proportion of polycrystalline quartz and rock fragments and low proportion of monocrystalline quartz and feldspar, that indicate the Sands may be derived from oceanic island due to abundant lithic fragments that are almost exclusively volcanic clasts. Lithic recycled sediments source refers to tectonically uplifted complex subduction zones behind volcanic arcs; these areas are dominated by sedimentary, metamorphic, and igneous rocks exposed due to tectonic uplift. (Dickinson,1970).

The collision between the Arabian Plate and the Eurasian Plate continued during the Pliocene. This convergence resulted in the formation of the Zagros Fold and Thrust Belt, where the Arabian Plate is colliding with the Iranian Plate. These events led to uplift and deformation of the

Plate as it is colliding with the Iranian Plate. These events led to significant uplift and deformation of the Zagros Mountains. Therefore, the origin of the deposits of the Mukdadya Formation in Iraq is believed to be from fluvial and alluvial fan environments that were active during the Miocene (Sissakian et al., 2021). Sediments were transported and deposited by rivers and streams that drained from the uplifted areas of the surrounding mountains. The formation is composed of gravel, sandstones, and mudstones that reflect a range of depositional environments, from braided river channels to floodplain deposits (Al-Juboury and McCann, 2008). This sedimentary deposit is a common type of molasse, which was formed in a rapidly sinking basin and is characterized by freshwater and lacustrine environments (Jassim and Goff, 2006).

5. Conclusion

1- Quartz is the main component of the Mukdadiya Formation sandstone. Two types of quartz, polycrystalline and monocrystalline, have angular to sub-angular with dominant straight and wavy extinction, that suggested they derived from plutonic igneous rock or metamorphic igneous.
2- The occurrence of Alkali feldspar (Potassium feldspars), including orthoclase and microcline, suggests semi-arid paleoclimate conditions or high relief source area, subjected to rapid erosion plagioclase in studied samples observed as very angular to sub angular. The fresh feldspars may indicate a fragmentation process from igneous rocks, accompanied by a short distance of transportation.
3- It is obvious that sedimentary rock fragments, particularly carbonate rock fragments, are the most abundant in the studied samples. This implies that they transformed from older layers with high carbonate content, which were exposed to the surface by tectonic activity such as folding and faulting with high relief.
4- Mukdadiya sandstone samples were determined to be quartzite. As a result, this sandstone is immature and suggests that the sediments were quickly deposited and moved a short distance from their source in the overthrust belt, the Sanandaj-Sirjan belt, or the northeastern overthrust belt, where the metamorphic fragments were most likely formed.
5- The stability of sandstone shows that the sediments are chemically and mechanically unstable.
6- Paleoclimate conditions indicate that all samples of Mukdadiya sandstone are semi-arid areas.

References

Abdulnaby, W., Mahdi, M., Al Al-Muhamed, R., Darweesh, N., and Hashoosh, A. 2021, . Geology of Bajalia Anticline of the Low Folded Zone of Iraq, Kuwait

Al-Banna, N. Y., 1982. Sedimentology of Injana Formation in selected areas from Northern Iraq, Unpublished. Sc. Thesis, University of Mosul, College of Science, 177 p.

Al-Dabbagh, N.O.F., 2018. Mineralogy and geochemistry of Injana and Mukdadiya Formation (Upper Miocene-Pliocene) in Zorbatyah area east iraq. Eastern Iraq . Unpubl.MSc.Thesis, Baghadad University , 84P.

Al-Badri, A., Dhiab, S.H., Faris, F.M., and Anwar, F., 1992. New names for some of the Middle Miocene-Pliocene formations of Iraq (Fat`ha, Injana, Mukdadiya and Bai Hassan formations). Iraqi Geological Journal, 25 (1), p 1 –7.

Al-Jassim, J.A., 1969, Sedimentological investigation of lower Bakhtiari Formation , in central Iraq , vnpubl M.Sc Thesis ,university of Baghdad ,84p.

Al-Juboury, A. I., 1994. Petrology and Provenance of the Upper Fars Formation, Northern Iraq. Acta. Geologica Universitatis Commenianae (Slovakia), Vol.50, pp. 45-53.

Al-Juboury, A.I., McCann, T., 2008. The Middle Miocene Fatha (Lower Fars) Formation, Iraq. Geo Arabia, 13(3), 141-174.

Al-Kalidi, R.M.S,2014. Petrography and Geochemistry of Mukdadiya Formation in Zawita 126P.

Al-Khafaji, S. J., & Mahdi, M. M. (2019). Geochemical, Mineralogical and Biological study of Holocene deposits in Almuthana province, southern Iraq. Iraqi Journal of Science, 1521-1529.

Al-Mutury, W. and Al-Asadi, M. 2008. Tectonostratigraphic History of Mesopotamian Passive Margin during Mesozoic and Cenozoic, South Iraq. Journal of Kirkuk University, 3: 31-50.

Al-Salmani, N. Z., & Tamar-Agha, M. Y. (2018). Petrography and Provenance of the Sandstone of Injana and Mukdadiya Formations (Upper Miocene/Pliocene) at Duhok Governorate, Northern Iraq. Iraqi Journal of Science, 59.

Al-Samaani,J.J.A.2011.Mineralogy and geochemistry of sandstone of Al-Mukdadiya formation in selected areas,north-east Missan. Unpubl.MSc.Thesis, Basrah University , 100p.

Al-Shammary, T. (2009). Sedimentological studies of the Mukdadiya formation south—east of Badra. Iraqi Journal of Science, 50(3), 369-375.

Al-Uqagdi, R.S., 2011. Sedimentology and Sequence Stratigraphy of Injana and Al-Muqdadyia Formations in Zakho and Ain Sefni areas/a comparative study. Unpubl. M.Sc. Thesis University of Mosul. Coll. Of Sc.149 P.

Arribas, J., Critelli, S., Le Pera, E. and Tortosa, A. ,2000. Composition of modern stream sand derived from a mixture of sedimentary and metamorphic source rocks (Henares River, Central Spain). Sedimentary Geology, Vol.133, pp.27-48.

Asiedu, D. K., Suzuki, S., and Shibata, T. (2000). Provenance of sandstones from the Wakino Subgroup of the Lower Cretaceous Kanmon Group, northern Kyushu, Japan. Island Arc, 9(1), 128–144. https://doi.org/10.1046/j.1440-1738.2000.00266.x

Augustsson C. 2021. Influencing factors on petrography interpretations in provenance research–acase study review .Geosciences 11, 205 p. https://doi.org/10.3390/geosciences11050205.

Basi, M. A. (2012). Sedimentological, Petrographical and Mineralogical Subsurface Study of Mukdadiya Formation, Central Part of Iraq. Iraqi Bulletin of Geology and Mining, 8(2), 87-98.

Bellen, R. C., Van Dunnington, H. V., Wetzel, R. and Morton, D. M., 1959. Lexique. Stratigraphque International; Asie paric, Internal. Geol. cong., Comm. Stratigraphy, 3 (3): 333 p.

Conolly, J. R. (1995). The occurrence of polycrystallinity and undulatory extinction in quartz in sandstones. Journal of Sedimentary Research, 135(1), 116–135.

Buday, T., 1980. The Regional Geology of Iraq (Stratigraphy and Paleontology). Dar Al-Kutb Publishing House, Mosul, Iraq, 443 p.

Bjorlykke, K., 1983. Digenetic reactions in sandstone. In: sedimentary digenesis (ED. By A. Parker and B.W. Sellwood), NATO ASI Series C; Vol. 115. Reidel, Dordrecht, p 169-214.

Boggs, S.Jr., 1995. Principles of Sedimentology and Stratigraphy, Prentice Hall, New Jersey. 774 p.

Boggs, S.Jr., 2009. Petrology of Sedimentary Rocks, 2nd edition Cambridge Univ. Press, Cambridge, 600 p.

Buday, T., 1980. The Regional Geology of Iraq (Stratigraphy and Paleontology). Dar Al-Kutb Publishing House, Mosul, Iraq, 443 p.

Demange, M. A. (2012). Mineralogy for Petrologists: optics, chemistry and occurrences of rock-forming minerals. CRC Press.

Dickinson, W. R. (1970). Interpreting detrital modes of graywacke and arkose. Journal of Sedimentary Research, 40(2), 695–707.

Dickinson, W. R., & Suczek, C. A. (1979). Plate tectonics and sandstone compositions. AAPG Bulletin, 63(12), 2164–2182.

Dickinson, W.R., Beard, L. S., Brakenridge, G.R., Erjavec, J.L., Ferguson, R.C., Inman, K.F., Ryberg, P.T., 1983. Provenance of North American Phanerozoic sandstones in relation to tectonic setting. Geological Society of America Bulletin, 94 (2), p 222-235.

Dickinson, W.R.,1985. Interpreting provenance relations from detrital modes of sandstones. In Provenance of arenites. Dordrecht: Springer Netherlands. Dordrecht, p 333-361.

Enad, T. H., 2007, Stratigraphical and sedimentological study of the Mukdadiya Formation in Badra area, Wasit Governorate, Unpublished. M.Sc. Thesis, University of Baghdad, 117P.

Folk, R. L., 1974. Petrography of Sedimentary Rocks. Austin, Texas, H Hemphill Publishing, 182 p.

Fouad, S.F.A., 2008. Geological map of Kany Rash Quadrangle, Sheet No. NJ-38-10 GEOSURV, Baghdad, Iraq..

Fouad, S.F.A., 2012b. Tectonic Map of Iraq, scale 1: 1000 000, 3rd edit. GEOSURV, Baghdad, Iraq.

Friedman, G.M., 1967. Dynamic processes and statistical parameters compared for size frequency distribution of beach and river sands. Journal of Sedimentary Research, 37(2), 327-354.

Garzanti E. 2016. From static to dynamic provenance analysis – Sedimentary petrology upgraded. In: Caracciolo L., Garzanti E., Von Eynatten H. & Weltje G.J. (Eds.): Sediment generation and provenance: processes and pathways. Sedimentary Geology 336, p 3–13. https://doi.org/10.1016/j.sedgeo.2015.07.010.

Garzanti E. 2019. Petrographic classification of sand and sandstone. Earth-Science Reviews 192,p 545–563. https://doi.org/10.1016/j. earscirev.2018.12.014.

Hendrix, M. S. (2000). Evolution of Mesozoic sandstone compositions, southern Junggar, northern Tarim, and western Turpan basins, northwest China: A detrital record of the ancestral Tian Shan. Journal of Sedimentary Research, 70(3), 520–532.

Ibbeken H. & Schleyer R. 1991. Source and Sediment. Springer, Berlin, p 1–286.

Ingersoll, R.V. and Suczek, C.A. 1979. Petrology and provenance of Neogene sand from Nicobar and Bengal fans, DSDP sites 211 and 218. Jour. of Sedi. Petrology, Vol.49, pp.1217-1228.

Jassim, S.Z.and Goff, J.C., 2006. Geology of Iraq. Dolin, Prague and Moravian Museum, Brno.341 p.

Mahdi, M. M., & Soltan, B. H. (2021). Determination of the Origin of Mukdadiya Formation's Gravels in Al-Teeb Region, East of Maysan Governorate, Southern Iraq, Based on Sedimentological and Paleontological Evidence. Iraqi Journal of Science, 2970-2982.

Mack, G.H. 1981. Composition of modern sand in humid climate derived from low-grade metamorphic and sedimentary foreland fold-thrust belt of north Georgia. Jour. of Sedi. Petrology, Vol.51, pp.1247-1258.

Moreland, G.C., 1968. Preparation of polished thin-section: In Hutchison, laboratory handbook of petrographic techniques, wiley Inter.Science.

Pettijohn, F. J., 1975. a Sedimentary Rocks, Harper and Row, 3 rd ed, New York, 628 p.

Pettijohn, F.J., Potter, P.E. and Siever, R., 1987. (Edit) Sand and sandstones. Springer- Verlag. New York, 553 p.

Saftić B., Velić J., Sztanó O., Juhász Gy. & Ivković Ž. 2003. Tertiary subsurface facies, source rocks and hydrocarbon reservoirs in the SW part of the Pannonian Basin (northern Croatia and south-western Hungary). Geologia Croatica 56, p 101–122.

Sadik, J.M., 1977. Sedimentological investigation of the Dibdibba Formation, southern and central Iraq., unpubl. M.Sc. Thesis, University of Baghdad ,148p.

Sissakian, V., Al-Jiburi, B., 2012. Stratigraphy of the High Fold Zone. Iraqi Bull. Geol. Min., Special Issue (6), 73-161.

Suttner, L. J. and Dutta, P. K., 1986. Alluvial sandstone composition and paleoclimate, Framework mineralogy. Jour. of Sedi. Petrology, Vol. 56, p 329-345.

Tucker, M. E., 1991. Sedimentray Petrology, an Introduction to Origin of Sedimentary Rocks, 2nd ed. Black Well Scintific Lid., 560 p.

Weltje G.J. 2006. Ternary sandstone composition and provenance: an evaluation of the 'Dickinson model'. In: Buccianti A., MateuFigueras G. & Pawlowsky-Glahn V. (Eds.): Compositional data analysis in the geosciences: from theory to practice. Geological Society of London, Special Publications 264, p 79–99. https://doi.org/10.1144/GSL.SP.2006.264.01.07.

Weltje G.J. & von Eynatten H. 2004. Quantitative provenance analysis of sediments: review and outlook. Sedimentary Geology 171, p 1–11. https://doi.org/10.1016/j.sedgeo.2004.05.007.

Young, S. W., 1975. Petrography of Holocene fluvial sand derived from regionally metamorphosed source rocks. Unpub. Ph.D. Dissertation. Indiana University, 144 p.

Zattin, M., & Zuffa, G. G. (2004). Unraveling the source rocks of the northern Apennines and southern Alps. Boll. Soc. Geol. It., 123, 67–76.

JJEES

JJEES (2026) 17 (2): 178-186
ISSN 1995-6681

Jordan Journal of Earth and Environmental Sciences

Public Perceptions on the Nexus of Climate Extremes, Drinking Water Quality, and Community Health in Khyber Pakhtunkhwa, Pakistan

Ibrar Hussain[1] , Farhat Ullah[2*] , Faisal Hayat[1] , Shamsul Arifeen[1] , Nida Naz[1]

[1] Department of Environmental Sciences, Abdul Wali Khan University Mardan, Pakistan.
[2] Department of Earth Sciences, Quaid-i-Azam University, Islamabad, Pakistan

Received on 7 August 2025; Accepted on 13 November 2025

Abstract

Climate change has intensified the frequency and severity of extreme weather events in Pakistan, especially in flood-prone areas, such as Charsadda and Nowshera in Khyber Pakhtunkhwa. This study examines local perceptions of the impacts of floods and droughts on drinking water quality and public health. A structured questionnaire was administered to 800 respondents (400 per district), and the data were analyzed using descriptive statistics. The results indicate that 66.3% of respondents in Charsadda and 70.8% in Nowshera were aware of climate change, though only 70% (Charsadda) and 65.5% (Nowshera) attributed it to human activities. Floods were perceived as the primary cause of water quality deterioration (44.5% in Charsadda and 47.8% in Nowshera), followed by droughts. Microbial contamination, unpleasant odor, and unusual taste were commonly reported, aligning with the WHO (2017) safety thresholds. Health effects were notable: 32.3% of respondents in Charsadda and 35.8% in Nowshera reported diarrhea during drought periods. Coping strategies varied: 42.3% in Charsadda and 47.8% in Nowshera used purification methods, although chlorine tablet utilization remained limited. These results highlight the urgent need for integrated water safety planning, strengthened public health preparedness, and climate-resilient infrastructure to mitigate localized vulnerabilities in flood-prone regions.

Keywords: *Climate Change, Kabul River, WHO, Floods, Pakistan*

1. Introduction

The impacts of climate change on water resources and public health are increasingly evident across Pakistan, particularly in flood-prone and ecologically sensitive regions. In recent years, extreme weather events such as floods, droughts, and prolonged heatwaves have disrupted drinking water systems, reduced water quality, and increased the risk of disease outbreaks in vulnerable communities (Noureen et al., 2022). According to the Climate Risk Index (2021) and Ullah et al. (2025), Pakistan ranks among the most climate-affected countries globally, with Khyber Pakhtunkhwa facing repeated flood disasters, especially in riverine districts such as Charsadda and Nowshera.

In these districts, a significant portion of the population relies on shallow groundwater sources, including hand pumps, dug wells, and boreholes, many of which are less than 40 feet deep and lack adequate protection against contamination. Research conducted by WHO (2017) and the Pakistan Council of Research in Water Resources (PCRWR, 2019) has shown that such sources are highly vulnerable to microbial pollution during and after floods. This risk is further exacerbated by limited awareness of water safety practices and insufficient institutional mechanisms to ensure access to clean water during emergencies (Ahmad et al., 2022). Although several national and international organizations, including UNDP, WaterAid, and WWF-Pakistan, have initiated programs focusing on water quality, climate resilience, and community-based management, many local communities still lack a clear understanding of the link between climate extremes and waterborne diseases. For instance, a WWF-Pakistan (2022) survey highlighted that only 61% of respondents in Khyber Pakhtunkhwa could accurately define climate change, and misconceptions attributing climatic events to supernatural causes remain widespread.

This study aims to assess how local communities in Charsadda and Nowshera perceive the impacts of climate extremes, specifically floods and droughts, on drinking water quality and public health. By analyzing survey data from 800 respondents, this research explores seasonal water shortages, common purification methods, institutional responses, and health challenges associated with unsafe water. These findings are intended to inform policymakers, NGOs, and disaster management authorities about local risk perceptions, coping behaviors, and the need for climate-adaptive water management in Khyber Pakhtunkhwa flood-prone regions.

* Corresponding author e-mail: farhatgeo1@gmail.com

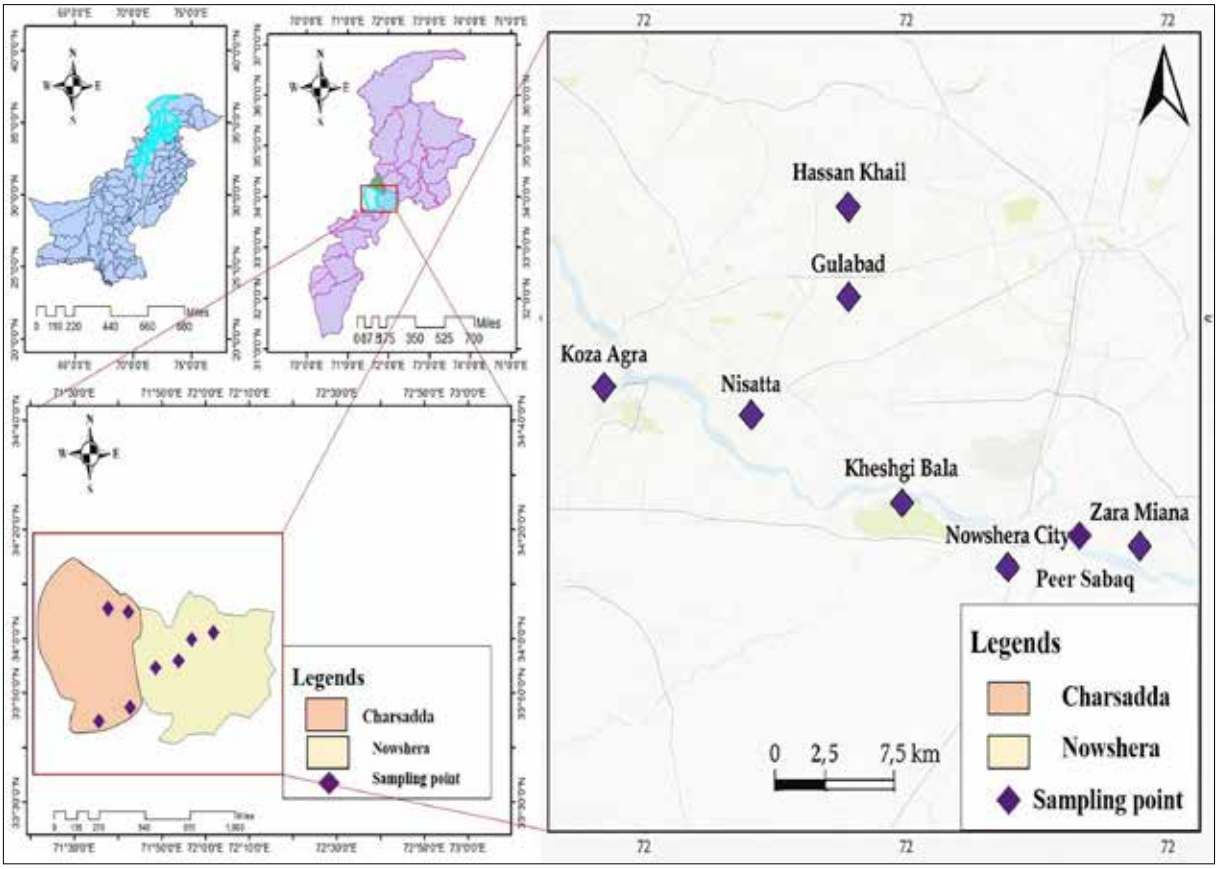

Figure 1. The map showing the sampling collection points from flood-prone districts of Khyber Pakhtunkhwa, Pakistan.

2. Methodology

This study was conducted in two flood-prone districts Charsadda and Nowshera, Khyber Pakhtunkhwa Pakistan as shown in figure 1. A total of 800 respondents were surveyed, with an equal number of samples from each district (400 respondents were from District Charsadda and 400 from Nowshera).

2.1. Sampling and Data Collection

Participants were selected using a random sampling technique to ensure a representative demographic spread. After gaining their assent, interviews were conducted with both male and female respondents using a structured questionnaire. The questionnaire was designed to capture perceptions related to the climate extremes, drinking water quality and public health.

2.2. Demographic Profile

Following participant consent, key demographic information including age, gender, and education level were recorded. In District Charsadda, the majority of the respondents were male 88.8%, while females accounted for only 11.3% of the sample. A comparable trend was observed in District Nowshera, where males comprised 92.3% of the participants, and females constituted merely 7.8%. The respondents from both districts also demonstrated diverse educational backgrounds. In Charsadda, 5% of the participants were illiterate, 8.5% had attained education up to the middle level, and 12% up to the intermediate level. Additionally, 62.5% held undergraduate degrees, 9% had completed a Master of Philosophy (M.Phil.), and 3% possessed a Doctor of Philosophy (Ph.D.) qualification. Conversely, in Nowshera, a higher proportion of respondents lacked formal education 9% or had education up to the middle level 18.5%. Moreover, 8.3% had completed intermediate education, 49.8% held bachelor's degrees, 10.3% had master's degrees, and 4.3% had earned Ph.D. qualifications, as depicted in Figures 2 and 3.

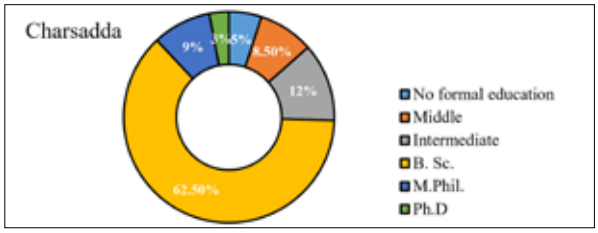

Figure 2. Educational background of the respondents from Charsadda District

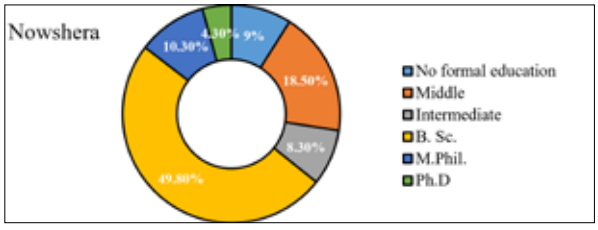

Figure 3. Educational background of the respondents from Nowshera District

2.3. Data Analysis

The data collected from the surveys were coded and analyzed using descriptive statistical methods. Frequencies and percentages were used to summarize and compare responses across the two districts. Charts and figures were developed to visualize the findings using SPSS software.

3. Results and Discussions

3.1. Public Awareness and Perceptions Towards Climate Change

The academic survey is a preliminary attempt to understand how residents in the study area perceive and understand climate change. In Charsadda, 66.3% of the population considered themselves aware of climate change, while 33.8% stated they were not aware of it at all. On the contrary, in Nowshera, 70.8% of respondents reported awareness of climate change, while 29.3% were unaware of it. Regarding the local level effects of climate change, 68.5% of respondents from Charsadda stated that they were aware of environmental changes in their setting, while 31.5% did not witness any local impacts. A greater percentage of Nowshera respondents confirmed the local impact of climate change on their environment (74.3%); the remaining 25.8% did not report any apparent effects. Regarding human activities, 70% of respondents from Charsadda believed that climate change is due to human activities; 30% did not share this belief. Among the Nowshera respondents, 65.5% agreed with the view of human-induced climate change, while 34.5% did not agree. Furthermore, the results show that in Charsadda, 73.3% felt that, in some way or another, climate change is related to water pollution, while 26.8% felt otherwise. In Nowshera, 66.8 % were found to be aware of this relationship, whereas the remaining 33.3 % were not aware of any connectivity with climate change. Overall, the findings reveal that respondents from Nowshera were less aware than those from other districts regarding local climate impacts, although they attributed fewer of those changes to human activity.

The above-mentioned data show that 66.3% of Charsadda and 70.8% of Nowshera respondents were aware of climate change, but fewer recognized its local impacts or human causes. These statistics show that communities in flood-prone areas have living experiences of climate variability, but their understanding of anthropogenic causes is limited (Gul et al., 2024; Iqbal and Nazir., 2023; United Nations Development Program, 2021; Water Aid Pakistan, 2022) Similarly, a World Wide Fund for Nature (WWF-2022) survey found that only 61% of respondents in Khyber Pakhtunkhwa could correctly define climate change. In both districts in this study, about one-third of people attributed climate change to divine or natural causes, thereby limiting the opportunities for grassroots-level action.

These results emphasize the need for targeted climate education using culturally appropriate language and platforms, such as schools, mosques, and radio (Sabra and Al-Moaz, 2022). Empowering people with climate knowledge is foundational to adaptive water behavior and resilience planning (Yadav, 2025).

3.2. Extreme Weather and Drinking Water Sources

The studies revealed notable variations in community perceptions between residents of Charsadda and Nowshera regarding the impacts of extreme weather events on drinking water quality. In Charsadda, floods were identified as the primary factor affecting water quality by 44.5% of respondents, followed by heatwaves (21.3%), droughts (19%), and storms (15.3%). In contrast, participants from Nowshera attributed poor water quality to floods (47.8%), droughts (20.3%), heatwaves (16.5%), and storms (15.5%) (Figure 4).

The depth of these water sources also varied between the two districts. In Charsadda, 13.8% of water obtained from depths of 10–20 feet, 20.3% from 20–30 feet, 28.3% from 30–40 feet, 12.8% from 40–50 feet, 16.8% from 50–80 feet, and 8.3% from depths exceeding 80 feet. Conversely, in Nowshera, 11.8% of respondents accessed water from 10–20 feet, 14.8% from 20–30 feet, 17% from 30–40 feet, 21% from 40–50 feet, 21.5% from 50–80 feet, and 14% from beyond 80 feet (Figure 6).

Survey participants also reported specific water quality issues experienced during or after flooding events. In Charsadda, the most frequently cited problems included unusual taste (34.5%), foul odor (28.8%), increased turbidity (19%), and bacterial contamination (17.8%). Similar concerns were raised in Nowshera, where 41.5% noted an unusual taste, 25.5% reported odor, 16% observed turbidity, and 17% reported bacterial contamination (Figure 7).

These findings indicate that flooding was perceived as the principal cause of deteriorating water quality in both districts, by 44.5% of respondents in Charsadda and 47.8% in Nowshera. The dominant water sources hand pumps, dug wells, and shallow boreholes were mostly situated at depths less than 40 feet, making them highly susceptible to contamination. This observation aligns with the World Health Organization (2017), which classifies wells less than 50 feet deep and lacking protective sealing as unsafe in flood-prone regions (Musche et al., 2018). Similarly, a field survey by the Pakistan Council of Research in Water Resources (PCRWR, 2019) in southern Khyber Pakhtunkhwa reported increased E. coli counts and turbidity levels in post-flood hand pump samples, particularly in areas without elevated platforms.

Overall, the results highlight the structural vulnerability of rural water infrastructure to extreme weather events. It is therefore essential for local governments and non-governmental organizations to prioritize interventions such as well deepening, installation of protective coverings, and community-level chlorination training to ensure the safety and sustainability of drinking water sources (Rasool et al., 2024).

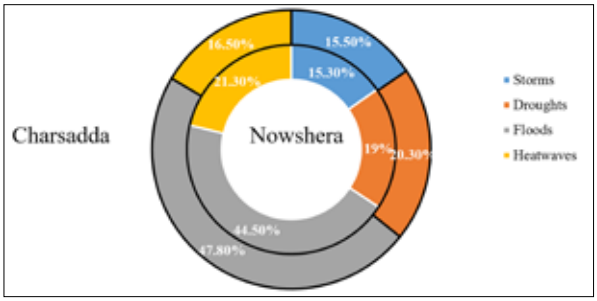

Figure 4. Perceived impact of Extreme weather on Drinking Water Quality

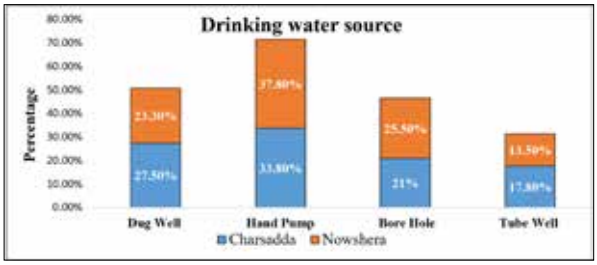

Figure 5. Primary Drinking Water Source of Charsadda and Nowshera Districts Quality

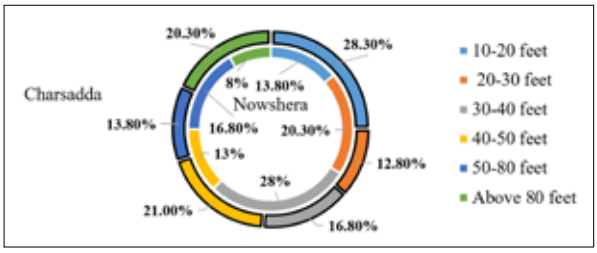

Figure 6. Depth Distribution of Water Source in the Kabul River Flood Plains.

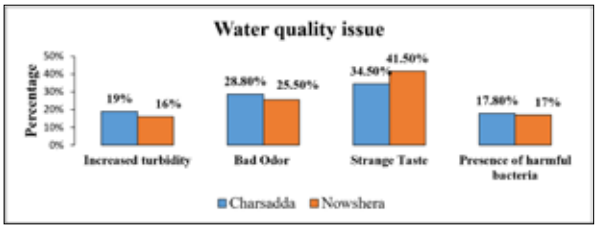

Figure 7. Water Quality Issues reported during or after floods Flood Plains.

3.3. Seasonal and Long-Term Changes in Water Quality

The survey results reveal the effects of extreme weather events on the long-term variation in drinking water quality. A higher proportion of respondents in Charsadda (73.5%) reported observing long-term changes in water quality, while 59% in Nowshera shared the same opinion. In Charsadda, 31% of respondents said that water quality was bad during floods, 21.5% during droughts, and 24.8% after heavy rainfall. However, 22.8% reported no major changes in water quality throughout the year. In Nowshera, by contrast, 35.3% reported that flooding affected water quality, while droughts were recalled by 26.5%, and heavy rains by 21.8%. Only 16.5% reported no significant changes in water quality throughout the year (Figure 8). These results align with the Food and Agriculture Organization of the United Nations (FAO, 2021) groundwater vulnerability maps, which identify Khyber Pakhtunkhwa's alluvial aquifers as prone to both contamination and seasonal drawdown. In similar studies in India's Bihar and Assam floodplains, post-monsoon water quality deterioration included increased turbidity, nitrate leaching, and pathogen load (Shamim and Chakraborty, 2025). To mitigate these trends, integrated watershed recharge zones, elevated storage tanks, and low-cost rainwater harvesting models used by UNICEF Bangladesh could be piloted in Pakistan's floodplain communities (Akbar et al., 2024; Nawaz et al., 2024).

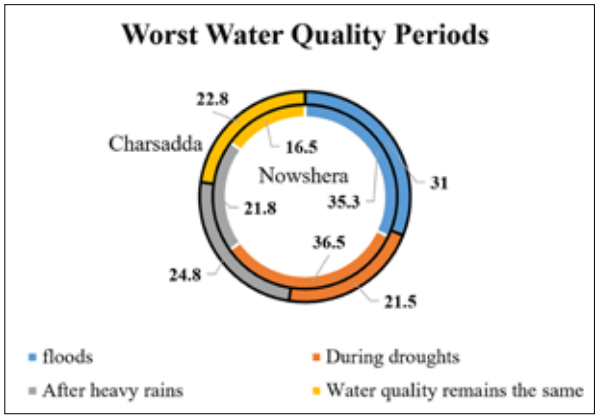

Figure 8. Perceptions of respondents on the worst period of water quality

3.4. Flood Impacts on Access to Safe Water

Flooding appeared to exert a considerable influence on drinking-water quality in both districts. In Charsadda, 65.8% reported that flooding indeed worsened water quality, while 34.3% observed no such adverse influence. In Nowshera, a similar trend was observed: 58.3% of respondents reported a flooding impact on water quality, while 41.8% said there was no such impact. The availability of clean water during flood events also differed. In Charsadda, 60.5% said flood-affected drinking water was unavailable, while 39.3% said it was available. The situation was much worse in Nowshera, where 73.3% reported no clean water during floods, while only 26.8% reported drinking water was available after floods.

Regarding pollution, 70.3% of respondents in Charsadda said their water sources were contaminated by flooding, while 29.8% reported no effect on their water. In Nowshera, 62.8% reported contamination of drinking water due to flooding; however, 37.3% reported no contamination. These outcomes are consistent with WaterAid (2019) flood response reports in Khyber Pakhtunkhwa and Punjab, where over 65% of shallow hand pumps failed to meet WHO microbial safety standards. Furthermore, MSF's (2010, 2011, 2022) post-flood health data from KP highlighted increased cases of diarrheal and skin diseases within 7–14 days of flood exposure, exacerbated by unsafe water use. The scale of disruption calls for decentralized water storage, chlorine tablet distribution, and emergency WASH mobile units as proposed in the NDMA Flood Response Framework (2023).

3.5. Government Response, Flood Control, and Community Awareness

In terms of government assistance, flood management initiatives, and community awareness during flood incidents, significant variations were noted between Nowshera and Charsadda. In Charsadda, slightly more than half of the participants (52%) reported receiving some government support to obtain clean drinking water following flooding, whereas 45% indicated they had not received any government support. In Nowshera, support seemed more prevalent, as 60.3% of participants reported receiving government support during the flood for clean drinking water, while 39.8% indicated they did not receive any support. In addition, when surveyed in Charsadda about

flood management systems, 45% of residents reported that certain flood control measures were available, while 64% believed these initiatives were either insufficient or ineffective. Conversely, 64% of participants in Nowshera acknowledged the existence of flood mitigation measures, while 36% reported that no such plans were available in their locality regarding public awareness and preparedness during floods, 63% of individuals in Charsadda reported being informed about flood-related information, whereas 37% acknowledged they were not. Awareness levels were relatively higher in Nowshera, where 75.3% of residents reported being well-informed during floods, while 24.8% reported lacking that information.

Government assistance for clean water was acknowledged by 52% of respondents in Charsadda and 60.3% in Nowshera. However, satisfaction with flood control infrastructure was mixed, and awareness of protective measures varied across districts. This reflects broader findings by the International Rescue Committee (2022), which noted significant delays in WASH service coordination during KP floods due to fragmented local responsibilities. International best practices, such as the WASH Cluster model used by UN OCHA in Mozambique and Pakistan (2022), emphasize pre-disaster coordination, clear role assignments, and resource mapping among stakeholders. Adoption of a similar approach at the district level in Khyber Pakhtunkhwa could vastly improve WASH service reliability.

3.6. Flood Frequency and Most Affected Areas

In Charsadda, 34% of respondents reported experiencing floods annually, 32% reported flooding every 2–4 years, 15.3% reported flooding every 5–10 years, and 18.8% reported flooding only rarely. Similarly, in District Nowshera, 37.3% of respondents experienced floods annually, 28.3% every two to four years, 19.8% every five to ten years, and 14.8% rarely experienced floods (Figure 9). Furthermore, in Charsadda, the most impacted regions were agricultural land (15.5%), residential areas (25.8%), water sources (31.8%), and roads and infrastructure (27%). In Nowshera, the impact on agricultural land was indicated by (21.5%) of the population, residential areas 29.5%, water sources by 35.3%, and roads and infrastructure by 13.8%, and these results showed that floods are a major and common occurrence in both districts, mostly affecting residential areas and water sources, as shown in figures 10 and 11. Annual flooding was reported by 34% of respondents in Charsadda and 37.3% of respondents in Nowshera. Most affected areas included water sources, homes, and roads. These findings are supported by NDMA's GIS-based Flood Hazard Maps, which confirm that settlements near the Kabul River in both districts fall within the high-risk red zone (Bibi et al., 2018). A comparative study of the Indus and Brahmaputra basins found that proximity of water sources to flood channels was the strongest predictor of post-flood waterborne disease outbreaks (Kumar et al., 2022; Atif et al., 2021).

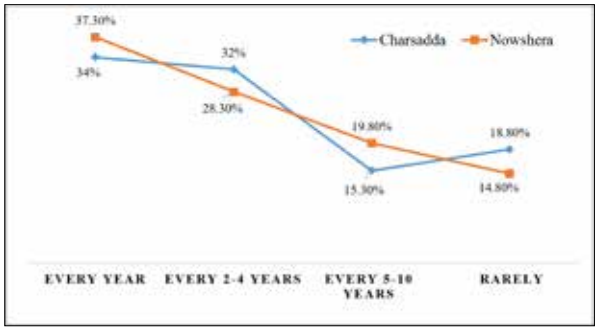

Figure 9. Frequency of flood occurrence in the flood prone districts

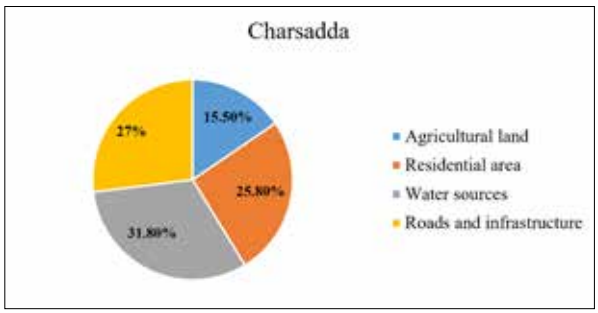

Figure 10. Most flood-affected areas in Charsadda

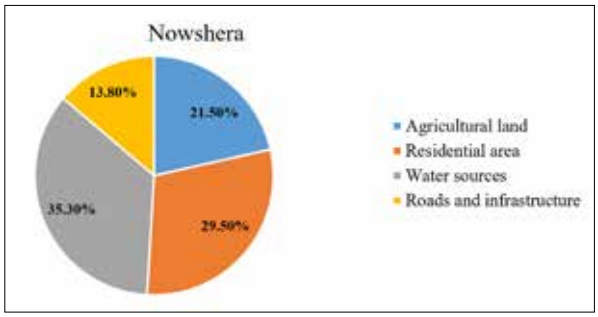

Figure 11. Most flood-affected areas in Nowshera

3.7. Water Management Practices During Floods

The survey identified significant issues concerning water management in Charsadda and Nowshera during flood occurrences. In Charsadda, 16.3% of participants reported disruptions to their water supply, whereas 34.8% reported pollution of water sources. 27% of participants reported overflowing drainage systems, while 22% indicated a lack of access to clean drinking water during flooding. In Nowshera, 20.3% of participants experienced interruptions in water supply, 29.3% managed polluted sources, 37.8% indicated drainage system spills, and 12.8% had no access to clean water (Figure 12). In both areas, residents employed various strategies to secure safe drinking water after flood incidents. In Charsadda, 21.8% of people boiled their water, 14% chlorine tablets or similar disinfection methods, 30% chose to purchase bottled water, and 34.3% depended on household filtration systems. In contrast, 28.3% of Nowshera inhabitants boiled their water, 12.4% utilized chlorine or similar methods, 20.8% bought bottled water, and 38.8% relied on filtration systems (Figure 13). Participants also recognized various organizations that oversee water quality during floods. In Charsadda, 16% of respondents attributed their support to local government bodies, 26.3% cited national agencies, 30.8% recognized non-governmental organizations (NGOs), and 27% cited engagement with local

community organizations. In Nowshera, 20.5% identified the local government's contribution, 28% mentioned national entities, 34.3% recognized NGOs, and 17.3% highlighted community initiatives (Figure 14). These results highlight the complex challenges communities face during flooding and underscore the adaptive methods and support systems essential to preserving water quality and access in both areas. During floods, 34.8% of respondents in Charsadda and 29.3% in Nowshera reported contamination of their drinking water sources. Filtration (34–38%), boiling (21–28%), and bottled water were used as coping strategies, though chlorine tablets remained underutilized. Similar behavior patterns were observed in the UNICEF 2022 KP WASH Assessment, which cited cost, supply chain gaps, and a lack of user confidence as major reasons for low disinfection rates.

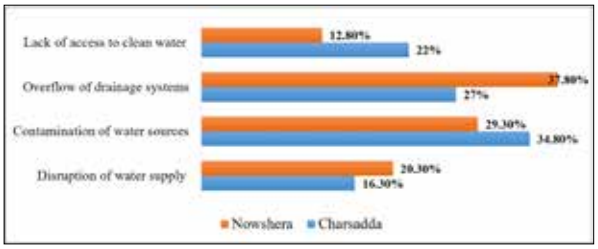

Figure 12. Major water management challenges during floods

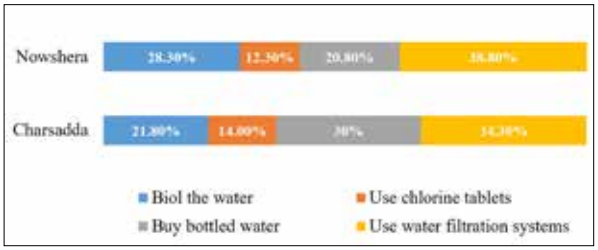

Figure 13. Household drinking water management after floods

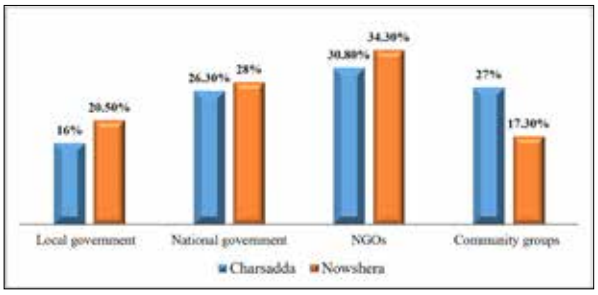

Figure 14. Effective organizations in water quality management

3.8. Public Preparation and Barriers to Water Quality Development

The survey revealed various obstacles and community responses linked to water quality control and readiness in areas vulnerable to flooding. In Charsadda, 13% of participants reported storing drinking water for potential floods, 31% implemented measures to clean and maintain their water sources, 32% built temporary barriers for protection, and 24% did not adopt any particular precautionary actions. In Nowshera, a somewhat larger percentage (18.3%) continued to use drinking water, 34.5% focused on conserving water sources, 19.5% constructed temporary flood barriers, and 27.8% took no precautions (Figure 15). Respondents from both areas identified multiple significant obstacles that impede initiatives to enhance water quality. Seventeen per cent of respondents in Charsadda and 22.5% in Nowshera expressed concerns about inadequate funding. A notable percentage also cited the lack of political commitment, with 30.5% in Charsadda and 32.8% in Nowshera. Public unawareness was reported by 29.3% of residents in Charsadda and 31.5% in Nowshera, whereas inadequate infrastructure was cited by 23.3% in Charsadda and 13.3% in Nowshera as a constraint (Figure 16). Various strategies were reported to address health risks health risks and avert waterborne diseases. In Charsadda, 26.8% of participants reported vaccination initiatives, 23.5% mentioned using mass media for awareness, 27.8% indicated emergency sanitation and water quality inspections, and 22% highlighted air quality assessments. In Nowshera, 30.3% of participants recognized vaccination programs, 28% acknowledged media campaigns, 31% noted emergency water and sanitation monitoring, and 10.8% mentioned air quality assessments (Figure 17). The main barriers identified were a lack of political will (30.5%), funding constraints (22.5%), low public awareness (31.5%), and weak infrastructure (13–23%). These constraints are nearly identical to those documented in the ADB 2022 Pakistan WASH Diagnostic Report, which emphasized how fragmented governance and underfunded Tehsil offices lead to structural failures. Globally, the International Water Association (IWA, 2022) suggests that local water utilities must be empowered with technical budgets, GIS-based monitoring, and disaster financing tools. Similar district-level reforms should be considered by KP's PHED and PDMA to address recurring infrastructure vulnerabilities.

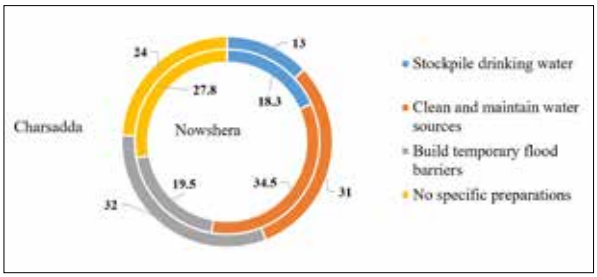

Figure 15. Community level preparation for water safety

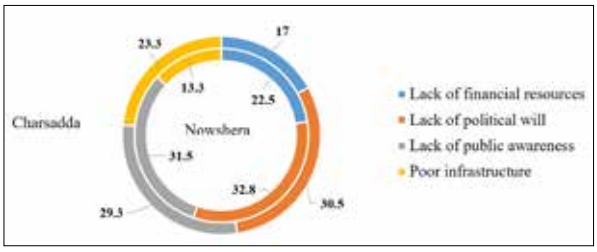

Figure 16. Key barriers to improving water quality in floodplains districts

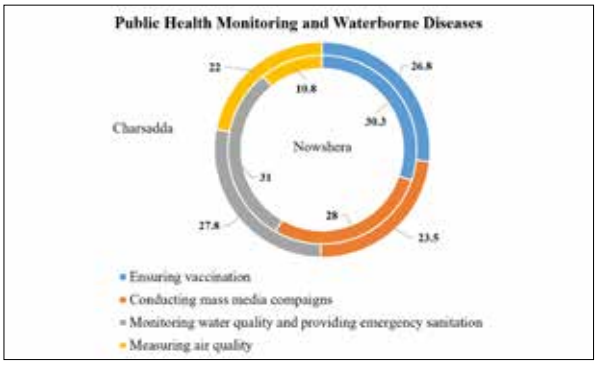

Figure 17. Public health monitoring and waterborne diseases prevention initiatives.

3.9. Seasonal Drinking Water Quality Challenges and Household Purification Methods

The survey examined seasonal water challenges, purification techniques, and their perceived efficacy in Charsadda and Nowshera. In Charsadda, 42.3% of families indicated they used water purification methods like boiling or filtration, whereas 57.8% did not practice any water treatment. Likewise, in Nowshera, 47.8% of participants reported that they treated their drinking water, while 52.3% did not report any treatment. When questioned regarding the success of these purification initiatives, 39.3% of residents in Charsadda and 46.5% of individuals in Nowshera believed that these actions improved water quality. Nonetheless, a greater percentage, 60.8% in Charsadda and 53.5% in Nowshera, indicated no significant enhancement due to purification techniques. The problem of seasonal water scarcity was also emphasized in both districts. In Charsadda, 40.5% of respondents faced water shortages at specific times each year, whereas 59.5% did not. In Nowshera, 45.8% indicated experiencing shortages, while 54.3% reported no such problems. Seasonal trends indicated that water shortages were considerably more frequent during the winter months. In Charsadda, 74.3% of participants indicated experiencing shortages in winter, while 25.8% reported the same in summer. In Nowshera, 61.3% faced shortages in winter, while 38.8% did so in summer.

3.10. Water Sources During Droughts and Associated Health Risks

During droughts, households in Charsadda and Nowshera implemented various strategies to obtain water for everyday needs. In Charsadda, 35% of households relied on groundwater sources, 25.3% utilized previously stored water, 14.8% bought water from local vendors, and 25% obtained water from a government supply. In Nowshera, 26.8% depended on groundwater, 30.3% utilized stored water, 13% acquired water from vendors, and 30% accessed water supplied by government agencies (Figure 18).

Health problems associated with drought-related water concerns were also apparent in both districts. In Charsadda, 32.3% of participants indicated diarrhea, 29.5% experienced cholera, and 18.3% faced skin infections. At the same time, 20% reported experiencing no major health issues during droughts. In Nowshera, health problems displayed a comparable pattern: 35.8% of participants had diarrhea, 32.3% acquired cholera, and 16.3% dealt with skin issues. A smaller group, 15.8%, reported no significant health issues during these dry spells. In addressing seasonal water shortages and associated health risks in drought-prone regions like Nowshera and Charsadda, replicating successful intervention models is critical (Figure 19). A notable example is the UNDP (2021) Community-Based Water Management Program in Tharparkar, Sindh, where solar-powered reverse osmosis plants and rainwater harvesting systems were introduced to ensure a sustainable water supply during droughts. Similarly, WWF-Pakistan's Water Stewardship Initiative in Punjab involved local communities in monitoring water quality, conserving groundwater, and adopting household-level filtration techniques, which significantly reduced the incidence of waterborne diseases (Khalid et al., 2024). These models highlight the effectiveness of decentralized water governance, public health integration, and community ownership. Applying such frameworks in KP, particularly with locally adapted solar desalination units, trained water committees, and mobile WASH clinics, could reduce health vulnerabilities, such as the high prevalence of diarrhea (35.8%) and cholera (32.3%), reported during droughts. Leveraging partnerships with NGOs, enhancing local infrastructure, and embedding these proven models into district-level policy can offer practical solutions tailored to regional needs.

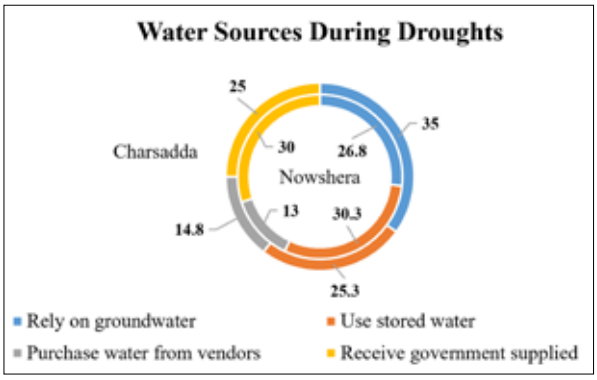

Figure 18. Water sources during droughts in the flood plains districts.

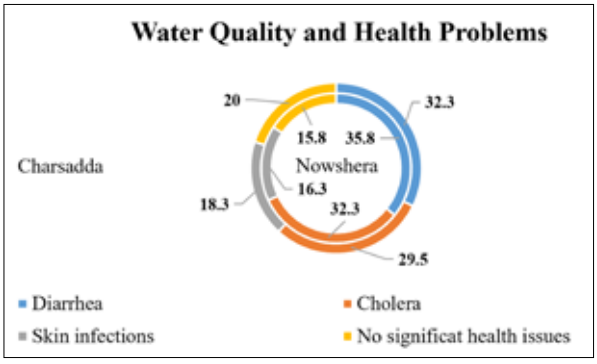

Figure 19. Water quality and health problems in the District Charsadda and Nowshera

4. Conclusion

In conclusion, the study highlights the significant challenges faced by communities in Charsadda and Nowshera regarding drinking water quality and public health during climate induced extreme weather events. Many families depend on shallow water sources, such as hand pumps and dug wells, which are easily polluted during floods. About 70% of people in Charsadda and 63% in Nowshera reported that drinking water became contaminated after floods. Common complaints included bad taste, foul smell, and dirty water. These unsafe conditions led to increased health issues such as diarrhea, cholera, and skin infections, which were reported by over 30% of people in both districts during droughts. Even though nearly half of the households used boiling or filtering methods, very few used chlorine tablets, which are known to be effective. Government and NGO support helped to some extent, but many people still lack clean water during emergencies. Overall, there is a clear need for safer water infrastructure, stronger public awareness, and better coordination among local agencies to protect public health during extreme weather conditions.

5. Recommendations

Based on the findings of this study, the following recommendations are proposed to improve drinking water safety and public health resilience in the context of climate extremes in flood-prone areas. First, water sources should be improved by digging deeper wells, properly sealing hand pumps, and building raised platforms to prevent floodwater from entering drinking water systems. At the household level, people should be encouraged and trained to use safe, simple water treatment methods such as chlorine tablets, boiling, and filtration. Awareness campaigns should be carried out in schools, mosques, and through local media to help people understand how climate change affects their health and water supplies. The government and NGOs should work together closely to provide clean water during emergencies and support long-term solutions. Local authorities should set up better planning and early-warning systems so that communities are better prepared. Finally, findings from this and similar studies should inform district and provincial governments in making water and health systems more resilient to climate change.

References

Ahmad, S., Zahra, J., Ali, M., Ali, S., Iqbal, S., Kamal, S., Aborode, A. T. (2022). Impact of water insecurity amidst endemic and pandemic in Pakistan: Two tales unsolved. Annals of Medicine and Surgery, 81.

Akbar, G., Ashraf, A., Hameed, S. (2024). Design and Evaluation of a Low-Cost Artificial Groundwater Recharge System Using Rainwater Harvested from Rooftop: A Case Study in Islamabad, Pakistan. Sustainability and Climate Change 17(4): 298-307.

Asian Development Bank (ADB). (2022). Pakistan: Water, sanitation, and hygiene sector assessment, strategy, and roadmap. Manila: ADB.

Atif, S., Umar, M., Ullah, F. (2021). Investigating the flood damages in Lower Indus Basin since 2000: Spatiotemporal analyses of the major flood events. Natural Hazards 108(2): 2357-2383.

Bibi, T., Nawaz, F., Abdul Rahman, A., Azahari Razak, K., Latif, A. (2018). Flood risk assessment of river Kabul and Swat catchment area: district Charsadda, Pakistan. The International Archives of the Photogrammetry, Remote Sensing and Spatial Information Sciences 42: 105-113.

Eckstein, D., Künzel, V., Schäfer, L. (2021). The global climate risk index 2021. Bonn Germanwatch.

FAO. (2021). Groundwater management in South Asia: Challenges and strategies. Rome: Food and Agriculture Organization of the United Nations.

Gul, S., Khan, N., Nisar, S., Ali, Z., Ullah, U. (2024). Impact of Climate Change-Induced Flood on Women's Life: A Case Study of 2022 Flood in District Nowshera, Khyber Pakhtunkhwa, Pakistan. Journal of Asian Development Studies 13(2): 1468-1482.

International Rescue Committee (IRC). (2022). WASH response report in KP flood-affected regions.

International Water Association (IWA). (2021). Resilient water and sanitation systems: Guidelines for decentralized management. London: IWA Publishing.

Iqbal, A., Nazir, H. (2023). Community perceptions of flood risks and their attributes: a case study of rural communities of Khipro, district Sanghar, Pakistan. Urban Climate 52: 101715.

Khalid, S., Hafeez, M., Aqib, S. (2024). Who is more water insecure? Gendered evidence from urban Pakistan. Frontiers in Water 6: 1423237.

Kumar, A., Mondal, S., Lal, P. (2022). Analysing frequent extreme flood incidences in Brahmaputra basin, South Asia. Plos one17(8): e0273384.

Médecins Sans Frontières (MSF). (2010Pakistan: Summary of MSF's flood response (July–October 2010). MSF UK/USA.

Médecins Sans Frontières (MSF). (2011). Pakistan: Six months after the floods — Special report. MSF Field Epidemiology Unit.

Médecins Sans Frontières (MSF). (2022). Pakistan Flood Update: Health response & water provision in floodaffected zones. (Sindh, Balochistan, Khyber Pakhtunkhwa) MSF South Asia.

Musche, F., Sandhu, C., Grischek, T., Patwal, P. S., Kimothi, P. C., Heisler, A. (2018). A field study on the construction of a flood-proof riverbank filtration well in India–Challenges and opportunities. International journal of disaster risk reduction 31: 489-497.

National Disaster Management Authority (NDMA). (2023). Monsoon contingency and flood response plan. Islamabad: NDMA Pakistan.

Nawaz Khan, M., Mukhtar, A. (2024). Water Management in Pakistan: Challenges and Way Forward. In The Water, Climate, and Food Nexus: Linkages, Challenges and Emerging Solutions (pp. 435-456). Cham: Springer International Publishing.

Noureen, A., Aziz, R., Ismail, A., Trzcinski, A. P. (2022). The impact of climate change on waterborne diseases in Pakistan. Sustainability and Climate Change 15(2): 138-152.

Pakistan Council of Research in Water Resources (PCRWR). (2019). Water quality status in Pakistan 2017–2019. Islamabad: Ministry of Science and Technology.

Rasool, A., Saeed, S., Ahmad, S., Iqbal, A., Ali, A. (2024). Empowering community participation for sustainable rural water supply: Navigating water scarcity in Karak district Pakistan. Groundwater for Sustainable Development 26: 101269.

Sabra, P., & Al-Moaz, M. A. (2022). Awareness of Climate Change-The role of art, education and culture in raising awareness of climate change. International journal of education and learning research, 5(1), 48-70.

Shamim, F., & Chakraborty, B. (2025). Temporal analysis of the Hooghly River's water quality: investigating pre-and post-monsoon scenarios in West Bengal, India. Water Science & Technology, 91(3), 266-279.

Ullah, W., Dong, H., Shah, A. A., Xu, C., Alotaibi, B. A. (2025). Unveiling the Multi-Dimensional Vulnerabilities of Flood-Affected Communities in Khyber Pakhtunkhwa, Pakistan. Water 17(2): 198.

UN OCHA. (2022). Pakistan floods: Humanitarian response plan and WASH cluster performance. New York: United Nations Office for the Coordination of Humanitarian Affairs.

UNDP Pakistan. (2021). Climate awareness and behavior change among rural households. Islamabad: United Nations Development Programme.

UNICEF Pakistan. (2022). Post-flood WASH assessment: Khyber Pakhtunkhwa province. Islamabad: UNICEF.

WaterAid Pakistan. (2022). Building resilience in flood-prone areas: A WASH perspective from northern Pakistan. Islamabad: WaterAid.

WaterAid. (2019). WASH in emergencies: Pakistan flood case

study. London: WaterAid Global.

WHO. (2017). Guidelines for drinking-water quality: 4th edition incorporating 1st addendum. Geneva: World Health Organization.

WWF-Pakistan. (2022). Community perception of climate change in Khyber Pakhtunkhwa. World Wide Fund for Nature – Pakistan.

Yadav, S. (2025). Empowering Communities for Climate Resilience: Bridging Knowledge and Action to Combat Climate Change. In Community Climate Justice and Sustainable Development (pp. 83-104). IGI Global Scientific Publishing.

JJEES

JJEES (2026) 17 (2): 187-198
ISSN 1995-6681

Jordan Journal of Earth and Environmental Sciences

Erosion-Accretion Dynamics and Displacement along the Jamuna River Part of Sirajganj District

Mst. Sadia Siddika Trina, Md. Inzamul Haque*, Md. Asikur Rahman, Md. Ashraful Islam Dewan, Most. Atia Parvin, Md. Anik Hossain

Dept. of Geography and Environment, Islamic University, Kushtia-7003, Bangladesh

Received on 5 February 2025; Accepted on 14 November 2025

Abstract

The Jamuna River is one of the largest rivers in Bangladesh, where erosion and accretion occur most frequently. This study analyzed LULC, evaluated the extent of erosion and accretion of the Jamuna River from 1988 to 2024, and assessed its effects, primarily on population displacement in Sirajganj district, where four upazilas are prone to bank erosion: Kazipur, Sirajganj Sadar, Belkuchi, and Chauhali. Landsat TM-5 and Landsat-8 imagery from three different periods (1988, 2006, and 2024) were obtained from the USGS to analyze LULC, CDS (change detection statistics), NDWI (normalized difference water index), and erosion and accretion. The results indicated that from 1988 to 2024, erosion totaled 18,813 hectares, accretion totaled 14,480 hectares, and 3,937 hectares remained unchanged. This represents a more significant erosion than accretion, resulting in the forced displacement of affected people. The CDS result for Sirajganj Sadar shows that the settlement area increased by 74.69% from 1988 to 2024, indicating that population movement from rural areas (such as agricultural or fallow land) to urban areas contributed to this shift. The total population of Sirajganj Sadar was 389,160 in 1991 and 631,877 in 2022, according to the Bangladesh Bureau of Statistics (BBS), reflecting substantial population growth. The population growth of Chauhali Upazila has been relatively steady but has declined over the last decade. In contrast, Kazipur Upazila's growth has increased very slowly during this period, indicating a shift in the population of these areas, which are more prone to bank erosion. This study quantifies the long-term (1988–2024) erosion and accretion dynamics of the Jamuna River in a highly vulnerable area of Bangladesh, directly linking these changes to population migration within specific affected upazilas in Sirajganj District. With its spatially explicit evidence of environmental change driving internal displacement, this integrated method provides important insights for targeted interventions that will help policymakers and stakeholders take practical steps to mitigate bank erosion and its impacts.

Keywords: *Jamuna River, Sirajganj, erosion and accretion, LULC Change, population displacement.*

1. Introduction

Riverbank erosion is a natural phenomenon in Bangladesh and other lower-confluence deltaic countries (Ali et al., 2021). Bangladesh is home to some of the world's most disaster-prone lands. Severe floods, powerful cyclones, and riverbank erosion caused by them have been a fact of life here. Geologically, Riverbank erosion is one of Bangladesh's most common natural disasters and probably occurs annually as a recurring, highly unpredictable event (Iva et al., 2017). It poses a significant threat by permanently depriving people of their roots and material wealth (Mollah & Ferdaush, 2015). River erosion is a typical geomorphological phenomenon in regions with constructed floodplains. Riverbank erosion is sometimes referred to as a "silent disaster" because it occurs more frequently each year than human-made catastrophes (Hassan, 2015).

The Ganges, Brahmaputra, and Meghna River systems form the largest delta in Bengal. River systems translocate approximately two billion tons of silt annually to the Bengal Delta (Hossain & Sakai, 2008). The largest braided river that meanders through Bangladesh's low-lying, sinking deltaic floodplain is the Old Brahmaputra, referred to as the "Jamuna" (Ashworth, 1996). Jamuna River, one of Bangladesh's major rivers, has deteriorated over the past decade due to varying rates of erosion and accretion (Hassan et al., 2017). Rivers are dynamic systems because they constantly alter course, so erosion and accretion are normal processes. Even if erosion can occasionally outpace accretion and ruin lives and livelihoods, the impoverished community typically suffers the most (Islam & Rashid, 2011). The multi-channel braided system of the Jamuna River is one of its defining features. It regularly changes, generating sandbars and altering the river's course (Nath et al., 2013). The lower Brahmaputra's Jamuna River experiences significant yearly erosion, resulting in major bankline migration, thousands of homeless families, and substantial land loss. For example, Jamuna's dynamic nature causes great suffering to the people who live along its course and on its islands (Baki & Gan, 2012). Over the past decade, the Jamuna River has caused the erosion of approximately 30 settlements, displacing one-third of the city's population and rendering 400,000 individuals homeless. During the monsoon season, the river Jamuna experiences a substantial increase in water flow, with

* Corresponding author e-mail: mihaque.iu@gmail.com

an average discharge of approximately 40,000 cubic feet per second. During this period, the Jamuna River experienced significant devastation, causing severe damage in Sirajganj District, which lies directly along its banks. Each year, tragedy results in a substantial number of individuals losing their livelihoods and agricultural land (Das, 2014). Following a complete loss due to the river, affected individuals relocate to neighboring districts or other areas (Shetu et al., 2016).

Nowadays, remote sensing and geographical information systems (GIS) techniques are essential tools for identifying LULC changes, disaster-prone areas, damage, and severity, as well as calculating the rate of change (Mohamad et al., 2018; Tobore et al., 2021; Al-Amoush et al., 2017). Despite uneven erosion rates, Bedini (2017) utilizes Landsat imagery and GIS tools to identify significant erosion along the coastline between the Semani and Shkumbini rivers and in Central Albania. A similar study, using Landsat TM and MSS satellite imagery in Chandpur district, Bangladesh, found that bar deposition in the Meghna River exceeded riverbank erosion, with an estimated 3,517 square meters of deposition between 1990 and 2002 (Nath et al., 2013). Using remote sensing, Uddin et al. (2011) measured morphological changes and susceptibility to erosion along the Jamuna riverbank. A study revealed that riverbank erosion has increasingly affected people in the riverine zone of the Jamuna, where Sirajganj Sadar was the most erosion-prone area (Rabbi et al., 2013). A spatial-temporal analysis of the erosion and accretion on the East and West Riverbanks of the Jamuna River was conducted by Hassan et al. (2017). They analyzed the spatial and temporal dynamics of erosion and accretion along the Jamuna River from 1995 to 2015, using Landsat imagery and Geographic Information System (GIS) techniques. Although considerable research has been conducted on riverbank erosion in Sirajganj, a comprehensive study is still lacking. Almost all previous studies on the Jamuna River have focused on either morphological dynamics, based on erosion and accretion along the bank line, or the socioeconomic aspects of the changes. Limited studies focus on the long-term spatiotemporal dynamics of erosion and deposition, with inadequate integration of advanced techniques like indexing (NDWI classification) for precise monitoring. Furthermore, while geoenvironmental impacts are explored extensively, comprehensive assessments of socio-economic consequences remain underrepresented, particularly regarding the livelihoods of affected communities. However, a significant gap remains in understanding how spatiotemporal land use and land cover (LULC) dynamics contribute to forced displacement due to erosion.

In this context, this study utilizes the Landsat TM Satellite and GIS to evaluate spatial and temporal changes in the Sirajganj district and calculate the erosion and accretion of the River Jamuna. Through digital image processing applied to temporal satellite images, the analysis enables researchers to evaluate the detection of river and erosion changes, while displaying the patterns and shifting river channels over time. Remote sensing provides a rapid, synoptic view of large areas, integrating with GIS techniques, making it an ideal tool for monitoring riverbank erosion and shoreline shifting at regular intervals (Sarkar et al., 2012). The bank line change analysis is crucial for predicting river path changes, assessing potential impacts on life and the environment, especially migration, and visualizing different spatial changes. So, the objectives of this study are to analyze the spatiotemporal variation of bank line shift of the Jamuna River to calculate the erosion-accretion rate from 1988 to 2024 and to explore the pattern of LULC changes in different upazilas of Sirajganj district. Furthermore, this study also tries to develop a population displacement scenario based on the riverbank line shift and LULC change in different parts of the study area.

2. Materials and Methods

2.1 Study Area

Sirajganj District is a district in the North Bengal region of Bangladesh, which is a part of the Rajshahi Division and is located between 24°01’ and 24°47’ north latitudes and between 89°15’ and 89°59’ east longitudes (Figure 1).

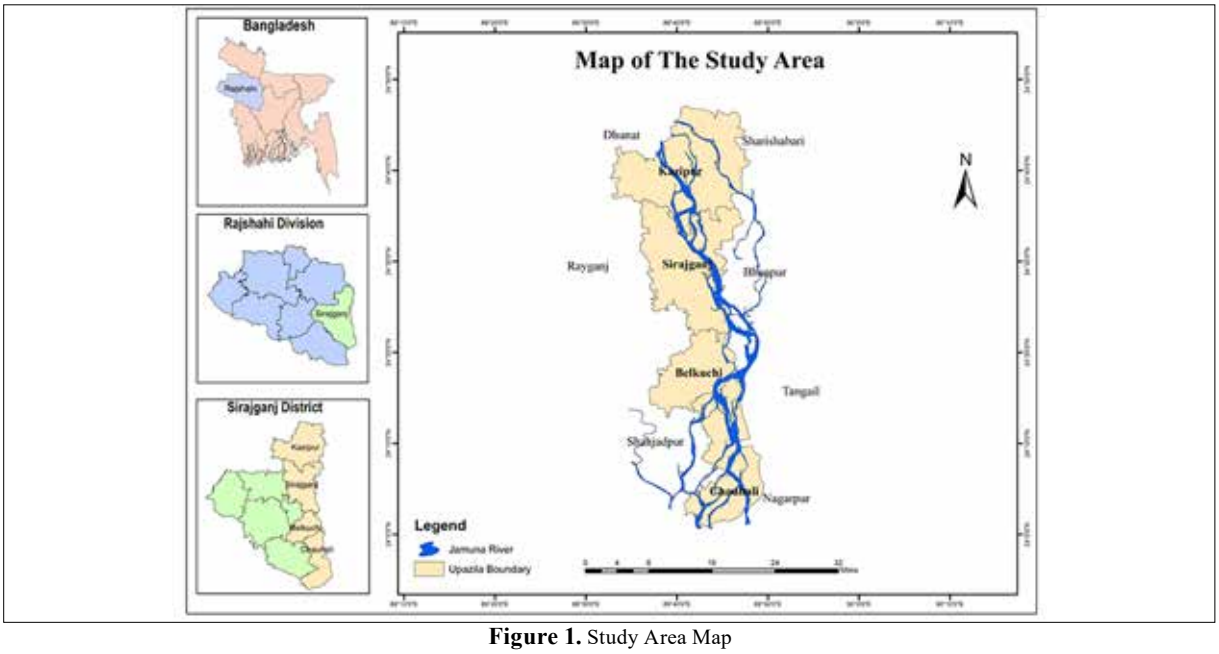

Figure 1. Study Area Map

This district comprises 9 upazilas: Tarash, Ullapara, Sirajganj Sadar, Shahzadpur, Raiganj, Kazipur, Chowhali, Belkuchi, and Kamarkhand. Four upazilas (Sirajganj Sadar, Kazipur, Chowhali, and Belkuchi) are more prone to riverbank erosion and are thus selected for the study. The study area encompasses 1,023.7 square kilometres, as illustrated in Figure 1.

2.2 Sources of Data

The data (Table 1) used in this study came from various secondary sources and included three Landsat images (spatial) and population data (non-spatial).

Table 1. Description of the collected data

Data Type	Year of Data	Data Source
Landsat imagery	1988, 2006, 2024	USGS (https://earthexplorer.usgs.gov/)
Population Data	1991, 2001, 2022	BBS (Bangladesh Bureau of Statistics)

2.3 Satellite image collection and pre-processing

The detail information about the collected satellite imageries are presented in Table 2. Landsat 5 TM (Thematic Mapper) and Landsat 8 OLI (Operational Land Imager) images of Sirajganj in 1988, 2006, and 2024 were collected from the USGS official website (https://earthexplorer.usgs.gov/). Pre-processing satellite images before change detection is crucial, as it aims to establish a more direct linkage between the data and biophysical phenomena (Coppin et al., 2004).

Table 2. Detailed Information of the Landsat Images used in this study

Satellite	Sensor Type	Path/Row	Date of acquisition	Spatial Resolution (m)	Cloud Cover (%)	Image Quality
Landsat 5	TM	138/43	1988-01-09	30	1.00	9
Landsat 5	TM	138/43	2006-01-26	30	0.00	7
Landsat 8	OLI/TIRS	138/43	2024-01-28	30	0.32	9

All Landsat data used in this study were acquired under clear atmospheric conditions (to get cloud-free images). The collected images were projected onto the Universal Transverse Mercator (UTM) coordinate system and stored as GeoTIFFs. PCS WGS (World Geodetic System) 1984 UTM Zone 45 N (datum) was the projection used for all the images. Data is processed using ENVI (Environment for Visualizing Images) version 5.3 software. First, metadata and radiometric calibration transform the Landsat scene's DN (Digital Number) into absolute radiance units (W m-2 sr-1). After that, atmospheric adjustment was performed using the FLAASH (Fast Line-of-sight Atmospheric Analysis of Spectral Hypercubes) module (Soto Carrión, 2022).

2.4 Methods

Figure 2 shows the detailed methodological framework of the study. Firstly, spatiotemporal changes in the study area were analyzed by LULC classification from 1988 to 2024. NDWI was also conducted to calculate the river's erosion and accretion. Finally, a migration scenario was developed based on the analysis of Change Detection Statistics (CDS) and Population data.

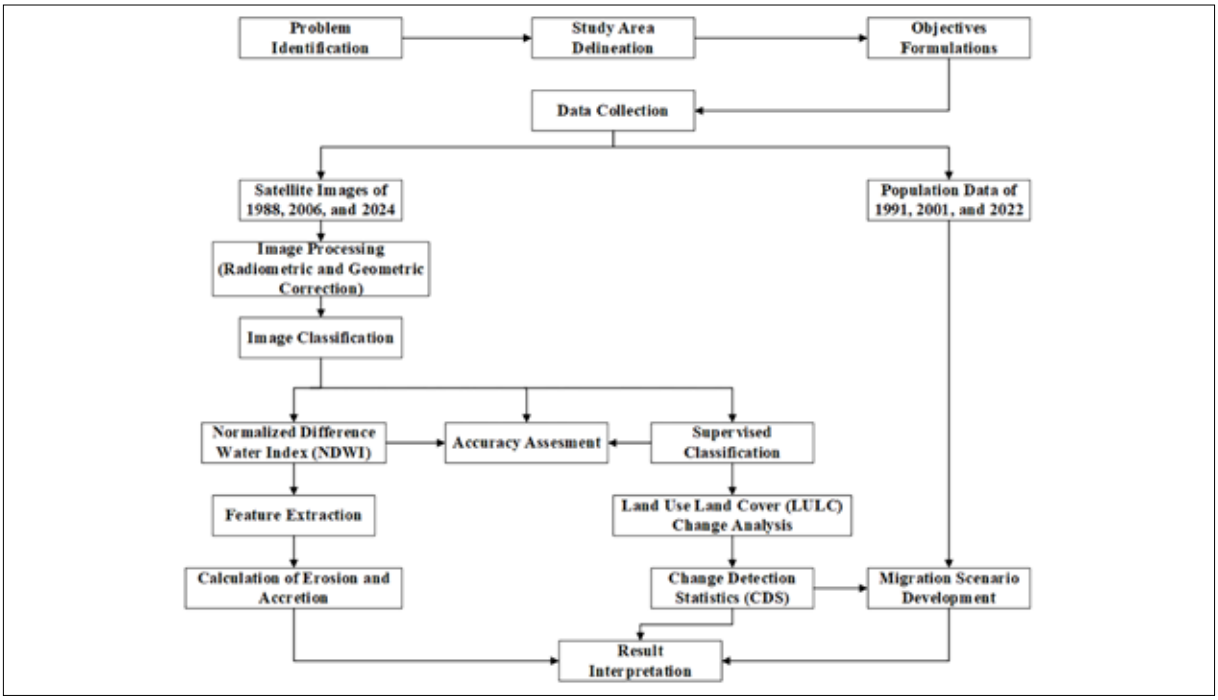

Figure 2. Methodological Framework

2.5 Satellite Image Classification

A classification scheme that identifies the LULC classes was considered when producing the LULC map using satellite imagery. The appropriate number of LULC classes varies, depending on the specifications of a particular project for a specific application (Shekar & Mathew, 2023). Six broad classifications (Agricultural land, vegetation, Water body, Char Land, Fallow Land, and Settlement) were employed to categorize the LULC of the study area. The following table (Table 3) contains a thorough overview of the classes. Each class was created based on texture, tone, and color.

Table 3. Details of the LULC classification scheme

S. No.	Class	Description
1	Agricultural Land	Places like parks and regularly tilled, cultivated croplands have high densities of grass, plants, and crops.
2	Vegetation	Reserve forest, plantation, etc.
3	Waterbody	Areas submerged in water include lakes, streams, ponds, reservoirs, and rivers.
4	Charland	Landmasses formed through the accumulation of massive sand, silt, and clay sediments over time and were carried by rivers.
5	Fallow land	Other people could eventually alter or use these areas, regardless of whether they have minimal vegetation. This group includes areas with sandy soils near rivers and streams, land with bare rock, and land without crops.
6	Settlement	Developed regions for roads, buildings, human habitation, and vegetation, aside from spaces created by humans, roadside trees, and trees planted around homes.

The training samples for each classification category were compiled. For each study year, nearly 260 training datasets were identified from the pre-processed images for LULC classes. Using ENVI (version 5.3) software, training samples were manually chosen from the pre-processed satellite images.

This study employed the supervised classification algorithm, the Maximum Likelihood Classifier (MLC). For the classification of medium-resolution satellite imagery, the MLC has been frequently used (Abusmier & Al-Kofahi, 2025; Anil et al., 2011; Ratnaparkhi et al., 2016; Zubair Iqbal & Javed Iqbal, 2018).

$$D = \ln(ac) - [0.5\ \ln(|Covc|)] - [0.5\ (X - Mc)\ T\ (Covc - 1)\ (X - Mc)] \quad (1)$$

Where the weighted distance or likelihood D of an unknown measurement vector X belongs to one of the known classes, and Mc is based on the Bayesian equation (Kantakumar et al., 2016).

2.6 Classification Accuracy Assessment

The accuracy assessment evaluates the classification of LULC images compared to reference data or maps (Foody, 2002). Google Earth is a valuable source of positional data for mapping land use and land cover in small geographical areas. A study conducted by Abineh and Zubairul (2015) found that its accuracy in assessing land use and land cover using Google Earth was over 75%. For accuracy assessment, 120 points were created in classified images by a stratified random method, and these points were compared with the reference map from Google Earth Pro. The classification accuracy was evaluated using a confusion matrix that included user accuracy, producer accuracy, overall accuracy, and the Kappa coefficient (Foody, 2020). The user, producer, overall accuracy, and Kappa statistics were calculated using specific formulas.

$$\text{User Accuracy} = \frac{\text{Number of Correctly Classified Pixels in each Category}}{\text{Total Number of Reference Pixels in that Category (The Row Total)}} \times 100 \quad (2)$$

$$\text{Producer Accuracy} = \frac{\text{Number of Correctly Classified Pixels in each Category}}{\text{Total Number of Reference Pixels in that Category (The Column Total)}} \times 100 \quad (3)$$

$$\text{Overall Accuracy} = \frac{\text{Total Number of Correctly Classified Pixels (Diagonal)}}{\text{Total Number of Reference Pixels}} \times 100 \quad (4)$$

$$\text{Kappa Coefficient (T)} = \frac{(TS \times TCS) - \sum(\text{Column Total} \times \text{Row Total})}{(TS \times TS) - \sum(\text{Column Total} - \text{Row Total})} \quad (5)$$

Where TS = Total Sample and TCS = Total Corrected Sample

2.7 Normalized Difference Water Index (NDWI)

This study utilized the NDWI to extract the river from the images, enabling the calculation of erosion and accretion. McFeeters (1996) developed the NDWI to enhance the water-related features of landscapes. The NDWI is calculated as:

$$NDWI = \frac{Green - NIR}{Green + NIR} \quad (6)$$

The water cover is mixed with impurities and varies spatially. Using the NDWI threshold for classification is an effective technique to distinguish water from other land cover types. In remote sensing processing, the classification method is widely used for extracting different land cover types (Qiao et al., 2012). McFeeters (1996) reported that NDWI values above zero are presumed to characterize water surfaces. In contrast, values lower than or equal to zero are considered non-water (e.g., agricultural land, vegetation, settlement, etc.) (Szabo et al., 2016). This study utilized the NDWI index to detect changes in land cover. The NDWI threshold range was reclassified into discrete classes by dividing it into five ranges and defining thresholds for NDWI classification (Table 4).

Table 4. The threshold value range used for NDWI classification

Feature	1988	2006	2024
Vegetation	-0.80 to -0.60	-0.73 to -0.44	-0.96 to -0.71
Agricultural Land	-0.53 to -0.44	-0.44 to -0.34	-0.73 to -0.37
Fallow Land	-0.39 to -0.33	-0.33 to -0.14	-0.35 to -0.16
Char Land	-0.22 to -0.02	-0.21 to -0.01	-0.15 to -0.008
Water	0.01 to 0.32	0.02 to 0.43	0.02 to 1.00

2.8 Feature Extraction and Calculation of Erosion and Accretion

After NDWI reclassification, the reclassified images were converted into polygon shapefiles for quantification using ArcMap 10.8.2. The transformed layers of the classified images from 1988, 2006, and 2024 were visually interpreted to determine the river boundaries. The unchanged area was calculated by intersecting the data from the previous year with that of the following year.

For erosion, the unchanged area was subtracted from the river area in 1988, 2006, and 2024, respectively. To quantify the amount of degraded land cover from 1988 to 2006, 2006 to 2024, and 1988 to 2024, attribute tables of these unchanged areas were summarized by computing the geometric union of polygon shape files for each pair of sequential years. Accretion was calculated according to the same procedure suggested by Mou et al. (2023) and Hassan et al. (2017).

2.9 Change Detection

Change detection is valuable in many LULC change detection applications, including cultivation, urban expansion, and landscape change (Salem et al., 2020). The most commonly used change detection methods include thematic change detection, image overlay, principal components analysis (PCA), image ratioing, NDVI differencing, and change vector analysis (Han et al., 2009). The ENVI 5.3 CDS tool was utilized in this study to evaluate the change detection in the study area. The CDS method utilizes two distinct images of the same scene taken at different times to identify changes over time. This study used three classified images of different years (1988, 2006, and 2024) to calculate changes in the study area. The change magnitude (Ci) in each class was determined using the following equation (Vivekananda et al., 2021):

$$Ci = Li - Bi \quad (7)$$

The percentage of change in each LULC class was calculated by dividing the change in a class by its coverage area in the base year and then multiplying by 100.

$$Pi = \frac{Li-Bi}{Bi} \times 100 \quad (8)$$

Where i = Number of classes in an image, Ci = Magnitude of change in class "i", Pi = Percentage of change in class "i", Li = Base image, Bi = Latest image

3. Results and Discussion

3.1 LULC change analysis

LULC patterns of Sirajganj District for the years 1988, 2006, and 2024 are shown in Figure 3, and Table 5 represents the area of the classified land cover. The changing trend of the classified land cover is summarized in Table 6. Agricultural Land in the study area shows an uneven trend. Agricultural land increased by approximately 89,842 hectares within the first 18 years (1988-2006) and decreased by approximately 81,700 hectares within the next 18 years (2006-2024). Over the 36-year period (1988-2024), agricultural land increased by approximately 8,141 hectares.

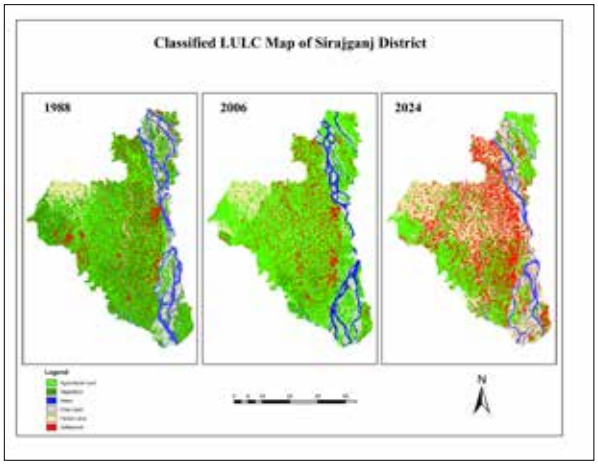

Figure 3. Classified LULC Map of Sirajganj District

Table 5. Calculated area of classified land use and land cover in Sirajganj District

LULC Type	Area (Hectare)		
	1988	2006	2024
Agricultural Land	68536.37	158379.17	76678.32
Vegetation	101167.30	16144.60	5268.15
Water	18888.07	16221.81	13996.82
Char Land	21721.56	14380.70	12776.83
Fallow Land	15684.06	17571.77	74028.52
Settlement	23965.75	27270.15	67216.82

Government policies, technological advancements, and rising demand for agricultural products led to an increase in agricultural land from 1988 to 2006 (Ali, 2007). However, from 2006 to 2024, a decline occurred, and the possible causes behind it were urbanization, industrialization, land conversion, and climate change (Haque et al., 2022). Despite these changes, the overall trend from 1988 to 2024 shows a positive development in agriculture. Over the past 36 years, the areas of vegetable, water, and char land decreased by approximately 9,5989, 4,891, and 8,944 ha, respectively. Fallow land and Settlement have increased by approximately 58344 and 43251 ha, respectively, over this period. Similarly, Haque et al. (2023) found a prominent decrease in char land beside the area of settlements, which increased over time in Sirajganj.

Table 6. LULC Change detection of the study area

LULC Type	Area Change (Ha)		
	1988-2006	2006-2024	1988-2024
Agricultural Land	89842.8	-81700.85	8141.95
Vegetation	-85022.7	-10876.45	-95899.15
Water	-2666.26	-2224.99	-4891.25
Char Land	-7340.86	-1603.87	-8944.73
Fallow Land	1887.71	56456.75	58344.46
Settlement	3304.4	39946.67	43251.07

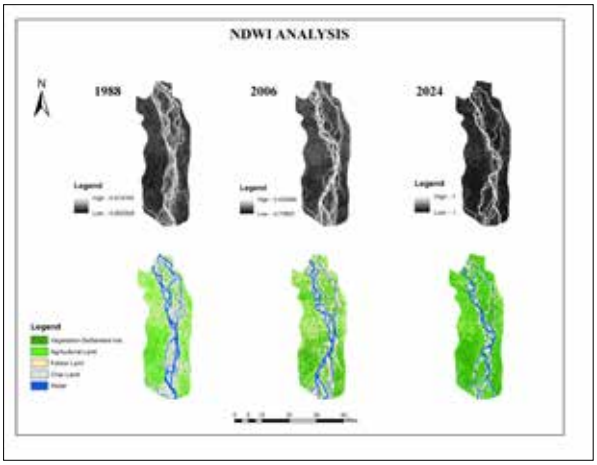

Figure 4. NDWI Analysis of Selected Area

3.2 NDWI Analysis

River areas were extracted using NDWI images. In this study, NDWI was used for three consecutive years (1988, 2006, and 2024) to extract the river from the study area for calculating erosion and accretion.

3.3 Accuracy Assessment Result

The accuracy assessment results for the classified images of the respective years (1988, 2006, and 2024) are presented in Table 7.

Table 7. Accuracy Assessment result of the LULC map

Kappa Coefficient	Overall Accuracy	Settlement	Fallow Land	Char Land	Water	Vegetation	Agricultural Land	Class Names	
0.76	77.50%	89.47%	68.97%	100.%	95.24%	100%	58.62%	Producers Accuracy	1988
		85.00%	100%	100%	100%	100%	85.00%	Users Accuracy	
		0.82	1.00	1.00	1.00	0.08	0.80	Conditional Kappa	
0.67	73.33%	78.26%	52.17%	100%	78.95%	73.33%	72.41%	Producers Accuracy	2006
		100%	75.00%	73.33%	100%	73.33%	51.22%	Users Accuracy	
		1.00	0.69	0.71	1.00	0.69	0.3567	Conditional Kappa	
0.82	85.83%	91.67%	79.17%	94.12%	100%	83.33%	75.76%	Producers Accuracy	2024
		91.67%	79.17%	100%	100%	33.33%	100%	Users Accuracy	
		0.89	0.74	1.00	1.00	0.29	1.00	Conditional Kappa	

The overall accuracy ranges from approximately 73% to 85%, with the kappa coefficient ranging from 0.6733 to 0.8272 from 1988 to 2024. Kappa values <40 percent are considered poor, 40-55 percent fair, 55-70 percent good, 70-85 percent very good, and >85 percent excellent (Ismail & Jusoff, 2008). Thus, according to these agreement scales, the classification indicates good to excellent agreement. The overall accuracy of the classified images is considered acceptable for this study.

3.4 Erosion and Accretion Scenario

Table 8 displays the erosion and accretion of the Jamuna River in Sirajganj for three time frames: 1988–2006, 2006–2024, and 1988–2024. Between 1988 and 2006, 17,199 hectares of erosion and 18,804 hectares of accretion occurred, with 5,551 hectares remaining unchanged. During the second assessment period between 2006 and 2024, 18,547 hectares experienced erosion, 12,609 hectares accreted, and 5,808 hectares remained unchanged. Between 1988 and 2024, the amount of erosion was 18,813 hectares, accretion was 14,480 hectares, and 3,937 hectares remained unchanged.

Table 8. Erosion, Accretion, and Unchanged Area of the study area

Year	Previous Years	Final Years	Unchanged Area (ha)	Erosion (ha)	Accretion (ha)
1988-2006	22750	24355	5551	17199	18804
2006-2024	24355	18417	5808	18547	12609
1988-2024	22750	18417	3937	18813	14480

Figure 5 illustrates the erosion and accretion of the study area over the past 36 years (1988-2024). The erosion and accretion rates have been acquired considering a three-time span- (1988-2006), (2006-2024), and the amount of erosion was 17199 ha, and the amount of accretion was 18804 ha, which means the erosion rate was less than the accretion rate. Similarly, Momen et al. (2020) found that the erosion of the Jamuna River was less than the accretion during the period of 1988-2003, indicating a contraction of the river during that time. The unchanged area represents the river that has not undergone significant erosion or deposition (Wohl, 2005). On the other hand, over the last 18 years (2006-2024), erosion was 18,547 ha, and the accretion was 12,609 ha, indicating that erosion was more significant than accretion. The amount of unchanged area was 5808 ha. Pahlowan & Hossain (2015) found similar results where the amount of erosion was more significant than the accretion from 2004 to 2014. That means that although the accretion was sometimes more significant than the erosion overall (36 years), the amount of erosion is high compared to accretion. Moreover, the 3937-ha area has not experienced significant erosion during this period.

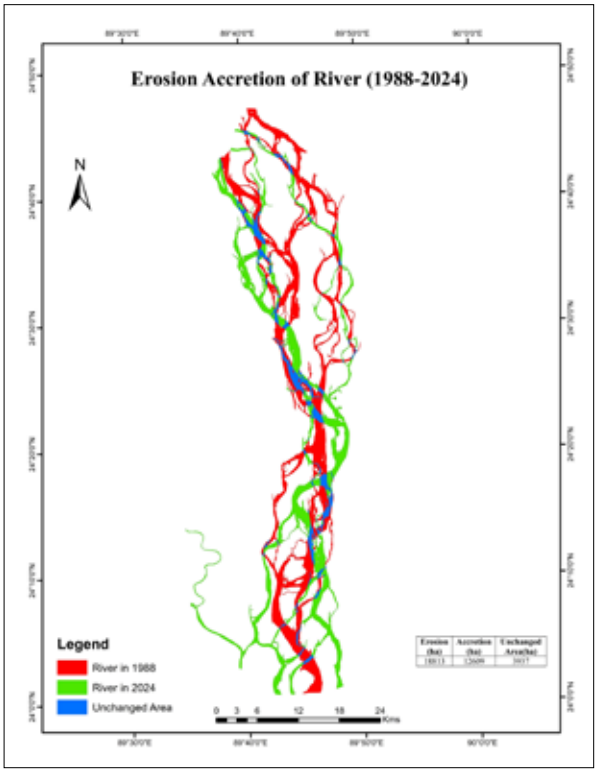

Figure 5. Erosion and Accretion of River (1988-2024)

Erosion, accretion, and unchanged areas in the study area were observed by analyzing Landsat images from 1988, 2006, and 2024. Figure 6 represents the highest eroded area, 18547 ha, from 2006 to 2024, and the highest accreted area, 18804 ha, from 1988 to 2006. The highest erosion may be attributed to increased river discharge, bank instability, human activities, etc., while the highest accretion may be due to significant sediment deposition or changes in river morphology, possibly influenced by upstream activities or natural river dynamics. A study found that dams and/or embankments in the river's vulnerable area altered the flow of water, reducing erosion and triggering deposition in the channel. On the contrary, sand mining caused river erosion (Lusiagustin & Kusratmoko, 2017).

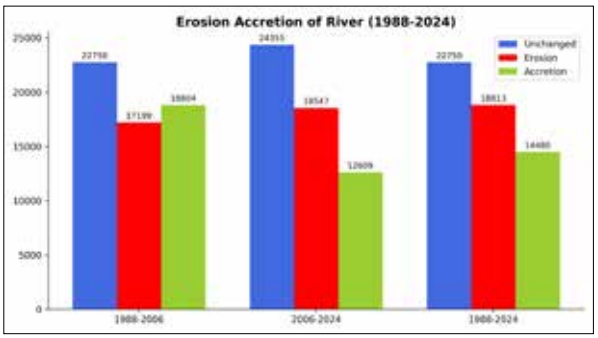

Figure 6. Erosion & Accretion of River from 1988-2024

3.5 Change Detection Statistics (CDS)

Tables 9 to 13 present change-detection statistics for Sirajganj District and its four upazilas (more prone to riverbank erosion) from 1988 to 2024. Between 1988 and 2006, there were significant changes in the fallow land, agricultural land, and vegetation in the Sirajganj District. 59.35% of vegetation and 59.07% of fallow land were converted into agricultural land, while 8.01% was converted into vegetation. Additionally, at this time, 48.11% of the water and 47.09% of the char land were converted to agricultural land. From 2006 to 2024, a major conversion was observed from vegetation to agricultural land, which was 57.71%. Another conversion of agricultural land (26.43%) was from fallow land. Considering water, the area converted into char and fallow land was about 20.93% and 28.28%, respectively. Moreover, conversion from char land to water and fallow land occurred, with respective amounts of 23.6% and 20.93%. Besides, 31.61% of agricultural land was converted into fallow land during this period.

Table 9. CDS of Percentage Change of LULC Between 1988 and 2024 (Sirajganj District)

	Area (Initial State_1988) in percentage								
Area (Final State_2024) in percentage	Class Names	Agricultural Land	Vegetation	Water	Char Land	Fallow Land	Settlement	Row Total	Class Total
	Agricultural Land	37.09	60.09	22.72	24.09	26.74	20.41	100	100
	Vegetation	2.18	4.33	4.1	3.66	1.46	0.97	100	10
	Water	2.56	2.39	18.41	14.35	6.33	3.77	100	100
	Char Land	1.93	1.81	14.84	17.49	6.37	3.06	100	100
	Fallow Land	28.58	16.69	27.00	28.5	43.22	20.57	100	100
	Settlement	27.65	14.69	12.93	11.90	15.88	51.22	100	100
	Class Total	100	100	100	100	100	100	0	0
	Class changes	62.91	95.67	81.59	82.51	56.79	48.78	0	0
	Image Difference	-29.42	-34.36	-27.65	-25.85	44.22	48.27	0	0

Significant changes in land cover were observed between 1988 and 2024 (Table 9). Considering agricultural land, the area was converted into fallow land and settlement, with conversion rates of 28.58% and 27.56%, respectively. Significant changes were observed from vegetation to agricultural land, fallow land, and settlement; their proportions are 60.09%, 16.69%, and 14.59%, respectively. From the water, about 22.72%, 14.84%, 27%, and 12.93% of areas were converted into agricultural land, char land, fallow land, and settlement, respectively. Besides, char land

was converted into agricultural land, water, fallow land, and settlement, and the conversions are 24.09%, 14.35%, 28.5%, and 11.90%, respectively. Moreover, 26.47% of fallow land was converted into agricultural land, and 15.88% was converted into settlement. During this period, 20.41% and 20.57% of the settlements were converted into agricultural and fallow land, respectively.

In Kazipur Upazila between 1988 and 2006, significant conversions from vegetation to agricultural land occurred. 67.97% of vegetation was converted into agricultural land in this period. 55.72% of water was converted into agricultural land. Similarly, char land was converted into agricultural land and water; the conversion amounts are 58.75% and 18.69%, respectively. In the meantime, 58.80% of fallow land was converted into agricultural land, and 42.32% of settlement was also converted into agricultural land. From 2006 to 2024, a significant conversion from vegetation to agricultural land was observed, representing a 43.36% change. During this period, 31.46% and 16.11% of agricultural land were converted to fallow land and settlement, respectively. 20.29% of water was converted into char land, and 29.42% into fallow land. Furthermore, 28.11%, 18.39%, and 23.43% of char land were converted to agricultural land, water, and fallow land, respectively. The change of fallow land into agricultural land was 26.69%. From 1988 to 2024 (Table 10), the primary conversions of agricultural land were vegetation (28.75%), water (37.78%), char land (38.18%), fallow land (38.59%), and settlement (24.19%). The conversion of char land was from vegetation (9.29%), water (10.55%), and fallow (11.59%). Fallow land was significantly converted from agricultural (35.24%), vegetation (29.48%), water (23.02%), and settlement (17.35%). The most extensive settlement conversion was from agricultural land (29.40%). Significant changes also were from vegetation (21.66%) and fallow (14.82%).

Table 10. CDS of Percentage Change of LULC Between 1988 and 2024 (Kazipur Upazila)

	Area (Initial State_1988) in percentage								
Area (Final State_2024) in percentage	Class Names	Agricultural Land	Vegetation	Water	Char Land	Fallow Land	Settlement	Row Total	Class Total
	Agricultural Land	21.38	28.75	37.78	38.18	38.59	24.19	100	100
	Vegetation	1.48	3.18	7.94	6.26	4.10	1.60	100	100
	Water	6.61	7.65	15.57	8.42	8.76	5.42	100	100
	Char Land	5.89	9.29	10.55	13.29	11.59	5.07	100	100
	Fallow Land	35.24	29.48	23.02	27.68	22.14	17.35	100	100
	Settlement	29.40	21.66	5.14	6.16	14.82	46.38	100	100
	Class Total	100	100	100	100	100	100	0	0
	Class changes	78.62	96.82	84.43	86.70	77.86	53.63	0	0
	Image Difference	76.42	-88.35	-45.53	-48.12	472.58	134.46	0	0

In Sirajganj Sadar, from 1988 to 2006, agricultural land experienced significant conversions from vegetation (73.48%), water (41.30%), char land (37.84%), fallow land (66.19%), and settlement (24.80%). A notable portion of water was converted from char land (28.13%), while 23.61% was converted into char land. Between 2006 and 2024, 37.93% of the vegetation was converted to agricultural land. 30.18% of char land was converted into water, while 18.47% was converted into char land.

Fallow land was significantly converted from agricultural (37.96%), vegetation (22.19%), water (25.88%), char land (25.57%), and settlement (54.04%). In the meantime, the settlement was primarily converted from agricultural land (34.19%), vegetation (23.15%), and fallow land (18.20%). From 1988 to 2024 (Table 11), vegetation (15.72%), char land (13.67%), and fallow land (16.27%) were the significant sources of conversion into agricultural land. 18.54% of char land and 10.41% of fallow land were converted into water.

Table 11. CDS of Areal Change of LULC Between 1988 and 2024 (Sadar Upazila)

	Area (Initial State_1988) in percentage								
Area (Final State_2024) in percentage	Class Names	Agricultural Land	Vegetation	Water	Char Land	Fallow Land	Settlement	Row Total	Class Total
	Agricultural Land	16.46	15.72	12.12	13.67	16.27	4.47	100	100
	Vegetation	0.43	0.70	3.29	4.43	2.66	0.43	100	100
	Water	5.46	6.65	24.88	18.54	10.41	2.83	100	100
	Char Land	2.59	5.25	18.73	21.73	6.35	1.52	100	100
	Fallow Land	33.21	39.48	25.37	27.09	21.64	11.59	100	100
	Settlement	41.86	32.20	15.60	14.54	42.67	79.16	100	100
	Class Total	100	100	100	100	100	100	0	0
	Class changes	83.54	99.30	75.12	78.27	78.36	20.84	0	0
	Image Difference	-42.80	-96.21	-19.96	-32.38	1031.21	156.46	0	0

Only a substantial amount of water (18.73%) was converted into char land. A substantial amount of vegetation (39.48%) was converted into fallow land, with significant conversion from agricultural land (33.21%), water (25.37%), char land (27.09%), and settlement (11.59%). Moreover, there is a considerable amount of conversion of settlement from agricultural land (41.86%), vegetation (32.20%), water (15.60%), char land (14.54%), and fallow land (42.67%).

Between 1988 and 2006, a significant change was observed in the fallow land of Belkuchi, where 68.32% of the fallow land was converted to agricultural land. Furthermore, vegetation (65.85%), water (41.91%), and char land (56.40%) were also converted into agricultural land. Between 2006 and 2024, in Belkuchi, 47.71% of vegetation and 25.07% of fallow land were changed into agricultural land. 16.40% and 24.90% of water turned into char and fallow land, respectively. On the other hand, 16.31% of char land turned into water. Also, 36.28% of char land was converted to fallow land. Agricultural land (35.46%), vegetation (22.51%), and fallow land (32.39%) were changed to settlement. From 1988 to 2024 (Table 12), a significant change occurred in agricultural land, with 47.90% converted to settlement. Also, 37.30% of vegetation, 15.47% of water, 23.56% of char land, and 26.27% of fallow land were converted into settlements. Vegetation (41.77%) and fallow land (25.74%) turned into agricultural land. 13.07% of char land and 17.81% of fallow land became water. Moreover, Water (25.06%) and char land (26.06%) were converted into fallow land.

Table 12. CDS of Percentage Change Between 1988 and 2024 (Belkuchi Upazila)

	Area (Initial State_1988) in percentage								
Area (Final State_2024) in percentage	Class Names	Agricultural Land	Vegetation	Water	Char Land	Fallow Land	Settlement	Row Total	Class Total
	Agricultural Land	39.07	41.77	22.68	23.60	25.74	7.29	100	100
	Vegetation	1.92	2.29	0.49	0.46	0.47	0.38	100	100
	Water	1.17	4.49	17.64	13.07	17.81	0.11	100	100
	Char Land	0.67	3.35	18.67	13.25	10.57	0.05	100	100
	Fallow Land	9.28	10.81	25.06	26.06	19.14	3.05	100	100
	Settlement	47.90	37.30	15.47	23.56	26.27	89.12	100	100
	Class Total	100	100	100	100	100	100	0	0
	Class changes	60.93	97.71	82.36	86.75	80.86	10.88	0	0
	Image Difference	36.47	-96.10	-40.51	-61.59	747.10	216.44	0	0

Between 1988 and 2006, in Chauhali, vegetation (46.30%), water (43.54%), char land (41.83%), fallow land (40.85%), and settlement (38.76%) were converted into agricultural land. Additionally, agricultural land (16.20%), vegetation (19.97%), char land (22.30%), and fallow land (24.89%) were converted into water. 15.20% of agricultural land, 19.14% of vegetation, and 21.50% of water were converted into char land. From 2006 to 2024, in Chauhali, 30.09% of the vegetation was converted into agricultural land. However, agricultural land (15.89%), char land (27.05%), and fallow land (15.00%) were converted into water. Besides 17.21% of agricultural land, 24.09% of water, and 16.69% of fallow land converted to char land. Surprisingly, agricultural land (28.29%), vegetation (19.83%), water (30.59%), and char land (34.13%) were turned into fallow land. On the other hand, 20.90% of agricultural land, 23.65% of vegetation, and 9.92% of water were converted to settlement. Between 1988 and 2024 (Table 13), in Chauhali, 31.12% of char land was converted to fallow land, which was a significant change.

Table 13. CDS of Percentage Change Between 1988 and 2024 (Chauhali Upazila)

	Area (Initial State_1988) in percentage								
Area (Final State_2024) in percentage	Class Names	Agricultural Land	Vegetation	Water	Char Land	Fallow Land	Settlement	Row Total	Class Total
	Agricultural Land	15.37	13.72	13.57	13.90	5.95	7.25	100	100
	Vegetation	4.31	4.48	1.46	1.48	1.56	3.33	100	100
	Water	17.07	17.27	18.99	20.06	30.22	8.72	100	100
	Char Land	11.78	18.33	20.34	21.02	22.73	8.68	100	100
	Fallow Land	24.14	28.43	30.81	31.12	30.33	24.27	100	100
	Settlement	27.34	17.77	14.83	12.41	9.20	47.75	100	100
	Class Total	100	100	100	100	100	100	0	0
	Class changes	84.63	95.52	81.01	78.98	69.67	52.25	0	0
	Image Difference	7.38	-91.33	-3.19	-34.26	510.75	836.85	0	0

Agricultural land (24.14%), vegetation (28.43%), water (30.81%), and settlement (24.27%) were converted into fallow land. However, agricultural land (17.07%), vegetation (17.27%), char land (20.06%), and fallow land (30.22%) turned into water. On the other hand, 11.78% of agricultural land, 18.33% of vegetation, 20.34% of water, 22.73% of fallow land, and 8.68% of settlement became char land. Furthermore, agricultural land (27.34%), vegetation (17.77%), water (14.83%), char land (12.71%), and fallow land (9.20%) were converted into settlements in this period.

3.6. Population Displacement Scenario

Due to riverbank erosion in various parts of the Sirajganj district, thousands have been displaced, resulting in increased poverty, food insecurity, and a lack of access to sanitation, healthcare, and drinking water facilities (Abrar & Azad, 2004; Rabbi et al., 2013). The erosion pushes people to migrate to other places like cities or the nearest towns and bound to live in the urban slum areas. There may not only be temporary migration but also permanent migration. CDS of Kazipur Upazila represents the settlement area increased by 22.10% from 1988 to 2024 (Table 12). In the Kazipur upazila of Sirajganj district, 21,961 people, constituting 9.35% of the total population, migrated permanently within neighboring areas due to the need for income and social connections (Mollah & Ferdaush, 2015). The CDS of Sirajganj Sadar indicates that the settlement increased significantly from 4.47% in 1988 to 79.16% in 2024, indicating an increase in the area by 74.69% (Table 10). This suggests a substantial growth in urban areas and settlements within the upazila. The increase in settlement areas is a strong indicator of urbanization, and population movement from rural areas (like agricultural or fallow land) to urban areas could contribute to this shift. A study was conducted on riverbank erosion and induced population migration of Sirajganj Sadar Upazila by Ali et al. (2021) where they found that sufferers migrated in the nearest union about 29.42% as they mostly preferred to migrate within a short distance, followed by Sirajganj Town 27.66%, Dhaka 20.35%, neighboring district 10.86% and others 11.71%, respectively. The displacement scenario can be hypothesized by examining the population growth of these upazilas, as shown in Figure 7. The population of all four areas increased significantly from 1991 to 2022.

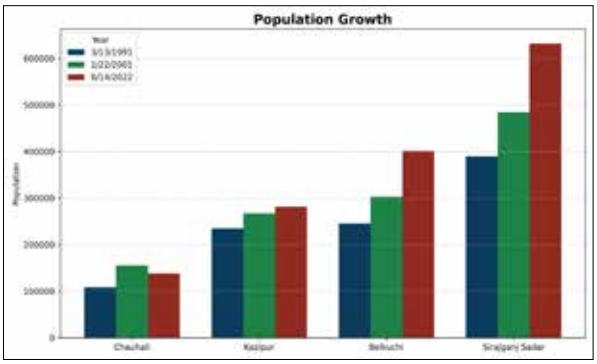

Figure 7. Population Growth of the Study Area

This is especially evident in Sirajganj Sadar, which has experienced the most substantial growth. Belkuchi upazila experienced a modest increase between 1991 and 2001, but the growth rate slowed between 2001 and 2022. Considering Chauhali and Kazipur, these areas have shown consistent population growth over this period. The population growth of Chauhali Upazila has been relatively steady, decreasing over the last decade, while Kazipur Upazila's growth has increased very slowly during the same period. On the other hand, Sirajganj Sadar has undergone the most dramatic population increase. The population has more than doubled since 1991, and the growth rate has been exceptionally high in the last decade. The total population of Sirajganj Sadar was 389160 in 1991 and 631877 in 2022. This indicates that people from other areas migrated to Sadar Upazila, leading to an increase in population and suggesting internal migration. In Sirajganj, after being affected by riverbank erosion, people immediately tend to migrate for safe shelter and later permanently for survival, where internal migration was observed, including men, women, and children, and the trends of settlement displacement are increasing day by day (Haque et al., 2023).

4. Conclusion

This study analyzed LULC and NDWI, calculated erosion and accretion, and its effects on population from 1988 to 2024 using satellite imagery and population data. The result represented that the amount of erosion increased, and accretion decreased over 36 years, which led to a change in the spatiotemporal characteristics of the study area and revealed the effects of erosion on population displacement. The LULC results showed that over 36 years, vegetation and char land decreased, while fallow land and settlement increased. The CDS result of Sirajganj Sadar representing the settlement area has increased tremendously by 74.69% during this period. The most significant effects of erosion were observed in Chauhali and Kazipur Upazila, as residents of these regions migrated temporarily or permanently to Sadar Upazila, causing Chauhali's population to decline in recent decades.

The findings underline the urgent need for sustainable land management strategies that balance development and environmental conservation. The implications are far-reaching, providing valuable data for policymakers, urban planners, and environmentalists to reduce negative impacts, design resilient land-use policies, and prioritize erosion control, water resource management, and ecological preservation strategies to ensure long-term regional sustainability. This study suggests that drivers of change and specific socioeconomic and policy data are needed to properly understand the underlying reasons for land transformation. The study did not account for climate change impacts, such as fluctuations in precipitation and temperature, and other hydro-morphological factors, which might have a considerable effect on erosion and accretion dynamics. Future research should use high-resolution satellite imagery and incorporate field surveys to enhance accuracy in LULC classification and erosion-accretion analysis. Alongside, collecting field data on migration patterns is crucial for understanding the actual migration scenario. Investing in land reclamation projects to recover and stabilize eroded areas, enhancing their utility for agriculture and settlement, will further aid in proactive erosion management.

References

Abineh Tilahun and I. Zubairul .2015. Use of Google Earth for Land Use mapping in the Case of Gish Abbay Sekela, West Gojjam, Amhara State, Ethiopia. International Journal of Society and Humanities (ISSN-2319-2070/VOL 6:1-6)

Abrar, C. R., & Azad, S. N. (2004). Coping with displacement: Riverbank erosion in northwest Bangladesh. University Press Limited.

Abusmier, S. A., & Al-Kofahi, S. D. (2025). Examining Land Use/Land Cover Dynamics in Zarqa Governorate Major Districts: Implications for Urban and Environmental Sustainability. Jordan Journal of Earth & Environmental Sciences, 16(1).

Ali, A. M. S. (2007). Population pressure, agricultural intensification, and changes in rural systems in Bangladesh. Geoforum, 38(4), 720-738. https://doi.org/10.1016/j.geoforum.2006.11.028

Ali, M. R., Ahmed, Z., Islam, A. H., & Rahman, M. M. (2021). River Bank Erosion, Induced Population Migration and Adaptation Strategies in the Sirajganj Sadar Upazila, Bangladesh. European Journal of Environment and Earth Sciences, 2(2), 39-47. https://doi.org/10.24018/ejgeo.2021.2.2.131

Anil, N. C., Sankar, G. J., Rao, M. J., Prasad, I. V. R. K. V., & Sailaja, U. (2011). Studies on land use/land cover and change detection from parts of South West Godavari District, AP–using remote sensing and GIS techniques. Journal of Indian Geophysical Union, 15(4), 187-194.

Archana, S., RD, G., & Nayan, S. (2012). RS-GIS based assessment of river dynamics of Brahmaputra River in India. Journal of Water Resource and Protection, 2012. https://doi.org/10.4236/jwarp.2012.42008

Ashworth, P. J. (1996). Mid-channel bar growth and its relationship to local flow strength and direction. Earth surface processes and landforms, 21(2), 103-123. https://doi.org/10.1002/(SICI)1096-9837(199602)21:2%3C103::AID-ESP569%3E3.0.CO;2-O

Baki, A. B. M., & Gan, T. Y. (2012). Riverbank migration and island dynamics of the braided Jamuna River of the Ganges–Brahmaputra basin using multi-temporal Landsat images. Quaternary International, 263, 148-161. https://doi.org/10.1016/j.quaint.2012.03.016

Bedini, E. (2007) Use of GIS and Remote Sensing to Detect Change along the Coastline Segment between Shkumbini and Semani Rivers, Central Albania. Proceedings of the 11th International Congress Bulletin of the Geological Society of Greece, XXXX, Athens, 24-26 May 2007, 1916-1924. https://doi.org/10.1088/1755-1315/169/1/012020

Coppin, P., Jonckheere, I., Nackaerts, K., Muys, B., & Lambin, E. (2004). Review ArticleDigital change detection methods in ecosystem monitoring: a review. International journal of remote sensing, 25(9), 1565-1596. https://doi.org/10.1080/0143116031000101675

Das, T. K., Haldar, S. K., Gupta, I. D., & Sen, S. (2014). River bank erosion induced human displacement and its consequences. Living Reviews in Landscape Research, 8(3), 1-35. https://doi.org/10.12942/lrlr-2014-3

Foody, G. M. (2002). Status of land cover classification accuracy assessment. Remote Sensing of Environment, 80(1), 185–201. https://doi.org/10.1016/s0034-4257(01)00295-4

Foody, G. M. (2020). Explaining the unsuitability of the kappa coefficient in the assessment and comparison of the accuracy of thematic maps obtained by image classification. Remote sensing of environment, 239, 111630.

Han, J., Hayashi, Y., Cao, X., & Imura, H. (2009). Evaluating Land-Use change in Rapidly Urbanizing China: Case Study of Shanghai. Journal of Urban Planning and Development. https://doi.org/10.1061/(ASCE)0733-9488(2009)135:4(166

Haque, M. A., Shishir, S., Mazumder, A., & Iqbal, M. (2023). Change detection of Jamuna River and its impact on the local settlements. Physical Geography, 44(2), 186-206. https://doi.org/10.1080/02723646.2022.2026075

Haque, M. N., Fatema, K., & Joy, M. A. R. (2022). Crop suitability analysis by adopting geo-spatial algorithm: a case study of Sirajganj district (flood-prone area) in Bangladesh. Arab Gulf Journal of Scientific Research, 40(4), 392-414. https://doi.org/10.1108/AGJSR-07-2022-0118

Hassan, M. A., Ratna, S. J., Hassan, M., & Tamanna, S. (2017). Remote sensing and GIS for the Spatio-temporal change analysis of the east and the West River Bank erosion and accretion of Jamuna River (1995-2015), Bangladesh. Journal of Geoscience and Environment Protection, 5(9), 79-92. https://doi.org/10.4236/gep.2017.59006

Hassan, M. S. (2015). Quantification of River Bank erosion and bar deposition in Chowhali Upazila, Sirajganj District of Bangladesh: A remote sensing study. Journal of Geoscience and Environment Protection, 4(1), 50-57. http://dx.doi.org/10.4236/gep.2016.41006

Hassan, S. T., Syed, M. A., & Mamnun, N. (2017). Estimating erosion and accretion in the coast of Ganges-Brahmaputra-Meghna Delta in Bangladesh. In 6th Int. Conference on Water & Flood Management (pp. 115-124).

Hossain, M. Z., & Sakai, T. (2008). Severity of flood embankments in Bangladesh and its remedial approach. Agricultural Engineering International: CIGR Journal. https://doi.org/10.1016/j.rse.2019.111630

Iqbal, M. Z., & Iqbal, M. J. (2018). Land use detection using remote sensing and gis (A case study of Rawalpindi Division). American Journal of Remote Sensing, 6(1), 39-51. https://doi.org/10.11648/j.ajrs.20180601.17

Islam, M. F., & Rashid, A. B. (2011). Riverbank erosion displacees in Bangladesh: need for institutional response and policy intervention. Bangladesh Journal of Bioethics, 2(2), 4-19. https://doi.org/10.3329/bioethics.v2i2.9540

Ismail, M. H., & Jusoff, K. (2008). Satellite data classification accuracy assessment based from reference dataset. International Journal of Geological and Environmental Engineering, 2(3), 23-29.

Iva, T. T., Hazra, P., Faisal, M., Saha, S., & Hossain, S. (2017). River bank erosion and its impact on population displacement in Bauphalupazila under Patuakhali district. Bangladesh. Journal of Science, Technology and Environment Informatics, 5(02), 371-381. https://doi.org/10.18801/jstei.050217.39

Kantakumar, L. N., Kumar, S., & Schneider, K. (2016). Spatiotemporal urban expansion in Pune metropolis, India using remote sensing. Habitat international, 51, 11-22. https://doi.org/10.1016/j.habitatint.2015.10.007

Lusiagustin, V., & Kusratmoko, E. (2017, July). Impact of sand mining activities on the environmental condition of the Komering river, South Sumatera. In AIP Conference Proceedings (Vol. 1862, No. 1). AIP Publishing. https://doi.org/10.1063/1.4991302

McFeeters, S. K. (1996). The use of the Normalized Difference Water Index (NDWI) in the delineation of open water features. International journal of remote sensing, 17(7), 1425-1432. https://doi.org/10.1080/01431169608948714

Mohamad, N., Khanan, M. F. A., Musliman, I. A., Kadir, W. H. W., Ahmad, A., Rahman, M. Z. A., ... & Zain, R. M. (2018, June). Spatio-temporal analysis of river morphological changes and erosion detection using very high resolution satellite image. In IOP conference series: earth and environmental

science (Vol. 169, No. 1, p. 012020). IOP Publishing. https://doi.org/10.1088/1755-1315/169/1/012020

Mollah, T. H., & Ferdaush, J. (2015). Riverbank erosion, population migration, and rural vulnerability in Bangladesh (a case study on Kazipur Upazila at Sirajgonj District). Environment and Ecology Research, 3(5), 125-131.

Momen, M. A., Uddin, M. E., & Tasnim, N. (2020).... seems incomplete. Please use the full reference (Momen, M. A., Uddin, M. E., & Tasnim, N. (2020, December). Assessment of Bank Erosion and Accretion of Jamuna River Using GIS and Remote Sensing. In Conference: 5th International Conference on Advances in Civil Engineering (ICACE-2020) at CUET, Chattogram, Bangladesh. 8p.)

Mou, M. A., Tusar, M. K., Haque, M. R., Chakraborty, S., & Ahmed, S. (2023). Assessment of Riverbank Erosion and Accretion and its Impact on the People of Chairman Ghat, Noakhali, Bangladesh. Journal of Sustainability and Environmental Management, 2(4), 220-230. https://doi.org/10.3126/josem.v2i4.61022

Nath, B., Naznin, S. N., & Alak, P. (2013). Trends analysis of river bank erosion at Chandpur, Bangladesh: a remote sensing and GIS approach. International Journal of Geomatics and Geosciences, 3(3), 454-463. https://doi.org/10.4236/gep.2016.41006

Pahlowan, E. U., & Hossain, A. T. M. S. (2015). Jamuna River Erosional Hazards, Accretion & Annual Water Discharge–A Remote Sensing & Gis Approach. The International Archives of the Photogrammetry, Remote Sensing and Spatial Information Sciences, 40, 831-835. https://doi.org/10.5194/isprsarchives-XL-7-W3-831-2015

Qiao, C., Luo, J., Sheng, Y., Shen, Z., Zhu, Z., & Ming, D. (2012). An adaptive water extraction method from remote sensing image based on NDWI. Journal of the Indian Society of Remote Sensing, 40, 421-433. https://doi.org/10.1007/s12524-011-0162-7

Rabbi, H., Saifullah, A. S. M., Sheikh, M. S., Sarker, M. M., & Bhowmick, A. C. (2013). Recent study on river bank erosion and its impacts on land displaced people in Sirajgonj Riverine area of Bangladesh. World journal of Applied Environmental chemistry, 2(2), 36-43.

Ratnaparkhi, N. S., Nagne, A. D., & Gawali, B. (2016). Analysis of land use/land cover changes using remote sensing and GIS techniques in Parbhani City, Maharashtra, India. International Journal of Advanced Remote Sensing and GIS, 5(1), 1702-1708. https://doi.org/10.23953/cloud.ijarsg.54

Salem, M., Tsurusaki, N., & Divigalpitiya, P. (2020). Land use/land cover change detection and urban sprawl in the peri-urban area of greater Cairo since the Egyptian revolution of 2011. Journal of Land Use Science, 15(5), 592-606. https://doi.org/10.1080/1747423X.2020.1765425

Shekar, P. R., & Mathew, A. (2023). Detection of land use/land cover changes in a watershed: A case study of the Murredu watershed in Telangana state, India. Watershed Ecology and the Environment, 5, 46-55. https://doi.org/10.1016/j.wsee.2022.12.003

Shetu, M. S. R., Islam, M. A., Rahman, K. M. M., & Anisuzzaman, M. (2016). Population displacement due to river erosion in Sirajganj district: impact on food security and socio-economic status. https://doi.org/10.3329/jbau.v14i2.32694

Soto Carrión, C., Zuñiga Negron, J. J., Paucar Ancco, J., Jiménez Mendoza, W., Ibarra Cabrera, M. J., Narváez Liceras, A., & Paucar Ancco, S. (2022). Multi-temporal analysis of the glacier retreat using landsat satellite images in the Nevado of the Ampay national sanctuary, Peru. Journal of Sustainable Development of Energy, Water and Environment Systems, 10(1), 1-15. https://doi.org/10.13044/j.sdewes.d8.0380

Szabo, S., Gácsi, Z., & Balazs, B. (2016). Specific features of NDVI, NDWI and MNDWI as reflected in land cover categories. Acta Geographica Debrecina. Landscape & Environment Series, 10(3/4), 194. https://doi.org/10.21120/LE/10/3-4/13

Uddin, K., Shrestha, B., & Alam, M. S. (2011). Assessment of morphological changes and vulnerability of river bank erosion alongside the river Jamuna using remote sensing. Journal of earth science and Engineering, 1(1).

Vivekananda, G. N., Swathi, R., & Sujith, A. V. L. N. (2021). Multi-temporal image analysis for LULC classification and change detection. European journal of remote sensing, 54(sup2), 189-199. https://doi.org/10.1080/22797254.2024.2350269

Wohl, E. (2005). Compromised rivers: understanding historical human impacts on rivers in the context of restoration. Ecology and Society, 10(2). https://doi.org/10.5751/ES-01339-100202

Tobore, A., Senjobi, B., & Oyerinde, G. (2021). Spatio Temporal Analysis and Simulation Pattern of Land Use and Land Cover Change in Odeda Peri-urban of Ogun State, Nigeria. Jordan Journal of Earth & Environmental Sciences, 12(4).

Al-Amoush, H., Al-Shabeeb, A. R., Al-Adamat, R., Al-Fugara, A. K., Al Ayyash, S., Shdeifat, A., ... & Rajab, J. A. (2017). The Use of GIS Techniques and Geophysical Investigation for Flood Management at Wadi Al-Mafraq Catchment Area. Jordan Journal of Earth and Environmental Sciences, 8(2), 97-103.

JJEES

JJEES (2026) 17 (2): 199-206
ISSN 1995-6681

Jordan Journal of Earth and Environmental Sciences

Assessment of Water Quality of Household Tanks in Jordan

Tuqa R. AL-Nawafleh and Kamel K. Al-Zboon*

Al-Balqa Applied University, Al-Huson University College, Environmental Engineering Department, P.O. Box 50, 21510 Al-Huson, Jordan.

Received on 11 January 2025; Accepted on 17 November 2025

Abstract

Ensuring the quality of household water tanks is crucial for safeguarding human health and maintaining environmental sustainability. This study aims to assess the physical, chemical, and biological parameters of water samples taken from 22 household tanks in Jordan. The findings revealed substantial bacterial contamination in water tanks, notably high levels of Pseudomonas in 11 samples, with counts exceeding 100 CFU/100ml, and total coliforms exceeding permissible limits in two samples. While most chemical and physical parameters were within acceptable ranges, instances of elevated alkalinity and turbidity were observed in some samples. The Water Quality Index (WQI) classifies most samples as "Excellent," representing 86% of the total, and 14% as "Good." It is recommended to implement periodic monitoring and maintenance programs to control biological pollution and ensure long-term improvements in water quality . It is vital to enhance public awareness of adequate tank maintenance practices among users, improve public health protection, and help implement sustainable water management initiatives to address climate change.

Keywords: *Water Quality Index (WQI), Household Storage Tanks, Water Management, Water Quality, Jordan*

1. Introduction

Jordan has been categorized as the second most water-poor country in the world in terms of water availability (Malkawi, 2005). Jordan's renewable water supply barely meets two-thirds of its population's water demands. The situation is exacerbated by rapid population growth and successive waves of refugees from neighboring countries experiencing conflict, resulting in overwhelming pressure on the already-stretched water supply. Unfortunately, the situation is expected to worsen due to climate change (USAID, 2023). The annual renewable water share is less than 100 m3 per person, significantly below the threshold limit of 500 m3. Despite over 98% of the population having access to an improved water source, access to a safely managed source is about 93%, and only 86% access to the piped network (Al-Kharabsheh and Al-Zboon, 2021; UNICEF, 2022). Urban water supply networks are facing mounting pressures due to escalating water needs driven by population expansion and economic development, and more recently compounded by the impact of climate change where water is supplied to the urban areas once a week. In rural areas, it is even less frequent, typically less than once every two weeks, with reduced frequency during the summer months (Constantine et al., 2017; UNICEF, 2022).

Household water tanks with capacities of 500 to 2000 liters are prevalent in developing urban regions, serving as a dependable, uninterrupted water for households. These tanks are typically situated at an elevated position, granting constant, pressurized access to water throughout the day (Schafer and Mihelcic, 2012). Given that tank water is sourced from the public network or by truck, it is essential to conduct thorough inspections and implement control measures before and during these practices to prevent contamination of the supplied water. Water consumers should be made aware of the potential risks associated with consuming the first rinse water that is supplied after the water supply has been resumed, and they should be guided on appropriate measures to minimize their exposure to chemical and microbial contaminants in tap water. To ensure water safety and prevent the spread of microbes, tank trucks designated for transporting potable water must undergo thorough inspection and sterilization before use. Regular monitoring of disinfectant residues and microbial contaminants in water transported by trucks is necessary. Awareness programs should be conducted to educate families on the maintenance practices needed to ensure the safety of their water tanks, thereby minimizing water quality deterioration (Salehi, 2022).

Water quality issues in storage facilities can be categorized into microbiological, chemical, or physical categories. The degradation of water quality in storage facilities is likely due to prolonged water storage. The extended holding times may create favorable conditions for microbial growth and chemical transformations. Water tanks, especially roof tanks, can pose a health hazard if they are not correctly sited, covered, and adequately maintained. These tanks have frequently exhibited poor bacteriological results and outbreaks of waterborne diseases (Al-Ghanim et al., 2014).

The problem of microbial regrowth in Jordan is compounded by the storage of water for extended periods, lasting up to two weeks, particularly during the summer season. Kirmeyer et al. (1999) reported that storage periods may extend to several months, significantly increasing the risk of quality deterioration due to chemical reactions such as reduced disinfectant residual, formation of disinfection

* Corresponding author e-mail: alzboon@bau.edu.jo, Kalzboon@yahoo.com

by-products, increased pH, taste and odor, corrosion, and hydrogen sulfide.

The household tanks predominantly used in Jordan are typically manufactured from galvanized iron and polyethylene. Long holding times decrease chlorine levels, and sediment buildup further enhances the likelihood of microbial growth in these storage tanks (Evison and Sunna, 2001).

Ogbozige et. al. (2018) investigated the impact of storage duration on chemical water quality across various container materials. The findings revealed that across all container materials examined, the maximum water retention period was approximately 21 days, except for clay-pot material, which had a retention period of no more than 6 days. Additionally, the study did not recommend the use of uncoated steel metal tanks. The conclusion reported that black plastic containers were more effective at maintaining water quality during storage than colored plastic containers, galvanized iron or coated steel containers, and clay pots.

Evison and Sunna (2001) investigated the regeneration characteristics of bacteria in various types of household storage tanks and the factors that affect their growth in Amman, Jordan. The results of the study showed that the bacterial count in water stored for 4 and 7 days increased significantly from log 1.7 to log 5.2 and log 5.7 CFU/mL, respectively. The regrowth of bacteria was mainly dominated by Actinomycetes, Pseudomonas species, and Moraxella spp. Interestingly, the different materials of the household tanks, such as polyethylene, fiberglass, and cast iron, did not significantly influence the total bacterial count of the stored water. The relationship between temperature and microbial regrowth suggests that conditions similar to ‘ ‘Jordan’s summer climate characterized by high ambient temperatures would likely exacerbate bacterial regrowth. However, the study revealed that temperature was the most crucial factor influencing microbial regrowth in household tanks. The higher the temperature, the higher the bacterial regrowth in the stored water.

A recent study in Jordan (Al-Nawafleh & Al-Zboon, 2025) examined the management of household water tanks in Irbid Governorate. It was found that while most households use plastic tanks, a substantial proportion still use galvanized iron tanks. Nearly half of homes do not regularly clean their tanks, which is directly related to contaminant levels in the water. This high contaminant level highlights the importance of proper tank maintenance to ensure safe storage, particularly in the Jordanian context.

This study was conducted during October–December 2022 and aimed to assess the quality of water in household tanks through chemical, physical, and biological analyses. This is to determine whether the water is suitable for drinking or other uses. The study provides recommendations to relevant authorities to raise awareness of the importance of drinking water of suitable quality and to take appropriate measures. To achieve the study’s objectives, water samples were collected from household tanks in the Irbid area and assessed for suitability for drinking.

2. Methodology

2.1 The Study Area

The Study area encompasses Irbid governorate, situated in the northern part of Jordan, covering approximately 1572 km² and located at the geographical coordinates of 32° 33’ 20” N, 35° 51’ 0” E (Figure 1). The climate in Irbid is Mediterranean, with hot and dry summers, cold and rainy winters. During the summer, temperatures can reach up to 35 °C, while during the winter, temperatures drop to around 5 °C and sometimes even to 0 °C. As of 2023, the population of the Irbid Governorate has reached around 2,135,000, making it the second-largest governorate in Jordan by population after the Capital Governorate. The governorate is divided into nine districts, namely, Qasabah, AL-Ramtha, AL-Koorah, Bani Kenanah, Bani Obeid, Aghwar Shamaliyah, Mazar Shamali, AL-Wastiyyah, and AL-Taybeh (DOS, 2024).

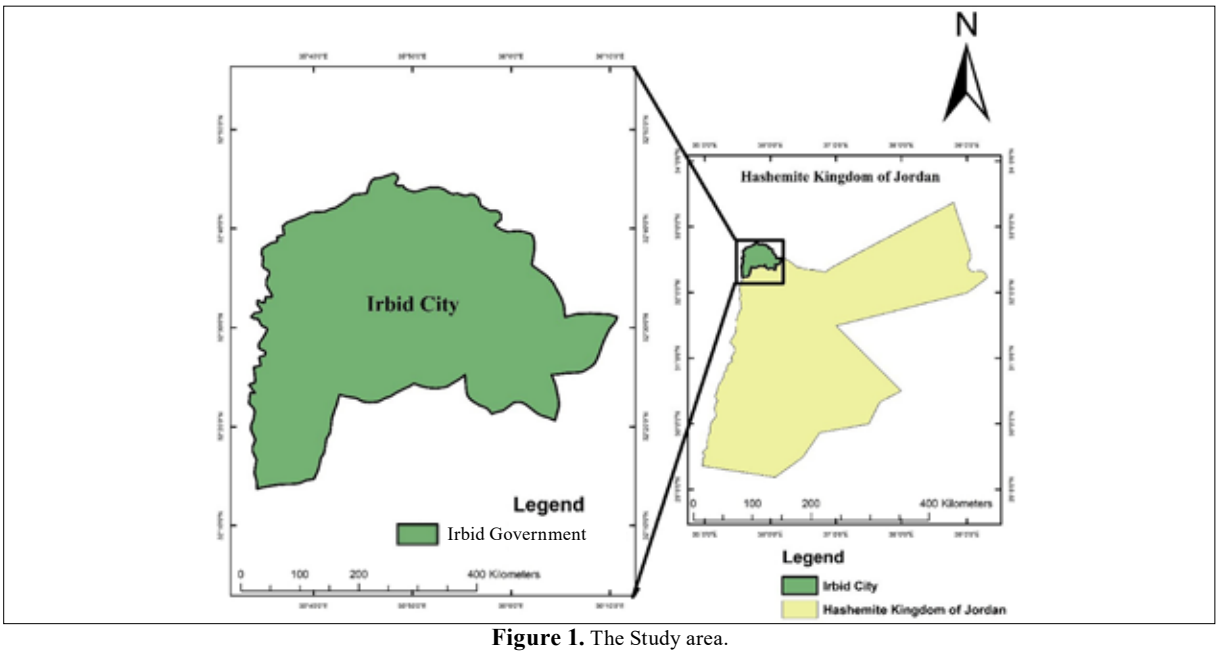

Figure 1. The Study area.

2.2 Water stress

Irbid District, the second-largest city in Jordan faces significant challenges related to water stress due to the influx of refugees from neighboring countries, which has intensified the demand for water in both urban and rural areas (UNHCR, 2021). Changes in precipitation patterns and rising temperatures, resulting from climate change, have also affected water availability, leading to prolonged droughts and reduced aquifer recharge rates (Bashabsheh and Alzboon, 2024). In this context, effective water management is crucial. The Yarmouk Water Company (YWC), responsible for water supply and wastewater management in Irbid and other northern governorates, plays a vital role in addressing these challenges through initiatives such as reducing leakage, ensuring water quality, promoting public awareness, and investing in modern technologies. YWC provided more than 96 million cubic meters of water in 2018 from surface and groundwater sources through more than 10,000km of the distribution networks (YWC, 2023).

2.3 Sampling

Twenty-two samples were collected from household water storage tanks between October 17, 2022 and December 11, 2022 from various locations in Irbid Governorate. The location of each sample was documented, using a global positioning system (GPS) device (Figure 2). All sampled tanks were supplied with water from the municipal network. For analysis, 2 liters of water were collected in two separate bottles: the first, with a capacity of 1.5 liters, was pre-sterilized for chemical and biological analysis at an environmental laboratory in Amman. The second bottle, with a capacity of 500 ml, was collected for analysis of turbidity, pH, electrical conductivity, dissolved solids, and alkalinity at the laboratory of Al-Balqa Applied University, Al-Huson College. All samples were placed in an ice box and analyzed within 12 hours.

Figure 2. Locations of samples.

2.4 Water Quality

This study aims to investigate water samples for physical parameters such as turbidity and electrical conductivity, and chemical parameters such as pH, hardness, TDS, alkalinity, Ca+2, Na+, PO4-2, Cl-, SO4-2, NO3-, K+, Mg+2, and biological parameters such as total coliform, E. Coli, and pseudomonas, then, to compare the results with the World Health Organization (WHO) standards and the Jordanian standard. Table 1 below shows the instruments used for measurement and the international and national standards.

Table 1. Physical, chemical, and biological water tests with the instruments used and the standards of JS and WHO.

Parameter	Instrument	WHO standard (WHO, 2022)	Jordanian standards (JS 286:2015)
EC	HI-98194 Multiparameter pH/ EC/ TDS	< 1200 µS/cm	< 700µS/cm
Turbidity	HI-93414 Turbidity & Free/Total Chlorine Meter	< 5 NTU	< 5 NTU
pH	HI-98194 Multiparameter pH/ EC/ TDS	6.5 - 8.5	6.5 - 8.5
Hardness	Titration with EDTA	< 600 mg/L as CaCO3	< 500 mg/L as CaCO3
TDS	HI-98194 Multiparameter pH/ EC/ TDS	< 1000 mg/L	1000 - 1300 mg/L
Alkalinity	Titration with strong H2SO4	< 200 mg/L as CaCO3	---------
Ca+2	930 Compact IC Flex	< 100 mg/L	75 – 200 mg/L
Mg+2	930 Compact IC Flex	< 50 mg/L	50 – 150 mg/L
Na+	930 Compact IC Flex	< 200 mg/L	200 – 300 mg/L
PO4-2	930 Compact IC Flex	< 0.1 mg/L	-----
SO4-2	930 Compact IC Flex	< 400 mg/L	< 500 mg/L
Cl-	930 Compact IC Flex	< 250 mg/L	200 – 500 mg/L
K+	930 Compact IC Flex	< 20 mg/L	< 12mg/L
NO3-	930 Compact IC Flex	< 50 mg/L	< 50 – 70 mg/L
Total coliform	Membrane filtration	0 MPN/100	< 1.1 MPN/100
E. Coli	Membrane filtration	0 MPN/100	< 1.1 MPN/100
pseudomonas	Membrane filtration	-------	-----

2.5 Water Quality Index (WQI)

Water Quality Index (WQI) is a numerical expression that shows the impact of various water quality parameters on the overall suitability of water for human consumption (Şener et al., 2021). WQI is a rating method that assesses how specific water quality parameters affect overall water quality. WQI indicates if water bodies pose a risk to different water uses. It is a single indicator of water quality that integrates collected

data based on weighted factors. By using WQI, we can use a single value as an indicator of water quality rather than examining tens of parameters.

WQI ranges from 0 to 100, classifying water quality as excellent, good, poor, very poor, or unfit for consumption (Nong et al., 2020). The WQI was proposed by Horton in 1965 to classify water quality based on the levels of measured physical, chemical, and biological indicators. These parameters may include temperature, pH, dissolved oxygen levels, turbidity, nutrients, heavy metals, and microbiological indicators (Akhtar et al., 2021). The Water Quality Index (WQI) is calculated using the Weighted Arithmetic Index method, as shown in the following equations (Bouslah et al., 2017).

$$WQI = \frac{\Sigma (Wn \times Qn)}{\Sigma Wn} \quad \text{(Equation \_2.1)}$$

$$Wn = \frac{K}{Sn} \quad \text{(Equation \_2.2)}$$

$$K = \left[\frac{1}{\Sigma\left(\frac{1}{Sn}\right)}\right] \quad \text{(Equation \_2.3)}$$

$$\boldsymbol{Qn = \left[\frac{(Vn - Vi)}{(Sn - Vi)}\right] \times 100} \quad \text{(Equation \_2.4)}$$

In equation 2.2, (Wn) represents the unit weight of water quality for a certain quality parameter. Sn is the standard permissible limit of the parameter (Table 1, Jordanian Standards), and K is a constant that can be determined from equation 2.3.

The constant K scales the unit weights appropriately, ensuring that the sum of all unit weights equals one.

In equation 2.4, Qn is the quality rating for a certain quality parameter, Vn is the estimated value of the certain quality parameter, and Vi is the ideal value of the parameter. The ideal (Vi0) value for drinking water is set to zero for all parameters except pH, which is set to 7.0 (Bouslah et al., 2017).

In this study, the Water Quality Index (WQI) will be determined based on fifteen parameters used in the analysis. These parameters include pH, Electrical Conductivity, Turbidity, Alkalinity, Hardness, Total Dissolved Solids, Calcium, Magnesium, Chloride, Sodium, Potassium, Nitrate, Phosphate, Sulfate, and Chloride. They have been selected as indicators for evaluating the overall water quality. Table 2 illustrates Water Quality Index (WQI) ranges, providing a way to interpret the overall water quality, based on the calculated WQI value.

Table 2. Water Quality Index (WQI) Classification (Brown et al., 1972).

WQI (Ranges)	water quality classification
0-25	Excellent
26-50	Good
51-75	Poor
76-100	Very poor
>100	Unfit for consumption

The ranges are typically divided into several categories, such as Excellent (WQI= 0-25) that signifies the high quality of water and safety for its various uses, including human consumption. Good category, (WQI= 26-50), indicates that the water may have minor deviations from ideal conditions for some parameters, but overall, it is still considered suitable for most purposes, including drinking. It suggests that the water is relatively clean and poses minimal health risks. Poor water quality, (WQI= 51-75), indicates that the water may have significant deviations from the desired standards for multiple parameters. It suggests that the water may require treatment or remediation before it can be used for certain purposes, particularly for human consumption. The presence of contaminants or pollutants may pose health risks. Very poor water quality, (WQI= 76-100), indicate that the water in this range exhibits substantial deviations from the desired standards for several parameters, indicating an elevated level of contamination or pollution. It implies that the water is unsuitable for most uses, including drinking, without extensive treatment or purification processes. Unfit for consumption (WQI>100): WQI values exceeding 100 indicate extremely poor water quality. Water falling within this range is unsuitable for consumption or most uses without thorough treatment (Horton, 1965).

3. Result and Discussion

3.1 Physical Parameters

Monitoring and managing the physical characteristics of water is essential to maintain its safety and suitability for various uses. The results obtained from analyzing the physical parameters of electrical conductivity (EC) and turbidity provide valuable insights into water quality) Figure 3(. There are many sources of turbidity in water tanks, such as air dust and bird waste in case of improper covering of the tanks. Also, the provided water may contain a significant level of turbidity. Turbidity is the cloudiness or haziness of water caused by particles such as sediment, organic matter, and microorganisms. High turbidity levels can reduce light penetration in water, affecting the disinfection process. Moreover, suspended particles can harbor harmful bacteria and viruses, making the water unsuitable for drinking (Hung et al., 2020). The maximum value of turbidity was 3.50 NTU in sample 13, and the minimum value (0.13 NTU) was found in samples 3 and 4, and the average turbidity was 0.88 NTU. All ‘samples’ values were within the permissible limit of 5 NTU according to both the WHO and Jordanian standards. Similarly, Luvhimbi et al. (2022) investigated the water quality of household containers and found that pH and EC ranged from 7.6 to 9.7 and from 19 to 903 µS/cm, respectively.

Electrical conductivity (EC) is a measure of a water sample’s ability to conduct an electrical current. It is an important indicator of dissolved salts and other ions in water, such as Ca, Mg, and Cl (Razman et al., 2022). Water can dissolve many inorganic and organic substances such as Na, K, Ca, Mg, SO4, and bicarbonates. These dissolved solids impart an undesirable color and taste to water. The figure below displays the data for 22 samples. Based on the present study, it has been determined that the electrical conductivity (EC) ranged from 536.0 µS/cm to866.0 µS/cm, with an average value of 707.8 µS/cm. The obtained results fall within the permissible limit of 1000µS/cm according to the (WHO). However, according to Jordanian standards, some values exceeded the allowable limit of 700µS/cm.

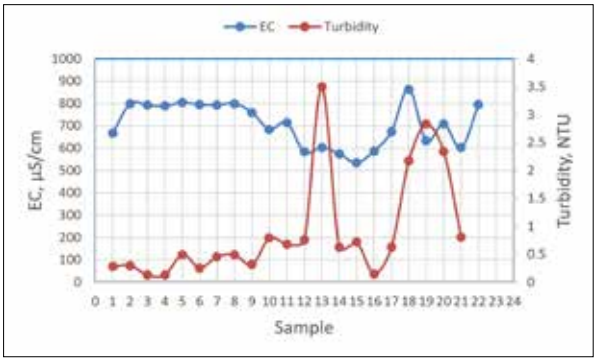

Figure 3. EC and Turbidity results for 22 samples.

3.2 Chemical parameters

Chemical quality refers to the concentration of different chemical substances in water. Assessment of the chemical composition is crucial because it greatly influences water suitability for drinking, industrial, and irrigation purposes. Many factors can affect the chemical composition of water, such as the type of roof material, tank cover, and storage method. Therefore, regular monitoring and assessment of the water's chemical quality are essential to ensure its safety and suitability for their intended uses. While most inorganic compounds are essential for human health and the formation of cells, organs, and tissues, elevated levels can cause adverse health effects. For example, Na is necessary to regulate fluid in the human body and to control muscle and nerve function; however, high levels of Na can cause high blood pressure and kidney and cardiovascular diseases (Luvhimbi et al., 2022). A low level of K is necessary for protein synthesis and carbohydrate metabolism; however, excessive levels can cause dangerous conditions such as cardiac arrest and reduced urine output (Ogoamaka and Osarumwense, 2022). Table 3 below illustrates the minimum, maximum, and average values for pH, hardness, Alkalinity, TDS, calcium, magnesium, nitrates, phosphates, sulfate, chloride, sodium, and potassium with the permissible limits for drinking water according to (WHO) and Jordanian standards.

Table 3. Results of chemical parameters for 22 samples.

Parameter	Min	Max	Average	WHO	JS
pH	7.3	8.3	7.7	6.5 - 8.5	6.5 - 8.5
Hardness	203.1	360	320.8	600 mg/L	500 mg/L
TDS	268	433	350	10000 mg/L	1000-1300 mg/L
Alkalinity	120	380	260.5	200 mg/L	-----
Ca+2	37.1	96.8	79.9	100 mg/L	75-200 mg/L
Mg+2	23.5	35.3	29.5	50 mg/L	50-120 mg/L
Na+	18.4	80.8	30.8	200 mg/L	200 – 300 mg/L
PO4	< 0.01	0.5	0.1	1 mg/L	-----
SO4-2	14.4	71.9	29.2	400 mg/L	500 mg/L
Cl-	37.3	133.9	56.2	250 mg/L	200 – 500 mg/L
K+	2.1	7.6	3.4	20 mg/L	12mg/L
NO3-	4.3	25.9	21.4	50 mg/L	50 – 70 mg/L

The pH values ranged from 7.3 to 8.3, with an average of 7.7. All values were within the allowable limits of WHO and Jordanian standards (6.5–8.5). For hardness, the maximum value was 360 mg/L, the minimum was 203.1 mg/L, and the average was 320.8 mg/L. All values were within the permissible limit according to WHO (600) and Jordanian standards (500). The TDS ranged from 268 mg/L to 433 mg/L, with an average of 350 mg/L, and all values were below the permissible limits for both standards. Water with a TDS level of more than 500 mg/L can cause many human health effects, such as gastrointestinal irritation (Ogoamaka and Osarumwense, 2022). The alkalinity was between a minimum value of 120 mg/L and a maximum value of 380 mg/L, with an average of 260 mg/L, where some values exceeded the permissible limit of WHO (200 mg/L).

The concentrations of magnesium and calcium were within the permissible limits of the WHO and Jordanian standards, with average concentrations of 79.9 mg/L and 29.5 mg/L for calcium and magnesium, respectively. The maximum concentrations reached 96.8 mg/L and 35.3 mg/L for both parameters. Excessive concentrations of Mg in drinking water result in osmotic diarrhea and laxative effects (Ogoamaka and Osarumwense, 2022). The sodium values were also within the permissible limits for both standards, with the highest value at 80.8 mg/L.

For SO4-2, Cl-, K+, and NO3-, the maximum values were lower than the permissible limits of the WHO and Jordanian standards, with max values of 71.9 mg/L, 133.9 mg/L, 7.6 mg/L, and 25.9 mg/L, respectively. A high level of Sulphate can cause cathartic or laxative effects on human health, while high concentration of NO3 causes blue baby syndrome, methemoglobinemia, and many health effects. The concentration of (PO4) ions in the water sample tested ranged from 0.01 mg/L to 0.5 mg/L, with an average concentration of 0.1 mg/L. It is worth noting that the maximum concentration of (PO4) was far below the permissible value set by the WHO, which is 1 mg/L. Overall, the results of chemical analyses were within the permissible limits set by the WHO and the Jordanian standard.

Luvhimbi et al. (2022) reported lower values of the chemical parameters in the water of household containers in South Africa, where the maximum values of Ca, K, Mg, and Na were 31.6, 1.8, 16.6, and 12.9 mg/l. The elevated levels of the chemical parameters in our study could be attributed to the longer storage period in the tank, which reaches 2 weeks during the summer season.

3.3 Biological Parameters

Household water tanks can be assessed based on several biological parameters, including the presence of microorganisms, such as bacteria, viruses, and parasites. The level of biological contamination in tap water is an essential aspect to monitor, as it can affect the quality and safety of the water supply. The present study measured total coliforms, E. coli, and pseudomonas. No contamination of E. coli was detected in the water storage tanks, as shown in Table 4. The investigation found that households' water storage tanks contained both Pseudomonas and total coliforms. Pseudomonas was found in 18 samples, 11 of which had concentrations greater than 100 CFU/100 ml, as shown in Table 4. This means the water in the storage tanks is unsafe to drink and must be cleaned before use.

Furthermore, some samples also contained total coliforms. Two of the samples had more than 100 CFU/100 mL, while 10 had less than 100 CFU/100 mL. However, it should be noted that both total coliform and Pseudomonas should be absent in drinking water according to the WHO guidelines. Luvhimbi et al., 2022, found that household storage tanks in Thulamela municipality, South Africa, contained high levels of total coliforms, with some samples exceeding 2000 MPN/100ml, whereas one sample showed a positive level of E. coli.

Table 4. Results of biological parameters for 22 samples

Sample	Total coliform	E. Coli	Pseudomonas
1	<1 CFU/100ml	<1 CFU/100ml	88 CFU/100ml
2	<1 CFU/100ml	<1 CFU/100ml	<1 CFU/100ml
3	<1 CFU/100ml	<1 CFU/100ml	5 CFU/100ml
4	<1 CFU/100ml	<1 CFU/100ml	5 CFU/100ml
5	<1 CFU/100ml	<1 CFU/100ml	40 CFU/100ml
6	<1 CFU/100ml	<1 CFU/100ml	< 1CFU/100ml
7	1 CFU/100ml	<1 CFU/100ml	262 CFU /100ml
8	<1 CFU/100ml	<1 CFU/100ml	2 CFU /100ml
9	<1 CFU/100ml	<1 CFU/100ml	33 CFU/100ml
10	<1 CFU/100ml	<1 CFU/100ml	8 CFU/100ml
11	13 CFU/100ml	<1 CFU/100ml	>100 CFU/100ml
12	19 CFU/100ml	<1 CFU/100ml	>100 CFU/100ml
13	>100 CFU/100ml	<1 CFU/100ml	>100 CFU/100ml
14	54 CFU/100ml	<1 CFU/100ml	>100 CFU/100ml
15	43 CFU/100ml	<1 CFU/100ml	>100 CFU/100ml
16	>100 CFU/100ml	<1 CFU/100ml	>100 CFU/100ml
17	49 CFU/100ml	<1 CFU/100ml	>100 CFU/100ml
18	44 CFU/100ml	<1 CFU/100ml	>100 CFU/100ml
19	33 CFU/100ml	<1 CFU/100ml	>100 CFU/100ml
20	49 CFU/100ml	<1 CFU/100ml	>100 CFU/100ml
21	14 CFU/100ml	<1 CFU/100ml	< 1 CFU/100ml
22	20 CFU/100ml	<1 CFU/100ml	10 CFU/100ml

3.4 Analysis of water quality index (WQI)

Table 5 illustrates the distribution of water quality index (WQI) values for 22 samples, along with their corresponding WQI categories. The WQI values ranged from 6.36 to 47.62, and the categories assigned are "Excellent" and "Good". Figure 4 shows that most of the water samples (86%) are classified as "Excellent", indicating a high level of water quality. A smaller proportion of samples (14%) fall within the "Good" range, still indicating satisfactory water quality. Notably, there are no samples classified as "poor," "Very poor," or "Unfit for consumption." In summary, the table provides an overview of the distribution of water quality in the given dataset. While most samples exhibit excellent water quality, there is still a need for improvement to address the smaller proportion of samples categorized as good. By focusing on pollution prevention, implementing effective water treatment measures, and adopting sustainable management practices, it is possible to ensure clean, safe, and reliable water for both human consumption and environmental sustainability.

Table 5. Water Quality Index (WQI) Analysis for 22 Samples

Samples	WQI value	WQI category
1	6.36	Excellent
2	7.55	Excellent
3	7.21	Excellent
4	7.09	Excellent
5	8.72	Excellent
6	7.29	Excellent
7	7.99	Excellent
8	7.05	Excellent
9	7.64	Excellent
10	10.26	Excellent
11	32.26	Good
12	18.32	Excellent
13	25.42	Excellent
14	18.48	Excellent
15	17.27	Excellent
16	20.91	Excellent
17	16.65	Excellent
18	20.04	Excellent
19	23.15	Excellent
20	20.62	Excellent
21	47.62	Good
22	42.69	Good

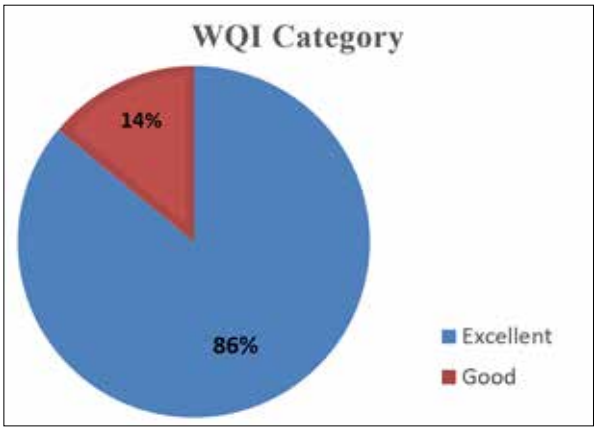

Figure 4. Percentage Distribution of Water Quality Status

4. Conclusion

Household water tanks are a common practice for water storage in developing urban regions, providing a dependable, uninterrupted water supply for households. The study of physical, chemical, and biological parameters of household water tanks in Jordan reveals critical insights into water quality. While electrical conductivity (EC) and turbidity levels are mostly within acceptable limits, some samples exhibit elevated turbidity due to sediment. Chemical analyses indicate that most parameters, including pH, hardness, TDS, and ion concentrations, comply with WHO and Jordanian standards, with occasional exceedances in alkalinity. Biological assessments highlight the presence of pseudomonas and total coliforms in several samples, underscoring the need for regular disinfection and maintenance. The Water Quality Index (WQI) classifies most samples as "Excellent," with a smaller fraction as "Good," emphasizing the overall high water quality but also the need for continuous monitoring and improvement to ensure safe, reliable drinking water.

Acknowledgement

The research reported in this publication was funded by the Deanship of Scientific Research and Innovation at Al-Balqa Applied University in Jordan under the Award Number DSR-2022#469

References

Akhtar, N., Ishak, M. I. S., Ahmad, M. I., Umar, K., Md Yusuff, M. S., Anees, M. T., and Ali Almanasir, Y. K. (2021). Modification of the water quality index (WQI) process for simple calculation using the multi-criteria decision-making (MCDM) method: a review. Water, 13(7), 905-915.

Al-Kharabsheh Noor M. and Al-Zboon Kamel K., 2021, Wastewater treatment and reuse in Jordan, 10 years of development, Desalination and Water Treatment, Volume 238, 2021, Pages 15-27.

Al-Nawafleh, T. R., & Al-Zboon, K. K. (2025). Management of household water tanks in Irbid Governorate of Jordan. Jordanian Journal of Engineering and Chemical Industries, 8(1), 28–35.

Al-Ghanim, K. A., Abd El-Salam, M. M., and Mahboob, S. (2014). Assessment of water quality for some roof tanks in Alkharj Governorate, KSA. Pak. J. Zool, 46(4), 1003-1012

Bashabsheh, A.Q., Alzboon, K.K. Impact of climate change on water resources in the Yarmouk River Basin of Jordan. J. Arid Land 16, 1633–1647 (2024). https://doi.org/10.1007/s40333-024-0069-0.

Bouslah, S., Djemili, L., and Houichi, L. (2017). Water quality index assessment of Koudiat Medouar Reservoir, northeast Algeria using Weighted Arithmetic Index Method. Journal of Water and Land Development, 35(1), 221–228.

Brown, R. M., McClelland, N. I., Deininger, R. A., and O'Connor, M. F. (1972). A water quality index—crashing the psychological barrier. In Indicators of Environmental Quality: Proceedings of a symposium held during the American Association for the Advancement of Science (AAAS) in Philadelphia, Pennsylvania, December (26) 31 173-182.

Constantine, K., Massoud, M., Alameddine, I., and El-Fadel, M. (2017). The role of the water tankers market in water stressed semi-arid urban areas: Implications on water quality and economic burden. Journal of Environmental Management, 188(2), 85-94.

Department of Statistics (DOS) (2024). Department of Statistics Estimated Population of the Governorate, Locality, Gender, and Household. Amman, Jordan.https://dosweb.dos.gov.jo/DataBank/Population/Population_Estimares/PopulationEstimates.pdf

Evison, L., and Sunna, N. (2001). Microbial regrowth in household water storage tanks. Journal-American Water Works Association, 93(9), 85-94.

Horton, R. K. (1965). An index number system for rating water quality. J Water Pollut Control Fed, 37(3), 300-306.

Hung, D. T., Thi Cuc, V., Thi Bich Phuong, V., Thi Thanh Diu, D., Thi Huyen Trang, N., Phuong Thoa, ... & Van Long, N. (2020). Evaluation of drinking water quality in schools in a district area in Hanoi, Vietnam. Environmental Health Insights, 14, 1178630220959672.

JSMO. Jordan Standards and Metrology Organization: Standard Specification """"Water-Drinking Water" "","" No. 286/2015. Jordan; 2015.

Kirmeyer, G. J. Kirby, L. Murphy, B. M. Noran, P. F. Martel, K. Lund, T. W. Anderson, J. L. MMedhurst, R. 1999, Maintaining Water Quality in Finished Water Storage Facilities. American Water Works Association Research Foundation and American Water Works Association, Denver, CO, USA.

Luvhimbi, N., Tshitangano, T.G., Mabunda, J.T. et al. Water quality assessment and evaluation of human health risk of drinking water from source to point of use at Thulamela municipality, Limpopo Province. Sci Rep 12, 6059 (2022). https://doi.org/10.1038/s41598-022-10092-4

Malkawi, S., (2005), 'Current reclaimed water uses in Jordan: Strategies, policies and 'standards', The Second Water Reuse Conference, June 6–9, 2005, Amman, Jordan.

Nong, X., Shao, D., Zhong, H., and Liang, J. (2020). Evaluation of water quality in the South-to-North Water Diversion Project of China using the water quality index (WQI) method. Water research, 178(1), 115-126.

Ogbozige, F. J., Ibrahim, F. B., and Adie, D. B. (2018). Effect of storage time and container material on potable water quality. Ife Journal of Science and Technology, 1(2), 59-71.

Ogoamaka Ezugwu and Osarumwense Akhimien, 2022, Review of the Effects of Water Characteristics and Quality on Human Health, International Journal of Current Science Research and Review, V5(3), 673-685.

Razman, N. A., Wan Ismail, W. Z., Abd Razak, M. H., Ismail, I., & Jamaludin, J. (2023). Design and analysis of water quality monitoring and filtration system for different types of water in Malaysia. International Journal of Environmental Science and Technology, 20(4), 3789-3800.

Salehi, M. (2022). Global water shortage and potable water safety; ' 'Today's concern and ' 'tomorrow's crisis. Environment International, 158(4), 106-115.

Schafer, C. A., and Mihelcic, J. R. (2012). Effect of storage tank material and maintenance on household water quality. Journal-American Water Works Association, 104(9), 521-529.

Şener, Ş., Varol, S., and Şener, E. (2021). Evaluation of sustainable groundwater utilization using index methods (WQI and IWQI), multivariate analysis, and GIS: the case of Akşehir District (Konya/Turkey). Environmental Science and Pollution Research, 28(35), 47991-48010.

UNICEF. (2022). Water, sanitation, and hygiene. Retrieved from www.unicef.org website: https://www.unicef.org/jordan/water-sanitation-and-hygiene

United Nations High Commissioner for Refugees (UNHCR). (2021). The Impact of Syrian Refugees on Jordan's Water Resources and Water Management Planning. Retrieved from UNHCR.

USAID. (2023, November 9). Water Resources & Environment | Jordan | U.S. Agency for International Development. Retrieved from www.usaid.gov website: https://www.usaid.gov/jordan/water-resources-environment.

World Health Organization WHO. (2022). Guidelines for drinking-water quality: Fourth edition incorporating the first and

second addenda. World Health Organization, 20 Avenue Appia, 1211 Geneva 27, Switzerland.

YWC, Yarmouk Water Company. (2023). Annual Reports and Publications. Retrieved from the Yarmouk Water Company website.

JJEES

JJEES (2026) 17 (2): 207-215
ISSN 1995-6681

Jordan Journal of Earth and Environmental Sciences

Tracking the temperature of Tharthar Lake and its effect on monthly evaporation using Landsat 8 images for the period (2022-2024)

K. A. Al-Qayyssi [1*], Ammar Y. Awad [1], Ahmed M. El kenawy[2]

[1]Department of Geography, College of Education for Humanities, University Of Anbar
[2]Instituto Pirenaico de Ecología, IPE-CSIC. Zaragoza, Spain

Received on 14 May 2025; Accepted on 17 November 2025

Abstract

Water is the basis of life and a key component of various economic activities upon which humans depend. Lakes are an important reservoir of freshwater worldwide, particularly in arid and semi-arid countries such as Iraq. One of the most significant challenges associated with water storage in Iraq is the substantial loss due to evaporation, estimated at 9 billion cubic meters annually. Hence, this study aims to estimate evaporation from Tharthar Lake, Iraq's largest water reservoir, with a capacity of approximately 85 billion cubic meters. Analysis of the L' 'Lake's imagery revealed relative variability in surface area, ranging from 1509.79 to 1574.59 km², primarily due to fluctuations in water inflow and outflow. Shallow areas showed greater thermal responsiveness, while deeper regions remained more thermally stable. The results indicated that monthly evaporation varied significantly, from a minimum of 90.45 mm in January to a maximum of 422.85 mm in August. Overall, the findings confirm that Tharthar Lake is highly influenced by ' 'Iraq's climatic regime, which is witnessing a steady annual increase in temperature. Overall, the use of thermal infrared sensors (TIRS) on Landsat 8 satellites is more effective than ground-based stations for monitoring lake surface temperatures across large temporal and spatial scales. This remote sensing approach enhances reliability while reducing both time and labor requirements.

Keywords: *Evaporation, water temperature, Tharthar Lake, arid environments, Iraq.*

1. Introduction

Lakes and reservoirs play a critical role in storing and regulating freshwater supplies, particularly in arid and semi-arid regions. These water bodies store 87-88% of Earth's liquid surface freshwater (Yao et al., 2020; Hirji & Duda, 2024), providing essential services such as water supply, food security, and climate resilience (Hirji & Duda, 2024). However, many lakes face threats from salinization, water diversion, pollution, and climate change (Williams, 1999; Williams, 2002). Recent studies reveal widespread declines in global lake water storage, attributed to climate warming, increased evaporation, and human water consumption (Yao et al., 2023; Zhao et al., 2024). These changes impact water availability, biodiversity, and ecosystem functions (Williams, 1999). Effective management of lakes requires integrated approaches that consider water quality, quantity, and basin-wide factors (Parparov & Hambright, 1996). Lakes also serve as sentinels and regulators of climate change, providing valuable data on environmental shifts (Williamson et al., 2009).

Iraq faces significant water resource challenges due to its arid climate, characterized by high temperatures and limited rainfall (Al-Maliki et al., 2022; Ali et al., 2024). The country has constructed large-scale water storage infrastructure, including dams and reservoirs, to meet agricultural, domestic, and industrial demands (Hamid et al., 2024). However, climate change is exacerbating water scarcity, with predictions of decreased precipitation, increased evapotranspiration, and potential drying of major rivers by 2040 (Al-Ansari, 2013; Al-Maliki et al., 2022). Studies have shown significant reductions in climatic water availability and increases in crop water demand across most of Iraq (Salman et al., 2020). These challenges are further compounded by population growth, urbanization, and inefficient water use (Ali et al., 2024). To address these issues, Iraq requires a strategic water management vision, including regional cooperation, improved agricultural practices, and investments in research and development (Al-Ansari, 2013).

The Iraqi government launched the Tharthar Dam Project in 1956 as one of the country's most important hydrological initiatives. The project was designed primarily for flood mitigation and water storage, diverting excess water from the Tigris River through the Samarra Dam Regulator into Tharthar Lake, and subsequently releasing it back into the Tigris and Euphrates Rivers via the Dividing Regulator. It involves developing natural depressions as reservoirs, along with constructing barrages, regulators, and dykes to control and manage water flow. To enhance operational efficiency, an expert system was developed for managing the Tharthar Lake system under varying hydrological conditions. As a result, the project plays a critical role in ' 'Iraq's water resource management strategy and its efforts to mitigate flood risks. Beyond its hydrological function, Tharthar Lake

* Corresponding author e-mail: kamal_algayssi@uoanbar.edu.iq

offers multiple socio-economic and environmental benefits, including irrigation of vast tracts of agricultural land, aquaculture development, tourism, groundwater recharge, and climate moderation.

Given the strategic importance of Tharthar Lake, the efficient monitoring and management of its water resources are essential, especially amid increasing climatic stress. One effective method for assessing changes in water temperature and evaporation is the use of remote sensing technologies—particularly Land Surface Temperature (LST) measurements derived from the Thermal Infrared Sensor (TIRS). TIRS detects infrared radiation through the thermal Bands 10 and 11 on the Landsat 8 and 9 satellites, providing high-resolution data that are crucial for hydrological and environmental research (Yang et al., 2020؛Aya,2025). The advancement of satellite technologies—with improved spatial resolution, shorter revisit times, and broader coverage—has significantly enhanced our understanding of energy and moisture exchanges between Earth's surface and the atmosphere (Oroud, 2019; Ahmed, 2022). These capabilities are especially valuable for estimating evaporation from water bodies by accurately capturing surface temperature data.

This study aims to assess seasonal and interannual variations in Land Surface Temperature (LST) over Tharthar Lake using data from the Thermal Infrared Sensor (TIRS) on Landsat 8 and 9, and to estimate corresponding evaporation rates under varying climatic conditions. It seeks to evaluate the impact of rising temperatures—driven by climate change—on surface water dynamics, with a particular focus on evaporation losses from the Lake. By analyzing spatial temperature patterns and thermal variability across the Lake's surface, the research identifies factors influencing heat distribution and water loss.

2- Study Area

The study area is situated within the Iraqi Al-Jazeera Plateau, spanning the administrative boundaries of Salah al-Din and Anbar Governorates (Figure 1). Geographically, it lies between longitudes 42°59′ to 43°42′ E and latitudes 33°39′ to 34°36′ N. Tharthar Lake, the largest freshwater lake in Iraq, is located between the Tigris and Euphrates rivers. It has a maximum storage capacity of approximately 85 billion cubic meters, with a water surface elevation of 65 meters above sea level and a surface area of 2,710 km² at full capacity. The dead storage volume is about 35.45 billion cubic meters, with a water level of 40 meters above sea level and a corresponding surface area of 1,589.17 km². The Lake serves as a vital flood control reservoir, storing excess water to protect cities along the Euphrates River. It also plays a critical role in the national water distribution system by regulating flows to both the Tigris and Euphrates rivers. The region experiences a semi-arid climate with extreme seasonal temperatures—averaging around 36°C in summer and dropping to 7°C in winter. According to ' 'Thornthwaite's drought index, the region's aridity coefficient ranges between 4.7 and 8.2 (Awwad & Remal , 2021؛ Al-Fahdawi et al,2022). Long-term precipitation data over 50 years show a declining trend, with a rate of -0.885 mm/year (Muslih, 2022؛ Oroud Altubeiri,2023 ؛Al-Timimi, et al,2024). Topographically, the basin features a notable elevation range, from 1,371 meters above sea level in the northern areas down to approximately 60 meters in the south, yielding a vertical relief of 1,311 meters. The total area of the lake basin is estimated at 32,237.93 km² (Figure 2).

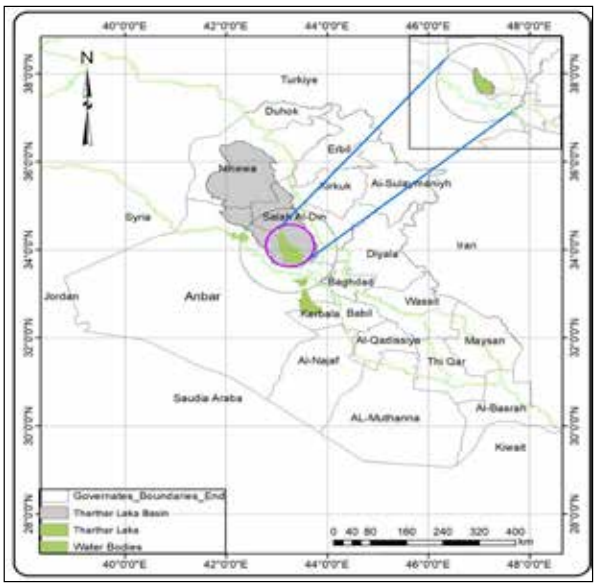

Figure 1. Location of the study area.

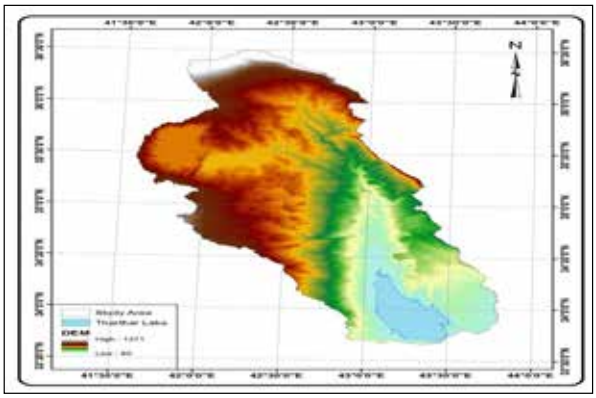

Figure 2. Topography of the study area.

3. Methods

Given the spatial and temporal variability of temperature across the Tharthar Lake region—and the limited availability of nearby meteorological stations—this study employed remote sensing techniques to monitor surface temperature and estimate evaporation rates. These spatial methods offer a reliable means of generating a geospatial database for water resource management in Iraq. By analyzing satellite-derived temperature and surface water extent over two hydrological years (October 2022–September 2024), the study aimed to develop scientific models that represent the L' 'Lake's dynamic thermal and hydrological behavior.

Two primary datasets were used. Landsat 8 Operational Land Imager (OLI) and Thermal Infrared Sensor (TIRS) images were obtained from the United States Geological Survey (USGS) database. A total of 24 images (one per month) were selected, each with a spatial resolution of 30 × 30 meters. In addition, hydrological records, including monthly inflow and outflow volumes, were sourced from relevant Iraqi governmental authorities. As the study area spanned

multiple Landsat scenes, mosaicking was performed using ArcGIS to unify the scenes into a single composite image.

The Normalized Difference Water Index (NDWI) was used to extract the Lake's surface area for each month. NDWI exploits the high reflectivity of water in the green band and its low reflectivity in the near-infrared (NIR) band:NDWI equation:(Jassim, 2017)

$$NDWI = \frac{Green - NIR}{Green + NIR}$$

Values closer to +1 indicate water bodies, while values near or below zero indicate land features such as vegetation or urban areas. NDWI was applied to each image to delineate the Lake's boundary and calculate its surface area monthly.

Monthly water levels and volumes were extracted from satellite images and cross-referenced with topographic maps of the Tharthar Lake basin. This enabled the estimation of water volume and elevation changes over the study period. To assess surface temperature dynamics, the thermal Band 10 from Landsat 8 was used following a multi-step procedure:

- Digital numbers (DN) from Band 10 were converted to spectral radiance using the following equation (Sajib et al., 2020): as Equation

$$L\lambda = ML \times Qcal + AL$$

where:

• LλL_{\lambda}Lλ = Spectral radiance (W/m²·sr·µm)

• ML=0.0003342M_L = 0.0003342ML=0.0003342, AL=0.1A_L=0.1AL=0.1 (band-specific calibration constants)

• QcalQ_{cal}Qcal = Band 10 DN value

- Radiance values were converted to Top-of-Atmosphere Brightness Temperature using (Allen et al., 2007), as Equation

$$TB = \frac{K2}{Ln} \times \frac{K1}{L\lambda + 1} - 273.15$$

Where:

• K1=774.8853K_1=774.8853K1=774.8853,K2=1321.0789K_2=1321.0789K2=1321.0789 (thermal conversion constants)

• TBT_BTB = Temperature in °C

- Emissivity was calculated using vegetation proportion derived from NDVI values as follows Equation (Al-Qayyssi,et al,.2024؛Yasir, et al., 2020)

$$Pv = square\frac{NDVI - NDVI\,min}{NDVI\,max - NDVI\,min}$$

Where:

• PvP_vPv = Proportion of vegetation

• ε\varepsilonε = Surface emissivity

- The Land Surface Temperature (LST) was computed using the formula (Ebtihal Taki et al., 2023):Equation

$$LST = \frac{TB}{1 + \lambda \times TB \div \rho} \times ln(\varepsilon)$$

Where:

• λ\lambdaλ = Central wavelength (11.5 µm for Band 10)

• ρ=14380\rho = 14380ρ=14380 (' 'Planck's constant constant)

• ε\varepsilonε = Land surface emissivity

- Monthly evaporation rates were estimated based on the extracted LST values using empirical relationships. In addition, water losses were computed using the Langer method, which accounts for local climatic conditions and surface area to determine evaporation losses over time.

4. Results and Discussion

The satellite-derived surface temperature data from Tharthar Lake over the two-year study period (October 2022 to September 2024) reveal pronounced seasonal and spatial thermal variability consistent with the characteristics of semi-arid continental climates. The observed peak surface temperatures of 33.8°C in July 2023 and 34.8°C in August 2024 are indicative of strong solar insolation and atmospheric conditions such as clear skies and low-pressure dominance during summer months. These findings align with previous studies in similar climatic regions, where solar radiation and prolonged daylight hours are key drivers of elevated lake surface temperatures (Kumar, R.,2018). Conversely, the lowest temperatures of 9.6°C and 8.7°C during January reflect typical winter cooling, influenced by the Siberian high-pressure system and Mediterranean depressions, which is consistent with known regional climatology (e.g., Al-Ansari et al., 2013).

The seasonal temperature amplitude exceeding 25°C plays a pivotal role in shaping the hydrological regime of Tharthar Lake, primarily by modulating evaporation rates. This strong thermal dynamic is critical because evaporation is the dominant form of water loss in such closed basins. The spatial temperature gradients further highlight the thermal heterogeneity of the Lake, with warmer, shallower southern and southwestern edges responding rapidly to seasonal warming, while deeper central regions maintain greater thermal inertia and stability due to water column mixing and depth effects (Salman,2020). This spatial variability in temperature not only affects evaporation but may also influence stratification, nutrient cycling, and aquatic habitat quality, underscoring the need to incorporate spatial heterogeneity in future hydrodynamic and ecological models of the Lake.

The observed seasonal fluctuations in lake surface area, with a notable increase in variability during the 2023–2024 water year, suggest an intensification of climatic influences, particularly evaporation and inflow variability. The larger seasonal shrinkage in surface area (83.48 km² difference) relative to the previous year reflects heightened sensitivity to changing meteorological conditions. Such patterns have been documented in other endorheic lakes worldwide, where seasonal evaporation and precipitation fluctuations drive dynamic surface area changes (Yang et al., 2020). The fact that surface area closely follows temperature and evaporation trends further validates surface temperature as a proxy for hydrological stress in the Lake.

Water level measurements indicate relatively stable but slightly declining trends, reflecting a balance between inflows, evaporation, and water management practices. The stabilization of levels between 38.1 and 38.4 m during 2023–2024 suggests

active management interventions aimed at maintaining lake volume, which is essential for sustaining local water supply and ecological functions. Such anthropogenic regulation is a common response to water scarcity in arid environments, but must be balanced against long-term sustainability given increasing climate variability.

Evaporation estimates derived from the Langer equation are consistent with temperature trends and demonstrate a clear increase in evaporative losses from one year to the next. The peak monthly evaporation rates above 400 mm in summer months, alongside total annual evaporation exceeding 2600 mm, emphasize the L' 'Lake's vulnerability to thermal stress and the resultant water loss. This increment of 56.47 mm in annual evaporation between the two years may appear modest but is significant given the cumulative impact on the L' 'Lake's water balance over time. Elevated evaporation rates during periods of low inflow magnify drought risk and can precipitate rapid lake level declines, negatively affecting water availability for agricultural, industrial, and domestic uses.

The pronounced thermal gradients and increasing evaporation underscore Tharthar ' 'Lake's sensitivity to climate change and highlight the importance of adaptive management strategies. The discussion of mitigation approaches such as surface covers (Rezazadeh et al., 2020) and windbreak plantations is highly relevant. These strategies have demonstrated effectiveness in reducing evaporation by creating physical barriers or altering microclimatic conditions, thereby conserving precious water resources in arid and semi-arid zones.

Rainfall variability, with a trend toward reduced and delayed precipitation, compounds the lake's hydrological challenges. The shift in rainfall timing and amounts disrupts the traditional hydrological regime, reducing the effectiveness of winter and early spring replenishment, which has been documented in other Middle Eastern basins affected by climate change(Al-Ansari et al., 2018). The combination of decreased rainfall and increased evaporation promotes hydrological drought and accelerates desertification processes, reinforcing the need for integrated water resource management that incorporates climate adaptation measures and sustainable water use policies.

Overall, while this study provides valuable insights, several limitations warrant consideration. Monthly satellite observations may miss shorter-term temperature and water-level fluctuations driven by episodic weather events, which could influence evaporation dynamics. Also, although satellite data are effective for large-scale monitoring, limited ground-truthing of temperature, evaporation, and water-level data may introduce inaccuracies. In addition, the Langer equation, while practical, is a simplified approach that may not capture all physical processes influencing evaporation, such as wind speed variability, humidity gradients, or lake surface roughness.

Albeit with these limitations, the study significantly advances understanding of climate-lake interactions in the Tharthar Basin and offers several implications. The identification of temperature and evaporation as key drivers of lake dynamics supports prioritizing thermal monitoring in future water resource plans and drought mitigation strategies. Also, highlighting increasing evaporation trends and rainfall shifts informs climate adaptation policies, emphasizing the need for diversified water supply and demand management. The findings provide scientific evidence for policymakers to enforce sustainable lake management and coordinate regional efforts to address climate-induced water scarcity. Overall, the study establishes a baseline for ongoing remote sensing monitoring and more detailed modeling of hydrological and ecological processes in arid lake systems.

Table 1. Water levels(m), surface area (km^2), and average temperature (°C) for the months covered by the study.

No	Date Of Capture	Visual Water Level Rise Start And End Of Month (M)	Water Volume InsideLake /Billion M3	Calculated Area From Satellite Visuals/Km2	Average Water Surface Temperature For Each Month
1	15/10/2022	39.22	35.22	1574.59	26.2
2	15/11/2022			1568.53	19.3
3	25/12/2022			1566.48	15.6
4	18/1/2023			1566.19	9.6
5	19/2/2023			1564.82	11.1
6	23/3/2023			1560.73	15.4
7	16/4/2023			1559.4	13.4
8	10/5/2023			1574.56	24.4
9	19/6/2023			1566.47	20.6
10	13/7/2023			1554.17	33.8
11	14/8/2023			1540.73	32.5
12	15/9/2023	38.4	33.19	1529.84	28.9
13	17/10/2023	38.1	32.69	1522.35	24.2
14	18/11/2023			1513.76	18.4
15	4/12/2023			1509.79	15.2
16	5/1/2024			1509.73	8.7
17	22/2/2024			1510.92	10.9
18	10/3/2024			1509.94	11.7
19	2/4/2024			1559.41	15.5
20	28/5/2024			1593.21	26.4
21	13/6/2024			1566.47	31.5
22	15/7/2024			1554.17	32.7
23	16/8/2024			1540.73	34.8
24	17/9/2024	38.4	33.18	1529.84	26.9

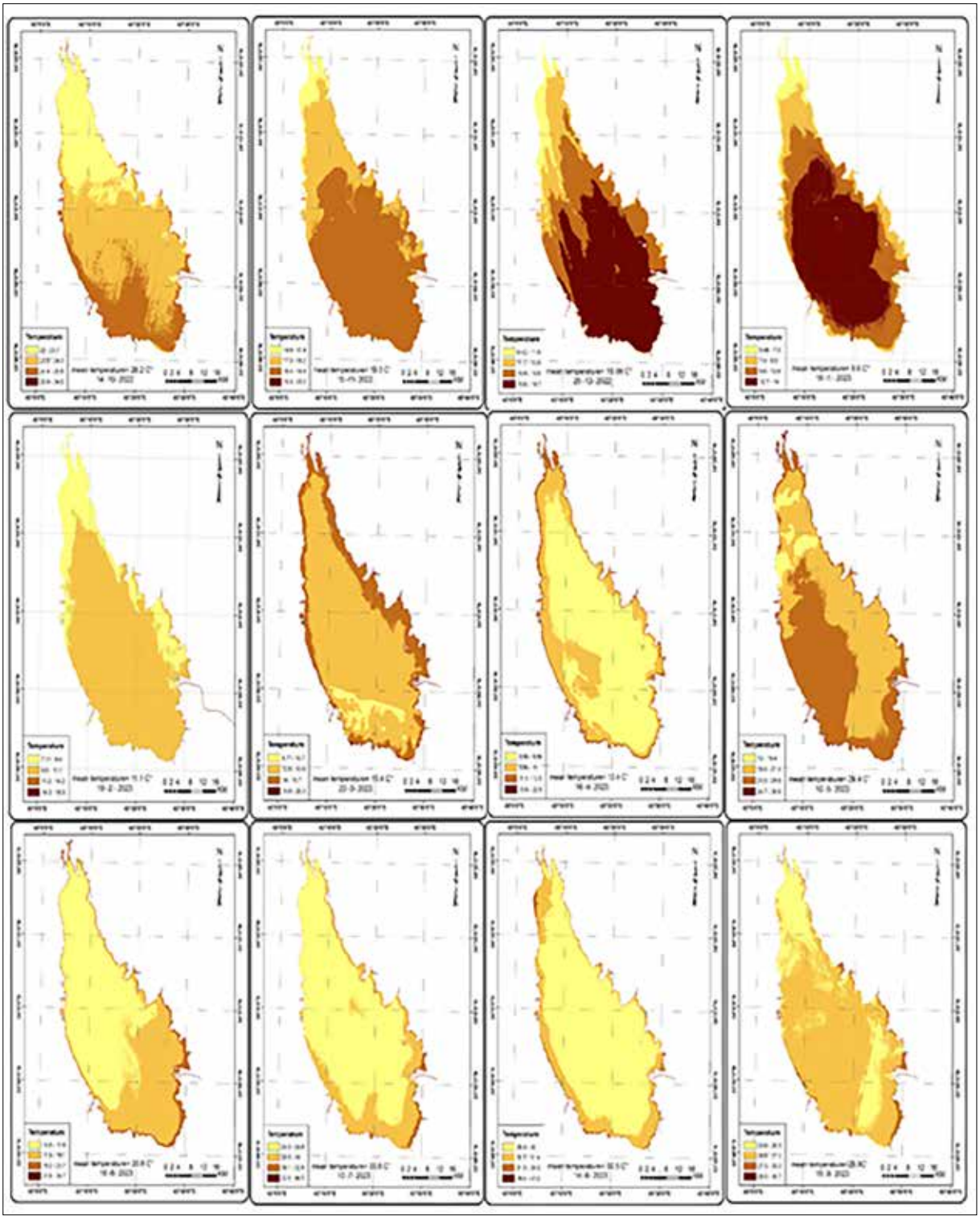

Figure 1. Variation of lake surface temperature for the period 2022-2024

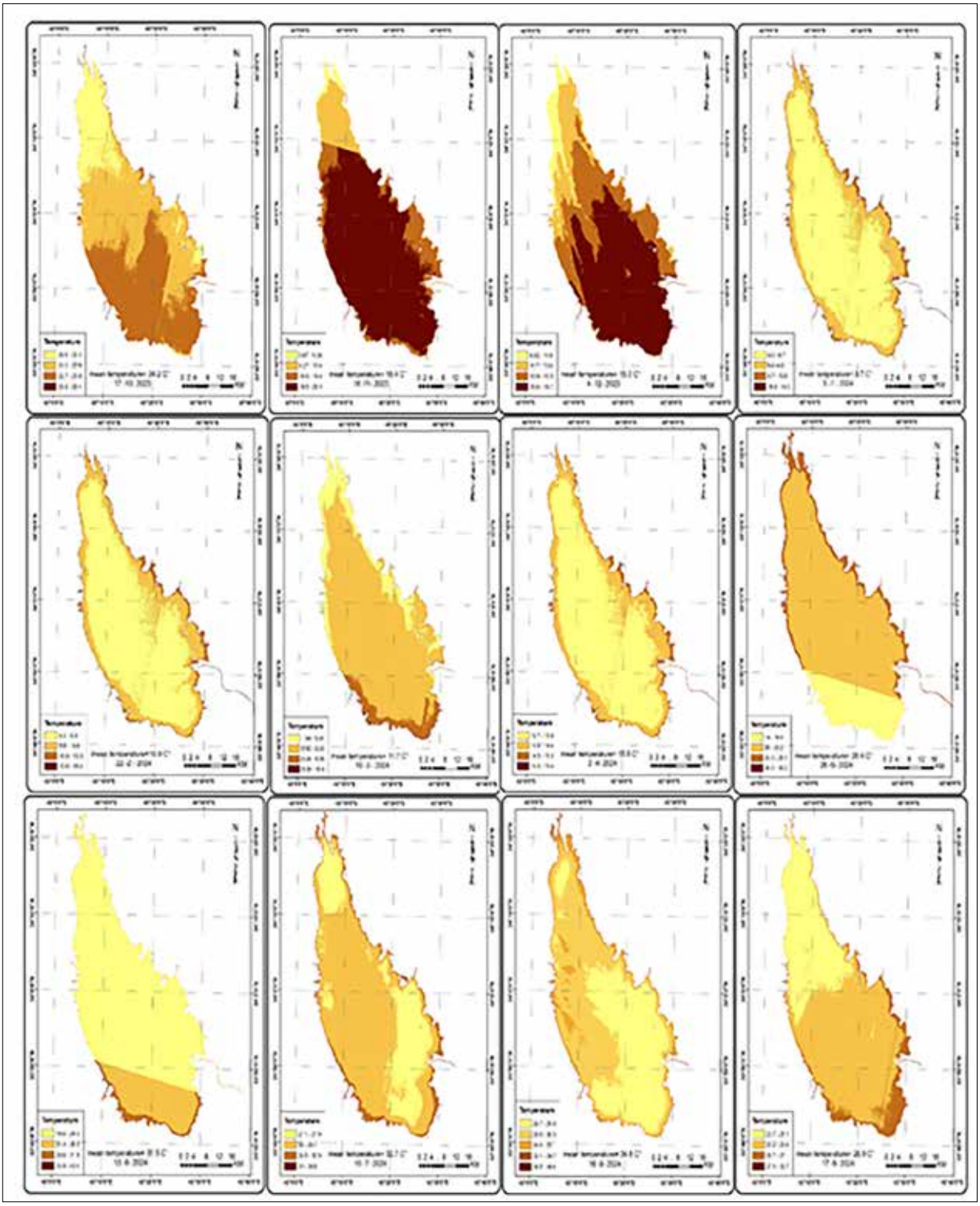

Continuing from Figure 1. Variation of lake surface temperature for the period 2022-2024

4 - Calculating evaporation using the Langer equation (simplified by Penman):

E = (700*(T+0.006h)/(100-A)+15(T-Td))/(80-T) (T-Td)= 0.0023h + 0.37 T + 0.53R+0.35Rann – 10.9

Where:

E = evaporation rate from the water surface (mm/day)

T = average temperature (°C)

Td = average dew point temperature (°C)

A = latitude (34)

h = elevation above sea level (45m)

R = monthly average daily temperature range (14.05 om)

Rann = average temperature of the warmest and coldest months (23.2) (Hassan, 2013)

The final monthly evaporation values were calculated using the Langer equation for the 2022-2023 hydrological year, as shown in Table 2. The highest calculated monthly evaporation values, 402.9 mm, were recorded during July due to the highest temperatures, while the lowest evaporation value, 123.7 mm, was recorded during January due to the lowest temperatures. In the 2023-2024 hydrological year, the highest total monthly evaporation value, 422.8 mm, was recorded during August, while the lowest monthly evaporation value, 90.4 mm, was recorded during February.

In addition, integrative analyzes between remote sensing data and hydrological modeling indicate that Lake Tharthar shows an increasing response to short- and long-term climate fluctuations, making it a sensitive system to any change in energy or water inputs. Determining the quantitative relationship between temperature change, evaporation rates, and changes in surface area provides a scientific basis for estimating early warning indicators of drought. These results also confirm the necessity of developing high-accuracy predictive models based on thermal and temporal data to improve water resources management and enhance the resilience of the ‘ ‘lake’s ecosystem in the face of accelerating climate change.

Table 2. Calculating monthly and annual evaporation using the Langer equation for the 2022-2023 hydrological year

Langer	Temp 0 C	T-Td	EVAP.mm/day	Evap.mm/month
Oct	26.2	14.46	9.25	277.53
Nov	19.3	11.91	6.32	189.47
Dec	15.06	10.34	4.89	146.78
Jan	9.6	8.32	3.26	97.80
Feb	11.1	8.88	3.68	110.48
Mar	15.4	10.47	5.00	150.10
Apr	13.4	9.73	4.37	131.04
May	24.4	13.80	8.43	252.85
Jun	20.6	12.39	6.86	205.67
Jul	33.8	17.28	13.43	402.91
Aug	32.5	16.82	12.63	378.90
Sep	28.9	15.46	10.59	317.80
Total				2661.35

Table 3. Calculating monthly and annual evaporation using the Langer equation for the 2023-2024 hydrological year

Langer	Temp 0 C	T-Td	EVAP.mm/day	Evap.mm/month
Oct	24.2	6.28	6.34	190.16
Nov	18.4	11.58	5.99	179.62
Dec	15.2	10.39	4.94	148.14
Jan	8.7	7.99	3.02	90.45
Feb	10.9	8.80	3.63	108.76
Mar	11.7	9.10	3.86	115.71
Apr	15.5	10.51	5.04	151.08
May	26.4	14.54	9.35	280.37
Jun	31.5	16.43	12.03	360.82
Jul	32.7	16.87	12.74	382.27
Aug	34.8	17.68	14.09	422.85
Sep	26.9	14.72	9.59	287.58
Total				2717.82

5. Conclusion

This study of Tharthar ' 'Lake's satellite-derived surface temperature and hydrological data over the two years from October 2022 to September 2024 reveals significant seasonal and spatial thermal variability characteristic of semi-arid continental climates. The pronounced temperature fluctuations, with summer peaks and winter lows, strongly influence evaporation rates and surface water dynamics. These patterns align with regional climatology, underscoring the dominant role of solar radiation, atmospheric pressure systems, and climatic seasonality in shaping lake thermal regimes. Spatial temperature heterogeneity highlights differential responses between shallow and deep lake zones, with implications for evaporation, water-column mixing, and aquatic ecosystem health. The observed increase in seasonal surface area variability and evaporation rates between study years indicates heightened sensitivity to climatic fluctuations, further stressing the vulnerability of closed-basin lakes like Tharthar to ongoing climate change.

Our findings provide crucial insights into climate-lake interactions in arid environments and establish a valuable baseline for ongoing remote sensing efforts and refined hydrological modeling. The demonstrated linkage between thermal dynamics, evaporation, and lake hydrology underlines the importance of integrating temperature monitoring into water management and climate adaptation policies. This research supports informed decision-making for sustainable water use. It highlights the urgency of coordinated regional strategies to mitigate climate-induced water scarcity in the Tharthar Basin and similar ecosystems.

References

Ahmed, K. (2022). Detection of the Bathymetry and Shoreline of Terkos Lake Turkey Using Digital Image Processing and GIS. Iraqi National Journal of Earth Science (INJES), 22(1), 55-64. doi: 10.33899/earth.2022.133434.1011

Al-Ansari, N. A. (2013). "Management of Water Resources in Iraq: Perspectives and Prognoses." Engineering 05(08): 667-684.

Al-Asadi, L. S. M., H. A. M. S. Al-Juboori and M. A. Fakhratov (2024). "Organizational and technological solutions for controlling concrete st ructures projects in the dry hot weather in Iraq." BIO Web of Conferences 107: 06012.

Al-Bayati, A. H. I., Hammad, J. A., Majdoub, R., & Jabbar, S. A. (2025, February). Pedological Study And Productive Capacity Of Some Soils Within The Euphrates River Sediments At The City Of Al-Ramadi In Iraq. In IOP Conference Series: Earth and Environmental Science (Vol. 1449, No. 1, p. 012097). IOP Publishing.

Al-Fahdawi, A. H. A., & Satam, A. T. M. (2022, October). A Study Of The Water Reality Of Managing The Euphrates River In Anbar Governorate In Light Of The Growing Water Demand For The Period (2020-2040). In AIP Conference Proceedings (Vol. 2400, No. 1). AIP Publishing.

Ali, S. H., A. R. Qubaa and A. B. M. Al-Khayat (2024). "Climate Change and its Potential Impacts on Iraqi Environment: Overvie w." IOP Conference Series: Earth and Environmental Science 1300(1): 012010.

Allen, R. G., Tasumi, M., & Trezza, R. (2007). Satellite-Based Energy Balance For Mapping Evapotranspiration With Internalized Calibration (METRIC)—Model. Journal Of Irrigation And Drainage Engineering, 133(4), 380-394.

Al-Maliki, L. A., S. K. Al-Mamoori, N. Al-Ansari, K. El-Tawel and F. G. Comair (2022). "Climate change impact on water resources of Iraq (a review of literatu re)." IOP Conference Series: Earth and Environmental Science 1120(1): 012025.

Al-Qayyssi, K. A., Mohammed, K. S., Al-Dulaimi, S. Z., & Al-Rawi, M. K. (2024). Estimating Soil Erosion in Al-Aubyth Valley Using Modern Techniques and the RUSLE Equation. Journal homepage: http://iieta. org/journals/ijdne, 19(5), 1551-1561. https://doi.org/10.36103/j93nst49

Al-Timimi, Y. K., Al-Lami, A. M., Basheer, F. S., & Awad, A. Y. (2024). Impacts Of Climate Change On Thermal Bioclimatic Indices Over Iraq. Iraqi Journal Of Agricultural Sciences, 55(2), 744-756. DOI: https://doi.org/10.36103/j93nst49

Awwad, A., & Ramal, K.(2021). Climatic Water Balance For Al-Rutba Provine - Western Iraq. Journal Of Alanbar University For Humanities,2021(2).109.

Aya, M., & Kadhim, A. (2025). Land Surface Temperature Estimation from Landsat Thermal Infrared Imagery in Karbala, Iraq. Iraqi National Journal of Earth Science (INJES), 25(1), 343-353. doi:10.33899/earth.2024.144879.1179

Blanken, P. D., Rouse, W. R., Culf, A. D., Spence, C., Boudreau, L. D., Jasper, J. N., & Verseghy, D. (2000). Eddy Covariance Measurements Of Evaporation From Great Slave Lake, Northwest Territories, Canada. Water Resources Research, 36(4), 1069-1077.

Ebtihal Taki, A. K., & Watheq Fahem, A. J. (2023). Land Surface Temperature Dynamics in Response to Changes in Land Cover in An-Najaf Province, Iraq. Korean Journal of Remote Sensing, 39(1), 99-110

from reanalysis and satellite-derived products: Implication for single-channel land surface temperature retrieval. Remote

Hamid, H. M., F. W. Al-Azawi and Z. F. Makki (2024). "Assessing Hydrological Characteristics in Iraq Dams." Pakistan Journal of Agricultural Research 37(1).

Hirji, R. F. and A. Duda (2024). "Integrated management of lakes, reservoirs, and their basins is critic al for a climate-resilient planet: an urgent wake-up call from collect ive amnesia." Water Policy 27(1): 66-87.

Jassim, Omar, Jamal. (2017). Estimating the storage capacity curve of Hamrin Dam Lake in Iraq using Geographic Information Systems and Remote Sensing. Jordan, Mutah University, Master's Thesis (unpublished).

Kinana Ghazi Haleme, Saadoun Zahir Al-Dulaimi, Abdul Salam Arif Abdul Razzaq,And Kamal Abed Ala Alah Algayssi, The Relationship Between Large-Scale Relative Vorticity Fields And Rainfall In Syria During The Period, 1980-2020.

Kong, X., Li, Y., Wang, L., & Liu, H. (2024). Lake Surface Temperature Retrieval Study Based On Landsat 8 Satellite Imagery—A Case Study Of Poyang Lake. Atmosphere, 15(4), 428.

Kumar, R., Verma, R., & Aggarwal, R. K. (2018). Empirical model for the estimation of global solar radiation for Indian locations. International Journal of Ambient Energy, 42(2), 124–130. https://doi.org/10.1080/01430750.2018.1525588

M, G. (2008). "Lake Management Perspectives in Arid, Semi-Arid, Sub-Tropical and Trop ical Dry climate."

Muslih, K. D. (2022). Annual And Monthly Trends Of Cooling And Heating Degree-Days In Four Different Cities In Iraq As An Index Of Energy Consumption. Asia-Pacific Journal Of Atmospheric Sciences, 58(1), 33–43.

Oroud, I. M. (2019). The Annual Surface Temperature Patterns Across The Dead Sea As Retrieved From Thermal Images. Arabian Journal Of Geosciences, 12(22), 695

Oroud, I. M., & Altubeiri, Z. S. A. (2023). Estimation Of Evaporation From The Surface Water Of The Gulf Of Aqaba Using Band 10 Onboard Landsat 8. Dirasat: Human And Social Sciences, 50(6).

Parparov, A. and K. D. Hambright (1996). "A Proposed Framework for the Management of Water Quality in Arid-Regio n Lakes." Internationale Revue der gesamten Hydrobiologie und Hydrographie 81(3): 435-454.

Ramel, K. A., AL Mehemdi, Y. H., & Awad, A. Y. (2024). Analysis Of The Trends Of Change In Temperature And Precipitation And Their Impact On Water In Anbar Governorate (1980-2023) https://doi.org/10.35516/hum.v51i5.10019

Rezazadeh, A., Akbarzadeh, P., & Aminzadeh, M. (2020). The effect of floating balls density on evaporation suppression of water reservoirs in the presence of surface flows. Journal of Hydrology, 591, 125323.

Sajib, M. Q. U., & Wang, T. (2020). Estimation Of Land Surface Temperature In An Agricultural Region Of Bangladesh From Landsat 8: Intercomparison Of Four Algorithms. Sensors, 20(6), 1778

Salman, S. A., S. Shahid, H. A. Afan, M. S. Shiru, N. Al-Ansari and Z. M. Yaseen (2020). “Changes in Climatic Water Sensing, 12(5), 791. https://doi.org/10.3390/rs12050791

Williams, W. D. (1999). “Salinisation: A major threat to water resources in the arid and semi-a rid regions of the world.” Lakes & Reservoirs: Science, Policy and Management for Sustainable Use 4(3-4): 85-91.

Williams, W. D. (2002). “Environmental threats to salt lakes and the likely status of inland sa line ecosystems in 2025.” Environmental Conservation 29(2): 154-167.

Williamson, C. E., J. E. Saros, W. F. Vincent and J. P. Smol (2009). “Lakes and reservoirs as sentinels, integrators, and regulators of clim ate change.” Limnology and Oceanography 54(6part2): 2273-2282.

Yang, J., Duan, S. B., Zhang, X., Wu, P., Huang, C., Leng, P., & Gao, M. (2020). Evaluation Of Seven Atmospheric Profiles From Reanalysis And Satellite-Derived Products: Implication For Single-Channel Land Surface Temperature Retrieval. Remote Sensing, 12(5), 791.

Yao, F., B. Livneh, B. Rajagopalan, J. Wang, J.-F. Crétaux, Y. Wada and M.Yasir, M., Hui, S., Rahman, S. U., Ilyas, M., Zafar, A., & Mehmood, A. (2020). Estimation Of Land Surface Temperature Using LANDSAT-8 Data-A Case Study Of District Malakand, Khyber Pakhtunkhwa, Pakistan. Journal Of Liberal Arts And Humanities, 1, 140-148.

Yasir, M., Hui, S., Rahman, S. U., Ilyas, M., Zafar, A., & Mehmood, A. (2020). Estimation Of Land Surface Temperature Using LANDSAT-8 Data-A Case Study Of District Malakand, Khyber Pakhtunkhwa, Pakistan. Journal Of Liberal Arts And Humanities, 1, 140-148

JJEES

JJEES (2026) 17 (2): 216-222
ISSN 1995-6681

Jordan Journal of Earth and Environmental Sciences

The Lateral and Vertical Variations in Petrophysical Properties of Zubair Formation in the East Baghdad Oil Field

Maan H. Abdullah Al-Majid[1*] and Bashar A. Al-Juraisy[2]

[1] Department of Petroleum Reservoir Engineering- College of Petroleum and Mining Engineering, University of Mosul, Mosul, Iraq.
[2] Department of Geology - College of Science, University of Mosul, Mosul, Iraq.

Received on 4 April 2025; Accepted on 19 November 2025

Abstract

The Zubair Formation is one of the main producing formations in the East Baghdad oil field, which is considered one of the largest producing oil fields in central Iraq, with its oil reserves exceeding 10 billion barrels. The formation is subdivided into sex parts according to lithological facies. This study aims to evaluate the petrophysical and geological characteristics of the Zubair Formation and to build three-dimensional models that show the distribution of these characteristics. Well logs data for three wells (EB-2, EB-4, and EB-16) were analyzed using the Interactive software (IP) to evaluate the formation's petrophysical properties. Porosity and permeability types were obtained by analyzing data from the three well logs. The results of two cross plots (Neutron Porosity-Density, and M-N) indicate that the lithology of the Zubair Formation is mostly sandstone, with small amounts of dolomite and limestone present in certain areas, and shale makes up a sizable portion of the volume (up to 50 %). In general, the Zubair Formation has a good total porosity (about 25% on average). Secondary porosity ranges from very low at the base to increasing towards the top of the formation. In contrast, effective porosity ranges from 0% to 15% depending on the shale content of the formation rocks. Permeability varies from low to high (2-600 md) depending on the porosity values and percentage of shale. The water and oil saturation of all formation units for the three studied wells ranged between (10-100 %). Three-Dimensional models of porosity, permeability, and saturation of water for the Zubair Formation have been made to view the distribution and variation of these properties in a three-dimensional view.

Keywords: *Lateral, Vertical, Petrophysical, Zubair Formation, East Baghdad, Oil*

1. Introduction

Well logging is one of the most widely used methods in petroleum engineering and geology because it has many advantages. It provides detailed information about many petrophysical and rock properties, and is much cheaper than coring or drilling. Many. Many studies have used well log data to evaluate the petrophysical characteristics of hydrocarbon-containing formations. For example, Albeyati et al. (2021) assessed the petrophysical properties of the Balad Oilfield in Iraq by combining all available data, including petrographic image analysis (PIA), well logs (resistivity, density, and gamma rays), and core data (permeability and porosity). Al-Majid (2022a) used a so-called velocity deviation log (VDL) derived from a porosity log to detect the presence of hydrocarbons in the Haritha Formation, which is considered one of the productive formations in the Qayyarah oil field in northern Iraq. Al-Mawla et al. (2023) used well log data to estimate porosity types and the percentage of shale in the Bajawan Formation, a productive formation of the Kirkuk field in northern Iraq. Al-Juraisy and Al-Majid (2025) also determined the petrophysical properties and oil content of the Hartha Formation in the Qayyarah field in northern Iraq. They identified three zones in the formation relative to the percentage of oil.

1.1. Location

The East Baghdad Oil Field comprises several oil fields spanning over 1,000 km2 and is situated east of the Baghdad Governorate. Al-Mansurrya and Al-Suwayrah regions, respectively, constitute its northern and southern borders (Figure 1). The East Baghdad Oil Field extends more than 100 km from northwest to southeast, with some areas exceeding 10 km in width.

1.2 Geology

Structurally, the East Baghdad field is an anticline affected by numerous longitudinal and transverse faults, which led to its division into independent sections containing different oil and gas reservoirs. It led to the development of the Arabian Peninsula's largest oil and gas reserves. Many NW-SE-trending faults in the field produce oil that originates from the Early Cretaceous sandstone parts of the Zubair Formation, the Late Cretaceous Tanuma Formation, and the Late Cretaceous Khasib Formation (Sharland et al., 2001).

Stratigraphically, the Zubair Formation section includes many rock types, such as sandstone, carbonates, siltstone, and shale, deposited in marine and lagoon environments (Ali and Jassim, 2023). The Zubair Formation is one of the lower Cretaceous deposits, characterized by sandstone and shale that alternate, with a few thin layers of limestone in the upper portion of the formation. Its age is regarded as Berriasian-Valanginian. In the study area, The thickness of the Zubair formation is roughly 400m, and Figure 2 shows the stratigraphic section of the formations in the field (Al-Haleem, 2010).

* Corresponding author e-mail: maan.abdalla@uomosul.edu.iq

Figure 1. The location map of the study area with the locations of studied wells (Modified from Al-Ameri and Al-Obaydi, 2011)

According to the final geological report of the Central Oil Company in the East Baghdad oil field (IPC,1982), the Zubair Formation was divided into six units (from A to Z) depending on the rock content of each unit.

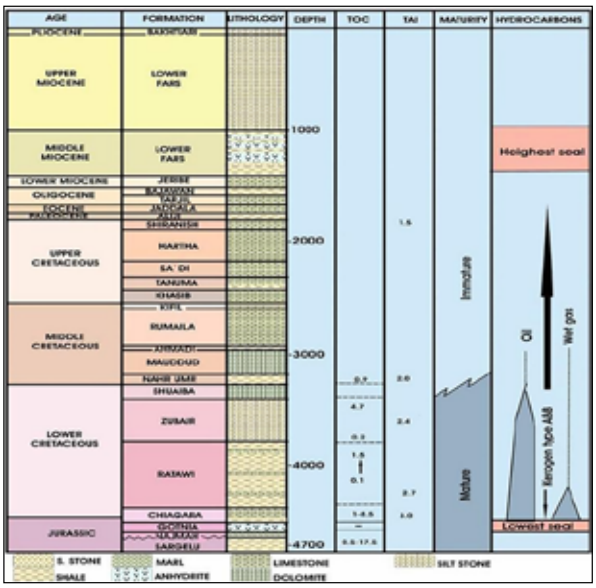

Figure 2. Stratigraphic section of East Baghdad Oil Field (Al-Haleem, 2010)

The primary aim of this study is to determine the amount of hydrocarbon in the Zubair Formation by analyzing petrophysical characteristics derived from well log data and creating three-dimensional models of these characteristics (porosity, permeability, and water saturation).

2. Materials and Methods

Well log data from three wells (EB-2, EB-4, and EB-16) in the East Baghdad Oil Field were used in this study, namely: Gamma ray, SP, porosity, and resistivity logs. All data used in this work were environmentally corrected to reduce the effects of mud cake, drilling mud, and other environmental factors. Many equations are used for calculating the required parameters and correcting them (Al-Majid, 2019, Al-Juraisy and Al-Majid, 2021, Al-Majid, 2021, Al-Majid, 2022a, Al-Majid, 2022b, Boddy and Smith, 2009, and Ebrahim, et al, 2023) (Table. 1). Several computer programs (Interactive Petrophysics (IP), Techlog, Petrel E&P, and NeuraLog programs) were used to facilitate and reduce the time spent in digitizing the data, preparing the data, well log analysis, data analysis, and results plotting.

Table 1. The measurement and correction equations used in this study

Porosity calculation $PHID = \frac{\rho ma - \rho b}{\rho ma - \rho f}$ ---------- (1) $PHIS = \frac{\Delta Tlog - \Delta Tma}{\Delta Tf - \Delta Tma}$ ---------- (2) $NPHID = \frac{NPHI + PHID}{2}$ ---------- (3) $PHIsec = (NPHID - PHIS)$ ----- (4)	ρma: density of the matrix (2.65 g/c^3 for sandstone). ρf: density of the fluid (1 g/c3 for fresh water). ρb: reading of density log. Δtf: fluid transit-time (189 μsec/ft for fresh water). Δtlog: sonic log reading of transit-time. Δtma: matrix transit-time (55.5 μsec/ft for Dolomite). PHID:density-porosity (using the density log data). NPHI: neutron porosity (using neutron log data). PHIS: primary porosity (obtained from sonic log data). PHIsec: secondary porosity. NPHID: neutron & density porosity.
Shale Volume calculation $IGR = \frac{GRlog - GRmin}{GRmax - GRmin}$ ---------- (5) $Vsh = 0.33 * [2^{(2*IGR)} - 1]$ ---------- (6)	IGR: gamma-ray index. Vsh: volume of the shale. GRlog: reading of gamma-ray log, GRmax: the maximum gamma-ray value. GRmin the minimum gamma-ray value.
Porosity corrections PHISc = PHIS − (Vsh × PHISsh) --- (7) NPHIc = NPHI − (Vsh × NPHIsh) -- (8) PHIDc = PHID − (Vsh × PHIDsh) -- (9) PHIE = NPHID × (1 − Vsh) ---- (10)	(PHISc; NPHIc; PHIDc): corrected porosities (PHISsh; NPHIsh; PHIDsh): shale porosity obtained from different logs PHIE: the effective porosity.
M & N lithology parameters $M = \left(\frac{\Delta tf - \Delta tlog}{\rho b - \rho f}\right) * 0.01$ ------ (11) $N = \frac{1 - NPHI}{\rho b - \rho f}$ ---------- (12)	M and N: lithology parameters
Permeability and saturation equations $K = 10000 * NPHID^{4.5} / Sw^2$ $Sw^n = \frac{a \cdot Rw}{NPHID^m \cdot Rt}$ ---------- (13) $So = 1 - Sw^n$ ---------- (14)	a: factor of the tortuosity (0.8 for sandstone). m: factor of the cementation (1.8 for sandstone). N: exponential of saturation (2 for sandstone). Rw: resistivity of formation water (obtained from Sp log). Rt: true formation resistivity (from resistivity logs); Sw: water saturation; So: oil saturation.

3. Results

3.1. Lithology

Lithology is one of the important parameters in evaluating geological formations. In order to delineate the lithology of the Zubair Formation in the study area, two types of cross-plots were used:

3.1.1 Neutron Porosity- Density (NPHI-RHOB) Cross plot

Neutron Porosity-Density cross-plots were applied to determine the main rock component of the Zubair Formation in the three studied wells by observing the assemblages of points around rock types (sandstone, dolomite, and limestone). Most of the points are located near the sandstone line (Figure 3). From Figure 3, it is clear that the main component of the Zubair Formation in the three wells is sandstone, with limestone and dolomite percentages varying from one well to another. As for the shale, it increased in well EB-4 compared to the other two wells.

3.1.2. M-N Cross plot

The two factors (M and N), calculated using equations 11 and 12, respectively, are assigned to the three wells to apply the M-N cross-plot, which shows the basic mineral compositions in the Zubair Formation (Figure 3).

From the M-N cross plots above, most of the points gather around the site of silica, which is the main mineral

composition of sandstone. This concentration means that the main parts of the formation are sandstone, which is consistent with the results of the NPHI-RHOB cross plots. Also, from Figure 3, it can be seen that some points are located in the limestone and dolomite zones, indicating the presence of layers of limestone and dolomite within the Zubair Formation.

So, according to the analysis of Figures 3 and 4, the Zubair Formation is mainly composed of sandstone interspersed with some layers of limestone and dolomite.

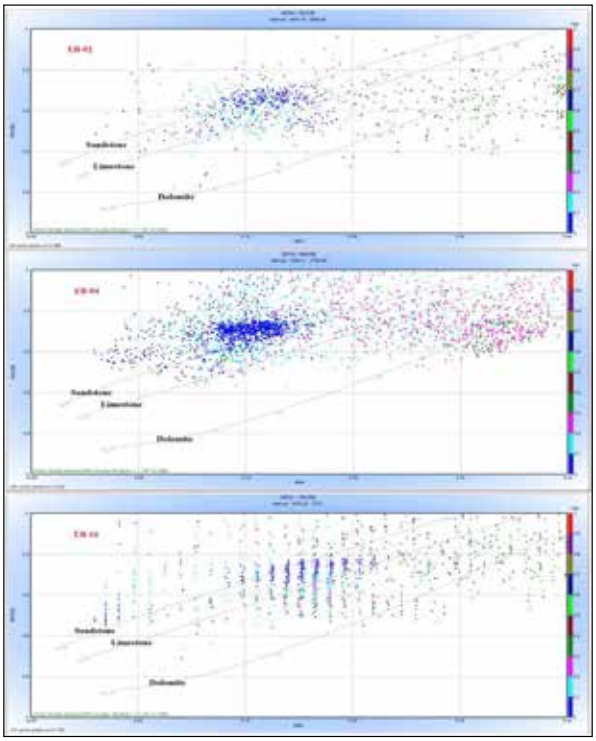

Figure 3. NPHI-RHOB cross plot applied on the three studied wells (EB-2, EB-4, and EB-16).

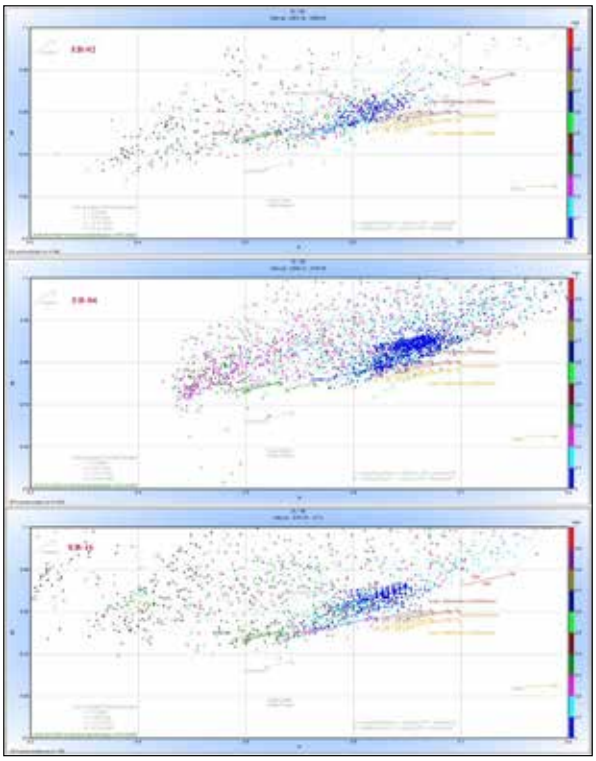

Figure 4. M-N Cross plot applied to the three studied wells (EB-2, EB-4, and EB-16).

3.2. Shale Volume

The shale volume (Vsh) is determinative in correcting porosity types and water saturation ratios based on shale content (Wahid et al., 2022). Vsh is calculated using the equations 5, and 6 respectively (Ajisafe and Ako, 2013). It is clear that there is an increase in the shale volume at the upper parts of the three wells, and in well EB-4 compared to other wells (figure 5).

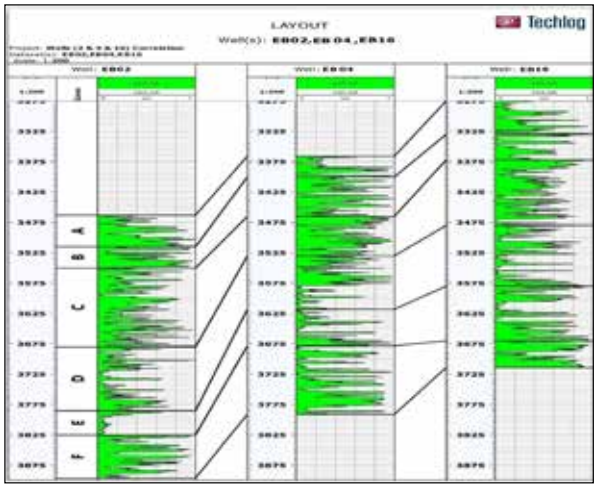

Figure 5. Shale volume of the three studied wells

3.3. Porosity

Three types of porosity have been calculated in this study:

3.3.1 Total porosity.

The total porosity (NPHID) values for wells EB-2, EB-4, and EB-16 have been calculated using equation 3. They are relatively high, reaching about 25%, especially in well EB-4, as its values are greater than those of the other two wells (Figure 6).

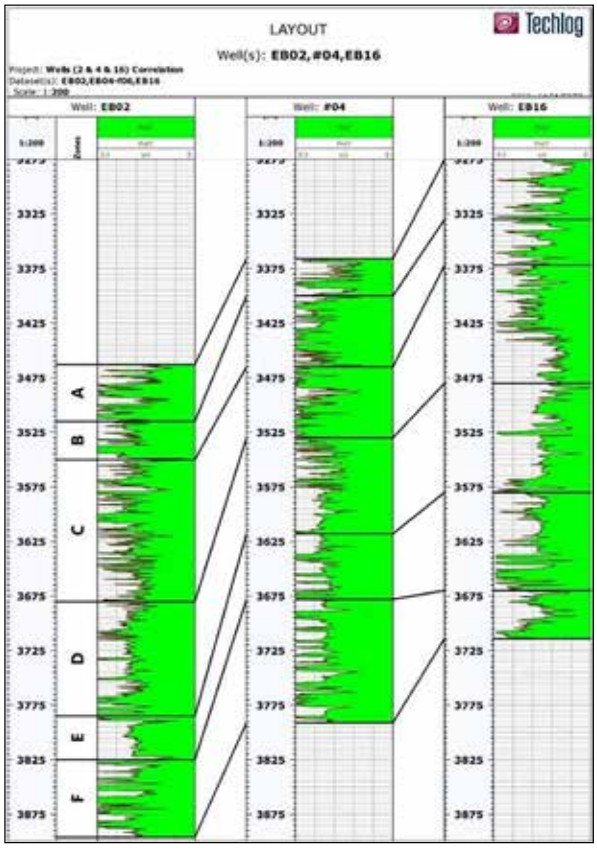

Figure 6. Total porosity values of the three studied wells.

3.3.2. Effective porosity

After accounting for the shale effect on total porosity, effective porosity (PHIE) values for the Zubair formation in the three studied wells are calculated using equation 10 (Figure 7). There was a close relationship between the total porosity values and the effective porosity values in the three wells

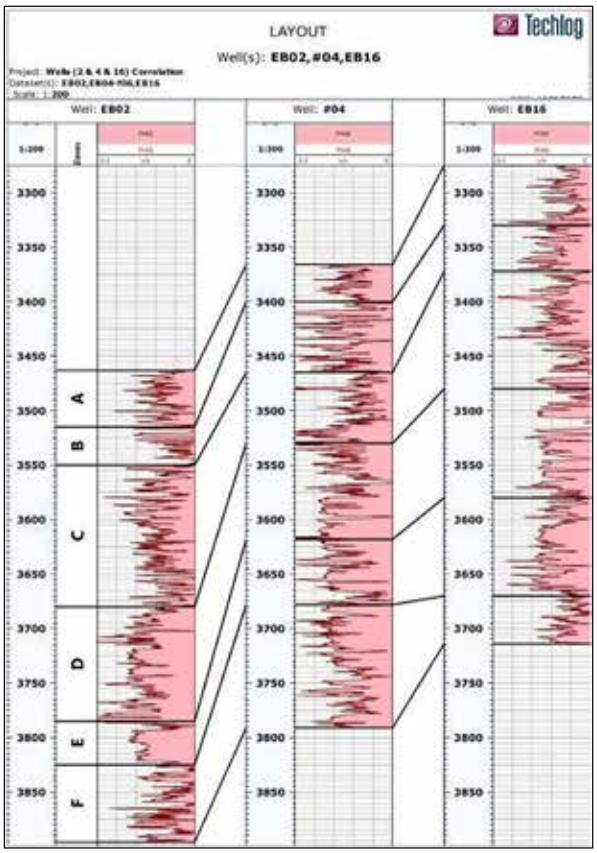

Figure 7. Effective porosity values of the three studied wells.

3.3.3. Secondary porosity

The secondary porosity values (PHIsec) are calculated using equation (4) as the difference between total and sonic porosities. The PHIsec values at wells EB-2 and EB-4 are almost equal in all units, while they are slightly larger in well EB-16 (Figure 8).

3.4. Permeability

The calculated permeability values for the three wells show that the highest permeability was observed in wells EB-4 and EB-16. The highest values (about 600 md) are observed at several units of well EB-4, while the lowest values are observed at most units of well EB-2. Figure 9 displays the three wells' permeability values.

3.5. Saturation

Determining water saturation (Sw) is an important characteristic that helps determine the amount of hydrocarbon in the oil reservoir (Mohammed et al., 2021). Water saturation is the fraction of the pore volume occupied by water. Improper calculation of water saturation leads to significant errors in the estimation of hydrocarbon saturation (1-Sw). There are several methods to determine water saturation, including dielectric measurements, nuclear measurements, the ratio technique (SP vs. Rxo/Rt), crossplots, F- overlays, Archie's equation, and shaly sand methods. In this study, Archie's formula was used to calculate the water and oil saturations of the Zubair Formation (equations 13 and 14, respectively). The results demonstrated that the water saturation values of Zubair Formation range between (10% - 100%) (Figure 10). This means that the percentage of saturation with hydrocarbon ranges between (100% - 10%). The highest hydrocarbon saturation appears in the C unit, followed by the A unit. There is a clear increase in water saturation in well EB-16, accompanied by a decrease in oil saturation

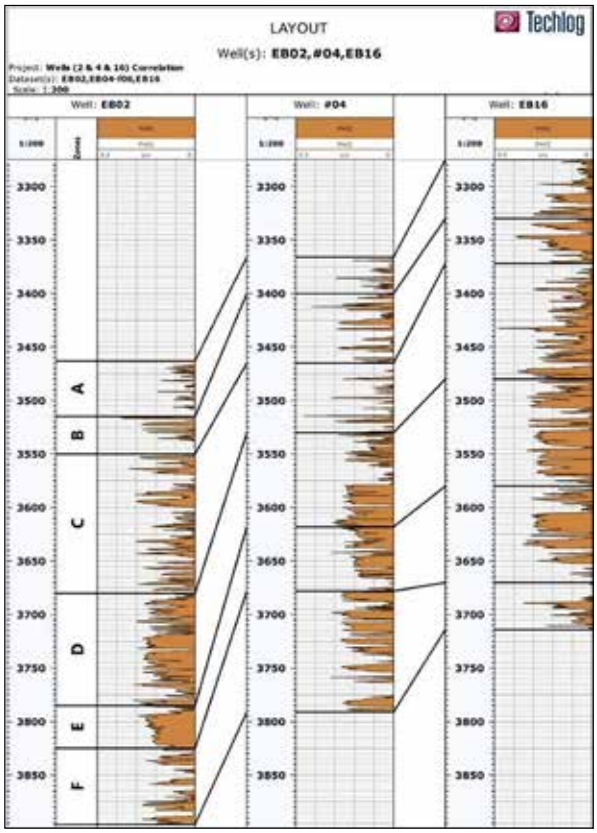

Figure 8. Secondary porosity values of the three studied wells in the study area

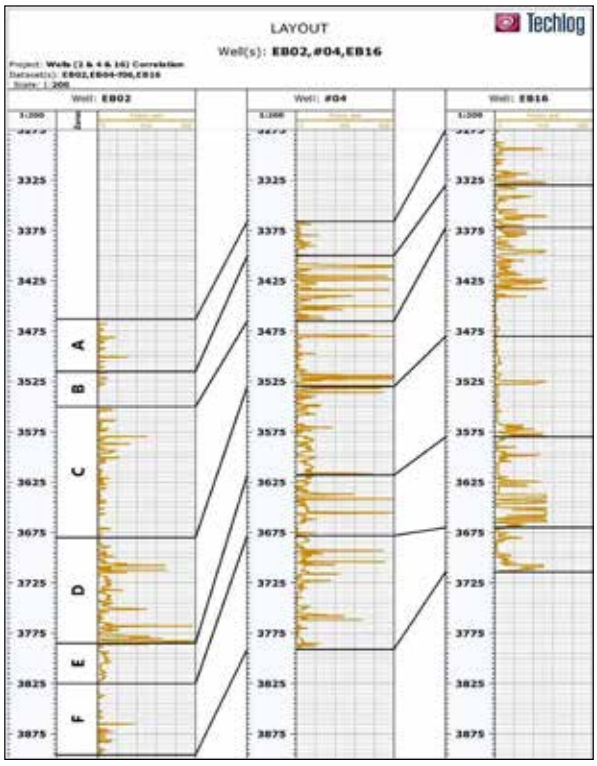

Figure 9. Permeability values for the three wells in the study area.

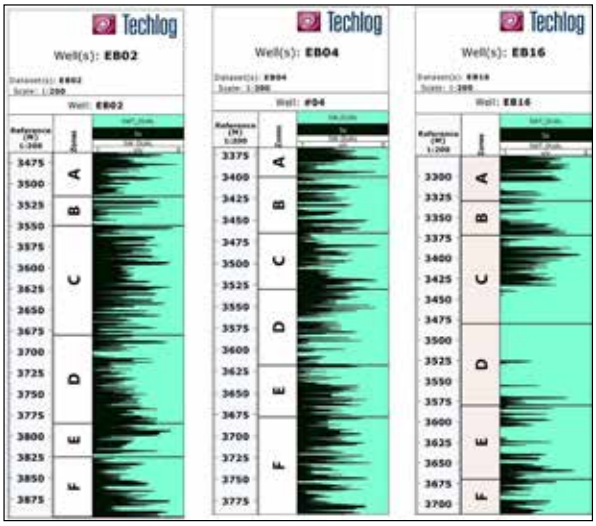

Figure 10. The saturation distribution in the three studied wells.

3.6. Petrophysical Modeling Process

Reservoir modeing in the oil and gas sector is the process of building a computer model of a petroleum reservoir to better estimate reserves, make field development decisions, forecast future production, install additional wells, and assess different reservoir management scenarios. A regular or irregular grid defines the array of distinct cells that make up a reservoir model, which depicts the reservoir's physical space. Although 1D and 2D models are occasionally employed, the array of cells is typically three-dimensional. Each cell has values for characteristics including water saturation, permeability, and porosity.

The process of assigning petrophysical property values (permeability, water saturation, and porosity) to every cell in a three-dimensional grid is known as petrophysical property modeling. For simulating the distribution of petrophysical characteristics in a reservoir model, Petrel provides a number of algorithms. Geostatistical techniques were used to construct the petrophysics model. Based on the porosity, water saturation, and permeability measurements, which were adjusted and evaluated in the IP software, models of these parameters were constructed. To account for the volume of data at hand, the Sequential Gaussian Simulation algorithm was employed.

3.6.1. Porosity Model

Total and effective porosity models of the Zubair Formation were built based on results from porosity logs. Each unit is characterized by a specific range of porosity values (Figure 11).

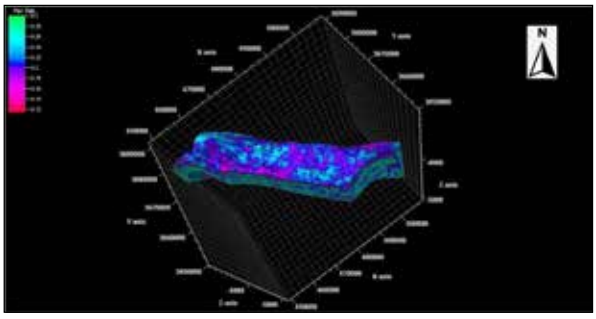

Figure 11. Total porosity model of Zubair Formation.

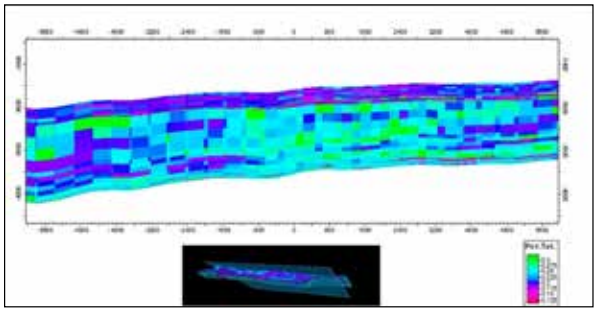

Figure 12. N-S cross-section shows the distribution of the total porosity of Zubair Formation.

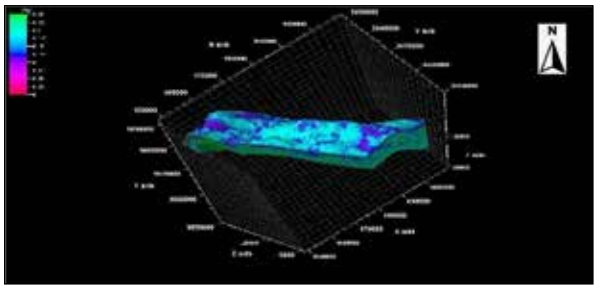

Figure 13. Effective porosity model of Zubair Formation.

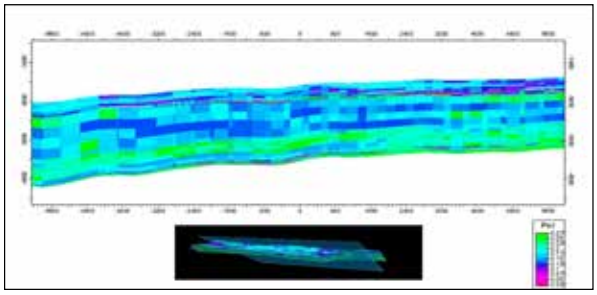

Figure 14. N-S cross-section shows the distribution of the effective porosity of the Zubair Formation

3.6.2. Permeability Model

Permeability is also considered one of the Petrophysical properties in formation evaluation. The method used to build the absolute permeability model was the Statistical Sequential Gaussian Simulation Algorithm, with normal score transforms and experimental variogram ranges calculated. The major direction azimuth is (-41°) as shown in Figure 15.

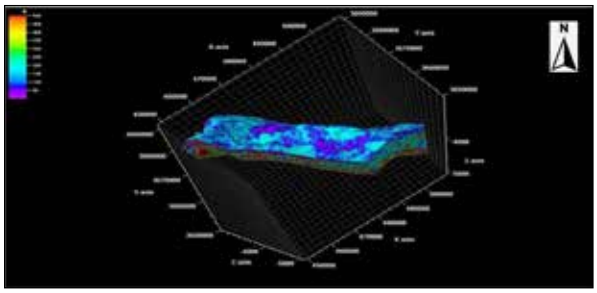

Figure 15. Permeability model of the Zubair Formation.

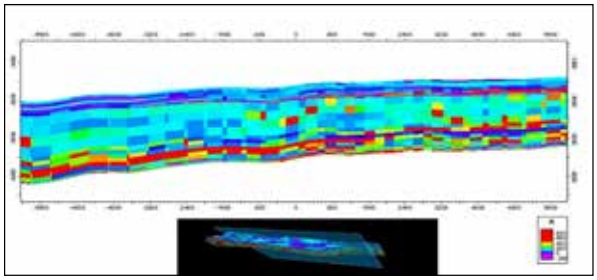

Figure 16. N-S cross sectionshows distribution of the permeability of Zubair Formation

3.6.3. Water Saturation Model

One of the petrophysical characteristics used to evaluate a deposit is water saturation. Water saturation values are used to describe each unit. Models of water saturation, environment, and porosity were found to match (Figure 17).

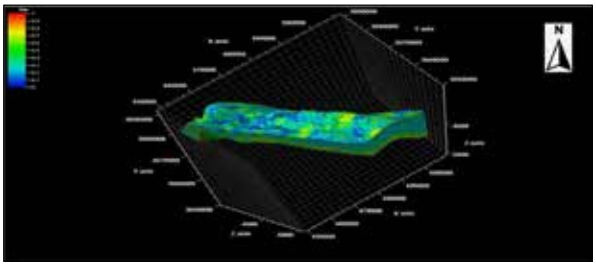

Figure 17. Water saturation model of Zubair Formation.

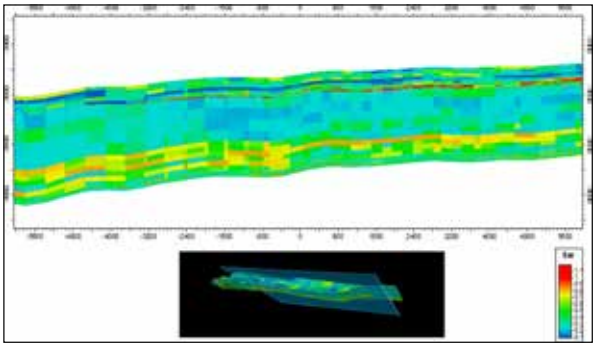

Figure 18. N-S cross-section shows the distribution of the water saturation of the Zubair Formation

4. Discussion

The Zubair Formation is considered lithologically complex, as it contains many rock types (Aqrawi et al., 2010). The proportions of these rocks vary from one region to another, and even within one region between one well and another (IPC,1982). This variation in lithology is clearly observed in the large dispersion of points on the NPHI-RHOB cross-plot (Figure 3) and the M-N Cross plot (Figure 4). This variation led to a large variance and overlap in the petrophysical properties calculated for the three study wells. However, in general, by observing the values of the calculated petrophysical parameters, we can distinguish some evidence as follows:

Regarding the total porosity, it can be noted that there is, in general, an increase in this type of porosity in most parts of the bottom of the formation) Figures 11&12). This is perhaps due to the increase in the proportion of clastic sediments in this part of the formation, as reflected in the sand-to-shale ratio.

It can also be noted that the increase in total porosity at the bottom of the formation is accompanied by an increase in effective porosity (Figures 13 and 14), and permeability (Figures 15 &16). On most sites, this increase may be related to the increase in the sandstone percentage.

Logically, an increase in water saturation indicates a decrease in hydrocarbon saturation (heavy oil at this site). The amount and method of oil distribution in the formation depend mainly on many factors, the most important of which are characteristics of the fluid and rock heterogeneity (Chioma et al., 2018). Therefore, it can be noticed that water saturation increases from the lower to the upper part of the formation. This may be due to the density of water being greater than that of oil, and the presence of oil with water in some of the upper areas of the formation may be due to the close density match between the heavy oil present in the reservoir and the density of water. In this case, heterogeneity plays an important role in the amount and distribution of the fluids, as less-dense fluids (oil) can move and distribute within small pores, while more-dense fluids (water) are unable to move and distribute within small spaces. Because the Zubair Formation contains many different and overlapping rocks, which mainly include sand rocks with large pore sizes and shale rocks with small pores, we note that there is overlap in the zones and amounts of oil, water saturation in most parts of the formation (Figure 10)

5. Conclusions

According to the interpretation results of the wells' data for the three studied wells, we can conclude the following:

- The Zubair Formation rocks consist mainly of sandstone, with interbedded layers of shale, siltstone, limestone, and dolomite.

- The formation rocks generally contain a relatively high percentage of shale, which is randomly distributed throughout the formation and varies between approximately 40% and 100%, reaching 100% in some parts of the formation while not exceeding 1% in others.

- The total porosity of the formation can be considered good, as it ranged between 15% and more than 30% in most parts of the formation

- The permeability of the formation rocks varied greatly between parts of the formation and from one well to another, ranging from 0 to 600 md, perhaps due to variations in the proportion of low-permeability shale within these rocks.

- Formation porosity contains a good range of hydrocarbon saturation (10-100%), and the variability of this hydrocarbon saturation depends on the amount and type of porosity in the formation's parts.

Acknowledgements

The authors are extremely grateful for the facilities provided by the Petroleum and Mining Engineering & College of Science at the University of Mosul, which have significantly improved the quality of this study.

References

Al-Ameri, T. K. and Al-Obaydi, R. Y. (2011). Cretaceous petroleum system of the Khasib and Tannuma oil reservoir, East Baghdad oil field, Iraq, Arab J Geosci 4:915–932.

Ajisafe, Y., Ako, B. (2013). 3D seismic attributes for reservoir characterization of "Y" field Niger Delta, Nigeria, Journal Applied Geology Geophysics, 1(2): 23–31.

Albeyati, F. M. O., Abdula, R.A., Fikret, T., (2021). Porosity and permeability measurements integration of the Upper Cretaceous in Balad Field, Central Iraq, Iraqi Geological Journal, 54(1B), 24-42.

Al-Haleem, A.A. (2010) .Compaction and migration of hydrocarbons in east Baghdad oil field. Kufa Journal of Engineering, 2(1): 81-96.

Ali, R.A., Jassim, H.K. (2023). Sedimentology and

geochemistry of Zubair Formation sandstone reservoir, East Baghdad Oilfield, central Iraq, Kuwait Journal of Science 50: 427–437

Al-Juraisy, B. A., and Al-Majid, M. H. (2021). Importance of Velocity Deviation Technique and Negative Secondary Porosity in Detection of Hydrocarbon Zones in Khasib Formation, East Baghdad Oil Field, Iraqi geological journal, 54 (2E), 86-103.

Al-Juraisy, B. A., and Al-Majid, M. H. (2025). Evaluation of Petrophysical Properties and Oil Content of Hartha Formation in Qayyarah Oil Field, Northern Iraq. Jordan Journal of Earth and Environmental Sciences (JJEES), 16 (3): 284-288.

Al-Majid, M. H., 2019, New Petrophysical Equations for Hartha-Tannuma Interval in the East Baghdad Oil Field, Iraqi national journal of earth science, 19(2):136-152.

Al-Majid, M. H., 2021, Petrophysical Properties Estimation of Euphrates Reservoir in Qayyarah Oil Field Using Core and Well Log Data, Iraqi geological journal, 54 (2E): 186-197.

Al-Majid, M. H. (2022a). The combination of velocity deviation and thorium normalization techniques to detect the Hartha Formation oil zones in the Qayyarah oilfield, AIP Conference Proceedings 2443, 030001.

Al-Majid, M. H. (2022b). Delineation of high compacted zones for Shuaiba Formation in East Baghdad oil field using porosity logs data, AIP Conference Proceedings 2443, 030019.

Al-Mawla, F.M., Al-Juraisy, B.A., Al-Hamidi, R.I., Q.M. (2023). The Use of Geophysical Well Logs in Determining the Some Petrophysical Properties of the Bajawan Formation in Selected Wells from the Kirkuk Field,Northern Iraq, 23(2): 168-188.

Aqrawi, A., Goff, J., Horbury, A., and Sadooni, F. (2010). The Petroleum Geology of Iraq. Scientific Press, 1st Edition, ISBN: 978-0-901360-36-8

Boddy, R., Samith, G. (2009). Statistical methods in practice, for scientists and technologists, Wiley, U.K. 248 p.

Chioma, O., Uko, E., Tamunobereton-ari, I. (2018). Determination of Lithology and Pore-Fluid of a Reservoir in Parts of Niger Delta Using Well-Log Data. IOSR Journal of Applied Physics, 10(2): 71-82

Ebrahim, D. M., Al-Majid, M. H., Al-Hamidi, R. E., Al-Hamdani, S. A. (2023). Porosity Type Determination Using the Velocity Deviation Technique for The Sheikh Allas Formation in The Kirkuk Oil Field, Northeastern Iraq, Iraqi National Journal of Earth Science, 23(2): 20-36.

Mohammed, M., Salih, H., and Mnaty, K. (2021). Reservoir Characterization of the Middle Cretaceous Mishrif Formation in the Buzurgan Oilfield, Southern Iraq. Iraqi National Journal of Earth Sciences. 21(2): 63-77. 10.33899/earth.2021.170388.

Sharland, P.R., Archer R., Casey, D.M., Davies R.B., Hall S.H., Heward, A.P., Horbury, A.D., and Simmons, M.D. (2001). Arabian Plate Sequence Stratigraphy. GeoArabia Special Publication 2, 371p.

Wahid, M. A., Elkadi, H. H., and Othman, M. M. (2022). Petrophysical Evaluation of the Lower Rudeis Formation in Shukheir Bay Field, Gulf of Suez, Egypt Using Open-Hole Well-Logs, Iraqi Geological Journal 55 (2A):1-18.

JJEES

JJEES (2026) 17 (2): 223-235
ISSN 1995-6681

Jordan Journal of Earth and Environmental Sciences

Identification of Social and Environmental Hotspots to Flood Risk on Cat Ba Island, Northern Vietnam

Phan Thi Mai Hoa[1, 2], Nguyen Quoc Phi[1*] and Nguyen Thi Cuc[1]

[1] Hanoi University of Mining and Geology, Hanoi, Vietnam
[2] Graduate University of Science and Technology, Vietnam Academy of Science and Technology, Vietnam

Received on 23 August 2025; Accepted on 1 December 2025

Abstract

This study identifies social and environmental hotspots associated with flood risk on Cat Ba Island, a climate-sensitive coastal region in Northern Vietnam. A spatial flood risk framework was developed by integrating the Analytic Hierarchy Process (AHP) with Geographic Information System (GIS) based Spatial Multi-Criteria Analysis (SMCA). Fourteen indicators representing terrain, hydrology, land use, and socio-demographics were standardized and weighted, with the AHP Consistency Ratio (CR = 0.04) confirming acceptable internal coherence. A Sentinel-1 SAR flood inventory from September 2024 was used for validation, showing a close match between the modeled risk zones and the observed inundation. Nearly all flooding (99.6%) occurred within the moderate-to-very high risk classes, while the low-risk zone experienced almost no inundation. Low-lying coastal areas, including Cat Ba Town and southern Tran Chau, emerge as the main hotspots due to dense settlement and limited drainage. Forested uplands show higher resilience. This study delivers the first empirically validated, high-resolution hotspot map for Cat Ba. It provides a clear, transferable framework to support climate adaptation and land-use planning in vulnerable island settings.

Keywords: *Analytic Hierarchy Process; Cat Ba Island; flood risk; Geographic Information System; social–environmental vulnerability.*

1. Introduction

Climate change poses profound threats to sustainable development globally, particularly through increasing flood risks that disproportionately affect coastal and island regions (Vousdoukas et al., 2023). Among these, small islands are considered highly vulnerable due to their low-lying topography, limited adaptive capacity, and exposure to sea-level rise, storm surges, and coastal erosion (Parmesan et al., 2022). In Southeast Asia, Vietnam is widely recognized as one of the most climate-exposed countries, with flood hazards threatening infrastructure, livelihoods, and economic resilience in both urban and rural areas (Boateng, 2012; Tuyet Hanh et al., 2020).

Cat Ba Island, the largest landmass in its archipelago and designated as a UNESCO Biosphere Reserve, represents a clear example of such vulnerability. Intensified flood events, resulting from rising sea levels, saltwater intrusion, and increasingly frequent typhoons, are placing increasing stress on critical infrastructure, including coastal roads and embankments, while directly impacting fisheries, tourism, and community well-being (Giang & Khanal, 2024).

Similar trends have been reported in other rapidly urbanizing settings, where increasing impermeable surfaces and limited drainage worsen flood impacts. (Oroud, 2025) shows that land-cover change in Amman has intensified runoff and concentrated flooding in low-lying districts. These conditions mirror what is now emerging on Cat Ba, where rapid tourism-driven expansion and inadequate drainage are increasing local flood susceptibility.

While significant attention has been given to physical exposure and hazard mapping, social vulnerability remains underexplored yet critical to climate risk. Socioeconomic conditions, such as high population density, limited access to services, and dependence on climate-sensitive livelihoods, can significantly limit communities' adaptive capacities (Cutter et al., 2012; Mai & Truong, 2022). In Vietnam, empirical studies indicate that combined pressures from flooding and salinization have intensified livelihood disruptions, triggered out-migration, and further deepened existing inequalities (Ta & Linh, 2024).

Although Vietnam's vulnerability to climate change has been widely acknowledged, most existing assessments focus on large-scale or provincial levels, lacking spatial granularity and place-specific insights. In particular, there remains a critical knowledge gap regarding fine-scale social vulnerability assessments for small islands such as Cat Ba, where localized socio-demographic characteristics and infrastructure limitations can substantially influence risk exposure (Dao & Dao, 2024; Van Phong et al., 2023).

This gap reflects broader global trends. Recent literature reviews have consistently identified enduring limitations in vulnerability assessments, particularly the insufficient incorporation of socioeconomic variables, the limited representation of localized contexts, and the lack of rigorous validation procedures (De Sherbinin et al., 2019). While an increasing number of studies have adopted integrated GIS-based frameworks, such as those utilizing AHP-based vulnerability assessments in Bangladesh (Ha-Mim &

* Corresponding author e-mail: nguyenquocphi@humg.edu.vn

Hossain, 2022), PCA combined with AHP models in Florida, USA (Xie & Meng, 2023), and multi-hazard mapping efforts in Romania (Ajtai et al., 2023; Chelariu et al., 2024). Most of these applications remain focused on urban or mainland regions. As a result, they seldom capture the compounded nature of social and environmental vulnerabilities in island communities.

National and regional vulnerability assessments are typically conducted at coarse spatial resolutions and depend on highly aggregated indices, which limit their relevance for local-scale adaptation. Existing reviews also note that most mapping efforts remain heavily oriented toward biophysical indicators, with only modest incorporation of social dimensions and very limited empirical validation against observed hazard impacts (Birkmann et al., 2022; Bukvic et al., 2020; De Sherbinin et al., 2019; Yarveysi et al., 2023). Against this backdrop, a fine-scale, empirically validated social–environmental vulnerability assessment for Cat Ba Island provides a useful complement to existing national and regional products.

Addressing this research gap, the present study applies a GIS-based Spatial Multi-Criteria Analysis (SMCA), integrated with the Analytic Hierarchy Process (AHP) to assess social vulnerability to flooding on Cat Ba Island. This integrated approach allows the combination of both environmental and socioeconomic indicators into a transparent, structured decision-making framework that is intuitive and adaptable to data-sparse environments. While advanced methods, such as machine learning, offer strong predictive performance, they often function as opaque "black boxes" that are difficult for local planners to interpret or adapt (De Sherbinin et al., 2019; Rudin, 2019; Uddameri & Hernandez, 2025). In contrast, the Analytic Hierarchy Process (AHP) provides a structured, transparent, and participatory framework that enables expert input and traceability, especially in data-scarce contexts (Ajtai et al., 2023). Accordingly, this study aims to (i) construct social and environmental hotspots to flood risk for Cat Ba Island using an integrated AHP and SMCA approach and (ii) validate its predictive performance using flood observations derived from Sentinel-1 Synthetic Aperture Radar (SAR) imagery. The findings are intended to support localized climate adaptation, risk reduction, and socially inclusive spatial planning in small island environments.

2. Study area

This study focuses on Cat Ba Island, the largest landmass in the Cat Ba Archipelago, located off the northeastern coast of Vietnam in Hai Phong Province, situated between 106°54′20″–107°07′20″E and 20°42′40″–20°52′40″N. Cat Ba Island and its surrounding islets cover a total area of approximately 173 km², as shown in Figure 1. The archipelago has a mean elevation of approximately 200 m above sea level, reflecting a dissected karst landscape dominated by steep ridges and narrow valleys (Van Quan et al., 2010). Demographically, Cat Ba Island has around 18,000–19,000 permanent residents. Recognized as a UNESCO Biosphere Reserve since 2004, the island encompasses diverse landscapes including karst limestone formations, tropical forests, and low-lying coastal zones (Hue et al., 2024). Its socioeconomic profile is shaped by a rapidly expanding tourism industry, small-scale aquaculture, and dispersed residential communities, many of which are situated in areas increasingly exposed to flood hazards (Hoang & Truong, 2023). Intensifying typhoons, shoreline erosion, and saltwater intrusion have placed mounting pressure on infrastructure systems and local livelihoods (Maliva, 2021), underscoring Cat Ba's significance as a representative site for assessing the intersection of climate-related social and environmental vulnerabilities.

Historical disaster records indicate that Cat Ba has experienced recurrent inundation in recent years. Typhoon Yagi in 2024 produced extensive flooding across Cat Ba Town and surrounding low-lying areas, disrupting transport and coastal infrastructure (VnExpress, 2024). More recently, prolonged rainfall in September 2025 caused additional inundation in Xuan Dam, Viet Hai, Cat Ba Town and Phu Long, with flood depths ranging from approximately 0.2 to 0.5 m and lasting for 1–3 hours (Newspaper, 2025). Such recurring events highlight the urgency of identifying social and environmental hotspots of flood risk on Cat Ba Island to inform adaptive planning and risk-reduction strategies.

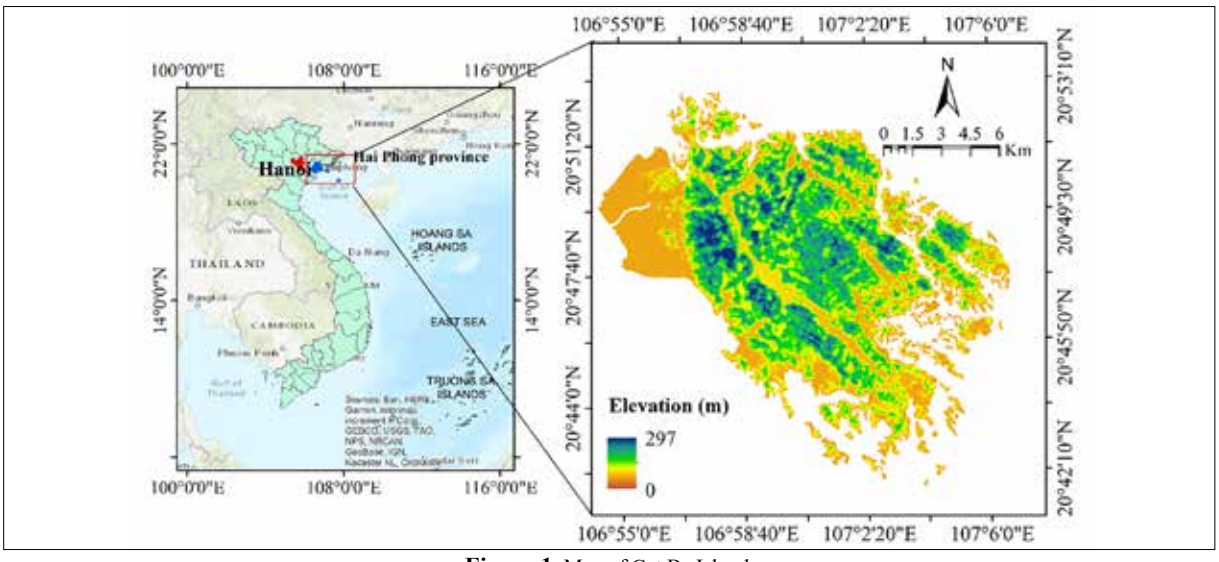

Figure 1. Map of Cat Ba Island.

3. Methodology

3.1. Materials

Fourteen spatial criteria were selected to represent key environmental and social factors influencing climate-related flood risk on Cat Ba Island. The criteria encompass terrain (elevation, slope), hydrological exposure (distance to rivers, rainfall, drainage density, stream power index, topographic wetness index), land cover (land use/land cover, NDVI, NDWI), and social exposure (population and building density, distance to services). Table 1 summarizes selected flood vulnerability indicators, including LULC, river proximity, slope, elevation, rainfall, NDWI, TWI, SPI, and NDVI, as well as their classification thresholds, data sources, and influence on vulnerability, based on expert knowledge and literature relevant to regional flooding.

Prior to analysis, each layer was standardized to a uniform vulnerability scale, ranging from 1 to 5, to ensure comparability, with higher scores indicating greater vulnerability (Table 1 and Figure 2). Direct factors, such as population density, were scored positively (higher values representing higher vulnerability), while inverse factors, such as distance to health facilities, were reverse-scored (greater distance indicating higher vulnerability). For example, elevation was reclassified so that low-lying coastal areas (<5 m) received very high vulnerability scores. In contrast, higher terrain was assigned lower scores, consistent with coastal flood risk assessments (Khan et al., 2025). Definitions of influence direction were determined to maintain consistency across criteria.

All indicators were processed and standardized on a 30-meter spatial resolution grid covering the entire Cat Ba Island study area. The resolution was selected to align with the spatial resolution of the primary base datasets, including the SRTM 30 m Digital Elevation Model, Sentinel-2 MSI (10–30 m), and the Google Dynamic World V1 (10 m resampled to 30 m). Below is a summary of the indicators used:

Land Use/Land Cover (LULC): Areas dominated by urban or impervious surfaces tend to have increased runoff and higher flood risk, whereas regions with natural vegetation or wetlands can enhance infiltration and mitigate flooding (Khodaei et al., 2025). We classified LULC types so that built-up or bare land areas receive higher vulnerability scores, while forested or wetland areas receive lower scores.

Distance to Rivers (DRi): Proximity to rivers elevates exposure to fluvial flooding (e.g., overbank flows and backwater effects). Locations closer to river channels are thus considered more vulnerable, as even moderate rain events can lead to flooding in adjacent lowlands (Khan et al., 2025; Miranda et al., 2023).

Slope: Flat or low-slope areas allow water to accumulate and stagnate, making them more prone to inundation, whereas steep slopes facilitate faster runoff and are generally less flood-prone (Khan et al., 2025; Tariq et al., 2022). We assigned higher vulnerability scores to gentler slopes.

Elevation: Low-elevation zones (especially <5 m above sea level) are highly susceptible to coastal flooding and storm surges, while higher-elevation areas are less exposed. Accordingly, lower elevations were scored as more vulnerable.

Rainfall (Annual): Regions with higher precipitation totals are likely to experience greater runoff volumes and flood frequencies. Areas on Cat Ba with higher long-term average rainfall were thus scored as having higher flood vulnerability. The mean rainfall for 2024 was derived through interpolation in ArcGIS.

Normalized Difference Water Index (NDWI): NDWI is a remote sensing index that emphasizes the presence of surface water and soil saturation by contrasting near-infrared and shortwave infrared reflectance. High NDWI values indicate the presence of standing water bodies or marshy conditions, signaling existing flood-prone or waterlogged areas (Abijith et al., 2025; Ji et al., 2009; Konapala et al., 2021). Areas with persistently high NDWI were considered more vulnerable.

Topographic Wetness Index (TWI): TWI models the potential for soil saturation and water accumulation based on terrain shape. Higher TWI values correspond to locations where water naturally converges and accumulates (e.g., valleys and depressions), thereby correlating with increased flood susceptibility (Abijith et al., 2025; Adnyana & Wiguna, 2025).

Stream Power Index (SPI): SPI measures the erosive power of flowing water and is related to slope and drainage area. Lower SPI values often identify low-gradient plains or wide valleys where water loses energy and can pond or overflow, increasing flood risk (Abijith et al., 2025; Kocsis et al., 2022). In our context, areas with low SPI (indicative of low slope and high potential water accumulation) were marked as more vulnerable.

Normalized Difference Vegetation Index (NDVI): NDVI quantifies vegetation density by measuring the difference in reflectance between near-infrared and visible red wavelengths. Areas with dense vegetation cover (high NDVI) can intercept rainfall, promote infiltration, and stabilize soils, thereby reducing runoff and flood severity. Conversely, sparsely vegetated or barren areas (low NDVI) exacerbate flood vulnerability due to higher runoff (Khan et al., 2025). Thus, lower NDVI areas were scored higher for vulnerability.

Drainage Density (DD): Drainage density represents the total length of streams and rivers per unit area. Regions with a high density of drainage channels may experience more concentrated runoff and potentially more severe flooding within those channels (Abijith et al., 2025; Rautela et al., 2023; Tetteh et al., 2024). High drainage density can be a double-edged factor: it indicates efficient water removal, but also means many areas are near a watercourse. In our scoring, extremely high drainage density areas were treated carefully, often in conjunction

with proximity to channels (as represented by the Distance to Rivers criterion).

Population Density (PopD): Higher population density indicates that more people and assets are exposed within a given area, raising the potential human impact of any flood event (Ibrahim et al., 2024). Densely populated neighborhoods on Cat Ba were thus given higher vulnerability scores, reflecting the higher stakes in those areas.

Building Density (BD): A high concentration of buildings often correlates with more impervious surfaces and reduced infiltration, which can increase runoff and flood intensity. Moreover, a greater number of structures means more property at risk. Areas with high building density were marked as more vulnerable to flooding (Son et al., 2023).

Distance to Nearest School: Schools and educational facilities often serve as emergency shelters or coordination centers during disasters. Communities located far from a school may have reduced access to safe shelters or organized relief in a flood event. Therefore, a greater distance from the nearest school was interpreted as higher social vulnerability (Isia et al., 2023).

Distance to Nearest Health Center: Access to healthcare is crucial during and after flood emergencies for treating injuries and illnesses. Communities that are farther from clinics or hospitals experience delays in receiving medical care. Thus, a longer distance to the nearest health center contributes to higher vulnerability (Zhran et al., 2024).

Each of these criteria was classified into five ordinal vulnerability classes (1-5) based on value ranges informed by previous studies and local expert consultations. This classification approach was iteratively refined to ensure that the resulting criteria maps aligned with local knowledge of past flood impacts, thereby increasing the reliability of our integrated assessment.

To quantify actual flood extents and validate the predictive accuracy of the composite flood risk zones, a flood inventory was generated using time-series Sentinel-1 SAR imagery. The change detection method was applied by calculating the backscatter difference between pre-flood and post-flood acquisitions, leveraging the sensitivity of SAR signals to surface water (Konapala et al., 2021). A threshold-based classification was then employed to isolate flooded pixels, with calibration based on field knowledge and visual interpretation of high-resolution optical imagery.

Table 1. Criteria for Vulnerability Assessment.

No.	Data	Classification level					Data sources
		Very low	Low	Moderate	High	Very high	
1	Elevation	0-30	30-74	74-120	120-169	169-297	Topographic maps (1:10.000 scale)
2	Slope	0-8.2	8.2-17.2	17.2-26.1	26.1-36.7	36.7-74	Topographic maps (1:10.000 scale)
3	Distance to rivers (DRi)	0-1203	1203-2203	2203-3159	3159-4270	4270-7080	OpenStreetMap (OSM)
4	Drainage density (DD)	0-0.08	0.08-0.3	0.3-0.6	0.6-0.9	0.9-1.5	OpenStreetMap (OSM)
5	Rainfall (annual)	231-260	260-277	277-290	290-302	302-325	CHIRPS daily rainfall dataset ("UCSBCHG/CHIRPS/DAILY")
6	NDVI	-0.25 -0.01	0.01-0.22	0.22-0.38	0.38-0.49	0.49-0.78	Landsat 8 imagery NDVI = (band 5- band4)/(band5+band4)
7	NDWI	-0.70–-0.44	-0.44–-0.33	-0.33–-0.16	-0.16-0.05	0.05-0.35	Sentinel-2 imagery of 2024
8	TWI	-4.9–-2.9	-2.9–-1.3	-1.3-0.9	0.9-3.8	3.8-10.5	Topographic maps (1:10.000 scale)
9	SPI	0-0.25	0.25-1	1-2.2	2.2-4.8	4.8-12.8	Topographic maps (1:10.000 scale)
10	Land use/land cover (LULC) - 2021	0-10	10-40	40-60	60-80	80-95	Google Dynamic World V1 (Sentinel-2)
11	Population density	2.5	2.5-4.9	4.9-41	41.66	66-215	National census (2019)
12	Building density	0-1431	1431-2483	2483-3535	3535-4821	4821-7451	Google Earth + Field Verification
13	Distance to nearest school	0-2918	2918-5551	5551-7955	7955-10244	10244-14595	Google Earth + Field Verification
14	Distance to nearest health center	0-76	76-252	252-487	487-803	803-1107	Google Earth + Field Verification

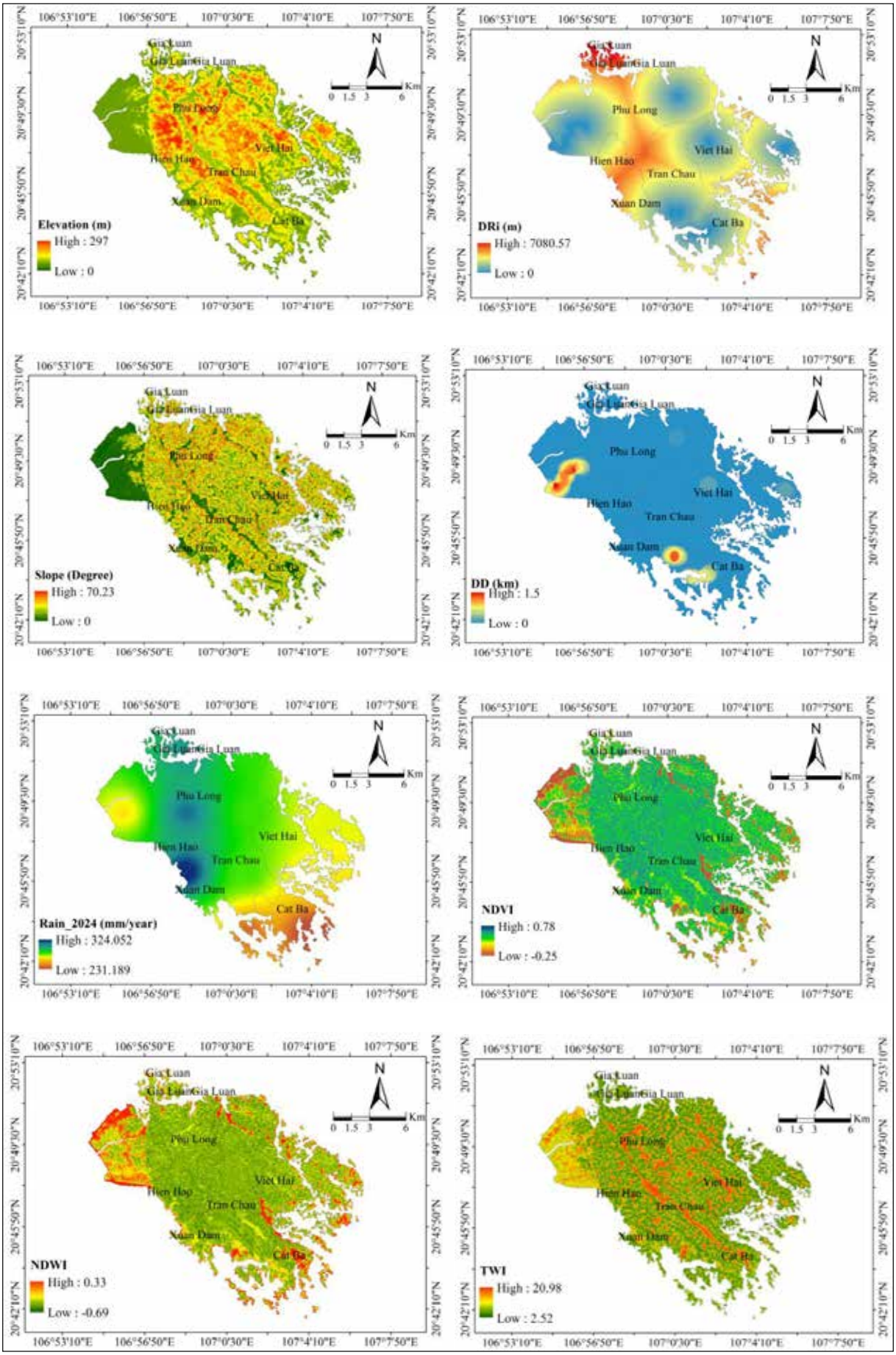

Figure 2. Input layers for flood vulnerability assessment and Sentinel-1 inundation map (Sept 2024).

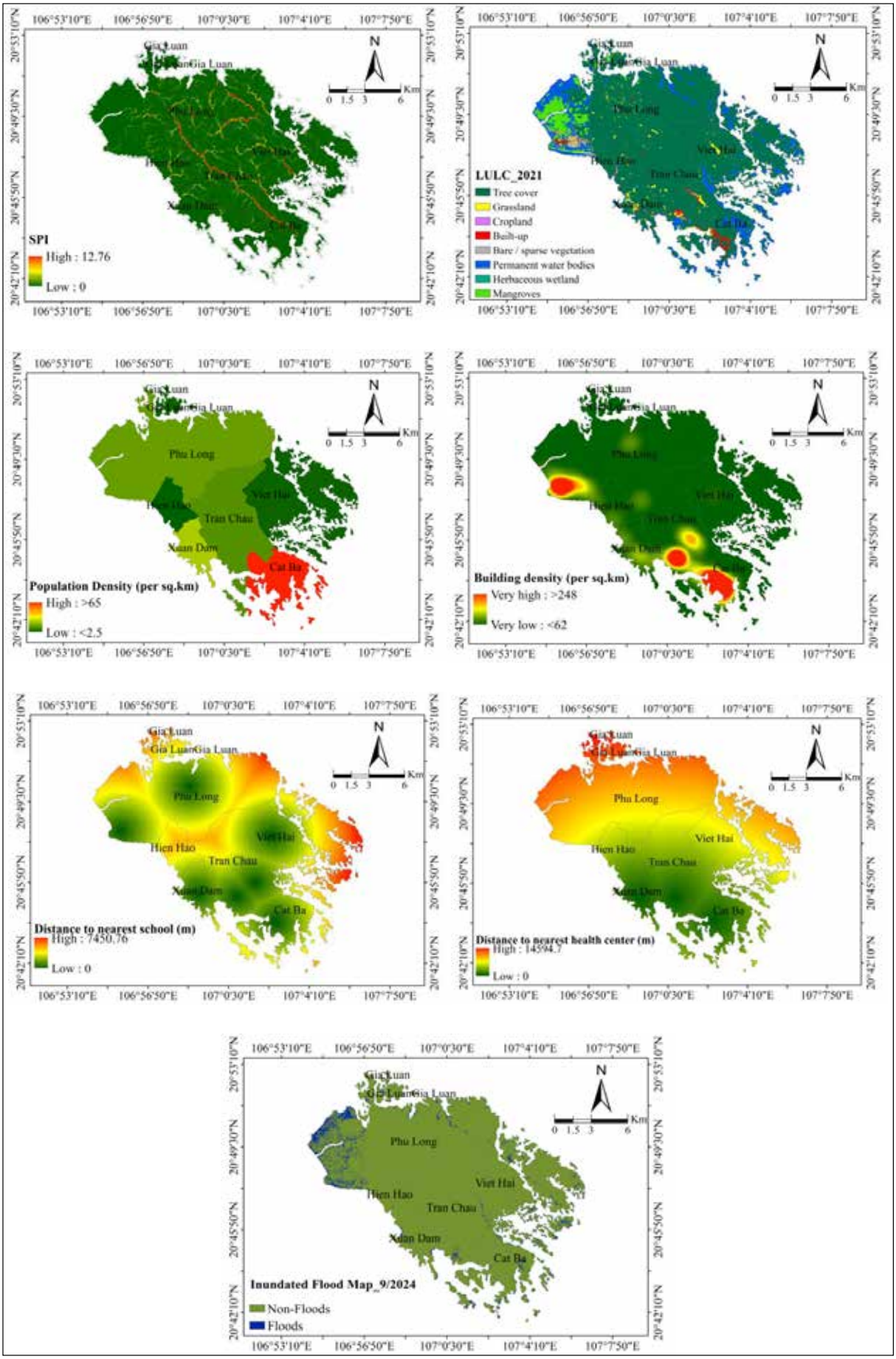

Continuing from Figure 2. Input layers for flood vulnerability assessment and Sentinel-1 inundation map (Sept 2024).

3.2. Method

To integrate the selected criteria and produce a composite flood vulnerability map, this study implemented a GIS-based Spatial Multi-Criteria Analysis (SMCA) combined with the Analytic Hierarchy Process (AHP) for factor weighting. The methodological workflow consisted of four key steps: data preprocessing, indicator standardization, expert-based weighting using AHP, and GIS-based weighted overlay analysis (Figure 3). The AHP method was selected for its capacity to systematically incorporate expert knowledge and local context into the evaluation model, which is particularly advantageous for place-specific assessment (Saaty, 1980). Unlike purely statistical techniques, AHP employs a structured pairwise comparison framework that captures expert judgments on the relative importance of factors, effectively reflecting local realities, such as prioritizing population density over minor topographic variations when assessing flood risk. The widespread application of AHP in climate vulnerability studies stems from its transparency and flexibility in integrating both qualitative and quantitative data (Al-Sababhah, 2023; Bharwani et al., 2013; Udie et al., 2018). Pairwise comparisons in this study were informed by a panel of local experts, including community planners and disaster risk management officials, to ensure alignment of the derived weights with practical experiences with climate hazards in the Cat Ba context.

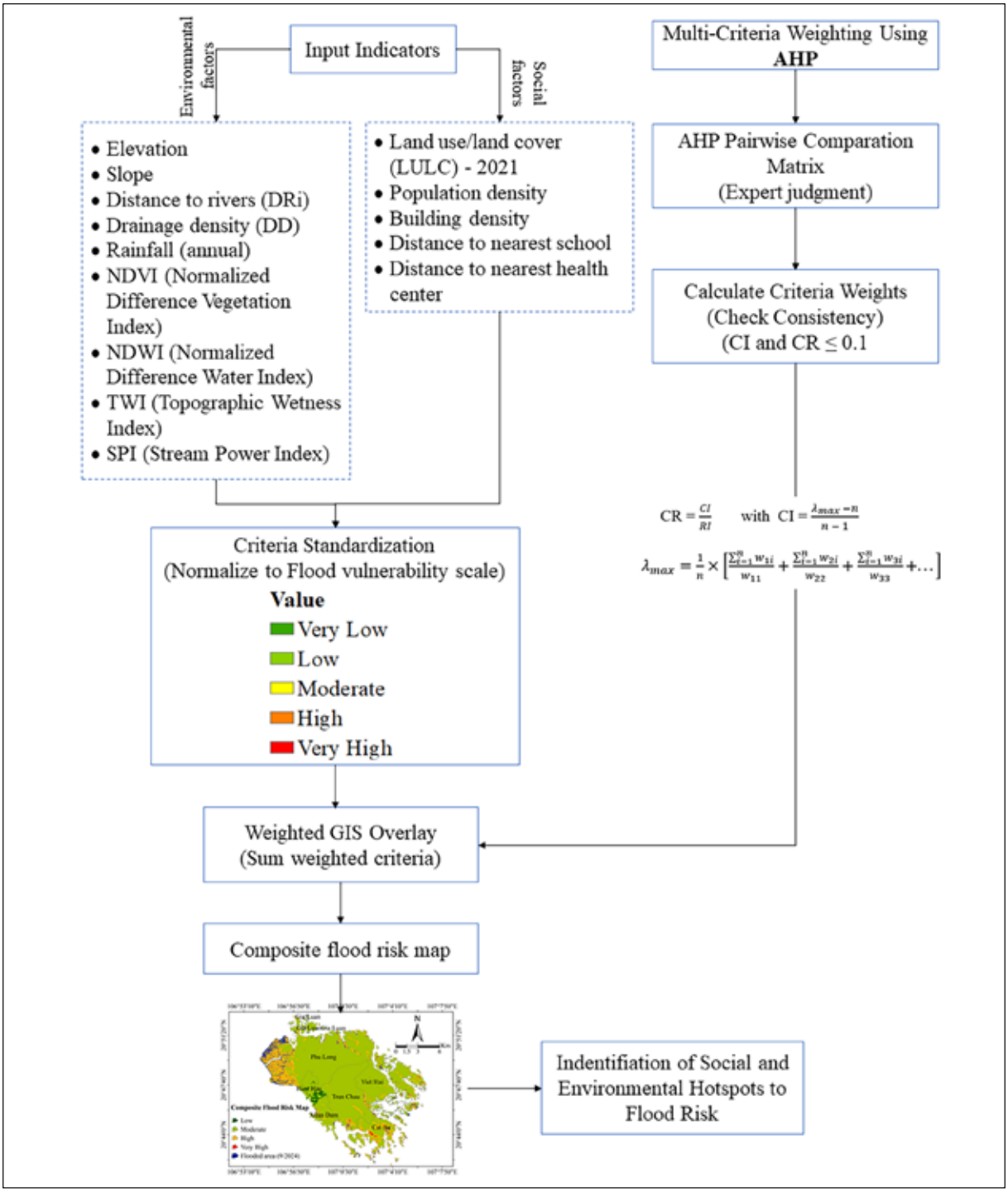

Figure 3. Workflow of the proposed approach to the composite flood risk map.

The Analytic Hierarchy Process (AHP), a structured multi-criteria decision-making (MCDM) technique, was adopted to rank and weight environmental and social factors influencing vulnerability.

Pairwise comparisons were conducted using Saaty's 1–9 scale (Figure 4), where a score of 1 reflects equal importance and a score of 9 indicates a strong preference for one factor over another (Saaty, 1980). Evaluations from a panel of disaster management and environmental experts were used to complete the comparison matrix, and the principal eigenvector was calculated to obtain normalized weights, representing the relative contribution of each criterion to overall vulnerability.

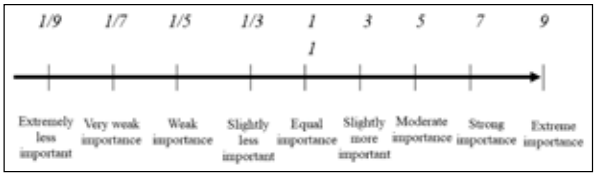

Figure 4. Standard AHP Intensity Scale (Saaty, 1980).

Consistency of expert judgments was verified by calculating the Consistency Ratio (CR), defined in Eq. (1). A CR below the recommended threshold of 0.1 indicated acceptable consistency, thereby ensuring the reliability of the derived weights (Saaty, 1980). In the present analysis, all matrices met this consistency requirement.

$$\mathrm{CR} = \frac{CI}{RI} \tag{1}$$

$$\text{with } \mathrm{CI} = \frac{\lambda_{max} - n}{n-1} \tag{2}$$

$$\lambda_{max} = \frac{1}{n} \times \left[\frac{\sum_{i=1}^{n} w_{1i}}{w_{11}} + \frac{\sum_{i=1}^{n} w_{2i}}{w_{22}} + \frac{\sum_{i=1}^{n} w_{3i}}{w_{33}} + \ldots \right] \tag{3}$$

where λmax is the principal eigenvalue of the comparison matrix, and nnn is the number of criteria. The CI measures the degree to which the judgments deviate from complete consistency.

The Random Index (RI), reflecting the average consistency of a randomly generated reciprocal matrix, is adopted from Saaty's guidelines (1980). For a comparison matrix of order n = 14, the corresponding RI value is 1.57 (Alonso & Lamata, 2006). Subsequently, Geographic Information System (GIS) techniques were employed to produce a composite social vulnerability map. Each spatial data layer representing a criterion was reclassified and multiplied by its corresponding AHP-derived weight. The weighted layers were then aggregated through linear combination to generate a continuous vulnerability index surface.

To support spatial interpretation, the continuous vulnerability surface was categorized into four discrete classes: Low, Moderate, High, and Very High vulnerability. Classification thresholds were determined using the Jenks Natural Breaks optimization method, which minimizes within-class variance and maximizes between-class differences (Komolafe et al., 2020). This method was chosen for its suitability in environmental and spatial data classification, particularly when values are not uniformly distributed. The resulting vulnerability classes reflect the relative severity of flood susceptibility across the study area and were validated against expert knowledge and observed inundation patterns.

The final classified flood vulnerability map was then overlaid with the Sentinel-1–derived flood inventory to assess predictive accuracy. This validation step involved spatial cross-tabulation between predicted vulnerability zones and actual flood extents, allowing for quantitative evaluation of model performance (Shivhare et al., 2024). The high degree of spatial alignment between predicted high-vulnerability zones and observed flooded areas provided empirical support for the reliability of the composite risk assessment.

4. Results and Discussion

4.1. Spatial Indicators of Flood Vulnerability

The spatial pattern of flood-related vulnerability on Cat Ba Island reflects the combined influence of environmental exposure, surface conditions, and settlement characteristics. High-vulnerability zones are concentrated in low-lying coastal centers such as Cat Ba Town and Xuan Dam, where dense construction, limited open space, and constrained drainage create conditions favorable for recurrent inundation. Conversely, upland communes such as Viet Hai and Gia Luan exhibit lower susceptibility due to intact vegetation and steeper terrain that facilitate runoff and enhance natural infiltration.

The results derived from the pairwise comparison matrix (Table 2) and the normalized weights (Table 3) show that built-environment and demographic indicators dominate the weighting structure, with population density, building density, and land-use characteristics ranking among the most influential criteria in the AHP evaluation. Population density (24.27%) and building density (18.12%) were the strongest contributors, followed by land use/land cover (12.80%) and NDWI (9.39%) (Table 3), indicating the role of urban expansion, impervious surfaces, and surface saturation in amplifying flood impacts. These findings align with previous work highlighting population pressure and urban form as central determinants of vulnerability in hazard-prone settings (Balaian et al., 2024; Cutter et al., 2012; Ma & Mostafavi, 2024). Hydrological indicators, such as proximity to rivers (6.55%) and drainage density (5.22%), exert secondary influence but remain important for explaining runoff concentration on valley floors and in constrained drainage corridors.

The spatial interaction between these factors produces a clear coastal–upland divide. Urbanized southern centers with extensive impervious cover show strong correspondence with high NDWI values and limited drainage pathways, resulting in concentrated flood hotspots. This pattern is also evident in Phu Quoc (Dao & Dao, 2024) and other tourism-driven island destinations (Du et al., 2015), where similar combinations of dense built-up areas and constrained drainage consistently amplify flood risk. Although rivers normally function as natural drainage corridors, poorly designed or undersized embankments can impede flow and intensify localized flooding, a pattern also observed in other urbanized watersheds (Zakir, 2024).

In contrast, forested uplands retain greater resilience due to higher vegetation cover and terrain gradients that limit water accumulation (Janzen et al., 2024; Justine & Seenath, 2025) on vegetation-mediated hazard mitigation.

Access to essential services, as reflected in the distance to schools (2.86%) and health centers (2.68%), further differentiates communities, highlighting areas where isolation may intensify the impacts of extreme events (Alabbad & Demir, 2025; Hamza et al., 2021).

Table 2. Pairwise comparison matrix.

Factors	Elevation	Slope	Distance to rivers	Drainage density	Rainfall (annual)	NDVI	NDWI	TWI	SPI	LULC	Population density	Building density	Distance to nearest school	Distance to nearest health center
Elevation	1	1	0.3	0.3	0.5	0.5	0.2	0.5	1	0.14	0.1	0.1	2	1
Slope	1	1	0.3	0.3	0.5	0.5	0.2	0.5	1	0.1	0.1	0.1	2	2
Distance to rivers	4	4	1	2	2	2	0.5	2	2	0.5	0.3	0.3	2	2
Drainage density	3	3	0.5	1	2	2	0.5	1	2	0.333	0.3	0.25	2	2
Rainfall (annual)	2	2	0.5	0.5	1	2	0.33	2	1	0.25	0.17	0.2	1	1
NDVI	2	2	0.5	0.5	0.5	1	0.3	2	2	0.25	0.14	0.20	1	1
NDWI	6	6	2	2	3	3	1	3	3	0.5	0.25	0.5	3	3
TWI	2	2	0.5	1	0.5	0.5	0.3	1	2	0.3	0.14	0.17	1	1
SPI	1	1	0.5	0.5	1.0	0.5	0.3	0.5	1	0.17	0.11	0.13	2	2
LULC	7	8	2	3	4.0	4	2	4	6	1	0.33	0.5	4	3
Population density	9	9	4	4	6	7	4	7	9	3	1	2	7	7
Building density	9	9	3	4	5	5	2	6	8	2	0.5	1	6	6
Distance to nearest school	0.5	0.5	0.5	0.5	1	1	0.3	1	1	0	0.1	0.2	1	2
Distance to nearest health center	1	0.5	0.5	0.5	1	1	0.3	1	1	0	0.1	0.2	0.5	1
SUM	48.5	49	16	20.17	28	30	12.33	31.5	39	9.10	3.65	5.83	34.5	34

Table 3. Normalization of matrix and final weights.

Factors	Elevation	Slope	Distance to rivers	Drainage density	Rainfall (annual)	NDVI	NDWI	TWI	SPI	LULC	Population density	Building density	Distance to nearest school	Distance to nearest health center	Weighted
Elevation	0.021	0.020	0.016	0.017	0.018	0.017	0.014	0.016	0.026	0.016	0.030	0.019	0.058	0.029	0.0225
Slope	0.021	0.020	0.016	0.017	0.018	0.017	0.014	0.016	0.026	0.014	0.030	0.019	0.058	0.059	0.0245
Distance to rivers	0.082	0.082	0.063	0.099	0.071	0.067	0.041	0.063	0.051	0.055	0.068	0.057	0.058	0.059	0.0655
Drainage density	0.062	0.061	0.031	0.050	0.071	0.067	0.041	0.032	0.051	0.037	0.068	0.043	0.058	0.059	0.0522
Rainfall (annual)	0.041	0.041	0.031	0.025	0.036	0.067	0.027	0.063	0.026	0.027	0.046	0.034	0.029	0.029	0.0373
NDVI	0.041	0.041	0.031	0.025	0.018	0.033	0.027	0.063	0.051	0.027	0.039	0.034	0.029	0.029	0.0350
NDWI	0.124	0.122	0.125	0.099	0.107	0.100	0.081	0.095	0.077	0.055	0.068	0.086	0.087	0.088	0.0939
TWI	0.041	0.041	0.031	0.050	0.018	0.017	0.027	0.032	0.051	0.027	0.039	0.029	0.029	0.029	0.0329
SPI	0.021	0.020	0.031	0.025	0.036	0.017	0.027	0.016	0.026	0.018	0.030	0.021	0.058	0.059	0.0289
LULC	0.144	0.163	0.125	0.149	0.143	0.133	0.162	0.127	0.154	0.110	0.091	0.086	0.116	0.088	0.1280
Population density	0.186	0.184	0.250	0.198	0.214	0.233	0.324	0.222	0.231	0.330	0.274	0.343	0.203	0.206	0.2427
Building density	0.186	0.184	0.188	0.198	0.179	0.167	0.162	0.190	0.205	0.220	0.137	0.172	0.174	0.176	0.1812
Distance to nearest school	0.010	0.010	0.031	0.025	0.036	0.033	0.027	0.032	0.013	0.027	0.039	0.029	0.029	0.059	0.0286
Distance to nearest health center	0.021	0.010	0.031	0.025	0.036	0.033	0.027	0.032	0.013	0.037	0.039	0.029	0.014	0.029	0.0268

Altogether, the results reveal a distinct spatial dichotomy: flood vulnerability clusters in urbanized, low-lying coastal zones, while forested upland areas exhibit lower susceptibility. This pattern reflects the interplay between built infrastructure, socioeconomic exposure, and natural buffering systems. And the AHP–SMCA framework effectively captures these spatial relationships and provides a robust basis for prioritizing climate-resilient planning on small islands.

4.2. Social-Environmental hotspots to flood risk on Cat Ba Island

This study underscores the value of integrating GIS-based Spatial Multi-Criteria Analysis (SMCA) with the Analytic Hierarchy Process (AHP) to assess flood-related environmental, social vulnerability at a fine spatial scale. The weighting of 14 indicators produced a consistency ratio (CR) of 0.04, well below the 0.1 threshold (Saaty, 1980), confirming the reliability of expert-based judgments. The AHP–SMCA framework proves especially suited to small island settings, offering a transparent and transferable tool for spatial risk diagnostics.

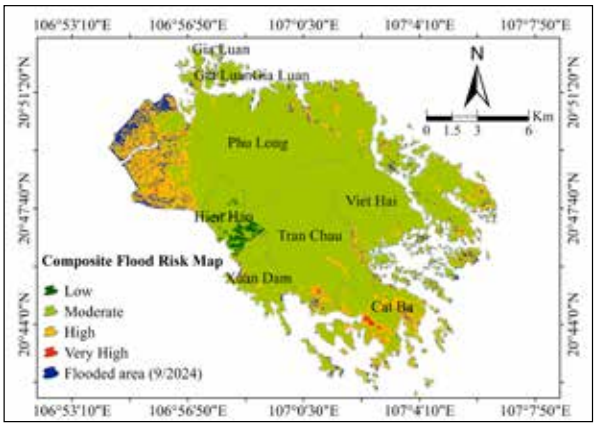

Figure 5. Composite Flood Risk Map of Cat Ba Island.

The comparison between the composite flood-risk map and the 2024 inundation footprint shows a strong correspondence in both magnitude and spatial pattern (Figure 5). Of the 172.85 km² study area, only 16.66 km² (9.6%) was flooded, and almost all of this inundation occurred within zones classified as moderate, high, or very high risk. The relationship between predicted risk zones and actual flood impacts becomes evident in Figure 6, where the extent of 2024 inundation is displayed alongside the area of each risk class. The low-risk class occupies just 0.06 km² (0.03% of the island) and contains only 0.00006 km² of flooding, confirming that areas mapped as low risk are effectively unaffected. Although the moderate-risk zone covers the largest share of the island (138.31 km²; 80%), it experienced only 5.91 km² of inundation (4.3% of its area). In contrast, the high-risk class (33.80 km²; 19.6%) contains 5.92 km² of flooding, accounting for 35.5% of the total inundation. The very-high-risk class shows the most pronounced contrast: although it occupies only 0.69 km² (0.4% of the island), the surrounding inundation associated with this class reaches 4.83 km², or nearly 29% of all observed flooding. These area ratios and the close spatial alignment show that flooded patches are concentrated mainly in low-lying coastal sectors classified as high or very high risk, whereas inland areas dominated by the moderate-risk class remain largely unaffected. Together, these patterns indicate that the composite flood-risk map effectively captures the principal flood-prone zones on Cat Ba Island.

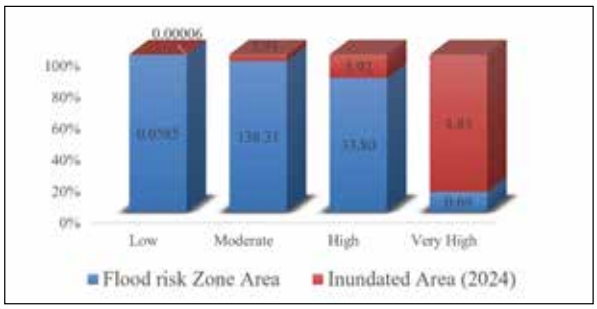

Figure 6. Discrepancy between flood risk zones and actual inundation (Sept 2024).

Several spatial hotspots aligned with the High and Moderate risk zones. In southern Tran Chau and Cat Ba town, high flood intensity was associated with low elevation, dense urbanization, and inadequate drainage systems. In Phu Long, both the ferry terminal area and western lowlands showed considerable exposure due to tidal backflow, estuarine influence, and functional infrastructure density. Meanwhile, southern Tran Chau, near Cat Ba town, displayed notable localized flooding patterns concentrated in natural depressions and valley floors, suggesting a combination of poor drainage and low-relief terrain.

By contrast, Hien Hao, which is located on the island's western flank, was predominantly classified as Very Low to Low flood risk, with minimal recorded inundation. This outcome can be attributed to several favorable physiographic and land cover characteristics. The area is dominated by elevated terrain, steep slopes, and dense vegetation, which facilitate rapid surface runoff and reduce water accumulation. Additionally, the absence of major urban infrastructure and minimal alteration of natural drainage patterns further mitigates the flood hazard in this sector. The contrast between Hien Hao and the southern lowland areas reinforces the role of topography, land use, and hydrological connectivity in defining localized flood risk.

Overall, these spatial patterns emphasize the need for targeted flood mitigation strategies that go beyond general zoning and address specific vulnerabilities in both densely developed and geomorphologically constrained areas of Cat Ba Island.

4.3. Discussion

The spatial distribution of social vulnerability on Cat Ba Island reveals a clear coastal-inland divide, carrying significant implications for both localized planning and broader theoretical discourse. High-vulnerability zones are primarily concentrated in low-lying, densely populated coastal communities (e.g., Cat Ba Town and Xuan Dam), whereas interior upland areas with intact forests and steeper terrain demonstrate markedly lower vulnerability. Figures 5 and 6 highlight that flood events in 2024 were largely confined to socially and environmentally vulnerable hotspots, thereby reinforcing the model's capacity to accurately delineate flood-prone zones on Cat Ba Island despite their

limited spatial extent. In essence, the GIS–AHP analysis not only pinpoints social–environmental hotspots of flood risk, but also empirically validates that elevated predicted vulnerability corresponds with a disproportionately high incidence of real-world flood impacts.

From a policy standpoint, this study provides a practical and spatially explicit framework for climate adaptation and spatial planning by identifying flood-prone social and environmental hotspots on Cat Ba Island. The results enable local authorities to prioritize high-risk zones such as Cat Ba Town and southern Tran Chau for targeted interventions such as drainage enhancement, climate-resilient infrastructure, and community-based preparedness strategies. Given the island's constrained evacuation capacity and infrastructure, strengthening adaptive capacity in urbanized coastal zones is especially urgent. Moreover, the findings underscore the need to regulate unplanned development in low-lying areas and to mainstream flood risk considerations into spatial planning processes. The overlay of flood data from 2024 further supports the critical protective role of upland forests and coastal mangroves, underscoring the value of nature-based solutions as cost-effective, complementary alternatives to conventional engineered defenses.

Beyond its practical applications, this study contributes to the theoretical understanding of flood vulnerability by illustrating how social and environmental factors interact to create concentrated risk in insular settings. On Cat Ba Island, high-exposure zones, which are characterized by dense populations, limited services, and poor drainage, closely align with areas of low elevation and intense land-use pressure. Together, these overlapping conditions give rise to well-defined social–environmental hotspots. This spatial overlap illustrates the compound nature of vulnerability, where socioeconomic stress and physical exposure reinforce each other. The contrast between flood-prone urban lowlands and more resilient upland areas highlights how vulnerability is highly place-specific and shaped by human–environment dynamics. By providing fine-scale, empirical evidence from a small island context, the study advances current frameworks by emphasizing the need for integrated approaches to climate risk that account for both social conditions and environmental constraints simultaneously.

The methodological contribution of this study lies in developing a transparent and replicable workflow that integrates AHP, GIS-based Spatial Multi-Criteria Analysis (SMCA), and Sentinel-1 SAR–derived flood data. The use of SAR imagery provided a robust validation layer, demonstrating that areas identified as highly vulnerable indeed corresponded with observed flood extents in 2024. By balancing expert-derived judgment with empirical satellite evidence, the approach ensures transparency and avoids the opacity of data-intensive "black box" models. Its reliance on open-access datasets and standard GIS techniques further enhances the transferability of the method to other small island settings facing similar constraints in monitoring capacity and planning resources. While the approach offers clear methodological and practical advantages, several limitations should be acknowledged to contextualize the findings and guide future research. Several methodological limitations warrant consideration. First, the use of 30-m resolution datasets may underrepresent micro-topographic depressions, drainage channels, and fine-scale urban structures that strongly influence local flood dynamics. Second, the AHP framework relies on expert judgment, which introduces a degree of subjectivity into the weighting process; although consistency checks were applied, the results may still vary depending on the composition and experience of the expert panel. Third, Sentinel-1 SAR imagery introduces potential uncertainty in steep or forested terrain, where layover, shadowing, and wet-surface backscatter can distort flood detection. Future work may address these limitations by incorporating higher-resolution elevation data, using multi-temporal SAR observations, and testing machine-learning classifiers. Such improvements would help enhance both the predictive accuracy and the broader applicability of the hotspot-based flood-risk framework.

5. Conclusion

This study demonstrates a practical and conceptually grounded approach for identifying social–environmental flood hotspots on Cat Ba Island by integrating expert-informed AHP weighting with spatial multi-criteria analysis. The framework advances current practice by linking social conditions with physical exposure in a single, transparent workflow that remains operational even in data-limited island environments. Validation with Sentinel-1 observations confirms that the model captures the spatial distribution of flood impacts, underscoring its suitability for risk screening and early-stage planning. More broadly, the approach offers a transferable tool for local governments seeking to prioritize adaptation measures, strengthen community preparedness, and safeguard natural buffers. Its emphasis on the combined social and environmental dimensions provides a useful direction for future climate-risk assessments on small islands, where tightly coupled human–environment dynamics shape vulnerability. Future work should build on this foundation by incorporating higher-resolution datasets and multi-event flood observations to enhance predictive robustness and support long-term climate adaptation strategies.

Acknowledgment

This research was funded and facilitated by the 2025 institutional science and technology project at Hanoi University of Mining and Geology, titled "Assessment of Social Vulnerability (SoVI) to Natural Hazards Using Google Earth Engine and Multi-temporal Remote Sensing Data in the Cat Ba Archipelago, Hai Phong City" (Project Code: T25-32). The authors express their sincere appreciation for this support.

References

Abijith, D., Saravanan, S., Parthasarathy, K., Reddy, N. M., Niraimathi, J., Bindajam, A. A., Mallick, J., Alharbi, M. M., & Abdo, H. G. (2025). Assessing the impact of climate and land use change on flood vulnerability: a machine learning approach in coastal region of Tamil Nadu, India. Geoscience Letters, 12(1), 1, https://doi.org/10.1186/s40562-025-00377-7.

Adnyana, I. M., & Wiguna, P. P. K. (2025). Modelling of flood hazard using topographic wetness index in Yeh Ho Watershed, Bali, Indonesia. I In Proceedings of the 10th International

Conference on Sustainable Agriculture, Food, and Energy (SAFE 2024), Jeju, Republic of Korea, 27–29 June 2024; Volume 159, p. 04002, https://doi.org/10.1051/bioconf/202515904002.

Ajtai, I., Ștefănie, H., Maloș, C., Botezan, C., Radovici, A., Bizău-Cârstea, M., & Baciu, C. (2023). Mapping social vulnerability to floods. A comprehensive framework using a vulnerability index approach and PCA analysis. Ecological Indicators, 154, 110838, https://doi.org/10.1016/j.ecolind.2023.110838.

Al-Sababhah, N. M. A. (2023). Integrated Evaluation of Soil Erosion-prone Areas Based on the GIS Technique and the Analytic Hierarchy Process on Hillside Slopes, Northwest of Jordan. Jordan Journal of Earth & Environmental Sciences, 14(2).

Alabbad, Y., & Demir, I. (2025). Understanding flood risk in public transit systems: Insights from accessibility and vulnerability analysis in Iowa. International Journal of Disaster Risk Reduction, 105615, https://doi.org/10.1016/j.ijdrr.2025.105615. (1-20.

Alonso, J. A., & Lamata, M. T. (2006). Consistency in the analytic hierarchy process: a new approach. International journal of uncertainty, fuzziness and knowledge-based systems, 14(04), 445-459, https://doi.org/10.1142/S0218488506004114.

Balaian, S. K., Sanders, B. F., & Abdolhosseini Qomi, M. J. (2024). How urban form impacts flooding. Nature Communications, 15(1), 6911, https://doi.org/10.21203/rs.3.rs-3650683/v1.

Bharwani, S., Taylor, R., Watkiss, P., & Devisscher, T. (2013). Decision Support Methods for Climate Change Adaptation: Analytic Hierarchy Process.

Birkmann, J., Jamshed, A., McMillan, J. M., Feldmeyer, D., Totin, E., Solecki, W., Ibrahim, Z. Z., Roberts, D., Kerr, R. B., & Poertner, H.-O. (2022). Understanding human vulnerability to climate change: A global perspective on index validation for adaptation planning. Science of the Total Environment, 803, 150065, https://doi.org/10.1016/j.scitotenv.2021.150065.

Boateng, I. (2012). GIS assessment of coastal vulnerability to climate change and coastal adaption planning in Vietnam. Journal of Coastal Conservation, 16(1), 25-36, https://doi.org/10.1007/s11852-011-0165-0.

Bukvic, A., Rohat, G., Apotsos, A., & de Sherbinin, A. (2020). A systematic review of coastal vulnerability mapping. Sustainability, 12(7), p. 2822, https://doi.org/10.3390/su12072822.

Chelariu, O.-E., Minea, I., & Iațu, C. (2024). Integrated assessment of geophysical and social vulnerability to natural hazards in North-East Region, Romania. Geomatics, Natural Hazards and Risk, 15(1), 2384607, https://doi.org/10.1080/19475705.2024.2384607.

Cutter, S. L., Boruff, B. J., & Shirley, W. L. (2012). Social vulnerability to environmental hazards. Social Science Quarterly 84, 242–261, https://doi.org/10.1111/1540-6237.8402002.

Dao, M. T., & Dao, M. T. (2024). Assessing the Vulnerability of Phu Quoc Island's Natural and Socioeconomic Systems to Climate Change. IOP Conference Series: Earth and Environmental Science, 1395, 012037, https://doi.org/10.1088/1755-1315/1395/1/012037

De Sherbinin, A., Bukvic, A., Rohat, G., Gall, M., McCusker, B., Preston, B., Apotsos, A., Fish, C., Kienberger, S., & Muhonda, P. (2019). Climate vulnerability mapping: A systematic review and future prospects. Wiley Interdisciplinary Reviews: Climate Change, 10(5), e600, https://doi.org/10.1002/wcc.600.

Du, S., Shi, P., Van Rompaey, A., & Wen, J. (2015). Quantifying the impact of impervious surface location on flood peak discharge in urban areas. Natural Hazards, 76(3), 1457-1471, https://doi.org/10.1007/s11069-014-1463-2.

Giang, P. Q., & Khanal, R. (2024). What next for marine ecosystem management in Vietnam: assessment of coastal economy, climate change, and policy implication. Environmental Research Communications, 6(2), 025002, https://doi.org/10.1088/2515-7620/ad19a5.

Ha-Mim, N. M., & Hossain, M. Z. (2022). Application of GIS and AHP-Based Integrated Methodology for Mapping and Characterizing Socioeconomic Vulnerability to Natural Hazards: A Case Study of Southwestern Coastal Bangladesh. In A System Engineering Approach to Disaster Resilience: Select Proceedings of VCDRR 2021 (pp. 187-203). Springer, https://doi.org/10.1007/978-981-16-7397-9_14.

Hamza, M., Eriksson, K., & Staupe-Delgado, R. (2021). Locating potential sources of capacity and vulnerability in geographically remote areas: Reflections based on three case studies. International Journal of Disaster Risk Reduction, 63, 102433, https://doi.org/10.1016/j.ijdrr.2021.102433.

Hoang, H. T. N., & Truong, H. Q. (2023). Assessing the Impact of Climate Change and the Resilience of Socio-ecological Systems: A Focus on the Red River Delta Biosphere Reserve in Vietnam. In The Vietnam-EU Economic and Trade Forum (pp. 321-342). Singapore: Springer Nature Singapore, https://doi.org/10.1007/978-981-99-8945-4_20.

Hue, L. M., Thao, V. T. P., Vy, N. K., Tra, D. T., & Nam, N. N. (2024). Land cover object change monitoring and environmental suitability confirmation in Cat Ba Biosphere Reserve of Vietnam. Biodiversity, 25(4), 324-336, https://doi.org/10.1080/14888386.2024.2385975.

Ibrahim, M., Huo, A., Ullah, W., Ullah, S., Ahmad, A., & Zhong, F. (2024). Flood vulnerability assessment in the flood prone area of Khyber Pakhtunkhwa, Pakistan. Frontiers in Environmental Science, 12, 1303976, https://doi.org/10.3389/fenvs.2024.1303976

Isia, I., Hadibarata, T., Jusoh, M. N. H., Bhattacharjya, R. K., Shahedan, N. F., Fitriyani, N. L., & Syafrudin, M. (2023). Identifying factors to develop and validate social vulnerability to floods in Malaysia: a systematic review study. Sustainability, 15(17), 12729, https://doi.org/10.3390/su151712729.

Janzen, S., Balzer, J., Merk, F., Eberle, C., Chabi, A., & Walz, Y. (2024). Moving towards a comprehensive evaluation of ecosystem-based disaster risk reduction: The example of agroforestry for flood risk reduction. Nature-Based Solutions, 5, 100104, https://doi.org/10.1016/j.nbsj.2023.100104.

Ji, L., Zhang, L., & Wylie, B. (2009). Analysis of dynamic thresholds for the normalized difference water index. Photogrammetric engineering & remote sensing, 75(11), 1307-1317, https://doi.org/10.14358/PERS.75.11.1307.

Justine, Y. E. D., & Seenath, A. (2025). Vegetative nature-based solutions for coastal flood risk management: Benefits, challenges, and uncertainties. Ocean & Coastal Management, 261, 107520, https://doi.org/10.1016/j.ocecoaman.2024.107520.

Khan, T. U., Nabi, G., Ullah, S., Akbar, A., Omifolaji, J. K., Achakzai, J. K., & Iqbal, A. (2025). Mapping flood resilience: a comprehensive geospatial insight into regional vulnerabilities. Frontiers in Water, 7, 1465505.

Khodaei, H., Nasiri Saleh, F., Nobakht Dalir, A., & Zarei, E. (2025). Future flood susceptibility mapping under climate and land use change. Scientific Reports, 15(1), 12394, https://doi.org/10.3389/frwa.2025.1465505.

Kocsis, I., Bilașco, Ș., Irimuș, I.-A., Dohotar, V., Rusu, R., & Roșca, S. (2022). Flash flood vulnerability mapping based on FFPI using GIS spatial analysis case study: Valea Rea catchment area, Romania. Sensors, 22(9), 3573, https://doi.org/10.3390/s22093573.

Komolafe, A., Awe, B., Olorunfemi, I., & Oguntunde, P. (2020). Modelling flood-prone area and vulnerability using integration of multi-criteria analysis and HAND model in the Ogun River Basin, Nigeria. Hydrological Sciences Journal, 65(10), 1766-1783, https://doi.org/10.1080/02626667.2020.1764960.

Konapala, G., Kumar, S. V., & Ahmad, S. K. (2021). Exploring Sentinel-1 and Sentinel-2 diversity for flood inundation mapping using deep learning. ISPRS Journal of Photogrammetry and Remote Sensing, 180, 163-173, https://doi.org/10.1016/j.isprsjprs.2021.08.016.

Ma, J., & Mostafavi, A. (2024). Urban form and structure explain variability in spatial inequality of property flood risk among US counties. Communications Earth & Environment, 5(1), 172, https://doi.org/10.1038/s43247-024-01337-3.

Mai, N. T., & Truong, D. D. (2022). Farming Households' Perception on Natural Disaster Impacts to Livelihoods and Adaptation Practices: A Case Study of Coastal Provinces in Central Vietnam. International Journal of Sustainable Development & Planning, 17(2), https://doi.org/10.18280/ijsdp.170223.

Maliva, R. (2021). Climate change and small islands. In Climate Change and Groundwater: Planning and Adaptations for a Changing and Uncertain Future: WSP Methods in Water Resources Evaluation Series No. 6 (pp. 155-176). Springer.

Miranda, F., Franco, A. B., Rezende, O., da Costa, B. B., Najjar, M., Haddad, A. N., & Miguez, M. (2023). A GIS-based index of physical susceptibility to flooding as a tool for flood risk management. Land, 12(7), 1408, https://doi.org/10.3390/land12071408.

Newspaper, H. P. (2025). Flood alert issued for low-lying areas in Hai Phong due to rising river levels. Retrieved 19/11/2025 from https://dangcongsan.vn/haiphong/tin-tuc-hoat-dong/canh-bao-lu-tren-cac-song-o-hai-phong.html?utm_source=chatgpt.com

Oroud, I. M. (2025). The Relative Impact of Urbanization Expansion and Climate Change on Flood Hazard in Amman City. Jordan Journal of Earth & Environmental Sciences, 16(1).

Parmesan, C., Morecroft, M. D., & Trisurat, Y. (2022). Terrestrial and Freshwater Ecosystems and Their Services. In: Climate Change 2022: Impacts, Adaptation and Vulnerability. Contribution of Working Group II to the Sixth Assessment Report of the Intergovernmental Panel on Climate Change [H.-O. Pörtner, D.C. Roberts, M. Tignor, E.S. Poloczanska, K. Mintenbeck, A. Alegría, M. Craig, S. Langsdorf, S. Löschke, V. Möller, A. Okem, B. Rama (eds.)]. Cambridge University Press, Cambridge, UK and New York, NY, USA, pp. 197–377, doi:10.1017/9781009325844.004.

Rautela, K. S., Kumar, D., Gandhi, B. B. G. R., Kumar, A., & Dubey, A. K. (2023). Flood Vulnerability Assessment Across Alaknanda River Basin using GIS-based combined analysis of geomorphometric approach and MCDM-AHP. Journal of the Geological Society of India, 99(11), 1604-1615, https://doi.org/10.1007/s12594-023-2512-9.

Rudin, C. (2019). Stop explaining black box machine learning models for high stakes decisions and use interpretable models instead. Nature machine intelligence, 1(5), 206-215, https://doi.org/10.1038/s42256-019-0048-x.

Saaty, T. (1980). McGraw-Hill; New York: 1980. The Analytic Hierarchy Process: Planning, Priority Setting, Resource Allocation McGraw-Hill, New York, 1980.

Shivhare, V., Kumar, A., Kumar, R., Shashtri, S., Mallick, J., & Singh, C. K. (2024). Flood susceptibility and flood frequency modeling for lower Kosi Basin, India using AHP and Sentinel-1 SAR data in geospatial environment. Natural Hazards, 120(13), 11579-11610, https://doi.org/10.1007/s11069-024-06614-0

Son, C. H., Lee, C. H., & Ban, Y. U. (2023). Analysis of the impact and moderating effect of high-density development on urban flooding. Heliyon, 9(12), https://doi.org/10.1016/j.heliyon.2023.e22695

Ta, K. L., & Linh, P. K. (2024). Integrating Women's Rights and Climate Migrant Protection: Bridging Gaps in Vietnam. Human Rights in the Global South (HRGS), 3(1), 79-100, https://doi.org/10.56784/hrgs.v3i2.109

Tariq, A., Yan, J., Ghaffar, B., Qin, S., Mousa, B., Sharifi, A., Huq, M. E., & Aslam, M. (2022). Flash flood susceptibility assessment and zonation by integrating analytic hierarchy process and frequency ratio model with diverse spatial data. Water, 14(19), 3069, https://doi.org/10.3390/w14193069.

Tetteh, A. T., Moomen, A.-W., Yevugah, L. L., & Tengnibuor, A. (2024). Geospatial approach to pluvial flood-risk and vulnerability assessment in Sunyani Municipality. Heliyon, 10(18).

Tuyet Hanh, T. T., Huong, L. T. T., Huong, N. T. L., Linh, T. N. Q., Quyen, N. H., Nhung, N. T. T., Ebi, K., Cuong, N. D., Van Nhu, H., & Kien, T. M. (2020). Vietnam climate change and health vulnerability and adaptation assessment, 2018. Environmental Health Insights, 14, 1178630220924658.

Uddameri, V., & Hernandez, E. A. (2025). Machine Learning for Flood Resiliency—Current Status and Unexplored Directions. Environments, 12(8), 259, https://doi.org/10.3390/environments12080259.

Udie, J., Bhattacharyya, S., & Ozawa-Meida, L. (2018). A conceptual framework for vulnerability assessment of climate change impact on critical oil and gas infrastructure in the niger delta. Climate, 6(1), 11, https://doi.org/10.3390/cli6010011

Van Phong, T., Nguyen, D. D., & Pham, B. T. (2023). Modeling and Mapping of Flood Susceptibility at Que Son District, Quang Nam Province, Vietnam using CatBoost. IOP conference series: materials science and engineering (Vol. 1289, No. 1, p. 012019). IOP Publishing, 10.1088/1757-899X/1289/1/012019.

Van Quan, N., Duc, T. T., & Van Huy, D. (2010). Landscapes and ecosystems of tropical limestone: case study of the Cat Ba Islands, Vietnam. Journal of Ecology and Environment, 33(1), 23-36, http://dx.doi.org/10.5141/JEFB.2010.33.1.023.

VnExpress. (2024). Cat Ba tourist island ravaged by Typhoon Yagi. Retrieved 19/11/2025 from https://e.vnexpress.net/photo/places/cat-ba-tourist-island-ravaged-by-typhoon-yagi-4791507.html?utm_source=chatgpt.com

Vousdoukas, M. I., Athanasiou, P., Giardino, A., Mentaschi, L., Stocchino, A., Kopp, R. E., Menéndez, P., Beck, M. W., Ranasinghe, R., & Feyen, L. (2023). Small Island Developing States under threat by rising seas even in a 1.5 C warming world. Nature sustainability, 6(12), 1552-1564, https://doi.org/10.1038/s41893-023-01230-5

Xie, W., & Meng, Q. (2023). An integrated PCA–AHP method to assess urban social vulnerability to sea level rise risks in Tampa, Florida. Sustainability, 15(3), 2400, https://doi.org/10.3390/su15032400

Yarveysi, F., Alipour, A., Moftakhari, H., Jafarzadegan, K., & Moradkhani, H. (2023). Block-level vulnerability assessment reveals disproportionate impacts of natural hazards across the conterminous United States. Nature Communications, 14(1), 4222, https://doi.org/10.1038/s41467-023-39853-z.

Zakir, H. M. (2024). Study on the groyne arrangement for protection of riverbank erosion of braided river in lowland area. Doctoral dissertation). Nagoya University.

Zhran, M., Ghanem, K., Tariq, A., Alshehri, F., Jin, S., Das, J., Pande, C. B., Pramanik, M., Hasher, F. F. B., & Mousa, A. (2024). Exploring a GIS-based analytic hierarchy process for spatial flood risk assessment in Egypt: A case study of the Damietta branch. Environmental Sciences Europe, 36(1), 184, https://doi.org/10.1186/s12302-024-01001-9.

JJEES

JJEES (2026) 17 (2): 236-246
ISSN 1995-6681

Jordan Journal of Earth and Environmental Sciences

Evaluating Lemon-Derived Biochar for Synthetic Dye Removal: A Green Approach to Water Treatment

Fawwaz Khalili[1], Omar Alnasra[1*], Omar Almaani[2], and Shrouq AlAzzeh[1]

[1] Department of Chemistry, Faculty of Science, The University of Jordan, Amman, Jordan.
[2] Department of Chemistry, Faculty of Science, Petra University, Amman, Jordan.

Received on 1 March 2025; Accepted on 15 December 2025

Abstract

Synthetic cationic dyes, such as crystal violet (CV) and methylene blue (MB), are persistent water pollutants that pose toxicological risks and impair aquatic ecosystems, while conventional activated carbons remain relatively expensive and are not always derived from sustainable sources. There is a particular lack of systematic kinetic and thermodynamic data for commercially available lemon-derived charcoals used under near-neutral pH conditions relevant to water treatment. This study evaluates the adsorption performance of a lemon-derived charcoal (LC) adsorbent for effectively removing CV and MB from aqueous solutions. The 'adsorbent's physico-chemical characteristics were determined by Fourier transform infrared (FTIR) spectroscopy, X-ray diffraction (XRD), thermogravimetric analysis (TGA), and scanning electron microscopy (SEM), confirming the presence of functional groups (e.g., hydroxyl, carbonyl, and phenolic) and a porous microstructure crucial for dye binding. Operational factors, including adsorbent dosage, contact time, and temperature, were examined to optimize adsorption. Kinetic results indicated that both dyes followed a pseudo-second-order model, consistent with a chemisorption-controlled rate. Isotherm analyses demonstrated a predominantly monolayer adsorption mechanism compatible with the Langmuir model, yielding maximum dye removal efficiencies of 82.24% for CV and 77.37% for MB. Thermodynamic assessment revealed that CV adsorption is exothermic, while MB adsorption is endothermic. Overall, these findings underscore the potential of commercially available lemon-derived charcoal as an eco-friendly and cost-effective adsorbent for mitigating dye pollution in wastewater treatment systems.

Keywords: *lemon charcoal; crystal violet; methylene blue; water treatment; waste recycling*

1. Introduction

The release of synthetic dyes, such as crystal violet (CV) and methylene blue (MB), from textile, pharmaceutical, and food industries is a significant source of water pollution. These cationic dyes are persistent, bioactive molecules that can cause eye and skin irritation, cyanosis, and potentially carcinogenic effects in humans and animals (Senthilkumaar et al., 2005; Saeed et al., 2010; Li et al., 2016; Ibrahim et al., 2019). In surface waters, their intense color reduces light penetration, suppressing photosynthesis and disrupting aquatic food webs, which ultimately degrades water quality and ecosystem stability (Wang et al., 2019; Cheng et al., 2022). As global concerns about water quality and environmental sustainability continue to grow, there is an increasing demand for efficient and cost-effective methods to remove these pollutants from water sources (Bikram et al., 2023). Adsorption is recognized as a promising approach for the removal of dyes from aqueous solutions due to its simplicity, effectiveness, and versatility (Gupta and Suhas, 2009; Al-Jboor and Khalili, 2011; Alnasra and Khalili, 2023). Over the past decade, researchers have made substantial progress in exploring novel adsorbent materials to address the dye removal challenge. Among these materials, activated carbon derived from agricultural waste products has garnered attention for its affordability, sustainability, and remarkable adsorption capabilities (Foo and Hameed, 2012; Öztürk and Bektaş, 2004).

Lemon charcoal, as a potential candidate in this context, is derived from lemon peels, which are often discarded as waste. Several studies have investigated the adsorption properties of lemon charcoal for various pollutants, showcasing its potential as a versatile adsorbent material (Foo and Hameed, 2012; Öztürk and Bektaş, 2004; Al-Qadri et al., 2024). The utilization of lemon charcoal as an adsorbent material not only offers a sustainable solution to waste management but also holds promise for efficient dye removal (Foo and Hameed, 2012; Ramutshatsha-Makhwedzha et al., 2022). The utilization of lemon peels in this study aligns with the global effort to minimize agricultural waste and repurpose it for environmental remediation. Lemon peels, often discarded as by-products of the citrus industry, are a valuable resource due to their high lignocellulosic content and bioactive compounds. This study demonstrates how these residues can be transformed into functional biochar, contributing to a circular economy model. Beyond lemon peels, future research should explore integrating other agricultural wastes, such as orange peels, banana skins, and sugarcane bagasse, to diversify potential adsorbent sources. Such efforts would not only reduce waste generation but also expand the scope of sustainable water

* Corresponding author e-mail: o_alnasra@ju.edu.jo

treatment technologies. This research aims to contribute to the existing body of knowledge by examining the adsorption capacity of LC specifically for CV and MB, two dyes with distinct chemical properties. Understanding the adsorption behavior of lemon charcoal towards these dyes is crucial for its practical application in wastewater treatment and environmental remediation. Moreover, it provides an opportunity to explore the underlying mechanisms governing the adsorption process, contributing to a broader understanding of adsorption phenomena.

2. Experimental

2.1 Chemicals and Preparation of the Adsorbent

All chemicals used in this study were of analytical grade. Commercial lemon-wood charcoal in granular form was purchased from a local supplier in Amman, Jordan, and is marketed simply as "LC". CV and MB were analytical-grade dyes, obtained from Gain Chemical Company (GCC) and s.d. Fine-Chem Ltd., respectively. According to the 'manufacturers' specifications, both dyes have dye content ≥ 90% and were used as received without further purification. Hydrochloric acid (HCl, 37%) was purchased from Tedia, and sodium hydroxide pellets (NaOH) from Merck KGaA.

LC was supplied as a pre-carbonized lemon-wood charcoal produced industrially by slow pyrolysis in limited oxygen. The manufacturer did not disclose the exact operating temperature or provide specific BET surface area or pore volume data; therefore, information on microstructure and porosity was inferred from the XRD, SEM, and TGA analyses presented in Section 3.1, which are consistent with a high-temperature (>400°C) woody biochar (Tintner et al., 2018; Dittmann et al., 2022). In our laboratory, the charcoal was gently ground in a Mini-Philips mill, sieved to select particles with sizes between 125 and 250 µm, rinsed several times with deionized water to remove fines and soluble impurities, and then oven-dried at 105°C for 24 h. No additional chemical activation or surface modification was applied, so that the adsorption performance reflects a readily available low-cost LC.

2.2 Instrumentation

A mini-Philips mining machine was employed to grind the adsorbent material. All mass measurements were conducted with precision using the RADWAG® AS 220 analytical balance. For LC characterization, a variety of advanced instruments were utilized. FTIR spectra were obtained using a Thermo-Nicolet NEXUS 670 FT-IR spectrophotometer. Thermal analysis, specifically TGA, was performed using a NETZCH STA 409 PG/PC thermal analyzer under a nitrogen atmosphere, with a heating rate of 20 °C per minute over the temperature range of 0 to 1000 °C. Powder X-ray diffraction (XRD) was conducted using a Philips 'X'Pert PW 3060 instrument, with controlled scanning parameters set at a rate of 1°/min over a 2θ range of 2° to 60°. The three-dimensional surface morphology was examined via scanning electron microscopy (SEM) using the 'NCFL's FEI QUANTA 600 FEG model. The concentrations of CV and MB in solution were determined spectrophotometrically using a METASH UV-Vis spectrophotometer model V-5100 equipped with a 1.0 cm quartz cell.

2.3 Calibration curves for dyes

In this study, calibration curves and their corresponding equations were derived by measuring the absorbance of standard solutions of CV and MB at specified concentrations. For CV, absorbance measurements were taken at a wavelength of 590 nm for solutions with concentrations ranging from 0.10 to 10.0 mg/L. For MB, absorbance was measured at 665 nm for solutions with concentrations between 1.0 and 15.0 mg/L. All calibration solutions were prepared in deionized water whose pH was adjusted to 7.0 ± 0.1 using minimal volumes of 0.1 M HCl or NaOH, matching the pH employed in the equilibrium adsorption experiments. Calibration plots, along with regression equations and coefficients of determination (R^2) are provided in Supplementary Figure S1 for both dyes. For any sample whose absorbance exceeded the linear range of the corresponding calibration curve, the solution was diluted with deionized water so that the final absorbance fell within the calibrated interval. Throughout this work, dye concentrations in aqueous solution are expressed in mg/L (for dilute aqueous solutions, 1 mg/L ≈ 1 ppm).

2.4 Adsorption experiments

A one-factor-at-a-time optimization strategy was employed to determine the optimal conditions for the batch adsorption experiments. In a typical run, 25.0 mL of dye solution (CV or MB), with initial concentrations of 10 mg/L for CV and 30 mg/L for MB, was used, and the pH of the solutions adjusted to values between 4 and 8 for CV and 3 and 8 for MB, using 0.1 M HCl or NaOH. The adsorbent, lemon-wood charcoal, was added in varying amounts (0.010–0.90 g) to the solutions in 100 mL plastic bottles, followed by agitation at 25 °C for 60 min. The effect of contact time was investigated separately by varying the contact time between 10 and 120 min. The suspensions were then filtered using nylon micro-filters (0.45 µm), and the concentration of unadsorbed dye in the filtrate was measured using the UV–Vis spectrophotometer. Adsorption isotherm experiments were also conducted at pH 7.0 and constant temperatures of 25.0, 35.0, and 45.0 °C with initial dye concentrations ranging from 3 to 20 mg/L for CV and 5 to 60 mg/L for MB. For isotherm experiments, the suspensions were shaken for 60 min to reach equilibrium and then filtered. The removal percentage of dyes was calculated as a function of pH, adsorbent dose, contact time, and temperature. Unless otherwise stated, each experimental condition was repeated three times and the mean value is reported. Method blanks (deionized water only), LC-only controls without dye, and dye solutions passed through 0.45 µm filters in the absence of LC were included in each batch to verify the absence of background signals and filtration losses at the measurement wavelengths.

Finally, kinetic and isotherm studies were conducted under optimal conditions for each dye to elucidate the characteristics of the adsorption reaction. Kinetic studies were carried out by monitoring dye uptake as a function of time (10–120 min) at fixed initial concentrations, while adsorption isotherms were examined at the concentration ranges specified above. The kinetic (PFO, PSO) and equilibrium (Langmuir, Freundlich, Dubinin–Radushkevich, and Temkin) models used in this work are widely reported in

the adsorption literature (Cheng et al., 2022; Gugushe et al., 2021; Mpupa et al., 2020).

2.5 Determination of the point of zero charge (pH_{pzc})

The point of zero charge (pH_{pzc}) of LC was determined using the pH-drift method. A series of 50.0 mL 0.01 M NaCl solutions was prepared, and their initial pH (pH_i) adjusted to the range 2.0–12.0 using 0.1 M HCl or 0.1 M NaOH. Then, 0.05 g of LC was added to each solution in 100 mL screw-cap bottles, and the suspensions were agitated at 25 ± 1 °C for 24 h. After equilibration, the final pH (pH_f) was measured. The difference $\Delta pH = pH_f - pH_i$ was plotted as a function of pH_i, and the pH_{pzc} was taken as the pH_i at which $\Delta pH = 0$.

2.6 Data analysis

All batch adsorption experiments were performed in triplicate (n = 3). Model parameters for kinetic and equilibrium studies were obtained by least-squares linear regression of the corresponding linearized equations. In the figures, data points represent mean values and the error bars correspond to ±1 standard deviation. The goodness of fit for each model was evaluated by the coefficient of determination (R^2).

2.7 Equilibrium and kinetic models

The equilibrium adsorption data were analyzed using the Langmuir, Freundlich, D–R, and Temkin isotherm models. In their non-linear forms, these models can be written as shown in Table 1. For parameter estimation, the corresponding linearized forms were used.

Table 1. Models for linear and non-linear sorption isotherms

Isotherm model	Non-linear equation	Linear equation	Reference
Langmuir	$q_e = \frac{q_m K_L C_e}{1 + K_L C_e}$	$\frac{C_e}{q_e} = \frac{1}{q_{max} K_L} + \left(\frac{1}{q_{max}}\right) C_e$	Langmuir, 1918
Freundlich	$q_e = K_F C_e^{1/n}$	$Log q_e = \log K_F + \frac{1}{n} \log C_e$	Freundlich, 1906
D-R	$q_e = q_m e^{-\beta \varepsilon^2}$	$\ln q_e = \ln q_{max} - \beta \varepsilon^2$	Dubinin, 1960
Temkin	$q_e = \frac{RT}{b_T} \ln(K_T C_e)$	$q_e = \frac{RT}{b_T} \ln C_e + \frac{RT}{b_T} \ln K_T$	Temkin, 1940

The following two models were used in kinetic evaluation to better understand how the dyes adsorb to LC sorbent:

Pseudo-first-order (PFO) [30]:

$$\ln(q_e - q_t) = \ln q_e - k_1 t \quad (3)$$

and pseudo-second-order (PSO) [21]:

$$\frac{t}{q_t} = \frac{1}{k_2 q_e^2} + \frac{t}{q_e} \quad (4)$$

3. Results and discussion

3.1. Physio-chemical properties of the adsorbents

The functional groups present on the LC were examined using FTIR spectroscopy. The analysis of the functional groups present on the surface of the LC was conducted using a potassium bromide (KBr) disk at a 10% ratio. The spectrum of the LC adsorbent, as illustrated in Figure 1, reveals that the predominant functional group specified in LC is as follows: A broad peak around 3413 cm^{-1} indicates the stretching of the O─H bond in hydroxyl surface functional groups on the LC surface (Nuhanović et al., 2019; Kar 2020; Janu et al., 2021; Roy et al., 2022). This O─H group is associated with phenols, alcohols, and carboxylic acids found in the chemical components of lemon wood, such as lignin, cellulose, hemicellulose, and organic acids (Šabanović et al., 2019). Low-intensity adsorption peaks at 2924 cm^{-1} and 2854 cm^{-1} suggest the presence of symmetric aliphatic C─H functional groups (CH_2 and CH_x) (Nuhanović et al., 2019; Ankona et al., 2021; Sirico et al., 2021; Ramutshatsha-Makhwedzha et al., 2022). These peaks, are likely linked to carbohydrate groups such as methoxy, methylene, and methyl groups (Rožič et al., 2014; Šabanović et al., 2019). Additionally, a double peak between 2339 and 2362 cm^{-1} is attributed to the stretching of CO_2 bonds (Stevens et al., 2008). A peak at 1841 cm^{-1} indicates the presence of ester functional groups, and a C═O bond near 1703 cm^{-1} likely originates from carbonyl groups (Alam et al., 2018; Hasan et al., 2021). The adsorption band in the range of 1613–1616 cm^{-1} corresponds to C═O stretching in esters, quinones, and ketones, as well as to conjugated C═C bonds (Rožič et al., 2014; Senophiyah-Mary et al., 2019; Roy et al., 2022). A peak around 1438 cm^{-1} suggests the presence of C─OH bonds (Alam et al., 2018), with similar peaks reported in studies on LC (Foroutan et al., 2021; Azadian and Gilani, 2023). Peaks in the range of 1315–1317 cm^{-1} may be attributed to CH_2 bending (Mariño et al., 2015). Stretching vibrations of C─O bonds, possibly from carbohydrates, appear at the broad peak at 1236 cm^{-1}. A small peak at 898 cm^{-1} is likely due to C─H stretching in the aromatic structures of lignin (Li et al., 2014), while the band near 875 cm^{-1} is associated with asymmetric stretching of CO_3^{2-} (Al-Hosney and Grassian, 2005; Kalina et al., 2022; Mishra et al., 2023). Distinctive peaks between 617 and 780 cm^{-1} correspond to C─H bending in phenyl rings (Stella Mary et al., 2016; Foroutan et al., 2021; Mishra et al., 2023).

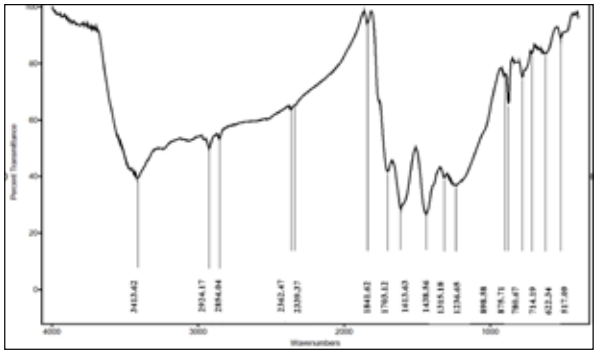

Figure 1. FTIR spectrum of LC for the investigation of the functional groups on the surface of the LC over a scanning range between 400 and 4000 cm-1

The thermogram in Figure 2a shows an initial mass loss below 200°C, which is attributed mainly to the desorption of physically adsorbed water and light volatile compounds. A further weight loss between approximately 200 and 400°C is associated with the decomposition of residual oxygen-containing surface groups and partially carbonized fragments remaining in the commercial charcoal. A more gradual mass loss between about 400 and 600°C likely reflects further dehydrogenation and condensation of aromatic structures. At higher temperatures, from 700 to 1000°C, the decomposition of inorganic carbonates (e.g., $CaCO_3$) and other mineral constituents contributes to the residual mass changes, leaving a predominantly carbonaceous and mineral residue (Gomide et al., 2020; Dittmann et al., 2022). TGA was used here to verify that LC is thermally stable under

the conditions employed for adsorption experiments and to obtain additional information on the degree of carbonization and ash content.

The crystal phase and microstructure of the synthesized LC were validated through XRD, with the diffractographic pattern providing a definitive confirmation of a broad background (Figure 2b), indicating a predominantly amorphous structure in the adsorbent with at least four sharp crystalline peaks. The range from 2θ = 2.00° to 2θ = 15.00° corresponds to the micro-crystallographic features of biochar-type adsorbents (Danish et al., 2018). Peaks at 2θ = 15.22°, 23.30°, 24.71°, 30.36°, 36.24°, 38.36°, 39.66°, 43.40°, 47.76°, and 48.74° are attributed to the crystalline graphite structure, while the peak at 29.65° is due to $CaCO_3$ in LC and the crystalline graphite-like structure (Xie et al., 2014; Jafri et al., 2018; Tintner et al., 2018; Oruç et al., 2019; Kar, 2020; Gabhi et al., 2020; Poonam and Kumar, 2020; Surya and Michael, 2021; Pérez et al., 2023).

The SEM images revealed that LC has a well-developed, irregular, and porous structure with many cavities. These images confirm that the wood cell and porosity morphologies remain prominent in the final biochar, with the adsorbent retaining much of the original wood cell structure. Moreover, the outer surface features varying pore sizes formed during pyrolysis. In Figure 2c (1000x magnification), the adsorbent shows wide and thick particles revealing characteristic wood structures, aligning with literature findings (Gomide et al., 2020). Figure 2d (4000x magnification) shows diverse pore sizes and shapes, indicating a high surface area (Kütahyalı and Eral, 2010; Azadian and Gilani, 2023).

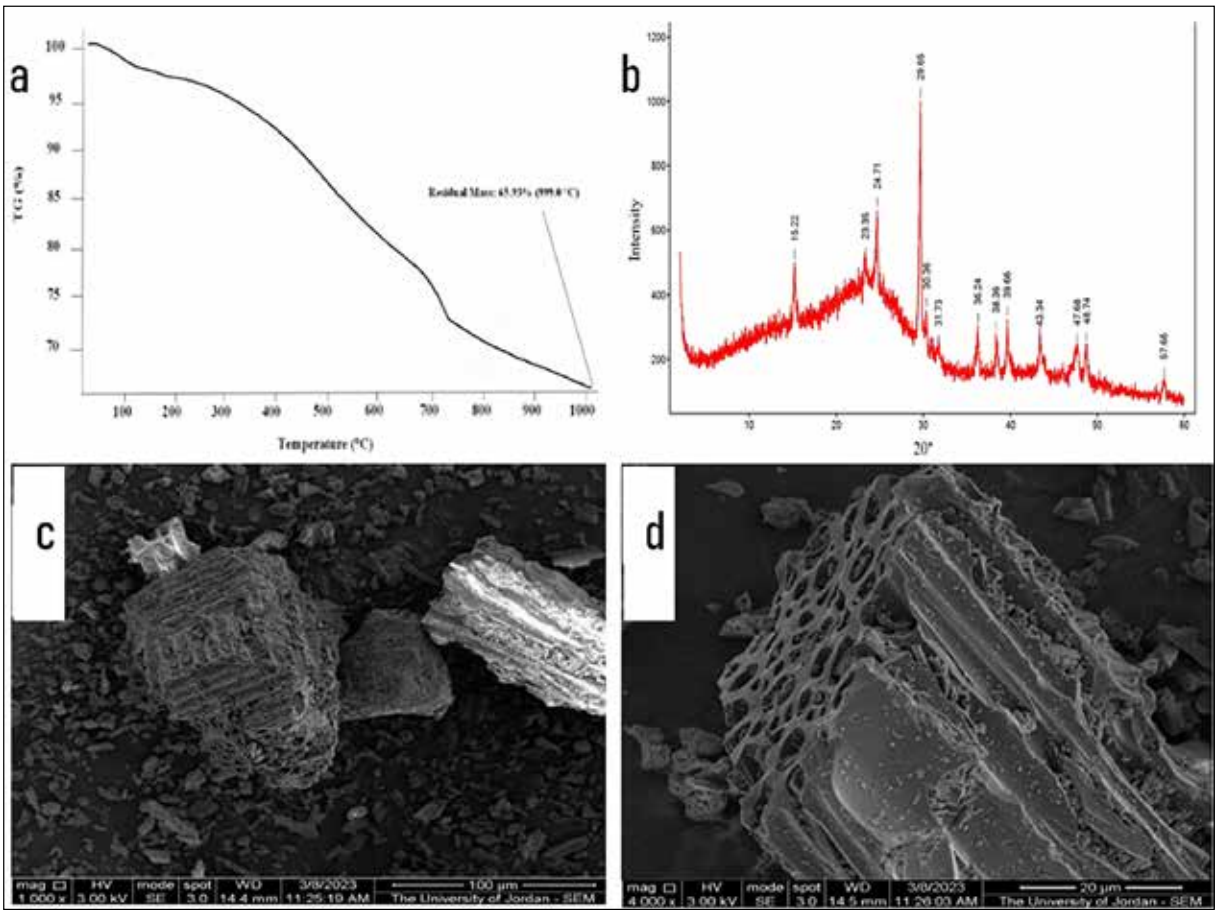

Figure 2. (**a**) TGA thermogram, (**b**) XRD spectrum, (**c**)–(**d**) SEM image

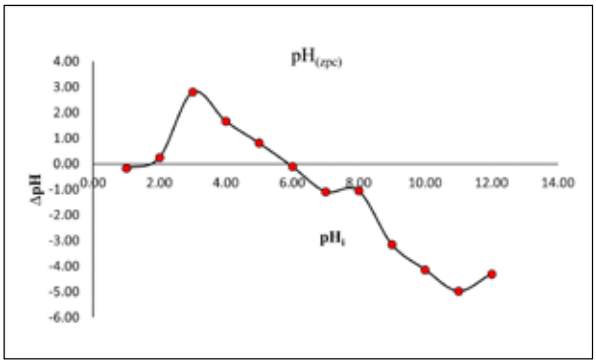

Figure 3. Determination of pH_pzc of LC by the pH-drift method. The intersection of the curve ($\Delta pH = pHf - pH_i$) with $\Delta pH = 0$ occurs at pH ≈ 6.

3.2. Evaluation of the adsorption performance of LC

3.2.1. Adsorption experiment studies

The solution pH strongly influences dye adsorption because it controls both the adsorbent surface charge and the ionization state of the dye molecules (Baloo et al., 2021; Gupta et al., 2021). In the present study, the removal of CV and MB was examined over pH 3–8, and only minor variations in uptake (< 5 %) were observed, indicating weak pH dependence (Supplementary Material, Figure S2). Both dyes remain cationic across these ranges—their ionizable functional groups (tertiary amine for CV, dimethylamino for MB) are protonated under neutral and mildly basic conditions, giving them a permanent positive charge. In contrast, LC possesses oxygen-containing surface groups (carboxyl,

phenolic, and lactonic) that progressively deprotonate above pH 3–4, imparting a net negative zeta potential to the surface (Rožič et al., 2014; Šabanović et al., 2019). Consequently, strong electrostatic attraction between positively charged dye molecules and the negatively charged LC surface is maintained throughout the investigated pH window. Only at pH > 8 would surface deprotonation saturation and hydroxide competition begin to reduce adsorption, but such conditions were not examined here. This mechanistic explanation aligns with prior studies on citrus-derived biochars and peels, which reported nearly constant adsorption of cationic dyes at neutral pH regions due to dominant electrostatic and π–π stacking interactions (Senthilkumaar et al., 2005; Foroutan et al., 2021; Ramutshatsha-Makhwedzha et al., 2022). Accordingly, pH 7.0 was selected for subsequent experiments as representative of natural and treated waters. As shown in Figure 3, the pH_pzc of LC was 6. Thus, the LC surface is expected to be positively charged at pH < 6 and predominantly negatively charged at pH > 6. Since the adsorption experiments were conducted mainly at pH 7.0 (> pH_pzc), electrostatic attraction between the cationic dyes (CV and MB) and negatively charged LC surface sites is favored, which is consistent with the high removal efficiencies observed.

The adsorbent dosage is another critical operational variable. The effect of LC mass (0.01–0.90 g) on the uptake of CV and MB is presented in Figure 4. For both dyes, the percentage removal increased markedly with increasing LC mass and reached a plateau at 0.10 g, at which the adsorbent became effectively saturated and further increases in dosage produced only marginal additional removal. The slight decrease in the uptake expressed as qe (mg g^{-1}) at higher dosages arises from the lower driving force per unit mass at constant initial dye concentration. On this basis, an LC mass of 0.10 g was selected for all subsequent experiments.

Contact time was then optimized. Adsorption of both dyes on LC was very fast, with most of the uptake occurring within the first few minutes and no significant changes observed up to 120 min (Supplementary Material, Figure S3). To ensure that equilibrium was fully attained under all investigated conditions, a contact time of 60 min was adopted for the kinetic, isotherm, and thermodynamic studies.

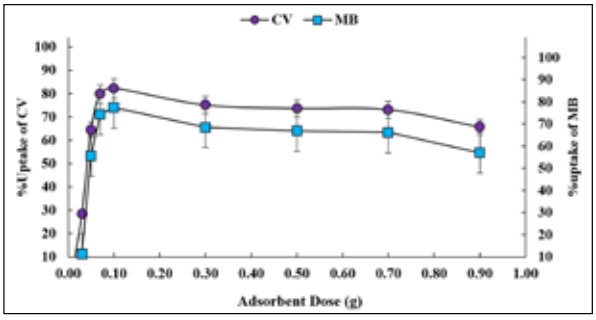

Figure 4. Effect of adsorbent does on % uptake of CV and MB on LC

3.2.2. Isotherms data studies

Equilibrium adsorption data for CV and MB were interpreted using the Langmuir, Freundlich, D–R, and Temkin models, which respectively describe monolayer adsorption on homogeneous sites, multilayer adsorption on heterogeneous surfaces, adsorption on energetically non-uniform sites, and adsorbate–adsorbent interactions (Langmuir, 1918; Freundlich, 1906; Dubinin, 1960). Isotherms were obtained at 25, 35, and 45 °C, and representative linear plots at 45 °C are shown in Figure 5. For both dyes, the equilibrium data fitted the Langmuir model very well (Figure 5a), indicating predominantly monolayer coverage, while the good agreement with the Freundlich and Temkin models (Figure 5b) reflects surface heterogeneity and non-negligible adsorbate–adsorbent interactions. The D–R model provided additional insight into the mean adsorption energy (E) and supported a predominantly physisorption-controlled process (Fig. 4c). The isotherms for the CV and MB dyes were studied at 25, 35, and 45 °C. The obtained data were assessed using the R2 coefficient, determined from the linear fits of the isotherm models. The isotherms were plotted as an illustrative example at 45°C (Figure 5) for both dyes. Figure 5a showed excellent agreement with Langmuir for both CV and MB dyes, indicating the presence of a monolayer and homogeneous adsorption sites. Also Figure 5b shows excellent fitting with the Freundlich model, suggesting the presence of heterogeneous sites for both dyes. The D-R model showed relatively good fit and supports the notion that LC contains both homogeneous and heterogeneous sites (Figure 5c).

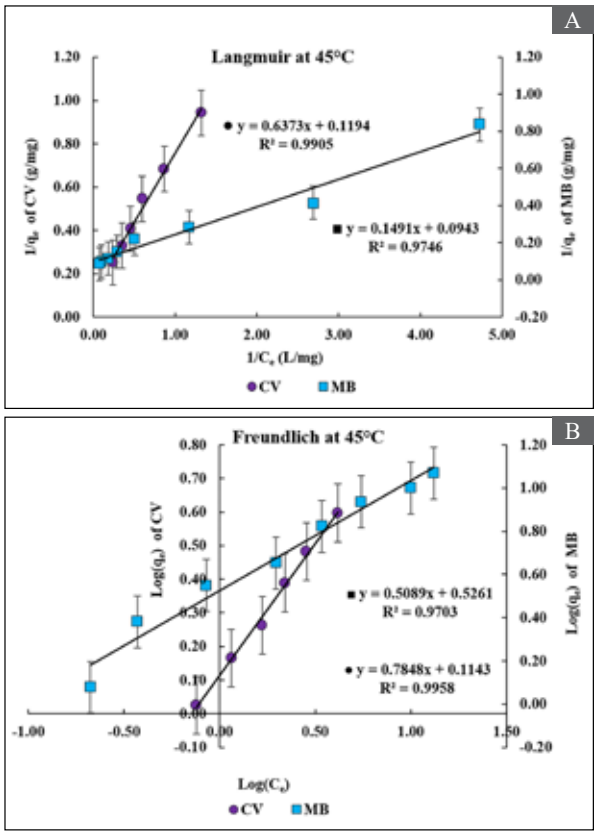

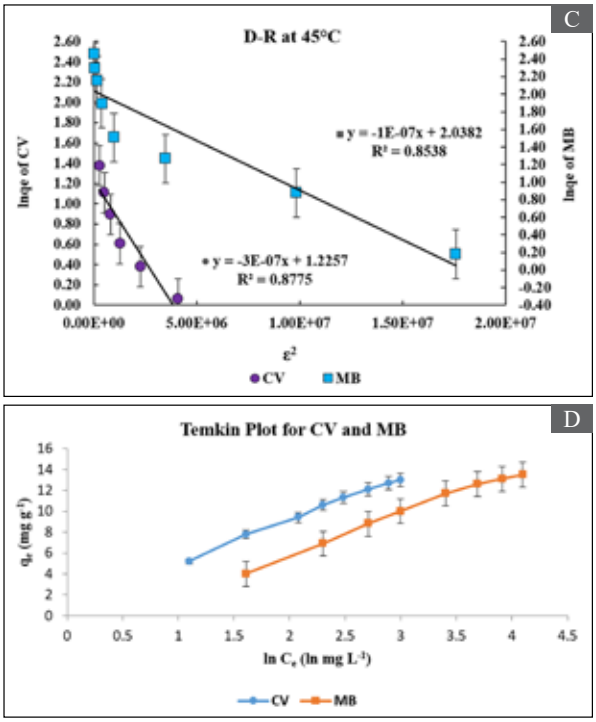

Figure 5. **a**) Langmuir **b**) Freundlich **c**) D-R **d**) Temkin models for CV and MB at 45 °C.

Table 1 presents adsorption isotherm parameters for the removal of CV and MB dyes using LC at different temperatures. For CV, the Langmuir isotherm showed the highest correlation coefficient (R2) values, particularly at 25 and 35°C (R2 = 0.991 and 0.993, respectively), suggesting monolayer adsorption as the dominant mechanism. The maximum adsorption capacity (qm) increased with temperature, indicating an endothermic process. The Langmuir separation factor (RL) values ranged from 0 to 1, indicating favorable adsorption. The Freundlich isotherm also showed high R2 values, indicating the possibility of heterogeneous adsorption. Freundlich constant (n) values greater than 1 indicate favorable adsorption conditions. In the D–R isotherm, the adsorption energy (E) was below 8 kJ/mol, implying a physical adsorption mechanism. The Temkin model provided a good fit across all temperatures, with R2 values exceeding 0.98, highlighting the influence of adsorbent-adsorbate interactions.

For MB, the Langmuir model also fitted the equilibrium data well at all three temperatures, with the highest R^2 observed at 45 °C (R^2 = 0.975). The Langmuir q_m value estimated at 25 °C is markedly higher than those obtained at 35 and 45 °C, leading to an apparent decrease from 25 to 35 °C followed by a slight increase from 35 to 45 °C. This non-monotonic behavior should be interpreted cautiously. Because the 25 °C isotherm was constructed over a relatively narrow C_e range and exhibits very high R^2, small experimental uncertainties in C_e can strongly affect the extrapolated q_m while leaving R^2 almost unchanged. Within the experimental scatter, the q_m values at 35 and 45 °C are of the same order of magnitude and consistent with the positive ΔH° obtained from the thermodynamic analysis, indicating that MB adsorption remains favorable at all three temperatures rather than being strongly enhanced specifically at 25 °C. The Langmuir separation factor (RL) values for MB remained between 0 and 1 at all temperatures, confirming favorable adsorption. Freundlich isotherm results also showed high R^2 values, indicating adsorption on a heterogeneous surface, and the n values > 1 reflect favorable adsorption conditions. The D–R model yielded adsorption energies E < 8 kJ mol^{-1}, consistent with a process dominated by physical adsorption, while the Temkin model gave good correlations (R^2 > 0.97), highlighting the role of adsorbent–adsorbate interactions.

The previous results indicate that adsorption capacity and isotherm model fit vary with temperature for CV and MB. For both dyes, the Langmuir and Freundlich models consistently provided the best description of the equilibrium data, suggesting the coexistence of monolayer adsorption on relatively homogeneous sites and additional uptake on heterogeneous surface sites. For CV, the increase in qm with temperature is consistent with the thermodynamic analysis and supports an endothermic adsorption process. For MB, the non-monotonic trend in qm (higher value at 25 °C followed by a decrease at 35 °C and a slight increase at 45 °C) should be interpreted cautiously in light of the limited Ce span and resulting sensitivity of the extrapolated qm at 25 °C. Overall, the isotherm analysis confirms that LC is an effective adsorbent for both CV and MB over the investigated temperature range, with adsorption primarily governed by physical interactions and surface heterogeneity.

To place the LC performance in context, it is useful to compare the present results with other citrus-derived and lignocellulosic adsorbents reported in the literature. Activated carbons and engineered biochars prepared from lemon and other citrus wastes often exhibit higher Langmuir capacities for cationic dyes under strongly optimized or chemically activated conditions (Foroutan et al., 2021; Ramutshatsha-Makhwedzha et al., 2022; Mishra et al., 2023). By contrast, the as-received lemon-wood charcoal used in this work, operated at near-neutral pH without additional activation, shows moderate capacities but achieves effective removal of both CV and MB with simple processing and low chemical input. This places LC among the class of low-cost, readily available sorbents whose main advantages are sustainability, ease of use, and operation under environmentally relevant conditions, rather than maximized capacity alone.

Kinetic studies

Pseudo-first-order (PFO) and pseudo-second-order (PSO) kinetic equations were used to describe the kinetic characteristics that control mechanisms of adsorption processes, such as mass transfer and chemical reactions. In pseudo-second-order reaction kinetics, the kinetic data from solid/solution sorption systems are described and correlated using this mathematical expression, which is currently the most widely used. By comparing the experimental qe values with the calculated PSO kinetic plots, it is possible to determine the viability of this model. CV shows excellent fitting to PSO with R2 of one (Figure 6), while it shows very poor correlation coefficient of 0.1954 for PFO. This means that the rate determining step in the adsorption of CV into LC involve a chemisorption process. Similarly, MB showed excellent agreement with PSO and very poor one with PFO. Also this means that the rate determining step in the adsorption of MB into LC is a chemisorption step.

Table 1. Langmuir, Freundlich, D-R isotherm, and Temkin parameters for LC towards CV and MB, at different temperatures.

CV														
T(°C)	Langmuir Isotherm				Freundlich Isotherm			D–R Isotherm				Temkin Isotherm		
	R2	q_m (mg/g)	K_L (L/mg)	R_L	R^2	n (g/L)	K_F (mg /g)	R^2	B (mol^2/kJ^2)	qm (mg/g)	E (kJ/ mol)	R^2	K_T (L/g)	b_T (kJ/mol)
25.0	0.991	2.76	14.92	0.51	0.966	3.40	2.53	0.875	1.70 E-08	2.85	5.42	0.982	0.07	1.44
35.0	0.993	3.18	1.00	0.74	0.984	3.32	1.10	0.784	2.07 E-08	2.41	4.92	0.991	0.11	1.38
45.0	0.893	8.38	0.19	0.86	0.996	1.27	1.30	0.878	3.17 E-07	3.41	1.26	0.999	0.29	4.72
MB														
T(°C)	Langmuir Isotherm II				Freundlich Isotherm			D–R Isotherm				Temkin Isotherm		
	R^2	q_m (mg/g)	K_L (L/mg)	R_L	R^2	n (g/L)	K_F (mg /g)	R^2	B (mol^2/kJ^2)	qm (mg/g)	E (kJ/ mol)	R^2	K_T (L/g)	b_T (kJ/mol)
25.0	0. 900	341.4	0.014	0.38	0.966	0.75	4.39	0.875	4.54 E-07	16.88	1.05	0.992	6.309E-03	18.98
35.0	0.936	4.31	1.00	0.63	0.985	0.56	0.06	0.784	5.71 E-06	9.88	2.96	0.975	2.256E+05	24.02
45.0	0.975	10.60	0.63	0.86	0.996	2.24	3.71	0.878	9.76 E-08	6.29	2.26	0.988	0.1248	9.68

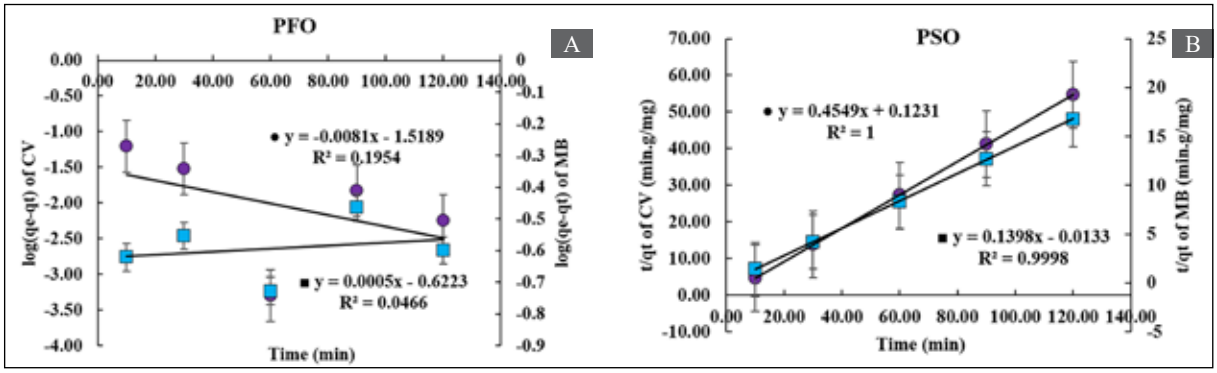

Figure 6. a) PFO **b**) PSO for the adsorption of CV and MB on LC

Table 2. Kinetic parameters for CV and MB adsorption on LC at 25 °C

CV			
Experimental qe = 2.200 (mg/g)			
Model	R2	k	Calculated qe (mg/g)
PFO	0.1954	k1= 1.87×10-2 min-1	0.028
PSO	1.0000	k2=5.96×10-1 g (mg.min)-1	2.198
MB			
Experimental qe = 7.189 mg/g			
Model	R2	k	Calculated qe mg/g
PFO	0.0443	k1= -1.38×10-3 min-1	0.030
PSO	1.0000	k2=1.19 g (mg.min)-1	7.189

Table 2 summarizes the kinetic parameters obtained for CV and MB with excellent agreement between experimental qe and calculated qe. It was 2.200 and 2.198 for CV, respectively, while for MB the values were 7.191 and 7.189, respectively. Also, it showed that the rate constant k2 (PSO) for MB is greater than that for CV. This means the rate of uptake for MB is larger than that of CV.

Thermodynamics

Thermodynamic parameters were evaluated from batch adsorption experiments conducted at initial dye concentrations of 10 mg/L for CV and 30 mg/L for MB, using equilibrium data obtained at 25, 35, and 45 °C. For each dye and temperature, the distribution coefficient was calculated as Kd = qe/Ce ($L\ g^{-1}$). The standard Gibbs free energy change was then obtained from $\Delta G° = -RT \ln Kd$, where (R) is the universal gas constant, and (T) is the absolute temperature. The enthalpy and entropy changes were determined from the 'van't Hoff relationship $\ln Kd = \Delta S°/R - \Delta H°/(RT)$ by plotting (ln Kd) versus (1/T) and performing linear regression. Table 3 shows the resulting thermodynamic parameters for CV and MB at different temperatures. These parameters offer insights into the feasibility, spontaneity, and thermal effects of the adsorption processes. The ln Kd values for CV decreased with increasing temperature, indicating reduced adsorption affinity at higher temperatures. The negative $\Delta G°$ values across all temperatures confirm that the adsorption process is spontaneous, with $\Delta G°$ decreasing as temperature increases. This suggests that higher temperatures weaken the spontaneity of adsorption, possibly due to desorption effects or decreased adsorbent-adsorbate interactions. The negative

ΔH° value (-148.19 kJ/mol) indicates that the adsorption of CV onto LC is exothermic. The negative ΔS° value (-0.46 kJ/mol·K) suggests decreased randomness at the solid-liquid interface during adsorption, consistent with dye molecules being immobilized on the LC surface. For MB, the ln Kd values increased with temperature, reflecting enhanced adsorption affinity at elevated temperatures. The ΔG° values are negative at all temperatures, confirming the spontaneous nature of the adsorption. Furthermore, the magnitude of ΔG° becomes more negative with increasing temperature, indicating greater spontaneity at higher temperatures. The positive ΔH° value (39.90 kJ/mol) demonstrates that the adsorption of MB is endothermic, implying that increased temperature facilitates the adsorption process. The positive ΔS° value (0.14 kJ/mol·K) indicates increased randomness at the solid-liquid interface during adsorption, possibly due to the displacement of water molecules by MB onto the adsorbent surface. The thermodynamic analysis reveals contrasting behaviors for CV and MB adsorption. While CV adsorption is exothermic and less favorable at higher temperatures, MB adsorption is endothermic and improves with temperature. These differences may stem from the distinct physicochemical interactions between each dye and the LC. The negative ΔG° values for both dyes highlight the viability of the biochar as an effective adsorbent for removing CV and MB from aqueous solutions, although the optimal temperature conditions differ for each dye.

Table 3. Thermodynamic parameters for CV and MB at different temperatures

CV						
T (°K)	1/T (°K^{-1})	ln K_d	K_d	ΔG° (kJ/mol)	ΔS° (kJ/mol)	ΔH° (kJ/mol)
298.15	0.0034	4.23	68.72	-11.46	-0.46	-148.19
308.15	0.0032	3.54	34.47	-6.90		
318.15	0.0031	0.45	1.57	-2.32		
MB						
T (°K)	1/T (°K^{-1})	ln K_d	K_d	ΔG° (kJ/mol)	ΔS° (kJ/mol)	ΔH° (kJ/mol)
298.15	0.0034	1.01	2.75	-2.20	0.14	39.90
308.15	0.0032	1.16	3.19	-3.61		
318.15	0.0031	2.03	7.16	-5.03		

Proposed adsorption mechanism

The combined characterization and adsorption results suggest that multiple interaction mechanisms contribute to the uptake of CV and MB on LC. FTIR analysis (Figure 1) indicates the presence of abundant oxygen-containing surface groups (e.g., hydroxyl, carbonyl, and carboxylic moieties) and aromatic structures, while XRD and SEM (Figure 2) reveal a largely amorphous carbon matrix with graphitic domains and a porous morphology. The measured pH_pzc of LC (pH ≈ 6; Figure 3) and the weak pH dependence of dye removal between pH 3 and 8 indicate that, at the working pH 7.0, the LC surface is predominantly negatively charged, favoring electrostatic attraction with the cationic forms of CV and MB. In addition to this electrostatic contribution, π–π stacking interactions between the aromatic rings of the dyes and the graphitic domains of LC, as well as possible hydrogen bonding between dye functional groups and surface oxygenated sites, are likely to play a role. The D–R adsorption energies (E < 8 kJ mol^{-1}; Table 1) and the temperature dependence of q_m and ΔG° (Table 3) point to a process dominated by physical adsorption, while the excellent fit of the pseudo-second-order kinetic model (Figure 6, Table 2) reflects the importance of surface interactions in controlling the overall rate. The somewhat stronger affinity observed for CV relative to MB under comparable conditions may be related to differences in molecular size, planarity, and charge distribution, which influence the balance of electrostatic and π–π interactions with the LC surface.

While this study emphasizes the removal of synthetic dyes, specifically CV and MB, the potential of LC extends beyond these applications. Biochar's porous structure and surface functional groups make it suitable for adsorbing a wide range of contaminants, including heavy metals, pharmaceuticals, and organic pollutants. Preliminary studies suggest that LC can effectively remove cadmium, lead, and arsenic ions from aqueous solutions, indicating its versatility as an adsorbent. In this work, LC was evaluated using synthetic single-dye solutions as a first step toward understanding its intrinsic adsorption behavior. Future studies should investigate the efficacy of LC in complex real water matrices, such as textile and mixed industrial wastewaters, and its potential for simultaneous removal of multiple pollutants. Additionally, an important practical consideration for any sorbent is its regenerability and service lifetime. In the present work, we did not perform systematic adsorption–desorption cycling experiments; our primary objective was to establish the intrinsic equilibrium, kinetic, and thermodynamic behavior of as-received LC toward CV and MB. Nevertheless, previous studies on citrus-derived biochars have shown that cationic dyes can be desorbed under mild alkaline or solvent treatment, with substantial retention of adsorption capacity over multiple cycles (Foroutan et al., 2021; Ramutshatsha-Makhwedzha et al., 2022; Mishra et al., 2023). Because regeneration efficiency and capacity retention directly determine the adsorbent cost per unit volume of treated water, future work will focus on quantifying LC reusability, mass loss, and energy input over repeated adsorption–desorption cycles, and on comparing these metrics with those of commercial activated carbon.

4. Conclusions

The conversion of lemon peels into biochar offers a cost-effective, environmentally responsible alternative to conventional adsorbents such as activated carbon. Nevertheless, the overall environmental impact of biochar production warrants scrutiny, especially regarding the energy requirements for pyrolysis and the possible release of volatile organic compounds. Incorporating renewable energy sources, such as solar or biomass, could help mitigate these challenges and enhance sustainability. In addition, a comprehensive economic analysis comparing lemon-derived biochar with conventional adsorbents would inform large-scale adoption for water treatment applications. This investigation confirms that LC is highly effective for removing CV and MB from aqueous solutions. Characterization by FTIR, SEM, TGA, and XRD demonstrated the presence of functional groups, a porous microstructure, satisfactory thermal stability, and an amorphous nature, all of which are suitable for adsorption. Both dyes followed the Langmuir and Freundlich isotherm models, with kinetics aligning with a pseudo-second-order mechanism indicative of chemisorption. Thermodynamic analyses revealed that CV uptake is exothermic and spontaneous at lower temperatures, while MB adsorption is endothermic, showing increased spontaneity at higher temperatures. LC exhibited a distinctly higher partition coefficient for CV (Kd = 68.72) than for MB (Kd = 2.75), making it particularly useful in treatments involving mixed-dye pollutants. By repurposing waste materials, this approach advances multiple United Nations Sustainable Development Goals, including SDG 6 (Clean Water and Sanitation) and SDG 12 (Responsible Consumption and Production). Although regeneration experiments were not carried out in this study, the literature on citrus-derived biochars indicates that regeneration can be achieved with moderate energy inputs, which is essential for maintaining competitive treatment costs relative to commercial activated carbon (Foroutan et al., 2021; Ramutshatsha-Makhwedzha et al., 2022). Accordingly, future research should focus on pilot- and field-scale assessments that explicitly quantify LC regeneration efficiency, cycling-induced capacity loss, and the resulting cost per unit volume of treated water, in addition to evaluating long-term performance in complex wastewaters.

Acknowledgment

This work has been carried out by Fawwaz I. Khalili during a sabbatical leave from the University of Jordan, chemistry department, with the support of the Deanship of Scientific Research.

Statements and Declarations

Data Availability

The authors confirm that the data supporting the findings of this study are available within the article and its supplementary materials.

Disclosure statement

No potential conflict of interest was reported by the authors.

References

Alam, M. S., Gorman-Lewis, D., Chen, N., Safari, S., Baek, K., Konhauser, K. O., & Alessi, D. S. (2018). Mechanisms of the removal of U(VI) from aqueous solution using biochar: A combined spectroscopic and modeling approach. Environmental Science & Technology, 52(22), 13057-67. https://doi.org/10.1021/acs.est.8b01715

Al-Hosney, H. A., & Grassian, V. H. (2005). Water, sulfur dioxide, and nitric acid adsorption on calcium carbonate: A transmission and ATR-FTIR study. Physical Chemistry Chemical Physics, 7(6), 1266. https://doi.org/10.1039/b417872f

Al-Jboor, M. M., & Khalili, F. I. (2011). Removal of nitrate ions from water using Jordanian lemon wood and olive seeds charcoal. International Journal of Arts and Sciences, 4(19), 283.

Alnasra, O. A., & Khalili, F. I. (2023). Synthesis and characterization of a nanosilica-cysteine composite for arsenic(III) ion removal. Acta Chimica Slovenica, 70(4), 674-89. https://doi.org/10.17344/acsi.2023.8160

Al-Qadri, F., Abdulrahman, J., Yahia, A., & Faleh, N. (2024). Bio adsorbent lemon peels charcoal to remove Fe(III) from water sources. Interciencia, 32(1), 3-20. https://doi.org/10.59671/Ch5fn

Ankona, E., Multanen, V., Nisnevitch, M., Billig, M., & Anker, Y. (2021). Investigation of pyrolysis kinetics and gaseous compounds emitted during charcoal production from woods commonly used in the eastern Mediterranean. Biofuels, Bioproducts and Biorefining, 15(3), 646-56. https://doi.org/10.1002/bbb.2188

Azadian, M., & Gilani, H. G. (2023). Adsorption of Cu2+, Cd2+, and Zn2+ by engineered biochar: Preparation, characterization, and adsorption properties. Environmental Progress & Sustainable Energy, 42(4), 14088. https://doi.org/10.1002/ep.14088

Baloo, L., Isa, M. H., Sapari, N. B., Jagaba, A. H., Wei, L. J., Yavari, S., Razali, R., & Vasu, R. (2021). Adsorptive removal of methylene blue and acid orange 10 dyes from aqueous solutions using oil palm wastes-derived activated carbons. Alexandria Engineering Journal, 60(6), 5611-29. https://doi.org/10.1016/j.aej.2021.04.044

Singh, B. J., Chakraborty, A., & Sehgal, R. (2023). A systematic review of industrial wastewater management: Evaluating challenges and enablers. Journal of Environmental Management, 348, 119230. https://doi.org/10.1016/j.jenvman.2023.119230

Cheng, S., Zhao, S., Xing, B., Liu, Y., Zhang, C., & Xia, H. (2022). Preparation of magnetic adsorbent-photocatalyst composites for dye removal by synergistic effect of adsorption and photocatalysis. Journal of Cleaner Production, 348, 131301. https://doi.org/10.1016/j.jclepro.2022.131301

Danish, M., Ahmad, T., Hashim, R., Said, N., Akhtar, M. N., Mohamad-Saleh, J., & Sulaiman, O. (2018). Comparison of surface properties of wood biomass activated carbons and their application against rhodamine B and methylene blue dye. Surfaces and Interfaces, 11, 1-13. https://doi.org/10.1016/j.surfin.2018.02.001

Dittmann, D., Saal, L., Zietzschmann, F., Mai, M., Altmann, K., Al-Sabbagh, D., Schumann,

P., Ruhl, A. S., Jekel, M., & Braun, U. (2022). Characterization of activated carbons for water treatment using TGA-FTIR for analysis of oxygen-containing functional groups. Applied Water Science, 12(8), 203. https://doi.org/10.1007/s13201-022-01723-2

Dubinin, M. M. (1960). The potential theory of adsorption of gases and vapors for adsorbents with energetically non-uniform surfaces. Chemical Reviews, 60(2), 235-41. https://doi.org/10.1021/cr60204a006

Foo, K. Y., & Hameed, B. H. (2012). Coconut husk derived activated carbon via microwave-induced chemical activation: Effects of activation agents on porous structure. Journal of

Hazardous Materials, 190, 8-14. https://doi.org/10.1016/j.cej.2011.12.084

Foroutan, R., Peighambardoust, S. J., Peighambardoust, S. H., Pateiro, M., Lorenzo, J. M. (2021). Adsorption of Crystal Violet dye using activated carbon of lemon wood and activated carbon/Fe3O4 magnetic nanocomposite from aqueous solutions: A kinetic, equilibrium, and thermodynamic study. Molecules, 26(8), 2241. https://doi.org/10.3390/molecules2608224

Freundlich, H. M. F. (1906). Over the adsorption in solution. The Journal of Physical Chemistry A, 57(385),1100-7.

Gabhi, R., Basile, L., Kirk, D. W., Giorcelli, M., Tagliaferro, A., Jia, C. Q. (2020). Electrical conductivity of wood biochar monoliths and its dependence on pyrolysis temperature. Biochar, 2(3), 369-78. https://doi.org/10.1007/s42773-020-00056-0

Gomide, R. A. C., De Oliveira, A. C. S., Rodrigues, D. A. C., De Oliveira, C. R., De Assis, O. B. G., Dias, M. V., & Borges, S. V. (2020). Development and characterization of lignin microparticles for physical and antioxidant enhancement of biodegradable polymers. Journal of Polymers and the Environment, 28(4), 1326-34. https://doi.org/10.1007/s10924-020-01685-z

Gugushe, A. S., Mpupa, A., Munonde, T. S., Nyaba, L., & Nomngongo, P. N. (2021). Adsorptive removal of Cd, Cu, Ni, and Mn from environmental samples using Fe3O4-ZrO2@APS nanocomposite: Kinetic and equilibrium isotherm studies. Molecules, 26(11), 3209. https://doi.org/10.3390/molecules26113209

Gupta, V. K., & Suhas, (2009). Application of low-cost adsorbents for dye removal—a review. Journal of Environmental Management, 90(8), 2313-42. https://doi.org/10.1016/j.jenvman.2008.11.017

Gupta, A., Sharma, V., Sharma, K., Kumar, V., Choudhary, S., Mankotia, P., Kumar, B., Mishra, H., Moulick, A., Ekielski, A., & Mishra, P. K. (2021). A review of adsorbents for heavy metal decontamination: Growing approach to wastewater treatment. Materials, 14(16), 4702. https://doi.org/10.3390/ma14164702

Hasan, M. N., Shenashen, M. A., Hasan, M. M., Znad, H., & Awual, M. R. (2021). Assessing cesium removal from wastewater using functionalized wood cellulosic adsorbent. Chemosphere, 270, 128668. https://doi.org/10.1016/j.chemosphere.2020.128668

Ibrahim, A., Fawal, G., & Akl, M. (2019). Methylene blue and crystal violet dyes removal (as a binary system) from aqueous solution using local soil clay: Kinetics study and equilibrium isotherms. Egyptian Journal of Chemistry, 62(3), 541-554. https://doi.org/10.21608/ejchem.2018.4113.1360

Janu, R., Mrlik, V., Ribitsch, D., Hofman, J., Sedláček, P., Bielská, L., & Saja, G. (2021). Biochar surface functional groups as affected by biomass feedstock, biochar composition, and pyrolysis temperature. Carbon Resources Conversion, 4, 36-46. https://doi.org/10.1016/j.crcon.2021.01.003

Kalina, M., Sovova, S., Hajzler, J., Kubikova, L., Trudicova, M., Smilek, J., & Enev, V. (2022). Biochar texture—a parameter influencing physicochemical properties, morphology, and agronomical potential. Agronomy, 12(8), 1768. https://doi.org/10.3390/agronomy12081768

Kar, K. K. (2020). Handbook of Nanocomposite Supercapacitor Materials I: Characteristics. Springer Cham, Switzerland. https://doi.org/10.1007/978-3-030-43009-2

Kütahyalı, C., & Eral, M. (2010). Sorption studies of uranium and thorium on activated carbon prepared from olive stones: Kinetic and thermodynamic aspects. Journal of Nuclear Materials, 396(2–3), 251-6. https://doi.org/10.1016/j.jnucmat.2009.11.018

Langmuir, I. (1918). The adsorption of gases on plane surfaces of glass, mica, and platinum. J Journal of the American Chemical Society, 40(9), 1361-403. https://doi.org/10.1021/ja02242a004

Li, J., Li, Y., Wu, Y., & Zheng, M. A. (2014). Comparison of biochars from lignin, cellulose, and wood as the sorbent to an aromatic pollutant. Journal of Hazardous Materials, 280:450-7. https://doi.org/10.1016/j.jhazmat.2014.08.033

Li, Q., Ma, X., Hu, C., & Zhai, J. (2016). Removal of methylene blue from aqueous solution with magnetite loaded multi-walled carbon nanotube: Kinetics, isotherms, and thermodynamics. Journal of Industrial and Engineering Chemistry, 39, 93-101.

Mariño, M., Lopes Da Silva, L., Durán, N., & Tasic, L. (2015). Enhanced materials from nature: Nanocellulose from citrus waste. Molecules, 20(4), 5908-23. https://doi.org/10.3390/molecules20045908

Mishra, A., Ojha, H., Pandey, J., Tiwari, A. K., & Pathak, M. (2023). Adsorption characteristics of magnetized biochar derived from Citrus limetta peels. Heliyon, 9(10), e20665. https://doi.org/10.1016/j.heliyon.2023.e20665

Mpupa, A., Nqombolo, A., Mizaikoff, B., & Nomngongo, P. N. (2020). Enhanced adsorptive removal of β-Estradiol from aqueous and wastewater samples by magnetic nano-Akaganeite: Adsorption isotherms, kinetics, and mechanism. Processes, 8(9), 1197. https://doi.org/10.3390/pr8091197

Nuhanović, M., Grebo, M., Draganović, S., Memić, M., & Smječanin, N. (2019). Uranium(VI) biosorption by sugar beet pulp: Equilibrium, kinetic and thermodynamic studies. Journal of Radioanalytical and Nuclear Chemistry, 322(3), 2065-78. https://doi.org/10.1007/s10967-019-06877-z

Oruç, Z., Ergüt, M., Uzunoğlu, D., & Özer, A. (2019). Green synthesis of biomass-derived activated carbon/Fe-Zn bimetallic nanoparticles from lemon (Citrus limon (L.) Burm. f.) wastes for heterogeneous Fenton-like decolorization of Reactive Red 2. Journal of Environmental Chemical Engineering, 7(4), 103231. https://doi.org/10.1016/j.jece.2019.103231

Öztürk, N., & Bektaş, T. E. (2004). Nitrate removal from aqueous solution by adsorption onto various materials. Journal of Hazardous Materials, 112(1–2), 155-62. https://doi.org/10.1016/j.jhazmat.2004.05.001

Pérez, S., Ulloa, M., Flórez, E., Acelas, N., Ocampo-Pérez, R., Padilla-Ortega, E., & Forgionny, A. (2023). Valorization of lemon peel wastes into a potential adsorbent for simultaneous removal of copper ion (Cu^{2+}) and Congo red from wastewater. Environmental Nanotechnology, Monitoring & Management, 20, 100795. https://doi.org/10.1016/j.enmm.2023.100795

Poonam, & Kumar, N. (2020). Experimental and kinetic study of removal of lead (Pb+2) from battery effluent using sweet lemon (Citrus limetta) peel biochar adsorbent. Environment, Development and Sustainability, 22(5), 4379-406. https://doi.org/10.1007/s10668-019-00389-2

Ramutshatsha-Makhwedzha, D., Mavhungu, A., Moropeng, M., & Mbaya, R. (2022). Activated carbon derived from waste orange and lemon peels for the adsorption of methyl orange and methylene blue dyes from wastewater. Heliyon, 8(8), e09930. https://doi.org/10.1016/j.heliyon.2022.e09930

Roy, H., Prantika, T. R., Riyad, M. H., Paul, S., & Islam, M. S. (2022). Synthesis, characterizations, and RSM analysis of Citrus macroptera peel-derived biochar for textile dye treatment. South African Journal of Chemical Engineering, 41, 129-39. https://doi.org/10.1016/j.sajce.2022.05.008

Rožič, M., Senji, I., & Miljanić, S. (2014). Methylene blue sorption characterization onto orange and lemon peels. The Holistic Approach to Environment, 4(3),97-110.

Šabanović, E., Muhić-Šarac, T., Nuhanović, M., & Memić, M. (2019). Biosorption of uranium(VI) from aqueous solution by Citrus limon peels: Kinetics, equilibrium, and batch studies. Journal of Radioanalytical and Nuclear Chemistry, 319(1), 425-35. https://doi.org/10.1007/s10967-018-6358-3

Saeed, A., Sharif, M., & Iqbal, M. (2010). Application potential of grapefruit peel as dye sorbent: Kinetics, equilibrium and mechanism of Crystal Violet adsorption. Journal of

Hazardous Materials, 179, 564-72. https://doi.org/10.1016/j.jhazmat.2010.03.041

Senophiyah-Mary, J., Thomas, T., Loganath, R., & Meenambal, T. (2019). Removal of copper from bioleachate of e-waste using lemon activated carbon (LAC) and comparison with commercial activated carbon (CAC). In: Ghosh SK (ed) Waste Valorisation and Recycling. Springer, Singapore, pp 385-395. https://doi.org/10.1007/978-981-13-2784-1_36

Senthilkumaar, S., Varadarajan, P. R., Porkodi, K., Subbhuraam, C. V. (2005). Adsorption of methylene blue onto jute fiber carbon: Kinetics and equilibrium studies. Journal of Colloid and Interface Science, 284, 78-82. https://doi.org/10.1016/j.jcis.2004.09.027

Sirico, A., Bernardi, P., Sciancalepore, C., Vecchi, F., Malcevschi, A., Belletti, B., & Milanese, D. (2021). Biochar from wood waste as an additive for structural concrete. Construction and Building Materials, 303, 124500. https://doi.org/10.1016/j.conbuildmat.2021.124500

Stella Mary, G., Sugumaran, P., Niveditha, S., Ramalakshmi, B., Ravichandran, P., & Seshadri, S. (2016). Production, characterization, and evaluation of biochar from pod (Pisum sativum), leaf (Brassica oleracea), and peel (Citrus sinensis) wastes. International Journal of Recycling of Organic Waste in Agriculture, 5(1), 43-53. https://doi.org/10.1007/s40093-016-0116-8

Stevens, R. W., Siriwardane, R. V., & Logan, J. (2008). In situ Fourier Transform Infrared (FTIR) investigation of CO2 adsorption onto zeolite materials. Energy Fuels, 22(5), 3070-9. https://doi.org/10.1021/ef800209a

Surya, K., & Michael, M. S. (2021). Hierarchical porous activated carbon prepared from biowaste of lemon peel for electrochemical double-layer capacitors. Biomass Bioenergy, 152, 106175. https://doi.org/10.1016/j.biombioe.2021.106175

Temkin, M. I., & Pyzhev, V. (1940). Kinetics of Ammonia Synthesis on Promoted Iron Catalysts. Acta Physicochim, 12, 327–356.

Tintner, J., Preimesberger, C., Pfeifer, C., Soldo, D., Ottner, F., Wriessnig, K., Rennhofer, H., Lichtenegger, H., Novotny, E. H., & Smidt, E. (2018). Impact of pyrolysis temperature on charcoal characteristics. Industrial & Engineering Chemistry Research, 57(46), 15613-9. https://doi.org/10.1021/acs.iecr.8b04094

Wang, T., Tang, X., Zhang, S., Zheng, J., Zheng, H., & Fang, L. (2019). Roles of functional microbial flocculant in dyeing wastewater treatment: Bridging and adsorption. Journal of Hazardous Materials. 384, 121506. https://doi.org/10.1016/j.jhazmat.2019.121506

Xie, Z., Guan, W., Ji, F., Song, Z., & Zhao, Y. (2014). Production of biologically activated carbon from orange peel and landfill leachate subsequent treatment technology. Journal of Chemistry, 1-9. https://doi.org/10.1155/2014/491912

JJEES

JJEES (2026) 17 (2): 247-254
ISSN 1995-6681

Jordan Journal of Earth and Environmental Sciences

Evaluation of Radiological Risk Parameters in the Soil along the Coastline of Arin Lake (Bitlis)

Şule KARATEPE ÇELİK[1*] , Sultan ŞAHİN BAL[2]

[1] Bitlis Eren University, Vocational School of Hizan, Bitlis, Turkey
[2] Bitlis Eren University, Department of Physics, Bitlis, Turkey

Received on 23 June 2025; Accepted on 25 December 2025

Abstract

This study examines natural (238U, 232Th, and 40K) and artificial (137Cs) radioactivity concentrations in 27 soil samples collected from the Arin Lake (Bitlis) coastline using an HPGe detector. For this purpose, dose calculations were performed, based on the radioactivity concentrations in the soil samples. The mean radioactivity concentration of ^{226}Ra, ^{232}Th, ^{40}K, and ^{137}Cs were 34.73±0.75, 32.43±0.67, 529.28±11.78, and 8.46±0.17 Bq.kg^{-1}, respectively. The radiological parameters with Ra equivalent (Ra_{eq}) value, the annual effective dose, and the absorbed dose values were lower than the recommended world mean. Furthermore, the radiological hazard indices Hin, Hex, and ELCR were below the specified limit values. In addition, the findings were compared to similar research in several other countries.

Keywords: *Radioisotopes, dose rates, Arin Lake, hazard indices*

1. Introduction

The living are continuously exposed to radiation from natural radioactive sources throughout their lives. This exposure arises from naturally occurring radioactive materials (NORMs) found in various components of Earth's environment, such as soil, water, and the atmosphere. Humans, as well as other living organisms, come into contact with these sources in their daily activities, leading to an inevitable accumulation of background radiation throughout their lifetimes (UNSCEAR 2000; Kuluöztürk et al., 2020; Özveren et al., 2020; Al-Momani et al., 2024). Naturally occurring radioactive materials (NORMs) such as ^{226}Ra, ^{232}Th, and ^{40}K are the radioisotopes that contribute most to background radiation. These radionuclides are produced by the natural decay of elements like uranium, thorium, and potassium in the Earth's crust (Baykara et al., 2011; Ibraheem et al., 2018; Abbasi et al., 2023; Yadav et al., 2023). Radioactivity levels differ from one location to another, owing to distinct geographical conditions and geological structures. For example, regions that contain uranium- or thorium-rich minerals tend to have higher levels of background radiation. In comparison, areas with different geological characteristics may show lower levels of natural radioactivity. (Özden et al., 2021; Yadav et al., 2023). Furthermore, artificial radioactive substances arise from nuclear weapon trials, accidents in nuclear reactors, and other nuclear studies. Among these, ^{137}Cs is of particular importance due to its long half-life and its impact on internal irradiation. These artificial sources have raised concerns about their long-term impacts on both ecosystems and human health (Kobya et al., 2015).

Regarding this subject in recent years, there has been extensive research into assessing the levels of radioactivity in soil, water, sand, and various food sources (UNSCEAR 2000; Ibraheem et al., 2018; Mehra et al., 2021; Tucakovic et al., 2023; Akça et al., 2014; Cambazoğlu et al., 2018). These studies are crucial for determining baseline radioactivity levels, which help in identifying regions with unusual radiation levels caused by natural variations or human activities (Tucakovic et al., 2023; Al-Harahsheh et al., 2020). Especially, many studies have been conducted to evaluate the natural and artificial radioactivity levels in soil samples collected from rivers, lakes, and coasts from different regions of the world (Kuluöztürk et al., 2020; Shadrin et al., 2020; Singh et al., 2021; Mantero et al., 2020; Al Shaaibi et al., 2023).

Lakes are vital water sources for aquatic life and humans. Lakes reflect the geological structure of the region in which they are located (Singh et al., 2021). The composition of soil along the lake coast is shaped by the lake's formation process and various atmospheric phenomena. The primary factor contributing to the radioactivity levels observed in sediment and coastal soil compositions in lakes is the presence of radioisotopes, such as ^{238}U, ^{232}Th, and ^{40}K in the soil and rocks. (Kobya et al., 2015). These radionuclides naturally occur in the Earth's crust, and their levels in lake ecosystems are influenced by surrounding geology and external environmental conditions (Baykara et al., 2011). These radioisotopes found in the soil contribute to the radioactive background level within the lake ecosystem. Though background radiation is low in intensity, continuous exposure can have lasting ecological impacts, particularly in environments where organisms are regularly exposed.

The objective of the study is to investigate both natural and artificial radioactivity levels in soil along the shoreline of Lake Arin. The study also aims to compare radioactivity

* Corresponding author e-mail: skaratepe@beu.edu.tr

concentrations in lakes, rivers, and coastal areas across different regions of the world and to identify areas that may pose radiological hazard indices. This research is driven by the need to track and comprehend the long-term effects of radiation exposure on ecosystems and human populations.

2. Materials and Methods

2.1. Study area

Arin Lake, located in the east of Türkiye, is within the borders of Bitlis province (Figure 1). It is located at 42°98' E and 38°45' N. This soda lake is situated south of the volcanic Nemrut Mountain and is surrounded by three villages. The lake serves as a breeding habitat for the endangered White-headed Duck, and it is recognized as a migratory route for numerous bird species. During the migration season, the most notable avian visitors include songbirds and flamingos (Nergiz & Durmuş, 2017). Furthermore, during the Ottoman period, soda production was carried out using resources from both Lake Van and Lake Arin, owing to the soda-rich nature of Lake Arin (Çelik & Bal, 2024).

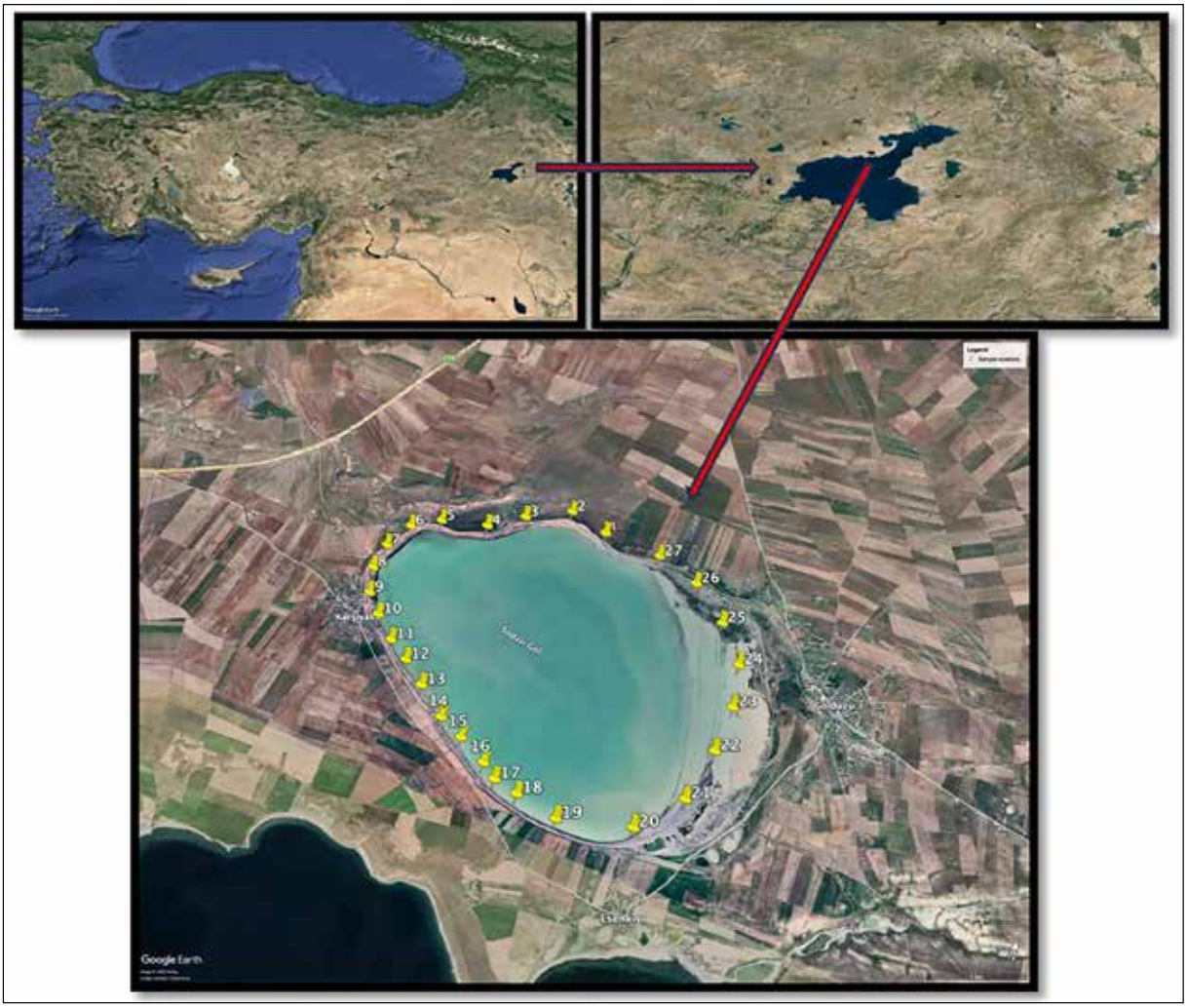

Figure 1. Map of the study area and location of the soil sample points.

2.2. Sampling and sample preparation

Twenty-seven soil samples were collected from Arin Lake and its surrounding areas. Figure 1 shows the sample locations from which there were obtained. The sample locations were determined using GPS. For soil samples, samples were collected from a depth of 10 to 15 cm below the surface (Satyanarayana et al., 2023). Additionally, each soil sample was dried before assessing activity levels. Roughly 1kg of each sample was transferred to the laboratory and labeled for identification. To prevent any alteration in the physical and chemical characteristics of the samples, all the samples were dried at 80°C for 24 h to remove moisture (IEAE 2003; Van et al., 2019). The samples were sieved through a 60-mesh screen for homogenous (Kuluöztürk et. al., 2020). When using a germanium detector, it is important that the particle size is equal and the sample is homogeneous. All samples were placed in 1 kg Marinelli containers suitable for measurement with a germanium detector.

2.3. Gamma Spectrometric Analysis

Radioactivity measurements of soil samples were performed using a high-purity gamma-ray detector system with a coaxial p-type HPGe detector (GEM50P4-83). It can measure gamma rays with energies between 40 keV and 10 MeV (Karakaya et. al., 2015). Relative efficiency is at least 50%, and the separation power is 1.90 keV at 1.33 MeV for ^{60}Co (FWHM). The detector is enclosed within a 10 cm-thick cylindrical lead shield to reduce background radiation (Karakaya et al., 2015). Additionally, lead shielding includes

a 1.5 mm thick copper and a 1 mm thick tin layer to stop the X-rays. Analysis was performed with MAESTRO32 (ORTEC) software (ORTEC 2006). Energy and efficiency calibrations were completed using standard sources (IAEA-375) obtained from the IAEA (Gilmore, 2008). Energy and efficiency calibrations of the detector were performed using a standard multi-nuclide gel source with a known activity of 1.365 μCi, containing isotopes such as ^{57}Co, ^{60}Co, ^{88}Y, ^{109}Cd, ^{139}Ce, ^{137}Cs, ^{203}Hg, ^{210}Pb, and ^{241}Am. The measurements were taken at 43,200-second (24-hour) intervals. The efficiency vs. energy graph is plotted and adjusted to fit the following equation (Kayakökü & Dogru, 2017; Özmen et al., 2014).

$$E_{ff}(E) = a + b \times log\ log\ (E)^2 + d \times log\ log\ (E)^3 \quad (1)$$

where a, b, c, and d are the optimal parameters identified by the fitting algorithm. Finally, the efficiency values required for calculating the activity concentration of the full-energy peaks were derived using this equation.

Each sample was counted for 50000 s to get acceptable counting data. ^{226}Ra, ^{232}Th, and ^{40}K isotopes were determined through the examination of gamma-ray lines at specific energy levels: 351.9 keV (^{214}Pb) and 609.3 keV (^{214}Bi) for ^{226}Ra, 911.2 keV (^{228}Ac) for ^{232}Th, 1460.8 keV for ^{40}K Observation was made at 661.7 keV to detect the ^{137}Cs isotope, which is an artificial radionuclide.

2.4. Radioactivity Concentration and Dose Calculations

The activity levels in samples were determined with the subsequent formula:

$$A(Bq.kg^{-1}) = \frac{N_S - N_B}{\varepsilon \times P_\gamma \times t} \times \frac{1}{m} \quad (2)$$

Where are counted per second (cps) for the sample and background, respectively. is the detector efficiency, is the γ-abundance, is the counting time (50000 s), and is the sample mass of 1kg (Kuluöztürk et al., 2020; Cambazoğlu et al., 2018).

The calculation of minimum detectable activities (MDA) was performed utilizing the following equation:

$$MDA(Bq.kg^{-1}) = \frac{2.71 + 4.65\sqrt{N_B}}{\varepsilon \times P_\gamma \times t} \quad (3)$$

Where is represented by the net peak areas in a specific energy range for the background, is the detector efficiency, and is the abundance associated with the energy, and t is counting time.

The calculated Ra equivalent value, which includes the weighted contributions from Ra, Th, and K, is an important parameter for comparing activity concentrations across all data. It was computed employing the following equation.

$$Ra_{eq}(Bq.kg^{-1}) = A_{Ra} + 1.43A_{Th} + 0.077A_K \quad (4$$

Where, A_{Ra}, $A_{Th,}$ and A_K represent the respective activity values for ^{226}Ra, ^{232}Th, and ^{40}K. The maximum recommended value of Ra_{eq} is 370 (UNSCEAR 2000).

To assess the attributes of gamma radiation in outdoor environments, the absorbed dose rate (D) in outdoor air, measured 1 meter above the ground, was computed from the activities of 238U, 232Th, and 40K using the following formula:

$$D(nGy/h) = 0.462C_U + 0.604C_{Th} + 0.417C_K \quad (5)$$

Where C_K, C_{Th}, and C_U represent the concentrations of ^{40}K, ^{232}Th, and ^{238}U activities, respectively.

Annual effective dose rate (AED) was defined as the value of radiation exposure to an individual over a year and provides an assessment of the potential health hazards associated with this radiation exposure (UNSCEAR 2000; Baykara et al., 2011)

$$AED(mSv/y) = D(nGy/h) \times 8760(h/y) \times 0.2 \times 0.7(,) \quad (6)$$

Where 0.2 is the outdoor time conversion factor, and 0.7 stands for the dose conversion factor in Sv to Gy. The global mean annual effective dose (AEDE) of outdoor terrestrial gamma radiation is 70 μSv.y-1 (UNSCEAR 2000; Al Shaaibi et al., 2023).

The external and internal hazard index (Hex) was calculated from the formula as follows (Krieger, R., 1985, Abbasi, 2023):

$$H_{ex} = \frac{A_{Ra}}{370} + \frac{A_{Th}}{259} + \frac{A_K}{4180} \leq 1 \quad (7)$$

$$H_{in} = \frac{A_{Ra}}{185} + \frac{A_{Th}}{259} + \frac{A_K}{4180} \leq 1 \quad (8)$$

Excess lifetime cancer risk (ELCR) was calculated with the following equation:

$$ELCR = AED \times DL \times RF \quad (9)$$

Where AED is the annual effective dose rate (μSv.y^{-1}), DL is the average life (70 years), and, for stochastic effects, RF (0.05 Sv−1) is used as the risk factor for cancer per Sievert in the population, as described by ICRP (ICRP 1990).

3. Results and Discussion

The radioactivity concentrations of the natural radioisotopes ^{226}Ra, ^{232}Th, and ^{40}K , and artificial radioisotopes ^{137}Cs in soil samples are given in Table 1 and Figure 2.

The samples exhibited varying levels of activity concentrations, ranging from 9.31±0.21 to 50.76±1.05 Bq.kg^{-1} for ^{226}Ra, 48.16±1.05 to 8.47±0.18 Bq.kg^{-1} for ^{232}Th, 97.55±2.46 and 896.13±17.87 Bq.kg^{-1} for ^{40}K, and 4.41±0.11 to 18.16±0.35 Bq.kg^{-1} for ^{137}Cs. The mean values were calculated to be 34.73±0.75, 32.43±0.67, 529.28±11.78, and 8.46±0.17 Bq.kg^{-1} for ^{226}Ra, ^{232}Th, ^{40}K, and ^{137}Cs, respectively. Examining both Table 3 and Figure 2 concurrently, the average activity concentrations of ^{226}Ra, ^{232}Th, and ^{40}K in the soil samples follow the order ^{226}Ra < ^{232}Th < ^{40}K. Sample 1 exhibited the highest activity concentrations of 226Ra, 232Th, and 40K, whereas sample 27 exhibited the lowest. The higher radionuclide values observed at sample numbers 1–6 can be attributed to the more pronounced accumulation of fine-grained sediment and chemical retention processes in this area. In soda lake conditions, high alkalinity may facilitate the adsorption of radionuclides into clay and carbonate phases, increasing sediment enrichment. Furthermore, surface runoff and erosion inputs from surrounding settlements and agricultural activities may have contributed to the accumulation of material transported from the basin in this section. The significant difference observed between closely located sampling points suggests micro-scale heterogeneity in the sediment.

Changes in clay and silt fractions can increase the specific surface area and, consequently, the retention of natural radionuclides. Furthermore, mineralogical composition, organic matter, redox conditions, and hydrodynamic deposition and resuspension processes, which depend on the flow regime, can lead to divergent concentrations even over short distances. Therefore, the difference between sample numbers 1 and 27 should not be explained solely by distance but should be evaluated in light of the combined effect of local sedimentological and geochemical conditions. Additionally, the lowest ^{137}Cs activity was obtained from sample 16. According to the UNSCEAR report, the activity concentrations of ^{226}Ra, ^{232}Th, ^{40}K, and ^{137}Cs have world mean values of 35 Bq.kg^{-1}, 30 Bq.kg^{-1}, 400 Bq.kg$^{-1,}$ and 51 Bq.kg$^{-1,}$ respectively (UNSCEAR 2000). As seen in Table 1, the ^{232}Th and ^{40}K activity values were slightly higher than these. However, the ^{226}Ra activity concentration was determined to be lower. In addition to natural radioisotopes, ^{137}Cs is an artificial radioisotope. It is emitted following nuclear weapons testing and nuclear power plant accidents. The measured 137Cs activity concentration was lower than the results in the other regions listed in Table 2.

Table 1. Radioisotope activity concentrations of soil samples in Arin Lake

Sample ID	Radioisotopes Activities (Bq.kg^{-1})			
	^{226}Ra (351.9–609.3 keV)	**^{232}Th** (911,2 keV)	**^{40}K** (1461,8 keV)	**^{137}Cs** (662 keV)
1	50.76±1.05	48.16±1.05	896.13±17.87	4.48±0.1
2	41.60±0.83	42.92±0.87	699.83±15.23	6.06±0.13
3	49.35±1.06	44.87±0.94	841.83±15.63	5.93±0.11
4	38.87±0.79	39.53±0.82	704.47±13.52	5.65±0.12
5	44.17±0.92	41.44±0.85	717.43±14.34	8.95±0.19
6	41.92±0.86	42.29±0.89	801.1±17.44	6.42±0.13
7	34±61±0.73	31.51±0.63	531.32±12.69	10.24±0.23
8	26.08±0.55	23.24±0.49	338.62±8.43	7.35±0.15
9	20.83±0.44	19.62±0.42	223.72±5.54	8.82±0.19
10	18.13±0.37	18.48±0.42	191.2±4.87	6.39±0.12
11	29.48±1.10	21.55±0.43	375.31±9.35	6.31±0.12
12	19.09±0.42	18.22±0.39	235.34±5.81	10.63±0.23
13	35.56±0.76	32.22±0.66	512.91±12.83	11.84±0.25
14	28.61±0.59	28.73±0.64	437.36±10.36	5.61±0.11
15	30.90±0.64	29.1±0.56	455.53±10.07	7.37±0.15
16	36.18±0.75	34.33±0.69	512.35±12.3	4.41±0.11
17	32.70±0.67	27.17±0.54	464.9±11.33	7.4±0.14
18	42.83±0.86	41.82±0.85	631.76±12.99	8.12±0.16
19	46.79±0.99	48.11±0.98	710.57±14.46	6.41±0.14
20	40.30±0.83	40.97±0.83	636.26±14.16	10.38±0.21
21	30.95±0.63	28.31±0.59	462.09±11.53	11.86±0.21
22	35.17±0.77	28.57±0.61	521.06±12.22	12.64±0.24
23	32.50±0.68	30.03±0.67	471.19±11.75	18.16±0.35
24	28.36±0.59	25.95±0.56	391.15±9.79	10.9±0.21
25	46.52±0.95	42.39±0.87	731.23±16.25	11.42±0.22
26	46.07±1.31	37.66±0.76	698.43±14.67	7.36±0.17
27	9.31±0.21	8.47±0.18	97.55±2.46	7.19±0.15
Min.	9.31±0.21	8.47±0.18	97.55±2.46	4.41±0.11
Max.	50.76±1.05	48.16±1.05	896.13±17.87	18.16±0.35
Mean	34.73±0.75	32.43±0.67	529.28±11.78	8.46±0.17
[1]World mean	35	30	400	51

[1](UNSCEAR 2000)

Additionally, it has been determined that similar results were obtained when comparing the activity concentrations of ^{40}K, ^{226}Ra, and ^{232}Th in this research with those in several other countries, as presented in Table 2. able 2 reveals wide variability in naturally occurring radionuclides reported in lake and coastal sediments across different geographical regions. In particular, the findings for ^226Ra and ^232Th are generally at a similar level to values reported in different aquatic environments such as Lake Eğirdir and the East Siberian Sea. They are consistent with the ranges reported for Lake Erçel and the Aegean coast. In contrast, ^40K is higher than the lower levels reported in Brazil; this may be related to the sediment's mineralogical composition and potassium-rich lithological inputs.

The frequency distribution of radionuclides ^{226}Ra, ^{232}Th, ^{40}K, and ^{137}Cs is illustrated in Figure 2. The histogram graphs in Figure 2 were generated using the IBM SPSS Statistics program.

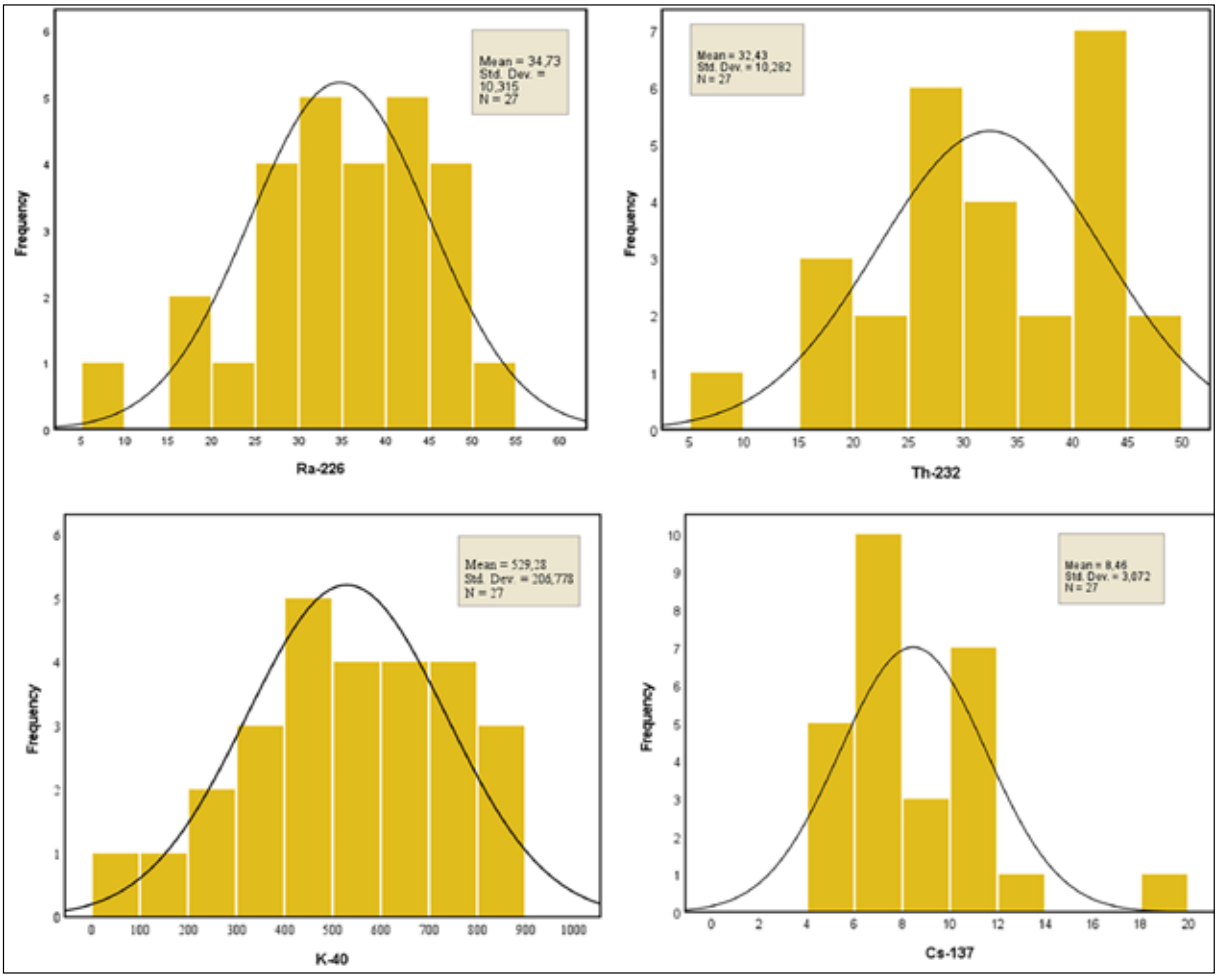

Figure 2. The frequency distributions of 226Ra, 232Th, 40K, and 137Cs radioactivity concentrations in the study area.

Table 2. Comparison the activity concentrations of ^{226}Ra, ^{232}Th, ^{40}K, and ^{137}Cs soil samples in Türkiye and several other countries

Region	^{226}Ra (Bq.kg^{-1})	^{232}Th (Bq.kg^{-1})	^{40}K (Bq.kg^{-1})	^{137}Cs (Bq.kg^{-1})	Reference
Erçel Lake, Turkiye	8.6–42.6	11.6–53.2	254.1–771.9	0.7–24.4	Yıldız et al. (2014)
Eğirdir Lake, Türkiye	34.13	27.32	363.28		Özseven et al. (2020)
East Antarctica	33	199	1150		Pal et al. (2021)
Saline Lakes, Crimea	65.68	34.95	287.42		Shadrin et al. (2020)
Qarun Lake, Egypt	10.21	11.05	927.44		Drawish et al. (2013)
Rize Türkiye	85.75	51.08	771.57	236.38	Dizman et al. (2016)
Aegean coast, Greece	9–31	9–67	426–740	0.8–2.6	Shahrokhi et al. (2021)
Gaeta Gulf, Italy	-	91.7	603.7	8.82	Desideri et al. (2002)
Brazil	62	82	179		Riberio et al. (2017)
Thailand	22.6	26.4	523.0	-	Malain et al. (2012)
East Siberian Sea, Russia	26.6	39.2	726	2.0	Ulyantsev et. al. (2023)
Oguta Lake, Nigeria	47.89	55.37	1023	-	Isinkaye et. al. (2015)
Iran	24.3	25.8	457.7		Kardan et. al. (2017)
This study	34.73	32.43	529.28	8.46	

The dose values resulting from the natural radioactivity of the soil samples, the hazard indices (Hin, Hex), and the ELCR were calculated as presented in Table 3.

According to Table 3, Ra_{eq} stemming from the natural radioactivity of the soil samples ranged from (28.93 to 188) Bq.kg^{-1} with a mean of 121.86 Bq.kg^{-1}. These values fall below the WHO-recommended global mean of 370 Bq/kg (WHO 2003).

ADR for the soil samples is in the range of 13.48-89.91 nGy.h^{-1}. The mean of 57.71 nGy.h^{-1} is below the global mean value of 60 nGy.h^{-1} (WHO 2003). Similarly, across all samples, AEDR values with a mean of 43.13 µSv.y-1 are significantly below the global mean of 460 µSv.y^{-1} (UNSCEAR 2000).

As seen in Table 3, H_{ex} and H_{in} both reach a maximum value of 0.33 and 0.42, respectively. Table 3 shows that the mean Hex is 0.24 and the mean H_{in} is 0.34. Both of these values are

below the permitted maximum limit value of 1 (WHO 2003). The calculated maximum lifetime cancer risk value is 0.39, with a mean of 0.25. The average value does not exceed the recommended threshold of 0.29 (UNSCEAR 2000).

Table3. Dose calculations and radiological hazard parameters of the soil samples

Sample ID	Ra_{eq} ($Bq.kg^{-1}$)	D ($nGy.h^{-1}$)	AEDR ($mSv.y^{-1}$)	H_{in}	H_{ex}	ELCR ($\times10^{-3}$)
1	188.63	89.91	110.26	0.65	0.51	0.39
2	156.86	74.33	91.15	0.54	0.42	0.32
3	178.34	85.01	104.25	0.62	0.48	0.36
4	149.64	71.21	87.33	0.51	0.4	0.31
5	158.67	75.35	92.41	0.55	0.43	0.32
6	164.08	78.32	96.05	0.56	0.44	0.34
7	120.58	57.18	70.12	0.42	0.33	0.25
8	85.39	40.21	49.31	0.3	0.23	0.17
9	66.11	30.8	37.78	0.23	0.18	0.13
10	59.28	27.51	33.74	0.21	0.16	0.12
11	89.2	42.29	51.86	0.32	0.24	0.18
12	63.27	29.64	36.35	0.22	0.17	0.13
13	121.13	57.28	70.25	0.42	0.33	0.25
14	103.37	48.81	59.86	0.36	0.28	0.21
15	107.59	50.85	62.36	0.37	0.29	0.22
16	124.72	58.82	72.13	0.43	0.34	0.25
17	107.35	50.9	62.43	0.38	0.29	0.22
18	151.28	71.39	87.55	0.52	0.41	0.31
19	170.3	80.31	98.49	0.59	0.46	0.34
20	147.88	69.9	85.72	0.51	0.4	0.3
21	107.01	50.67	62.14	0.37	0.29	0.22
22	116.15	55.23	67.74	0.41	0.31	0.24
23	111.72	52.8	64.76	0.39	0.3	0.23
24	95.59	45.09	55.29	0.33	0.26	0.19
25	163.44	77.59	95.15	0.57	0.44	0.33
26	153.7	73.16	89.72	0.54	0.42	0.31
27	28.93	13.48	16.54	0.1	0.08	0.06
Mean	**121.86**	**57.71**	**70.77**	**0.42**	**0.33**	**0.25**
[1]World mean	**370**	**60**	**460**	**<1**	**<1**	**0.29**

1(WHO 2003; UNSCEAR 2000)

4. Conclusion

In this research, the radioactivity levels of the natural radionuclides (226Ra, 232Th, and 40K) and the artificial radionuclide (137Cs) were investigated in soil samples collected from the coast of Arin Lake using a HPGe detector system.

The results show that the average concentration of ^{226}Ra is lower than the global average, while ^{232}Th and ^{40}K are higher. The high levels of ^{232}Th and ^{40}K may be due to the volcanic nature of Süphan Volcano and the region's geological structure, especially in the use of potassium-based fertilizers. These factors contribute to the high soil concentrations observed.

Despite some elevated levels, the calculated radiological parameters, including absorbed dose rate (D), radium equivalent activity (Ra_{eq}), and annual effective dose rate (AEDR), remained within safe limits as recommended by UNSCEAR (UNSCEAR 2000). In addition, radiological hazard indices, such as the internal (Hin) and external (Hex) hazard indices, and the excess lifetime cancer risk (ELCR) are below the permissible threshold values.

In conclusion, although certain natural radionuclides were above global averages, the overall radiological risk is minimal, indicating that the area does not pose substantial health risks according to the parameters analyzed.

Acknowledgments

This research received financial support from the Scientific Projects Department of Bitlis Eren University (BEBAP 2022.18).

References

Abbasi, A., Zakaly, H. M., and Alotaibi, B. M. 2023. Radioactivity concentration and radiological risk assessment of beach sand along the coastline in the Mediterranean Sea. Marine Pollution Bulletin 195: 115527. https://doi.org/10.1016/j.marpolbul.2023.115527.

Akça, S., Küçükönder, E., Karatepe, S., and Doğru, M. 2014. Radioactivity levels in some mushroom species and consequent doses. Asian Journal of Chemistry 26(3): 879.

Al-Harahsheh, S., and Al-Dalabeeh, M. (2020). Measurement of radon levels in the groundwater of Al-Rusaifah City in Zarqa governorate using liquid scintillation counter. Jordan Journal of Earth and Environmental Sciences, 11, 98-102.

Al-Momani, I. F., and Ali, S. M. 2024. Investigation of Heavy Metals in Indoor Dust from Irbid, Jordan. Jordan Journal of Earth & Environmental Sciences, 15(2).

Al Shaaibi, M., Ali, J., Tsikouras, B., and Masri, Z. 2023. Environmental radioactivity assessment of the Brunei Darussalam coastline of the South China Sea. Environmental Pollution 323: 121288. https://doi.org/10.1016/j.envpol.2023.121288.

Baykara, O., Karatepe, Ş., and Doğru, M. 2011. Assessments of natural radioactivity and radiological hazards in construction materials used in Elazig, Turkey. Radiation Measurements 46(1): 153–158. https://doi.org/10.1016/j.radmeas.2010.11.019.

Canbazoglu, C., Ilter, S., Sahin Bal, S., Karatepe, S., and Dogru, M. 2018. A preliminary study on radioactivity concentrations and dose assessment of some anticarcinogenic medicinal plants used in Turkey. Fresenius Environmental Bulletin 27: 793–798.

Çelik, Ş. K., and Bal, S. Ş. 2024. An evaluation of radon concentrations in Arin Lake, Bitlis. Water, Air, & Soil Pollution 235(2): 94.

Desideri, D., Meli, M. A., Roselli, C., and Testa, C. 2002. Geochemical partitioning of actinides, 137Cs and 40K in a Tyrrhenian sea sediment sample: Comparison to stable elements. Journal of Radioanalytical and Nuclear Chemistry 251: 37–41.

Dizman, S., Görür, F. K., and Keser, R. 2016. Determination of radioactivity levels of soil samples and the excess of lifetime cancer risk in Rize Province, Turkey. International Journal of Radiation Research 14(3): 237–244. https://doi.org/10.18869/acadpub.ijrr.14.3.237.

Gilmore, G. R. 2008. Practical Gamma-ray Spectroscopy, 2nd ed. John Wiley & Sons Ltd.

Ibraheem, A. A., El-Taher, A., and Alruwaili, M. H. 2018. Assessment of natural radioactivity levels and radiation hazard indices for soil samples from Abha, Saudi Arabia. Results in Physics 11: 325–330.

IAEA-TECDOC-1360. 2003. Collection and preparation of bottom sediment samples for analysis of radionuclides and trace elements. IAEA-TECDOC-1360, Vienna.

International Commission on Radiological Protection (ICRP). 1990. Recommendations of the International Commission on Radiological Protection. In ICRP Publication 60. Pergamon Press, Annals of ICRP, Oxford.

Isinkaye, M. O., and Emelue, H. U. 2015. Natural radioactivity measurements and evaluation of radiological hazards in sediment of Oguta Lake, South East Nigeria. Journal of Radiation Research and Applied Sciences 8(3): 459–469.

Karakaya, M.Ç., Doğru, M., Karakaya, N., Vural, H.C., Kuluöztürk, F., and Bal, S.Ş. 2015. Radioactivity concentrations and dose assessments of therapeutic peloids from some Turkish spas. Clay Minerals 50(2): 221–232.

Kardan, M. R., Fathabdi, N., Attarilar, A., Esmaeili-Gheshlaghi, M. T., Karimi, M., Najafi, A., and Hosseini, S. S. 2017. A national survey of natural radionuclides in soils and terrestrial radiation exposure in Iran. Journal of Environmental Radioactivity 178: 168–176.

Kayakökü, H., and Doğru, M. 2017. Radioactivity analysis of soil samples taken from the western and northern shores of Lake Van, Turkey. Applied Radiation and Isotopes 128: 231–236.

Kobya, Y., Taşkın, H., Yeşilkanat, C. M., Varinlioğlu, A., and Korcak, S. 2015. Natural and artificial radioactivity assessment of dam lakes sediments in Çoruh River, Turkey. Journal of Radioanalytical and Nuclear Chemistry 303: 287–295.

Krieger, R. 1985. Radioactivity of construction materials. Betonwerk Fertigteil-Technik 47: 468–473.

Kuluöztürk, M. F., Çelik, Ş. K., and Doğru, M. 2020. Assessment of gamma radiation levels of beach sands in Bitlis region of Lake Van. Arabian Journal of Geosciences 13: 1–7. https://doi.org/10.1007/s12517-020-05600-7.

Malain, D., Regan, P. H., Bradley, D. A., Matthews, M., Al-Sulaiti, H. A., and Santawamaitre, T. 2012. An evaluation of the natural radioactivity in Andaman beach sand samples of Thailand after the 2004 tsunami. Applied Radiation and Isotopes 70(8): 1467–1474.

Mantero, J., Thomas, R., Holm, E., Rääf, C., Vioque, I., Ruiz-Cánovas, C., and Isaksson, M. 2020. Pit lakes from Southern Sweden: Natural radioactivity and elementary characterization. Scientific Reports 10(1): 13712.

Mehra, R., Kaur, S., Chand, S., Charan, C., and Mehta, M. 2021. Dosimetric assessment of primordial radionuclides in soil and groundwater of Sikar district, Rajasthan. Journal of Radioanalytical and Nuclear Chemistry 330: 1605–1620.

Nergiz, H., and Durmus, A. 2017. Effects of habitat change on breeding waterbirds in Arin (Sodali) Lake, Turkey. Applied Ecology and Environmental Research 15(3): 1111–1118.

ORTEC. 2006. Maestro-32: Multi-channel analyzer software, a65-b32 model. https://www.ortec-online.com/-/media/ametekortec/manuals/a65-mnl.pdf.

Özden, S., and Aközcan, S. 2021. Natural radioactivity measurements and evaluation of radiological hazards in sediment of Aliağa Bay, İzmir (Turkey). Arabian Journal of Geosciences 14: 1–14.

Özmen, S. F., Cesur, A., Boztosun, I., and Yavuz, M. E. L. E. K. 2014. Distribution of natural and anthropogenic radionuclides in beach sand samples from Mediterranean coast of Turkey. Radiation Physics and Chemistry 103: 37–44.

Özseven, A., Akkurt, I., and Günoğlu, K. 2020. Determination of some dosimetric parameters in Eğirdir Lake, Isparta, Turkey. International Journal of Environmental Science and Technology 17: 1503–1510.

Pal, R., Patra, A. C., Bakshi, A. K., Dhabekar, B., Reddy, P. J., Sengupta, P., and Sapra, B. K. 2021. Investigations on baseline levels for natural radioactivity in soils, rocks, and lakes of Larsemann Hills in East Antarctica. Environmental Monitoring and Assessment 193: 1–21.

Ribeiro, F. C., da Lauria, D. C., do Rio, M. A., da Cunha, F. G., de Oliveira Sousa, W., de Albuquerque Medeiros Lima, E., and Franzen, M. 2017. Mapping soil radioactivity in the Fernando de Noronha archipelago, Brazil. Journal of Radioanalytical and Nuclear Chemistry 311: 577–587.

Satyanarayana, G. V. V., Sivakumar, N. S., VidyaSagar, D., Murali, N., Rao, A. D. P., and Narayana, P. L. 2023. Measurement of natural radioactivity and radiation hazard assessment in the soil samples of Visakhapatnam, Andhra Pradesh, India. Journal of the Indian Chemical Society 100(1): 100856.

Shadrin, N., Mirzoeva, N., Sidorov, I., Korotkov, A., and Anufriieva, E. 2020. Natural radionuclides in bottom sediments of the saline lakes: What factors determine their concentration? Environmental Earth Sciences 79(8): 168.

Shahrokhi, A., Adelikhah, M., Chalupnik, S., and Kovács, T. 2021. Multivariate statistical approach on distribution of natural and anthropogenic radionuclides and associated radiation indices along the north-western coastline of Aegean Sea, Greece. Marine Pollution Bulletin 163: 112009.

Singh, K. K., and Vasudevan, S. 2021. Reconstruction of sedimentation rates based on the chronological framework of Lake Pykara, Tamil Nadu, India. Environmental Monitoring and Assessment 193(7): 428.

Tucaković, I., Karanović, G., Coha, I., Pavičić-Hamer, D., and Grahek, Ž. 2023. Radionuclides in commercial children's food Ulyantsev, A., Ivannikov, S., Bratskaya, S., and Charkin, A.

2023. Radioactivity of anthropogenic and natural radionuclides in marine sediments of the Chaun Bay, east Siberian Sea. Marine Pollution Bulletin 195: 115582.

UNSCEAR. 2000. United Nations Scientific Committee on the Effects of Atomic Radiation: Sources and effects of ionizing radiation. Volume I: Sources; Volume II: Effects. Report to the General Assembly, with scientific annexes. United Nations Sales Publications E.00.IX.3 and E.00.IX.4, United Nations, New York.

Van, T. T., Bat, L. T., Nhan, D. D., Quang, N. H., Cam, B. D., and Hung, L. V. 2019. Estimation of radionuclide concentrations and average annual committed effective dose due to ingestion for the population in the Red River Delta, Vietnam. Environmental Management 63: 444–454.

WHO. 2003. World Health Organization, guidelines for drinking water quality, vol. 3-Chapter 9 draft. Switzerland, Geneva.

Yadav, M., Jindal, M. K., Bossew, P., and Ramola, R. C. 2023. Geological control of terrestrial background radiation in Garhwal Himalaya, India. Environmental Geochemistry and Health 45(11): 8379–8401.

Yadav, M., Jindal, M. K., and Ramola, R. C. 2023. Study of radionuclides in rock samples from Ukhimath area and its correlation with soil and water data. Chemistry Africa 6(4): 2165–2173.

Yıldız, N., Oto, B., Turhan, Ş., Uğur, F. A., and Gören, E. 2014. Radionuclide determination and radioactivity evaluation of surface soil samples collected along the Erçek Lake basin in eastern Anatolia, Turkey. Journal of Geochemical Exploration 146: 34–39.

JJEES

JJEES (2026) 17 (2): 255-265
ISSN 1995-6681

Jordan Journal of Earth and Environmental Sciences

Spectroscopic Prediction of Soil Iron Oxides, Organic Carbon, and Calcium Using VIS-NIR and PLSR in Northern Jordan

Abdulla Al-Rawabdeh [1*], Abdel Rahman Alsaleh [1,2], Muheeb Awawdeh [1]

[1]Laboratory of Applied Geoinformatics, Department of Earth and Environment Sciences, Yarmouk University, Irbid, Jordan.
[2]Department of Civil and Environmental Engineering, Khalifa University of Science and Technology, Abu Dhabi, United Arab Emirates

Received on 22 October 2025; Accepted on 31 December 2025

Abstract

Soil spectroscopy has not yet been applied in Jordan as a proxy for assessing soil properties. In this study, forty surface soil samples were collected using a cluster random sampling method and analysed for three key soil properties —free iron oxides (Fed), soil organic carbon (SOC), and calcium (Ca), owing to their critical roles in soil fertility and known spectral responsiveness in the VIS-NIR range. Spectroscopy data (325 to 1075 nm) were acquired using a field spectroradiometer, and several pre-processing techniques were applied to enhance correlation accuracy and minimize noise. The analyzed soils were classified under the USDA soil texture system as clay, silty clay, silty clay loam, and clay loam. Geochemical results showed: Fe_d% (0.4- 1.28, mean 0.89), SOC% (1.09- 3.96, mean 1.69), and Ca% (0.08- 10.65, mean 3.19). Partial least squares regression (PLSR) analysis was employed to predict these soil properties from spectral reflectance data, yielding a high coefficient of determination (R^2) for both model calibration and validation. The spectral signals of Fe_d, SOC, and Ca were found to be significant across different wavelengths of the VIS–NIR region, confirming their spectral activity. The performance of the PLSR models was validated, and the spectral signals of Fe_d, SOC, and Ca were found to be significant across various wavelengths within the visible and near-infrared (VIS–NIR) region (325–1075 nm). The applied spectral pre-treatment techniques and characteristic variable selection methods notably enhanced model performance and predictive accuracy. The findings demonstrate that VIS–NIR spectroscopic analysis can serve as a reliable and efficient alternative to traditional laboratory methods for determining key soil properties in northern Jordan. This study represents an important step toward establishing a national spectroscopic library of soil materials in Jordan.

Keywords: *soil; field spectroscopy; partial least squares regression; iron oxides; soil organic carbon; Jordan.*

1. Introduction

Soil forms the uppermost layer of the Earth's surface and develops gradually over time (Plummer et al., 2016). Traditional soil survey methods rely on field sampling at multiple locations in the field, followed by laboratory analyses to determine soil properties, and interpolation techniques to map these properties across the study area. However, such methods are costly, time-consuming, and often yield low- accuracy interpolation results because they fail to fully capture spatial variations in soil characteristics (Zhang et al., 2017).

Modern techniques, including remote sensing and geographical information systems (GIS), have been developed to estimate soil properties indirectly and present the results in digital format. Remote sensing techniques can accurately estimate several physical and chemical soil properties- such as texture, organic matter (OM), moisture content, salinity, and iron content (Kumar et al., 2013), while significantly reducing cost and time compared to traditional mapping. Nevertheless, unlike conventional approaches that analyze deeper soil horizons, remote sensing typically examines only the upper few centimeters of the surface soil layer (Fathololoumi et al., 2020).

Because different materials exhibit unique reflectance and absorption behaviors at specific wavelengths, they can be distinguished by their spectral reflectance signatures. Soil spectral reflectance is influenced by both the chemical and physical properties (Kumar et al., 2013; Pereira et al., 2017). Several external factors, such as land cover, vegetation, and land use can affect soil reflectance and should be considered to avoid misinterpretation of results (Kumar et al., 2013). In dryland environments, where such influences are minimized, soil properties, such as moisture content and organic carbon, can be more reliably estimated from reflectance analysis under controlled laboratory conditions (Pereira et al., 2017).

In recent years, numerous studies have employed hyperspectral and multispectral remote sensing techniques to investigate soil properties. For example, Camargo et al. (2015) analyzed the spatial variability of clay, iron oxide, and adsorbed phosphate in Brazilian Oxisols using diffuse reflectance spectroscopy with a PerkinElmer Lambda 950 spectrophotometer. Using partial least squares regression (PLSR), they achieved high correlations between VIS–NIR spectral reflectance (380–2500 nm) and the measured soil attributes. Similarly, Demattê et al. (2015) investigated UV-VIS-NIR Spectroscopy as an alternative soil mapping technique, obtaining promising calibration and validation accuracy that confirmed its suitability for soil attribute estimation in Brazil. The study area was divided into two

* Corresponding author e-mail: abd_rawabdeh@yu.edu.jo

subareas: Soil samples from subarea 1 were used for model calibration, while those from subarea 2 were reserved for validation. The resulting models demonstrated high predictive accuracy, confirming that remote sensing provides a reliable and efficient alternative to conventional soil mapping methods. Forkuor et al. (2017) combined remote sensing and laboratory analysis to assess six soil characteristics, which are cation exchange capacity (CEC), soil organic carbon (SOC), silt, clay, nitrogen, and sand across a 580 km² watershed in southwestern Burkina Faso. Their study demonstrated that Landsat 8 and RapidEye satellite data, particularly in the SWIR and NIR bands, were highly predictive of soil variability.

Yu et al. (2018) generated geochemical soil property maps in China using hyperspectral imagery from the space-borne HJ-1A satellite, supplemented by field spectra collected with an SVC HR1024 spectroradiometer and validated through laboratory analysis. The authors mapped organic carbon, phosphorus, nitrogen, and potassium using a stepwise regression model, achieving high predictive performance. In northern Jordan, Landsat-8 and Sentinel-2 imagery were used combined with support vector machine (SVM) classification, to analyze spatial variations in soil surface colour. They observed strong correlations between red soil distribution, precipitation gradients, and geomorphological features. This approach proved effective for quantifying soil colour variations related to climatic and geomorphological factors.

Previous spectroscopic studies conducted in northern Jordan have primarily focused on qualitative or semi-quantitative relationships between soil spectral characteristics and surface properties such as soil color and iron oxide presence, using instruments such as the ASD FieldSpec® 3 Hi-Res spectroradiometer (e.g., Sahwan et al., 2021). While these studies demonstrated the sensitivity of visible-range spectroscopic data to surface soil attributes, they did not develop quantitative predictive models linking field-acquired spectra to laboratory-measured geochemical soil properties. Moreover, their findings revealed a strong relationship between visible-range spectral data and free iron oxides, whereas no significant correlation with soil organic carbon was reported.

The present study advances beyond spectral–color associations by integrating field spectroscopy with laboratory analyses and Partial Least Squares Regression (PLSR) to quantitatively predict free iron oxides (Fed), soil organic carbon (SOC), and calcium (Ca). The primary goal of this research is to evaluate soil spectral reflectance as a proxy for laboratory-based soil property estimation by modeling the relationships between VIS–NIR spectra and key geochemical parameters. Previous large-scale soil mapping efforts in Jordan, such as the National Soil Map and Land Use Project (NSMLUP, 1989–1995; MoA, 1995), relied mainly on USDA soil classification and produced limited-resolution maps (1:250,000) covering selected regions (Ababsa, 2013). Consequently, the adoption of advanced remote sensing-based techniques is essential for generating accurate, high-resolution digital soil maps.

Therefore, the main objective of this research is to assess the feasibility of using VIS–NIR field spectroscopy as a quantitative alternative to conventional laboratory soil analyses in northern Jordan. By developing and validating PLSR-based predictive models for key soil fertility indicators—free iron oxides, soil organic carbon, and calcium—this study provides a methodological framework to support future digital soil mapping initiatives. Rather than presenting a comprehensive national soil spectral library, the outcomes of this research represent a foundational contribution toward such an initiative, demonstrating the potential structure, performance, and limitations of spectroscopy-based soil characterization under Jordanian environmental conditions.

2. Materials and Methods

2.1 Soils in Jordan

The spatial distribution of soils in Jordan is primarily controlled by climate and topography. The country's climate ranges from arid and desert conditions in the eastern and southern regions to sub-humid Mediterranean conditions in the northern and western highlands. Jordan's geological diversity contributes significantly to its soil variability, as the landscape comprises various lithologyical units, including chalk, limestone, sandstone, chert, marl, and assorted Pleistocene and Holocene deposits such as alluvial, eolian, and lava flows materials (Bender et al., 1974). The contrasting physical and chemical characteristics of these parent materials result in a wide range of soil properties across the country (Bender et al., 1974). A substantial portion of Jordan's soils developed on carbonate-rich and basaltic rocks, which are common in the northern and eastern regions (Ababsa, 2013).

Several classification systems have been applied to categorize Jordanian soils. Table 1 summarizes the classifications proposed by Moorman (1959) and their corresponding equivalences in the Food and Agriculture Organization of the United Nations (FAO, 2006) and the United States Department of Agriculture (USDA, 1999) classification systems. The USDA Soil Taxonomy is particularly relevant, as it is internationally recognized for its hierarchical structure and practical applicability. This system classifies soils progressively from orders (the broadest level, e.g., Alfisols, Mollisols) down to suborders, great groups, subgroups, and soil series, the latter representing local-scale soil types with specific physical and chemical properties (Cordova et al., 2005).

Table 1. Comparison of soil classifications in Jordan as proposed by Moorman (1959) and their equivalents according to the FAO (2006) and USDA (1999) systems (after Cordova et al., 2005).

Moorman, 1959	FAO, 2006	USDA, 1990
Red Mediterranean soils (Mediterranean woodlands and forest-steppe soils)	Luvic calcisols Vertic luvisols Calcic luvisols Chromic luvisols Chromic cambisols	Xerochrepts, Xerothents, Chromoxererts
Yellow Mediterranean soils (soils in transition to steppe)	Calcic calsixerolls Calcic phaeozems Luvic phaeozems	Calsixerolls Xerochrepts
Yellow soils (steppe and desert soils)	Luvic xerosols Calcic fluvisols Calcic regosols	

2.2 Study Area

The study area is situated within the administrative boundaries of the Greater Irbid Municipality in northern Jordan (Figure 1) and covers an approximate area of 185 km². Geographically, it extends between 32°26′00.17″ N – 32°39′44.87″ N and 35°51′17.52″ E – 35°58′40.49″ E. The region experiences a semi-arid Mediterranean climate, with most of the annual rainfall occurring between October and April (Al Qudah et al., 2015). The average temperature ranges from 8.0-15 °C in winter to 22-31 °C in summer (Al-Bakri et al., 2012).

According to the National Soil Map and Land Use Project (NSMLUP, 1989–1995), the dominant soil types in the area include calcixerollic, lithic, typic xerochrepts, and typic and entic chromoxererts (Ababsa, 2013). Geomorphologically, the study area lies within the Houran Plains, characterized by extensive flat terrain with thick red, clay-rich soils developed over basaltic and carbonate parent materials (Al Qudah et al., 2015). These soils play a vital role in regional agriculture and hydrological processes, making the area suitable for assessing soil spectral variability and geochemical composition.

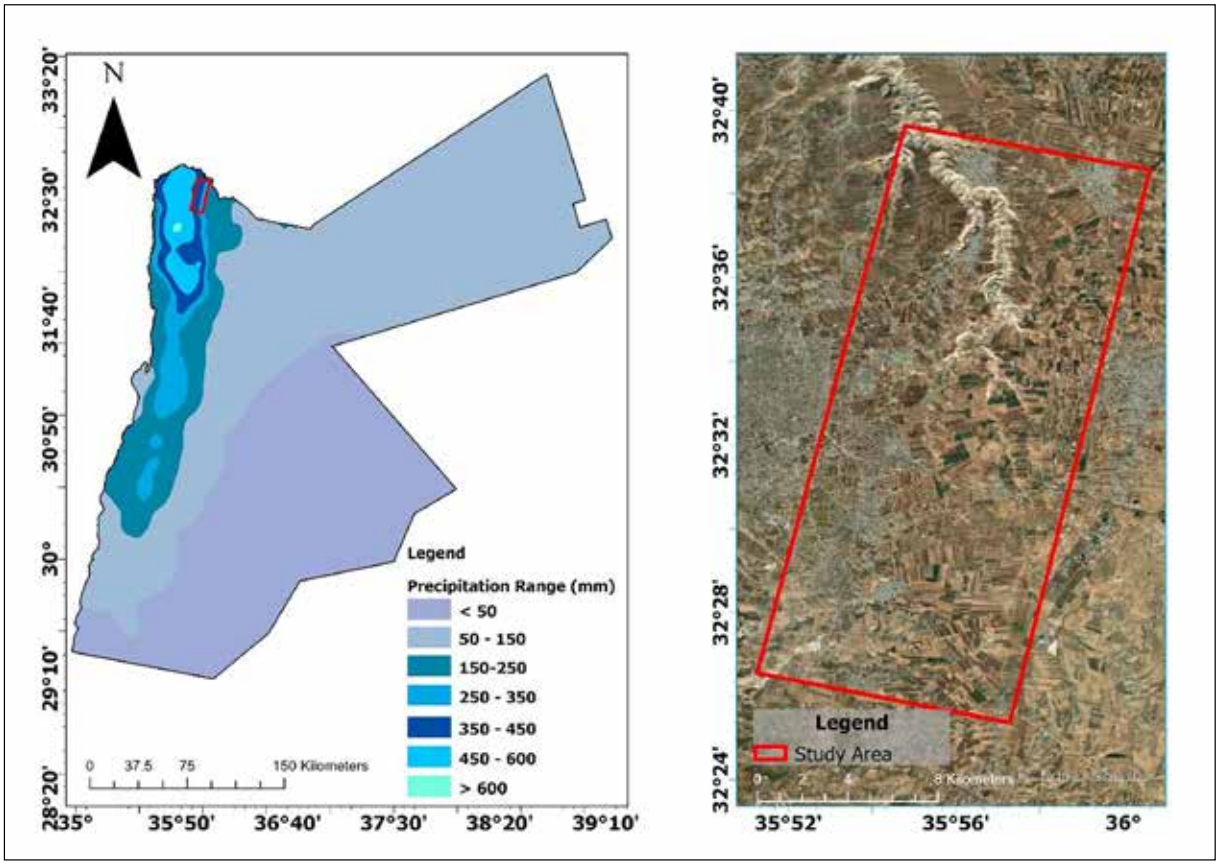

Figure 1. Map showing annual precipitation and the location of the study area in northern Jordan (derived from Landsat-8 imagery).

Most of the study area is covered by soil deposits; however, several rock formations are also exposed, belonging to the Balqa and Ajloun Groups (Figure 2). The Balqa group consists of six formations that are predominantly composed of chert beds and fossiliferous chalk, which is notably rich in vertebrate remains (Alnimrat et al., 2022). In contrast, only the Wadi As Sir Formation of the Ajloun Group is exposed within the study area. This formation is characterized by bedded chert, chalk, limestone, phosphorite, dolomite, and porcelanite (Abed, 2017).

These lithological units serve as the parent materials for the region's soils. The nature of the parent material exerts a significant influence on the concentration and type of nutrient elements within the soil —an effect that is more pronounced in young soils and diminishes as soils age and undergo weathering. Understanding the mineralogical composition of these rocks is therefore essential for interpreting their role in soil genesis and the region's geochemical variability (Singh and Schulze, 2015).

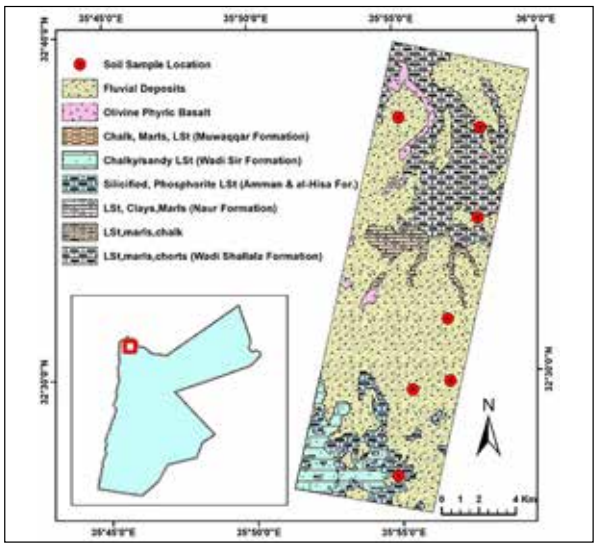

Figure 2. Simplified geological map of the formations exposed within the study area, northern Jordan, modified after Moh'd (1997) and Abdelhamid (1993).

2.3 Data Collection

Soil samples and corresponding spectra data were collected from the field using an ASD Handheld 2 Spectroradiometer (Figure 3). The spectral reflectance measurements were conducted prior to plowing season to ensure undisturbed soil surface conditions and reliable calibration. Following each spectral acquisition, approximately 2 kg of surface soil was collected from the same sampling point and sealed in labeled plastic bags for subsequent physical and geochemical analyses. The ASD HandHeld 2 Spectroradiometer (Figure 4) is a portable non-destructive field instrument capable of rapid measurements within the visible to near-infrared (VIS–NIR) range of 325–1075 nm, covering 751 spectral bands. To maintain data accuracy, the instrument was calibrated every 10 minutes using a white reference panel. Several precautionary steps were taken to minimize external noise and measurement error. Field operators wore dark clothing to reduce light scattering, and the spectroradiometer sensor was maintained at a fixed height of approximately 2.0 m above the soil surface, oriented toward the sun to minimize shadow effects and ensure stable illumination during measurements. . Measurements were also conducted away from electrical lines and reflective surfaces to prevent external electromagnetic and optical interference.

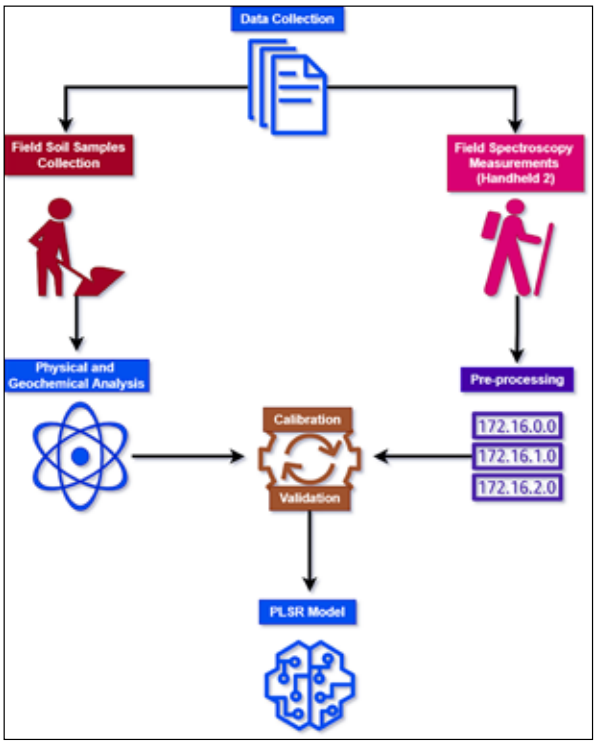

Figure 3. Flowchart illustrating the methodological framework adopted in this study, including field data collection, laboratory analysis, and statistical modeling procedures.

The soil sampling locations (Figure 5) were carefully selected to represent the diversity of soil types across the study area and to minimize the influence of vegetation on the soil's spectral signal. Sites with minimal vegetation cover were prioritized to avoid interference from plant material during spectral measurements. Two temporal constraints guided data collection: 1) measurements were conducted during periods of lowest vegetation cover, and 2) sampling occurred only when solar radiation was sufficient, following the recommendations of Cropscan™ (2001). All field measurements were carried out around noon, when the sun was near its zenith and cloud cover was minimal, to ensure consistent illumination conditions. A clustered random sampling strategy was adopted to ensure representative coverage of soil variability across the study area. Seven sampling clusters were selected based on differences in dominant soil types, land-use patterns, and geomorphological settings, as identified from existing soil and geological maps, and field reconnaissance. Within each cluster, approximately five to six surface soil samples were collected at randomly selected locations, resulting in a total of forty samples. This sampling design was chosen to capture both local-scale variabilities within clusters and broader spatial heterogeneity across the study area, while minimizing the influence of vegetation cover on the soil spectral signal.

Figure 4. Calibration process of the ASD HandHeld 2 Spectroradiometer using a white reference panel to ensure measurement accuracy during field data acquisition.

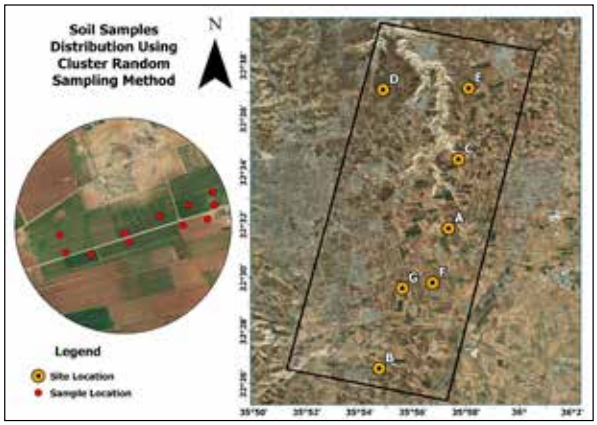

Figure 5. Spatial distribution of soil sampling clusters across the study area, illustrating the locations of the seven sampling sites. Site A is shown as an example of the randomly collected soil samples within a cluster.

2.4 Laboratory Analysis

Laboratory analyses were conducted to quantify the key soil properties targeted in this study and to provide reference measurements for calibrating and validating the spectroscopic models. The collected soil samples were subjected to standardized chemical analysis procedures to determine soil organic carbon (SOC), total calcium (Ca),

and free iron oxides (Fed). These parameters were selected due to their relevance to soil fertility, pedogenic processes, and their known spectral responsiveness in the VIS–NIR region. The analytical methods applied for each parameter are described in detail in the following subsections.

2.4.1 Soil Organic Carbon (SOC)

Soil organic carbon (SOC) plays a vital role in determining soil physical structure, influencing aggregation, porosity, and overall fertility (Sparks et al., 1996). Soil organic matter exists at various stages of decomposition, encompassing microbial biomass as well as plant and animal residues. The Walkley and Black (1934) wet oxidation method, as described in Sparks et al. (1996), was used to quantify SOC in the collected samples. The absorbance of calibration standards and sample solutions was measured at 600 nm using a Thermo Electron Corporation spectrophotometer housed in the Department of Earth and Environmental Sciences, Yarmouk University.

2.4.2 Calcium Content (Ca)

Calcium is a fundamental element for plant growth, contributing to cellular structure and fruit firmness, and indirectly influencing chlorophyll production through its interaction with iron (Fan et al., 2016). The sodium carbonate fusion method (Sparks et al., 1996) was employed to decompose the soil samples and estimate total calcium (Ca) and iron (Fe) contents. The digested samples were subsequently analyzed using a PerkinElmer AAS 200 atomic absorption spectrophotometer available in the Department of Chemistry, Yarmouk University.

2.4.3 Free Iron Content (Fed)

The citrate–bicarbonate–dithionite (CBD) extraction method was applied to determine free iron oxides (Fed) in the soil samples, as recommended for large sample sets (Sparks et al., 1996). The iron concentration in the extracted CBD solution was quantified using a PerkinElmer AAS 200 atomic absorption spectrophotometer at the Department of Chemistry, Yarmouk University.

2.5 Statistical analysis

The statistical analysis was conducted using Unscrambler® X v10.4 to develop a robust regression model that predicts unknown geochemical values for soil samples based on their spectroscopic attributes. Unscrambler® X is a commercial software package designed for multivariate data analysis, particularly useful in analytical applications such as near-infrared (NIR) spectroscopy, where it supports both calibration and predictive model development for real-time material analysis. In this study, two primary datasets were employed: 1) Response matrix (Y): geochemical data obtained from laboratory analyses, and 2) Predictor matrix (X): spectral reflectance data derived from field spectroscopy measurements. The analytical workflow comprised five main stages: 1) pre-processing of the spectral data to enhance signal quality and remove noise; 2) application of partial least squares (PLS) regression to model relationships between spectral and geochemical variables; 3) model calibration using reference data to establish the predictive relationship; 4) model validation to evaluate accuracy and generalizability; 5) model testing to assess the final predictive performance.

In addition to the coefficient of determination (R^2), model performance was evaluated using the root mean square error of calibration (RMSEC), root mean square error of cross-validation (RMSECV), residual prediction deviation (RPD), and bias. RMSEC and RMSECV were used to quantify calibration accuracy and prediction uncertainty, respectively, while RPD—defined as the ratio between the standard deviation of the reference data and RMSECV—was used as an indicator of model robustness. According to commonly accepted criteria, RPD values greater than 2 indicate good predictive performance, whereas values between 1.4 and 2 suggest moderate predictive capability.

Model bias was calculated as the mean difference between predicted and measured values to assess systematic over- or underestimation. Bias values close to zero indicate unbiased predictions.

The optimal number of latent variables (PLSR factors) was determined by minimizing RMSECV and avoiding overfitting, following the guidelines provided in Unscrambler® X. Only factors that contributed significantly to reducing prediction error were retained in the final models.

The inclusion of these diagnostic metrics demonstrates that the developed PLSR models for free iron oxides (Fed), soil organic carbon (SOC), and calcium (Ca) exhibit satisfactory calibration accuracy, acceptable prediction uncertainty, and stable generalization performance based on their VIS–NIR spectral signatures.

2.5.1 Pre-processing of the spectroscopic data

Spectral pre-processing was applied to the raw VIS–NIR reflectance data to reduce noise, correct for instrumental and environmental effects, and enhance the correlation between spectral variables and laboratory-measured soil properties. All transformations were performed using Unscrambler® X v10.4 following recommended procedures for field-acquired soil spectra.to optimize the relationship between the spectral data matrix and the laboratory-measured contents of free iron oxides (Fed), soil organic carbon (SOC), and calcium (Ca).

A series of transformations was applied sequentially: Baseline correction was first applied to adjust for spectral offsets, caused by variations in illumination intensity and sensor positioning. The minimum reflectance value within each spectrum was used as a reference, ensuring spectral normalization and improving inter-sample comparability.

Correlation Optimized Warping (COW) was subsequently employed to correct minor wavelength shifts along the spectral axis (x) resulting from sensor instability and field measurement conditions. Default segment length and slack parameters recommended by Unscrambler® X were used, which improved spectral alignment and reduced misregistration between samples.

A multiplicative Scatter Correction (MSC) was applied to minimize scattering effects related to differences in soil particle size, surface roughness, and moisture conditions (Unscrambler® X, 2014). MSC improved model linearity

by reducing multiplicative and additive scattering, leading to improved calibration stability, particularly for Fed and Ca models. While SOC data were excluded from this stage due to their specific response characteristics.

A deresolve transformation was then implemented to reduce spectral resolution and suppress high-frequency noise while preserving diagnostically relevant spectral features. This step reduced collinearity among adjacent wavelengths and improved model robustness without loss of predictive information.

Finally, Orthogonal Signal Correction (OSC) was applied to remove spectral variance uncorrelated to the response variables. OSC effectively filtered non-informative components from the X-matrix, resulting in improved signal-to-noise ratios and enhanced prediction accuracy during cross-validation.

The combined application of these pre-processing steps resulted in higher coefficients of determination (R^2) and reduced prediction errors in PLSR models compared to those, developed using raw spectra, confirming their effectiveness in improving model performance.

2.5.2 Model Calibration

The PLSR model calibration was conducted using diagnostic parameters such as score plots, loading plots, and regression coefficients to evaluate model structure and performance. The PLSR approach organizes samples along model components based on the variation within the predictor matrix (X)—representing the spectral data—and the response matrix (Y)—representing the laboratory-measured soil properties. PLS loadings describe how each variable in the X- and Y-spaces is contributing to the model components, providing insight into the correlation structure between spectral variables and soil attributes. To identify potential outliers, the X–Y relationship plot (t-scores from X versus u-scores from Y) was examined to detect samples that deviated significantly from the general data trend. Each variable was weighted by its regression coefficient, reflecting its importance in predicting a specific Y-response. The regression coefficients also served as indicators of model interpretability and predictive strength. Ideally, the predicted versus reference (measured) plot should exhibit a linear relationship with a slope near 1 and a correlation coefficient (R^2) close to unity, indicating high model accuracy. In a predicted-versus-reference plot, the predicted values should show a straight-line relationship with the measured values, ideally with a slope of 1 and a correlation of 1 or near 1. These diagnostic parameters were employed to iteratively exclude outlier samples, irrelevant variables, and spectral noise, ultimately producing a stable and optimized PLSR model with maximum predictive accuracy (Unscrambler® X, 2014).

2.5.3 Model Validation

Model validation is a critical step in assessing the reliability and predictive performance of a regression model that has been calibrated using empirical data. Validation estimates the level of uncertainty associated with future predictions and determines how effectively the model can predict new observations of the same type as those used in its development. A model is considered valid when its prediction uncertainty is minimal, and its performance remains stable across independent datasets (Unscrambler® X, 2014).

In cases where a large number of samples are available (typically more than 50), independent validation or test-set validation can be applied. However, in this study, the dataset consisted of 33 samples, which was insufficient for reliable independent testing. Therefore, a cross-validation approach was adopted as a more suitable alternative. Cross-validation systematically partitions the dataset into subsets, iteratively using one subset for testing and the remainder for model calibration. This approach provides a robust measure of model accuracy and generalization capability, particularly when working with limited sample sizes.

2.5.4 Partial Least Squares Regression (PLS Regression)

The PLSR method, also known as Projection to Latent Structures (PLS), models the predictor (X) and response (Y) matrices simultaneously to extract latent variables from X that best predict the corresponding variables in Y. These latent variables, referred to as factors, are analogous to the principal components in Principal Component Analysis (PCA) but are specifically optimized to maximize the covariance between X and Y (Unscrambler® X, 2014).

Unlike Principal Component Regression (PCR), which first performs PCA on the X-matrix and then regresses the resulting component scores (T) against the Y data, PLSR integrates these steps. This simultaneous modeling approach allows PLSR to capture the most relevant spectral information while minimizing residual error, often achieving high predictive accuracy with fewer factors than PCR. Consequently, PLSR provides an efficient and robust framework for establishing quantitative relationships between soil spectral reflectance data and their corresponding laboratory-measured properties.

3. Results and Discussion

This section presents and discusses the results obtained from both laboratory analyses and spectroscopic modeling. It is organized into three main parts: first, the spatial variability and descriptive statistics of the laboratory-measured soil properties are reported; second, the performance of the spectral pre-processing and PLSR models is evaluated using calibration and validation metrics; and finally, the predictive results are interpreted in relation to soil spectral behaviour and compared with findings from previous studies. The discussion highlights the strengths and limitations of the developed models and their implications for soil spectroscopy applications in semi-arid environments.

3.1 Laboratory Analysis

Soil organic carbon (SOC) is primarily derived from the biological decomposition of plant residues and other organic materials within the soil (Jenkinson, 1966). The upper soil horizon (<30 cm) typically contains the highest SOC concentrations, as it is directly influenced by climatic factors and human activities such as cultivation, grazing, and fertilization (Batjes, 2006).

The laboratory analyses revealed substantial variation

in SOC content across the study area (Table 2). SOC values ranged from a minimum of 1.0% in sample no. 31 (Site E) to a maximum of 3.9% in samples no. 14 and 20 (Sites B and C), with a mean of 1.69%. This considerable variation likely reflects spatial differences in organic matter inputs, biological activity, and local microclimatic conditions.

The coefficient of variation (CV) for SOC was 36.1%, indicating high variability among the samples. Such variation suggests that SOC distribution within the study area is influenced by both land-use practices and environmental heterogeneity, consistent with findings from similar semi-arid Mediterranean landscapes.

Table 2. Descriptive statistics of soil properties analyzed in the study.

Soil parameter	n	Min	Max	Mean	SD	CV
SOC %	40	1.09	3.96	1.69	0.61	36.17
Ca %	40	0.08	10.65	3.19	2.22	69.83
Fed %	40	0.40	1.28	0.89	0.22	24.92

n, number of samples; SD, standard deviation; CV, coefficient of variation (=Mean/SD* 100%)

The results of the sodium carbonate fusion analysis are summarized in Table 2. The total calcium (Ca) content exhibited substantial variability, ranging from a minimum of 0.08% in sample no. 25 (Site D) to a maximum of 10.6% in sample no. 9 (Site A), with a mean value of 3.19%. The coefficient of variation (CV) was 69.83%, indicating an extremely high degree of dispersion among the samples. This pronounced variability likely reflects differences in carbonate content, soil management practices, and microenvironmental conditions across the study sites.

In contrast, the total iron (Fe) content across sites A to E was relatively uniform. This consistency suggests that iron concentration in the soils is primarily governed by parent material composition and pedogenic processes, which appear to be similar across the sampled locations.

Generally, free iron in soils originates from secondary iron oxides, either absorbed or precipitated onto mineral surfaces or bound in iron–organic matter complexes. Iron occurs in two oxidation states—ferrous (Fe^{2+}) and ferric (Fe^{3+})—both of which play essential roles in plant metabolism, respiration, and photosynthesis (Jones, 2020). The relative proportions of these oxidation states are strongly influenced by soil pH and pore-water content.

The analysis of free iron oxides (Fed) revealed a variation with values ranging from 0.40% (sample no. 13, Site B) to 1.28% (sample no. 28, Site D) (Table 2). These differences likely reflect localized variations in drainage conditions, oxidation–reduction dynamics, and organic matter associations, which collectively influence iron mobility and availability in the soil matrix.

3.2 Pre-processing and Correlation models

The relationships between the hyperspectral reflectance data and the three selected soil properties—free iron oxides (Fed), soil organic carbon (SOC), and calcium (Ca)—were examined through Partial Least Squares (PLS) regression analysis. After applying the pre-processing procedures described in Section 2.5.1, a robust and stable PLSR model was developed for each soil property.

Model validation was subsequently performed to assess model stability and to evaluate the predictive confidence for estimating unknown soil samples. The validation results confirmed that the applied preprocessing transformations effectively enhanced the correlation between spectral signatures and laboratory-measured soil parameters, yielding reliable predictive models for Fed, SOC, and Ca.

3.2.1 Pre-processing of the spectroscopic data

Several spectral transformation techniques were applied to the raw hyperspectral data to enhance signal quality, remove noise, and achieve optimal correlations between spectral reflectance and the measured soil properties (Figure 6a–d).

Baseline correction was first applied to adjust for spectral offsets and normalize reflectance intensity (Figure 6a). The Correlation Optimized Warping (COW) method was then used to realign the spectra and correct minor wavelength shifts along the x-axis (Figure 6b). Subsequently, Multiplicative Scatter Correction (MSC) was implemented to minimize scattering effects caused by differences in particle size and surface roughness (Figure 6c). Finally, the Deresolve transformation was applied to reduce excessive spectral resolution and eliminate high-frequency noise, thereby improving data smoothness and model interpretability (Figure 6d). These pre-processing steps collectively enhanced the stability and accuracy of the subsequent PLSR models developed for Fed, SOC, and Ca prediction.

3.2.2 Correlation between soil properties and reflectance data (PLS regression)

Three stable Partial Least Squares Regression (PLSR) models were developed for predicting free iron oxides (Fed), soil organic carbon (SOC), and calcium (Ca) content, each demonstrating credible validation accuracy and strong predictive confidence.

For Fed, the PLSR model achieved coefficients of determination (R^2) of 0.82 for calibration and 0.85 for cross-validation, using only three latent factors (Figure 7c–d). The first two PLSR factors explained 88% of the variance in the X-matrix (spectral data) and 82% in the Y-matrix (Fed concentrations) (Figure 7a). The score plot showed a clear, consistent distribution of samples across the first two factors, confirming the model's robustness.

The regression coefficient plot identified the spectral bands most influential in predicting Fed (Figure 7b). The important X-variables (spectral bands) were characterized by strong positive or negative regression coefficients, distributed intermittently along the wavelength axis. According to Liu (2019), soil iron oxides exhibit maximum positive correlations at 585, 747, 1153, 1380, and 2187 nm. In this study, the critical wavelengths associated with iron oxides were distributed primarily across the visible and near-infrared (VIS–NIR) region (325–1075 nm). This pattern aligns with findings by Heller and Ben-Dor (2020), who noted that both soil organic matter (SOM) and Fed are spectrally active within the 400–1000 nm range, often

exhibiting overlapping effects.

To enhance model precision, spectral wavelengths that overlapped significantly with SOM reflectance characteristics were excluded from the set of important variables, thereby isolating the spectral contribution of Fed and improving model interpretability.

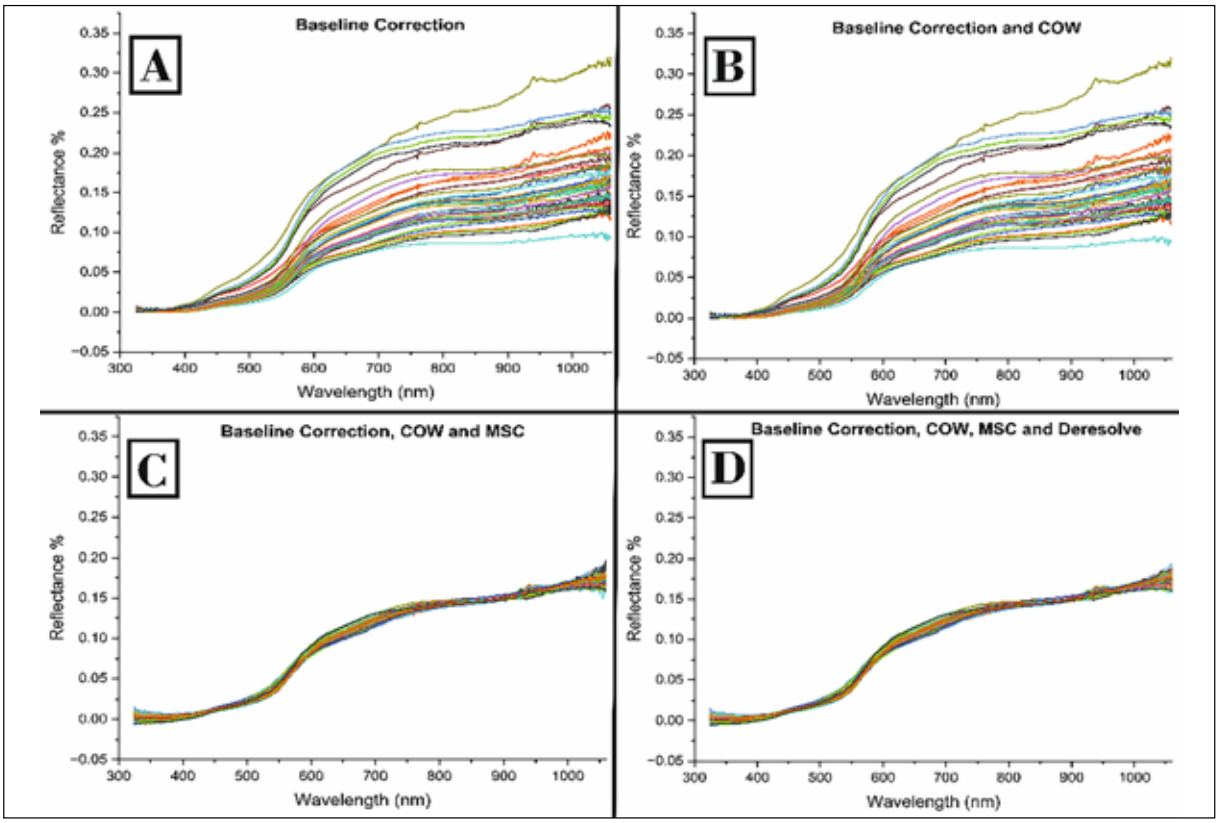

Figure 6. Pre-processing transformations applied to the spectroscopic data: (a) baseline correction to adjust spectral offset, (b) correlation optimized warping (COW) to correct wavelength shifts, (c) multiplicative scatter correction (MSC) to remove scattering effects, and (d) deresolve transformation to reduce high-frequency noise and improve signal smoothness.

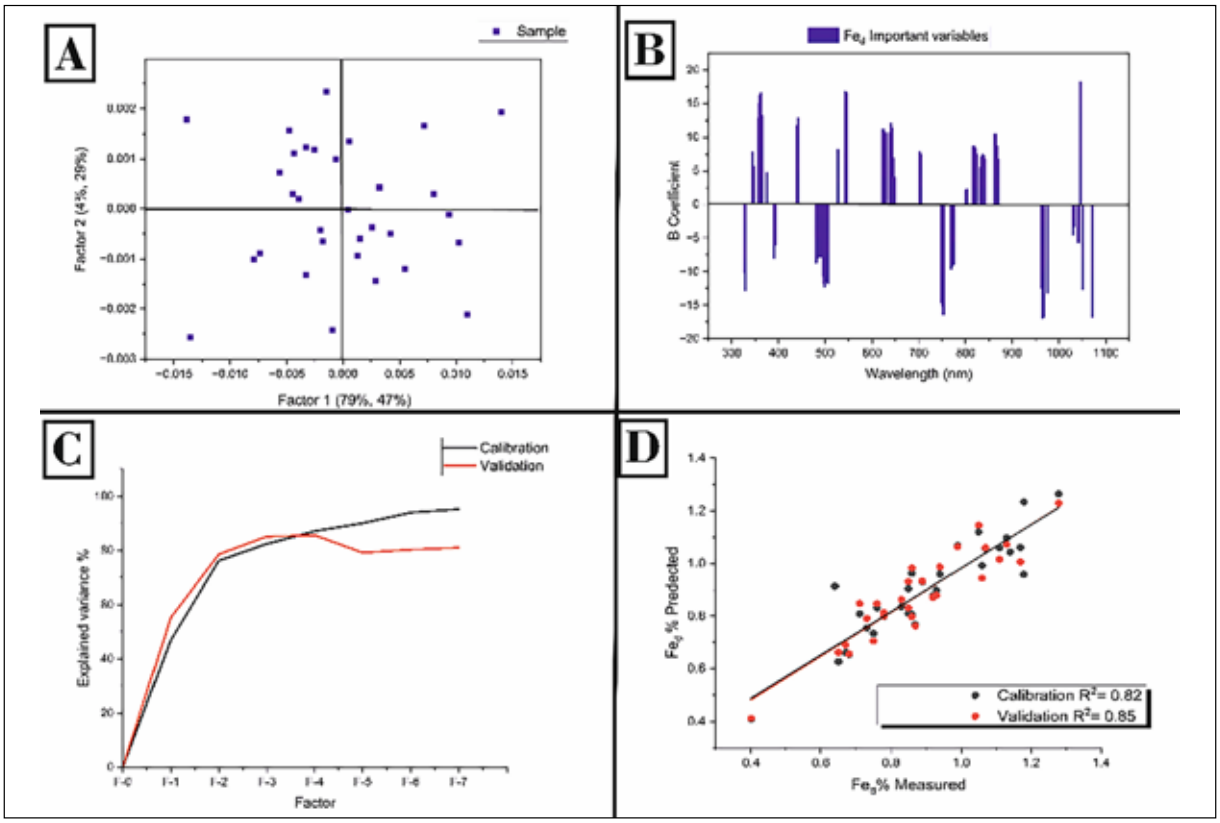

Figure 7. Partial Least Squares Regression (PLSR) model for free iron oxides (Fed) developed using 32 soil samples.

The strong predictive performance of the Fed model is consistent with previous studies that report high sensitivity of visible wavelengths to iron oxide absorption features (e.g., Sahwan et al., 2021; Heller and Ben-Dor, 2020). The relatively high RPD values obtained for Fed indicate robust model reliability, reflecting the pronounced spectral activity of iron oxides in the VIS–NIR region.

The PLSR model for soil organic carbon (SOC) demonstrated strong predictive performance, achieving a coefficient of determination (R^2) of 0.83 for calibration and 0.72 for cross-validation, with four latent factors employed (Figure 8b–c). The score plot illustrates the distribution of samples along the first two factors, where Factor 1 accounted for 100% of the variance in the X-matrix (spectral data) and 36% of the variation in the Y-matrix (SOC), while Factor 2 explained an additional 34% of the variance in Y (Figure 8b).

According to Xu et al. (2020), SOC is highly correlated with spectral features in the visible and near-infrared (VIS–NIR) regions, particularly at wavelengths around 400, 530, 610, 800, 1000, and 1100 nm. In the present study, the identified spectral bands for SOC prediction (Figure 8b) closely align with these ranges. The selected wavelengths are associated with variations in chromophores and the optical properties of humic acids (Xu et al., 2020). Moreover, the significant wavelengths observed in the NIR region correspond to vibrational overtones of C–H, O–H, and N–H bonds, which are characteristic of organic carbon compounds.

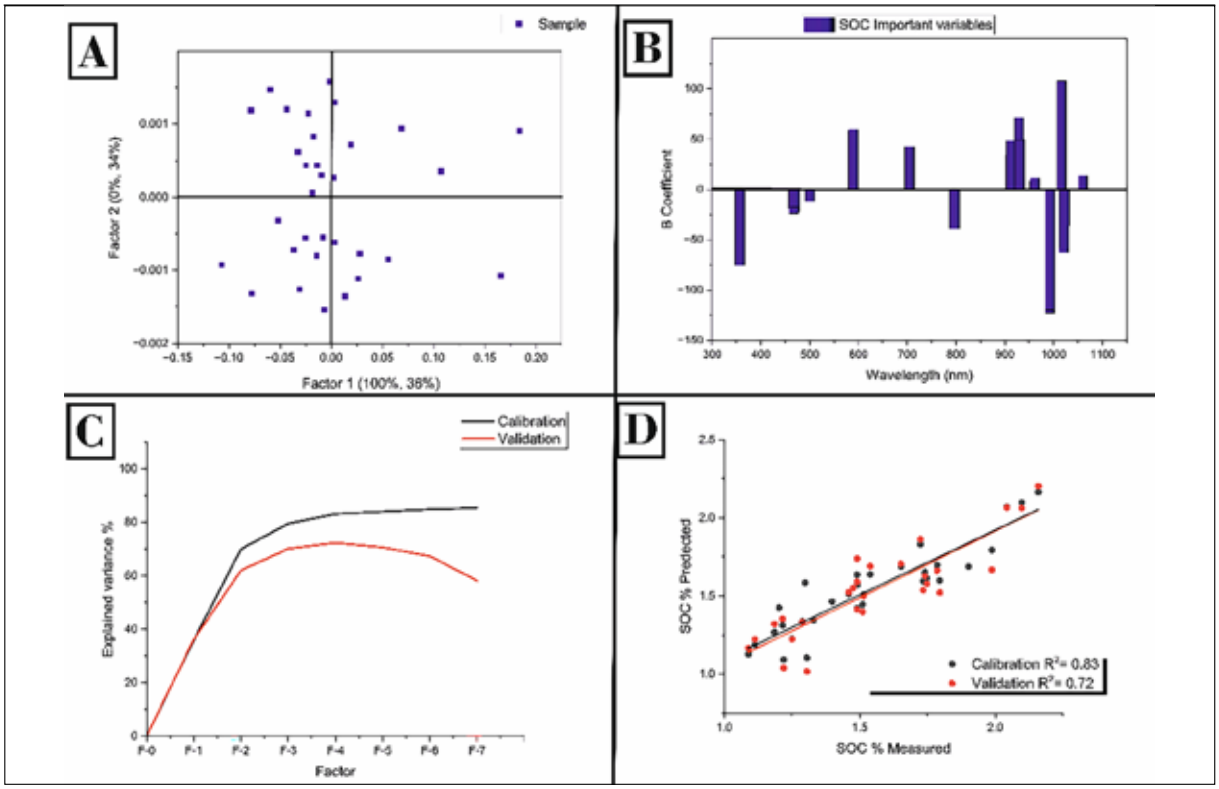

Figure 8. Partial Least Squares Regression (PLSR) model for soil organic carbon (SOC) developed using 32 soil samples. The model achieved an R^2 of 0.83 for calibration and 0.72 for cross-validation, utilizing four latent factors to explain the spectral–SOC relationship.

The SOC model exhibited lower validation accuracy compared to Fed and Ca, which can be attributed to the complex and indirect spectral behavior of organic carbon. SOC absorption features often overlap with those of iron oxides and soil moisture, reducing model specificity, particularly in semi-arid soils with relatively low organic matter content. Similar limitations have been reported in other VIS–NIR studies conducted in arid and semi-arid environments (Xu et al., 2020; Gomez, 2008)

The PLSR model developed for calcium (Ca) achieved a coefficient of determination (R^2) of 0.87 for calibration and 0.79 for validation (Figure 9a, c–d). The model utilized three latent factors, which explained 93% of the variance in the X-matrix (spectral data) and 58% of the variance in the Y-matrix (calcium content). The score and regression coefficient plots revealed a clear distribution of samples across the first two factors, as well as the key spectral variables contributing to Ca prediction (Figure 9b).

The correlation between calcium and VIS–NIR spectral reflectance is not yet fully understood. However, in this study, the most significant spectral bands correlated with Ca were identified within the visible to near-infrared range after data pre-processing, showing both positive and negative relationships (Figure 9b). According to Gomez (2008), important wavelengths for estimating $CaCO_3$ content in soils are typically observed near 500, 600, and 1430 nm, which are closely associated with soil colour—an attribute linked to calcium carbonate concentration. Gomez (2008) identified additional spectral features within the VIS–NIR range, notably in the visible wavelengths (approximately 500–650 nm) related to soil color variations and in the near-infrared region around 1400 nm, which are indirectly influenced by carbonate minerals. The consistency between these spectral regions and those identified in the present study further supports the applicability of VIS–NIR spectroscopy for estimating calcium-related soil properties..

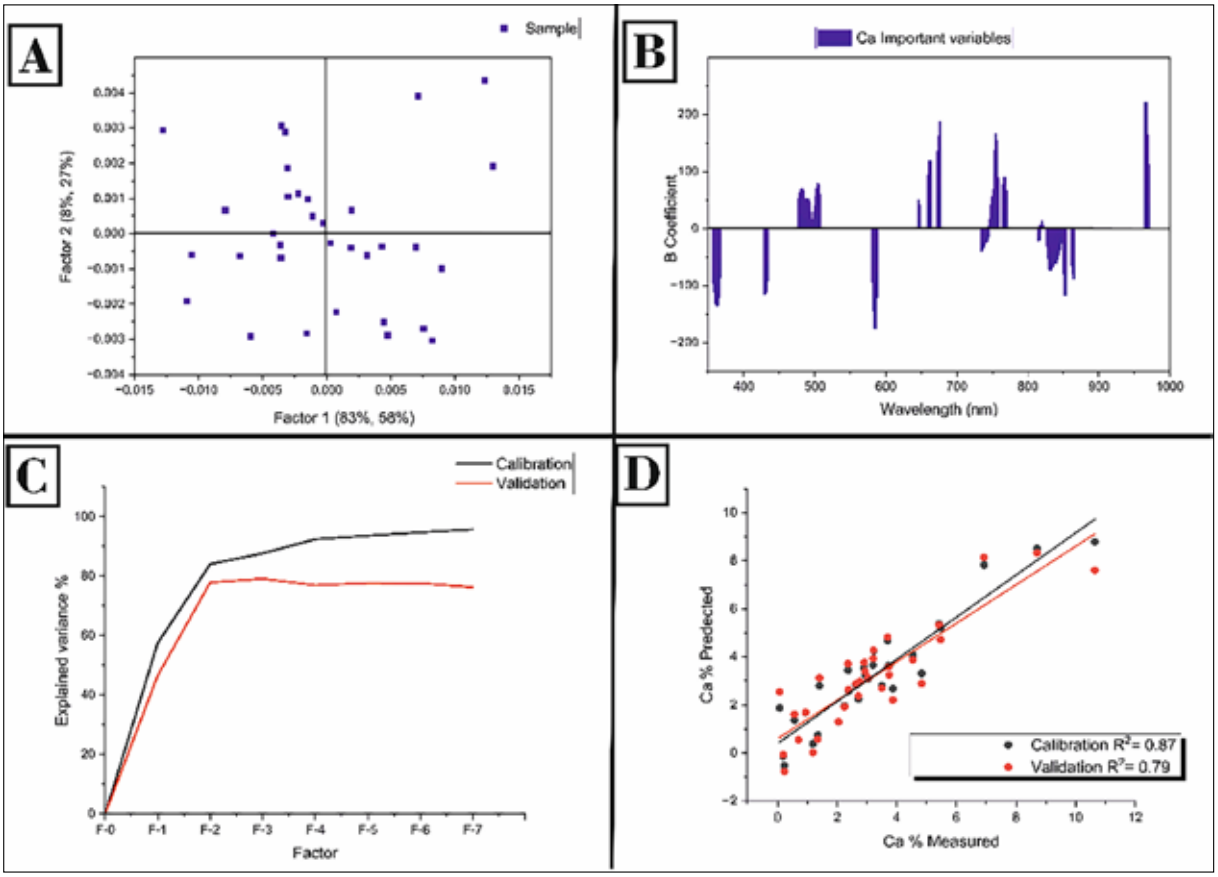

Figure 9. Partial Least Squares Regression (PLSR) model for calcium (Ca) developed using 32 soil samples. The model achieved R^2 values of 0.87 for calibration and 0.79 for validation, with three latent factors explaining 93% of the variance in X and 58% in Y.

The Ca model showed strong calibration performance, likely due to the influence of calcium carbonate on soil brightness and colour, which indirectly affects VIS–NIR reflectance. However, the moderate validation performance suggests that Ca prediction remains sensitive to soil texture and mineralogical variability.

4. Conclusions and Recommendations

This study demonstrates the robustness and efficiency of VIS–NIR field spectroscopy combined with Partial Least Squares Regression (PLSR) for characterizing selected soil properties under semi-arid Mediterranean conditions in northern Jordan. Based on correlations within the 325–1075 nm spectral range, three PLSR models were successfully developed to predict free iron oxides (Fed), soil organic carbon (SOC), and calcium (Ca), showing satisfactory calibration and validation performance.

The results revealed distinct, intermittent spectral responses associated with each soil property across the VIS–NIR region, confirming that Fed, SOC, and Ca are spectrally active and can be reliably modeled using multivariate regression. These findings highlight the potential of soil spectroscopy as a rapid and effective alternative to conventional laboratory analyses for soil property estimation.

Importantly, this research should be viewed as a preliminary but essential step toward the development of a soil spectral database in Jordan. Although the present dataset is spatially limited, it establishes a validated methodological foundation for future large-scale sampling, model generalization, and integration with remote sensing platforms. Expanding the approach to include a wider range of soil types and geographic regions will be necessary to support the development of standardized spectral calibration models and, ultimately, a comprehensive national soil spectral library.

Furthermore, integrating satellite-based and unmanned aerial vehicle (UAV) platforms with soil spectroscopy has the potential to significantly enhance data acquisition efficiency and spatial coverage. Such integration would enable the generation of high-resolution digital soil maps, supporting precision agriculture and sustainable land management. The availability of up-to-date spectroscopy-based soil information would assist farmers and decision-makers in optimizing crop selection, irrigation practices, and fertilization strategies, thereby improving agricultural productivity and resource efficiency in Jordan.

References

Ababsa, M.; Kohlmayer, C. Atlas of Jordan: History, Territories and Society; Presses de l'Ifpo: Beirut, Lebanon, 2013.

Abdelhamid, G. Geological Sheet of Irbid; Natural Resources Authority: Amman, Jordan, 1993.

Abed, A.M. An overview of the geology and evolution of Wadi Mujib. Jordan Journal of Natural History 2017, 4, 6–28.

Al Qudah, K.; Abu-Jaber, N.; Jaradat, R.; Awawdeh, M. Artificial rainfall tests, soil moisture profiles, and geoelectrical investigations for the estimation of recharge rates in a semi-arid area (Jordanian Yarmouk River Basin). Environmental Earth Sciences 2015, 73, 6677–6689. https://doi.org/10.1007/s12665-015-4094-3

Al-Bakri, J.; Saoub, H.; Nickling, W.; Suleiman, A.; Salahat, M.; Khresat, S.; Kandakji, T. Remote sensing indices for monitoring land degradation in a semiarid to arid basin in Jordan. Proceedings of SPIE 2012, 8538. https://doi.org/10.1117/12.974438

Alnimrat, R.M.; Alqudah, M.; Al-Shereideh, S.; Alsaleh, A.R.S. Geochemical and petrological analyses of the phosphorite deposits (Amman/Al Hisa Formation) from northwest Jordan. Arabian Journal of Geosciences 2022, 15, 1211. https://doi.org/10.1007/s12517-022-10238-5

Batjes, N.H. Soil carbon stocks of Jordan and projected changes upon improved management of croplands. Geoderma 2006, 132, 361–371. https://doi.org/10.1016/j.geoderma.2005.05.009

Bender, F. Geology of Jordan; Gebrüder Borntraeger: Berlin, Germany, 1974.

Camargo, L.A.; Júnior, J.M.; Barrón, V.; Alleoni, L.R.F.; Barbosa, R.S.; Pereira, G.T. Mapping clay, iron oxide and adsorbed phosphate in Oxisols using diffuse reflectance spectroscopy. Geoderma 2015, 251, 124–132. https://doi.org/10.1016/j.geoderma.2015.03.017

Cordova, C.E.; Foley, C.; Nowell, A.; Bisson, M. Landforms, sediments, soil development, and prehistoric site settings on the Madaba–Dhiban Plateau, Jordan. Geoarchaeology 2005, 20, 29–56. https://doi.org/10.1002/gea.20041

CropScan™. Multispectral Radiometer (MSR): User's Manual and Technical Reference; CropScan™: Rochester, MN, USA, 2001.

Demattê, J.A.M.; Alves, M.R.; Gallo, B.C.; Fongaro, C.T.; Souza, A.B.; Romero, D.J.; Sato, M.V. Hyperspectral remote sensing as an alternative to estimate soil attributes. Revista Ciência Agronômica 2015, 46, 223–232. https://doi.org/10.5935/1806-6690.20150026

Fan, S.-S.; Chang, F.-H.; Hsueh, H.-T.; Ko, T.-H. Measurement of total free iron in soils by H_2S chemisorption. Journal of Analytical Methods in Chemistry 2016, 2016, 1–7. https://doi.org/10.1155/2016/8015452

FAO; ISSS; ISRIC. World Reference Base for Soil Resources; FAO: Rome, Italy, 2006.

Fathololoumi, S.; Vaezi, A.R.; Alavipanah, S.K.; Ghorbani, A.; Saurette, D.; Biswas, A. Improved digital soil mapping using multitemporal satellite data fusion. Science of the Total Environment 2020, 721, 137703. https://doi.org/10.1016/j.scitotenv.2020.137703

Forkuor, G.; Hounkpatin, O.K.L.; Welp, G.; Thiel, M. High-resolution mapping of soil properties using remote sensing variables. PLOS ONE 2017, 12, e0170478. https://doi.org/10.1371/journal.pone.0170478

Gomez, C.; Lagacherie, P.; Coulouma, G. Continuum removal versus PLSR for clay and $CaCO_3$ estimation. Geoderma 2008, 148, 141–148. https://doi.org/10.1016/j.geoderma.2008.09.003

Heller Pearlshtien, D.; Ben-Dor, E. Effect of organic matter on the spectral signature of iron oxides. Remote Sensing 2020, 12, 1960. https://doi.org/10.3390/rs12121960

Jenkinson, D.S. Studies on the decomposition of plant material in soil. Journal of Soil Science 1966, 17, 280–302. https://doi.org/10.1111/j.1365-2389.1966.tb01462.x

Jones, J.D. Iron availability and management considerations. Crops & Soils 2020, 53, 32–37. https://doi.org/10.1002/crso.20015

Kumar, N.S.; Anouncia, S.M.; Prabu, M. Application of satellite remote sensing for soil fertilization assessment. International Journal of Online Engineering 2013, 9. https://doi.org/10.3991/ijoe.v9i2.2436

Liu, J.; Sun, Z. Hyperspectral characteristics and estimation of soil iron oxide content. IOP Conf. Ser.: Earth Environ. Sci. 2019, 300, 022147. https://doi.org/10.1088/1755-1315/300/2/022147

Ministry of Agriculture (MoA). The Soils of Jordan; Ministry of Agriculture: Amman, Jordan, 1995.

Moh'd, B. Geological Sheet of Irbid; Natural Resources Authority: Amman, Jordan,

Moorman, F. Report on the Soils of East Jordan; FAO: Rome, Italy, 1959.

Pereira, P.; Brevik, E.; Muñoz-Rojas, M.; Miller, B. Soil Mapping and Process Modeling for Sustainable Land Use Management; Elsevier, 2017. https://doi.org/10.1016/C2016-0-04317-6

Plummer, C.C.; Carlson, D.; Hammersley, L. Physical Geology; McGraw-Hill, 2016.

Sahwan, W.; Lucke, B.; Kappas, M.; Bäumler, R. Soil surface colors using Landsat-8 and Sentinel-2. European Journal of Remote Sensing 2018, 51, 850–862. https://doi.org/10.1080/22797254.2018.1512114

Sahwan, W.; Lucke, B.; Sprafke, T.; Vanselow, K.A.; Bäumler, R. Spectral features and iron oxides in soils. European Journal of Soil Science 2021, 72, 80–97. https://doi.org/10.1111/ejss.12947

Singh, B.; Schulze, D.G. Soil minerals and plant nutrition. Nature Education Knowledge 2015, 6, 1.

Sparks, D.L. et al. Methods of Soil Analysis, Part 3; SSSA, 1996. https://doi.org/10.2136/sssabookser5.3

The Unscrambler® X. User Manual v10.3; CAMO Software, 2014.

USDA. Soil Taxonomy; USDA, 1999.

Walkley, A.; Black, I.A. Determination of soil organic matter. Soil Science 1934, 37, 29–38. https://doi.org/10.1097/00010694-193401000-00003

Xu, L. et al. Estimation of organic carbon using Vis–NIR spectroscopy. Remote Sensing 2020, 12, 3394. https://doi.org/10.3390/rs12203394

Yu, H. et al. Prediction of soil properties using hyperspectral data. Archives of Agronomy and Soil Science 2018, 64, 546–559. https://doi.org/10.1080/03650340.2017.1369526

Zhang, G.; Liu, F.; Song, X. Digital soil mapping: Progress and prospects. Journal of Integrative Agriculture 2017, 16, 2871–2885. https://doi.org/10.1016/S2095-3119(17)61762-4

JJEES

JJEES (2026) 17 (2): 266-276
ISSN 1995-6681

Jordan Journal of Earth and Environmental Sciences

Spatio-Temporal Dynamics of Land Surface Temperature and Urbanization Impacts in Bathinda City, Punjab (1990–2022)

Gurvinder Singh[1], Rohan Kumar[1], Jai Sukh Paul Singh[1], Swati Sharma[2*], Ajay Roy[1]

[1] Lovely Professional University, Phagwara, Punjab, India
[2] Center of Excellence, SEnSRS, Indian Institute of Technology (IIT), Ropar, Punjab, India

Received on 6 October 2025; Accepted on 12 January 2026

Abstract

This study examines the relationship between changing patterns of Land Surface Temperature (LST), land use/land cover (LULC) change, and vegetation index (NDVI) in Bathinda City, Punjab, India, over 32 years (1990–2022). Using the Landsat data, LST and NDVI were calculated for four years (1990, 1999, 2010, and 2022) and analyzed alongside the dynamics of LULC maps classification. Results show that the mean LST increased significantly from 31.2°C in 1990 to 36.6°C in 2022, indicating a rising urban heat island (UHI) effect. At the same time, vegetation cover declined sharply, with NDVI maximum values dropping from 0.71 to 0.46, while built-up and open lands expanded. Regression analysis confirmed a strong negative correlation between NDVI and LST, especially in 1990 (R^2 = 0.5604), but this relationship weakened in 2022 (R^2 = 0.1259), showing that vegetation alone can no longer explain urban heating. Spatial analysis shows that higher LST values are associated with urban and industrial zones, while cooler areas are linked to vegetation and water bodies. The findings highlight the impacts of rapid urbanization without sustainable planning as a major driver of LST rise in the study area. This study recommends integrating green infrastructure into urban development policies to reduce UHI effects.

Keywords: *Spatio-Temporal, LST, LULC, NDVI, UHI*

1. Introduction

Urbanization is now a strongly human-driven process that continuously alters the physical characteristics of the land surface and disrupts climate patterns in many parts of the world (Oke, 1982; Grimmond, 2007). As the cities are growing and with the increase of population, especially near the urban centers, ultimately the surrounding croplands and natural green areas are getting replaced by infrastructures such as roads, buildings, etc., which are inhibiting the natural capacity of a landmass to reflect the heat (Imhoff et al., 2010; Abusmier & Al-Kofahi, 2025). The increased absorption of natural light by built-up elements has increased the overall Land Surface Temperature (LST) in urban areas, which has led to the problem of Urban Heat Island (UHI) formation, making the urban centers hotter than the scattered settlements and vegetated areas (Voogt & Oke, 2003; Zhou et al., 2014). The UHI formation has caused many other issues, including increased power consumption, heatstroke among kids and the elderly, fire events in many urban areas due to overconsumption of cooling appliances, increased water consumption, and water scarcity in urban centers. (Santamouris, 2015; Li et al., 2019).

In India, the situation of urban expansion is critical, particularly in Tier II cities (Manesha et al., 2021), where the construction and development projects are not monitored as per standard building and environmental codes (Bhan & Jana, 2013; Tamrakar et al., 2024), ultimately leading to dense settlements with a more LST-elevating scenario. The added-on effects of soaring LST in cities are destroying natural vegetation, as plant water intake increases while resources are limited (Rao et al., 2021).

Bathinda, a fast-developing city located in the arid agro-climatic region of Punjab, is a very suitable example for studying LST dynamics over time and the resultant UHI effect. It is an important urban center, part of the Indo-Gangetic alluvial plains and has a semi-arid climate with large seasonal temperature ranges, thus sensitive to local environmental land-cover change, as well as anthropogenic heat sources (Majumder et al 2021). The establishment of major infrastructure, such as the Guru Nanak Dev Thermal Power Plant and an oil refinery, and associated industrial and residential growth has intensified built-up surfaces while reducing vegetation cover. Bathinda experienced substantial LULC transition in the form of growth in residential areas, commercial clusters, and industrial expansions. Studies based on geospatial technologies have noted an alarming decline in vegetation cover and an increase in settlement areas, culminating in a rise in localized surface temperature. 'Bathinda's climate is represented by extreme summer temperatures and low rainfall. When combined with rapid urban expansion, these climatic conditions contribute to increased thermal stress. This study offers insight into the thermal behavior of the land surface, which can be applied to other climatic zones in India.

Voogt and Oke (2003) studied the LST surface and atmospheric UHI mechanisms, heat reradiation, reflectance, and absorption from vegetated areas compared to the built-up area. Weng et al. (2004) mapped LST dynamics

* Corresponding author e-mail: swati.9238@gmail.com

by employing Landsat ETM+ imagery and LULC change analysis in Indianapolis. Similarly, Yuan and Bauer (2007) worked on high-resolution thermal data for change analysis in temperature patterns. Imhoff et al. (2010) studied the UHI effects across U.S. cities and confirmed its correlation with the increased LST after urban expansion activities. The UHI phenomenon in India has recently been a new hazard studied by many researchers: Kikon et al. (2016) applied the NDVI analysis to detect UHI formation in Guwahati, India; Pal and Ziaul (2017) studied spatio-temporal changes in LST in Kolkata using multi-year Landsat datasets; Sethi et al. (2024) combined NDVI and LST trends to analyze the impacts of urban sprawl in Bhubaneswar, India. Momeni and Saradjian (2007) and Bao et al. (2023) developed emissivity correction models using NDVI and LULC layers to enhance UHI analysis. Sobrino et al. (2004) and Jiménez-Muñoz et al. (2009) proposed a split-window algorithm for LST estimation in UHI analysis. Mallick et al. (2013) and Bao et al. (2023) used NDVI, Normalized Difference Built-up Index (NDBI), and Normalized Difference Water Index (NDWI) to examine LST dynamics and their correlation with heat gradients across varying LULC patterns. Rajasekar and Weng (2009) explored the role of bare soil and built-up areas in thermal amplification using ASTER imagery for Chennai. Tran et al. (2006) explored inter-city LST changes in relation to spatial variations in LULC layers. Buyantuyev and Wu (2010) reported urbanization patterns in Phoenix, USA that led to a lowering of groundwater levels and to evapotranspiration exceeding rainfall, thereby exaggerating the UHI impacts in the study area.

Despite this growing body of research, a critical gap remains. Most studies either lack temporal depth, analyzing only one or two years, or fail to integrate vegetation and moisture indices in a comprehensive way (Manjunath & Jagadeesh, 2024; Tamrakar and Sharma, 2024; Okoduwa & Amaechi, 2025). The methodological inconsistency across different sensors (Landsat, MODIS, ASTER) and the majority research interest in the Tier-1 cities like Delhi, Mumbai, Bangaluru makes long term analysis difficult, especially for cities located in arid and peri-urban regions of India like Bathinda city that requires a detailed LULC study for absolute calibrations of LST fluctuation, (Zhou et al., 2014; Li et al., 2019).

The primary objective of this study is to assess the spatio-temporal evolution of LST in Bathinda City from 1990 to 2022 using multi-temporal Landsat data. The LULC and vegetation indices, such as NDVI, were classified to evaluate their relationship with varying LST over the selected time period. Finally, the results estimate the intensity of the UHI effect and compare thermal differences between urban and peri-urban zones over the temporal timeline. Additionally, it seeks to identify the key LULC and biophysical factors influencing LST distribution through regression-based statistical modeling.

This study presents the first long-term (1990–2022) LST analysis for Bathinda City, Punjab, integrating environmental indices: NDVI-based emissivity and LULC patterns across multiple temporal timelines, and spectral indices for improved accuracy. Regression models are used to quantify LST–landscape relationships, offering data-driven insights. Overall, it offers a unique methodological and contextual contribution to urban remote sensing in arid Indian cities.

2. Study Area

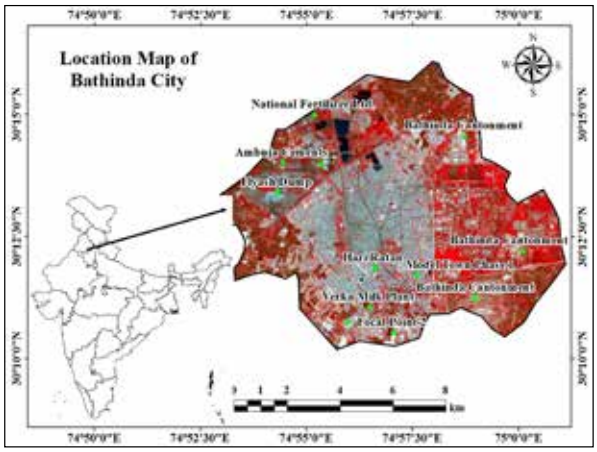

Figure 1. Map depicting the location of the study area, Bathinda City

Bathinda city is the oldest city of Punjab, situated between ”29º46’11” and ”30º35’08” north latitude and from ”74º37’49” and ”75º22’54” east longitude (Figure 1). It is located in the south-western part of Punjab and lies within the Indo-Gangetic alluvial plains. The region is mostly flat with gentle slopes, and the average elevation ranges from 200 to 220 meters above sea level. There are no hills or natural elevations; the landscape is mainly modified by human activities such as canals, embankments, and urban structures. The climate of Bathinda is semi-arid, characterized by very hot summers, mild winters, and low rainfall. In the summer months, especially May and June, the temperature often crosses 45°C, and hot winds called ‘’’loo’ are common in this region. Winters are cooler with minimum temperatures falling to 4–5°C. The annual average rainfall is about 400–500 mm (Sharma et al., 2017), which occurs mainly during the monsoon period from July to September, but the rainfall is often erratic and unevenly distributed. Soils in this region are sandy to sandy loam in texture, generally low in organic matter, and prone to salinity in some areas. Vegetation in Bathinda is mostly planted rather than natural, and trees are commonly found along roadsides, parks, and canals (Ahmad, 2023). The natural green cover is very sparse due to the dry climate. The main land-use pattern in and around Bathinda is agriculture, with wheat, cotton, and mustard as the dominant crops, supported by canal and tube-well irrigation. However, in recent years, the urban sprawl has converted agricultural lands into residential and commercial plots. Urbanization in Bathinda has picked up pace since the 1990s (Guite, 2019) due to industrial growth, improved transport connectivity, and the establishment of major public-sector units, such as thermal power plants and the Guru Gobind Singh Oil Refinery. This growth is mostly unplanned, with residential colonies and commercial buildings expanding on the periphery without proper infrastructure. The central areas are becoming overcrowded, and green spaces are

continuously shrinking, raising concerns for heat stress and environmental degradation. In the backdrop of impending climate change, where temperature extremes and weather unpredictability are expected to worsen, understanding urbanization patterns and their impacts on local land and climate systems becomes urgent. Bathinda, situated in a sensitive agro-climatic zone, needs immediate attention to climate-resilient urban planning, sustainable land use, and environmental monitoring to protect people and the ecosystem from rising heat and water-related stresses.

3. Materials and Methods

This study investigates the spatio-temporal evolution of LST and its role in UHI formation in Bathinda City, located in the south-western region of Punjab, India, over 32 years from 1990 to 2022. The research leverages geospatial techniques and satellite datasets to examine how thermal conditions have changed in Bathinda City, Punjab, due to rapid industrialization and urban growth.

The methodology involves processing multi-temporal satellite images, followed by LULC classification, NDVI variations in the study area based on analysis of thermal bands from Landsat sensors, and an urban–rural long-term temperature gradient estimate indicating UHI intensity. Further, multivariate statistical classification and modeling are used to identify key driving factors influencing LST patterns, including both natural and human-induced variables. The workflow is represented in Figure 2, providing a systematic overview of data input, processing, and analysis stages.

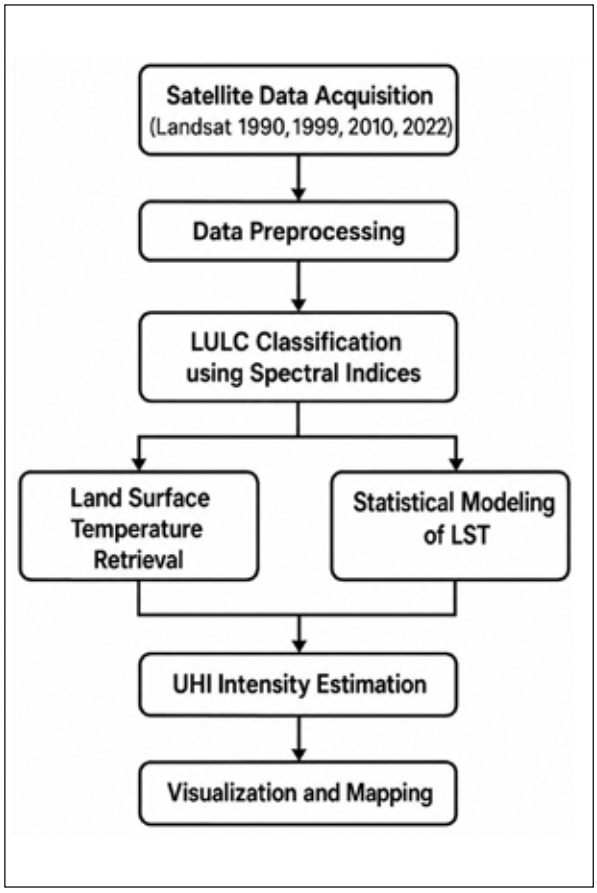

Figure 2. Diagram representing the overall methodology flowchart

Table 1. Details of Satellite Data Used in the Study

S.No	Satellite	Sensor	Year	Acquisition Date	Spatial Resolution	Bands Used	Cloud Cover	Season
1	Landsat 5	TM	1990	10 May 1990	30 m (optical & TIR)	Bands 1–7	<10%	Pre-monsoon
2	Landsat 5	TM	1999	15 May 1999	30 m (optical & TIR)	Bands 1–7	<10%	Pre-monsoon
3	Landsat 5	TM	2010	12 May 2010	30 m (optical & TIR)	Bands 1–7	<10%	Pre-monsoon
4	Landsat 8	OLI/TIRS	2022	08 May 2022	30 m (resampled TIR)	Bands 1–11	<10%	Pre-monsoon

3.1 Satellite data and pre-processing

In this study, multi-temporal satellite imageries were acquired from USGS Earth Explorer that included Landsat 5 TM bands for the years 1990, 1999, and 2010 and Landsat 8 OLI/TIRS for 2022 (Table 1). These data were selected for their temporal precision in the long-term analysis of the urban heat regime, and match the key stage of the urban change that happened in Bathinda City post the Indian financial reforms undertaken in 1991. Imagery was acquired from March to June (the pre-monsoon season in this region) to minimize vegetation masking and ensure seasonal surface temperature variation. The images acquired were Level-2 products; thus, no radiometric or atmospheric corrections were required. Individual band layers were stacked to generate single composite images for each scene, followed by assigning them UTM Zone 43N and WGS 84 projected coordinates. The projected images were then clipped to the area surrounding Bathinda City. All this was ensured by ensuring that each scene had <10% cloud cover and a pixel dimension of 30m x 30m. Open-source software, QGIS version 3.28, was used for pre-processing.

3.2 LULC classification using spectral indices

To accurately extract LULC classes from multi-temporal satellite images, a hybrid classification technique was adopted, which combines spectral index thresholding with supervised classification based on the Maximum Likelihood Classifier (MLC). This method helped better separate different land types, especially in a mixed, dry area like Bathinda. Five major LULC categories were defined for classification: built-up area, vegetation, agricultural land, open/barren land, and water bodies. To strengthen discrimination among these classes, a set of normalized spectral indices was computed from Landsat imagery reflectance bands. These included the NDVI, which is calculated as (NIR − RED) / (NIR + RED) and is effective for identifying vegetative cover; the NDBI, computed as (SWIR − NIR) / (SWIR + NIR), to highlight urban and constructed areas and the NDWI, calculated as (GREEN − NIR) / (GREEN + NIR), which helps in detecting water bodies. LULC classification was carried out using QGIS (version 3.28) with the Semi-Automatic Classification Plugin.

These spectral indices were utilized in combination

with original image bands to define clear, representative training samples for supervised classification. The classified outputs for each time period were subjected to accuracy assessment using the Kappa coefficient. Ground-truth points collected from field surveys and high-resolution Google Earth imagery were used for validation, particularly for the 2022 dataset, while historical images were used with visual interpretation for earlier years. This methodology ensured that the LULC maps generated were both consistent and reliable for temporal analysis.

3.3 LST retrieval from Landsat data

The single-channel algorithm (QGIS SCP plugin) was applied to estimate LST from thermal bands of Landsat 5 (Band 6) and Landsat 8 (Band 10). The process involved radiance calculation, conversion to brightness temperature, and surface emissivity correction using NDVI-derived emissivity models.

Radiance and Brightness Temperature Calculation

For Landsat 5 TM, radiance (L_λ) was calculated using:

$$L\lambda = \left(\frac{(L_{max} - L_{min})}{(QCAL_{max} - QCAL_{min})}\right) \times (QCAL - QCAL_{min}) + L_{min} \quad (1)$$

Where:

L_λ - Spectral radiance (W/m²·sr·µm)

QCAL - DN values

L_{max},L_{min} - Spectral radiance scaling constants from metadata

Brightness Temperature (BT) in Kelvin:

$$T_B = \frac{K_2}{ln\left(\frac{K_2}{L_\lambda} + 1\right)} \quad (2)$$

For Landsat 8 TIRS, top of atmospheric radiance (TOA) was calculated as:

$$L_\lambda = M_L \times Q_{cal} + A_L \quad (3)$$

BT from TOA radiance:

$$T_B = \frac{K_2}{ln\left(\frac{K_2}{L_\lambda} + 1\right)} - 273.15 \quad (4)$$

Where K_1, K_2, M_L and A_L are radiometric calibration constants available in the scene metadata (MTL file).

Surface Emissivity Estimation and LST Correction

To correct for surface emissivity (ε), the NDVI-based method was adopted. The proportion of vegetation (PV) was calculated as:

$$PV = \left[\frac{(NDVI - NDVI_{min})}{(NDVI_{max} - NDVI_{min})}\right]^2 \quad (5)$$

Surface emissivity (ε): =0.004×PV+0.986

Final LST in Kelvin:

$$LST = \frac{T_B}{1 + \left(\frac{\lambda . T_B}{\rho}\right) \ln(\varepsilon)} \quad (6)$$

Where:

λ =10.8µm (central wavelength for Band 10)

ρ = h × c/σ =1.438×10^{-2}m·K

h = 6.626×10^{-34}Js, c=2.998×10^8 m/s, σ =1.38×10^{-23} J/K

3.4 Urban Heat Island (UHI) Intensity Estimation

Urban heat island intensity was calculated using a binary zonal contrast method in QGIS software by delineating:

Urban core zones (high-density built-up areas)

Peripheral rural buffer zones (non-urban areas with vegetative/agricultural land)

$$UHI_{intensity} = LST_{urban} - LST_{rural} \quad (7)$$

4. Results and Discussion

4.1 Changes in Land Use and Land Cover (LULC)

Table 3. Land use land cover classes 1990, 1999, 2010 and 2022

Category Name	Area (Km²)	Area (Km²)	Area (Km²)	Area (Km²)
Agriculture	17.58	8.32	9.66	9.38
Built Up	17.79	23.99	26.56	28.86
Open Land	13.99	29.11	16.66	25.75
Vegetation	38.57	27.21	35.91	24.83
Water Body	2.07	1.37	1.21	1.18
Total	**90**	**90**	**90**	**90**

LULC maps for the years 1990, 1999, 2010 and 2022 were generated with overall accuracies of 83%, 85%, 89% and 82%, respectively. The Kappa values for these years were 0.79, 0.81, 0.86, and 0.77, respectively. The results of the LULC analysis reveal substantial change, as reflected in the generated LULC maps (Figures 3 & 4). Separately, spatial expansion maps were prepared as depicted in Figure 5. The proportions of the following 5 classes of LULC: vegetation, agricultural land, built-up area, open land and water bodies were found to be 43%, 20%, 20%, 15% and 2% respectively for the year 1990. LULC analysis of 1999 indicated a marked change: vegetation class decreased to 30%, agricultural land class decreased to 9%, built-up area increased to 26%, and open land class increased to 33%. It also indicated roughly no change in the area under the water body class. By 2010, the vegetation class again increased to 40%, the agriculture area class roughly remained the same at 11%, the built-up area further increased to 30%, the open land class at 18%, and the water body at 1%. Further analysis of the imagery from 2022 showed that vegetation dropped to 28%, the agriculture class remained stagnant at 10%, built-up area increased to 32%, open land increased to 29%, and waterbody remained at 1% (Table 2). LULC results for the period 1990-2022 clearly indicate that the built-up area, which was 17.79 km² in 1990,

increased to 28.86 km² in 2022. During the same period, open land increased by 84%. In contrast, there was a noticeable decline in natural and agricultural land cover: vegetation cover decreased by 36%, agricultural land decreased by 47%, and water bodies decreased by 43%. Figure 5 shows that in 1990, Bathinda City was limited to a 2 km circle; by 1999, it had started growing at the southeast and northwest flanks. But from 1999 onwards, the city limits have started growing in all direc.tTill till, 2010 it remained like, thatfrom but 2010 on,wards more foccity growth city was seethe west-southwest directiontions. Over the past 32 years, Bathinda city has changed a lot. Natural land is now less, and built-up and open land are more.

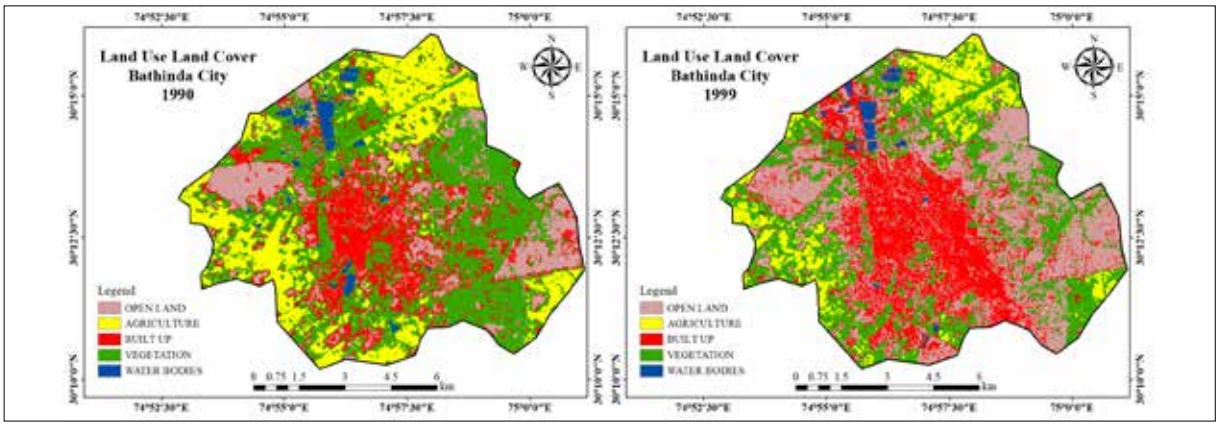

Figure 3. LULC classes of Bathinda city for the years 1990(left) and 1999 (right)

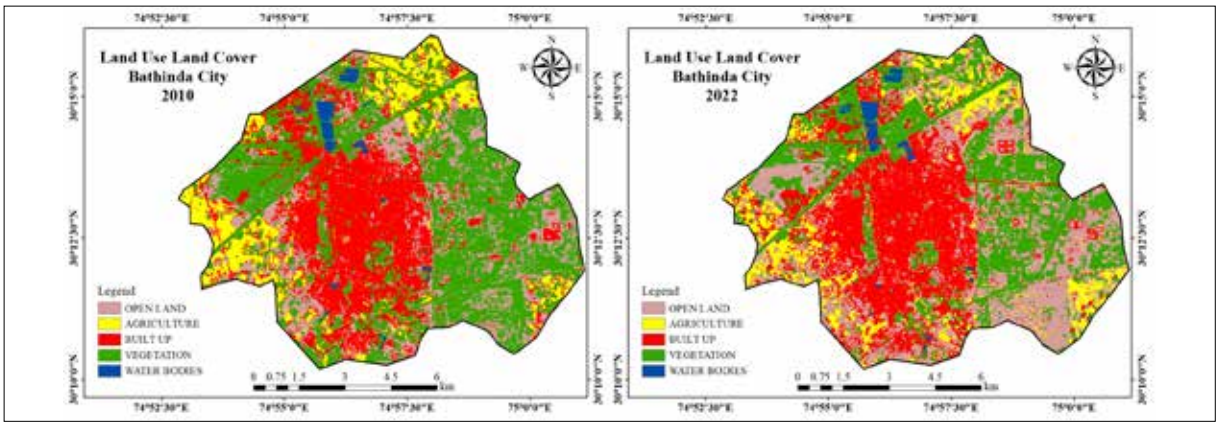

Figure 4. LULC classes of Bathinda city for the years 2010(left) and 2022 (right)

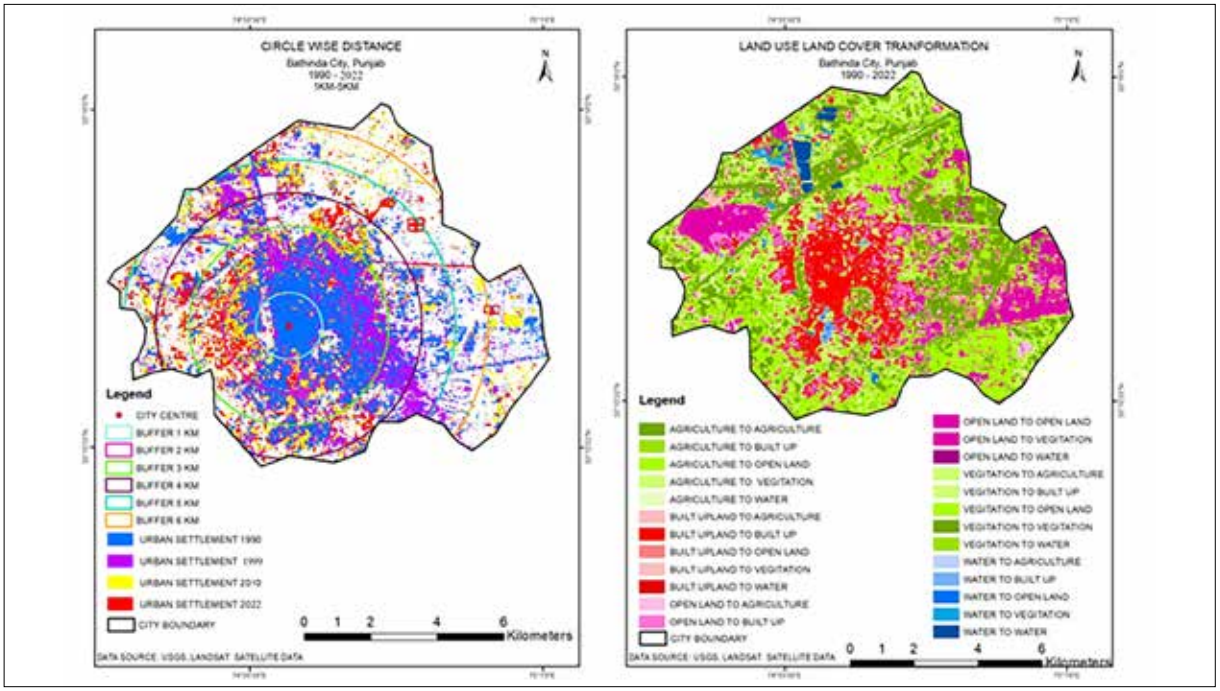

Figure 5. Spatial expansion from 1990 to 2022 (Left), Land Transformation from 1990 to 2022 (Right)

4.2. Land Surface Temperature (LST) Trends

The LST of Bathinda city has increased from 1990 to 2022. This change is clearly visible in the LST maps for the years 1990, 1999, 2010, and 2022 (Figures 6 & 7). In 1990, the average LST was about 31.2°C. By 2022, this increased to around 36.6°C. This shows that the city has become hotter over the last 32 years. The hottest areas were mostly in the city center and in industrial or built-up zones. These areas had more concrete and buildings, which absorb and trap heat. In contrast, the cooler areas were near vegetation, agricultural land, and water bodies. These natural surfaces help to keep the land cool by allowing evaporation and shading. The maps also show that the hot zones have spread outward from the center over time. In 1990, the high LST was mostly limited to the middle part of the city. By 2022, these hot areas had expanded in almost all directions, especially towards the west and southwest, where new development took place. This increase in temperature and the spreading of hot zones suggest a rise in the UHI effect, in which cities become hotter than surrounding rural areas due to buildings, roads, and less greenery. In summary, LST increased by more than 5°C between 1990 and 2022. Built-up areas are hotter, green/water areas are cooler, and hot zones now cover a larger part of the city, not just the center. Built-up areas are hotter, green/water areas are cooler, and hot zones now cover a larger part of the city, not just the center. These results show how urban growth and land changes have directly affected the temperature pattern in Bathinda.

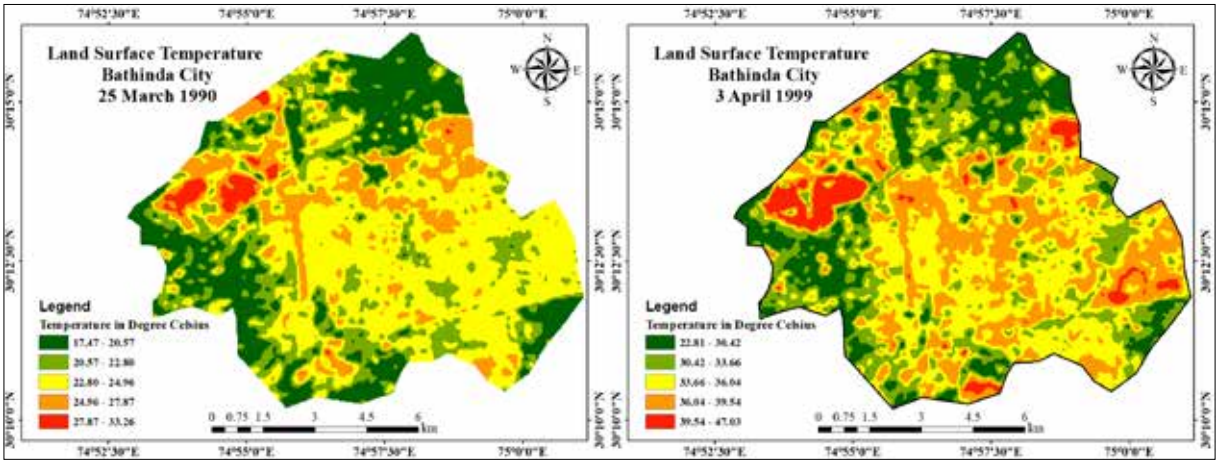

Figure 6. LST map derived from the Landsat sensor for the years 1990 (left) and 1999 (right) of Bathinda City

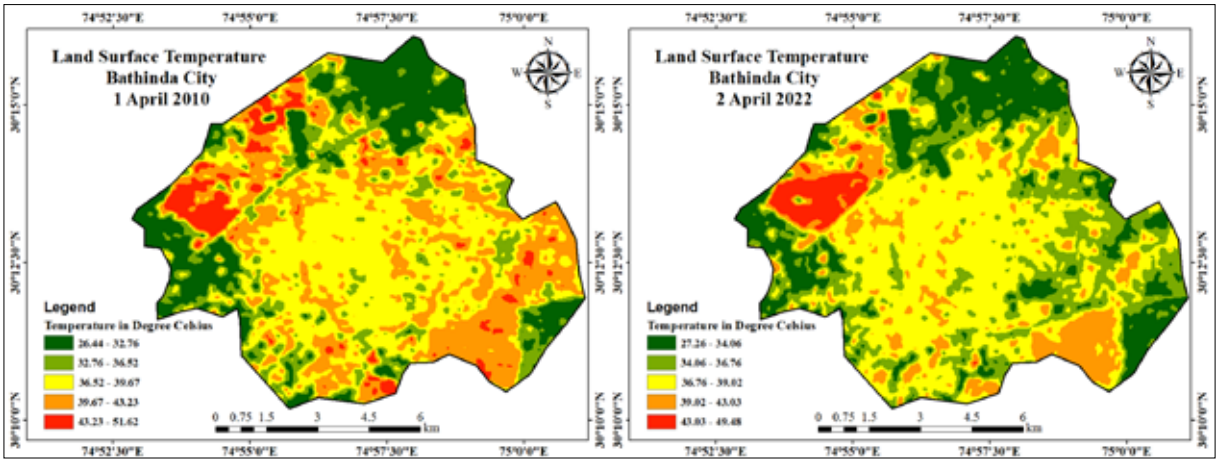

Figure 7. LST map derived from Landsat sensor for the year 2010 (left) and 2022 (right) of Bathinda City

4.3. NDVI Trends

The NDVI maps for 1990, 1999, 2010, and 2022 (Figures 8 & 9) show that green cover (vegetation) in Bathinda has decreased over time. In 1990, the maximum NDVI value was 0.71, indicating areas with dense green vegetation. The minimum NDVI value was –0.39, indicating the presence of non-vegetated areas, such as buildings, roads, or water. By 2022, the maximum NDVI had dropped to 0.46, and the minimum increased to –0.12. This difference means the greener areas became less green, and the non-vegetated areas increased. In 1990, more vegetation was observed in the northern and south-western parts of the city, as well as around the Cantonment area. Some green patches were visible in the center as parks. In 2022, these green zones had reduced in both size and health (lower NDVI values), and more areas showed lower NDVI values, indicating less or no vegetation. The central parts of the city and areas near industrial zones like the thermal power plant and National Fertilizer Limited (NFL) showed very low NDVI values in all years, especially in 2022, because of more buildings and very little greenery. The maps indicate that vegetation has decreased in both quantity and quality; NDVI values are declining each decade; and built-up and barren areas are increasing, while dense green areas are shrinking.

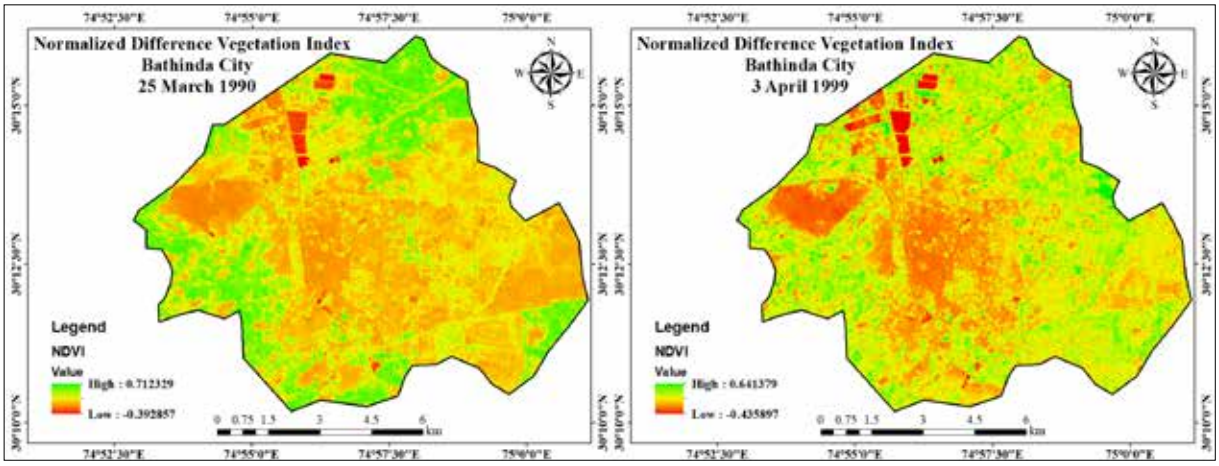

Figure 8. NDVI map derived from the Landsat sensor for the years 1990 (left) and 1999 (right) of Bathinda City

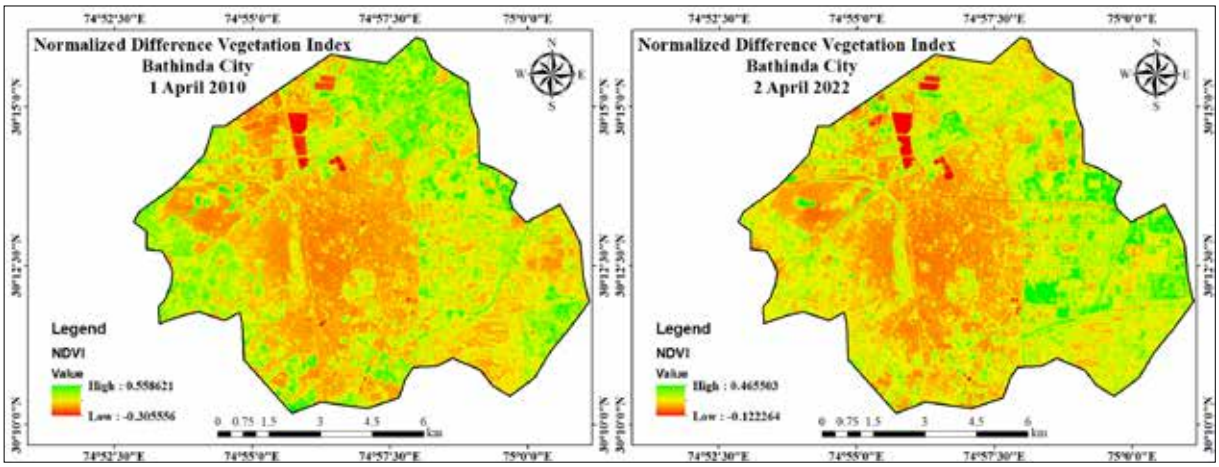

Figure 9. NDVI map derived from the Landsat sensor for the years 2010 (left) and 2022 (right) of Bathinda City

These results show that natural green cover is declining, which may lead to higher land surface temperatures and greater heat in the city, as discussed in the previous section.

4.4. Relationship between NDVI and LST

This section looks at how green cover (NDVI) and LST are related. We used scatter plots and regression analysis to study this for the years 1990, 1999, 2010, and 2022. The results are shown in Figures 10-13. In all four years, the relationship was negative, meaning that when NDVI is high (more vegetation), LST is low, and when NDVI is low (less vegetation), LST is high. The regression equations and R^2 values (which indicate the strength of the relationship) are shown in Table 3.

Table 3. Regression equations and R^2 values:

Year	Regression Equation	R^2 Value	Slope
1990	LST = 24.69 – 9.26 × NDVI	0.5604	–9.26
1999	LST = 36.35 – 12.24 × NDVI	0.1818	–12.24
2010	LST = 39.90 – 20.43 × NDVI	0.3251	–20.43
2022	LST = 39.26 – 13.31 × NDVI	0.1259	–13.31

From the Table, the strongest relationship was in 1990 (R^2 = 0.56). This result means NDVI explained 56% of the change in LST. In 2022, the relationship became much weaker (R^2 = 0.13). NDVI explained only 13% of the LST variation. This variation shows that in earlier years, green cover had a strong impact on land temperature. But over time, as the city developed and more concrete replaced greenery, other factors, (such as buildings, traffic, and roads) began to affect LST more than vegetation alone. The slope of the regression line was the steepest in 2010 (–20.43), indicating that a small change in vegetation caused a large change in temperature that year. This change might be due to rapid development and vegetation loss during that time. The effect of vegetation on LST was strong in the past, but weaker now due to more built-up land and other urban factors.

5. Discussion

5.1. Interpretation of LST and Urbanization Patterns

The LST maps for 1990, 1999, 2010, and 2022 (Figures 6 & 7) show that the temperature in Bathinda city has increased significantly over the last 32 years. In 1990, the average LST was about 31.2°C, but by 2022, it had reached about 36.6°C. This strong increase of more than 5 degrees Celsius shows a clear sign of the UHI effect. The hotter areas in the city are mostly where there is more built-up land and open land, especially in the city center and in industrial zones, such as near the Thermal Power Plant and the NFL area. These places have very little vegetation, so they absorb and keep more heat. The cooler areas are found near vegetated zones, agricultural fields, and water bodies. These natural surfaces help cool the land by releasing moisture and reflecting less heat. But over the years, these cooler areas have reduced in size. From the LULC maps (Figures 3 and 4), we can see that the built-up area increased from 20% in 1990 to 32%

in 2022. Vegetation decreased from 43% to 28%, and open land increased from 15% to 29%. This decrease means that natural land, such as trees and farms, is being replaced by concrete, roads, and bare land, which causes temperatures to rise. Also, urban expansion shifted from the city center to the northwest and southwest, especially from 1999 to 2022 (Figure 5). As the city grew, the hot zones also expanded, matching the direction of new construction.

The LST trend in Bathinda city closely relates to the city's progressive industrialization. In the early 1990s, a few agro-based units and thermal power infrastructure were in place, which evolved substantially over the years with the establishment of major energy and manufacturing facilities and planned industrial estates. Large industrial installations were commissioned in the 2000s, leading to the transformation of vegetated land to built-up land with high heat retention capacity. This study has clearly revealed thermal hotspots aligning with industrial corridors and urban zones. So, the rise in LST is closely connected with how the land is changing. More buildings and less green cover are making the city hotter. This is a serious issue for health, comfort, and the environment, and it shows that urban growth must be better planned to control rising temperatures.

5.2. NDVI decrease and green cover loss

The NDVI maps from the years 1990, 1999, 2010, and 2022 (Figures 8 & 9) show that green cover in Bathinda city has decreased a lot over time. In 1990, the maximum NDVI value was 0.71, but in 2022, it dropped to 0.46. This means there are fewer dense green areas now. The minimum NDVI value also changed: it was –0.39 in 1990 and became –0.12 in 2022. This shows that even the driest or most barren areas are becoming more common. In the NDVI map of 1990 the north, southwest, and cantonment area had high NDVI values. These were green and healthy zones. By 2022, many of these areas had turned into built-up or open land, and their NDVI values became low. The reason behind this drop in NDVI is seen in the land use change. This means green areas were either cut down for construction, turned into barren plots or used for roads and infrastructure. This change affects not only the look of the city, but also the environment. The NDVI maps clearly show this transformation and prove that green cover is shrinking fast in Bathinda. This also helps to explain why LST has increased, because less vegetation means more heat.

5.3. NDVI–LST relationship over time

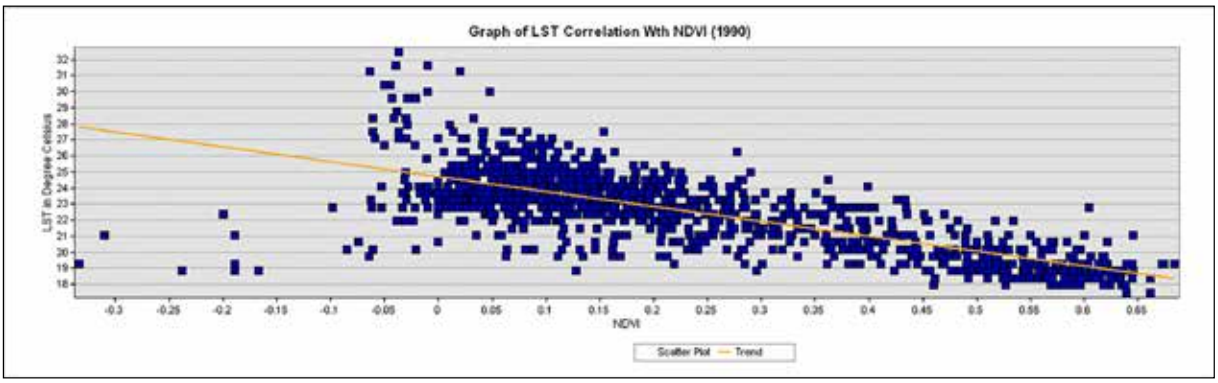

Figure 10. Scatter Diagram of 1990 showing the NDVI relationship with LST

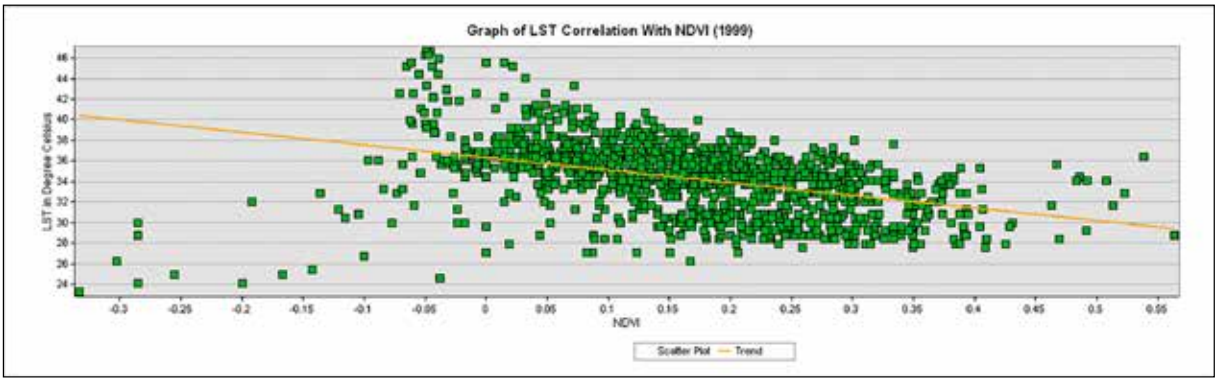

Figure 11. Scatter Diagram of 1999 showing the NDVI relationship with LST

The relationship between NDVI and LST was studied for 1990, 1999, 2010, and 2022 using scatter plots and regression analysis (Figures 10-13). In all four years, we found a negative relationship between NDVI and LST. This relationship means when NDVI is high, LST is low, and when NDVI is low, LST is high. This result is expected because vegetation helps to cool the land through evapotranspiration and shade. This change shows that NDVI and LST were strongly correlated in the past, but over time the relationship has weakened. 'That's because in 1990, the city had more vegetation and agriculture, so NDVI played a big role in cooling the surface. But in 2022, the city has more built-up areas, concrete roads, and industrial zones. These things also raise the temperature, but are not shown in NDVI. So now, LST depends on many urban factors, not just vegetation. NDVI alone cannot explain the high temperatures we see in today's urban landscape.

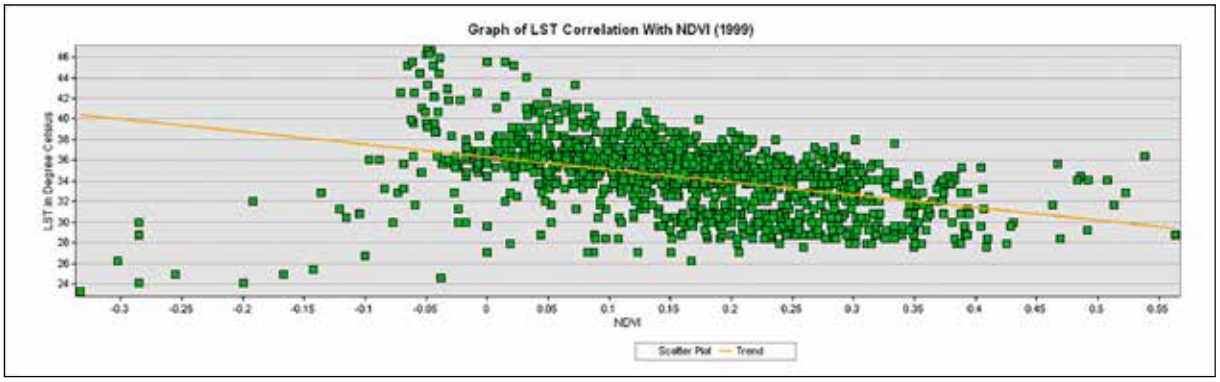

Figure 12. Scatter Diagram of 2010 showing the NDVI relationship with LST

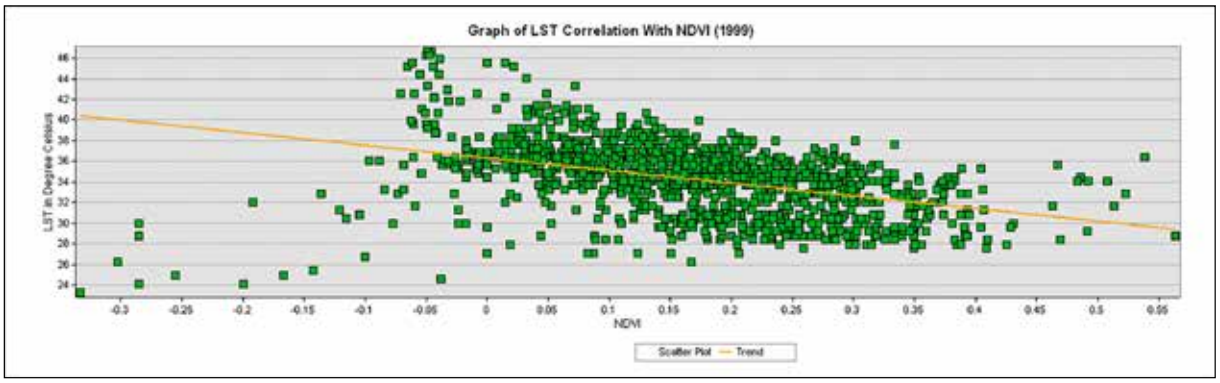

Figure 13. Scatter Diagram of 2022 showing the NDVI relationship with LST

The study clearly shows that urban growth in Bathinda has reduced green areas and increased LST. This is dangerous for the city's climate, health, and future development. The loss of vegetation and the rise in built-up and open land have intensified the urban heat island effect. If this continues, the city will face more heat stress, poor air quality, and health problems. To reduce these effects, urban planning should focus on saving and increasing green cover. This greening can be done by protecting parks, planting trees, and keeping green buffers around roads and buildings. Open land, which is rising in many parts, should not be left barren—it should be turned into green spaces or used wisely. New construction should include cool roofs, shaded areas, and less concrete. The city must also regularly monitor land use and temperature using satellite data , as done in this study. This strategy can help planners and government officials make smart decisions to manage heat and control unplanned expansion. Green and climate-friendly policies are now urgent, especially in rapidly growing cities like Bathinda.

6. Conclusion:

This study clearly shows that Bathinda city has become much hotter over the last 32 years due to urban growth and loss of vegetation. The Land Surface Temperature (LST) increased from 31.2°C in 1990 to 36.6°C in 2022, mainly in areas where built-up and open land have replaced green zones. The NDVI values dropped, showing a sharp decline in vegetation. The negative relationship between NDVI and LST shows that green cover helps reduce surface temperature. However, over time, this link weakened, indicating that vegetation alone cannot explain the city's temperature rise. The regression model errors increased, showing the limitation of using only NDVI to predict LST in urban areas. It is clear that other factors, such as buildings, roads, and land-use changes, also play a significant role in increasing temperatures. This study shows that remote sensing and satellite data are powerful tools to monitor land changes and support smart city planning. The results reflect the need to increase the urban vegetation, namely, parks, trees along the streets and green buffer zones that can reduce the thermal stress in dense urban pockets. Rejuvenation of barren land, former industrial land, etc., with green cover could further reduce local heat accumulation. Major causes of heat accumulation include unscientific roofing and impervious surfaces, which can be addressed through reflective roofing and reduced impervious surfaces in high-LST zones, lowering surface temperatures. These findings can assist town planners in the development of a sustainable urban environment.

Author Contribution

SN	Name of author	Contribution
1	Gurvinder Singh	Conceptualized this study. He collected satellite images, produced land-use and NDVI maps, and prepared the first draft of the report.
2	Dr. Rohan Kumar	Worked on the method to calculate LST and studied how LST changed over time.
3	Dr. Jai Sukh Paul Singh	Worked on a correlation study between NDVI and LST to improve the report with scientific inputs
4	*Dr. Swati Sharma	Worked on processing satellite data, creating maps, and preparing the final draft.
5	Ajay Roy	Helped in making clean and clear maps, organizing data, and finding related studies for background support.

Acknowledgment:

We would like to thank Lovely Professional University (LPU), Punjab, for its logistical and research support during this research. The university provided us with access to computers, software, the internet, and the library, which helped us accomplish this work.

Conflict of Interest:

The authors declare that there is no conflict of interest related to this study.

Funding Statement:

No funds were acquired for this work.

References

Ahmad, N. (2023). Spatio-Temporal Change Detection Analysis of Land Use Land Cover of Bathinda District, Punjab, India. Biosciences Biotechnology Research Asia, 20(2), 571-590.

Abusmier, S. A., & Al-Kofahi, S. D. (2025). Examining Land Use/Land Cover Dynamics in Zarqa Governorate Major Districts: Implications for Urban and Environmental Sustainability. Jordan Journal of Earth & Environmental Sciences, 16(1).

Okoduwa, A. K., Amaechi, C. F., & Enuneku, A. A. (2025). Assessing Land Use/Land Cover and Predicting Future Scenarios in Kano Metropolis, Northern Nigeria. Jordan Journal of Earth & Environmental Sciences, 16(3).

Bao, G., Qin, Z., Bao, Y., Zhou, Y., Li, W., & Sanjav, A. (2014). NDVI-based long-term vegetation dynamics and its response to climatic change in the Mongolian Plateau. Remote Sensing, 6(9), 8337-8358.

Bao, Y., Li, Y., Gu, J., Shen, C., Zhang, Y., Deng, X., & Ran, J. (2025). Urban heat island impacts on mental health in middle-aged and older adults. Environment International, 109470.

Bhan, G., Anand, G., Arakali, A., Deb, A., & Harish, S. (2013). Urban housing and exclusion. India exclusion report, 14, 77-108.

Buyantuyev, A., & Wu, J. (2010). Urban heat islands and landscape heterogeneity: linking spatiotemporal variations in surface temperatures to land-cover and socioeconomic patterns. Landscape ecology, 25, 17-33.

Chandra, S., Sharma, D., & Dubey, S. K., (2018). Linkage of urban expansion and land surface temperature using geospatial techniques for Jaipur City, India. Arabian Journal of Geosciences, 11, 1-12.

Grimmond, C. S. B. (2007). Urbanization and global environmental change: local effects of urban warming. The Geographical Journal, 173(1), 83–88.

Guite, L. S. (2019). Assessment of urban sprawl in Bathinda city, India. Journal of Urban Management, 8(2), 195-205.

Imhoff, M. L., Zhang, P., Wolfe, R. E., & Bounoua, L. (2010). Remote sensing of the urban heat island effect across biomes in the continental USA. Remote Sensing of Environment, 114(3), 504–513.

Jiménez-Muñoz, J. C., & Sobrino, J. A. (2009). Split-window coefficients for land surface temperature retrieval. International Journal of Remote Sensing, 30(8), 2147–2165.

Kaur, R., & Pandey, P. (2022). Spatial trends of surface urban heat island in Bathinda: a semiarid city of northwestern India. International Journal of Environmental Science and Technology, 1-22.

Kikon, N., Singh, P., Singh, S. K., & Vyas, A. (2016). Assessment of urban heat islands (UHI) of Noida City, India using multi-temporal satellite data. Sustainable Cities and Society, 22, 19–28.

Li, X., Zhou, Y., Asrar, G. R., Imhoff, M., & Li, X. (2019). Surface urban heat island response to urban expansion. Science of The Total Environment, 657, 710–720.

Majumder, A., Setia, R., Kingra, P. K., Singh, M., & Singh, S. (2021). Estimation of land surface temperature using different retrieval methods for studying the spatiotemporal variations of surface urban heat and cold islands in Indian Punjab. Environmental Development and Sustainability, 23, 15921–15942. https://doi.org/10.1007/s10668-021-01321-3

Mallick, J., Rahman, A., & Singh, C. K. (2013). Modeling urban heat islands in heterogeneous land surface and its correlation with impervious surface area by using night-time ASTER satellite data in highly urbanizing city, Delhi-India. Advances in Space Research, 52(4), 639-655.

Manesha, E. P. P., Jayasinghe, A., & Kalpana, H. N. (2021). Measuring urban sprawl of small and medium towns using GIS and remote sensing techniques: A case study of Sri Lanka. The Egyptian Journal of Remote Sensing and Space Science, 24(3), 1051-1060.

Manjunath, D. R., & Jagadeesh, P. (2024). Dynamics of urban development patterns on thermal distributions and their implications on water spread areas of Vellore, Tamil Nadu, India. Frontiers in Sustainable Cities, 6, 1462092.

Momeni, M., & Saradjian, M. R. (2007). Evaluating NDVI-based emissivities of MODIS bands 31 and 32 using emissivities derived by Day/Night LST algorithm. Remote Sensing of Environment, 106(2), 190-198.

Oke, T. R. (1982). The energetic basis of the urban heat island. Quarterly Journal of the Royal Meteorological Society, 108(455), 1–24.

Pal, S., & Ziaul, S. (2017). Detection of land use and land cover change and land surface temperature in English Bazar Municipality, India. The Egyptian Journal of Remote Sensing and Space Science, 20(1), 125–145.

Rao, Y., Dai, J., Dai, D., & He, Q. (2021). Effect of urban growth pattern on land surface temperature in China: A multi-scale landscape analysis of 338 cities. Land Use Policy, 103, 105314.

Santamouris, M. (2015). Regulating the damaged thermostat of the cities—Status, impacts and mitigation challenges. Energy and Buildings, 91, 43–56.

Sethi, S. S., Vinoj, V., Gogoi, P. P., Landu, K., Swain, D., & Mohanty, U. C. (2024). Spatio-temporal evolution of surface urban heat island over Bhubaneswar-Cuttack twin city: a rapidly growing tropical urban complex in Eastern India. Environment, Development and Sustainability, 26(6), 15381-15402.

Sharma, D. A., Rishi, M. S., Keesari, T., Pant, D., Singh, R., Thakur, N., & Sinha, U. K. (2017). Distribution of uranium in ground waters of Bathinda and Mansa districts of Punjab, India: inferences from an isotope hydrochemical study. Journal of Radioanalytical and Nuclear Chemistry, 313, 625-633.

Sobrino, J. A., Jiménez-Muñoz, J. C., & Paolini, L. (2004). Land surface temperature retrieval from LANDSAT TM 5. Remote Sensing of Environment, 90(4), 434–440.

Tamrakar, Y., & Sharma, S. (2024). A review of spatial analysis techniques used for LULC change detection over Delhi NCR in the past two decades. Geospatial technology to support communities and policy: pathways to resiliency, 263-287.

Tamrakar, Y., Das, I. C., & Sharma, S. (2024). Machine learning for improved drought forecasting in Chhattisgarh, India: a statistical evaluation. Discover Geoscience, 2(1), 84.

Tran, H., Uchihama, D., Ochi, S., & Yasuoka, Y. (2006). Assessment with satellite data for urban heat island in Asian mega cities. International Journal of Applied Earth Observation and Geoinformation, 8(1), 34–48.

Voogt, J. A., & Oke, T. R. (2003). Thermal remote sensing of urban climates. Remote Sensing of Environment, 86(3), 370–384.

Weng, Q., Lu, D., & Schubring, J. (2004). Estimation of land surface temperature–vegetation abundance relationship for urban heat island studies. Remote Sensing of Environment, 89(4), 467–483.

Yuan, F., & Bauer, M. E. (2007). Comparison of impervious surface area and normalized difference vegetation index as indicators of surface urban heat island effects. Remote Sensing of Environment, 106(3), 375–386.

Zhou, D., Zhao, S., Liu, S., Zhang, L., & Zhu, C. (2014). Surface urban heat island in China's 32 major cities: Spatial patterns and drivers. Remote Sensing of Environment, 152, 51–61.

Zhou, D., Zhao, S., Liu, S., Zhang, L., & Zhu, C. (2014). Surface urban heat island in China's 32 major cities. Remote Sensing of Environment, 152, 51–61.

Majumder, A., Setia, R., Kingra, P. K., Singh, M., & et al. (2021). Estimation of land surface temperature using different retrieval methods for studying the spatiotemporal variations of surface urban heat and cold islands in Indian Punjab. Environmental Development and Sustainability, 23, 15921–15942. https://doi.org/10.1007/s10668-021-01321-3

JJEES

JJEES (2026) 17 (2): 277-286
ISSN 1995-6681

Jordan Journal of Earth and Environmental Sciences

A new approach for studying vulnerability to Groundwater pollution using DRASTIC and AHP in the Biyeme Upper Stream Watershed, Yaoundé, Cameroon

François Ntep [1,2*], Jean Ghislain Tabue Youmbi [1,2], Gabriel Alain Assoa Angoa[2]

[1] National Advanced School of Mines and Petroleum Industries, University of Maroua, P.O. Box 08 Kaele, Cameroon
[2] Department of Mining Petroleum Gas and Water Resources Exploration, University of Maroua, P.O. Box 08 Kaele, Cameroon

Received on 3 February 2025, Accepted on 18 January 2026

Abstract

This research work presents the results of an assessment of the vulnerability of groundwater to surface pollution in the Biyeme UpperStream Watershed (BUW). A method based on a geographic information system and the DRASTIC and AHP models was used to study this vulnerability. Located in the south-west of the city, the study area covers the part of Yaoundé where the population suffers from an inadequate supply of drinking water and where agriculture and/or livestock farming are the main means of subsistence. This research approach is based on continuous monitoring of average monthly data from 52 wells and 05 springs over 05 years, from 2015 to 2020. Assess the degree of vulnerability of groundwater to pollution in different areas of the catchment using each of the different methods and then compare them. In addition, a hierarchical analytical process was used to determine the assessment coefficients for each parameter. The main results show that the best outcome was achieved with DRASTIC-AHP. Regardless of the method used, vulnerability is highest in the upstream part of the basin; groundwater catchments in these areas must therefore be protected from contamination before they are sited.

Keywords: *Groundwater Vulnerability; DRASTIC and DRASTIC-AHP models; Biyémé Upper Stream Watershed; Yaoundé, Cameroon.*

1. Introduction

Water is a finite resource under pressure from pollution, inadequate sanitation, increased frequency of groundwater droughts, overexploitation of groundwater at unsustainable rates, inadequate water infrastructure, increased food demand from a growing population, increased water consumption, and irrigation (Ghazavi and Ebrahimi, 2015; Hazaymeh and Lange, 2024). Agricultural and residential activities have made groundwater in the BUW vulnerable to pollution. Previous groundwater vulnerability assessment studies have shown that urban areas are increasingly vulnerable to groundwater contamination (Singh et al., 2015; Ghazavi and Ebrahimi, 2015; Hazaymeh and Lange, 2024). For several decades, the world's population has been growing rapidly, and Africa accounts for about 17.4% of that population. This growth systematically leads to increased consumption of renewable and non-renewable natural resources. To manage these resources effectively, we need to ensure that they are of good quality (Singh et al., 2015; Ghazavi and Ebrahimi, 2015; Hazaymeh and Lange, 2024). To do this, we need to understand and study the parameters that control groundwater vulnerability and identify areas likely to be contaminated. This study aims to produce groundwater vulnerability maps for the BUW. Groundwater uses in urban areas include not only abstraction by public services, but also private self-supply for residential, commercial, industrial and agricultural purposes (Alam et al., 2012). Urban self-supply of water and the direct use of local wells by low-income households are often vital to a large proportion of a city's inhabitants (Kumar et al., 2015; La Vigna, 2022). A number of approaches have been developed to assess the vulnerability of groundwater. Three primary methods exist by which groundwater vulnerability is commonly assessed: (1) a subjective overlay and index method based on the rating of individual hydrogeological factors (Alam et al., 2012); (2) process based mathematical models that are data intensive (Neshat et al., 2014a) (3) statistical models that describe the contamination potential for a specified geographical region using the available data in the regions of interest (Alam et al., 2012).

2. Materials and methods

2.1. Study area

The BUW is located between 03°48'00″ and 03°51'58″ North latitude and between 11°27'36″ and 11°30'00″ East longitude, covering an area of 14.00 ha. It is part of the Mfoundi division (Fig.1). The hydrographic network constitutes a set of perennial rivers. The geological substratum is composed of a set of fractured Pan-African geotectonic units, constituting aquiferous reservoirs exploitable through wells and boreholes (Bissaya et al., 2018). Yaoundéé is characterized by strongly accented relief, with a mean altitude of 730 m. Soils are red and ferralitic in the majority.

* Corresponding author e-mail: francoisntep10@gmail.com

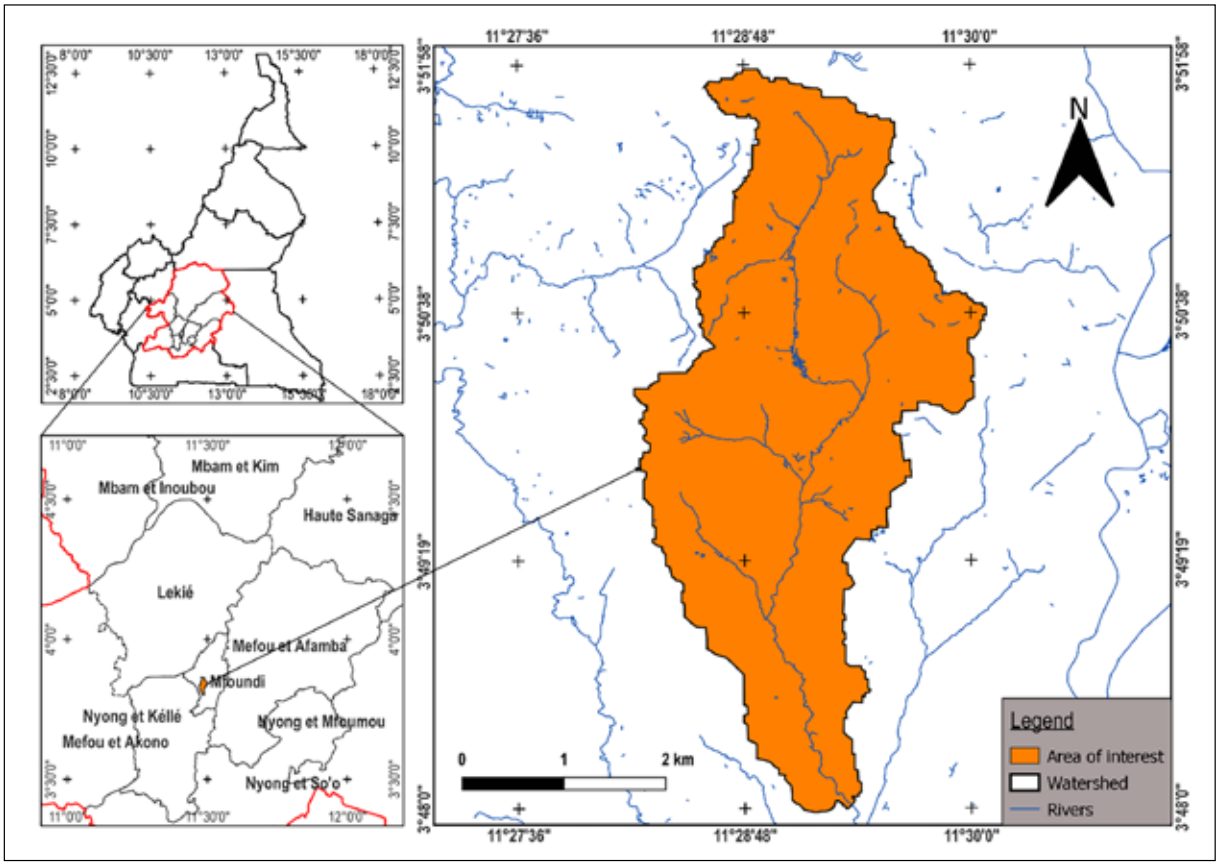

Figure 1. Geographical location of the Biyeme Upstream Watershed

The average inter-annual rainfall for the period from 1991 to 2021 is about 1727.00 mm. Potential Evapo-Transpiration (PET) has been calculated, using the Thornthwaite (1948) in (Fouépé et al., 2011; Ntep et al., 2021), and the average inter-annual PET is 964.00 mm. ééFigure 2 shows the variations in monthly rainfall in Yaoundé town from January to December, based on meteorological data recorded at the Yaoundé Air Force Station (Fouépé et al., 2011; Ntep et al., 2021). Heavy rainfall is drained by a set of perennial rivers, causing inundations of the valley bottom. The climate is equatorial, with two rainy seasons.

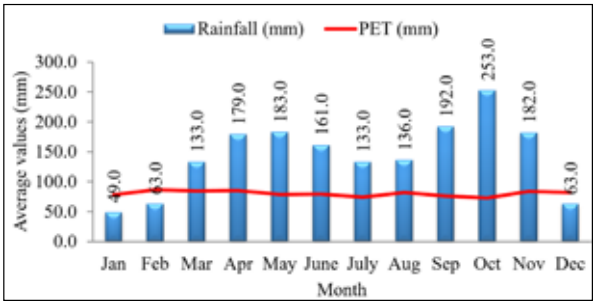

Figure 2. Monthly average rainfall and PET in Yaoundé city

The geology comprises crystalline basement rocks such as paragneiss, migmatitic gneiss, and schists of Proterozoic age, metamorphosed during the Pan-African orogeny at the northern margin of the Congo Craton (Bissaya et al., 2018). These medium- to high-grade metasediments are deeply weathered to form a lateritic soil profile up to 20 m thick (Fouépé et al., 2011; Kringel et al., 2016; Ntep et al., 2021). The bedrock is covered by alluvial hydromorphic clay and sand in the valleys and ferralsols on the hillsides (Bissaya et al., 2018). The hydrogeological setting consists of an unconfined porous aquifer overlying a fractured gneiss aquifer of much lower productivity. The seasonal dynamics of unconfined groundwater flow are described by Ntep et al. (2021), who reported average groundwater level fluctuations of 0.49 m in valleys, 0.65 m on slopes, and 1.3 m on plateaus between the rainy and dry seasons. The groundwater surface generally follows the relief well. Kringel et al. (2016) charted the rapid expansion of the urban area. The population is expected to approach 2.5 million inhabitants at a growth rate of 5.7%. The relief in éYaounde is undulating terrain with differences between 20 and 40 m at an average altitude of 730 m and seven prominent “inselbergs” with steep slopes (Fig.3).

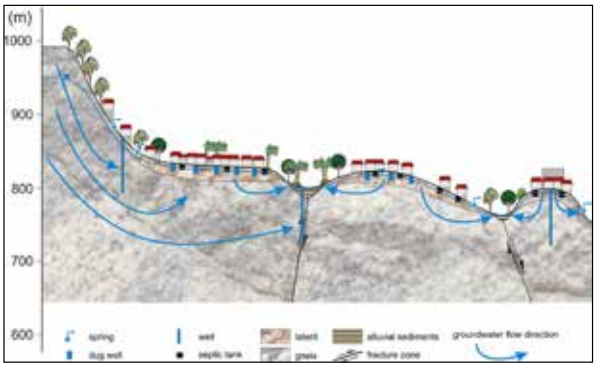

Figure 3. Sketch of the hydrogeological arrangement of terrain, aquifers, drainage network of Yaounde in relation to urban settlement and decentralized installations of water supply and discharge; groundwater surface and flowlines only approximate - not to scale (Kringel et al., 2016).

2.2. Research methods and data collection

2.2.1. AHP method

The Multi-Criteria Decision Analysis (MCDA) is a process that integrates and transforms the judgment of a decision-maker and geographical data into useful and appropriate information for environmental decision-making (Focazio, 2002; Costa et al., 2019; Kargaranbafghi et al., 2020). It provides decision options, from the most preferred to the least preferred, using many techniques, such as the Analytic Hierarchy Process (AHP) and the set-theoretic approach (Velasquez and Hester, 2013; Gangadharan et al., 2016; Kargaranbafghi et al., 2020). To achieve this, Saaty (2001) developed the AHP. The AHP is an efficient tool for multiple decision-making, helping the decision-maker set priorities and make the best decision. The principle of this analysis is to compare the elements of each criterion 2 by 2 using a comparison scale. The aim here is to calculate new scores that will then be assigned to each criterion. Several combinations have been made DRASTIC-AHP. In the DRASTIC-AHP method, the original DRASTIC scores are taken into account, and the weights of detailed parameters were established by ranking their importance and appropriateness based on their contribution to groundwater vulnerability assessment. Once the hierarchy has been established, multiple pairwise comparisons based on the standardized comparison scale of nine levels were estimated for all seven parameters. To achieve the desired results, there is a procedure to follow in Figure 4 and Table 1.

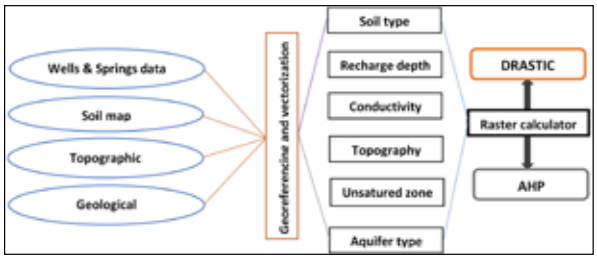

Figure 4. Flowchart of methodology for groundwater pollution vulnerability analysis (Oroji, 2018) modified.

Table 1. Comparison scale

Numeric scale or intensity	Verbal scale or definition	Comment
1	Equal importance of two elements Equally important	Both elements compete in the same way toward the goal
3	One element is a little more important than the other Slightly more important	Experience and personal judgment slightly favor one element over the other.
5	One element is more important than the other Strongly important	Experience and personal judgment really favor one element over the other
7	One element is much more important than the other Significantly more important	One element is largely dominant, and this dominance is demonstrated in practice.
9	One element is absolutely more important than the other Absolutely more important	The dominance of one element over another is demonstrated and absolute
2,4,6	Intermediate value between two judgments	Used to refine one's judgment
Reciprocity	If element i is assigned one of the previous numbers when compared to element j, then j will have the opposite value when compared to i	

2.2.1.1 Binary comparisons

Compare the relative importance of all the elements belonging to the same level of the hierarchy, taken two by two, in relation to the element of the level immediately above;

- For each comparison, choose the most important criterion and express your judgment as to its importance.
- The measure for determining relative importance could be expressed on a scale of 1 to 9.

Table 2 gives the scale values for comparing ratings when assessing the importance of two elements.

Table 2. Scale values for comparing the rating given when assessing the importance of two elements (Arauzo, 2017).

Expressing one criterion in relation to another	Rating
Same importance	1.00
Moderately important	3.00
Highly important	5.00
Very important	7.00
Extremely important	9.00
Moderately less important	0.33
Strongly less important	0.20
Less important	0.14
Extremely less important	0.11

2.2.1.2 Comparison judgment matrix

The criteria comparison given in Table 1 is transformed into a judgment matrix by transcribing the evaluation values into the corresponding columns (Table 3). The value "a" is entered in cell "i" column and "j" row of a criterion considered important. Then the value ratio of "1/a" is entered in the cell considered less important in the comparison.

Table 3. Judgment matrix for depth parameter

Depth (m)	1.50-4.50	4.50-9.00	9.00-15.00	15.00-23.00
1.50 - 4.50	1.00	3.00	5.00	5.00
4.50 - 9.00	0.33	1.00	3.00	5.00
9.00 - 15.00	0.20	0.33	1.00	3.00
15.00 - 23.00	0.20	0.20	0.33	1.00
Total	1.73	4.53	9.33	14.00

a = value found in the intersection of cell i column and j row, and noted (a_{ij}).

C_1, C_2 to C_n = comparison criterion set in row "i" and column "j" corresponding to the evaluation comparison value C_i and C_j.

$$A = [a_{ij}] = \begin{bmatrix} 1 & a_{12} & \cdots & a_{1n} \\ \frac{1}{a_{12}} & 1 & . & a_{2n} \\ \vdots & . & \ddots & \vdots \\ \frac{1}{a_{1n}} & \frac{1}{a_{2n}} & \cdots & 1 \end{bmatrix} \quad (1)$$

The matrix in the previous table is as follows:

$$A = \begin{bmatrix} 1.00 & 3.00 & 5.00 & 5.00 & \square \\ 0.33 & 1.00 & 3.00 & 5.00 & \square \\ 0.20 & 0.33 & 1.00 & 3.00 & \square \\ 0.20 & 0.20 & 0.33 & 1.00 & \square \\ \square & \square & \square & \square & \square \end{bmatrix} \quad (2)$$

Calculating the vectors of the priority

This outcome involves calculating the eigen vectors of the matrix obtained from the previous evaluations. Tables 4 and 5 give the respective division of each element of the matrix by the total of its column and the calculation of the average of the elements in each row of the previous matrix.

Table 4. Division of each element of the matrix by the total of its column

Depth (m)	1.50-4.50	4.50-9.00	9.00-15.00	15.00-23.00
1.50 - 4.50	0.58	0.66	0.54	0.36
4.50 - 9.00	0.19	0.22	0.32	0.36
9.00 - 15.00	0.12	0.10	0.11	0.21
15.00 - 23.00	0.12	0.04	0.04	0.10

Table 5. Calculation of the average of the elements in each row of the previous matrix

Depth (m)	1.50-4.50	4.50-9.00	9.00-15.00	15.00-23.00	Priority
1.50-4.50	1.00	3.00	5.00	5.00	2.32
4.5-9.00	0.33	1.00	3.00	5.00	1.20
9.00-15.00	0.53	0.27	0.13	0.10	0.53
15.00-23.00	0.20	0.20	0.33	1.00	0.27

Calculating of the intrinsic value λmax

The matrix A is multiplied by the elements of the priority vector (x), x is the eigenvalue of the priority vector (n), and the average of the values found is calculated. The result is called the λmax value. Let a_{ij} = the judgment matrix of the value of the element (i) in the ith row and the element (j) jth column. The normalised value aij is equal to

$$aij = Wi/Wj \text{ , and } a_{ij} = 1, aji = Wj/Wi = 1/aij \text{ ,} \quad (3) \text{ reciprocal}$$

Wi = contribution to the selection of the best choice and to each of the criteria

Wj = contribution of the specific criteria to the main objective.

Jhariya et al. (2019), then Saaty (2001), suggested that the largest eigen value

$$[\lambda max = a]ji = Wj/Wi = 1/aij \quad (4)$$

The results of the Judgment matrix for the depth parameter and the division of the elements of the sum vector weighted by the priority corresponding to each criterion are shown in Table 6.

Table 6. Weighted sum corresponding to each criterion's priority

Depth (m)	1.50-4.50	4.50-9.00	9.00-15.00	15.00-23.00	Priority
1.50-4.50	0.58	0.66	0.54	0.36	0.53
4.50-9.00	0.19	0.22	0.32	0.36	0.27
9.00-15.00	0.12	0.10	0.11	0.21	0.13
15.00-23.00	0.12	0.04	0.04	0.10	0.10

This is how we calculate the average value of λmax

$$[(4.36 + 4.28 + 4.12 + 4.06)]/4 = 4.20 \quad (5)$$

Random Index [RI]

Jhariya et al. (2019) then Saaty (2001), developed a scale in which random indexes [RI] were established by making random judgment across a large number of replications. This [RI] number represents the average of the indices calculated across replications for different square matrix sizes (N). The reading of the [RI] value is indicated by a random index in Table 7. N =5 RI= 1.12

Table 7. Random index

N	1	2	3	4	5	6	7	8	9	10	11	12	13	14	15
RI	0.00	0.00	0.58	0.90	1.12	1.24	1.32	1.41	1.45	1.49	1.51	1.48	1.56	1.57	1.59

Calculating the Coherence Index (CI)

The various steps involved in calculating the new ribs result in redundant comparisons, aimed at improving the quality of the result. The CI is a tool that provides information about the validity of the results.

$$IC = (\lambda max - N)/(N-1) CI = (\lambda max - N)/(N-1) \quad (6)$$

with N=5, CI= 0.07

Calculating the Coherence Ratio (CR)

The coherence ratio is the ratio of the coherence index calculated on the matrix corresponding to the decision-maker's judgments and the random index of a matrix of the same dimension. If CR ≤ 10% or 0.10, the matrix is considered to be sufficiently coherent. If this value exceeds 10%, the assessments may need to be revised.

$$CR = IC/IARC = CI/RI \quad (7)$$

with CI= 0.07 and RI=0.9, so CR<10%,

The degree of consistency of the comparison is acceptable. Once the new coastlines have been validated, we apply the same principle as in the DRASTIC method to calculate the vulnerability indices. This gives:

$$S = \sum\_(i=1)\^N \square W\_(i) \ X\_i \qquad S = \sum_{i=1}^{N} W_i \ X_i \quad (8)$$

with S as the index, Wi as the parameter weight, and Xi as the criterion rating.

The higher the scores, the higher the values of the vulnerability indices and the more vulnerable the areas.

2.2.1.3. Mapping of vulnerability zones using the DRASTIC-AHP method

The new vulnerability indices have been calculated using the AHP method, as illustrated above. The DRASTIC-AHP and AHP-AHP vulnerability maps are thus obtained using Table 8.

Table 8. Classification of vulnerabilities according to the DRASTIC-AHP method (Magha et al., 2021)

Value	Degree of Vulnerability
0.10	Very Low
0.20	Low
0.30	
0.40	Medium
0.50	
0.60	
0.70	High
0.80	
0.90	Very high

2.2.2. DRASTIC method

This method takes into account the litho-petrophysical parameters of the layers overlying the water table (Aller et al., 1987; Babiker et al., 2005; Sarah, 2016). Each parameter is assigned a weight, and each reference value or range of values is assigned a slope; the weighted slope is obtained by simply multiplying the two. The result will be a cartographic rendering produced in ARCGIS software from a grid designed in EXCEL. The vulnerability index will be calculated according to the following equation (9), and Table 8 provides the attribution of notes for the DRASTIC model indicators (Chi et al., 2017).

$$I = DvDw + RvRw + AvAw + SvSw + TvTw + IvIw + CvCw \quad (9)$$

Where "v"is the rib and "w" the weight.

Table 9. Attribution of notes for DRASTIC model indicator (Aller et al., 1987; Oroji, B., 2018).

Range	Rating		Range	Rating		Range	Rating	
Confining Layer	1	Zone vadose	0.0-1.5	10	Depth to water (m)	0.04-4.1	1	Conductivity (m)
Silt/Clay	3		1.5-4.5	9		4.1-12.3	2	
Shale	3		4.5-9.0	7		12.3-28.7	4	
Limestone	3		9.0-15.0	5		28.7-41	6	
Sandstone	6		15-22	3		41-82	8	
Bedded Limestone. Sandstone	6		22-30	2		>82	10	
Sand and Gravel W. Silt	6		>30.4	1		10	10	Topography (m)
Sand and Gravel	8		Thin or Absent	10	Soil media	2-6	9	
Basalt	9		Gravel	10		6-12	5	
Massive Shale	2	Aquifer media	Sand	9		12-18	3	
Metamorphic/Igneous	3		Peat	8		>18	1	
Weathered Metamorphic Igneous	4		Shrinking Clay	7		0-50	1	Recharge (mm)
Glacial Till	5		Sandy Loam	6				
Bedded Sandstone. Limestone	6		Loam	5		50-100	3	
Massive Sandstone	6		Silty Loam	4				
Massive Limestone	8		Clay Loam	3		100-175	6	
Sand and Gravel	8		Muck	2				
Basalt	9		No shrinking Clay	1		175-225	8	
Karst Limestone	10					>225	9	

2.3 Maps validation

For several authors, Lerner (2004), Shrestha et al. (2016), Aydi (2018), and Khosravi et al. (2018), the validation of the maps is based on chemical analyses of the various water samples taken. A comparison is made between the distribution of water quality and the spatial distribution of water vulnerability derived from the vulnerability maps. Areas of low vulnerability are associated with low-quality water, while areas of high vulnerability are associated with polluted water. Once the necessary data were collected to prepare the vulnerability map, the DRASTIC vulnerability index was computed by linearly combining all seven model parameters. Data analysis and model implementation included assigning sensitivity ratings to mapped attributes and combining or overlaying individual characteristic maps to create the final cumulative vulnerability map using GIS (Shrestha et al., 2016; Khosravi et al., 2018).

2.4. Comparison of the maps obtained

According to Aller et al. (1987) and Babiker et al. (2005), comparing assessment methods comes down to determining whether the methods are correlated two by two and which method offers the greatest margin of safety. Surface analysis is used to determine the difference between the vulnerability maps produced by the different methods. This analysis assumes that the index values are identical from one map to another and that the maps are consistent.

3. Results and Discussion

3.1. Results

3.1.1. DRASTIC results

DRASTIC parameters were collected, analyzed, and overlapped to generate a groundwater vulnerability map as follows:

3.1.1.1. Depth (D)

The depth of groundwater is the vertical distance between the ground surface and the water level. This parameter determines the time required for water-soluble pollutants to penetrate from the ground to the aquifer. Thus, near-surface aquifers are likely to become contaminated faster than deeper aquifers (Chandoul et al., 2008). The th was directly measured by subtracting the water surface level from the top aquifer level. The depths vary between 5.0 m and 9.0 m. Depths of 7.0 m are the most represented, while depths of 5.0 m are the least, with less vulnerability observed regarding depth to water layer". The different ratings assigned to each interval are given in Table 9, and the map in Figure 5 shows the depths in the BUW during the monitoring period. From Figure 5, it can be observed that shallow aquifers occupy a very small percentage of the basin area and are confined to the upper part of the basin.

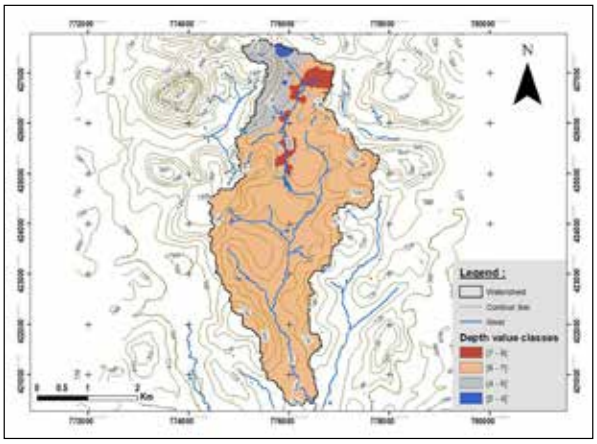

Figure 5. Mapping of depths to water table in the BUW.

3.1.1.2. Recharge (R)

According to Mansaray et al. (2015) then Nkembe & Defo (2022), three types of recharging mechanisms are generally defined. The variability of recharge estimation methods poses a significant challenge in choosing the most suitable one. Mansaray et al. (2015) then Nkembe & Defo (2022), demonstrated that the judicious choice of these methods should relate to a technique on a spatiotemporal scale, a range of values representative of the geological and hydrogeological conditions in the field, and the validity of the methods based on various techniques. The piezometric level fluctuation method enables quantification of effective infiltration in free water tables. It enables establishing a link between precipitation and variations in the piezometric level of the water table. The Water Table Fluctuation (WTF) method requires knowledge of the storage coefficient and the piezometric amplitude of the water table over time, which are deduced from the topographic level of each well. Recharge is estimated by the WTF method. Figure 6 shows the representation of recharge in the basin during the monitoring period. Over almost the entire study area, recharge ranged from 0.005 mm to 0.20 mm per day. Table 9 shows the ratings assigned for recharge using the DRASTIC method. Layers of precipitation, soil, and slope percentage were overlaid. According to DRASTIC ratings, the net groundwater recharge layer indicates medium to high vulnerability (Sarah, 2016). From Figure 6, it can be concluded that in this basin, the recharge values decrease from the upstream to the downstream of the main draining river.

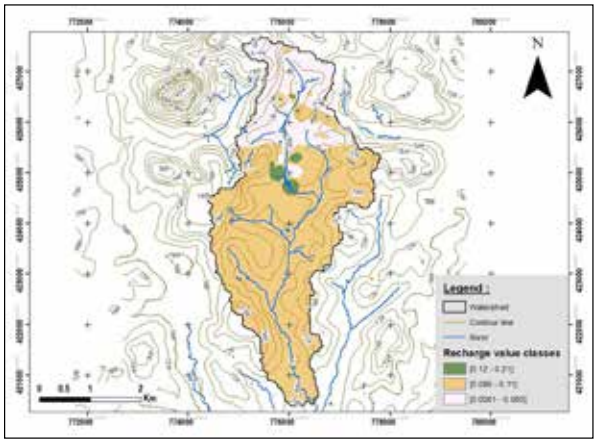

Figure 6. Mapping of the recharge variation in the BUW.

3.1.1.3. Aquifer media

The aquifer media reflects the characteristics of the constituents of the aquifer vadose zone that affect water flow within the aquifer and control pollutant attenuation processes (Chandoul et al., 2008). The BUW aquifer is essentially composed of granular elements derived from the alteration of the gneiss. The materials are, therefore, for the most part, a heterogeneous mixture of fine to coarse sand in equal proportions with the products of altered metamorphites. Figure 7 shows the distribution of materials in the aquifer, and Table 9 shows the corresponding rating.

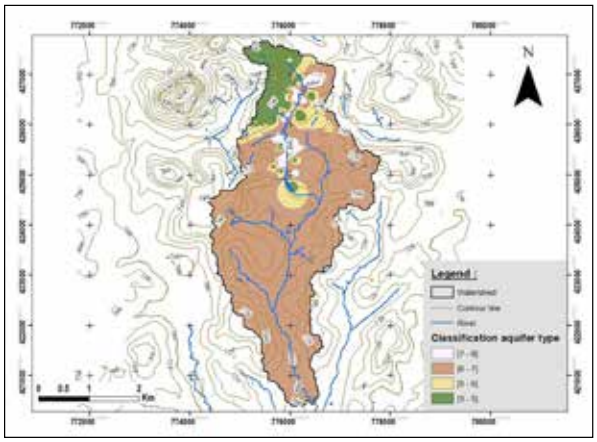

Figure 7. Mapping of the aquifer materials in the BUW.

3.1.1.3. Aquifer media

The aquifer media reflects the characteristics of the constituents of the aquifer vadose zone that affect water flow within the aquifer and control pollutant attenuation processes (Chandoul et al., 2008). The BUW aquifer is essentially composed of granular elements derived from the alteration of the gneiss. The materials are, therefore, for the most part, a heterogeneous mixture of fine to coarse sand in equal proportions with the products of altered metamorphites. Figure 7 shows the distribution of materials in the aquifer, and Table 9 shows the corresponding rating.

3.1.1.4. Soil type

Soil has a significant effect on the amount of recharge; therefore, it affects the ability of a pollutant to move vertically in the vadose zone. According to Aller et al. (1987) and Sarah (2016), fine-grained materials such as clay and silt reduce soil permeability and, thus, limit the movement of contaminants. The various soil formations have been estimated from Figure 8 and highlighted using the classification provided in Table 9 of the DRASTIC rating.

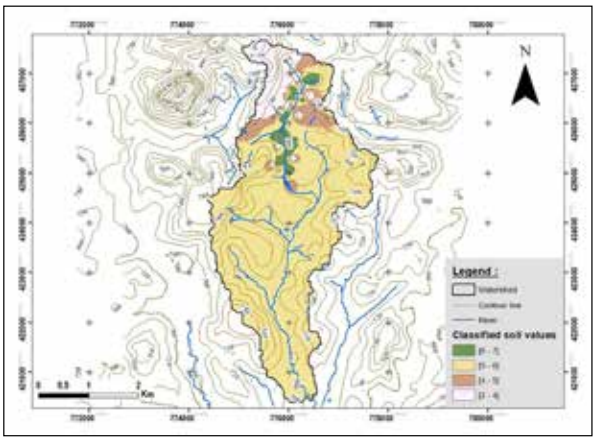

Figure 8. Mapping of the soil type in the BUW.

3.1.1.5. Topography

Although the BUW belongs to highly geomorphological units at altitudes of over 700 m, almost all the slopes are between 5 and 6% (Fig.9). Slopes in excess of 6% cover the North-West of the basin. There are only a few areas with slopes exceeding 10%. The land slope is a critical factor that determines the amount of surface runoff. As a result, low-slope areas tend to retain water for a longer period, leading to greater infiltration and, thus, a higher pollution potential (Moges and Dinka, 2012).

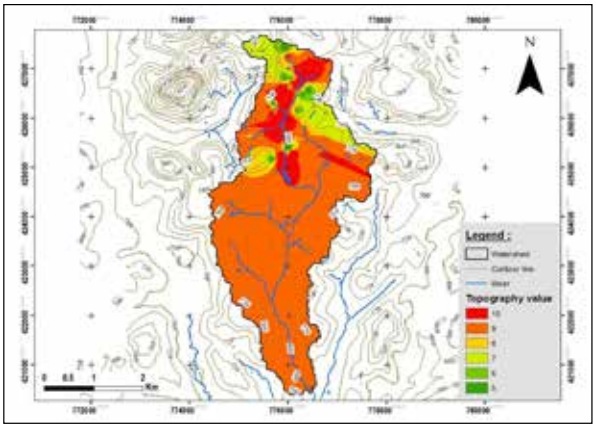

Figure 9. Mapping of the topography classes in the BUW.

3.1.1.6. Impact of the vadose zone

The vadose zone is composed of silty and clayey sands in almost equal proportions. It is made up of sands and clays in the South-West, East, Center to North, and North-West of the study area, and sands and silts from the center to the South-East and North-West of the basin. The sand-silt-clay combination is scattered in the northern part of the study area. According to Aller et al. (1987) and Sarah (2016), fine-grained materials such as clay and silt reduce soil permeability and, thus, limit the movement of contaminants. Figure 10 shows a cartographic representation of the vadose zone classes in the basin.

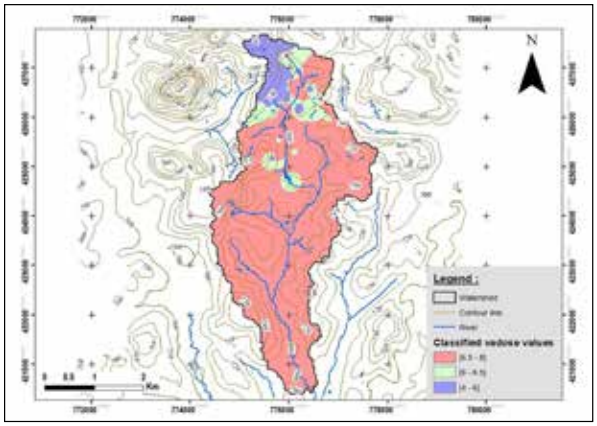

Figure 10. Mapping of the vadose zone classes in the BUW.

3.1.1.7. Hydraulic conductivity

This parameter plays an essential role in the rate of dispersal and migration of pollution (Chandoul et al., 2008). Higher hydraulic conductivity indicates greater infiltration and movement of water and contaminants into the aquifer, increasing the potential for pollution. The map in Figure 11 shows the conductivity classes recorded in the BUW.

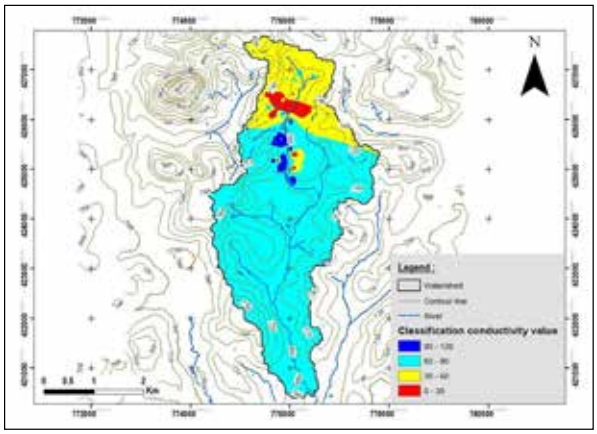

Figure 11. Mapping of the conductivity classes in the BUW.

3.1.1.8. Mapping of DRASTIC vulnerability areas

Calculation of the DRASTIC vulnerability indices gave values ranging from 70 to 159, with percentages of 23.5 and 66.99, respectively. These indices, calculated as a percentage, show the existence of three classes of vulnerability: low, medium, and high (Table 10). The high vulnerability class covers approximately 88% of the surface area of the BUW (Fig.12). The DRASTIC parameter weights are given in Table 10.

Table 10. Evaluation criteria of degree of vulnerability models.

Vulnerability	Method					
	DRASTIC		AHP-AHP		DRASTIC-AHP	
	Area		Area		Area	
	ha	(%)	ha	(%)	ha	(%)
Low	0.3	02	1.8	13	0.7	05
Medium	1.4	10	11.9	85	11.2	80
High	12.3	88	0.3	02	2.1	15

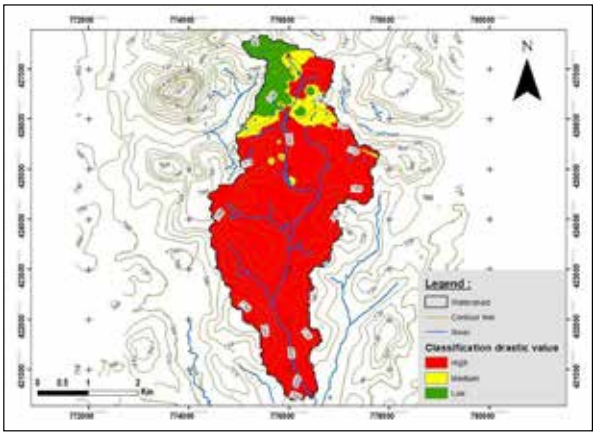

Figure 12. The DRASTIC model vulnerabilities classes map in the BUW.

3.1.2. AHP-AHP result

Figure 13 shows the vulnerability of the study area using the AHP-AHP method. As with previous methods, there are three classes of vulnerability. The medium vulnerability class covers approximately 70% of the basin's total surface area. The low- and high-vulnerability classes cover the rest of the area.

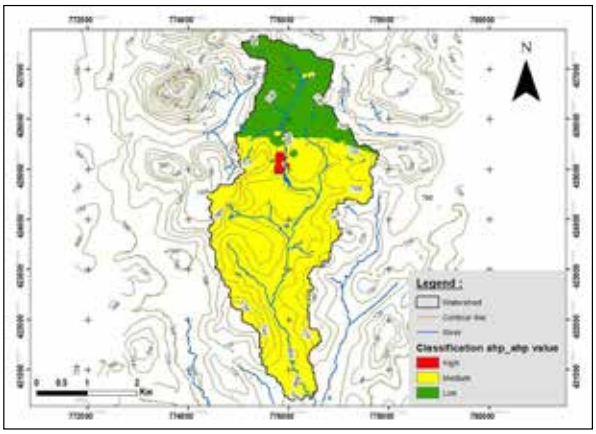

Figure 13. The AHP-AHP model vulnerabilities classes map in the BUW.

3.1.3. DRASTIC-AHP result

Figure 14 shows the vulnerability situation obtained using the DRASTIC-AHP method. It shows three classes of vulnerability, with the medium class predominating. The high and low classes occupy about 20% of the basin's surface area. According to this index, this aquifer has low vulnerability potential.

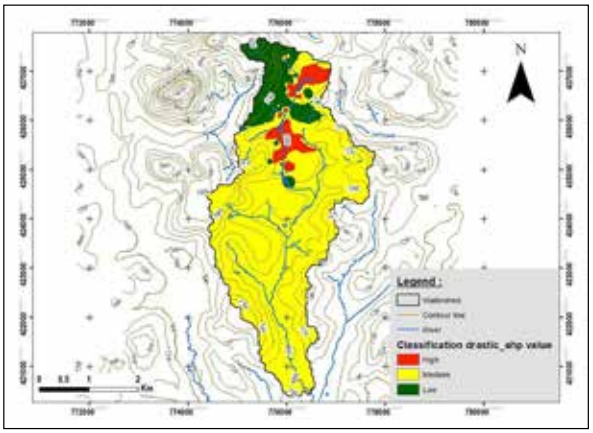

Figure 14. The DRASTIC-AHP method vulnerability classes map in the BUW.

3.2. Discussion

According to Mansaray et al. (2015), Sarah (2016), Nkembe & Defo (2022), and the rest of the city of Yaoundé, the BUW is essentially alluvial, made up of sand, silt, and clay. The sand particle size varies from 0.05 mm to 2.0 mm, the silt from 0.002 mm to 0.05 mm, and the clay fraction consists of a mixture of clay and sand. The relative proportions of sand, silt, and clay that make up this soil. Many soil properties are influenced by texture, including drainage, water holding capacity, aeration, susceptibility to erosion, organic matter content, cation exchange capacity, pH buffering capacity and soil thickness (Mansaray et al., 2015; Nkembe & Defo, 2022). According to the results, the category 0.04 to 4.1 m/day as hydraulic conductivity values, has the largest area. Therefore, the amount of hydraulic conductivity is low, and since the potential for vulnerability is directly related to this parameter, the amount of vulnerability is low. The geological structure of the sand of the aquifer media contains most of the region, which is graded eighth in the aquifer media ranking. A large percentage of the study area is composed of sandy loam texture, which according to the soil texture rankings, is ranked sixth and has a moderate vulnerability. The quantity of water that a given soil can store, mainly influenced by soil texture and organic matter content. In general, soils with particles of silt and clay have a greater capacity to retain water. Similarly, soils richer in organic matter have a greater water retention capacity (Moges and Dinka, 2012). Which leads to groundwater contamination in this basin due to poor drainage of runoff water (Moges and Dinka, 2012). The table 6 compares the different methods. Whatever the method, only three classes of vulnerability were detected. In the DRASTIC method, the vulnerability class dominates over the other two, whereas the average vulnerability class predominates in the AHP-AHP and DRASTIC-AHP methods, in almost equal proportions in the basin and for this study period. It can therefore be seen that the AHP-AHP and DRASTIC-AHP methods minimise the vulnerability of subsurface groundwater in this Biyeme upper stream basin compared with the DRASTIC derived method and are therefore the most suitable for decision-making in the context of groundwater protection in general and in this basin in particular. Some parameters were obtained indirectly and by interpolation, in particular recharge, conductivity and lithology, which may explain the discrepancies in the final results. According to the method used, the predominant classes of vulnerability are medium and high. The areas of very low vulnerability are located on the higher ground, where the soil profile is well developed with sufficient clay, low conductivity and low recharge. It should be noted that these maps are decision-making aids for the efficient management of groundwater resources. They can be used to establish resource protection areas.

4. Conclusions

Groundwater vulnerability assessments of the entire basin are found to be realistic and suitable for the area. However, despite its success in some case studies, the DRASTIC method has some disadvantages. The influence of regional characteristics (geology, hydrology, hydrogeology, land use etc.) is not accounted for in the method, so the same weights and rating values are used everywhere. This research paper also provides an overview of the vulnerability

of drinking water supply systems, which is quantified using a quantitative vulnerability assessment index. Groundwater resources, which account for 96% of the world's freshwater, are highly valuable because they are potable and require minimal treatment. However, this resource remains under-exploited in poor and developing countries. Given the complaints of people living in urban areas about untimely water cuts and water rationing, the management of water resources in these countries needs to be seriously questioned. To this end, strategies and policies have been put in place to address this problem, notably through the PAEPYS (Projet d'Alimentation en Eau Potable de la ville de Yaoundé à partir de la Sanaga). This project will eventually supply 315.000 m^3 of water per day to the urban and peri-urban populations of Yaounde city. Unfortunately, this project relies on surface water resources, yet underground resources also exist and could serve as a potential source of supply for the populations in situations where the CAMWATER water distribution network is absent or non-operational. This could help communities to become self-sufficient in terms of drinking water supply on a sustainable and, above all, permanent basis. For this reason, it should first be protected. Although it lies deep underground, this water is just as vulnerable as surface water. Potential sources of pollution have been identified. Household waste and poorly regulated septic tanks are the main sources of groundwater vulnerability in the BUW. The concentration of populations in medium-slope areas could explain why the high-vulnerability classes in these waters are present in medium- to low-slope areas. This mapping enabled three classes of vulnerability to be assessed: low, medium and high, based on the natural parameters of the aquifer. The "very high" class is absent, whatever the method. The DRASTIC method might be considered a helpful approach for qualitatively evaluating vulnerability to different sources of pollution and assisting planners and decision-makers in preserving groundwater resources in the BUW. According to this evaluation, the DRASTIC-AHP method has higher accuracy than the other methods, with 88% accuracy. For this reason, it can be concluded that the modified-DRASTIC-AHP method gave more valid and accurate results than other methods for the alluvial aquifer vulnerability assessments. The groundwater vulnerability maps for the BUW area are ideal for future land-use planning studies. Detailed and frequent groundwater quality monitoring in highly vulnerable areas should be performed to monitor changing levels of pollutants. In addition, local administrators should conduct education programs and awareness-raising activities for the farmers. However, other quantitative, process-based models are recommended for precise outcomes.

Nomenclature

BUW = Biyeme Upper Stream Watershed;

NASMPI = National Advanced School of Mines and Petroleum Industries;

PET = Potential Evapo Transpiration;

AHP = Analytic Hierarchical Process;

WTF = Water Table Fluctuation

CAMWATER = Cameroon water utilities.

Acknowledgments

The author is really grateful to the reviewers and editors for their stimulating and constructive suggestions.

Conflict of interest statement

The author declares that he has no known competing financial interests or personal relationships that could have influenced the work reported in this paper.

References

Alam, M., Rais, Aslam, S.M. (2012). Hydrochemical Investigation and Quality Assessment of Ground Water in Rural Areas of Delhi, India. Environmental Earth Sciences, 66, 97-110. https://doi.org/10.1007/s12665-011-1210.

Aller, L., Bonnet, T., Lehr, J., Petty, R. and Hackett, G. (1987). DRASTIC: a standardized system for evaluating groundwater pollution potential using hydrogeological settings. Report No 600/287/035, EPA, Washington, USA. J. Environ Protection Agency.

Arauzo, M. (2017). Vulnerability of groundwater resources to nitrate pollution: A simple and effective procedure for delimiting Nitrate Vulnerable Zones. Sci Total Environ; 575:799-812. doi:10.1016/j.scitotenv.2016.09.139.

Aydi, A. (2018). Evaluation of groundwater vulnerability to pollution using a GIS-based multi-criteria decision analysis. Groundw Sustain Dev. 7:204-11. doi:10.1016/j.gsd.2018.06.003.

Babiker, I.S., Mohamed, M.A.A., Hiyanna, T. and Kato, A. (2005). A GIS Based DRASTIC Model for Assessing Aquifer Vulnerability in Kakamigahara Heights, Gifu Prefecture, Central Japan. Science of the Total Environment, 345, 127-140. http://dx.doi.org/10.1016/j.scitotenv.2004.11.005.

Bissaya, R., Ghogomu, R.T., Akissebini, S.M. (2018). Geomorphological approach in active tectonics for the cartography of landslide and rock fall hazards in the North-West part of the region of Yaounde-Cameroon. The International Journal of Engineering and Science (IJES). Volume 7, 4 (2018) PP 73-96.

Chandoul, E.R., Trabelsi, N., Bouaziz, S. and Ben Dhia H. (2008). "Spatial Analyst" pour le calcul et la cartographie de la vulnérabilité des eaux souterraines à la pollution selon la méthode DRASTIC. Application sur la nappe phréatique de Gabès Nord, La conférence Francophone ESRI, Versailles.

Chi, Z., Yuntao, W., Li, Y. and Ding, W. (2017). Vulnerability Analysis of Urban Drainage Systems: Tree vs. Loop Networks Sustainability, 9, 397.

Costa, C.W., Lorandi, R., Lollo, J.A., Santos, V.S. (2019). Potential for aquifer contamination of anthropogenic activity in the recharge area of the Guarani Aquifer System, southeast of Brazil. Groundwater for Sustainable Development. Vol. 8 p. 10–23. DOI 10.1016/j.gsd.2018.08.007.

Focazio, M.J. (2002). Assessing groundwater vulnerability to contamination: providing scientifically defensible information for decision makers (Vol. 1224). US Dept. of the Interior, US Geological Survey.

Fouépé, A., Ndam Ngoupayou, J.R., Riotte, J., Takem, J.E., Mafany, G., Maréchel, J.C., Ekodeck, G.E. (2011). Estimation of groundwater recharge of shallow aquifer on humid environment in Yaounde, Cameroon using hybrid water-fluctuation and hydrochemistry methods. Environ Earth Sci 64: 107–118 doi 10.1007/s12665-010-0822-x.

Gangadharan, R, Nila Rekha, P., Vinoth, S. (2016). Assessment of groundwater vulnerability mapping using AHP method in coastal watershed of shrimp farming area. Arab J Geosci 2:107

Ghazavi, R. and Ebrahimi Z. (2015). Assessing groundwater vulnerability to contamination in an arid environment using DRASTIC and GOD models. International Journal of Environmental Science and Technology, (12), 2909–2918.

https://doi.org/10.1007/s1376 2-015-0813-2.

Hazaymeh and Lange (2024). A review on water quality aspects of urban rainwater harvesting in Jordan/ JJEES 15 (3): 199-207.

Jhariya, D.C., Kumar, T., Pandey, H.K., Kumar, S., Kumar, D., Gautam, A., Baghel, V. and Kishore, N. (2019). Assessment of Groundwater Vulnerability to Pollution by Modified DRASTIC Model and Analytic Hierarchy Process. Environmental Earth Sciences, 78, 610. https://doi.org/10.1007/s12665-019-8608-2.

Kargaranbafghi, F., Kheirandish Ravari, M., Rahimi Shahid, M. (2020). Seismic hazard analysis of Zarand city using AHP-GIS. Italian Journal of Engineering Geology and Environment 1: 5-16.

Khosravi, K., Sartaj, M., Tasai, F., Singh, V., Kazakis, N., Melesse A. (2018). A comparison study of DRASTIC methods with various objective methods for groundwater vulnerability assessment. Sci Total Environ. 642 : 1032-49. doi:10.1016/j.scitotenv.2018.06.130.

Kringel, R., Rechenburg, A., Kuitcha, D., Fouépé, A., Bellenberg, S., Kengne, I.M., Fomo MA. (2016). Mass balance of nitrogen and potassium in urban groundwater in Central Africa, Yaounde/Cameroon. Science of the Total Environment 547, 382–395 http://dx.doi.org/10.1016/j.scitotenv.12.090.

Kumar, P., Bansod, B.K.S., Debnath, S.K., Thakur, P.K., Ghanshyam, C. (2015). Index-based groundwater vulnerability mapping models using hydrogeological settings: a critical evaluation Environmental impact assessment review, 2015 51 38.

La Vigna F. (2022). Urban groundwater issues and resource management, and their roles in the resilience of cities Hydrogeology Journal https://doi.org/10.1007/s10040-022-02517-1.

Lerner, D.N. (2004). ”””””””””””””Urban groundwater pollution. International contributions to hydrogeology IAH”” ”””””””””””, 24. A. A. Publ., 277 pp.

Magha, A., Awah, M., Nono, G., Tamfuh, P., Wotchoko, P., Adoh, M. and Kabeyene, V. (2021). Assessment of Groundwater Quality for Domestic and Irrigation Purposes in Northern Bamenda (Cameroon). Journal of Water Resource and Protection, 13, 1-19. doi: 10.4236/jwarp.2021.131001.

Mansaray, A., Gogra, A. and Massaquoi A. (2015). The Recharge Potential of Groundwater in the Mokonde Community in Southern Sierra Leone. Natural Resources, 6, 543-552. doi: 10.4236/nr.2015.611052.

Moges, S.S. and Dinka, M.O. (2012). Assessment of groundwater vulnerability mapping methods for sustainable water resource management: An overview. Journal of Water and Land Development DOI: 10.24425/jwld.140389, No. 52 (I–III): 186–198.

Neshat, A., Pradhan, B., Pirasteh S., Shafri, HZM (2014a). Estimating groundwater vulnerability to pollution using a modified DRASTIC model in the Kerman agricultural area, Iran. Environ Earth Sci 71(7):3119–3131.

Ntep, F., Tabue Youmbi, J.G., Feumba, R., Ewodo Mboudou, G., Ngos III, S. (2021). Analyse piézométrique et suivi de la pollution des ressources en eau des aquifères de subsurface du Bassin Versant Amont de la Biyeme (BVAB) Yaoundé Cameroun. Afrique SCIENCE, 18, 6, 132 – 149 pp.

Nkembe, S.E., Defo, C. (2022). Assessment of piezometric distribution and vulnerability of groundwater to pollution in a tropical environment: the case study of the aquifer of Santchou, Cameroon, Central Africa. Sustainable Water Resources Management, 8(2): 48. https://doi.org/10.1007/s40899-022-00605-4.

Oroji, B. (2018). Groundwater vulnerability assessment using GIS-based DRASTIC and GOD in the Asadabad plain. J. Mater. Environ. Sci., Volume 9, Issue 6, Page 1809-1816.

Saaty, T. (2001). Decision Making for Leaders: The Analytic Hierarchy Process for Decisions in a Complex World. RWS Publications, Pittsburg.

Sarah, W. (2016).”A Vulnerability Framework for Assessing the Risks to Water Supply Systems Under Climate Uncertainty in the Urban North eastern United States” Doctoral Dissertations. https://doi.org/10.7275/7872988.0.

Shrestha, S., Kafle, R. and Pandey V. (2017). Evaluation of index-overlay methods for groundwater vulnerability and risk assessment in Kathmandu Valley, Nepal. Sci Total Environ. 575:1-12. doi: 10.1016/j.scitotenv.2016.09.141.

Singh, P., Tiwari, A.K., Singh, P.K. (2015). Assessment of groundwater quality of Ranchi township area, Jharkhand, India by using water quality index method. Int J Chem Tech Res 7 (01): 73–79.

Velasquez, M. and Hester, P.T. (2013). An analysis of multi-criteria decision-making methods. International Journal of Operations Research. Vol. 10(2) p. 56–66.

المملكة الأردنية الهاشمية

صندوق دعم البحث العلمي

الجامعة الهاشمية

المجلة الأردنية
لعلوم الأرض والبيئة

JJEES

مجلة علمية عالمية محكمة

المجلد (١٧) العدد (٢)

http:// jjees.hu.edu.jo/

ISSN 1995-6681

المجلة الأردنية لعلوم الأرض والبيئة

مجلة علمية عالمية محكمة

المجلة الأردنية لعلوم الأرض والبيئة: مجلة علمية عالمية محكمة ومفهرسة ومصنفة، تصدر عن عمادة البحث العلمي في الجامعة الهاشمية وبدعم من صندوق البحث العلمي - وزارة التعليم العالي والبحث العلمي، الأردن.

ترسل البحوث إلكترونيا إلى البريد الإلكتروني التالي:

رئيس تحرير المجلة الأردنية لعلوم الأرض والبيئة

jjees@hu.edu.jo

لمزيد من المعلومات والأعداد السابقة يرجى زيارة موقع المجلة على شبكة الانترنت على الرابط التالي:

www.jjees.hu.edu.jo

المملكة الأردنية الهاشمية صندوق دعم البحث العلمي الجامعة الهاشمية

JJEES

المجلة الأردنية لعلوم الأرض والبيئة

المجلد (17) العدد (2)

مجلة علمية عالمية محكمة تصدر بدعم من صندوق دعم البحث العلمي

ISSN 1995-6681 jjees.hu.edu.jo حزيران 2026